UNIVERSIDAD NACIONAL DE COLOMBIA

Simulation of Nitrogen Injection as an Enhanced Recovery Method in a Tight Natural Fracture Sandstone Reservoir with Compositional Fluids

Carlos German Herrera Guevara

Universidad Nacional de Colombia
Petroleum Engineering Department
Medellín, Colombia
2016

Simulation of Nitrogen Injection as an Enhanced Recovery Method in a Tight Natural Fracture Sandstone Reservoir with Compositional Fluids

Carlos German Herrera Guevara

A Thesis submitted in partial fulfillment of the
requirements for the Degree of
Master of Science in Petroleum Engineer

Advisor:
Ph.D Juan Manuel Mejia Cardenas

Investigation line
Enhance Oil and Gas Recovery
Research Group
Flow & Transport Dynamics

Universidad Nacional de Colombia
Petroleum Engineering Department
Medellín, Colombia
2016

Con todo el amor a mi madre Gloria Herrera

y mis adorados abuelitos Nidia Guevara y Jaime Herrera

quienes poco a poco me enseñaron
a valorar y agradecer las pequeñas cosas de la vida.

El verdadero viaje de descubrimiento
no consiste en buscar nuevos caminos
sino en tener nuevos ojos. M. Proust

AKNOWLEDGEMENTS

The Advance Reservoir Engineering job requires integrating the knowledge of several disciplines; I was able to fulfill the objectives of this thesis with the generous help, advice and support of all Engineers and scientists mentioned below, and also with the love of my family which I am immensely grateful.

To my wife Angela Betancur for her continuous support and optimism that let me achieve this goal. To Ines Soto for creating the conditions that help me to optimize the project time.

I want to thank EQUION ENERGIA LIMITED and ECOPETROL S.A for providing access to data, information and computational resources that made this project possible. I am especially grateful to H. Aguirre for helping me improve every day my technical skills.

Thanks to the Senior EOR Reservoir Engineer Alonso Ocampo for his valuable and outstanding insights into the project scope and to the Senior Petroleum Engineer and EQUION's Subsurface Vice president Victor Castro for sharing his global view about the benefits that this project could bring to Colombia's Energy and sustainability Strategy.

I am highly grateful to EQUION's subsurface Technology Leader Fabio Tarazona for continuously promoting the studies that may change the future of our country.

I am highly grateful to my advisor Juan Manuel Mejia for his kind and gentle orientation in the simulation engineering work.

Thanks to Dr. Z. Gutierrez, the Geologist that made possible a geological modeling approach for Piedemonte fields as a natural fracture system. Thanks to J. Alzate and M. Martinez for their valuable comments which helped me find consistency within the data for the construction of the natural fracture model. I also want to thank R. Linares for sharing his view and understanding of the geological structures. All of them had a great and positive attitude towards sharing their knowledge to me. Thanks to the petrophysicist C. Moya for her valuable insights into the petrophysical uncertainty and to the continuous respectable technical challenge she posed to me.

I am also thankful to the Reservoir Engineers B. Perez, for his robust data analysis support; and to R. Gaviria for his advice in natural fracture reservoir simulation modeling and his clever guidance. Thanks to C. Lopez and J. Marin for their high quality insights into the geomechanical behavior of a natural fracture and the understanding of the critically stressed fractures, that were highly important to develop this work; and also for their unselfish personality.

I would like to thank R. Osorio from Ecopetrol for his valuable and wise comments about PDM fluid behavior. Special thanks to Amy Broome from Landmark for her outstanding professional and trustworthy support in the surface nitrogen facility set up. And Dr. J. Gilman for his generous thoughts related to the fracture porosity and fracture spacing.

CONTENTS

TABLE LIST

FIGURES LIST

NOMENCLATURE

Parameters

i	Pseudo-intensity of the critical Stressed Fractures	# fractures
I	Intensity of the critical Stressed Fractures	# fractures/ft
Pc	Capillary Pressure	psia
Sgt	Gas trap Saturation	%, or Fraction
N_2	Nitrogen	%, or Fraction
CO_2	Carbon dioxide	
μm	Micro meters	
λ	Pore throat size or inter-porosity coefficient	
e_0	Fracture Aperture (width)	
k	permeability	md
k air	Permeability to air	md
km	Matrix permeability	md
k_f	Effective Fracture permeability	md
$k_{f,in}$	Intrinsic fracture permeability	md
ϕ_m	Matrix porosity	%, or Fraction
ϕ_f	Fracture porosity	%, or Fraction
kr	Relative permeability	Fraction
krgo	Relative permeability of gas in the presence of oil	Fraction
krgw	Relative permeability of gas in the presence of water	Fraction
krwo	Relative permeability of water in the presence of oil	Fraction
krwg	Relative permeability of water in the presence of gas	Fraction
Swi	Initial water saturation	%, or Fraction
Sorw	Residual oil saturation during a water displacement process	%, or Fraction
Sorg	Residual oil saturation during a gas displacement process	%, or Fraction
Sorm	Residual oil saturation during a miscible displacement process	%, or Fraction
xi	Molar fraction of component i in the liquid phase	Fraction
yi	Molar fraction of component i in the vapor phase	Fraction
zi	Total molar fraction	Fraction
ρ	Fluid density	gr/cc
u	Volumetric velocity	
M	Commonly known as Molecular weight	

	but in Molecular Mass units
V_b	Bulk (total) volume
qmfi	Transfer Molar rate between the matrix (+ as for source) and the fracture (- as for sink)

Definitions

Sheet	Pauto Complex is formed by a series of initial un-communicated similar formations called sheets.
Compartment	Each sheet can have partially communicated sectors

Abbreviations

QOP	Oil Production Rate	stbd
QGP	Gas Production Rate	Mscfd
QGI	Gas Injection Rate	Mscfd
QWP	Water Production Rate	stbwd
COP	Cumulative Oil Production	Mstb
CGP	Cumulative Gas Production	MMscf
CWP	Cumulative Water Production	
HC	Hydrocarbon	
N2	Nitrogen	
CSLS	Cumulative Gas Sales	MMscf
SLSG	Gas Sales Rate	
PAVH	Average Pressure weight by HC PV	psia
PV	Pore Volume	
WCUT	Water Cut	Fraction
API	API Gravity	
BHP	Bottom Hole Pressure	psia
THP	Well Head Pressure	psia
GOR	Gas Oil Ratio	Scf/stb
Rs	Gas dissolved in oil at standard conditions.	Scf/stb
PDM	Piedemonte	
NRU	Nitrogen Rejection Unit	
NTG	Net to Gross	Fraction
ASU	Air Separation Unit	
FFM	Full Field Model	
DPDP	Dual Porosity/Dual Permeability Model (*Implicit* fracture Model)	
DFM or DFN	*Discrete* Fracture Model or *Discrete* Fracture Network	
SP	Single Porosity	
FRM	Floreña Mirador	
FRB	Floreña Barco	
FRG	Floreña Guadalupe	
EOR	Enhanced Oil Recovery	
EGR	Enhanced Gas Recovery	

MMP	Minimum Miscibility Pressure	psia
MDT	Refers to a reservoir pressure test from the MDT tool.	
M	Molecular Weight	lbm/ lbm mol
PLT	Production Logging Tool	
PBU	Pressure Build up	
PC	Critical Pressure	
PTA	Pressure Transient Analysis	
TVDss	True Vertical Depth sub sea	
TC	Cortical Temperature	
PVT	Pressure Volume Temperate	
VISCOM	Matrix Oil Viscosity	
VISCOF	Fracture Oil Viscosity	
DENOM	Matrix Oil Density	
DENOF	Fracture Oil Density	
ZC	Critical Compressibility	
SOM	Matrix Oil Saturation	Fraction
SGM	Matrix Gas Saturation	Fraction
SOF	Fracture Oil Saturation	Fraction
SGF	Fracture Gas Saturation	Fraction
EoS	Equation of State	
sp	single porosity	
dp	dual permeability	
UBI		
e.g.	It is the abbreviation for the Latin phrase exempli gratia (for example)	
m.a	It is the abbreviations for the Latin phrase Mega Annum, Absolute millions of years.	
χ	Excess Permeability	

Sub index

i	Component (pseudo-component) or x axes direction
d	Domain (m: matrix or f: fracture.
m	Matrix domain
f	Fracture domain
l	direction
o	oil
g	gas
w	water
ft	feet
in	inches
psi(a)	Pounds square inches (absolute)
cm	centimeters
kmts	kilometers
nm	nanometers
x	Refers to the matrix of fracture

SUMMARY

The main motivation for this work to me comes from the reservoir engineering challenge to understand the impact of nitrogen injection in the flow of compositional fluids that are in a natural fracture system at field level. Hopefully this project could be translated and incorporated for Colombia's energy supply and sustainability benefits, and bringing other important derived beneficial consequences like creating jobs opportunities.

Initially, the shape factor was considered to be constant throughout this work, but later this restriction was eliminated. A new contribution of this work was to propose and implement a simple methodology to construct a robust dual porosity/dual permeability reservoir simulation model based on the apparent aperture estimation at initial conditions. This was done to estimate the apertures when image logs or when other information are not available.

The aperture match is obtained by relating the excess permeability with the critical stressed fracture intensity, fracture porosities and shape factors, which also contribute to the understanding of the behavior of nitrogen injection into a compositional fluid in the matrix/fracture system. This study can be treated as a basic but solid step towards the understanding of fluid flow anisotropy created during the injection process in Pauto and Floreña fields with the aim to maximize the value of these assets.

The deductive philosophy approach (from the global concepts to the detail) rules the engineering problem solution proposed in this project. This work is divided in 3 main sections. Those steps (chapters) were considered essential to follow, in order to understand the impact of natural fractures within a tight matrix system for the flow of gas and oil, considering a compositional system under a nitrogen injection process.

- General Aspects of Pauto and Floreña Fields (**Chapter 1**).
- Model Description (**Chapter 2**).
- Nitrogen Injection (**Chapter 3**).

General Aspects of Pauto and Floreña Fields

This 1st Chapter describes the basics about the natural fracture system, the understanding and full integration of geology, petrophysics, fluids distribution and production mechanisms in the context of available information, conceptual models and correlations. This was done in order to fill the gaps where no information was available to understand and build the conceptual model of the natural fracture system of Piedemonte fields.

Thin section images, Image and Sonic Logs, Permeability from Basic Core Analysis compared with pressure transient analysis are indicators that suggest that Pauto and Floreña Fields are highly impacted in fluid flow due to the presence of natural fractures.
Three important findings are described as follows:

- A new theoretical graph using a simple correlation to estimate the fracture porosity and the spacing with different apertures was proposed and implemented. This was done by assuming a vertical well, the equation uses the number of fractures, the dip of the fractures and the thickness of the structure, see Section 1.6.2.2.

- Two small workflows to link the information are proposed: 1) to use the maximum information from the capillary pressure measurements (see Section 1.6.3) to estimate the conventional and unconventional fluid flow threshold 2) a quality control in the pressure transient analysis (see Section 1.6.5) to avoid possible misleading natural fracture interpretations was also proposed.

- Knudsen threshold of 0.1 suggests that the fluid flow in the tight matrix is conventional (Darcy flow) even if the permeabilities are below 0.1 md, see Section 1.6.3.2.

- Ways on how to link information like fracture intensity, fracture orientation; low tracer velocities among other (see Section 1.8) were shown. This information also helps to find correlations like excess permeability with the critical stressed fractures, see Figure 1-13.

Model Description

The 2nd Chapter describes the fundamental equations used to model a natural fracture system which helps to use the commercial software as a "gray box" tool, based on the conceptual model built in the 1st Chapter.

The model description section is composed of the physical and mathematical model details that show the strengths and limitations of the reservoir model, see Section 2.3, which is used in Chapter 3.

The Computational Model and the Full Field Model sections describe the construction of the dual porosity/dual permeability model using measured data (Chapter 1) and the history matching of a single porosity model and its conversion into a dual porosity/dual permeability model using the proposed workflow, see Section 2.8. The model description and workflow proposed in this Chapter were required to achieve the objectives of this study related to the nitrogen injection evaluation in a natural fracture system.

2 main important findings are presented:

- An easy and successful workflow theory and application to build a dual porosity/dual permeability reservoir model was developed and implemented. This workflow allows the estimation of shape factors that are consistent with the initial excess permeability and spacing. This was done by adjusting the apparent aperture (e_0) and fracture intensity (I) by knowing the matrix permeability, using Eq. 2-45 described in Section 2.8. The equation that links all the process is given by the following equation:

$$\chi = I \frac{k_{f,in}}{k_m} e_0 + 1$$

Generally the aperture is generated stochastically in geo-statistical models. The intension of the proposed approximation in this study is to tie all variables in order to keep consistency with the KH from logs and PBU (Pressure Build Ups), which is not achieved with the stochastic models (see Figure 2-19).

- Even with a very close match in production and pressure between the single porosity and dual porosity/dual permeability, 2 main differences in the modeling were observed: 1) a higher vertical condensate segregation generated in the fracture system compared with the single porosity system (see Figure 2-36 and Figure 2-39) and 2) a reduction in the mobility of the liquid drop out generated in the matrix (see Figure 2-37).

Nitrogen Injection

This 3rd chapter describes the impact of different uncertainty parameters. The Gas Trap Saturation and the vertical matrix permeability are the most important uncertainty variables that affect the condensate and gas flow through the porous media in these reservoirs when the re-cycling lean gas injection is replaced by nitrogen injection, see Figure 3-29.

Several conclusions are reported in Section 3.8. The 3 Main Numerical results selected show that:

- The maximum incremental gas sales are not due to N_2 overriding phenomena but due to a maximum injection limit that is achieved in the system (see Figure 3-11, Plot 2) which is 200 MMscfd of N_2 injection with 200 MMscfd of gas sales (see Figure 3-8 Case 7).

- Condensate Liquid losses generated by N_2 injection can be reduced by having a higher amount of CO_2 in the N_2 stream. The minimum condensate losses results with CO_2 injection as the oil production losses respect to the base case are ~4 MMstb in 10 years with a constant gas sales plateau (see Figure 3-44) which additionally gives the maximum incremental gas sales of 0.9 Tcf in 10 years.

- The vertical matrix permeability (kmV) is one of the most influential parameters that affect the results. When kmV is increased by a factor of 10 it generates a better sweep efficiency of the matrix system compared with the reference case, which results in an increase in the cumulative oil production of 16 MMstb in 10 years.

INTRODUCTION

Background

Pauto and Floreña fields have produced since 2001 and are characterized by having folded structures which have been generated due to compressive forces of tectonic plates. These fields have been identified as naturally fractured as the relation in fracture/matrix permeability is higher than 10 (see Figure 1-41).

Additional to the structural and petrophysical complexities, the hydrocarbon compositional behavior is also complex. For Pauto field, gas condensate is much more predominant; while in Floreña has volatile oil and gas condensate regions, see Section 1.7.

To produce these reservoirs, gas re-injection has been proved to be one of the most efficient methods to maximize the oil recovery **[16]**[1], but this option limits the access to gas resources due to the re-injection process, see Figure 1-56.

This work proposes the option to replace the re-injected gas by nitrogen in order to have access to these gas volumes. Injection of non-hydrocarbon fluids has been reported to have good results as an Enhanced Oil and Gas Recovery (EOR/EGR) in several fields like Catarell-Mexico **[9, 10]**, Jay-USA **[12]**, Habshan-Abu-Dhabi **[13, 14],** Anschutz Ranch-USA and the Rocky Mountains fields-USA **[1-7]**, generating significant benefits in total hydrocarbon recovery.

The proposed method of nitrogen injection in the Colombian eastern foothills is not a new idea by itself. Projects like this have been explored in laboratory tests, and have been taken up to some simulation degree in the past for Cupiagua Sur **[15],** Cusiana **[17]** and Cupiagua fields [**18**]. Its feasibility has been considered following generic screening criteria **[19]**, namely the type of formation, depth, reservoir pressure, porosity, permeability, API, reservoir temperature, oil viscosity, and oil saturation; however these applications have not been implemented due to gas market conditions and specially for the cost of effective technology available for the N_2 separation from the air (e.g Air Separation Units –ASU-) and from the hydrocarbons (e.g the Nitrogen Rejection Units Technologies – NRU-).

A disadvantage of N_2 injection is that it increases in the Minimum Miscibility Pressure (MMP) when combined with the condensate that already exists in the reservoir (see Figure 3-1), compared with the CO_2, methane or a lean gas that is re-injected. Despite this, some advantages of nitrogen injection for pressure support and sweep are: 1) readily available, being ~80% of the air the source, 2) much more economic compared with methane, lean gas and CO_2, 3) reduces considerably corrosion risk compared with CO_2, being N_2 an inert gas which highly simplifies surface management, making this injection option a very good candidate to be used in an EOR/EGR technique.

[1] Chapter 3 References.

Fracture apertures are a key element to build a natural fracture system as it affects the fracture porosity and permeability. Generally, the aperture can be estimated from micro-electric image logs when wells are drilled with water based muds, using sonic logs with oil base muds with still some limitation to estimate the apertures or in the laboratory. Those ideal cases to estimate apertures are not fully available for these fields.

Therefore, to the best of our knowledge, this work is the first published attempt that proposes and implements a methodology and equations to build a compositional and natural fracture full field simulation model to identify its impact in the nitrogen injection as an enhanced recovery method. Measured and interpreted data was used to link the flow capacity, critical stressed fracture intensity and orientation to build a dual porosity/dual permeability model with estimated apparent apertures resulting from the workflow proposed in this study.

Problem Description

In order to have access to hydrocarbon gas volumes in Pauto and Floreña fields with the minimum oil losses, one option is to replace the re-injected gas with nitrogen, as this element is abundant and relatively easy to access. One additional complexity that these reservoirs have is the role that natural fractures with a tight matrix play in the sweep efficiency at a micro level and in production at a macro level.

Hence, the proposal is to model a nitrogen injection flow using a compositional and dual porosity/dual permeability reservoir simulation model to allow a systematic study to understand how the total hydrocarbon recovery efficiency is affected by using nitrogen as an Enhanced Recovery method in Piedemonte fields.

In this way, the hypothesis is that it is possible to pose a mathematical model that allows the study of the physical mechanisms of pressure and displacement of nitrogen injection in a compositional and naturally fractured reservoir. Ultimately allow identifying the impact that the main matrix/fracture variables have in the total gas and oil recovery.

Objectives

The general and specific objectives of this work are described as follows:

- **General**

  To model the nitrogen injection process in a naturally fractured system to quantify the hydrocarbon recovery factor.

- **Specifics**

1. To develop the mathematical model for a compositional and naturally fractured system using a commercial tool.

2. To evaluate the impact of nitrogen injection rates in the recovery efficiency for the Piedemonte field using a reservoir simulation model.

3. To evaluate the impact that the main uncertainty variables in a dual porosity/dual permeability model have in the recovery efficiency of the nitrogen injection process for the Piedemonte field using a reservoir simulation model.

See Chapter 3 for the general objective. See Chapter 2 for the specific objective 1. See Section 3.6 for the specific objective 2 and Section 3.7 for the specific objective 3.

1. GENERAL ASPECTS OF PIEDEMONTE FIELDS

1.1 Introduction

The objective of this chapter is to present a general understanding of Pauto and Floreña fields in the context of their behavior as a natural fracture system in the presence of compositional fluids; this will build the foundations to build the conceptual and numerical natural fracture model.

Several factors coming from geological, petrophysical, geomechanical and reservoir engineering interpretations highlight the importance that natural fractures have on productivity and injectivity for Pauto and Floreña Fields. Basic parameters coming from previous information classifies Piedemonte fields as a Type 2 natural fracture system "in which matrix provides the essential storage capacity and the fractures provide the essential permeability" following Nelson and Gilman criteria **[1]**, where the excess permeability are in the order of 10.

Integration of reservoir management and engineering with geological, petrophysical and geomechanical interpretation is a key factor to understand the impact that natural fractures play on the fluid flow within the system. An effective combination of different data, information and knowledge coming from various disciplines is achieved by using, in an integrated way, seismic, micro-seismic, image logs, sonic logs, pressure transient analysis, cores, micro photography (to detect micro-fractures), capillary pressure, seismic structural interpretation, fluid losses during drilling, geo-statistical approaches, tracer analysis, and production-injection history understanding.

Also, the adequate use of correlations has been found to be useful to fill the gaps where data is not available, those correlations are:

- For Pauto and Floreña, fracture distribution observations suggest good correlation of decreasing the critical stressed fracture intensity with depth, see Figure 1-13.

- Capillary pressure curves were used to infer critical parameters that affect the fluid flow in the matrix, such as the relative permeability and maximum gas trap saturation, see Section 1.6.3 and Section 1.6.4.

1.2 Previous Studies

Fields Rio Chitamena, Cusiana, Cupiagua Sur, Cupiagua and Piedemonte (Pauto and Floreña) are located in the Colombian Eastern Cordillera foothills, inside Casanare area. The studies done for those fields will be used as reference to understand the differences and complexities compared to Pauto and Floreña. Some published references related to Pauto and Floreña fields are available in the geological **[2]** and petrophysical **[3, 4]** context, but little work has been published in terms of reservoir engineering **[5, 6]**. A summary of those works are:

In 2009, Linares **[2]** presented a way to understand the generation of Pauto and Floreña geological structures. It was based on different balanced cross sections related to the geological compartments combining 2D and 3D Seismic. This conceptual geological model was used to build the dynamic model in 2013, which is used in this work. It is also shown here that there is high uncertainty on the shape and size of those sheets (compartments) and reservoirs, due to poor resolution of seismic data.

Palencia et al. **[3, 4]** presented in 2012 a first approach to define a methodology that estimates petrophysical parameters and define the lower limit where the matrix contributes to the flow. For the porosity, they found that 75% of samples above 1.7% porosity de-saturate above 60 psi, and 25% samples that de-saturate were believed to be due to rock fabric and presence of micro-fractures; 70% of the samples above 2.5% porosity showed fluorescence and 60% of the wells shows production above 3% of porosity. For the permeability, it was sustained that the matrix contributes to the flow of wells even for permeabilities lower than 1 md which was corroborated by a correlation between the flow meters, resistivity logs and cores.

Jolly **[5]** in 2002 performed a gas (single phase) discrete fracture reservoir simulation modeling (DFM) for Barco Floreña. This model was used to match the PBU data using a spacing of 25 to 350 ft in the NW-SE direction and 10 to 140 ft in the NE-SW direction, with apertures of 0.1 cm and porosities of 1%. He highlights that the anisotropy that is created with the open fractures aligned to the maximum stress will have a high impact in the vertical permeability. He suggested to perform further investigations related to the spatial variability of the fractures, the physics of the gas condensate flow within the matrix and fracture, and the up-scaling of discrete fracture networks.

Ahmad **[6]** performed in 2013 a pressure build up history match using a 2D radial black oil and compositional reservoir simulation model for PDM using the matrix/fracture skin and rate dependent skin as regression variables. An equivalent natural fracture system with layers of 0.1 ft. (3.048 cm) thickness for the fracture system were used, with 4% porosity for the matrix and fracture, and 0.04 md for the matrix permeability and ~$1x10^3$ md for fracture permeability. It was found that relative permeability does not affect the well test match but have effects on the long term production.

1.3 Geology

1.3.1 Location

Piedemonte (PDM) fields (Pauto and Floreña) are located in the eastern Colombian foothills, in Casanare state. As areal scales are important in this work, Figure 1-1 shows a size comparison of PDM fields with Bogota Capital District, presented as a didactical way to compare the area scale of the fields.

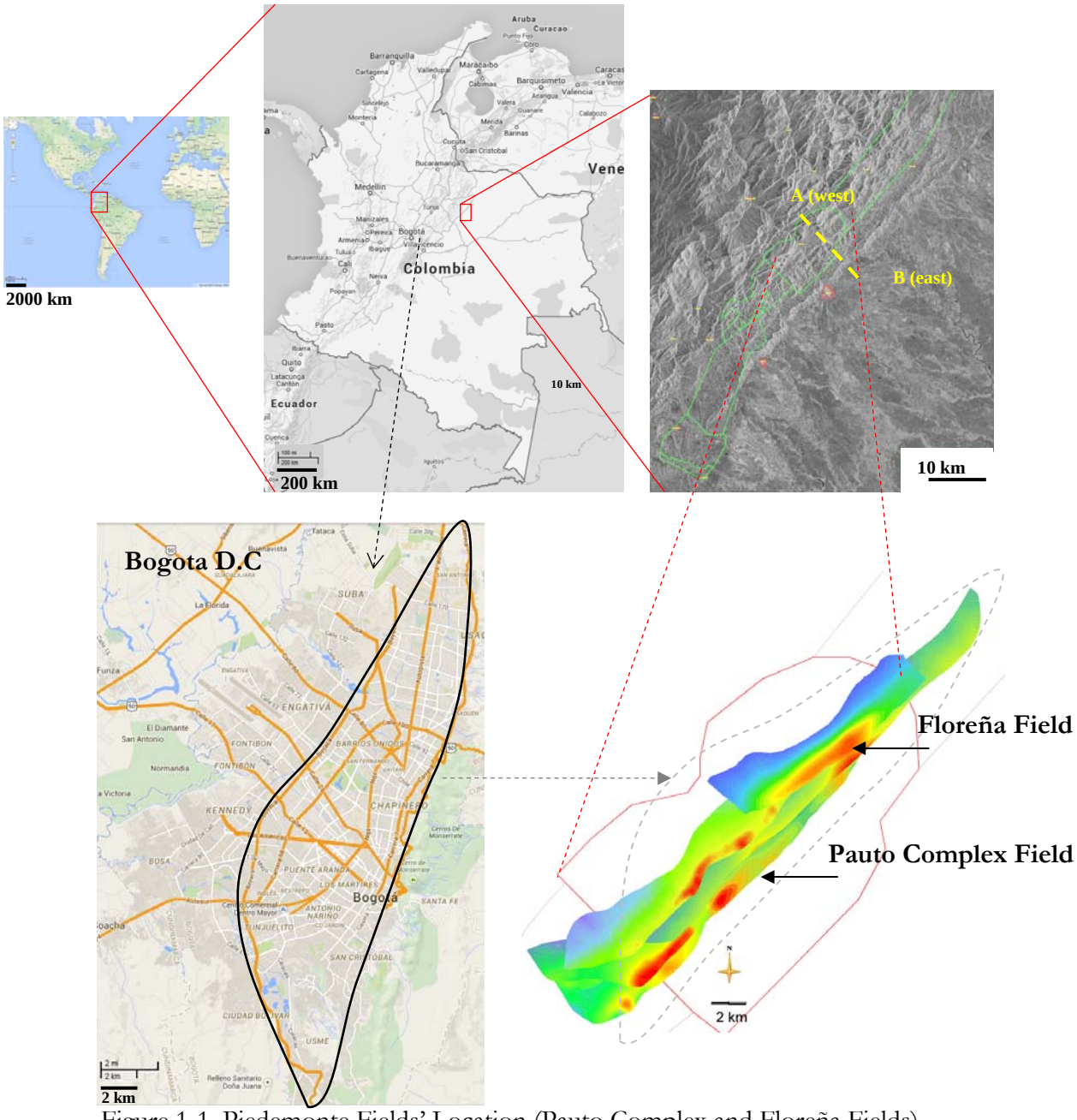

Figure 1-1. Piedemonte Fields' Location (Pauto Complex and Floreña Fields).

1.3.2 Structural Geology

Geological complexities in the subsurface are reflected in the geomorphology (e.g. mountains and rivers) of the sector, see Figure 1-2.

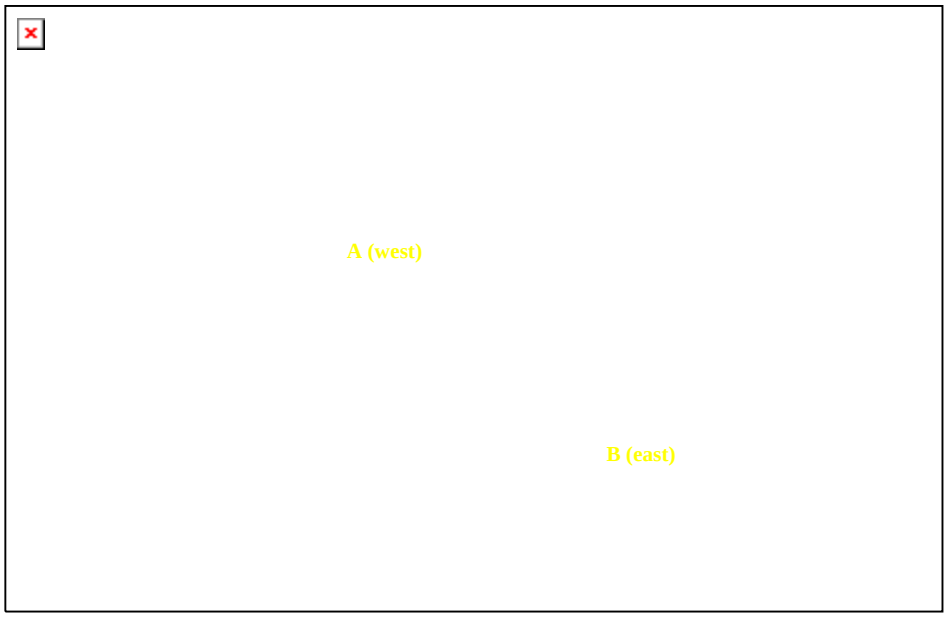

Figure 1-2. Pauto and Floreña Fields' Geomorphology - Google Earth Satellite Image.

In the context of this work, the location is relevant due to the impact that the main tectonic plates' compressions have on the reservoirs' formation, namely generated by the Nazca, Caribbean and South American continental plates **[8]**.

The geological evolution developed a folded structure composed of Cretaceous to present-day rocks. Those structures are limited to the west by the Guaicáramo fault and to the east by the Nuchía syncline. The historical evolution and deformation of these structures generate an uncertainty when the structural models of the fields are defined **[9]**. For that reason, several models have been created with time once new information of the field is available.

The Eastern Colombian Cordillera foothills have 3 deformation regions: one is Cusiana, the second is Cupiagua and the third one is comprised by the Piedemonte fields which are forethrust structures given by sheets (compartments) in a duplex arrangement (Volcanera, Pauto, and Floreña structures, see Figure 1-3).

- **Pauto:** The seismic reflections are noisy and with poor quality data (see Figure 1-3) due to the structural folding, faulting complexities and aspects like discontinuities, high dips, abrupt topography, and extensive overburden formations that affect several attributes that are required for a good seismic resolution and interpretation. Several other static (e.g logs) and dynamic (e.g PBU´s) information is used to define

structures, faults, fractures and many other important characteristics of reservoirs, including baffles[2], channels and contacts **[2]**.

- **Floreña:** This structure belongs to a folding fault asymmetric anticline related to a fault. The limits of Floreña are: on the top el Morro structure, below the Pauto structures, to the west the Guaicáramo Fault and Nuchía Fault to the east, see Figure 1-3.

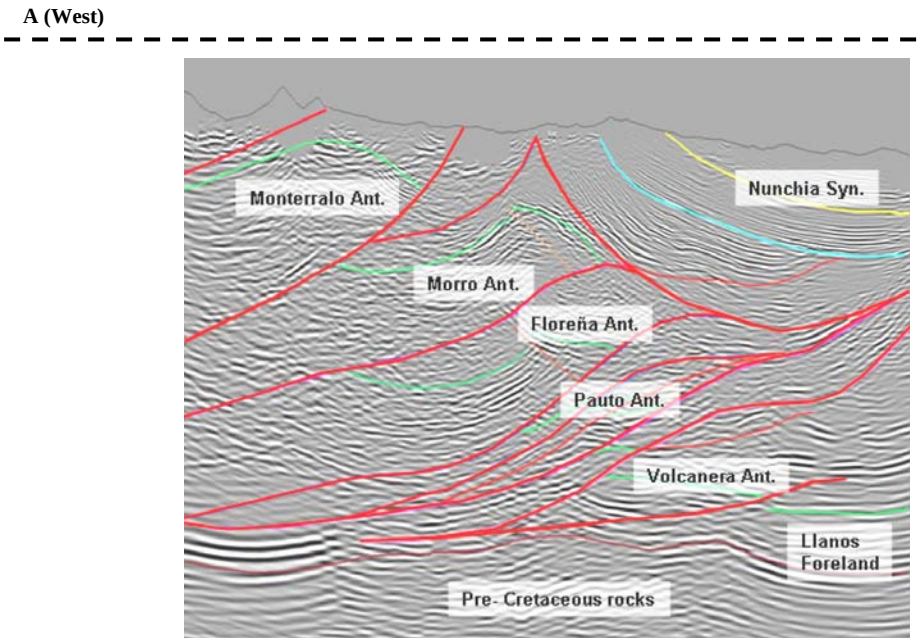

Figure 1-3. 3D Seismic – Pauto and Floreña X-Section (from Linares, 2009).

[2] Baffles: Portions of the reservoir with very low transmissibility, either because of a very low rock quality or its structure (e.g tear faults).

Figure 1-4 shows a 2D X-Section geological interpretation for Floreña and for Pauto Complex sheets **[2]**. Each color represents the formations that compose the fields.

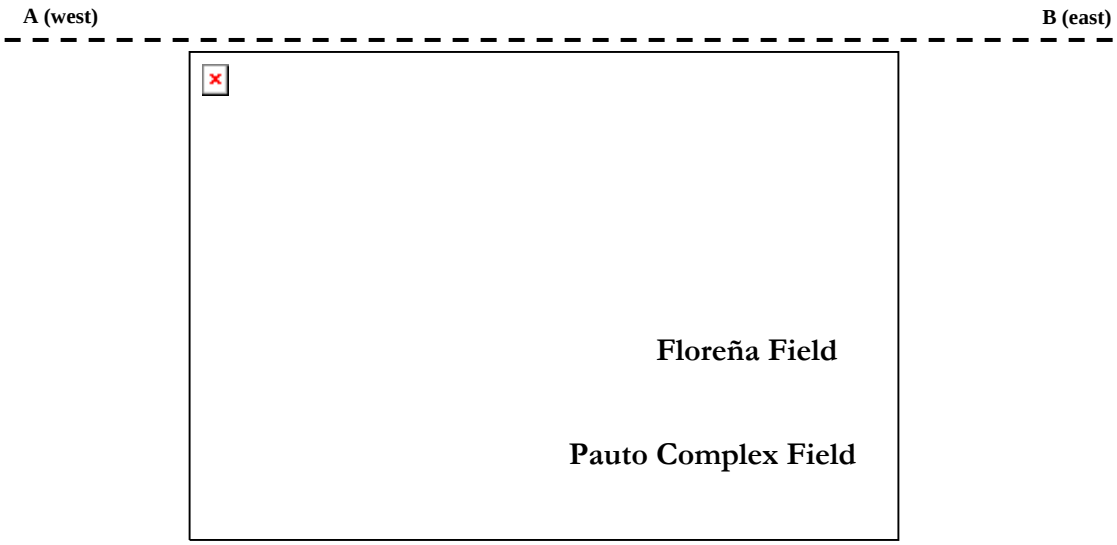

Figure 1-4. Structural Map Interpretation (from Linares, 2014).

Figure 1-5 shows a possible interpretation of Piedemonte structures made by Linares **[2]** at the end of 2014. Figure 1-5 shows structures that are long, quite narrow and aligned to the 45^0 axes in the SW-NE direction. In Figure 1-5 the top of the structure is highlighted in red

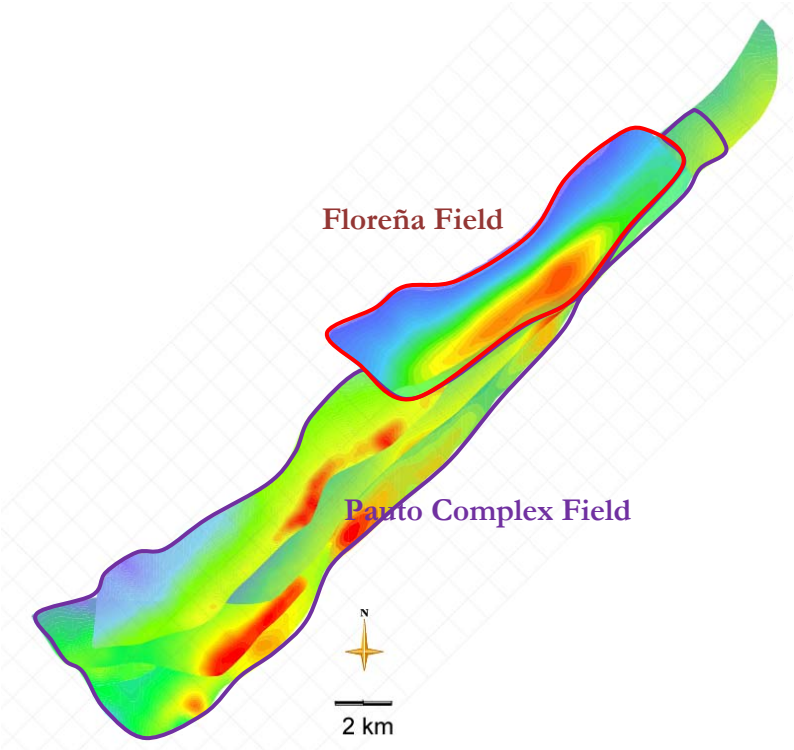

Figure 1-5. Pauto and Floreña Structures (from Linares, 2009).

Finally, Figure 1-6 shows a simple schematic[3] of the Piedemonte Pauto Complex sheets and Floreña reservoirs. This is done in order to show a simpler understanding of the sheets (compartments) and the target reservoirs.

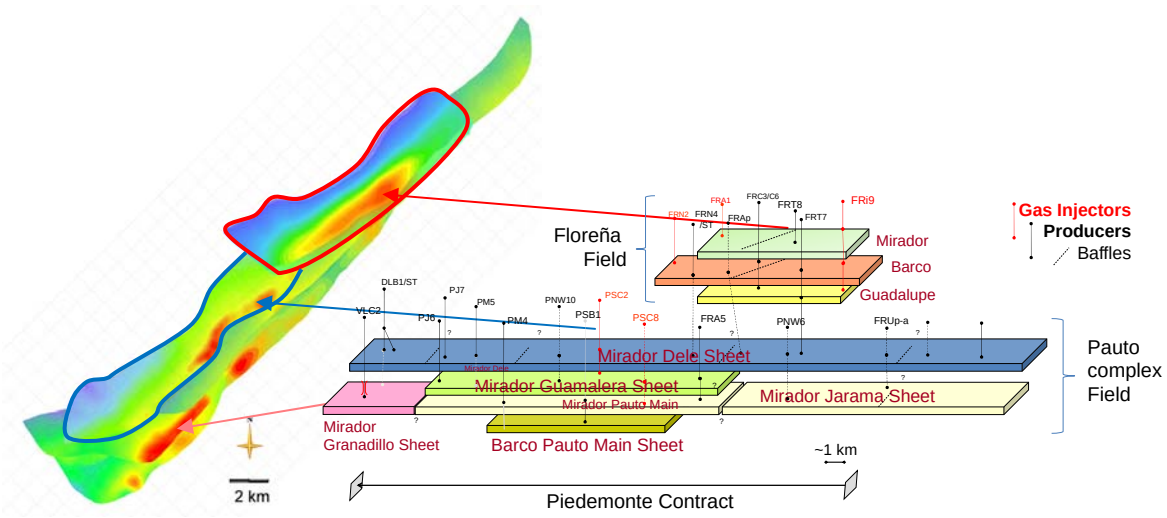

Figure 1-6. Schematic of Pauto Complex Sheets and Floreña Reservoir.

1.3.3 Stratigraphy and Depositional Environments

The stratigraphy in the Llanos Colombian Foothills has several units ranging from the Paleozoic, Cretaceous and Tertiary ages, separated by discordances **[2]** (see Figure 1-7[4]).

The main reservoirs are, from top to bottom, Mirador, Barco and Guadalupe Formations. As source rocks we have Gachetá, Guadalupe Mudstone and Los Cuervos Formations. Even C8 unit from Carbonera Formation, which is the principal seal rock in the area, could be a source rock.

[3] Map created by F. Osorio and I. Castiblanco April 2014.
[4] Stratigraphy column source: R. Linares [2].

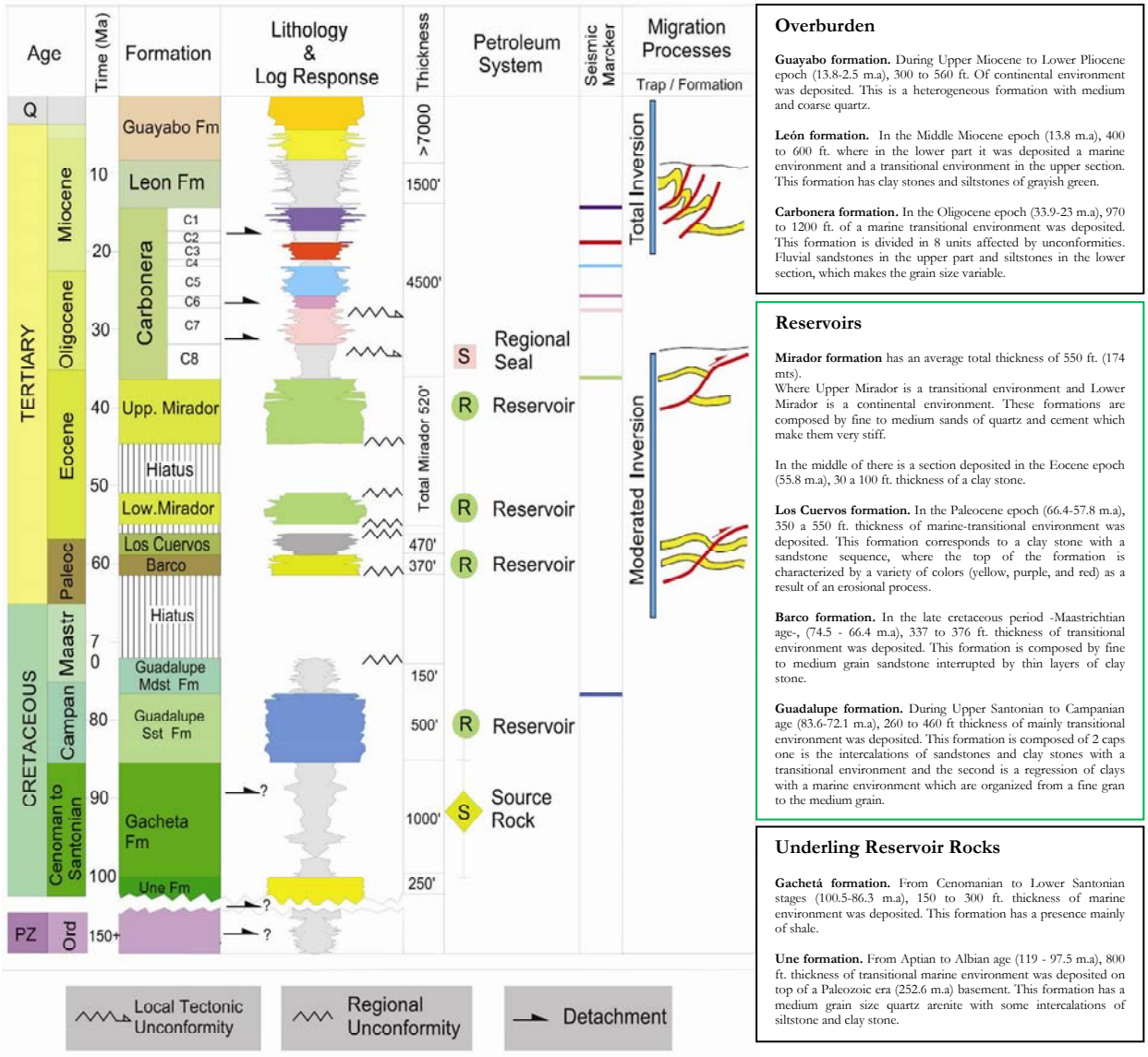

Overburden

Guayabo formation. During Upper Miocene to Lower Pliocene epoch (13.8-2.5 m.a), 300 to 560 ft. Of continental environment was deposited. This is a heterogeneous formation with medium and coarse quartz.

León formation. In the Middle Miocene epoch (13.8 m.a), 400 to 600 ft. where in the lower part it was deposited a marine environment and a transitional environment in the upper section. This formation has clay stones and siltstones of grayish green.

Carbonera formation. In the Oligocene epoch (33.9-23 m.a), 970 to 1200 ft. of a marine transitional environment was deposited. This formation is divided in 8 units affected by unconformities. Fluvial sandstones in the upper part and siltstones in the lower section, which makes the grain size variable.

Reservoirs

Mirador formation has an average total thickness of 550 ft. (174 mts).
Where Upper Mirador is a transitional environment and Lower Mirador is a continental environment. These formations are composed by fine to medium sands of quartz and cement which make them very stiff.

In the middle of there is a section deposited in the Eocene epoch (55.8 m.a), 30 a 100 ft. thickness of a clay stone.

Los Cuervos formation. In the Paleocene epoch (66.4-57.8 m.a), 350 a 550 ft. thickness of marine-transitional environment was deposited. This formation corresponds to a clay stone with a sandstone sequence, where the top of the formation is characterized by a variety of colors (yellow, purple, and red) as a result of an erosional process.

Barco formation. In the late cretaceous period -Maastrichtian age-, (74.5 - 66.4 m.a), 337 to 376 ft. thickness of transitional environment was deposited. This formation is composed by fine to medium grain sandstone interrupted by thin layers of clay stone.

Guadalupe formation. During Upper Santonian to Campanian age (83.6-72.1 m.a), 260 to 460 ft thickness of mainly transitional environment was deposited. This formation is composed of 2 caps one is the intercalations of sandstones and clay stones with a transitional environment and the second is a regression of clays with a marine environment which are organized from a fine gran to the medium grain.

Underling Reservoir Rocks

Gachetá formation. From Cenomanian to Lower Santonian stages (100.5-86.3 m.a), 150 to 300 ft. thickness of marine environment was deposited. This formation has a presence mainly of shale.

Une formation. From Aptian to Albian age (119 - 97.5 m.a), 800 ft. thickness of transitional marine environment was deposited on top of a Paleozoic era (252.6 m.a) basement. This formation has a medium grain size quartz arenite with some intercalations of siltstone and clay stone.

Figure 1-7. General Stratigraphy (from Linares, 2009).

1.3.4 Lithology

The estimated matrix and fracture porosities for Mirador and Barco formations from petrology analysis **[10]** are presented in this section.

- **Mirador**

Mirador is mainly made of quartz (>95%) with small quantities of Chert in it, with heavy minerals and ductile materials.

There are 3 main components in the matrix: mono crystalline quartz grains makes up 88% and polycrystalline quartz grains 2%, and the rest in silica volume could be 9% of

siliceous cement; and ~1% of kaolinite acting in the cement, which increases with the amount of fine quartz grains.

Figure 1-8 shows the fracture porosities from petrographic analysis which has values of 0.34%, 0.36%, 0.4%, 0.7%, 1% and 1.1% at ambient conditions.

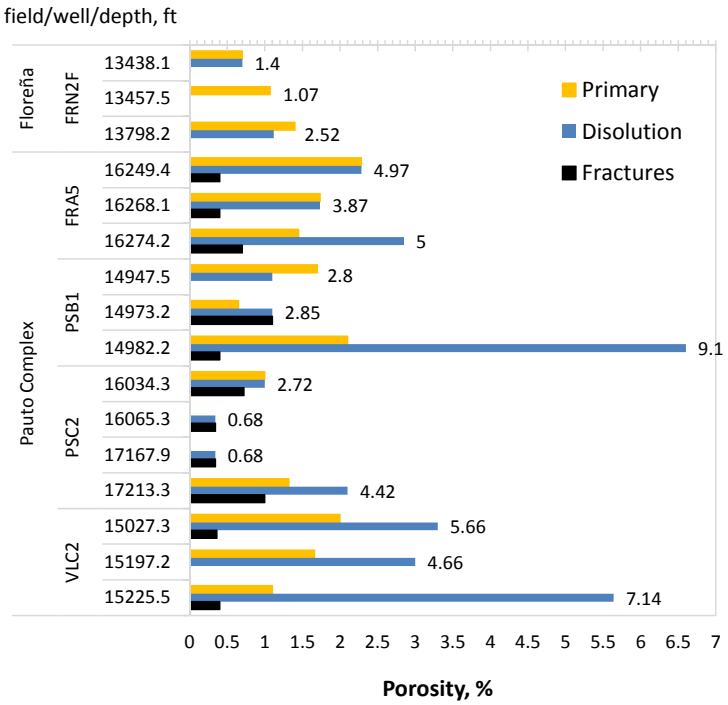

Figure 1-8. Mirador Porosity Types from Petrographic Analysis (from Mesa, 2002).

Figure 1-9 shows a thin section from Mirador formation where the following observations can be made:

- **Mirador matrix porosity range is 0.68% – 9.1%[5],** generated by 3 factors: primary pores, kaolinite dissolution and **micro-fractures porosities which are between 0.3% and 1%.**

- Different fracture types are observed: perpendicular and parallel to the bedding planes, and inclined fractures related to shear zones (see Plot D).

- Figure B. In the stylolite fractures, it is quite common the presence of TAR obstructing the fracture space. This happens because these fractures occurred during burial compaction, and presumably happened previous to hydrocarbon expulsion or migration processes (so this does not contribute to effective porosity).

[5] Notice that the porosity obtained by this method, is at ambient conditions and is done in 2D so, some linear assumptions are made to estimate the porosity.

Figure A
ϕ Total: 7.14%
(→) 0.36% *perpendicular* fractures to the bedding plane.

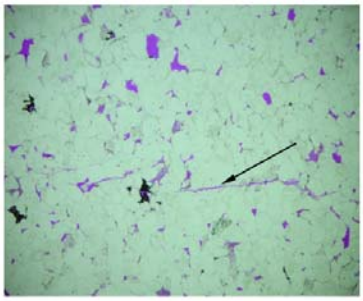

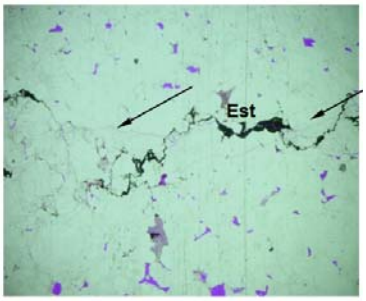

Figure B
ϕ Total: 2.74%
(→) 0.68% *parallel* fractures associated to stylolite (Est).

Figure C
ϕ Total: 2.81%
(→) 1.068% *parallel* fractures to the bedding plane.

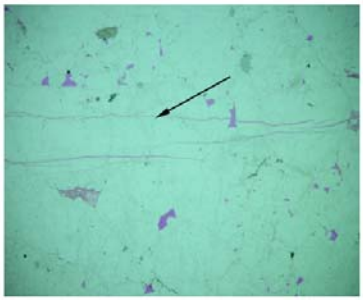

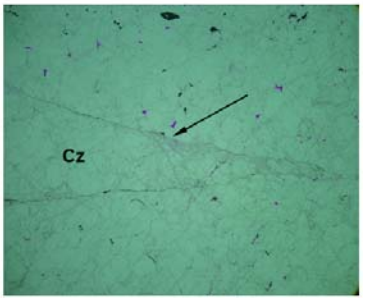

Figure D
ϕ Total: 0.68%
2 *inclined* micro-fractures related to a shear zone.

Figure 1-9. Pauto Mirador Thin Sections - Micro-fractures Types (from Mesa, 2002).

- **Barco**

Barco is mainly made up of quartz grain with very small proportions of Chert, heavy minerals and ductile materials in Floreña and Pauto fields.

There are 2 main components of the matrix: mono crystalline and Polycrystalline grains of quartz with 10 to 15% in volume of siliceous cement; and ~3.72% of kaolinite acting as cement, which increases with the amount of fine quartz grains.

Barco has better porosity values (~1.38 – 6.08%) than Mirador, with porosity generation from dissolution (see Figure 1-12).

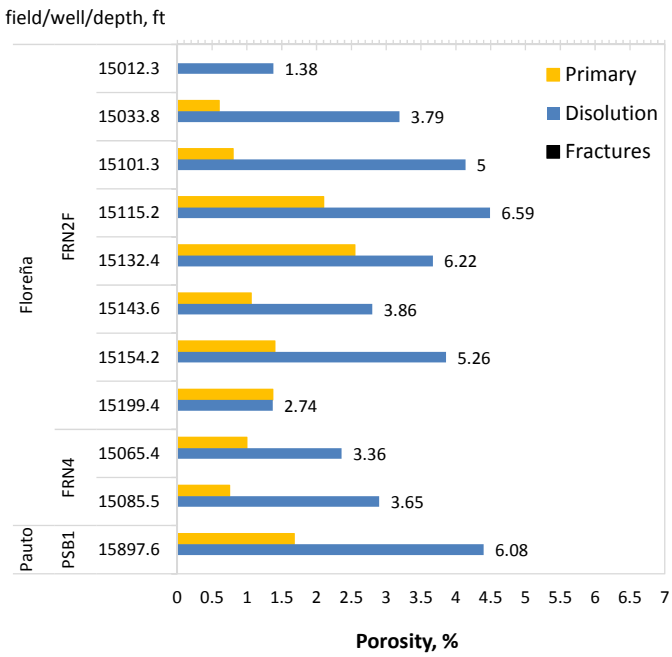

Figure 1-10. Barco Porosity Types (from Mesa, 2002).

1.3.5 Fracture Characteristics

The fracture systems have 5 main characteristics, those are: intensity, spacing, orientation, length and aperture (width).

1.3.5.1 Intensity

Fracture intensity[6] could be gathered by using two criteria. One is the identification of fractures using image logging[7] (see blue and black dots in Figure 1-14), and the second is by selecting which of those fractures have a high probability to contribute to the flow (critical stress fracture theory **[11, 12, 13]**, see red dots Figure 1-11).

For the purpose of fluid flow and modeling, the second criterion was used in this evaluation. The Barton, et al method **[11]** is used to estimate the critically stressed shear fractures for the wells that have available Sonic and Dip measurements. This method consists in using the Mohr-Coulomb failure criteria to detect the fractures that have a high probability to contribute to the flow (see Plot A in Figure 1-11).

Marin and Lopez **[12]** did this work to identify the probable critically stressed fractures that contribute to the flow. The models uses the initial reservoir pressure as reference with sensitivities to the friction coefficient from 0.52 to 0.6.

[6] By definition, fracture intensity is measured in the vertical direction while the fracture density is estimated volumetrically.
[7] Image logs have different resolution depending on the physical attribute used to determine the fractures. Most of the image logs which have been used to estimate the orientation and intensity of the fractures in these fields come from the UBI (Ultrasonic Borehole Images). It is possible that the UBI only register one portion of the total open fractures, meaning that there is an implicit uncertainty in the amount of open fractures determined by this methodology.

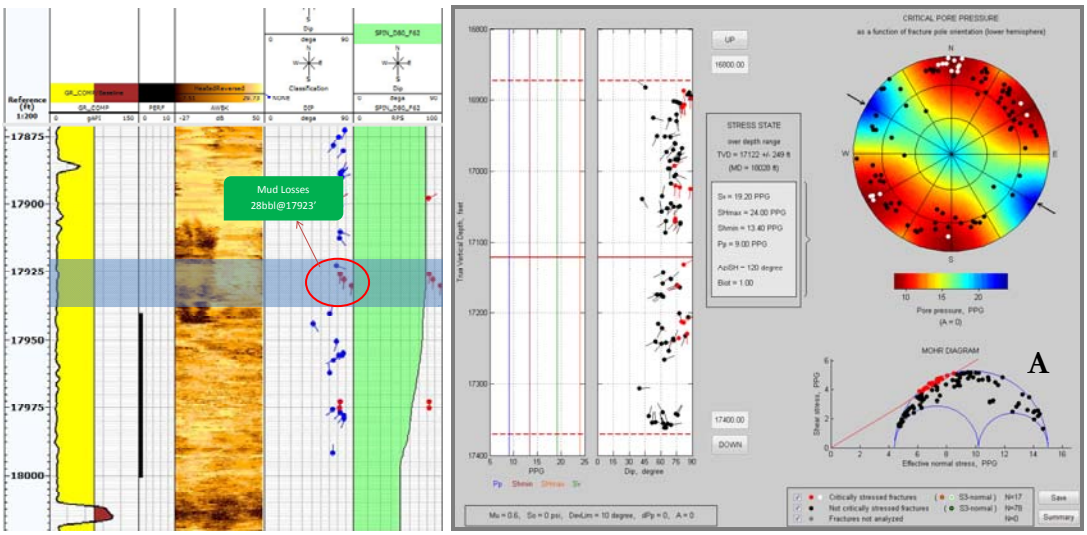

Figure 1-11. Example of Pauto Critically Stressed Fracture Well 1 Mirador Dele (from Lopez et al., 2014).

Figure 1-12 shows the total fractures measured for each well (see figure on top). Using the interpretation made by Lopez **[13]** it was selected the critically stressed fractures[8] (see bottom graph). It is observed that the critically stressed fractures that could contribute to the flow are between 5 to nearly 10 fractures per well (bottom graph) compared with the total average fractures per well of 100 (Figure on top), this means that only an average of 10% of the total observable fractures contributes to the flow.

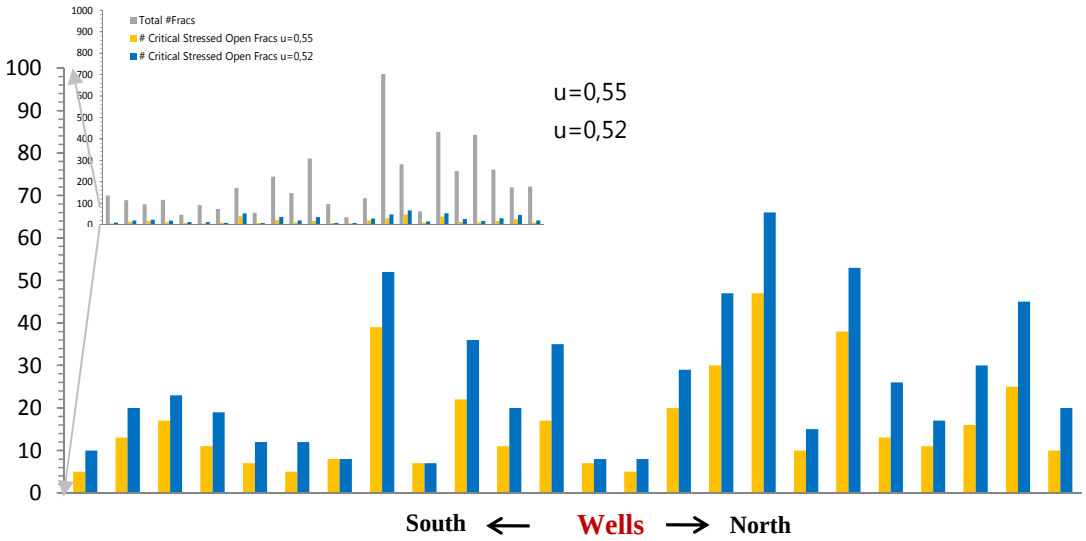

Figure 1-12. Fracture Intensity Interpretation Summary (from Lopez et al., 2015).

Figure 1-13 shows the relation between the KH obtained from pressure transient analysis (PBU) divided by the KH from logs, which is defined as the excess permeability (χ).

[8] This interpretation avoids the estimation of the fractures that will be included in the reservoir simulation model..

Figure 1-13 shows 3 plots on the top, those plots shows a trend of the fracture flow capacity, the number of critically stressed fractures and the excess permeability with depth.

From the reservoir engineering perspective, the impact of the formation units and structures presented in Figure 1-7 are translated into the understanding of the stresses/strain behavior and its impact on the rocks deposited in each of the periods. As each formation will have different thicknesses and ages (which impacts its brittleness and stiffness[9] – Lithological and mechanical drivers for fractures) and different deposition environments (which impacts the rock quality - lithological drivers for fractures). One hypothesis is that those parameters have direct implications in the naturally fractures observations (See Plot 2 in Figure 1-13).

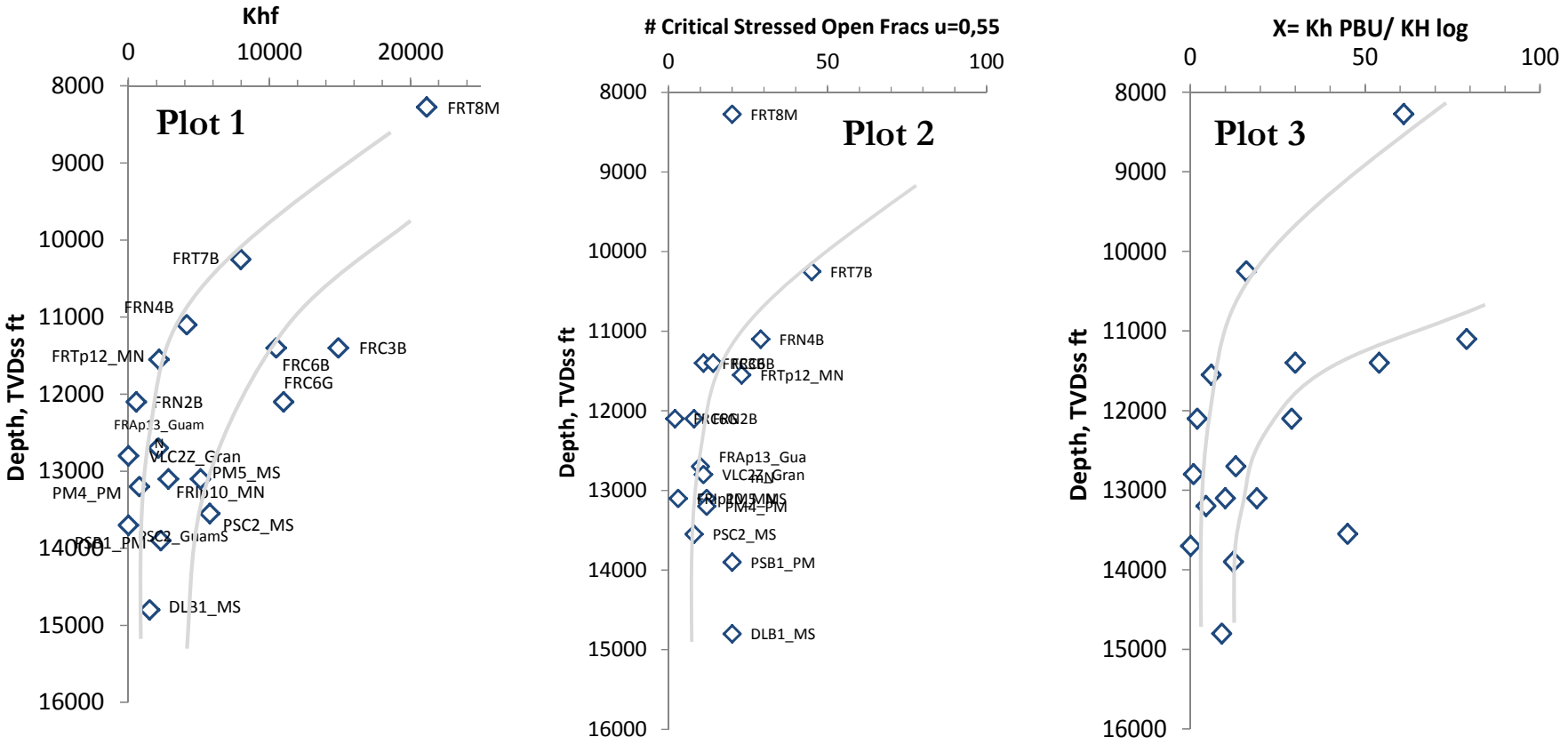

Figure 1-13. Correlation of Open Stressed Natural Fractures, Excess Permeability and Depth.

[9] As a reference, the young modulus is in the order of 1x10-6 psia (high stiffness) and the Poisson's ratio is in the order of 0.2 (low deformation), making the PDM sandstones brittle compared with shale.

1.3.5.2 Spacing

Spacing is the average separation between fractures of a unique family.

As reference Jolly **[5]** in 2002 used spacing from 25 to 350 ft in the NW-SE direction and 10 to 140 ft in the NE-SW direction for Barco reservoir simulation study.

The low Seismic resolution information of these fields makes the identification of fault spacing in the horizontal plane difficult which generates a high uncertainty in the structural driver. Figure 1-14 shows some interpretations that suggest spacing between 2 to 4 kms in a macro scale **[2]**.

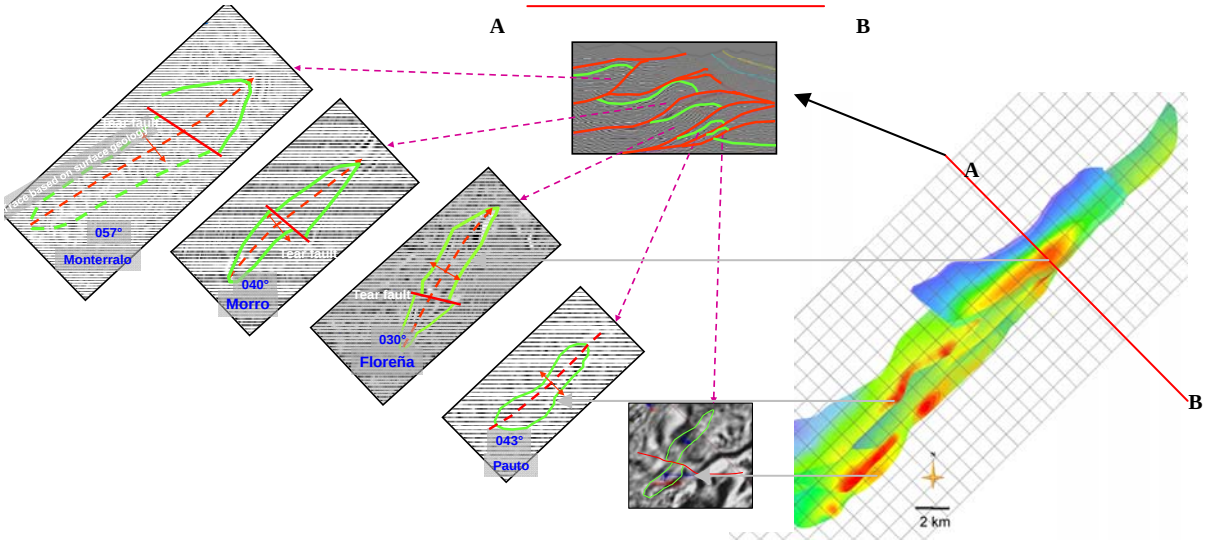

Figure 1-14. Horizontal Compartmentalization. Mega Fracture Spacing (from Linares, 2009).

Figure 1-15 is an aerial photograph of Mirador outcrop, analyzed by Gutierrez in 2015, which gives an initial estimation of fracture spacing between 100 to 300 m.

Figure 1-15 also shows a circle in solid line to represent a typical radius of investigation of 300 mts, obtained from PBU interpretations (see Figure 1-58).

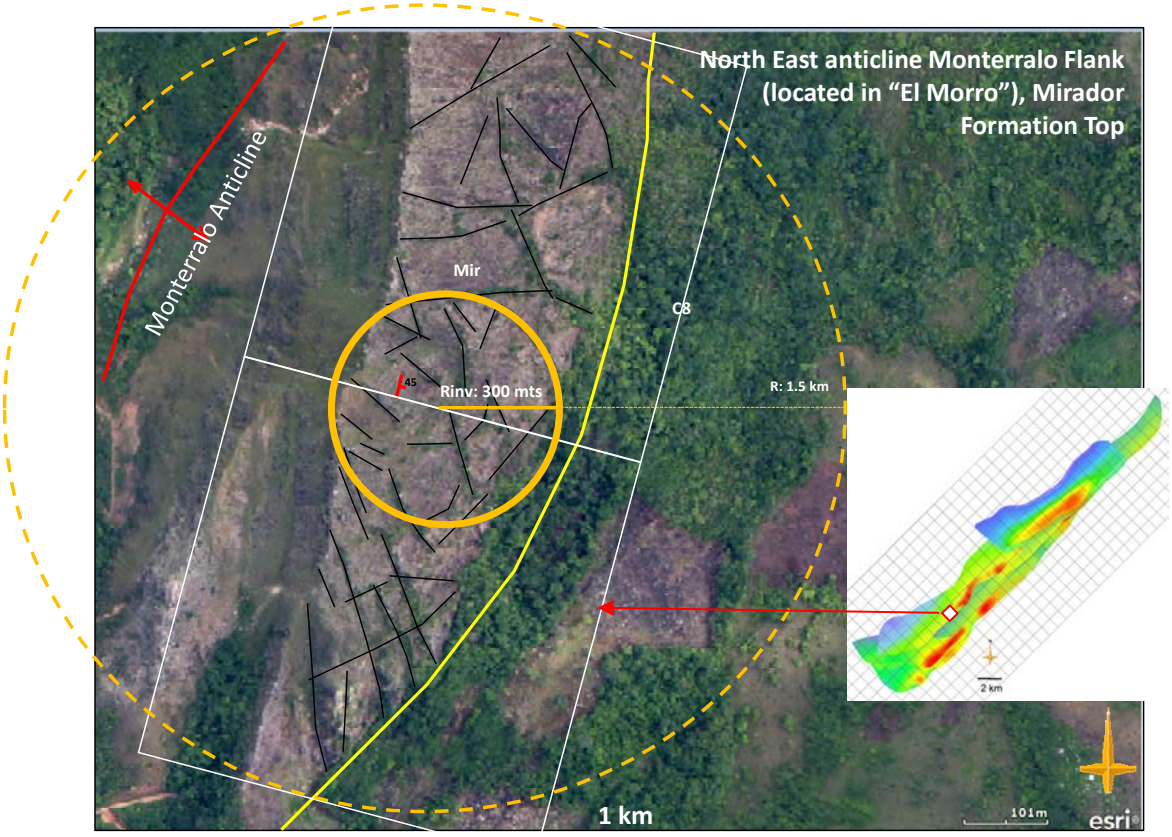

Figure 1-15. Aerial Photograph of Mirador Outcrop in Llanos foothills. Macro Fracture Spacing (from Gutierrez, 2015).

Continue increasing the resolution of the fracture spacing observations, the Figure 1-16 shows the fracture clusters. Also it shows the rose diagram color to highlight predominant direction of the fractures and the dip of the fractures. The red color in the rose diagram is for the fractures that are almost vertical (80^0).

Figure 1-16 shows a horizontal projection of some of the wells. The natural fractures clusters highlighted have range of spacing between them from 2 meters up to 30 m **[14]**.

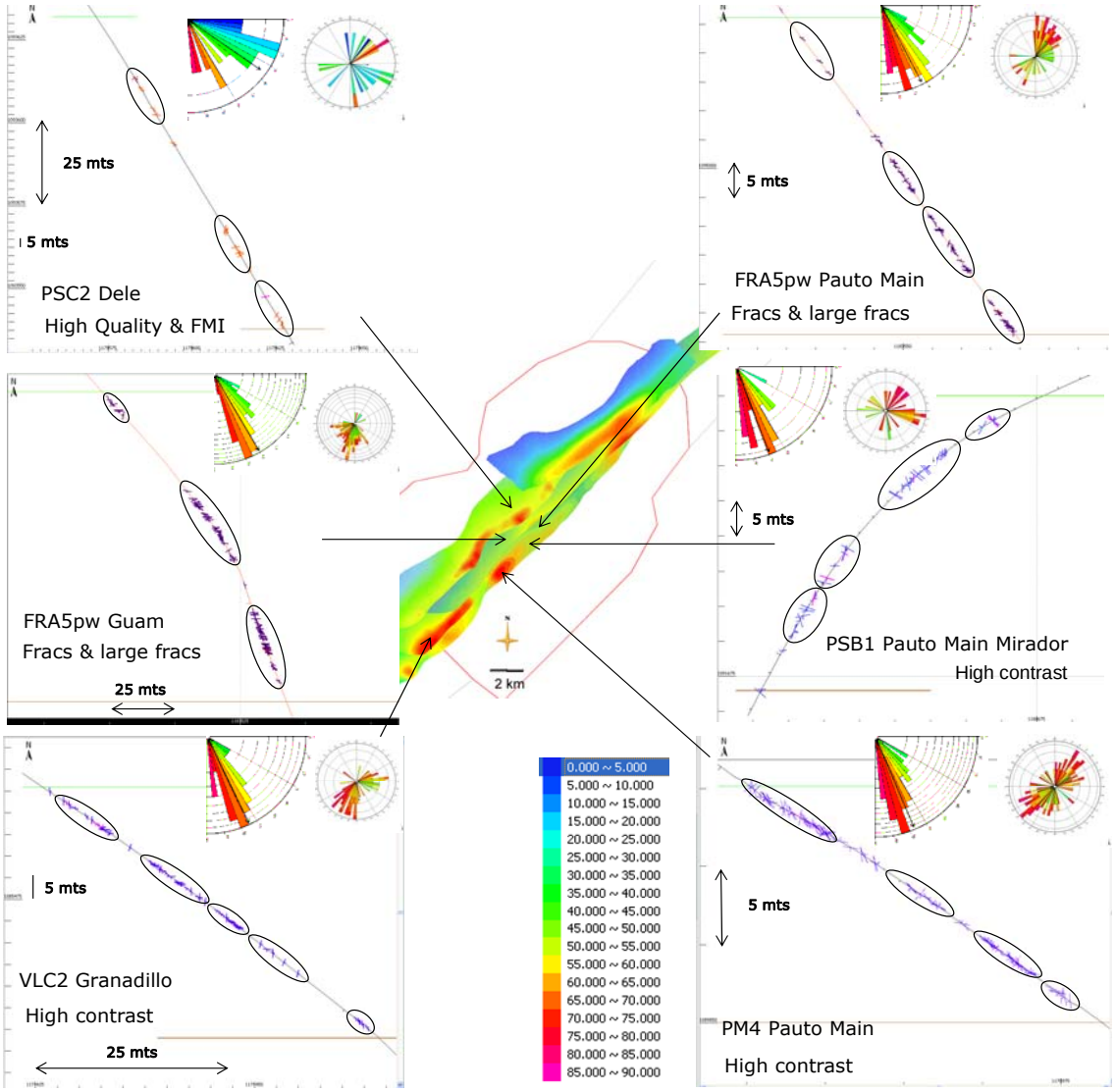

Figure 1-16. Fracture Spacing by Clusters using Logs (from Alzate, 2012).

Figure 1-17 shows a fractured core with the scale in inches. This Figure shows a couple of representative high dip angles with a spacing of ~1 in. Other cores not presented here show visible fractures from 1 to 10 ft.

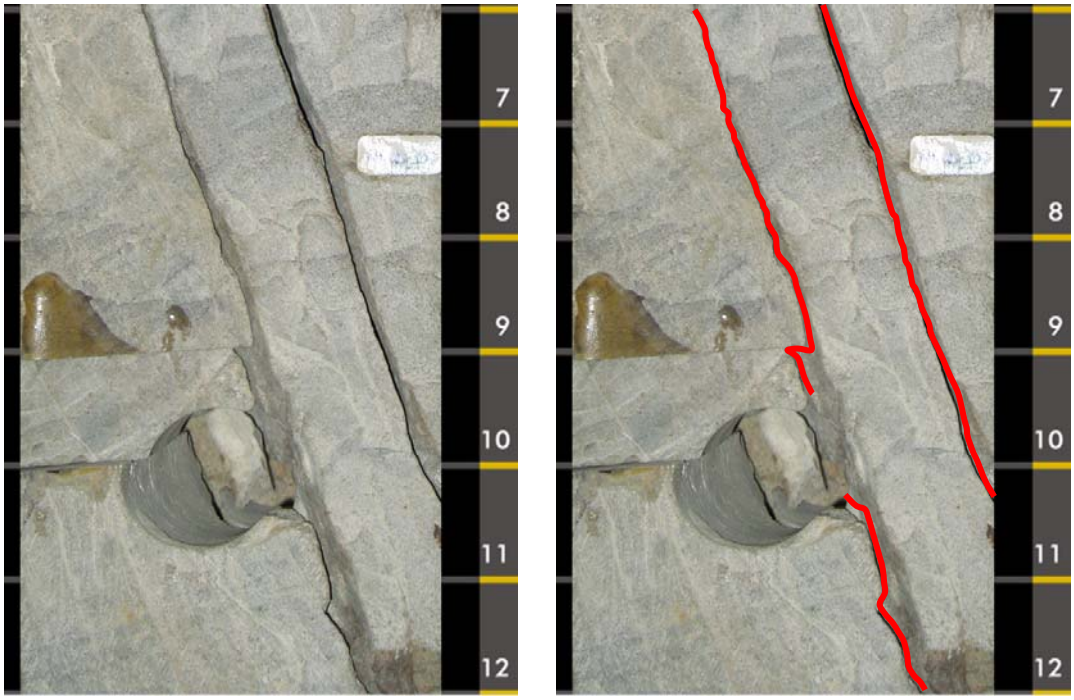

Figure 1-17. Fractured Core Samples DLB1.

When building a full field reservoir simulation model, the fracture spacing is done by software that captures the logs and fracture intensity, and stochastically defines the fracture spacing. This stochastic approximation does not keep consistency between the flow capacity of the well and the aperture of the fractures.

In this project, the fracture spacing was not available, so it was necessary to constrain the spacing values by using a correlation. Here, the objective is to have a step in the natural fracture construction workflow to have reliable fracture spacing.

Figure 1-18 represents a schematic of the simple model proposed which can be compared with Figure 1-17 where a real fracture system is shown.

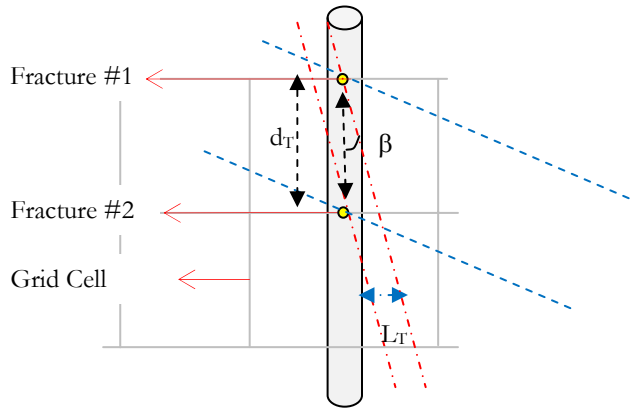

Figure 1-18. Fracture Orientation impact sketch on Fracture Spacing.

The Equation 1-6 presented just applies the Pythagoras theorem to estimate the distance between the fractures (L_T) using the dip (β) and the vertical distance between them (d_T), see Figure 1-18. This correlation is a key step in the integrated information workflow[10].

$$L_T = d_T \cdot Tan(\beta) \qquad 1\text{-}1.$$

Where

L_T : is the theoretical spacing.
d_T : is the theoretical distance between the fractures
β : is the dip of the fracture

Assuming a vertical well, the Figure 1-19 was created as a new theoretical plot[11] for vertical fractures to estimate the theoretical fracture porosities related to the theoretical fracture spacing expected in the near wellbore.

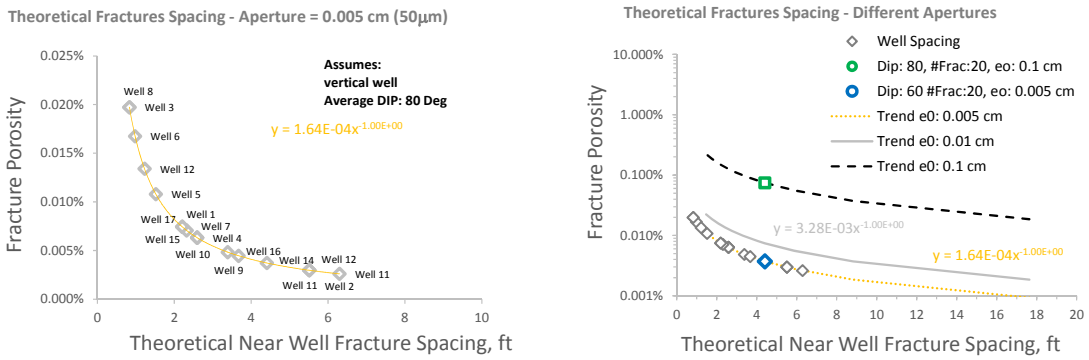

Figure 1-19. Theoretical Minimum Fracture Porosity vs. Maximum Spacing.

1.3.5.3 Orientation

Figure 1-20 and Figure 1-21 show a summary of the fractures' interpretation using image logs[12] for Pauto and Floreña respectively. Four families of fractures are identified by Alzate **[14]** for this field:

- Family 1 and 2: Two main fracture families were found: one with a SW dipping and another with a NE dipping.

[10] Notice that the aperture uses corresponds to 0.01 cm (100 microns) and a very high value of 0.1 cm (1000 microns). The intension was to show that apertures in the order of 0.1 cm as reported in **Reference 5** are too high, which generates very high fracture porosities. Also the aperture of 100 microns could be considered as the highest values compared with the estimations that will be presented though this project as the example presented in Figure 1-13 where the apertures of the fractures are in the order of 35 to 50 microns.

[11] Through this document, there are different theoretical plots that should be used for consistency, one is the aperture vs. porosity, and the others are the inter-porosity vs. shape factor, aperture vs. fracture permeability. This work proposes these new simple but highly useful theoretical plots that will constraint the spacing and the fracture porosity.

[12] Image logs like the FMI (Full-bore Formation Micro-imager) and UBI (Ultra Sonic Borehole Imager).

The interpretation suggests that those fracture families are conjugate fractures with a strike of N60W. Additionally, some micro-seismic events near an injector show a SE-E orientation for the maximum horizontal stress (see Figure 1-54) which correlates with the orientation of these fractures.

Regional maximum stress direction is N60W (135° Azimuth), favors the existence of many critically stressed natural fractures (see Figure 1-11). In general, these fractures have a high dip angle (80°).

Notice that family 1 and 2 generate an impact in the spacing between the fractures as the fractures will be closer at higher dips, see Figure 1-18.

- Family 3: A fracture family with a NE-SW strike which are almost parallel to structure orientation.

- Family 4: A fracture family with an N-S strike.

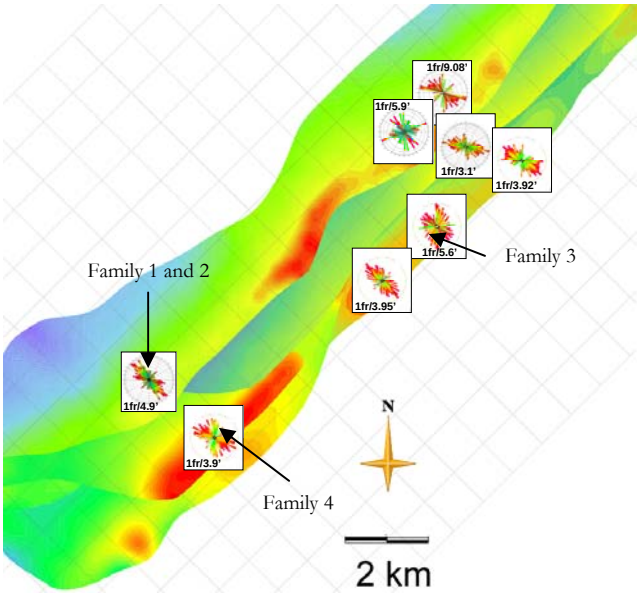

Figure 1-20. Pauto Complex Fracture Orientation (from Alzate and Linares, 2012).

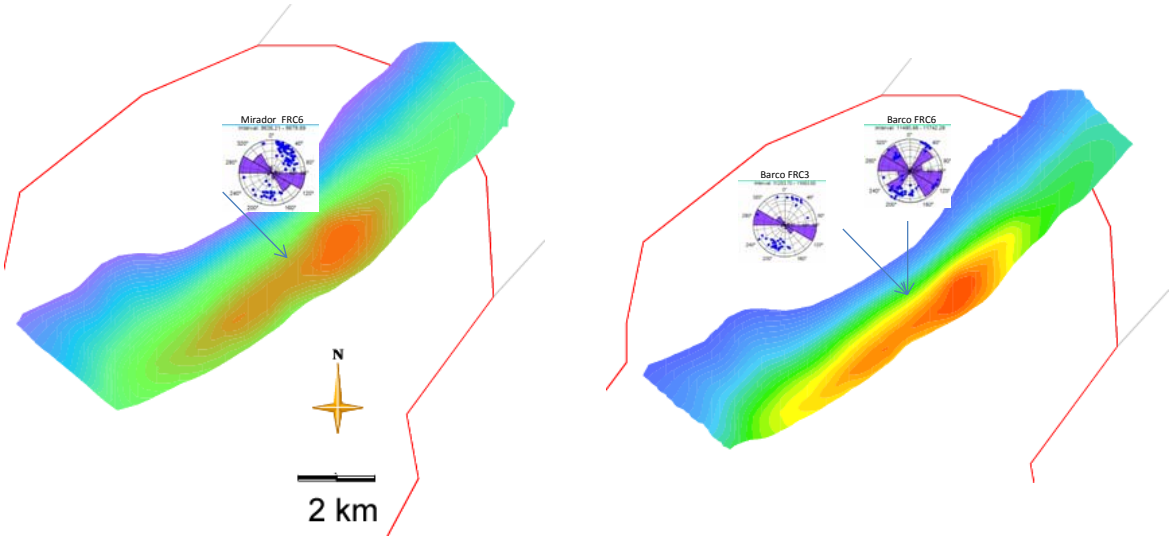

Figure 1-21. Floreña Fracture Orientation (from Alzate and Linares, 2012).

1.3.5.4 Length

The length of the fractures determines how much the fractures are interconnected.

From outcrops, the natural fractures have lengths from 100 m up to 500 m (see Figure 1-15).

Figure 1-22 shows the micro-fractures lengths from petrologic analysis which has a range of length between 1.01 and 5 mm **[10]**.

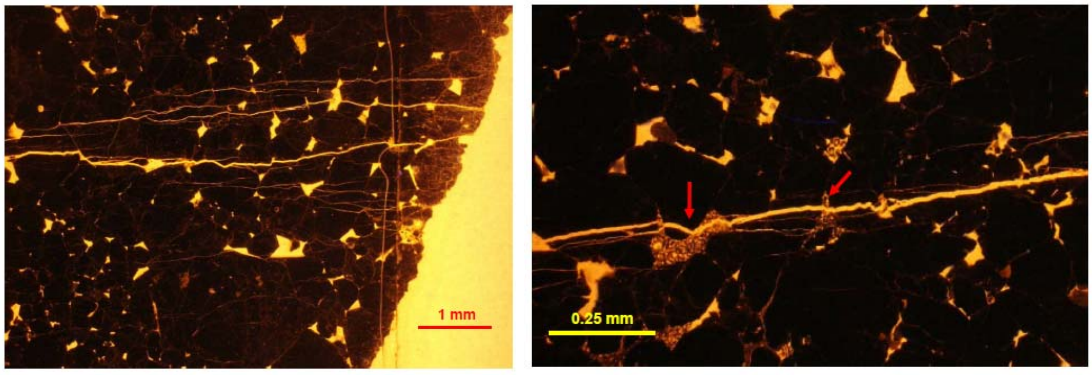

Figure 1-22. Micro-fracture length (from Mesa, 2002).

Figure 1-23 shows a tortuous shape of the micro-fractures.

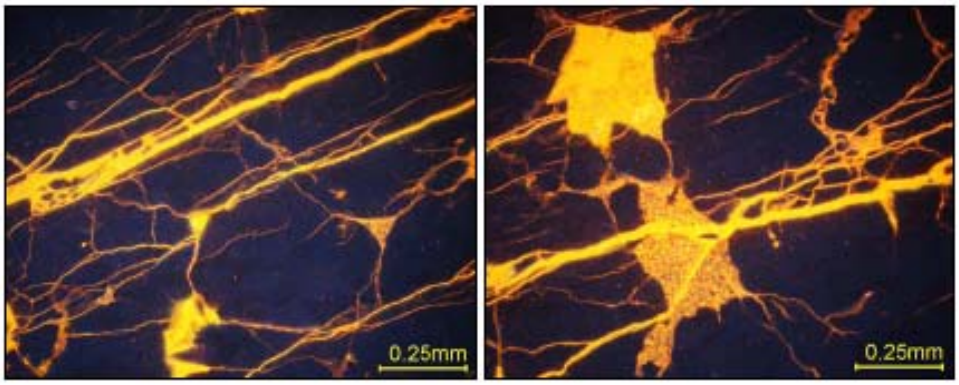

Figure 1-23. Micro-fracture tortuosity (from Mesa, 2002).

1.3.5.5 Aperture (width)

Fracture apertures are a key element to build a natural fracture system as it affects the fracture porosity and permeability. Generally, the aperture can be estimated from image logs when the wells are drilled with water based muds, but there is still a limitation to estimate the apertures and fracture porosities with oil base muds as it requires

This attribute helps to set some constraints to the fracture porosity and permeability by using ideal conditions of fractures.

- **Fractures**

Figure 1-28 shows the Core Special Analysis[13] performed in 2009 by Lopera et al. **[11].** It shows a permeability change with the change in the effective stress (see Plot 1). Afterwards in 2013, Marin and Lopez **[12]** matched these data to the Barton permeability model **[17]** to relate the fracture permeability with the fracture aperture at different normal stresses (see Plot 2), the apertures have a range from 0.002 cm (20 μm) up to 0.05 cm (500 μm).

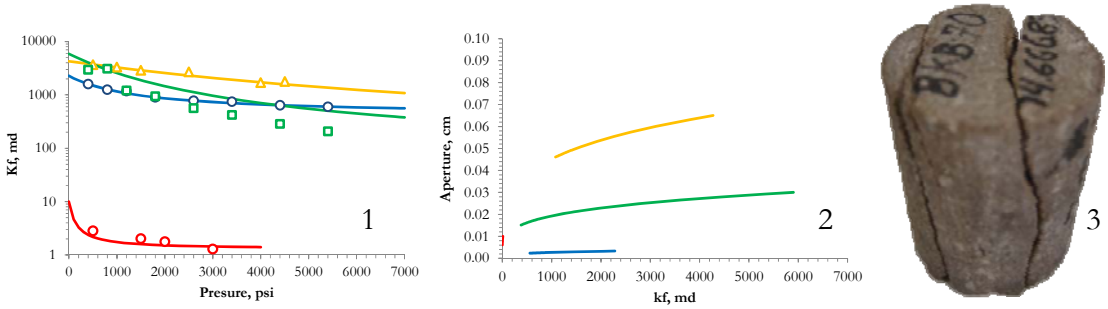

Figure 1-24. Fracture Apertures from Laboratory Test (from Lopera and Marin, 2009).

For the purpose of this study, to calibrate the fractures apertures, the Figure 1-25 was created by combining Plots 1, Plot 2 and Plot 3 from Figure 1-13.

[13] Fractures plug example used in the laboratory. In Plot 3 Figure 1-28, the fractures may look wide open as they are at ambient conditions.

Figure 1-25 shows 3 trend lines which were obtained by using Equation 1.8. As an example, this analysis shows that the wells that are along the red line have an initial global estimate of apertures in the order of 35 microns, and the green line shows wells that could have apertures in the order of 70 μm.

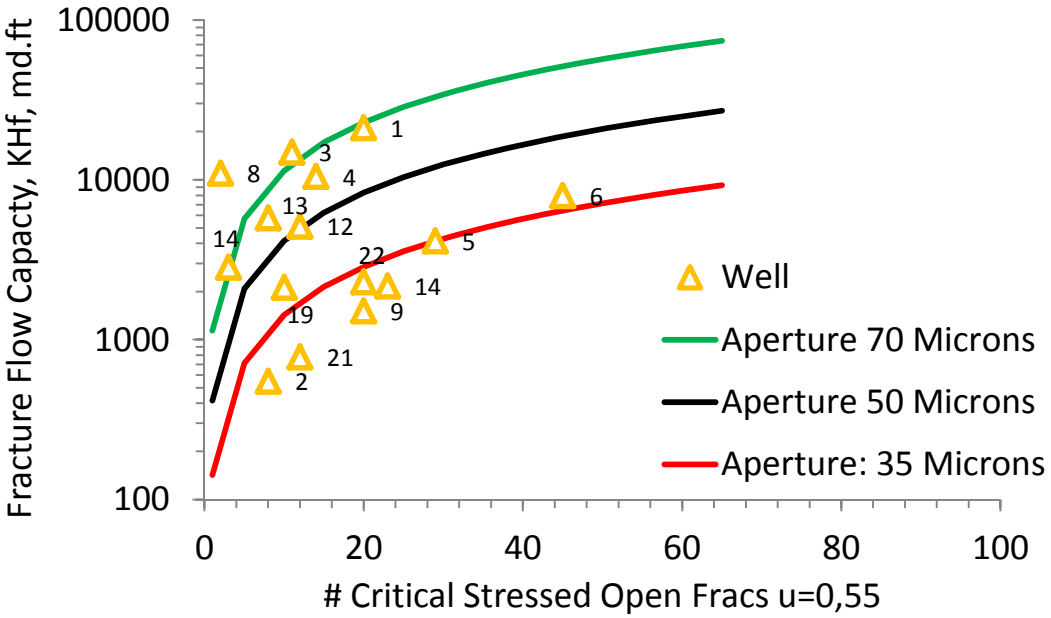

Figure 1-25. Apertures Estimated from the Critical Stress Fracture and Fracture flow Capacity.

- **Micro fractures**

Cobaleda **[13]** in 2002 analyzed 300 samples with the Scan Electron Microscopy (SEM), the results shows that the major fracture apertures are around 0.5 μm which were localized mainly in the border of the grains. Micro-fractures in the order of less than 2 μm were reported as scares. As a reference, pores have sizes from ~0.1 to ~1 μm, see Figure 1-30.

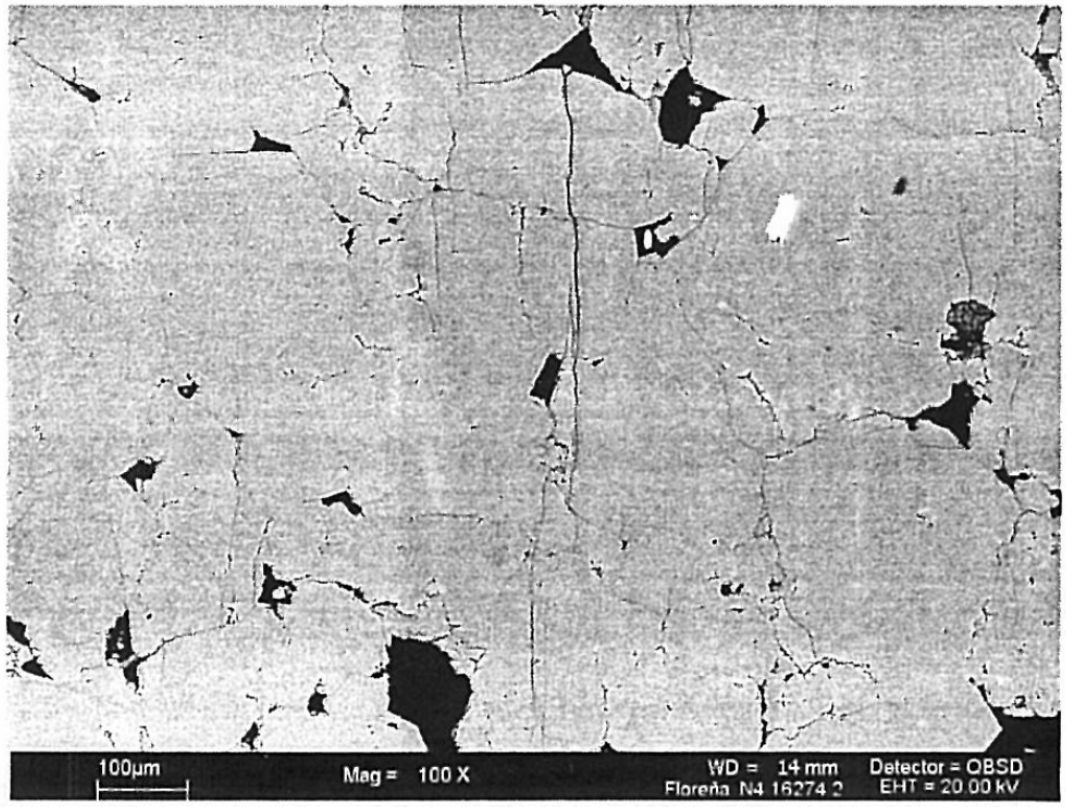

Figure 1-26. Micro-fracture Aperture (from Cobaleda, 2002).

1.4 Initial Reservoir Pressure and Fluid Contacts

Figure 1-27 show the initial reservoir pressure varying with depth and a general view of the initial reservoir fluids. The estimated Water Oil Contact (WOC) shows one of the boundary limits of the reservoir, the other boundary limit is defined by the main faults presented in Figure 1-3.

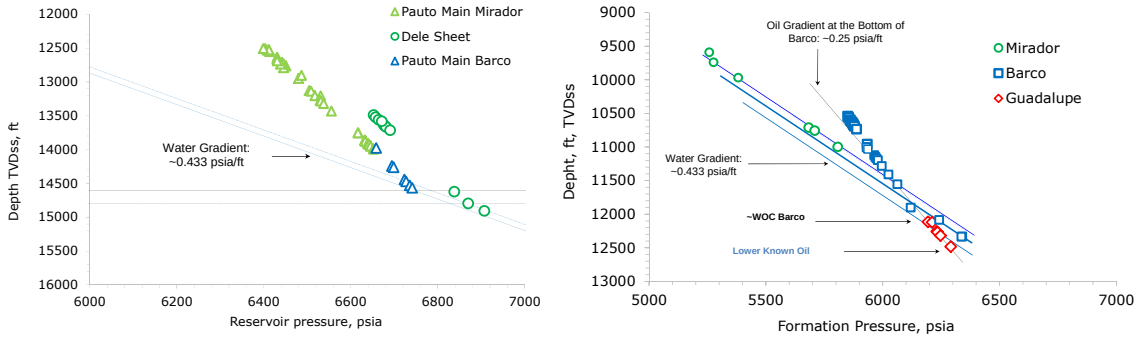

Figure 1-27. Pauto Complex and Floreña Initial Pressure and Water Oil Contacts.

1.5 Petrophysics

Five main petrophysical attributes are described in this section. They are the rock compressibility, the porosity and permeability relationship, the capillary pressure, the relative permeabilities for the oil, gas and water phases. Also it was included the inter-porosity and storage which are the fracture coefficients obtained from pressure transient analysis and are related to the fracture porosity and permeability.

1.5.1 Rock Compressibility

The matrix[14] rock compressibility for conventional reservoir (C_r) simulation is the same as the $C_{bp,m}$ term used in geomechanics to represent the matrix bulk rock compressibility. The bulk rock compressibility is defined as the change if the pore volume with respect to the pore pressure at constant confining pressure and is expressed in the Eq. 1-2.

$$C_r = C_{bp,m} = \frac{1}{V_b}\left(\frac{\partial V_b}{\partial P_p}\right)_{P_c} \qquad 1\text{-}2.$$

Where b refers to bulk, p to pore, m to matrix. V_b is the bulk volume, P_p is the pore pressure and P_c is the confining pressure[15].

Figure 1-28 shows the rock compressibility measurements for Piedemonte rocks **[18]**. The rock compressibility has a range at 6000 psia from 6x10^{-5} to 2 x10^{-5}.

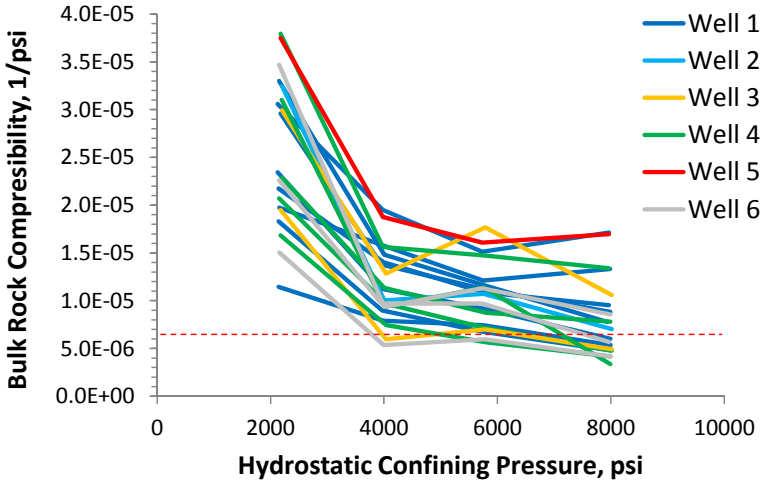

Figure 1-28. Compressibility for Floreña and Pauto (from Mogollón, 2002).

[14] No measurement of the fracture compressibility is available. Generally, the fracture compressibility could be 10 times higher than the matrix compressibility **[17]**.

[15] Pc is only used in this equation as the confining pressure; please avoid any confusion with the Capillary Pressure abbreviation.

1.5.2 Matrix Capillary Pressure

It is possible to link capillary pressure, pore throat radius and diameter with the flow, permeability and gas trap saturation by using the following workflow:

- Estimate the pore throat radius estimation, see Figure 1-29 and Figure 1-30.
- Then, the pore throat is correlated with the Knudsen number given the Eq. 1-3 to identify the flow regime, see Figure 1-32 and Figure 1-33.
- Then, infer the gas trap saturation and the relative permeability shape of the water, see Figure 1-34 and Figure 1-44 respectively.

1.5.2.1 Pore Throats

Only matrix capillary pressure is available for PDM which is used to estimate the initial water saturation as a basic approach, see Figure 1-29.

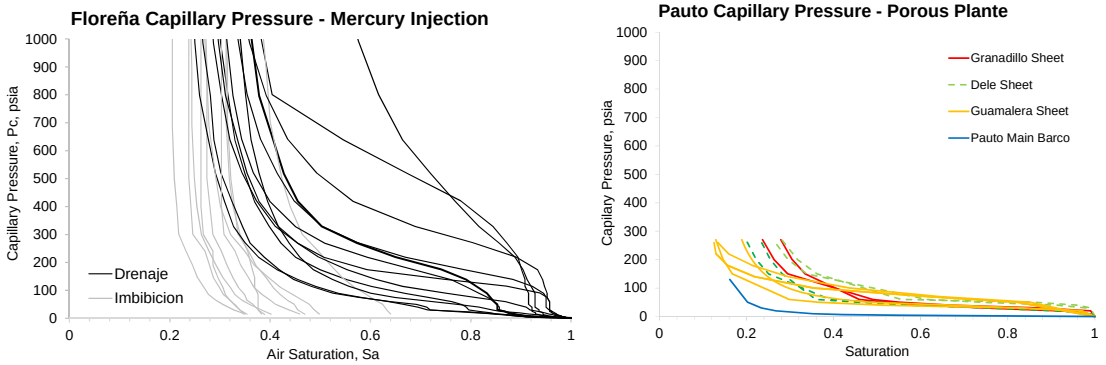

Figure 1-29. Floreña (left side graph) and Pauto (right side graph) Capillary Pressure.

Figure 1-30 shows the pore throat radius for Floreña (left side graph) and Pauto (right side graph). The average pore throats are in the order of 1 µm.

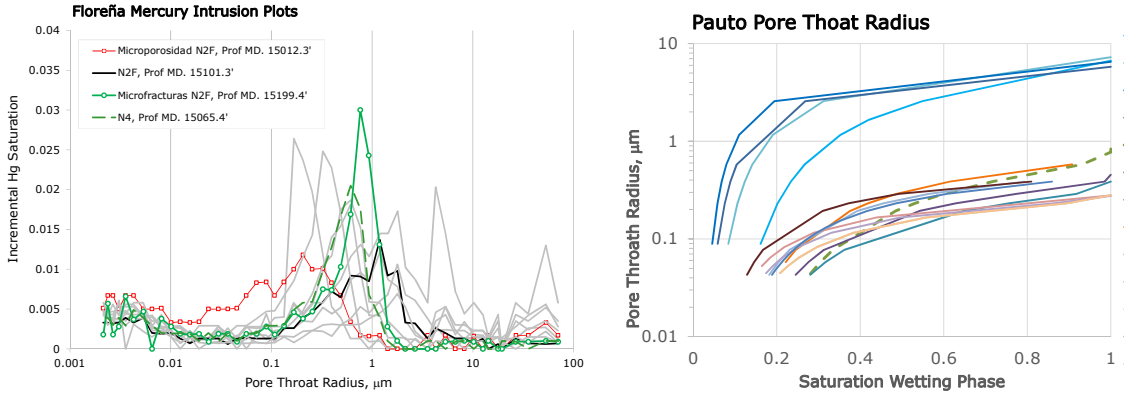

Figure 1-30. Floreña (left side graph) and Pauto (right side graph) Pore Throat Radius.

On the other hand, Figure 1-29 suggests that capillary pressures for Pauto (right side plot) have better rock qualities than Floreña (left side plot). This apparently irreconcilable data is attributed to the presence of micro-fractures **[11]** in Pauto Matrix, as it is evident in the stress-strain data in Figure 1-31 that Pauto seems to be affected more by the micro-fractures than Floreña.

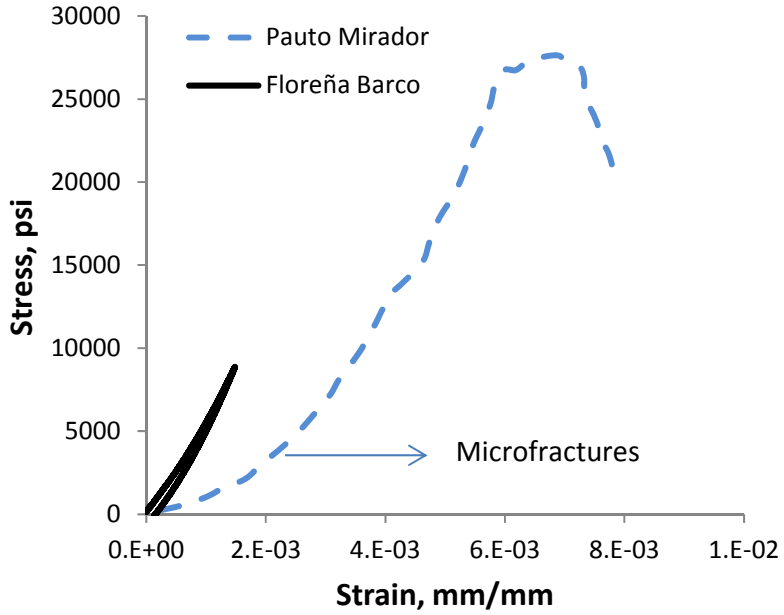

Figure 1-31. Floreña (Solid Line) and Pauto (Dashed Line) Stress and Strain Plot.

1.5.2.2 Flow Regimes Thresholds

The limits for tight gas and other definitions for conventional and unconventional can be determined by different methods, the proposed one in this work is by using the Knudsen number.

The Knudsen number relates the importance of the pore throat radius and molecular radius in the flow type regime characterization.

As a matter of reference, the average molecular diameter of CH_4 is in the order of 0.38 nm, while the pore throats sizes are in the order of 1000 nm (1 μm)[16]. By definition the Knudsen number is given by:

$$k_n = \frac{\lambda}{d} \qquad 1\text{-}3.$$

[16] The pore throat size are (0.001 cm: 0.01 mm: 10 μm: 10.000 nm, see Figure 1-30) compared to the lower fracture width (0.0001 cm: 0.001 mm: 1 μm: 1000 nm, see Figure 1-26). These are high enough compared to the molecular size of methane (**~0.38 nm**), which is a close approach to assume continuous flow.

Where k_n is the Knudsen adimensional number.

λ : gas mean free pathway, nm (it was assumed a value of 0.61@6000psi).

d : pore throat diameter, nm.

Figure 1-32 and Figure 1-33 show the relation of the non-dimensional Knudsen Number (k_n) with the pore throat radius and wetting phase saturation. It can be observed that even if the permeabilities are low, the Knudsen criterion **[20]** suggests that a continuous flow in the matrix will be dominant throughout most of the production's life. Notice that the porous plate does not achieve high pressure values, which limit the k_n estimation, see Figure 1-32.

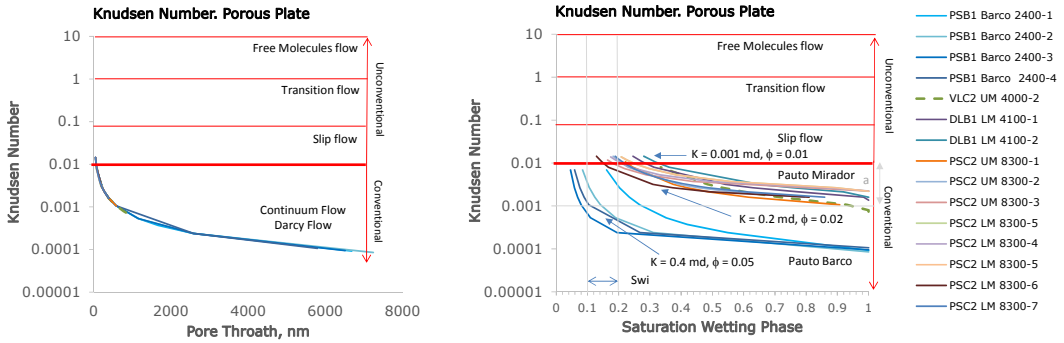

Figure 1-32. Pauto Complex - Knudsen Number.

Figure 1-33 (left side), shows a window for slip flow (unconventional physical modeling) for the gas phase between the initial water saturation of 21% and the 34% using the Knudsen threshold criteria. The measurements made with mercury injection on Floreña samples increase the resolution, where a slip flow could happen below 34% of wetting phase saturation.

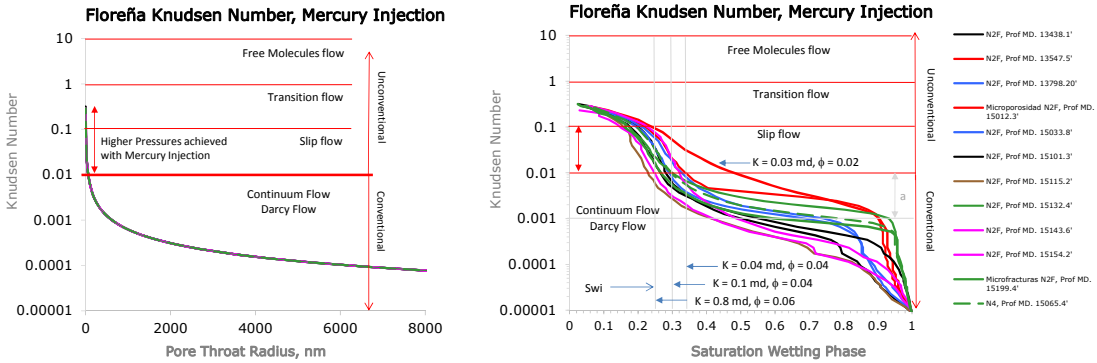

Figure 1-33. Floreña Barco - Knudsen Number.

k_n will be affected in case a multiphase flow happens, as the presence of a second phase will change the effective pore throat diameter, see Eq. 1-14.

1.5.2.3 Maximum Gas Trap Saturation

Maximum gas trap saturation (S_{gt}) is a parameter that highly impacts the relative permeability to gas due to hysteresis during the imbibition process.
Figure 1-34 shows the estimated S_{gt} for Pauto and Floreña Fields using the correlation developed at Heriot Watt University **[28]**. The correlation is a function of the capillary pressure measured and applies to the matrix system (without micro-fractures).

$$S_{gt} = C_1 \cdot \ln\left(\sqrt{(C_2 k)^{0.6}} \cdot \frac{|\log(\lambda)|}{S_{w,1\mu}}\right) \quad 1\text{-}4.$$

$$\rightarrow \lambda = \left(\frac{P_{c2} \diagup P_e}{S_{w2} - S_{we}}\right) \quad 1\text{-}5.$$

Where

S_{gt}	: Maximum Gas Trap Saturation.[17]		
C_1	: Constant 1.	C_2	: Constant 2.
P_{c2}	: Capillary pressure 2.	P_e	: Entry Capillary pressure.
S_{w2}	: Water Saturation 2.	S_{we}	: Entry water saturation.
$S_{w,1\mu}$	: Water saturation at 1 micron.	k	: Permeability.
λ	: Pore throat size.		

Figure 1-34 also shows the results compared with some measurements made for Cusiana, Cupiagua and other reported data in the literature **[29]**.

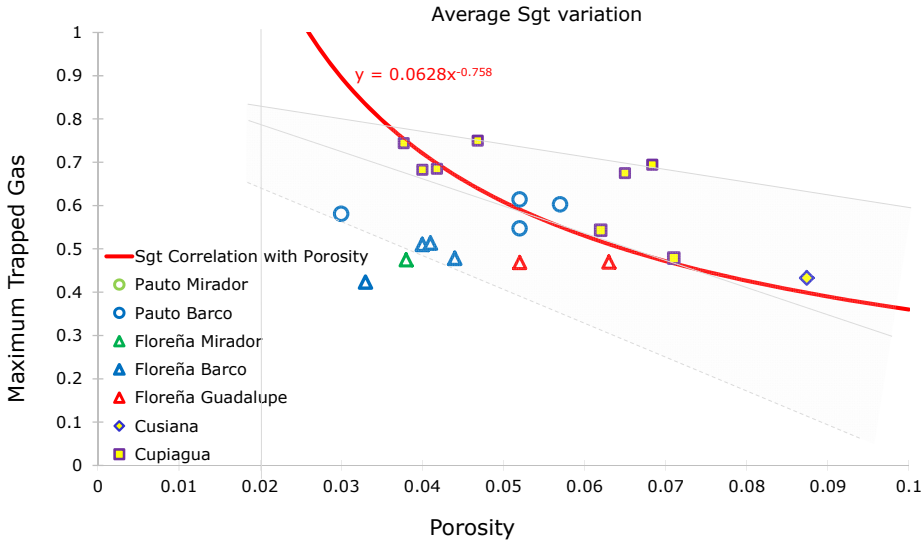

[17] Notice that this is the maximum gas trap saturation that will be used in the hysteresis process so, the gas trap saturation will be changing through time depending on the drainage and imbibition processes that happens in the reservoir.

Figure 1-34. Estimated Max Gas Trap Saturation Values for PDM Fields.

1.5.3 Porosity and Permeability

As reference for the matrix petrophysical properties, the Figure 1-35 shows a core comparison of a Sample with Fractures and a sample without fractures.

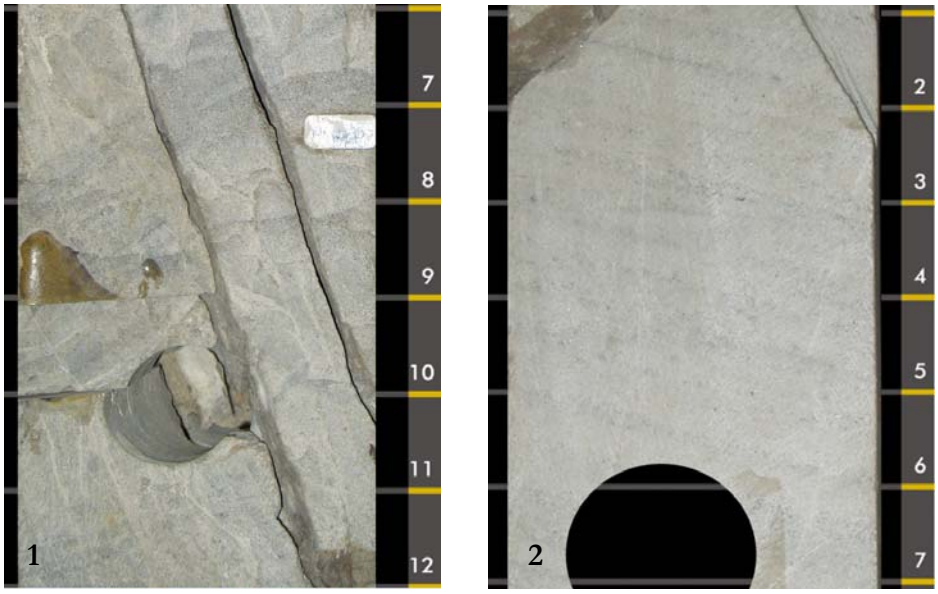

Figure 1-35. Core Sample with Fractures (fractures highlighted in the right side).

1.5.3.1 Matrix porosity and permeability

Figure 1-36 shows the Klinkemberg permeability at 4500 psia. In the right side vertical access of this Figure it is shown as reference the conventional and unconventional limits:

- Floreña field has a range between 0.01 and 0.055 fraction units for the matrix porosity, and 0.002 to 6 md for the matrix permeability. See the blue triangles in Figure 1-36.

- Pauto field has a range of matrix porosity that is between 0.002 to 0.055 fraction units and 0.002 to 2.78 md for the matrix permeability, see the yellow dots in Figure 1-36. Figure 1-36 shows that Pauto porosities and permeabilities are lower than Floreña petrophysical properties.

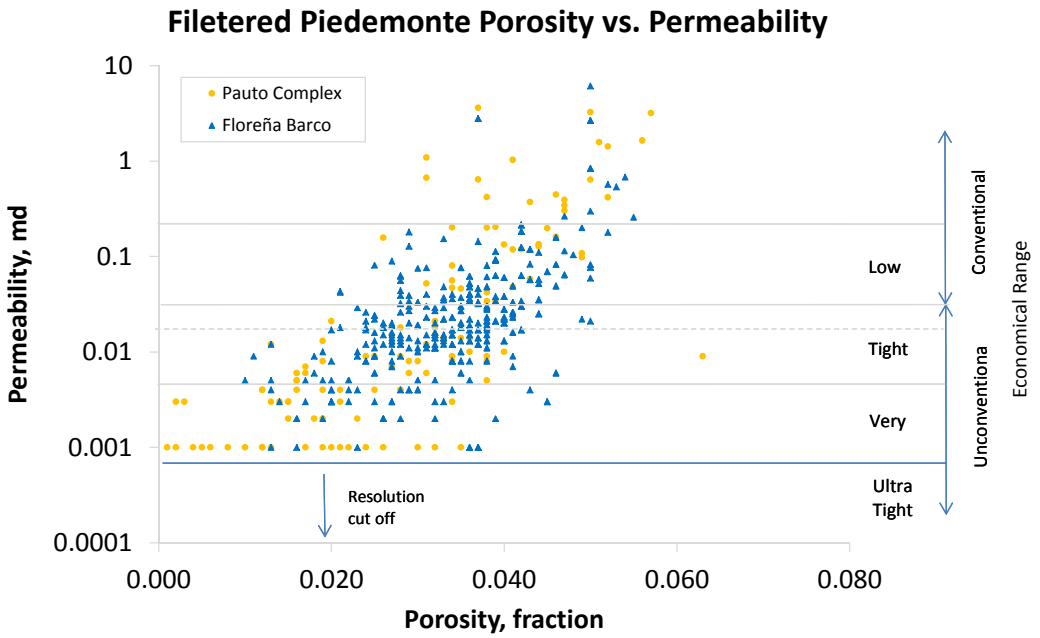

Figure 1-36. Porosity and Permeability from plugs with Economical Convectional and Unconventional Limits and Ranges.

There are two known ways to define the threshold for the conventional and unconventional flow, one is using the economical limit and the second is using the physical limit. Figure 1-37 shows the combination of both criteria where it can be observed that both limits are quite close one to each other.

The economical threshold to identify the limits of conventional and unconventional[18] reservoirs was given by Golan **[19]** and uses the permeability as limits.

The physical threshold to identify the limits of conventional and unconventional was presented by Nazari **[20]** which includes the flow equations and the Knudsen adimensional physical limits.

In this project, Nazari criterion will be used combined with the capillary pressures in the Section 1.5.2 to conclude that the matrix of Piedemonte fields is closer to the conventional than the unconventional tight gas reservoir fluid flow.

Figure 1-37 also shows the range where Piedemonte values are located in the conventional and unconventional definition.

[18] Notice that the permeability driver to define the tight gas limit as unconventional comes from the definition given by the Unites States government to determine taxes credits **[20]**, but it does not capture the physics as the Knudsen number criteria which is one option to define if the flow will be conventional (e.g Darcy Flow) or unconventional (e.g slip flow, Transitional or molecular).

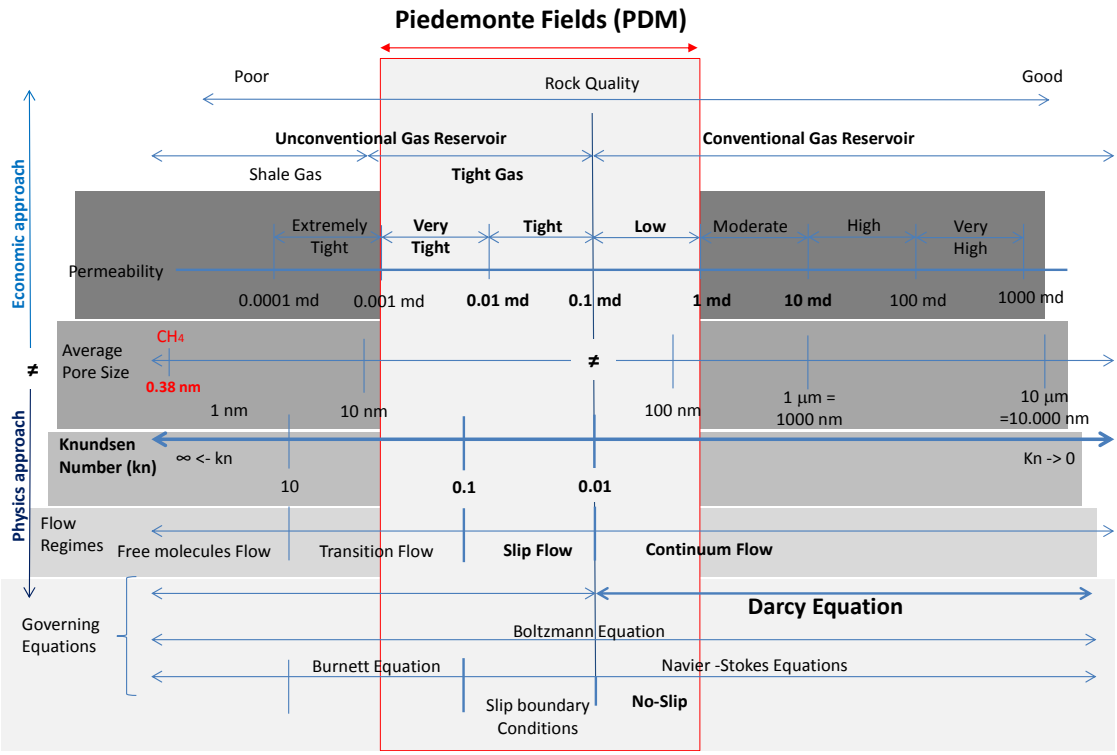

Figure 1-37. Physical and Economical Tight Gas Definition and Ranges (after Golan, 1991 and Nazari, 2015).

1.5.3.2 Fracture Porosity and Permeability

Neither direct fracture porosity nor permeability data are available for PDM fields at the time this study was performed.

Knowing in advance that none of the following methods would directly estimate the exact porosity and permeability of the fractures, it was necessary to perform different analysis to define probable ranges for those parameters that would impact the flow capacity of the wells.

- **Fracture Porosity**

A correlation to relate the matrix and fracture porosity is given by Eq. 1-6 **[23, 24]**.

$$\phi_T = \phi_m + \phi_f - \phi_m \phi_f \qquad 1\text{-}6.$$

The Eq. 1.6 can be simplified by assuming that $\phi_m \phi_f$ is near 0.

$$\rightarrow \phi_T \sim \phi_m + \phi_f \qquad 1\text{-}7.$$

Figure 1-38 shows the conceptual model to estimate the fracture porosity. It assumes a matrix surrounded by a fracture

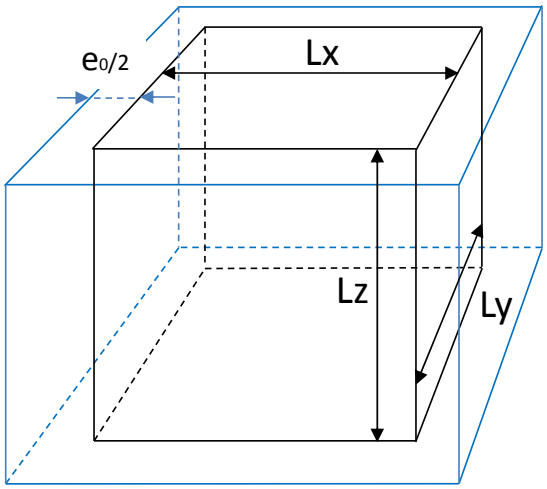

Figure 1-38. Fracture Conceptual Model to estimate the fracture porosity (from V.Golf, 1982).

Eq. 1-8 shows the theoretical fracture porosity based on the conceptual model presented in Figure 1-38. This equation shows the dependence of fracture porosity with scale.

$$\phi_f = e_0\left(\frac{1}{L_x}+\frac{1}{L_y}+\frac{1}{L_z}\right) \qquad 1\text{-}8.$$

Eg. 1-9 shows a simplified equation to estimate the fracture porosity by assuming a parallel fracture

$$\rightarrow \phi_f \approx \frac{e_0}{L} \qquad 1\text{-}9.$$

Where fracture porosity, ϕ_f (fraction) is a function of:

L_x, L_y, L_z : Matrix block size dimensions in the x, y and z direction, ft.
e_0 : Fracture aperture (width), ft.

When no information is available, a general rule suggests that $\phi_f < 0.1 \cdot \phi_m$ when $\phi_m < 10\%$ **[23]**.

- **Fracture Permeability**

Figure 1-39 shows the conceptual model of an inclined fracture[19].

[19] Figure adapted from Reference **[23]**.

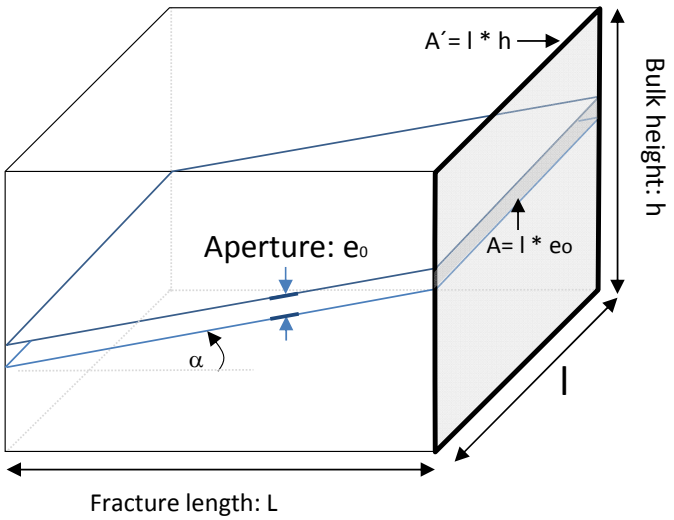

Figure 1-39. Fracture Conceptual Model to estimate the fracture permeability (from V.Golf, 1982).

Eq. 1-10 shows the Darcy´s equation following the conceptual model description presented in Figure 1-39 with $A' = h \cdot l$.

$$q_D = \frac{(h \cdot l) \cdot k_f}{\mu} \frac{\Delta P}{L} = \frac{A' \cdot k_f}{\mu} \frac{\Delta P}{L} \qquad \text{1-10.}$$

Where

k_f : is the **effective fracture permeability**, md.

A' : is the area of the cell (e.g DX and DZ[20] if the path flow is in y direction), noted as A' for apparent.

h : is the bulk height, ft

Eq. 1-11 shows the Poiseuille´s Equation following the conceptual model description presented in Figure 1-39 with $A = e_0 \cdot l$.

$$q_P = C_2 N_f \frac{e_0^2 \cdot (e_0 \cdot l)}{12\mu} \frac{\Delta P}{L} = C_2 N_f \frac{e_0^2 \cdot A}{12\mu} \frac{\Delta P}{L} = C_2 N_f \frac{e_0^3 \cdot l}{12\mu} \frac{\Delta P}{L} \qquad \text{1-11.}$$

Where

C_2 : 3.3 x 10^{-6}

N_f : Number of critically stressed fractures in DZ, for this case.

e_0 : Fracture aperture (width), mm.

[20] DZ in some references is the thickness expressed as h, flow direction DY as L, and perpendicular flow direction DX as l.

A : is the area of the fracture (e.g DX and e_0 if the path flow is in y direction).

If $q_D = q_P$ then the Eq 1-12 represents the effective fracture permeability based on Poiseuille´s Equation[21] including the number of critically stress fractures and the constant to estimate the effective permeability in md. This equation implies that if the aperture is increased 2 times then the permeability increases to the power of 3[22].

$$k_f = C_2 N_f \frac{e_0^3}{12h} \quad \text{1-12.}$$

Eq 1-12 is transformed in Eq 1-13 by including the angle of the fracture

$$k_f = N_f \cdot \left(C_1 \cdot \frac{e_0^3}{h} \cos^2(\alpha) \right) \quad \text{1-13.}$$

Where:

C_1 : Conversion factor in Darcy units, 8.44 x10^6 for e_0 in cm, 5.44x10^7 for e_0 in inches.[23]

α : The angle between the pressure gradient and the fracture plane [°][24].

Organizing the Eq 1-13

$$k_f = N_f \cdot \left(C_1 \cdot e_0^2 \cos^2(\alpha) \right) \cdot \frac{e_0}{h} \quad \text{1-14.}$$

Eq 1-15 represents the **intrinsic fracture permeability** $k_{f,in}$ (in Darcies).

$$k_{f,in} = C_1 \cdot e_0^2 \cos^2(\alpha) \quad \text{1-15.}$$

Eq. 1-16 results from including Eq. 1-9 into Eq. 1-14 helps to validate if the fracture effective permeability and the fracture porosity (e.g Core analysis and PBU interpretation).

$$k_f = N_f \cdot \left(C_1 \cdot e_0^2 \cos^2(\alpha) \right) \cdot \phi_f \quad \text{1-16.}$$

Eq. 1-17 results from including Eq. 1-9 and Eq. 1-15 into Eq. 1-16.

$$k_f = N_f \cdot k_{f,in} \cdot \phi_f \quad \text{1-17.}$$

[21] This equation does not consider the roughness and friction.

[22] Example, for a fracture with a h (bulk height) of 250 ft and aperture of 0.1 mm (100 μm), the effective fracture permeability (kf) is 12 md; if the aperture is twice the value (0.2 mm), then the kf is 106 md.

[23] Example, for a fracture width of 0.1 mm, the k_{ff} is 844 Darcies.

[24] Notice that the dip angle does not only impact the fracture permeability but also the spacing, as it was explained in Figure 1-19.

The Eq. 1-12 is then transformed in Eq. 1-18 following the conceptual model description presented in Figure 1-39.

$$k_f = N_f \cdot \left(C_1 \cdot e_0^2 \cos^2(\alpha)\right)\frac{A}{A'} \qquad 1\text{-}18.$$

A slight modification of Eq. 1-18 helps to validate the input of the effective permeability into the reservoir simulation models, in order to validate possible ranges of KH. Eq. 1-8 shows the relationship between the number of fractures, the intrinsic fracture permeability and the total area of the grid cell and the area of the fracture.

$$k_f = N_f \cdot k_{f,in} \cdot \frac{A}{A'} \qquad 1\text{-}19.$$

Eq 1-20 shows how to evaluate the total permeability:

$$k_T = k_f + k_m \qquad 1\text{-}20.$$

Where

k_T : is the total permeability, md.
k_f : is the Fracture permeability, md.
k_m : is the Matrix permeability, md.

Eq 1-21 shows how to estimate the total flow capacity.

$$kH_T = kH_f + kH_m \qquad 1\text{-}21.$$

Where

kH_T : is the Total flow capacity of the well, Darcy.
kH_f : is the Fracture permeability, md.
kH_m : is the Matrix flow capacity of the matrix, Darcy.

- Formation pressure was measured using a Dual Packer technology in a fracture location using the critically stressed fracture interpretation **[12, 14]**. After taking fluid samples and checking that no mud was circulating anymore, it was possible to infer a combined matrix-fracture permeability in the order of ***40 md***, this value could be used as a reference to identify possible values for fracture permeability in-situ, see Figure 1-40

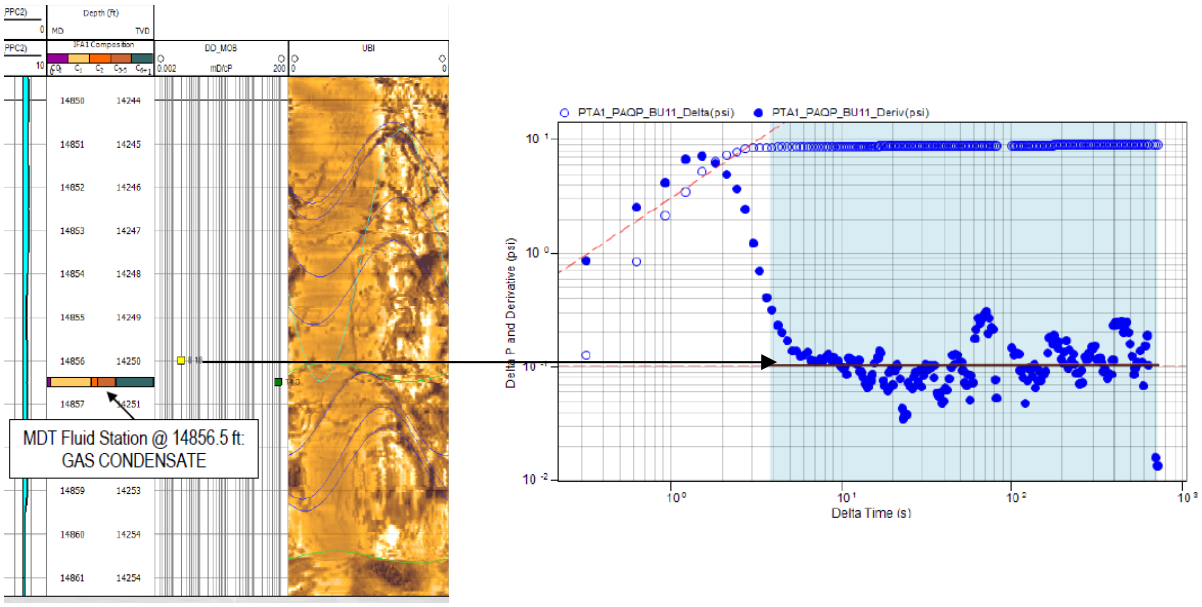

Figure 1-40. Permeability from formation pressure build up (from Lopez et al., 2014).

- The left side graph in Figure 1-41 shows for each well the KH from logs and Pressure Build up – PBU. The right side graph and the relation between the KH obtained from pressure transient analysis (PBU) divided by the KH from logs; this relation is defined in this document as the excess permeability.

  A simple methodology for calibrating the wells' KH is done by calculating the permeability using the porosity from logs. Following this, a practical relation is used between the matrix KH and the PBU-obtained KH above the saturation pressure, which gives the excess permeability that helps to identify the sector that is affected by natural fractures.

  This technique has a limitation, which is that it does not actually relate the fracture intensity with log measurements, and sometimes, the KH obtained from PBU is affected by the mobility due to condensate banking. Besides, this KH is an overall average of the effective flow capacity of the movable fluids in the reservoir.

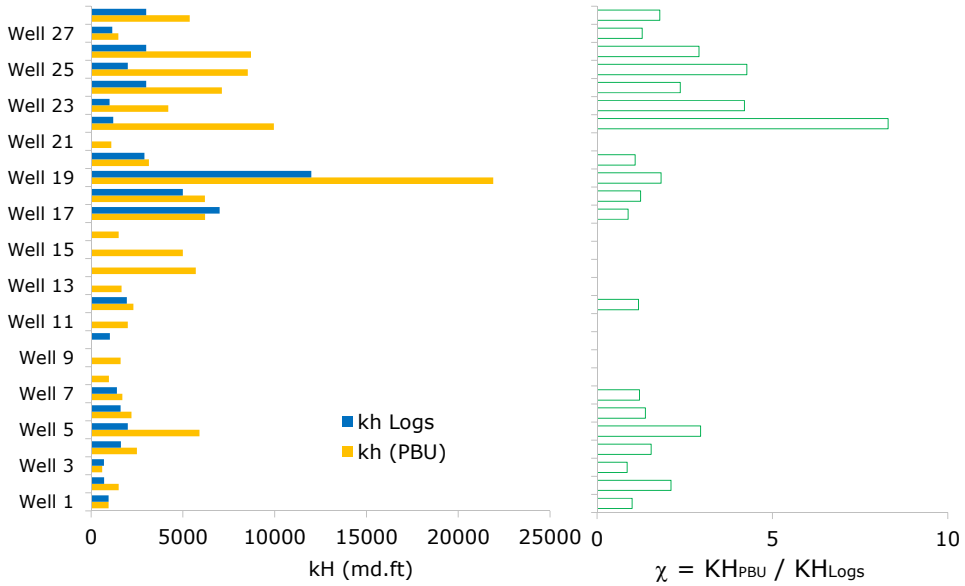

Figure 1-41. Flow Capacity from Transient Analysis and Excess Permeability for PDM Wells.

- Notice the permeability and porosity work around workflow could be done with the fracture coefficients from PBU (Pressure Build Up) information, see Section 1.5.5.

1.5.4 Relative Permeability

1.5.4.1 Matrix Relative Permeability

Three gas-oil drainage tests for relative permeability measurement are available with dead oil; these relative permeabilities represent the displacement of oil by gas under an immiscible process.

A consistency check from the end points of gas-oil experiments and capillary pressure measurements was performed to obtain the water-oil relative permeability values, as those were not available.

- **Gas-Oil Relative Permeability**

Figure 1-42 shows the 3 drainage[25] gas-oil relative permeability measurements available for the matrix of Pauto and Floreña.

[25] Drainage means that the plugs were initially saturated with water, then displaced by oil and finally displaced by gas under unsteady state conditions. This test could simulate the gas injection process in a volatile oil system.

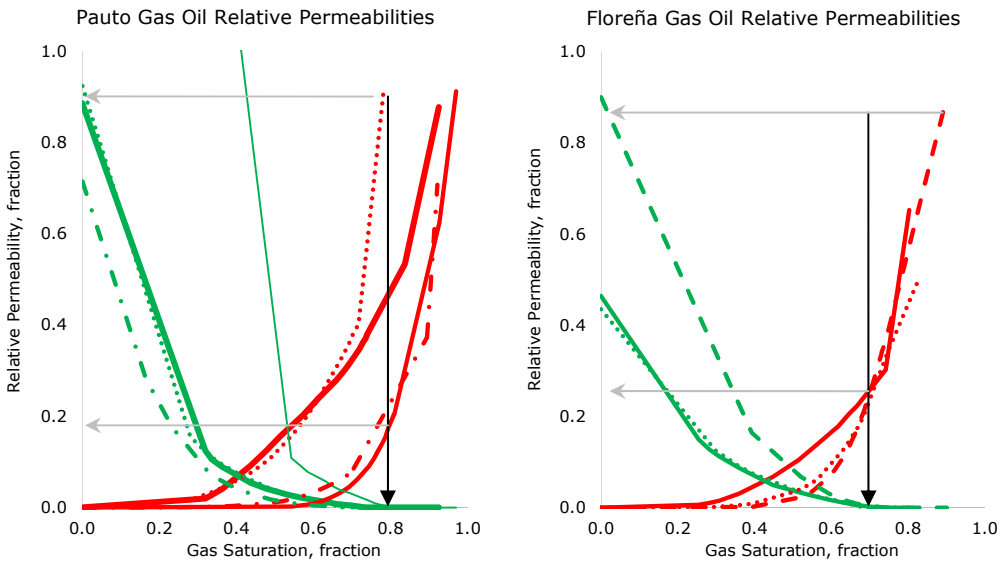

Figure 1-42. Pauto and Floreña Gas Oil Relative Permeability.

The sum of oil and gas relative permeabilities shows a general impact in the effective hydrocarbon permeability; see the arrows in Figure 1-43.

For Pauto, a slight change in gas saturation (Sg~80%) that could be due to a liquid drop out (So ~20%, see Figure 1-50) generates a huge impact in the total hydrocarbon permeability (from 0.9 to 0.5).

The arrows in Figure 1-43 suggest that a slight liquid drop out (see Figure 1-50) generates a high impact in gas relative permeability. Something similar happens for the flow in the matrix in Floreña, with the difference that the impact seems to be lower for rocks with an air permeability of 0.03 md and porosity of 0.03 compared with Pauto.

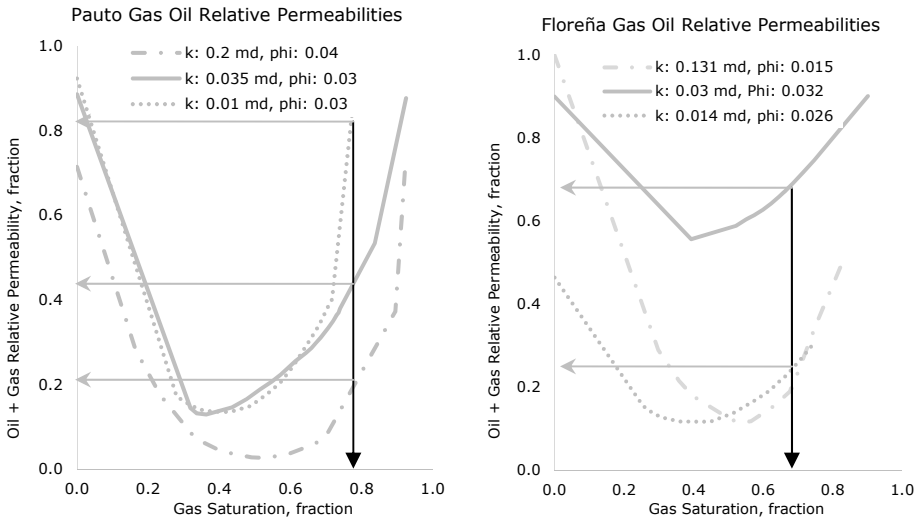

Figure 1-43. Sum of Gas and Oil Relative Permeability for Pauto and Floreña.

- **Water Oil Relative Permeability**

The Corey and Brooks **[31]** correlation was used to build the water-oil relative permeabilities. The exponents where double checked using a slightly modified version of Fatt and Dykstra correlation **[32]**, see Eq. 1-22.

Figure 1-44 shows the obtained water relative permeability curve from capillary pressure assuming a contact angle of 30° and an interfacial tension between water and oil of 30 mN/m. The Corey exponent obtained after the match for the water (n_w) was 2 for Pauto and 5 for Floreña.

$$k_{rwt} = k_{rwt}@S_r \cdot \frac{\int_0^{Swt} \frac{dS}{P_c^{2/(1+b)}}}{\int_0^1 \frac{dS}{P_c^{2/(1+b)}}} \qquad 1\text{-}22.$$

Where:

S_r : is the residual saturation.
P_c : is the capillary pressure.
S : is the saturation.
k_{rwt} : is the relative permeability to the wetting phase.
$k_{rwt}@S_r$: is the relative permeability end point at residual saturation.

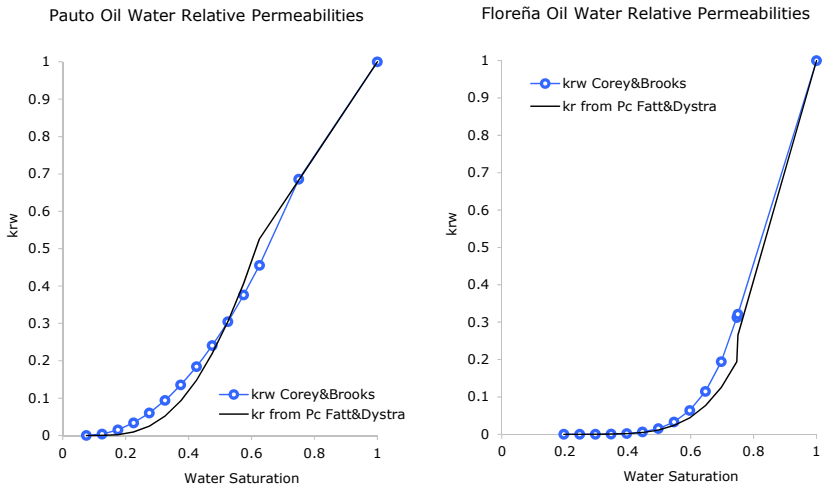

Figure 1-44. Water Oil Relative Permeability for Pauto and Floreña.

1.5.4.2 Fracture Relative Permeability

No fracture relative permeability was available. This parameter and its uncertainty will be discussed in Chapter 2, Section 2.6.3.5.

1.5.5 Pressure Transient Fracture Coefficients

Eqs. 1-23 to 1-26 shows a very short summary of the Inter-porosity coefficient (λ) and Storage coefficient (ω) parameters that could be obtained from the characteristic type curve pressure derivative function for a dual porosity and dual permeability system **[33]**.

The Inter-porosity coefficient (λ) is defined by Eq. 1-23 and shows the relationship of the shape factor - σ (i.e the fracture spacing[26]) and the excess permeability (i.e the fracture and matrix permeability relation):

$$\lambda = \sigma \frac{k_m}{k_f} r_w^2 \qquad 1\text{-}23.$$

Eq. 1-24 is reorganized to estimate the fracture permeability.

$$\rightarrow k_f = \sigma \cdot k_m \frac{r_w^2}{\lambda} \qquad 1\text{-}24.$$

Eq. 1-25 shows the Storage coefficient (ω) which is one of the parameters to classify the natural fracture system: Basically ω defines the percentage of the fracture storage capacity:

$$\omega = \frac{\phi_f C_f}{\phi_f C_f + \phi_m C_m} \qquad 1\text{-}25.$$

Then, Eq. 1-26 is reorganized to estimate the fracture porosity.

$$\rightarrow \quad \sim \phi_f = \left(\frac{\omega}{1-\omega} \right) \cdot \phi_m \qquad 1\text{-}26.$$

Figure 1-45 was built using Eq. 1-23, which shows the theoretical values expected for the shape factor and inter-porosity coefficients at different excess permeability values for Piedemonte reservoirs.

[26] See Eq. 2-13, Section 2.4.6.for further information.

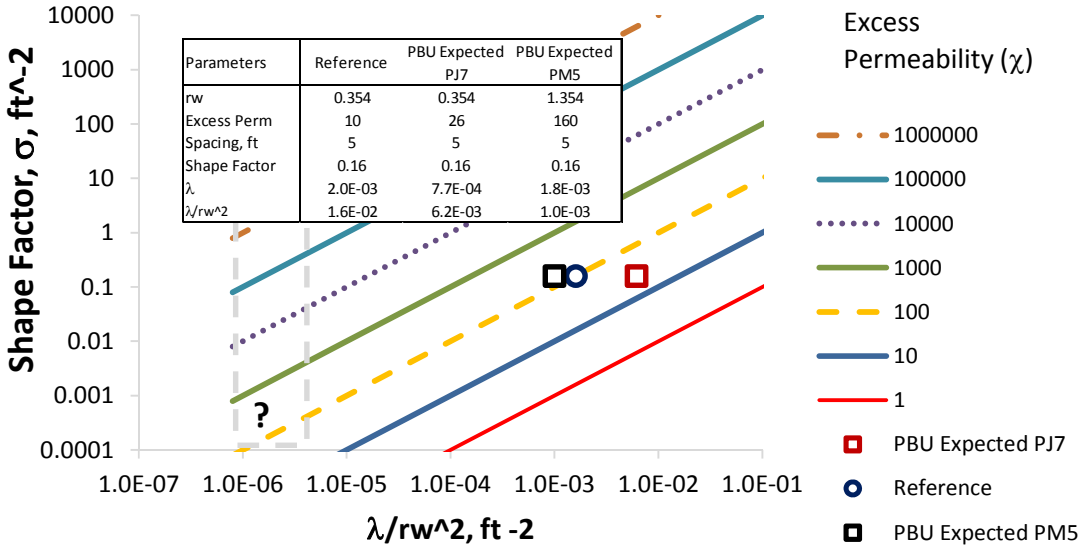

Figure 1-45. Theoretical Inter-porosity and Shape Factors with different Fracture Spacing.

Figure 1-46 shows 2 well cases where the pressure transient analysis shows the shape of the derivative of the pressure transient with time[27] that seems to have the dual porosity/dual permeability behavior.

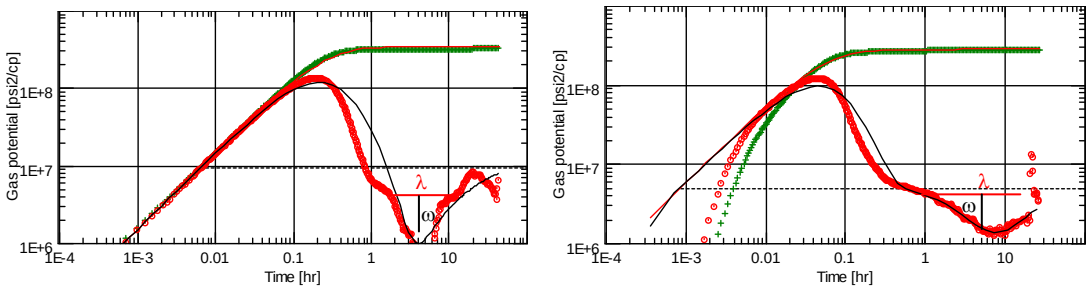

Figure 1-46. Pressure Transient Analysis. Well 1 (left side plot), Well 2 (right side plot).

Additionally to the classical analysis presented in Figure 1-46, a further analysis was performed using Figure 1-47 and Figure 1-48. It was concluded that those characteristic pressure derivative shapes are not related to a natural fracture signature. The analysis is presented as follows:

- First, the PBU interpretations as a natural fracture system give the Inter-porosity (λ) average values for both wells in the order of ~$1x10^{-6}$, see Figure 1-46. This value is very far from theoretical values which are in the order of $1x10^{-2}$, see Figure 1-47 **[33]**. The inter-porosity ~$1x10^{-6}$ values of are not consistent **[1]** with the excess permeability (χ) estimations that are in the order of 100.

[27] Escobar **[34, 35]** performed an interpretation of these 2 wells, concluding a dual porosity/dual permeability behavior.

In other words, in order to have Inter-porosity values in the order of $1x10^{-6}$ it would require to have an excess permeability (χ) in the order of 10.000 and 100.000, which are not realistic values for sandstones with gas production and for PDM sandstones as well.

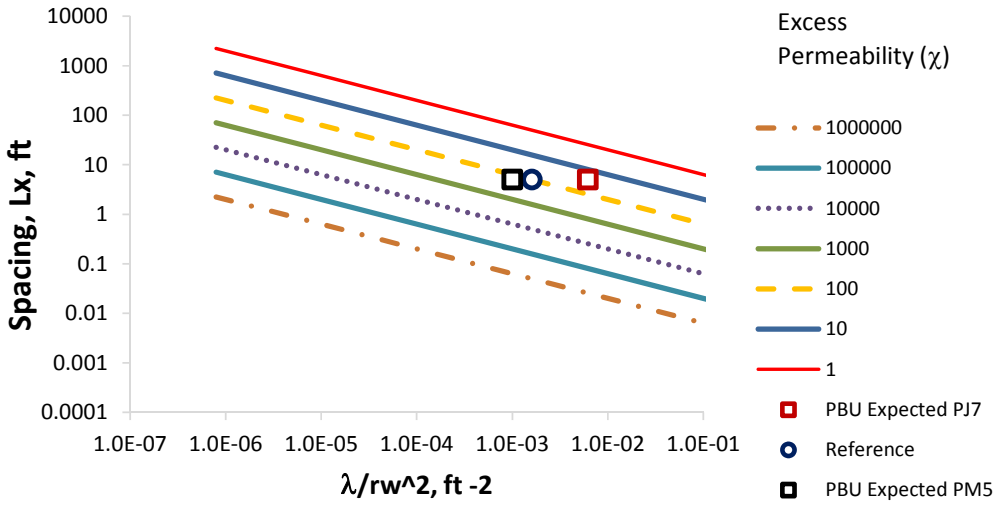

Figure 1-47. Theoretical Inter-porosity and Spacing with different Excess Permeabilities.

- Second, from PBU analysis the storage coefficient value in the order of 0.1 estimated for PM5 using Eq. 1-8 and Eq. 1-26 requires aperture values in the order of 20 cm, which is quite unrealistic and generates a huge uncertainty in the dual permeability behavior, see Figure 1-25.

  As a reference, theoretical values for fracture porosities are 0.01% for apertures of 0.005 cm as showed in Figure 1-48 with apertures in the order of 50 microns.

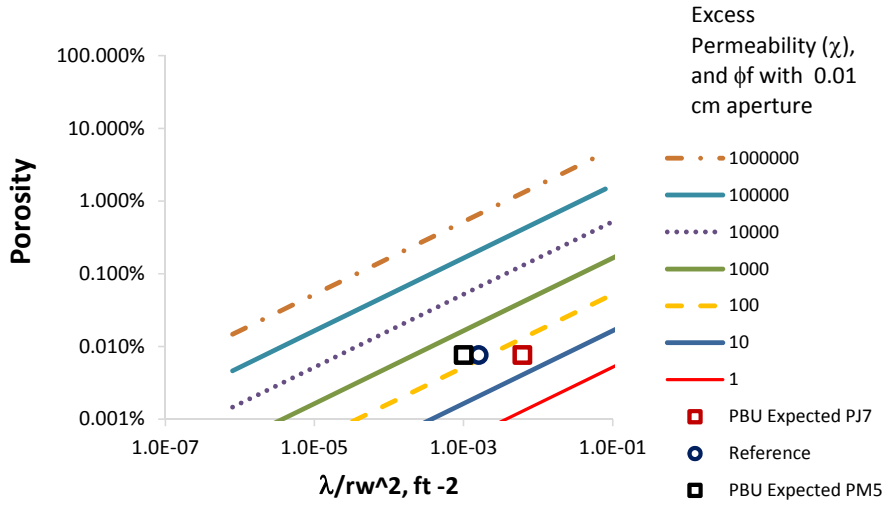

Figure 1-48. Theoretical Inter-porosity and Porosity with different Excess Permeabilities with a Selected Aperture.

Table 1.1 shows the inferred values for □ and □ from the only 2 PBU interpretations, using the average information from Section 1.3.5.2 (Fracture Spacing) and Section 1.5.3 (matrix porosity and permeability) to infer the fracture porosity and permeability using the output interpreted data:

Table 1.1. Estimated Fracture Factors and Parameters.

Well	PJ7	PM5	Comments
Inter-porosity coefficient, □, ft	$1.2x10^{-6}$	$2.5x10^{-7}$	From PBU interpretation **[33,34]**
Storage coefficient,□□	0.001 - **0.01** - 0.05	**0.09** - 0.12	From PBU interpretation **[33,34]**
KH, md	1000	5500	From PBU interpretation **[33,34]**
□m, fraction	3.5%	3.5%	From Logs, Figure 1-36
Shape Factor, □	$2.6x10^{-4}$	$3.1x10^{-4}$	From Eq. 1-20
Spacing (Lx) Estimated, ft	125	115	From Eq. 2-13
□f estimated	0.035%	0.35%	From Eq. 1-22
Aperture Estimated, cm	2	20	From Eq. 1-8
km assumed, md	0.1	0.1	From Figure 1-36
kf estimated, md	2.7	16	From Eq. 1-12
Excess Permeability, kf/km	27	160	From PBU and Logs/cores
Radius where DPDP begins, ft	252	670	From PBU interpretation **[33,34]**
End of wellbore storage, hr	1	0.3	From PBU interpretation **[33,34]**

Perez and Herrera **[37]** in 2015 build a gas condensate and a dual porosity/dual permeability single well reservoir simulation model to understand possible pressure derivative responses, see Figure 1-49. The sector model simulation highlights some important observations, such as:

1) The characteristic natural fracture behavior is shown at earliest times, < 1 hr.

2) Comparing the measured PBU data (see Figure 1-46) with the dual porosity/dual permeability sector model behavior (see Figure 1-49), the dual porosity/dual permeability behavior could be hidden by the wellbore storage, which has a period of around ~1 hr.

4) In order to have high fracture porosities (near 1%), it is required to have a low spacing between the fractures (high fracture density), see black line with circles and its relationship with Eq. 1-23 and Eq. 2-13).

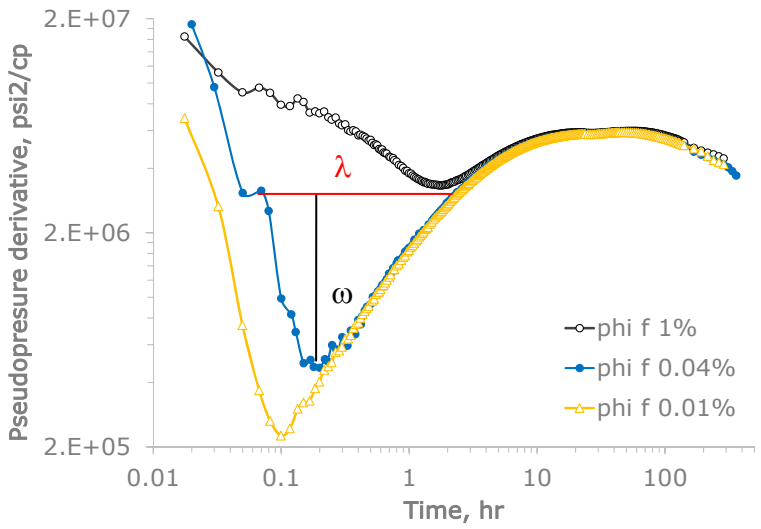

Figure 1-49. PDM Sector Model - Pressure Transient Simulation Analysis (from Perez et al., 2015).

1.6 Fluid Characterization

One of the importance of modeling the compositional fluids is to capture the mobility of the fluids under different pressure regimes (e.g in a blow down or a gas injection processes). Huge changes in the oil and gas saturations, viscosities and densities when the pressure changes in these systems.

The Ecuacion of estate was calibrated by Several CCE (Constant Composition Expantion), CVD (Constant Volume Depletion), Multi-stage separator, swelling and backward multicontact tests with hydrocarbon gas **[38]**.

To represent the changes in compostion with depth it was generated the compositional gradients for each compartmet. The following items show a very brief description of the fluid properties for Pauto Complex and Floreña fields.

- **Pauto:** In general terms, Pauto is a gas condensate system that has different sheets (compartments) with an average yield of 140 stb/MMscf.

  Dele is the only sheet that suggests a possible volatile oil section. Figure 1-50 shows an example of the Constant Composition Expansion (CCE) match obtained with an adjusted EoS. This figure also shows some selected oil and gas parameters from the CVD.

  Figure 1-50 also shows that the maximum liquid drop out of 20%. This liquid drop out generates a reduction in almost 50% in the gas relative permeability highlighted with the arrows in Figure 1-42 and Figure 1-43.

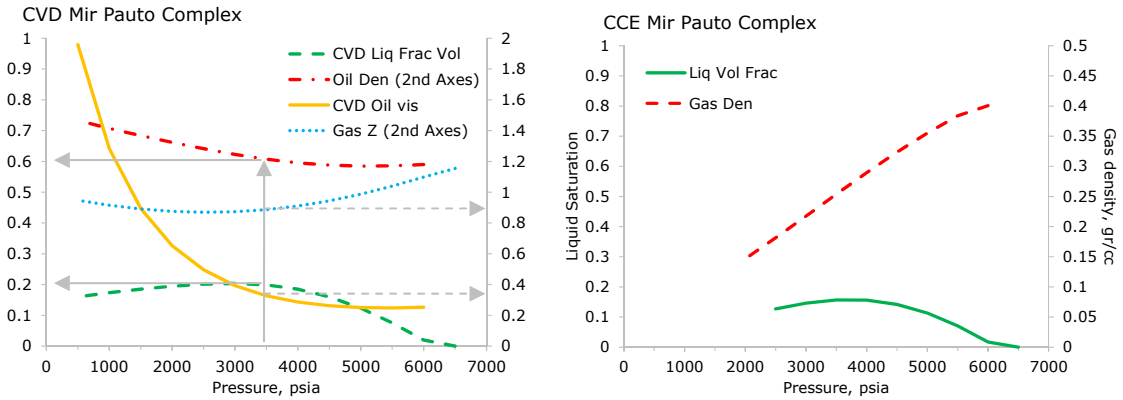

Figure 1-50. Pauto Complex General Match (left) and Fluid Properties (right).

- **Floreña:** This field has 3 reservoirs, see Figure 1-6.

  Mirador is a gas condensate with a similar yield to Pauto.

  Barco is a little more complex than Mirador, as it has a strong compositional gradient with depth. Barco has a gas condensate cap with an average yield of 192 stb/MMscf and a volatile oil section with a Solution Gas (Rs) of ~2530 stb/scf.

  Guadalupe contains a volatile oil with a Rs of ~1785 stb/scf.

  Figure 1-51 shows the compositional gradient currently available for Floreña field. Guadalupe (red line) shows a higher degree of under-saturation compared with Barco (blue lline).

  The EoS is matched with several PVT tests **[38]**. It was selected for the gas condensate zone, a CCE graph (right side figure) which shows the gas density (red line) change with the liquid drop out, this happens due to a loss of heavy components in the gas phase. For the oil section (light dashed green line)[28] there is a huge change in oil viscosity (yellow line) when the pressure drops below the bubble point, meaning that there is significant gas libetation from the oil.

[28] One of the factors that seem to affect the fluid distribution in Floreña field is that Floreña structure is much more fractured than Pauto Complex), which probably helped to generate a volatile oil section with a gas retrograde cap, see Figure 1-13

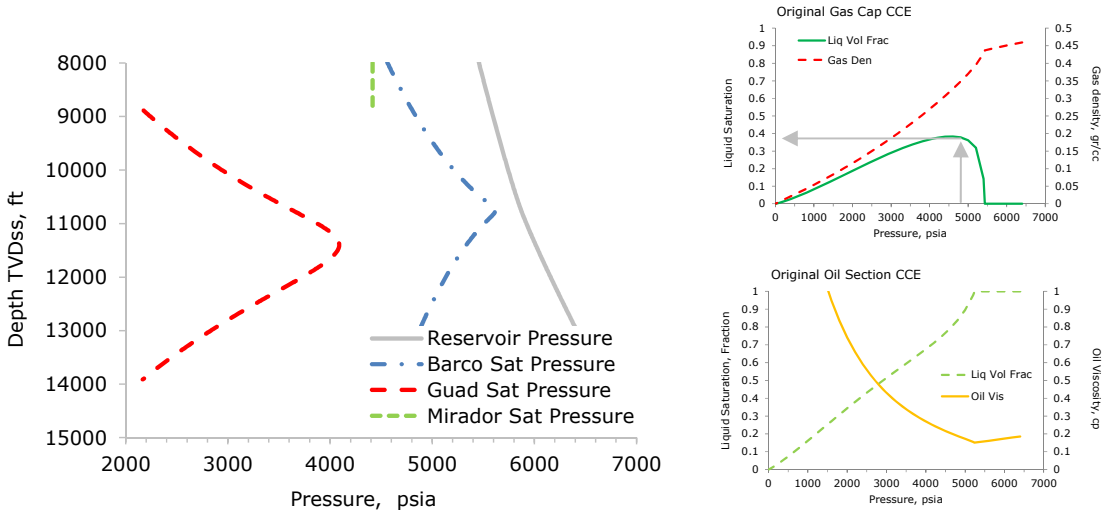

Figure 1-51. Floreña General Fluid Properties.

1.7 Production Mechanism

More than just highlighting the production history and events, it was selected some specific observations about Piedemonte production which made them particularly attractive to study the effects of natural fractures.

Production, geology and reservoir engineering integration for Pauto and Floreña helps to understand the fields by integrating pressure measurement, production/injection, tracer analysis and seismic attributes interpretation.

- **Pauto**. Different sheets and reservoirs in Pauto show different production mechanisms like:

There is a correlation between the water production and the fracture's orientation, also there is an observable correlation where closer the well is to an aquifer higher is the water production[29], see Figure 1-52.

[29] Other Fields located in this trend show that even if the wells are closer to the aquifer, the water production does not increase through time due to the fracture orientation (e.g Cusiana in the middle of the structure **[40]**).

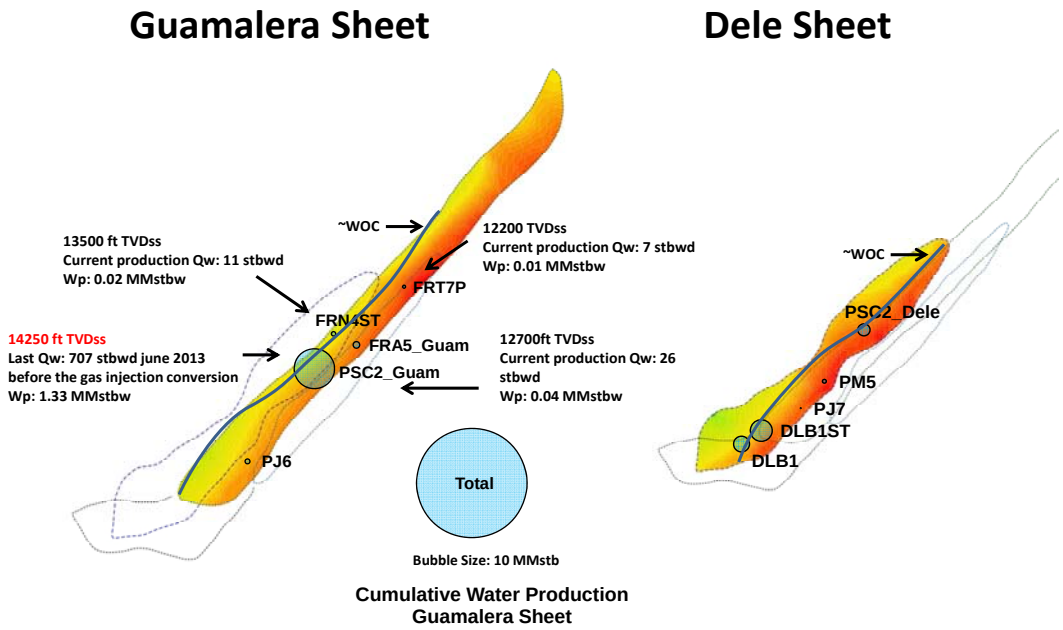

Figure 1-52. Pauto Water Production.

Injection/production Analysis: A weak correlation in the volumetric sweep from the injector and the producers has not been observed up to date (2016), see Producer 1 and Producer 2 in Figure 1-53.

Figure 1-53 highlights with an arrow the only tracer detection in Pauto field that was detected between the gas injector and the producer 1. This suggests a probable orientation of the higher transmissibility fractures being NW-SE (Familiy 1 and 2 presented in Figure 1-20). The tracer's velocity was **~2 ft/day (0.0008 cm/sec)**, which is very low compared to Floreña tracer's velocity: **~89 ft/day (~0.0315 cm/sec**).

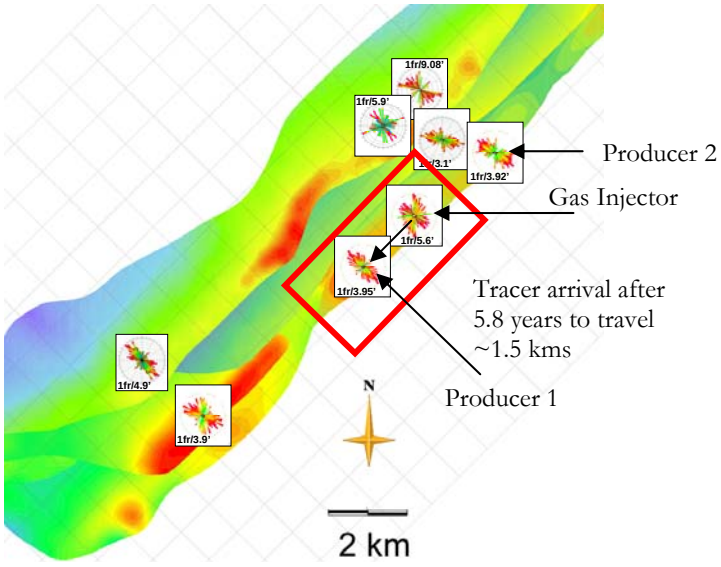

Figure 1-53. Pauto Tracers.

Micro-seismicity data **[39, 40]** has been used combined with the critical stress fracture theory **[11]** to explain why this weak connectivity is happening between the injectors and producers in Pauto. Figure 1-54 shows a preferential path in the maximum stress direction[30], which in some way helps to increase the displacement efficiency.

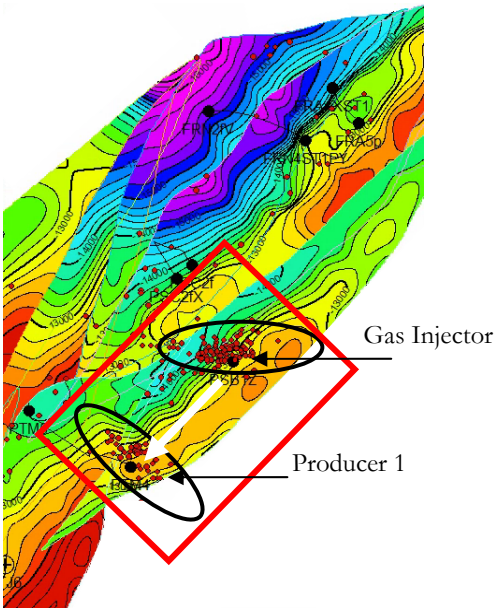

Figure 1-54. Pauto Complex Micro-seismicity.

Pressure build ups (PBUs) shows that there is a pressure support between the injector and producer 2 but the tracers have not been detected meaning that only pressure support is happing in this area. Also as presented in Section 1.5.5, the pressure derivative does not show the characteristic dual porosity/dual permeability shapes.

In the context of low or tight sand pressure behavior for Pauto, the pressure transient wave moves 1,000 times slower than one performed in a 100-md reservoir in a gas reservoir with a permeability of 0.1 md, this means that the pressure support (e.g pressure transient analysis) will be faster than the displacement (e.g tracer analysis).

- **Floreña**

Figure 1-55, Figure 1-56 and Figure 1-57 shows the analysis of the same pair of producer/injector in Floreña field.

Correlation between the water production and the fractures' orientation: A characteristic water production in the flank well (Producer 3) of Barco and Guadalupe (see Figure 1-60) shows that the production increases rapidly but then stabilizes at 1300 stbwd, this behavior suggests a typical fracture communication with the aquifer which is related to the water constant production rate due to a constant pressure drop between the aquifer and the producing well.

[30] Refers to M. Zback **[11]** for further information about the global stress regime maps.

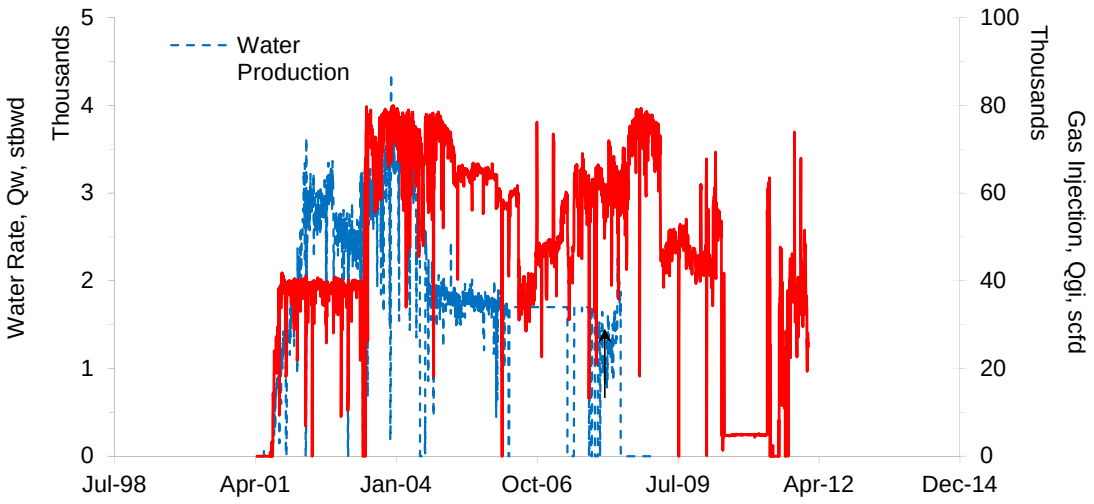

Figure 1-55. Floreña Water Breakthrough.

Injection/production Analysis: Southern wells of Floreña have a strong displacement communication, this behavior shows a high correlation between the injected gas and the produced fluids, see Figure 1-56.

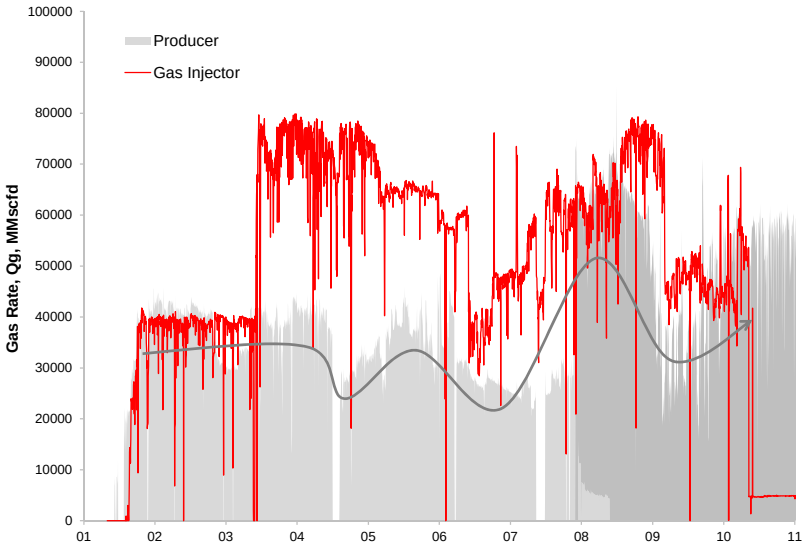

Figure 1-56. Floreña Correlation between Injection/Production.

Micro-seismic events in the injector were not detected (lack of geophones) so, tracers have been used to detect the connectivity between the injectors and producers, see Figure 1-57. The average travel velocity of the tracer is 89 ft/day (0.0315 cm/sec). This travel velocity is too high compared with other fields like Cusiana which has a travel velocity range between 5-10 ft/day.

These tracers seem to be controlled by a series of discontinuities oriented from NW-SE between injector 2 (Crestal well) and Producer 3 (Flank well), see right side graph in Figure 1-57.

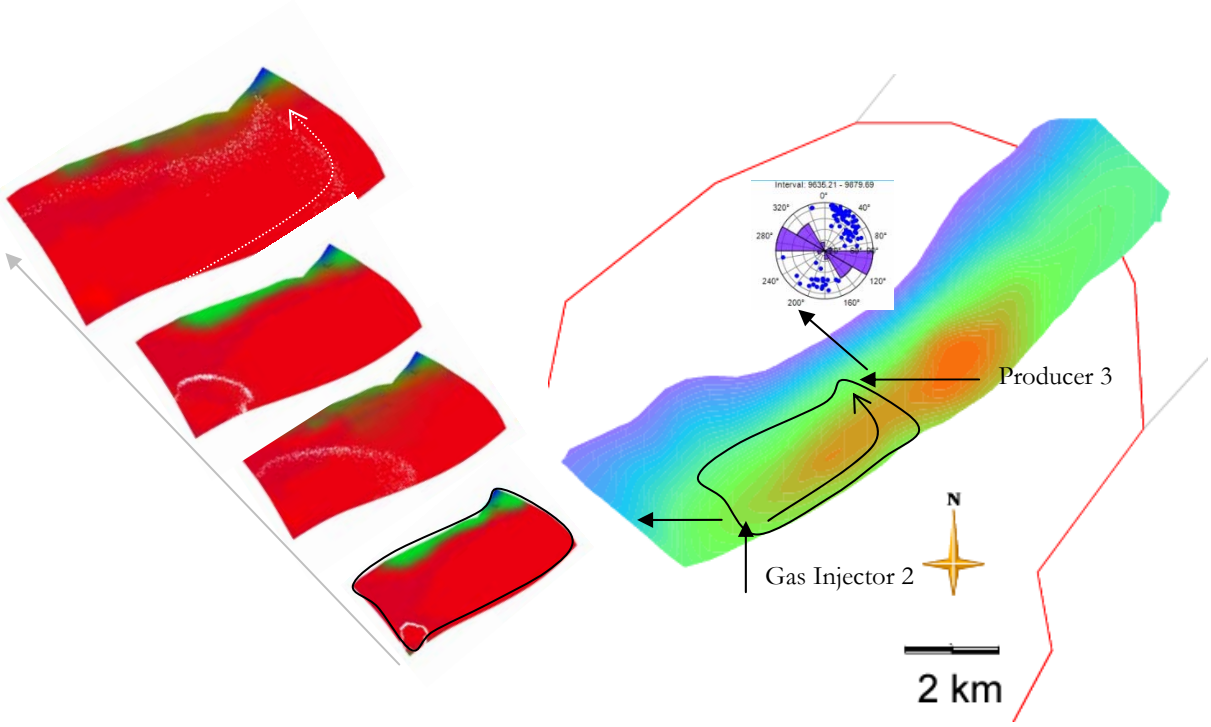

Figure 1-57. Floreña Tracers.

Pressure build ups (PBUs): Figure 1-58 shows the radius of investigation reached after 12 hours for different wells in Pauto and Floreña and its relationship with the KH. This radius can be as high as 100 mts.

The correlation that is presented uses the classical equation of the radius of investigation (r_{inv}) from pressure transient analysis theory. The correlation uses an average net thickness of 250-500[31] ft for the upper and lower trends respectively, which is the possible KH range that could represent the matrix system as an initial approach.

$$r_{inv} = \frac{0.029 \cdot 0.3048}{1000} \cdot \sqrt{\frac{k_t t}{\phi_t \mu c_t}} \qquad 1\text{-}27.$$

Where

t : is in hours
k_t : is in md.
μ : is in cp.
r_{inv} : is in km.
c_t : 5.5×10^{-4} (assuming a c_g : 6×10^{-4} psi^{-1}, and c_f : 6×10^{-6} psi^{-1}).

[31] Using simple average values: Lowest KH matrix was estimated with k * h gross * NTG = 1 md * 500 ft * 1 = 500 md.ft,

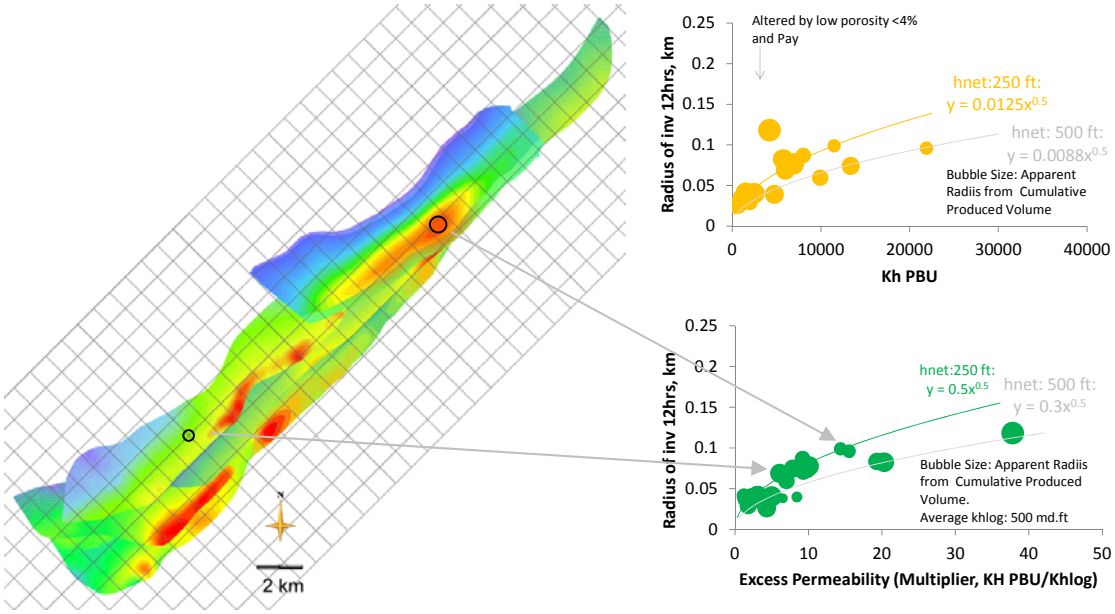

Figure 1-58. Drainage Radius vs. Excess permeability.

As reference, the Figure 1-15 shows the possible amount of fractures that a pressure transient test could capture in 12 hours in a radius of investigation of 100 mts.

1.8 Summary and Conclusions

Though this chapter it was presented the geological, petrophysical, fluids and production analysis to show a complete reservoir characterization. The following aspects are highlighted:

1. It is proposed a new theoretical correlation to estimate the fracture porosity and the fracture spacing with different fracture apertures see Figure 1-19.

   The correlation assumes a vertical well and uses the number of critically stressed fractures, the dip of the fractures and the thickness of the structure, see Figure 1-18.

   This approximation helps to delimit and constraint the fracture petrophysical parameters and is used in this study as a key piece of information to perform the quality control for the spacing in the reservoir simulation model.

2. To check for consistency of the Inter-porosity (□) and storage coefficients (□) for a dual porosity/dual permeability system it was added 2 additional steps in the workflow in the PBU analysis. The steps 1st uses the theoretical Inter-porosity and Spacing equation that links different Excess Permeabilities, and 2nd step uses the theoretical Inter-porosity and Porosity equation that links different Excess Permeabilities with a Selected Aperture.

   The Inter-porosity (□) and storage coefficients (□) from PBU interpretations as a natural fracture system are the order of $1x10^{-6}$ and 0.1 respectively which means that it is required the excess permeability (χ) to be ~10.000 with apertures in the order of 2 to 20 cm. Those interpretations are not consistent with the theoretical fracture porosities ranges from 0.02%, see Figure 1-19.

3. It was included a workflow to link the capillary pressure, pore throat radius and diameter with the flow and gas trap saturation. The importance of this workflow is that it gives the ability to build a reservoir simulation model either for injection or for a full depletion case, see Section 1.5.2.

   By using drainage capillary pressures it was possible to infer the 3 important parameters that affect the fluid flow in the matrix: 1) It was estimated the Corey exponents of 2 and 5 for the water relative permeability for in Pauto and Floreña fields respectively, see Figure 1-44. 2) It was estimated an average maximum gas trap saturation of 40%, see Figure 1-34. 3) It was inferred that almost all the flow behavior in the matrix is conventional, see Figure 1-32 and Figure 1-33.

4. A window between the initial water saturation of 10% and 30% of the slip flow (unconventional modeling) threshold was identified using the dimensionless Knudsen Number combined with the capillary pressures for Pauto field, see Figure 1-32. Above 30% of the wetting phase saturation, the flow is continuous (Darcy flow) even if the permeabilities are lower than 0.1 md.

5. A window between the initial water saturation of 21% and 34% of the slip flow (unconventional modeling) threshold was identified using the dimensionless Knudsen Number combined with the capillary pressures for Floreña field, see Figure 1-33. Above 34% of the wetting phase saturation, the flow is continuous (Darcy flow) even if the permeabilities are lower than 0.1 md.

6. The correlation used for the gas trap saturation underestimates this end point up to 0.2 fraction units where matrix porosities are below 50%, see Figure 1-34.

7. A correlation between a critically stressed fracture distribution and the excess permeability decreasing with depth was found. This correlation could be related to the structural deformation concept, where the current shallowest formations have a higher and much more complex deformation history (i.e Floreña field) compared with current deeper formations (i.e Pauto sheets), see Figure 1-13.

8. Even if low natural critically stressed fractures are present in each well (between 5 to 30 fractures/well, see Figure 1-12), the high dip (80^{o}, see Figure 1-16) make them almost vertical, which directly reduces the spacing (see Figure 1-18). This condition generates relatively fracture porosities in the order of 0.02%, see Figure 1-19.

9. Preferential fracture orientation NW-SE combined with Injection/Production analysis could explain why tracers that travel between injectors and producers have a faster response in Floreña (113 cm/sec, see Figure 1-57) compared to Pauto Complex field (0.0008 cm/seg, see Figure 1-53). This has a direct effect on oil and gas production, and pressure support related to the gas injection performance in both fields, as the injection along the strike direction in Pauto seems to delay the gas breakthrough in the producers.

1.9 References

1. J. GILMAN ET AL. A New Classification Plot for Naturally Fractured Reservoirs. Canadian Unconventional Resources Conference. SPE 146580. Alberta, Canada. 15-16 November 2011.

2. R. LINARES ET AL. New Insights into the Piedemonte License Triangle Zone in the Llanos Foothills – Colombia. X Simposio Bolivariano Exploración Petrolera en Cuencas Subandinas. ACGGP. July 2009.

3. C. PALENCIA AND J. ALZATE. Petrophysical Data Review. Equion Energia LTDA. Internal Report. C, Colombia. August 2011.

4. C. PALENCIA ET AL. Building a Petrophysical model for a Low Porosity and Highly Tectonized Reservoir. Field Case: Pauto Complex – Colombia. Society of Petrophysicist and well log analysis. SPWLA. Cartagena, Colombia. 2012.

5. R. JOLLY Floreña Fracture Characterization and Modeling. Equion Energia LTDA. Internal Report. Bogota, Colombia. October 2002.

6. S. ALAVIAN. VLC2 Well Test History Matching, Equion Energia LTDA. Internal Report. Bogota, Colombia. PERA. Trondheim, Norway. June 2013.

7. T. BRATTON ET AL. The Nature of Naturally fractured Reservoirs. Oilfield Review. Denver, USA. 2006.

8. M. COOPER ET AL. Development and Tectonic History of the Llanos Basin, Eastern Cordillera, and Middle Magdalena Valley, Colombia.. The American Association of Petroleum Geologists. AAPG Bulletin, V. 79, No. 10, pg. 1421–1443. October 1995.

9. F. SAVINI ET AL. Active-hide-related Deformation and its Role in Hydrocarbon Exploration and Development-insights from HCA Modeling. Dipartimento di Scienze Geologiche, Univesita. AAPG Memoir 82, pg. 453-472., Roma Tre, Rome, Italy. 2004.

10. G. MESA ET AL. Estudio Petrológico de 27 Secciones Delgadas De Los Pozos Floreña N2f, Floreña N4, Floreña A5, Pauto Sur B1, Pauto Sur C2 Y Volcanera C2z Formaciones Barco Y Mirador Cuenca De Los Llanos. Equion Energia LTDA. Internal Report. Piedecuesta, Santander, Mayo 2002.

11. M. ZOBACK. Reservoir Geomechanics. Department of Geophysics, Stanford University. 2007.

12. C. LOPEZ AND J. MARIN. Critically Stressed Fractures in PDM. Equion Energia LTDA. Internal Report. Bogota, Colombia. 2014.

13. G. COBALEDA. Geometria Poral en Corazones. May 2002. Ecopetrol y Equion Internal Report. Bogota, Colombia.

14. C. LOPEZ. Aplicabilidad del daño Geomecánico para el Complejo Pauto y Floreña. Equion Energia LTDA. Internal Report. Bogota, Colombia. May 2015.

15. J. ALZATE. Pauto Fractures. Well Comparison. - Mirador Formation. Equion Energia LTDA. Internal Report. Bogota, Colombia. 2012.

16. S. LOPERA, A. RESTREPO, A. OCAMPO. Use of Divergent fluids as an Alternative for Enhanced Recovery in Naturally Fractures Cores. SPE 122061. Cartagena, Colombia. June 2009.

17. N. BARTON, S. BANDIS AND K. BAKHATAR. Strength, Deformation and Conductivity coupling of rock Joints. Int. J. Rock Mech. Min. Sci. & Geomech. Abstr. Vol. 22, No 3. pg. 121-140. 1985.

18. M. MOGOLLÓN. Determinación de Compresibilidad del Volumen Poroso a Muestras de Los Pozos Floreña 2nf, A5, 4n, Pauto Sur B1, C2 y Volcanera C2. Equion Energia LTDA. Internal Report. ICP. Marzo 2002.

19. R. BAKER ET AL. Canadian Bakken IOR/CO2 Pilot Projects. Presented at 20th Annual CO2 Flooding Conference. Midland, Texas, USA. December 11-12, 2014.

20. R. NAZARI. Nano and Micro Gas flow Measurement and Prediction. Unconventional Gas and Gas-condensate Recovery Studies. Heriot Watt University. Edinburgh, Scotland. 14-15 May 2015.

21. Guidelines for Application of Petroleum Resources Management System. Sponsored by SPE, AAPG, WPC, SPEE, and SEG. November 2011.

22. L. ZHANG ET AL. Development of a New Compositional Model with Multi-Component. Journal of Natural Gas Science and Engineering. Elsevier. October 2014.

23. V. GOLF-RACHT. Fundamentals of Fractured Reservoir Engineering. Amsterdam: Elsevier Scientific. Amsterdan – Oxford – New York. 1982.

24. C. KOSSAC. Simulation of Naturally Fractures Reservoirs. Oil Recovery Mechanisms and Numerical Simulation. Houston, USA. March 2005.

25. R. DEAN ET AL. Simulations of Naturally Fractured Reservoirs. SPE 14110-PA. May 1988.

26. J. THOMEER. Introduction of a Pore Geometrical Factor Defined by the Capillary Pressure Curve. SPE 1324-G. Dallas, USA. Oct. 4-7 1959.

27. J. CLAVIJO. Pauto and Floreña Capillary Pressure Match with Thomeer Correlation. Equion Energia LTDA. Internal Report. Bogota, Colombia. 2013.

28. A. DANESH, D.H TEHARNI, M. JAMIOLAHMADY ET AL. Gas Condensate Recovery Project - Final Report, pg 3.54. Heriot Watt University. Institute of Petroleum Engineering. Edinburgh, Scotland. 2002 – 2005.

29. F. AKINDELE ET AL. Enhanced Gas Recovery from Water-Drive Reservoirs-Methods and Economics. SPE 11104. 1982.

30. T. BLASINGAME. The characteristic flow behavior of Low-Permeability Reservoir systems. Texas A&M University. SPE Unconventional Reservoirs Conference. SPE 114168. Keystone, USA. 10-12 February 2008.

31. H. GODA. Using a Modified Brooks-Corey Model to Study Oil-Water Relative Permeability for Diverse Pore Structures. SPE 88538. October 2004.

32. M. HONARPOUR, ET AL. Relative Permeability of Petroleum Reservoirs. Second Edition, Florida, U.S.A. pg. 16 - 19. 1987.

33. L. PEREZ. Integration of Well Test Analysis into Naturally Fractured Reservoir Simulation. Submitted to the Office Of Graduate Studies of Texas A&M University in Partial Fulfillment of the Requirements for the Degree of Master of Science. Austin, USA. August 2005.

34. F. ESCOBAR. Interpretación Prueba de Restauración de Presión Pozo Pauto M5. Equion Internal Report. Bogota, Colombia. Octubre 14 de 2012.

35. F. ESCOBAR. Interpretación Prueba de Restauración de Presión Pozo Pauto J7. Equion Internal Report. Bogota, Colombia. Septiembre 26 de 2013.

36. J. GILMAN. Practical Aspects of Simulation of Fractured Reservoirs. International Forum on Reservoir Simulation. Littleto, pg. 15, CO, USA. June 23-27 2003.

37. B. PEREZ, C. HERRERA AND C. LOPEZ. Single Well Reservoir Simulation Considering: compositional effects, dual porosity/dual permeability and geomechanical modeling. Equion Energia LTDA. Internal Report. Bogota, Colombia. 2015.

38. S. MARTINSEN AND C. WHITSON. Pauto Complex Fluid Characterization and fluid Initialization. PERA. Equion Energia LTDA. Internal Report. February 2009.

39. E. RIVERA. Micro-sismicidad Aplicada al Monitoreo de Yacimientos Sometidos a la Inyección de Fluidos. Tesis de grado Universidad Industrial de Santander. Bucaramanga. 2013.

40. J. OSORIO. Correlation between micro-seismicity and Reservoir Dynamics in a Tectonically Active Area of Colombia. SPE 115715. Denver, USA. September 2008.

41. R. BEAUHEIM. Well testing in fractured media: flow dimensions and diagnostic plots. Journal of Hydraulic Research Vol. 42 Extra Issue, pg. 69-76. 2004.

2. MODEL DESCRIPTION

2.1 Introduction

The scope with the construction of this reservoir model was to model Pauto Complex and Floreña fields as dual porosity/dual permeability reservoirs to estimate the anisotropic fluid flow behavior compared to the conventional single porosity modeling (SP –equivalent model–) and its impact in the oil-gas and water production predictions. A commercial software tool was used to include several features of this complex system as a first step towards the understanding of the impact natural fractures have on these fields.

In spite of knowing that other approximations could in theory be much more rigorous, like using a discrete fracture modeling, they will bring certain limitations, as those models require high and enough quality data to map the discrete fractures and may require high processing time, which is not possible in PDM fields due to a low quality seismic data, see Section 1.3.

The static and dynamic integration is a key part prior building a fit for purpose reservoir model. For this case, The dual porosity/dual permeability model (DPDP) was found to give enough initial resolution to handle aspects such as the high uncertainty in the structures, the amount of natural fractures going from micro-fractures to meso-fractures, the number fluid pseudo-components (12 pseudo-components) and the understanding of production/ injection/pressure changes during a stable process (middle production region).

Initially, the shape factor was considered to be constant in this work, but this restriction was eliminated by adding a concept that links the fracture properties to create a simple but practical equation and methodology which helps populate the consistent DPDP model, see Eq. 2-44 and Figure 2-19.

The method is based on finding the fracture spacing and apparent aperture -e_0- that match the excess permeability (see Figure 2-27), which affects fracture porosity estimations. It was found that the high critically stressed fracture intensity created in the model (see Figure 2-21) is related to high fracture dips, which generates theoretical fracture spacing lower than 10 ft, see Figure 2-23 and Figure 2-24.

This methodology proved to tie well different field production behaviors while keeping as simple as possible the natural fracture description, see Section 2.7.2.2. It was found that even if the production and pressure match between the SP and DPDP where very close, 2 main differences in the modeling were observed: 1) a higher vertical condensate segregation generated in the fracture system compared with the single porosity system (see Figure 2-36 and Figure 2-39) and 2) a high reduction in the mobility of the liquid drop out generated in the matrix (see Figure 2-37) compared with the single porosity system.

2.2 State of the Art

It was assumed that the nitrogen injection process in Piedemonte fields (Pauto Complex and Floreña) will be impacted by the naturally fractured system. Following the identification of the previous aspect, some relevant studies related to nitrogen injection and modeling of naturally fractured reservoirs were selected:

There is an extensive work in compositional modeling which cannot be explained in detail through this chapter. Whitson and Brule **[1]** present a detailed work about compositional characterization, PVT behavior and gas injection processes, which are then emphasized by Castillo and Montoya **[2]** describing the fundamental equations to build a compositional simulation model.

A. Castillo and J. Montoya **[2]** in 2003 developed a full description of a compositional reservoir simulation model in cylindrical coordinates with the purpose of studying the condensate banking effect. One of the relevant conclusions remarks the strong influence of the absolute permeability on the pressure behavior, which directly affects the evolution of the condensate bank and the deliverability of wells.

Through time, several authors have worked on naturally fractured systems. Barenblatt in 1960 proposed the first continuous dual porosity model and then it was adapted by Warren and Root **[3]** in 1963 for petroleum industry applications. The Warren and Root model describes the matrix as a source of fluids to the fracture and then the fracture transports the fluids to the well. Several other modifications, upgrades and new theories have been done and published by Sahimi **[4]** in 2009, including single fracture models, network models, fractal models, discrete models, mechanical models, percolation models and lattice models.

Beliveau et al. **[5]** in 1961 highlighted two important drivers that control the recovery factor: 1) the magnitude (anisotropy) and heterogeneity of the fracture permeability and 2) the connection between the matrix and the fracture (i.e the shape factor).

Then Ringen et al **[6]** in 2005 performed a brief summary on the importance of fracture aperture in capillary continuity. He reported that Saidi A. M in 1987 found that a maximum aperture of 0.05 mm was necessary to achieve capillary continuity, and then Sajadian et al in 1998 found that by increasing the apertures of the fractures from 0.5 mm to 2.6 mm, hydrocarbon recoveries were reduced.

Bratton **[7]** in 2006 and then Utria **[8]** in 2007 presented a methodology and workflows that integrate the geological understanding of the intrinsic variables that govern natural fractures in the reservoir (e.g fracture spacing, distribution, aperture) with the reservoir engineering work in order to understand the effects that fractures have on decline rates, productivity and injectivity, among other aspects. They highlight that empirical correlations using petrophysics (e.g rock and facie characterization) and geology (e.g structural shape and history, and curvature maps) are required to understand the drivers that generate conductive natural fractures.

Ayala et al **[9]** in 2009 did a reservoir simulation analysis for a gas condensate in a natural fracture system. They concluded that fractures has a much higher depletion rate than the matrix does, having a high liquid dropout in the fracture. The matrix generates liquid drop out around it, generating a fluid blockage inside, thus affecting the recovery factor. This outcome can be much more drastic when the matrix has very low permeability; in these cases, molecular diffusion could play a more important role compared to the hydraulic pressure diffusion within the matrix and fracture.

Later Amudense **[10]** in 2012 studied the effect of capillary pressure and relative permeabilities in natural fractures, where the balance between the capillary and gravitational forces determines the distribution of fluids. He concluded that with X-shaped fracture relative permeabilities, the oil sweep is less uniform. Furthermore, the gas-oil capillary pressure could even duplicate the oil sweep.

Mun-Hong **[11]** in 2013 described a very complete work comparing the dual porosity and dual permeability (DPDP) model with the discrete fracture-matrix model (DFM). Some important observations included that, if good geological information is available, it is better to build a DFM rather than a DPDP model, as it gives the most accurate results. DPDP tends to homogenize more the fluid flow compared to DFM, generating large errors in production's composition behavior.

For more than 45 years, the petroleum industry has been developing several reservoir simulation software tools with the aim of modeling different geological shapes, petrophysical characteristics and fluid-rock interactions with complex physics and mathematical solutions and strategies.

Akand **[12]** presents a review of ten standard SPE comparative studies that have been done for different cases and with different software vendors (e.g VIP, CMG, Nexus, Eclipse, Sensor among others). The selection of the reservoir simulation software depends on several user factors, such as 1) the surface and subsurface coupling, 3) the cost, 4) the speed, 5) and the robustness to capture the rock and fluids' physics.

Following the five previous five criteria, Nexus^{R} Reservoir Simulation Software was selected, which claims to have significant improvements compared with prior generation simulators **[13]**, including the gridding, phase behavior of compositional fluids, the dual porosity and dual permeability modeling and the reservoir and surface network conectivity.

2.3 Conceptual and Physical Model

Since there is a wide range in natural fracture scales and a high uncertainty related to the structural shapes/sizes and the relationship between the rock types and the structural models (see Section 1.4 and 1.5), a dual porosity/dual permeability model comes to be an approximation that helps to handle the uncertainty **[5]**.

- **Conceptual Model.**

The conceptual model based on Chapter 1 shows 7 main aspects:

1. Fracture density is higher when curvature is higher.

2. Deeper the structure is, lower is the critical stressed fracture intensity, see Figure 1-13.

3. Main fractures that contribute to the flow are conjugate and almost vertical (80^o), see Figure 1-16. This has a high impact in the fracture vertical permeability, porosity and fracture spacing that probably generates some fluid segregation.

4. Higher permeability in the E-W direction compared to the S-N direction seems to be one of the reasons for low tracer velocities in Pauto, late breakthrough times and better displacement, see Figure 1-53.

5. Gas Trap Saturation has a major impact in the fluid flow due to low porosities (Figure 1-34).

6. There are leaner gas condensate fluids in Pauto compared with Floreña, see Section 1.6.

7. Wells are aligned almost to the axes as the structures are narrow, see Figure 1-52.

- **Physical Model.**

The following items present the identified assumptions and limitations that will ultimately condition the results of the mathematical model (differential model). For this case the assumptions are:

1. Water Oil Capillary Pressures are included.
2. Gravity effects are included. The matrix is considered to be in capillary equilibrium as the horizontal fractures are few; the main fractures are vertical with small apertures.
3. Two phase compositional fluid flow (oil and gas) and one phase (water) are considered with a volumetric approach (water considered to be inert).
4. Single and dual porosity/dual permeability modeling.
5. Flow in 3 dimensions in Cartesian coordinates.
6. Variable grid size cells in x, y and z to represent the structures.

7. Porosity and Permeability Heterogeneity grid population.
8. Newman type boundary conditions (no flow in the boundaries – closed system).
9. Fluid compositional grading is included.
10. Driver Mechanism: Fractures that contribute to the fluid flow are only related to curvature maps which are matched to flow capacities from PBU information.

The limitations of this model are:

1. The rate dependent correlation for the oil and gas relative permeability is not included **[14, 15, 16]**.
2. Neither Hysteresis nor imbibition in gas-oil capillary pressure changes was included.
3. Geomechanical dynamic modeling[32] is not included.
4. Other Driver Mechanisms to identify fractures that contribute to the flow are not considered due to lack of information like changes in the stresses in every point of the reservoir.
5. Equal and constant rock compressibility and the same for the matrix and fracture systems.
6. No micro-fracture modeling was included. It was assumed that the matrix implicitly contains the micro-fractures[33] properties.
7. Other complex fluid interactions like asphaltenes, dissolution of other phases in water and molecular diffusion phenomena are not included.

2.4 Fluid Flow Mathematical Model

The first step in order to select the physical model comes from the information available to build it, see Chapter 1. As it has been shown, the uncertainty related to seismic (see Section 1.4.2) and rock typing characterization (see Section 1.6) is huge, so the continuous dual porosity/dual permeability (DPDP) modeling approach was selected, rather than the discrete fracture modeling, as the DPDP modeling can handle the uncertainty in a simple way. Also see Appendix A.1, where the equation and models are explained in detail.

The fluid flow model is made of 4 sub-models **[2]**.

- The Molar conservation equation.
- The Momentum equation (Darcy Law).
- The Equation of State (Peng Robinson Equation).
- The Compositional flow equation.
- The Transfer function equation between the matrix and the fracture.

[32] No changes of shape factor with pressure -and time- are considered; no changes in the estimated initial apparent apertures (which impacts the fracture permeability and relative permeability) with changes in stresses – varying pressure with time- either. Even if the geomechanical dynamic modeling was not incorporated, geomechanical static concepts and sensitivities were used, such as fracture orientation, dipping and dip azimuth, which impact the vertical permeabilities, fracture porosities, spacing, shape factors and fluid behaviour.

[33] Please see the stress-strain plot (Figure 1-34) presented in Section 1.5.3.1 for further information about the comparison between the capillary pressures and its relationship with the assumption of micro-fractures.

The assumptions made for oil, gas and water phases are described as follows:

- **For the hydrocarbon phases.**

The differential model begins with the molar conservation equation[34], where the constitutive equations like Darcy's flow equation and the equation of state are included.

This arrangement implicitly assumes that changes in pressure will generate compositional changes that affect the fluid properties, including density, viscosity and interfacial tensions, which directly impact the mobility of oil and gas phases in the porous medium (this cannot be represented with a black oil approximation, especially under gas injection).

- **For the water phase.**

In this case, it is assumed that water could be modeled using the volumetrically (*Bw*), as density changes with pressure are very low compared to the hydrocarbon ones. In addition, water is considered to be an inert phase as it does not interact with the oil and gas phases.

2.4.1 Molar Conservation Equation

The molar balance equation for the i^{th} species in the oil and gas phases is:

$$-\frac{\partial}{\partial x_j}\left(x_i \frac{\rho_o}{M_o}\varphi u_{o,j} + y_i \frac{\rho_g}{M_g}\varphi u_{g,j} \right)_X = \bar{q}_{hci} \pm \bar{q}_{mfi} + \frac{\partial}{\partial t}\left(x_i \frac{\rho_o}{M_o}\phi S_o + y_i \frac{\rho_g}{M_g}\phi S_g \right)_X \qquad 2\text{-}1.$$

where

$\bar{q}$	refers to the rate per unit volume and time.
$\bar{q}_{hci} > 0$	rate for the sink (positive flow for producer wells).
$\bar{q}_{mfi} > 0$	rate from the matrix to the fracture.
$X = m, f$	represent the matrix and fracture spacing respectively.
x_i and y_i	are the molar fractions of component i in the oil and gas phase respectively.
M_o and M_g	are the Molecular Weights for oil and gas phases respectively.
ρ_o and ρ_g	are the density of oil and gas phases respectively.

2.4.2 Momentum Equation (Darcy's Law)

Darcy's law defined the inertia (momentum) effect on the fluid flow, representing the hydraulic flow rate of oil, gas and water.

[34] The molar conservation was selected as it was assumed that no chemical reactions happen in the reservoir.

$$u_j = -\frac{k_j k_d}{\mu_\alpha}\frac{\partial \Phi_\alpha}{\partial x_j} \qquad 2\text{-}2.$$

Where the velocity $v_{\alpha d}$ is function of:

$k_{r\alpha d}k_d$: Effective permeability to α phase.

μ_α : Dynamic viscosity of α phase.

$\frac{\partial \Phi_\alpha}{\partial d}$: The hydraulic potential between the matrix and fracture and the gravitational forces for α phase.

The flow potential of phase α is defined as the sum of the kinetic potentials (Φ_α) given by the hydraulic pressure (P_α) and the gravitational potential $\left(\rho_\alpha \frac{g}{g_c} D\right)$.

With $\Phi_\alpha = P_\alpha - \rho_\alpha \frac{g}{g_c} D$

2.4.3 Compositional Flow Equation

The compositional equation is required to estimate the global composition (Z_i) when the reservoir pressure is below the saturation pressure (dew point or bubble point).

$$\frac{\partial}{\partial x_j}\left[\left(\lambda_{c,j}\right)\nabla P_o + \left(\frac{y_i \rho_g}{M_g}\frac{k_j k_{rg}}{\mu_g}\frac{\partial P_{cgo}}{\partial x_j}\right) - \left(\frac{x_i \rho_o \gamma_o}{M_o}\frac{k_j k_{ro}}{\mu_o} + \frac{y_i \rho_g \gamma_g}{M_g}\frac{k_j k_{rg}}{\mu_g}\right)\frac{\partial z}{\partial x_j}\right]_X = \tilde{q}_{hci} \pm \bar{q}_{mfi} + \frac{\partial\left(\phi \Gamma Z_i\right)_X}{\partial t} \qquad 2\text{-}3.$$

Where

$X = m, f$ represents the matrix and fracture spacing respectively.

Γ is defined as: $\Gamma = \frac{\rho_o S_o}{M_o} + \frac{\rho_g S_g}{M_g}$

$\lambda_c = \lambda_{cx} \cdot \vec{i} + \lambda_{cy} \cdot \vec{j} + \lambda_{cz} \cdot \vec{k}$ is the compositional mobility defined as: $\lambda_{cx} = \frac{x_{io}\rho_o}{M_o}\frac{k_x k_{ro}}{\mu_o} + \frac{y_{ig}\rho_g}{M_g}\frac{k_x k_{rg}}{\mu_g}$

2.4.4 Phase Equilibrium

From Peng-Robison's Equation of State (EoS) applied to this specific case, the required oil and gas densities are calculated from Eq. 2-4.

$$\frac{\partial \rho_\alpha}{\partial t} = c_\alpha \rho_\alpha \frac{\partial p_\alpha}{\partial t} \qquad 2\text{-}4.$$

Where

c_α : is the compressibility factor.
α : is the oil or gas phase.

The phase equilibrium **[2]** also provides the composition inside the matrix and fractures at different pressures, which is critical information to estimate the viscosity, compressibility and saturations.

2.4.5 Saturation Equation

As described by Peñuela **[17]**, the oil and gas phases' saturations are related to the liquid (L) and gas (V) molar fractions with Eq. 2-5 and Eq. 2-6.

$$S_o = \frac{L\rho_g}{L\rho_g + V\rho_o} \qquad 2\text{-}5.$$

$$S_g = \frac{V\rho_o}{L\rho_g + V\rho_o} \qquad 2\text{-}6.$$

Where

S : is the saturation.
V : is the Vapor (gas) molar fraction.
L : is the Liquid molar fraction.
ρ : is the density and subscripts o and g are the oil and gas phases, respectively.

2.4.6 Governing equation for the water phase

Water PVT behavior is assumed to be slightly compressible, with a weak formation volume factor (*Bw*) dependence of pressure. In addition, water is considered to be an inert phase as it that does not interact with the oil and gas phases. The conservation equation for the water phase reads:

$$\frac{\partial}{\partial x_j}\left[\rho_w \frac{k_j k_{rw}}{\mu w}\nabla\Phi_w\right]_X = \bar{q}_w \pm \bar{q}_{mfw} + \frac{\partial}{\partial t}\left(\rho_w \phi S_w\right)_X \qquad 2\text{-}7.$$

2.4.7 Matrix-Fracture Transfer Function Equation

Figure 2-1 shows the classical representation of a natural fracture described by Warren and Root[35] in 1963 **[3]**. Plot 1 (left side graph) shows a representation of the fractured reservoir rock and Plot 2 (left side graph) shows how that reservoir rock is divided in several grid cells. The cells with Δx, Δy and Δz dimensions are then subdivided further to represent the fractured system. The subdivisions are done by using the spacing between the fractures named as Lx, Ly and Lz.

The transfer function is an elegant but simple concept that has the ability to capture implicitly the fluid flow between the matrix and the fracture in which has implicitly included the fracture spacing in a factor named the shape factor. In general terms, the shape factor describes the matrix surface created due to the amount of fractures.

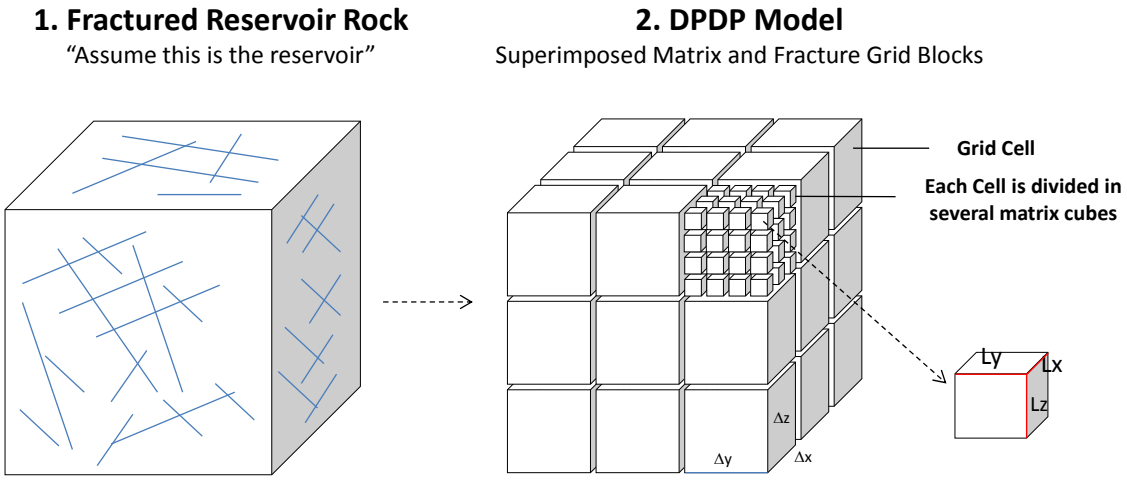

Figure 2-1. Fracture Spacing Conceptual Model (after Warren and Root, 1963).

The basic transfer function between the matrix and the fracture **[19]** is defined by:

$$\bar{q}_{mf\alpha i} = \frac{\sigma}{\mu}\left[P_{f\alpha} - P_{m\alpha} - \gamma_\alpha\left(D_f - D_m\right)\right] \qquad 2\text{-}8.$$

Where:

D	: Depth.
$P_{f\alpha}$	: Fracture pressure of α phase.

[35] Figure 2-1 is the mathematical representation given by Eq. 2-8 which represents the flow between the matrix and fracture that coexists mathematically in the same space.

$P_{m\alpha}$: Matrix pressure of α phase.

γ_{α} : Gradient of α phase.

The extended equation for compositional fluids is given by **[18]**.

$$q_{mf\alpha i} = T_{mf} \frac{k_{r\alpha} x_{\alpha i} \rho_{\alpha}}{\mu_{\alpha}} \left[P_{f\alpha} - P_{m\alpha} - \gamma_{\alpha} \left(D_f - D_m \right) \right] \quad \text{2-9.}$$

Where $q_{\alpha i}$ represents the amount of fluid transferred from the matrix to the fracture due to a pressure gradient between both systems, accounting also for gravitational effects. This flux is function of:

T_{mf} : Transmissibility between the matrix and the fracture.

$k_{r\alpha}$: Matrix Relative permeability of α phase.

ρ_{α} : Matrix Molar density of α phase.

$x_{\alpha i}$: Matrix Molar fraction of *i* component in α phase.

μ_{α} : Matrix Viscosity of α phase.

The transmissibility between the matrix and the fracture is defined as:

$$T_{mf} = C_1 \cdot \bar{k}_{mf} \sigma \cdot \left(\Delta x \Delta y \Delta z \cdot NTG_f \right) \quad \text{2-10.}$$

Where T_{mf} is function of:

$C_1 = 0.001127$: Constant accounting for field units.

$\bar{k}_{mf}$: Average permeability, md.

σ : Shape factor (matrix surface contacted are by the fractures), ft^{-2}.

$\Delta x \Delta y \Delta z \cdot NTG_f$: Net fracture volume, ft^3.

- **The average permeability** has the following function:

$$\bar{k}_{mf1} = \bar{k}_{mf} = \frac{1}{3} \left[\frac{k_{mx} k_{fx}}{k_{mx} + k_{fx}} + \frac{k_{my} k_{fy}}{k_{my} + k_{fy}} + \frac{k_{mz} k_{fz}}{k_{mz} + k_{fz}} \right] \quad \text{2-11.}$$

This can be simplified if $k_{fx} >> k_{mx}$

$$\bar{k}_{mf2} = \bar{k}_{mf} = \frac{1}{3} \left[k_{mx} + k_{my} + k_{mz} \right] \quad \text{2-12.}$$

- **The shape factor** is a mathematical concept that uses the fracture spacing to represent how much the matrix is fractured. This factor impacts the flow transfer between the matrix and the fracture as showed in Eq. 1-10.

  The shape factor is related to the surface area created by the fracture system in 3 directions. Coats Equation **[18]** includes the effect of multiphase flow as follows:

$$\bar{k}_{mf}\sigma = 8\left[\frac{k_{mx}}{L_x^2}+\frac{k_{my}}{L_y^2}+\frac{k_{mz}}{L_z^2}\right]\left(1-\phi_f\right) \qquad 2\text{-}13.$$

  Gilman **[20]** uses the term $k_m\sigma$ as a threshold to identify if the model behaves as a natural fracture system ($k_{mf}\sigma < 0.1$). $k_m\sigma$ was extended to $\bar{k}_{mf}\sigma$ as Eq. 2-12 implies that $k_m \approx \bar{k}_{mf}$.

  Where

  L_x, L_y *and* L_z : represents the rock matrix dimensions in *x*, *y* and *z* directions.

Figure 2-2 shows the conceptual model example for Piedemonte, where:

- Plot 1 shows the grid cells of the model.
- Plot 2 shows one example of the model's grid cell.
- Plot 3 shows a simplified sketch of the cell that has matrix and fractures which is the equivalent graph presented in Figure 2-1.
- Plot 4 shows how the fractured cell begins to have a mathematical description in Δx, Δy, Δz dimensions. As an example, the grid cell has 9 sub-division to represent 3 fractures in the *x* direction, 3 fractures in the *y* direction and 3 fractures in the vertical direction. This is created by introducing the spacing variable L showed in Plot 5.

Plot 4 shows that lower the spacing is, the higher is the fracture density and higher the shape factor (see Eq. 2-13) and higher the transmissibility between the matrix and the fracture (see Eq. 2.10).

Also, lowering the matrix permeability, the shape factor is lower, as well as the transmissibility between the matrix and the fracture Eq.2-13.

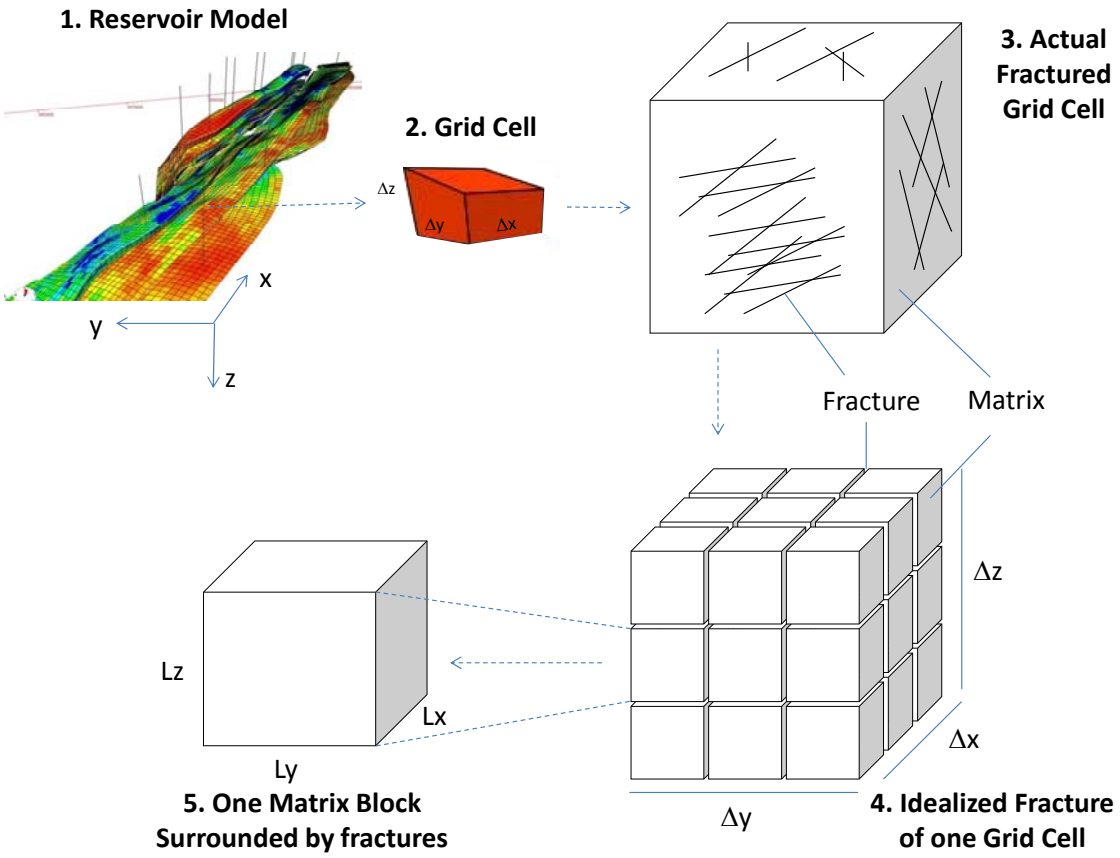

Figure 2-2. Sketch of the Shape Factor (Sigma Factor). Idealized Representation of Fractured Reservoirs (after Warren and Root, 1963).

2.5 Numerical Model

Figure 2-3 shows a flow diagram to solve the system with an IMPES strategy (Implicit pressure Explicit Saturation).

In general terms, the input data is used to solve the Liquid-Vapor Equilibrium. Afterwards, the pressure equation is solved, which internally begins to iterate (internal iterations) until the solution converges and continues to the next time step (external iterations).

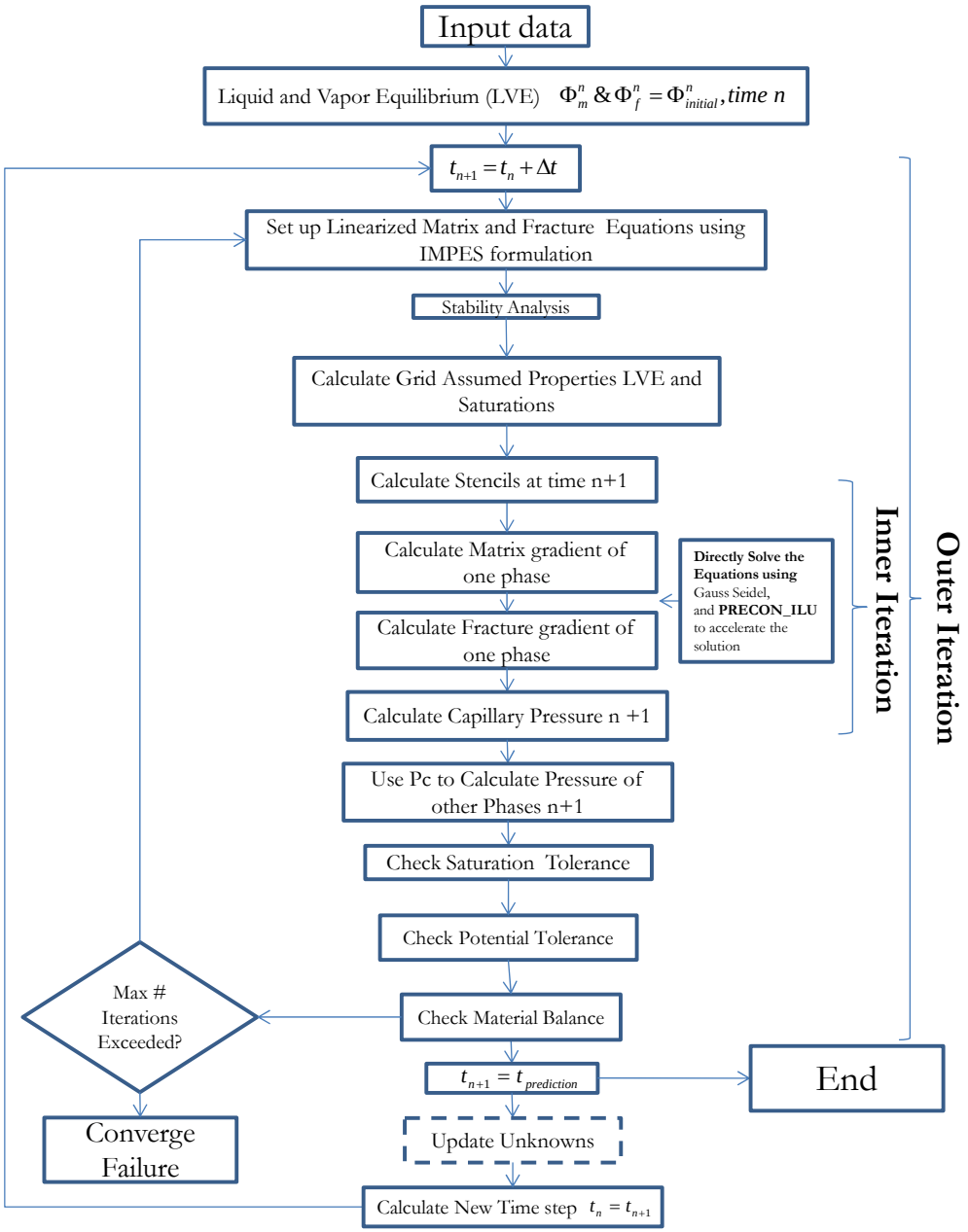

Figure 2-3. Flow Chart for the General Solution of pressure and saturation equations in a compositional and natural fracture system.

Figure 2-4 shows the flow chart to solve the Liquid and Vapor Equilibrium. In every time-step, the pressure changes and there is a flow from one grid cell to another, thus changing the global composition (Z_i).

This is one of the important steps to account for the condensate banking generation around the well[36], and for the liquid and vapor changes in every grid cell.

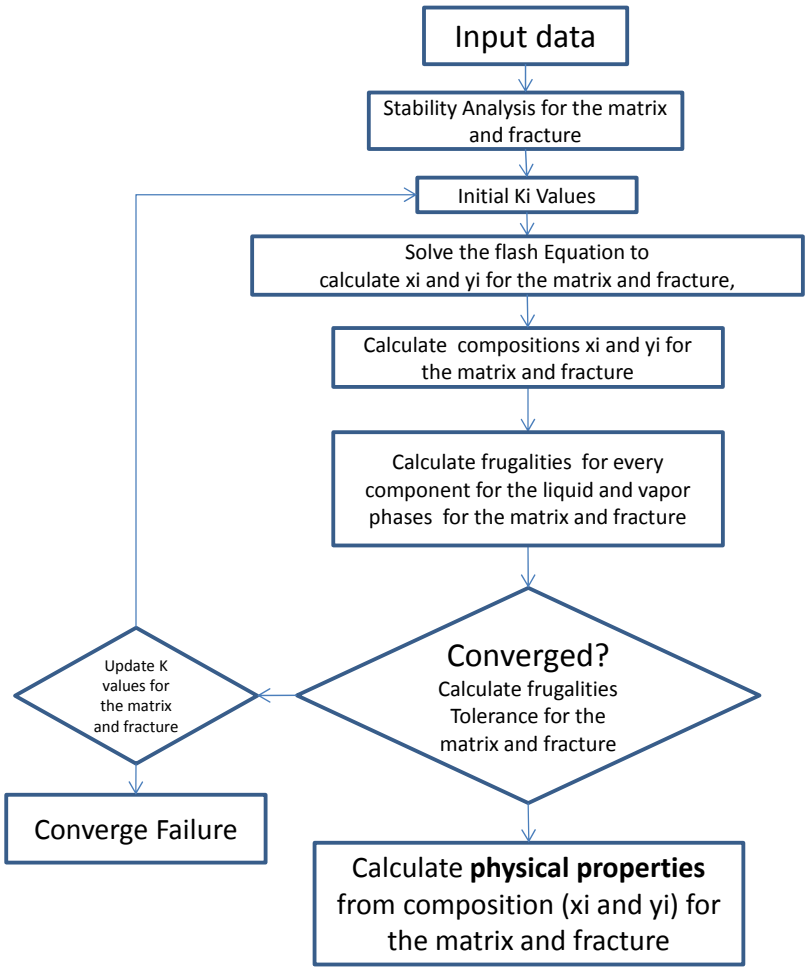

Figure 2-4. General Flowchart for the Liquid Vapor Equilibrium Solution.

The flash calculation is thoroughly described by Castillo and J. Montoya **[2]** by using the theory described by Whitson and Brule **[1]**. In the flash calculation the equations converge to a relationship between the oil composition, the global composition, the equilibrium constants (k-values) and the molar fraction of the gas phase showed in Eq. 2-14.

$$x_i = \frac{Z_i}{V(k_i - 1) + 1} \qquad 2\text{-}14.$$

[36] This special workflow combined with the accumulation term in the compositional equation, generates higher saturations in the grid cells, compared to the maximum liquid dropout obtained from the CCE or CVD tests, see Figure 1-50 and Figure 1-51 as a reference.

2.6 Full Field Model Description

This section describes the subsurface, wells and facilities systems, giving more emphasis on the subsurface set up, as this is the main driver of this study.

2.6.1 Grid Description

Figure 2-5 and Figure 2-6 show a horizontal and 3D view of the reservoirs and sheets (compartments) of this study.

The Figures use a ternary diagram as a color code to show in the same graph the distribution of oil, gas and water phases, which have a range from 0 to 1.0 saturation fraction, being red 100% gas saturation, blue 100% water and green 100% oil.

- **Pauto**

See Figure 1-6 with Figure 2-5 to understand the spatial distribution of Pauto complex sheets.

Figure 2-5 also shows the vectors with the direction of positive flow in the x, y and z axes that will be used as in the Section 3 for the flow analysis.

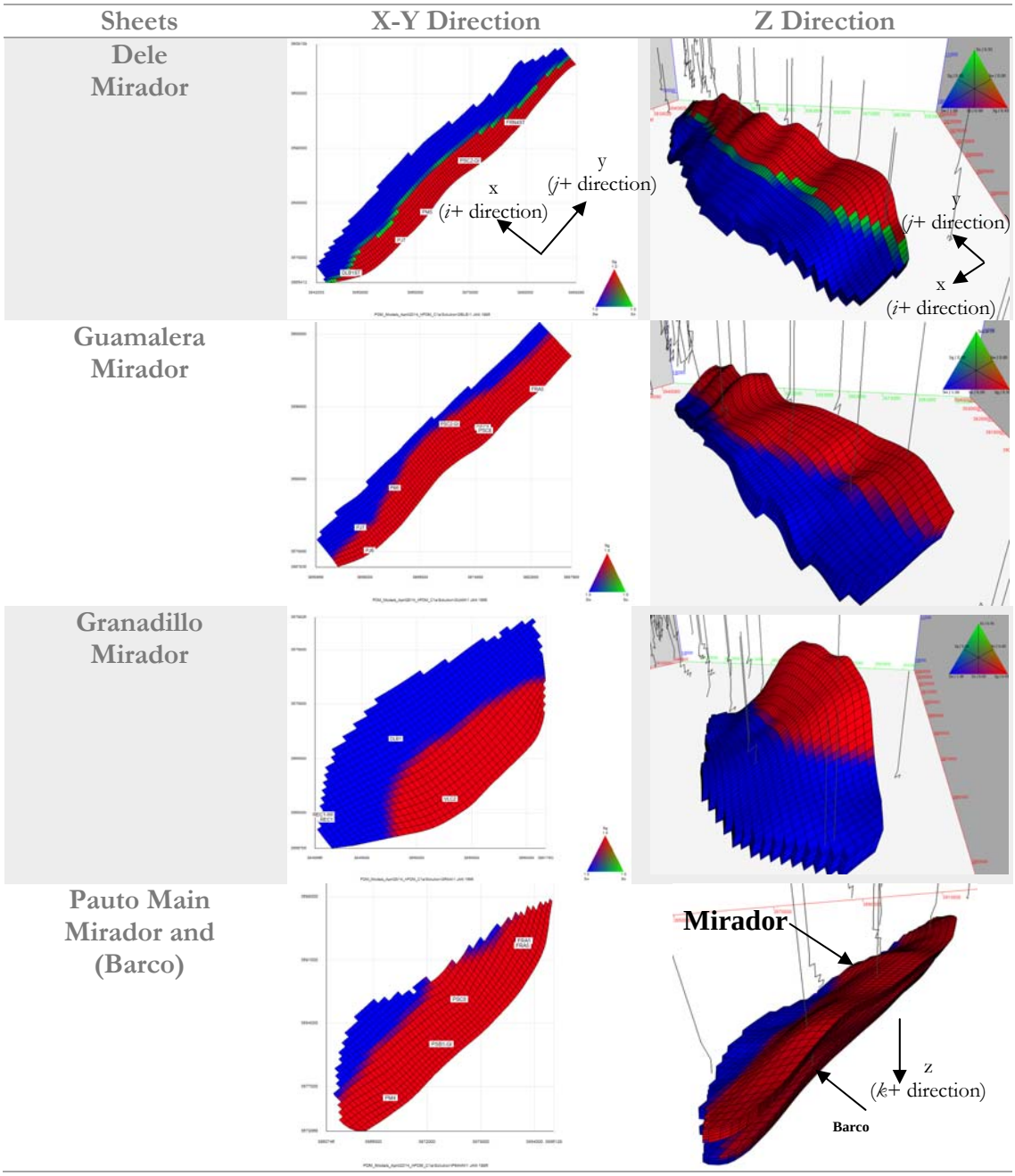

Figure 2-5. Pauto Complex 3D Saturation distribution.

- **Floreña**

Figure 2-6 shows the gas section of Mirador Floreña and the gas/oil sections in Barco and Guadalupe in Floreña field. Those compositional gradients are presented in Figure 1-51.

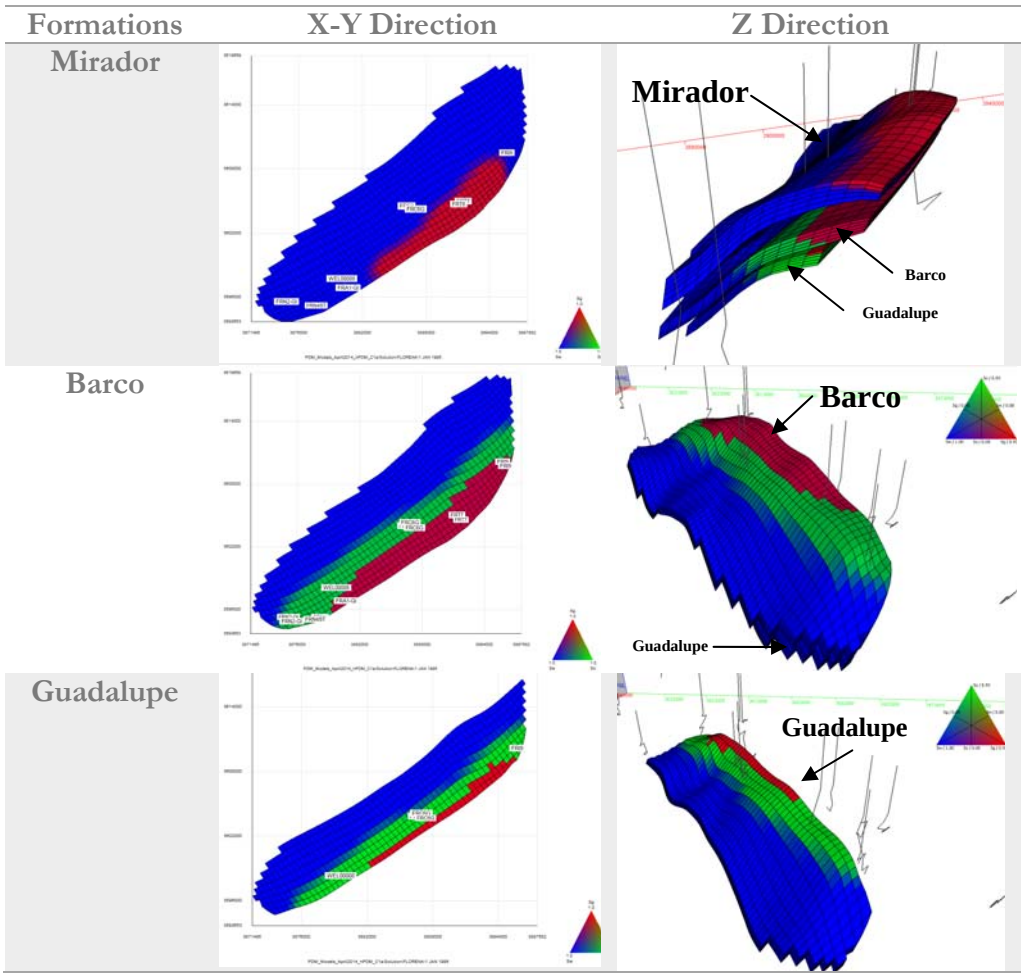

Figure 2-6. Floreña 3D Saturation Distribution.

2.6.1.1 Grid Purposes

The following models were built in order to evaluate the impact matrix and fracture properties have in the fluid flow compared to the equivalent single porosity model, and also to investigate the impact that natural fractures have on the N_2 injection scheme.

Single Porosity Refined Model (spF1[37]): To represent the gas gravity segregation it was build the model with better refinement in the vertical direction.

The computational time: 8.3 hr for the refined model compared with 0.4 hr for the coarse model (spC1) see Figure 2-30. The refined model was used to compare the results with the vertical coarse model, see Figure 2-7.

Single Porosity Vertical Coarse Model (spC1): The vertical coarsen model is used to evaluate the recoverable oil and gas volumes and its behavior in the history match section. The grid cells' size of this model is described in Figure 2-8 and Figure 2-9

[37] See nomenclature section, F for fine and C for Coarse, dp for dual porosity and 1a is the simulation case.

Dual porosity and dual permeability Vertical Coarse Model (dpC1): In the author's knowledge, this is the first approach that has been made with the PDM full field model to compare the equivalent single porosity model (SP) with the dual porosity/dual permeability model (DPDP).

2.6.1.2 Layer description

The coarse model was generated by grouping the cells of the refined reservoir model only in the vertical direction, as it is shown in Figure 2-7.

The scale at the right of the figure represents the oil saturation for a south-to-north vertical view of Mirador and Barco formations for Floreña field, where just slight variations in the oil distribution are observed at initial conditions (see the white arrow in Figure 2-7).

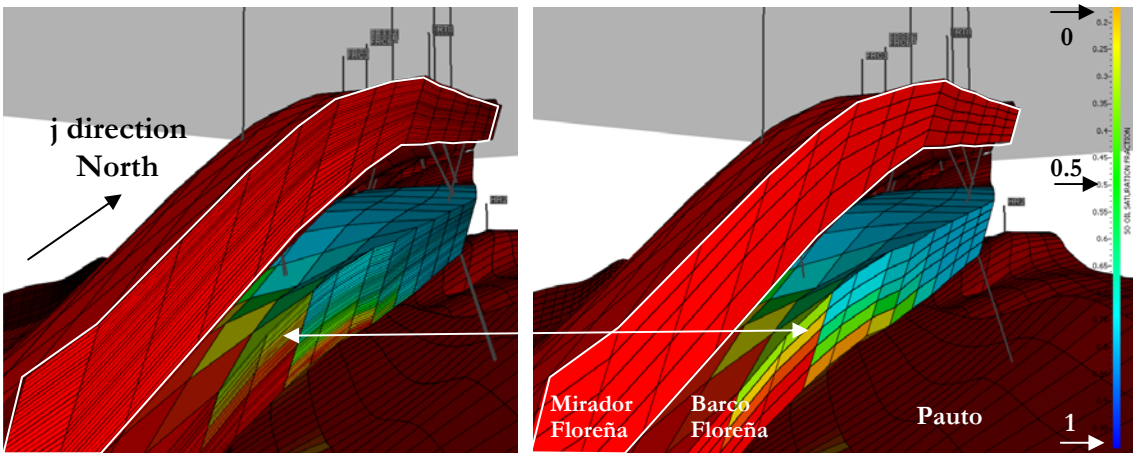

Figure 2-7. Floreña 3D View - Refined Model (left side graph, □ z~: 30 ft) vs. Coarse Model (right side graph, □ z~ 150 ft).

2.6.1.3 Grid block Sizes and orientation

The grid generation had the aim of representing the shape of the structure but trying as much as possible to have regular grid cells to avoid the numerical dispersion in the simulations.

Figure 2-8 shows the size of the Fine and Coarse grids for all the compartments respectively in the z direction where the fine model (spF1) has an average of ~30 ft per cell in the z direction while the coarse model (spC1) has an average of ~150 ft per cell.

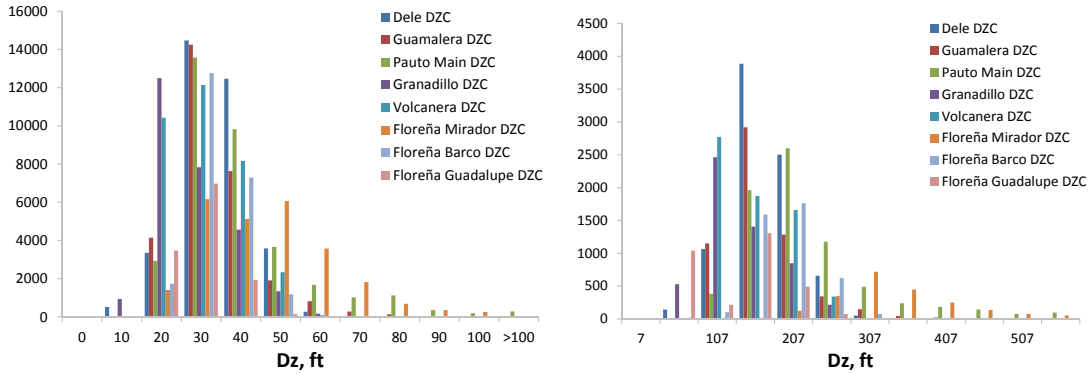

Figure 2-8. Grid Block sizes in z direction Histogram- Refined (left side graph, □ z~ 30 ft) and Coarse (right side graph, □ z~ 150 ft).

Figure 2-9 shows the histogram for all the compartments in which the variance of the grid length in the *x* direction (see left side graph) is lower compared with the grid length in the *y* direction (see right side graph).

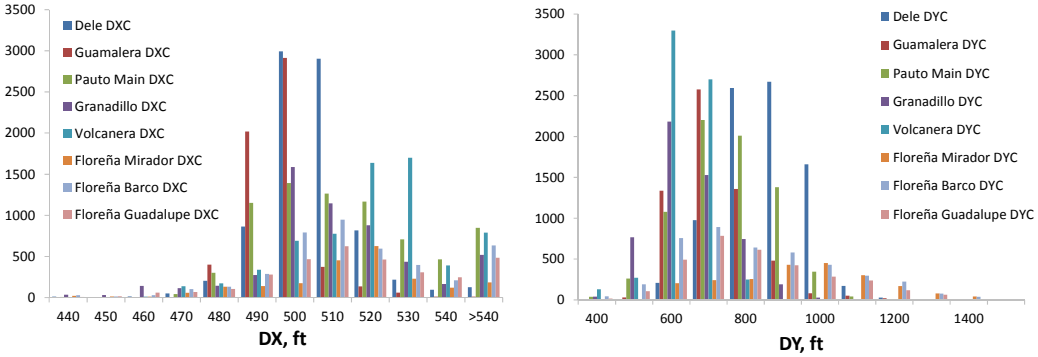

Figure 2-9. Grid Block sizes in x (left □ x~ 500 ft ±50 ft) and y (left □ y~ 700 ft ±300 ft) directions, same for the Coarse and Refined Grids.

2.6.1.4 Number of Cells

Table 2.1 shows a reduction in a factor of ~5 in the number of cells, from 350,000 cells for the refined model down to almost 70,000 cells for the Coarse model, which is translated into a computational saving time of ~15 times for the single porosity model, see Figure 2-30.

The dual permeability model has 70,000 cells for the matrix and 70,000 cells for the fracture, but with a considerable time increase in the history and in the prediction stages, as observed in Figure 2-30.

Table 2.1. Number of Grid Cells.

Model	Active Grid Blocks	Grid Block Connections
SP Refined: hm_spF1s:	351.690	969.612
SP Coarsen: hm_spC1s)	68.699	186.090
DPDP Coarse Model : hm_dpC1):	MATRIX : 70.291 FRAC : 70.291	MATRIX : 186.090 FRAC : 189.499

2.6.2 Initial and Boundary Conditions

2.6.2.1 Initial Conditions

Same reservoir pressure variation with depth and compositional grading presented in Figure 1-27, **Error! Reference source not found.**Figure 1-50 and Figure 1-51.

$$P = P_i \ \forall(x, y, z), t = 0$$

2.6.2.2 Boundary Conditions

It was used the Newman-type boundary conditions for a closed system where no flow goes through the boundaries. The boundary conditions are represented by Eq. 2-17, Eq. 2-18 and Eq. 2-19.

$$\left(\frac{\partial \Phi_o}{\partial x}\right)_{x=0,y,z} = 0\,, \qquad \left(\frac{\partial \Phi_o}{\partial x}\right)_{x=Dx,y,z} = 0\,, \quad \forall(y,z) \qquad \text{2-15.}$$

$$\left(\frac{\partial \Phi_o}{\partial y}\right)_{y=0,x,z} = 0\,, \qquad \left(\frac{\partial \Phi_o}{\partial y}\right)_{y=Dy,x,z} = 0\,, \quad \forall(x,z) \qquad \text{2-16.}$$

$$\left(\frac{\partial \Phi_o}{\partial z}\right)_{x,y,z=0} = 0\,, \qquad \left(\frac{\partial \Phi_o}{\partial z}\right)_{x,y,z=Dz} = 0\,, \quad \forall(x,y) \qquad \text{2-17.}$$

2.6.3 Petrophysics

This section describes the values selected for the reservoir simulation model, which were based on experimental data and information presented in the section 1.5.

2.6.3.1 Rock Compressibility

Based on the information presented in Figure 1-28 it was assumed constant matrix and fracture rock compressibility value of 6 x 10^{-6} psi^{-1}@6000psia.

2.6.3.2 Porosity and Permeability

The Figure 2-10 represents the theoretical fracture porosity with different apertures, this graph was created using Eq. 1-8, see Section 1.5.3. Then, the data available from transient analysis, petrophysics and petrography were used to delimit the fracture spacing selection (Lx, Ly and Lz). Notice that fracture permeability and porosity are highly dependent of the scale.

In Figure 2-10, the red dot shows a maximum porosity value of 1%, from petrographic analysis described in Section 1.3. The blue square shows the value used by Jolly **[21]**. Both points highlight the possible upper bound for fracture porosity values.

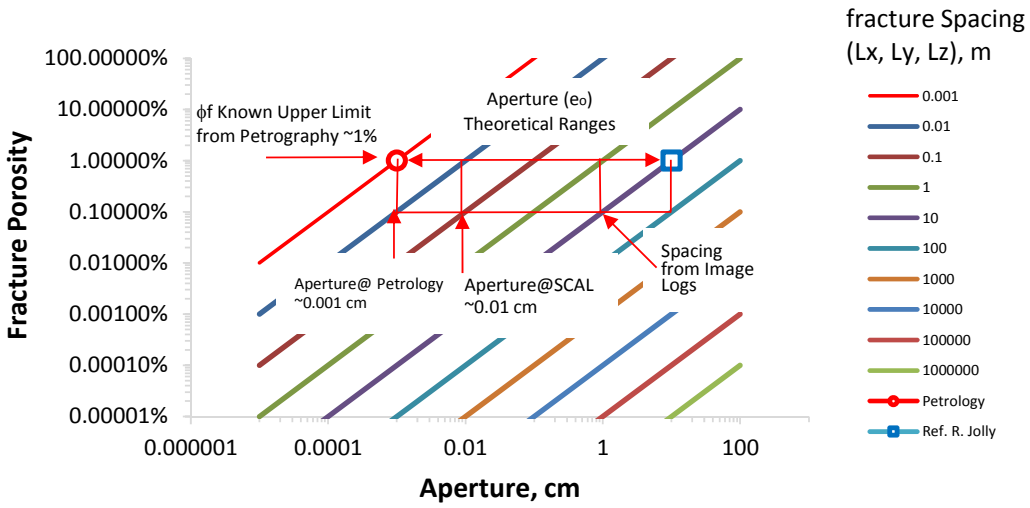

Figure 2-10. Theoretical Porosity and Aperture with different Fracture Spacing.

Figure 2-11 shows the porosity and permeability conventional cross plot for each sheet's matrix and fracture. The matrix porosity-permeability comes from a geo-statistical work **[22]**, while the fracture porosity is theoretically obtained using Eq. 1-8.

The fracture's permeability comes from geo-statistical work that was performed to match the PBU data and applying Eq. 1-11.

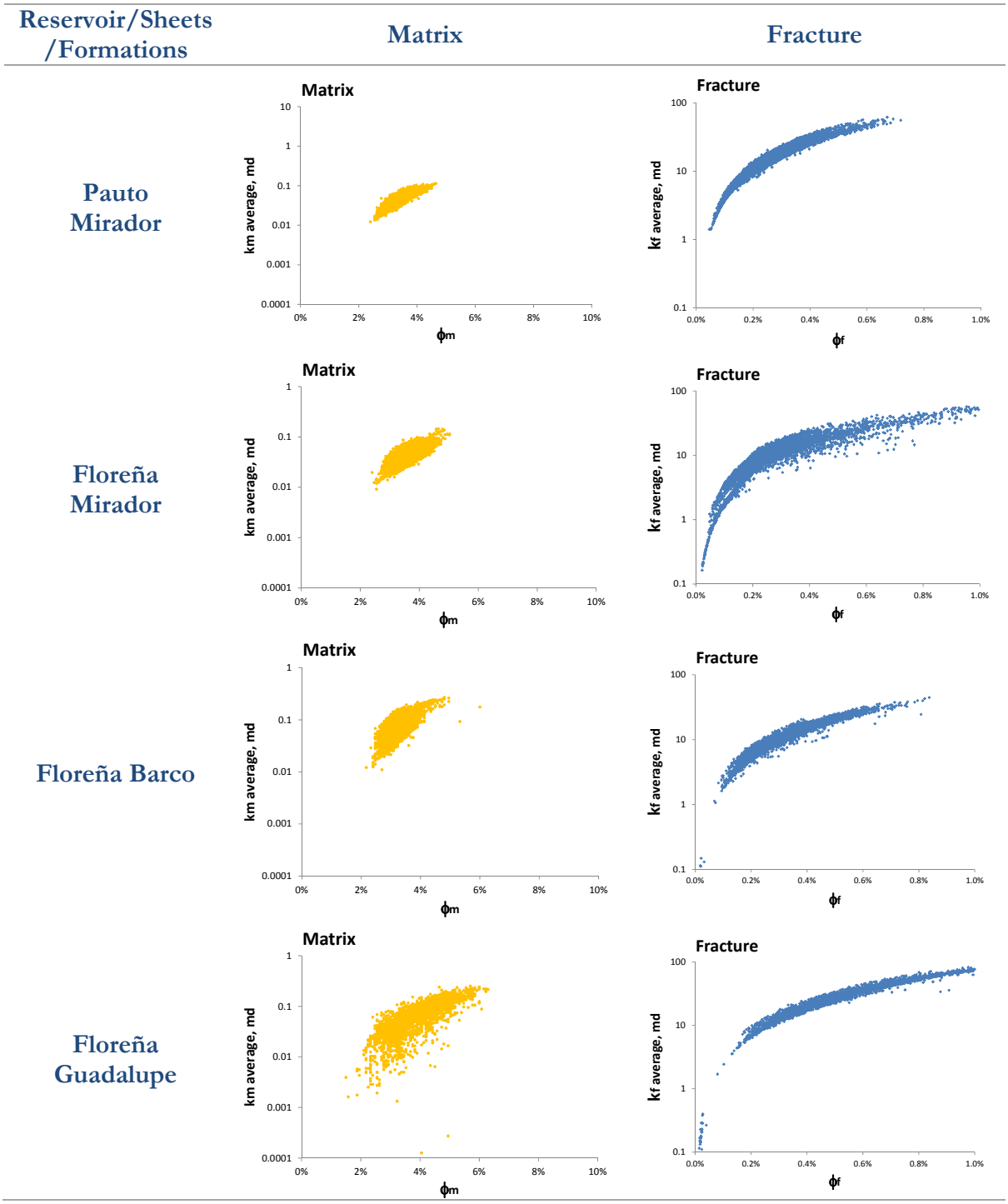

Figure 2-11. Pauto and Floreña Porosity and Permeability X-Plots.

2.6.3.3 Heterogeneity and Anisotropy

- **Heterogeneity**

Figure 2-12 shows the anisotropy created with the effective fracture permeability. See also Appendix C for complimentary plots.

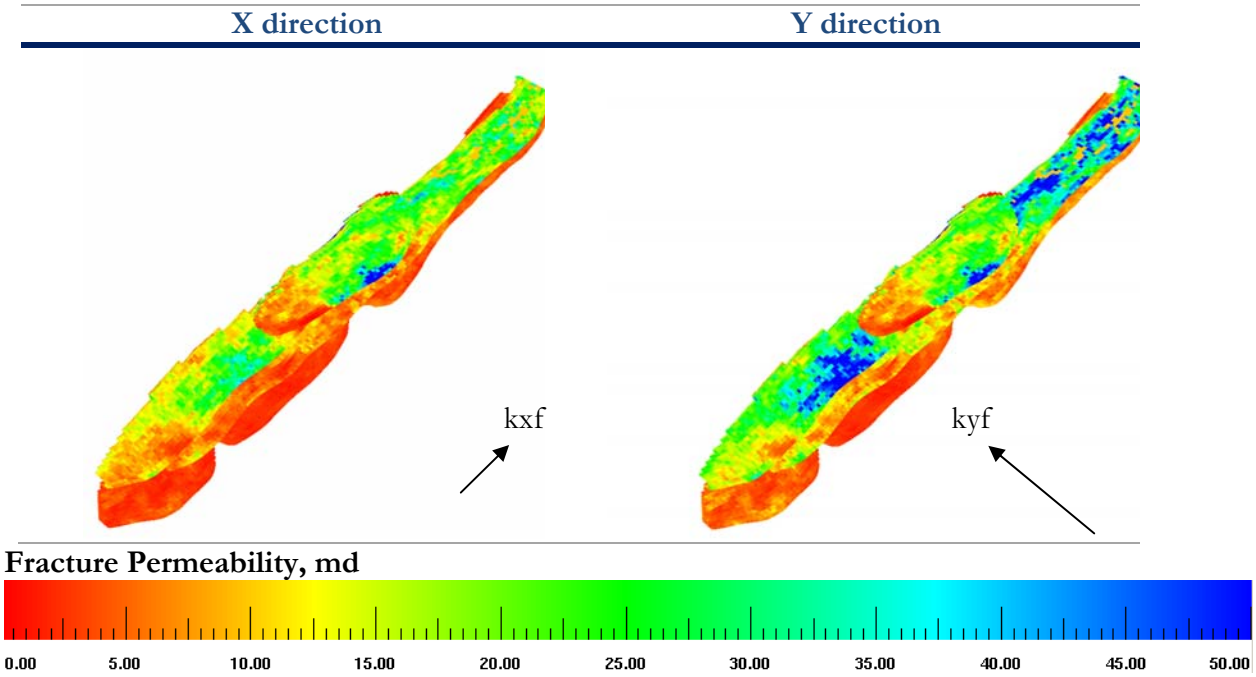

Figure 2-12. PDM Effective Fracture Permeability.

As mentioned by Beliveau et al. **[5]**, an important aspect that controls the recovery factor is the magnitude of the fracture's permeability heterogeneity.

Two methodologies were selected to estimate the heterogeneity of the model: the Dykstra Parsons approximation which only considers one parameter and Lorentz which compares 2 parameters.

The first methodology uses the Dykstra-Parsons coefficient defined as:

$$V_{DP} = \frac{\bar{k} - k_{\sigma}}{\bar{k}} \qquad 2\text{-}18.$$

Where:

V_{DP} : Dykstra-Parsons Heterogeneity Factor.
$\bar{k}$: Permeability Percentile 50.
k_{σ} : Permeability Percentile 84.1.

The second methodology uses Lorentz Heterogeneity, which is a graph of a flow zone indicator that includes the cumulative storability ($Phi \cdot h$) compared to the cumulative flow capacity ($k \cdot h$). This concept is used and combined with the Gini coefficient which is conventionally used to estimate the disparity between 2 individuals **[23]**.

The Brown equation **[23]** is used to estimate the Gini coefficient:

$$V_G = \left| 1 - \sum_{j=0}^{j=n-1} \left((Phi \cdot h)_{k+1} - (Phi \cdot h)_k \right) \left((k \cdot h)_{k+1} - (k \cdot h)_k \right) \right| \qquad 2\text{-}19.$$

Where:

V_G : Gini coefficient which quantifies the Lorentz Heterogeneity.

$Phi \cdot h$: Cumulative proportion of the storability, for data available from j=0 to n; with $(Phi \cdot h)_0 = 0$, $(Phi \cdot h)_n = 1$

$k \cdot h$: Cumulative proportion of flow capacity, for the data available from j=0 to n; with $(k \cdot h)_0 = 0$, $(k \cdot h)_n = 1$

Usually, the heterogeneity factor is used in the vertical direction within petrophysical models, but for this study, the Heterogeneity Index was adapted in order to be used in the 3D model.

The convention gives a value of 0 to represent complete homogeneity, and a value of 1 to represent complete heterogeneity. Figure 2-13 shows that both methodologies estimate an intermediate heterogeneity of around 0.5.

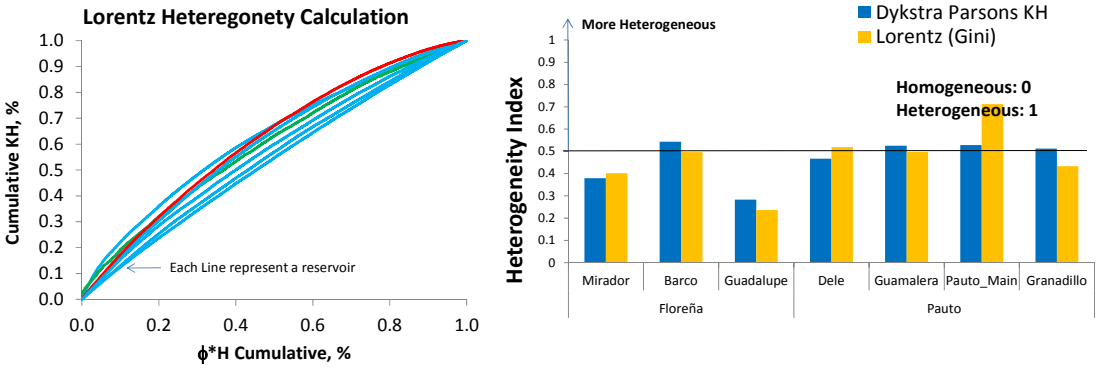

Figure 2-13. Heterogeneity factor of the 3D simulation model.

- **Anisotropy**

A simple approach was used to implement constant permeability anisotropy in the model, as this information was not available to validate a variable anisotropy in each of the grid cells (e.g interference tests).

It was assumed that the fracture's permeability should be decomposed in 3 vectors following the x, y and z direction.

Figure 2-14 shows how the permeability in the y direction is aligned with the rose diagram coming from the fracture's main directions for Pauto Field (also see Figure 2-12).

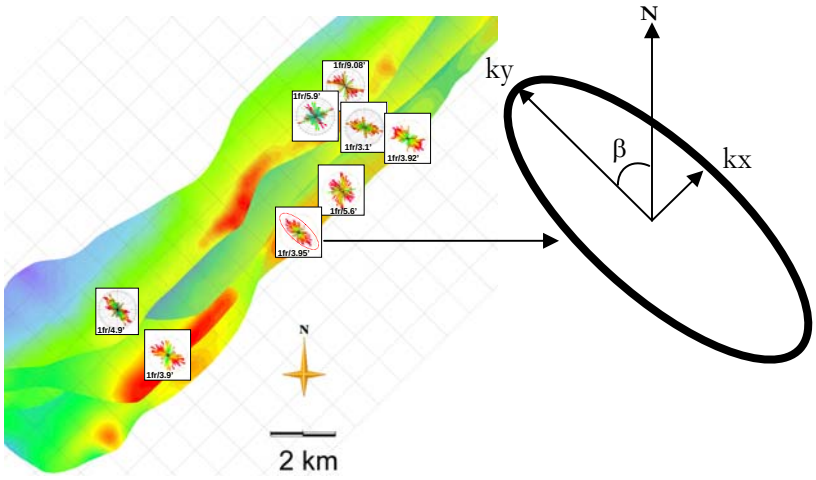

Figure 2-14. Fracture Permeability Anisotropy Example.

Eq. 2-20 and Eq. 2-21 represent the permeability split in the x and y direction using the main dip azimuth[38] of the fractures (□) which are oriented NW-SE.

$$k_{fx} = k_f \cdot \text{sen}(\beta) \qquad 2\text{-}20.$$

$$k_{fy} = k_f \cdot \cos(\beta) \qquad 2\text{-}21.$$

The bulk fracture permeability comes from the difference between the total permeability from PBU and the matrix permeability estimations from logs/cores. The anisotropy is estimated by:

$$a_f = \frac{k_{fy}}{k_{fx}} \rightarrow k_{fy} = a_f k_{fx} \qquad 2\text{-}22.$$

[38] It was assumed in this work, for practical purposes that the orientation of the grid is are very close to the azimuth direction of the fractures.

Eq. 2-23 uses the assumption of a radial flow to relate the bulk permeability and the permeability in x and y direction[39].

$$k_f = \sqrt{k_{fx} k_{fx}} \qquad 2\text{-}23.$$

Using Eq. 2-24 with a general dip azimuth ($\square$) of 30°, an average horizontal anisotropy factor[40] of 1.73 was estimated, which means that the permeability in the y direction is 1.73 times higher than the permeability in the x direction.

For the case where the x and y permeabilities are the same, and in order to include the anisotropy for permeability while keeping the same KH for the system, it is required to include Eq. 2-22 into Eq. 2-23, with a factor of $1.73^{1/2}$.

$$k_f = \sqrt{a_f k_{fy} k_{fy}} \qquad 2\text{-}24.$$

2.6.3.4 Capillary Pressure Selection

Figure 2-15 shows the selected water-oil capillary pressures for Floreña and Pauto fields used for the static initialization and dynamic approach.

Additionally, Capillary pressure curves are presented up to 1000 psia, which is the maximum possible capillary pressure observed from the initial pressure conditions presented in Figure 1-27.[41]

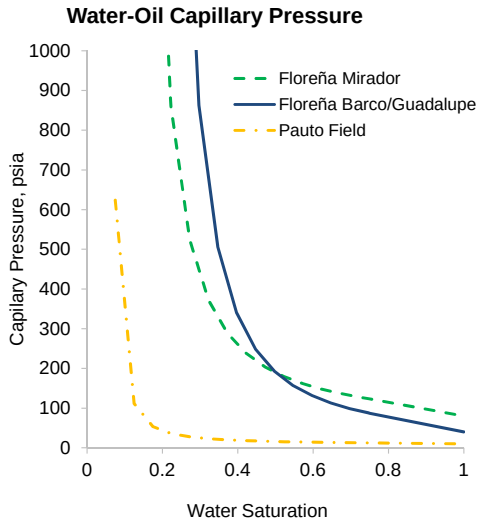

Figure 2-15. Pauto Complex and Floreña Water Oil Relative Capillary Pressure.

[39] A similar analysis is presented in **[25]** pg. 434. Evaluation of Anisotropy in a Fractured Reservoir.
[40] This permeability could link the travel time of the tracers in Pauto ~2 ft/day which traveled in the x direction (north south, see Figure 1-53) and the tracers velocity in Floreña field that travelled in the y direction (east –west, see Figure 1-57) with a velocity of 89 ft/day.
[41] The stress-strain plot presented in Figure 1-31 shows further information about the comparison between the Capillary pressures and its relation with the micro-fractures' assumption.

2.6.3.5 Relative Permeability

Figure 2-16 and Figure 2-17 show the selected gas-oil and water-oil relative permeabilities for the full field model; see Section 1.5.4 for further information.

These relative permeability curves were based on the history matching case obtained with the single porosity model, taking into account other considerations, such as the range of matrix permeability and porosity used in the tests.

Additionally, Figure 2-16 and Figure 2-17 shows with dashed lines a sum of the relative permeabilities. This curve shows the losses in the effective permeability due to changes in saturation.

- **Gas-Oil Relative Permeability**

The reservoir simulation software used at the moment when this project was evaluated did not have available rate dependent relative permeability curves, which are important to adequately model the fluid flow in gas condensate reservoirs **[14, 15, 16]**.

The relative permeability rate dependent parameters (coupling effect) found by Gomez and Herrera **[24]** was used to create the near wellbore relative permeabilities.

When the dual porosity dual permeability model was created, the wellbore relative permeabilities showed in Figure 2-16 were used for the fracture system, and the reservoir relative permeabilities were used for the matrix system.

Heriot Watt Experiments **[15]** show evidence that the flow in the fractures have more influence by inertial effects rather than the coupling effects. The present study did not use the common X shape for fracture relative permeability as it was assumed that the fractures dominate the flow.

Gas Oil kr	1. Reservoir (and Matrix)	2. Wellbore (and Fracture)
1. Pauto field Mirador and Barco formations	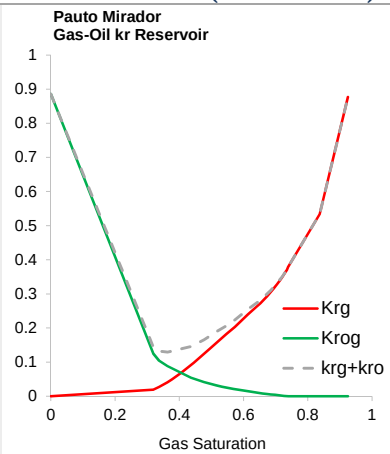	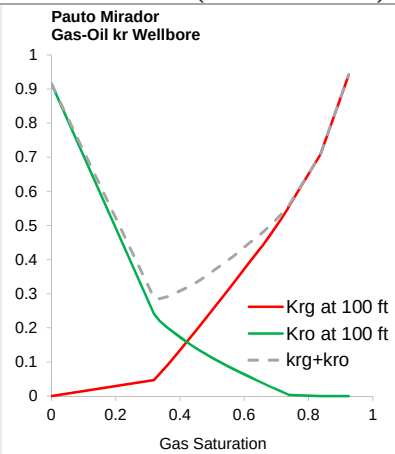
2. Floreña field Mirador formation	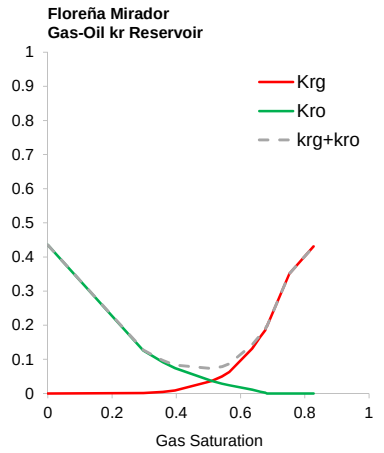	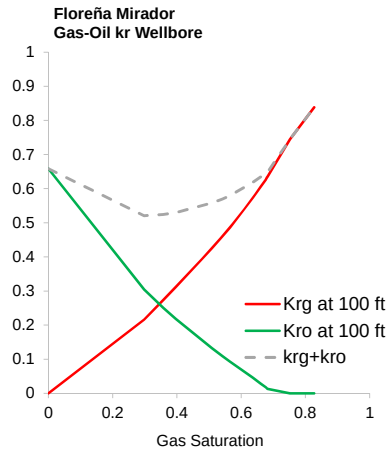
3. Floreña field Barco and Guadalupe formations	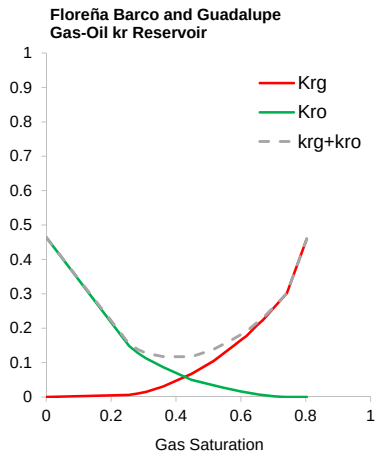	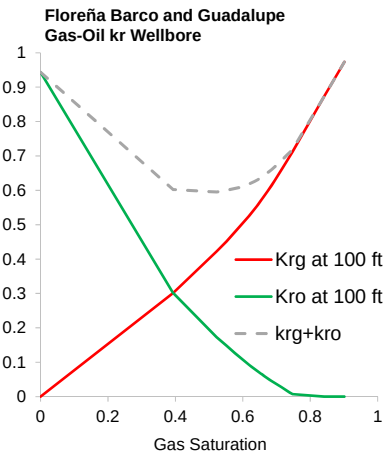

Figure 2-16. Floreña and Pauto Gas-Oil Reservoir Relative Permeabilities.

- **Water Oil Relative Permeability**

Figure 2-17 shows the water – oil relative permeabilities used for Floreña and Pauto Complex fields.

For Pauto Mirador and Barco formation, the same relative permeabilities were assumed, as no information was available. The shape and end-points come from the analysis presented in Section 1.5.4.

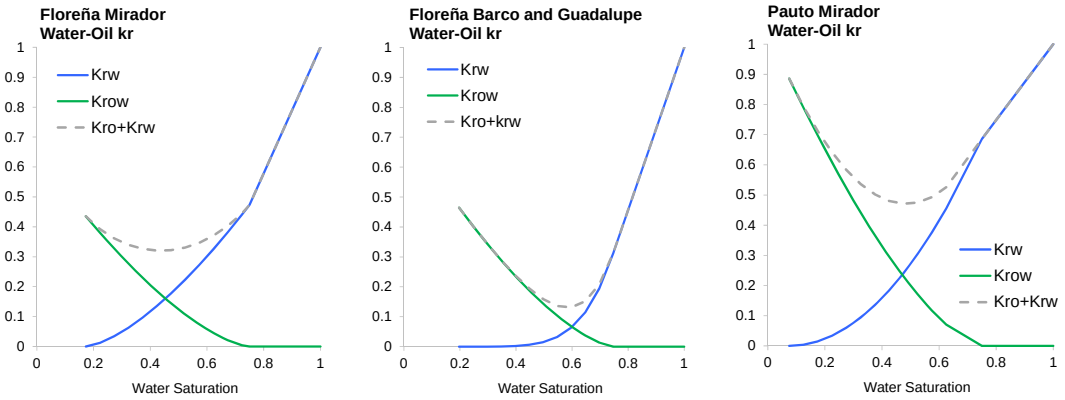

Figure 2-17. Floreña and Pauto Water- Oil Relative Permeabilities.

2.6.4 Fluid Properties

Table 2.2 shows the parameters used in Peng-Robinson's EoS of 3 Parameters. The number of fluid pseudo-components will be later used in the results section to visualize the changes in composition in the grid cells.

Table 2.2. Internal EoS Parameters.

# Pseudo-Component	Pseudo-Component	M	TC	PC	ZC
1	CO2	44.01	87.75	1069.51	0.27433
2	N2	28.014	-232.51	492.84	0.29178
3	C1	16.043	-116.66	667.03	0.2862
4	C2	30.07	89.91	706.62	0.27924
5	C3	44.097	206.02	616.12	0.2763
6	C4	58.123	292.6	541.14	0.27724
7	C5-6	77.638	413.33	479.33	0.26939
8	C7-10	117.787	598.28	410	0.2695
9	C11-14	174.53	739.54	320.18	0.2732
10	C15-20	239.55	868.05	238.61	0.25763
11	C21-29	338.129	973.99	192.66	0.27705
12	C30+	545.598	1081.68	166.98	0.36811

Binary interaction coefficients (BIP´s) were used from an analogue field for this study. These values are similar to those presented by Whitson and Brule[42] **[1]**.

[42] Due to confidentiality, it was not possible to show the values. See **Chapter 4 in Reference 1** where similar parameters are available.

2.6.5 Wells and Facilities

- **Wells**

  - Gas rate control was used in the model, which means that the oil will be estimated by flash calculations using the equations of state.

  - Skin Factors and KH comes from Pressure Transient Analysis (PBU) above the saturation pressure.

- **Facilities**

A basic representation of the surface facilities set up is shown in Figure 2-18. In this network there are 3 separators (see SEP1 node) and the NGL-LPG Plant was modeled in the NGL node.

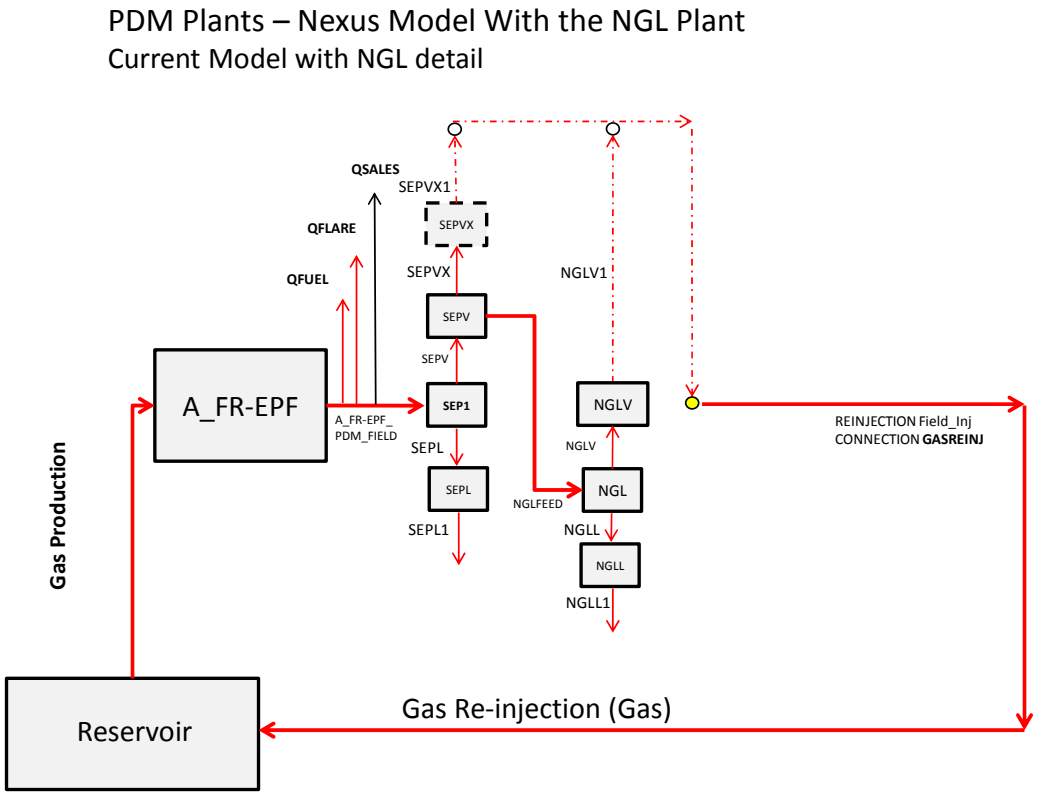

Figure 2-18. Facilities Sketch before N_2 Injection Case.

2.7 Workflow for a Dual Porosity/Dual Permeability Full Field Simulation Model Construction

Workflow Theory Section.

Generally fracture apertures are generated stochastically using geo-statistical models which do not tie the fracture porosity and permeability with the apertures of the fractures. The aim of the proposed approximation of this study is to tie all variables to keep consistency with the KH estimated from logs and Pressure Build Ups, see Figure 2-19

One of this work's new contributions is to propose and implement a simple methodology to construct a robust dual porosity/dual permeability reservoir simulation model based on the apparent aperture estimation when it is not possible to infer it from image logs or when there are other information limitations.

The workflow proposed in this study to build the dual porosity/dual permeability model is based on a good control of the wells' flow potential. That flow potential is highly related to the excess permeability and number of critically stressed fractures, which in turn is related to the apparent aperture that also limits the storage coefficient and that directly impacts the fracture porosity and fracture spacing.

Quality Control Steps.

This workflow includes a quality control graphs which uses standard plots in each of the workflow steps. The steps of the workflow are as follows:

1. Find a function or a correlation for spacing, see Figure 1-19.
2. Find and select a fracture driver mechanism, see Figure 2-20.
3. Find a correlation between the critical stress fractures and the main fracture driver mechanism (e.g structural curvatures, see Figure 2-21).
4. Check Pressure Transient Coefficients: inter-porosity vs. shape factor at different excess permeabilities (see Figure 2-22).
5. Check apertures vs. fracture porosities at different spacing (see Figure 2-23 and Figure 2-24).
6. Check spacing vs. apparent apertures at different excess permeabilities, see 1st column in Figure 2-23 and Figure 2-24.
7. Check apparent apertures vs. fracture porosities see 2nd column in Figure 2-23 and Figure 2-24.
8. Check shape factors, see Figure 2-25 and Figure 2-26.
9. Assume apertures that will be adjusted to match the excess permeabilities (see Figure 2-27).
10. Identify the natural fracture classification by checking the Gilman plot: Excess permeability vs. storage coefficients and Nelson plot: % Fracture permeability vs. storage coefficients, (see Figure 2-28 and Figure 2-29).
11. Finally, calibrate previous steps by checking again for consistency in the limits and constraints between the excess permeability, storage coefficients, inter-porosity

factors, shape factor (spacing), fracture porosities, fracture permeabilities and apertures using general rules **[20]**, laboratory and field data analysis (see Chapter 1).

2.7.1 Workflow Theory

One of the most important assumptions made is that the excess permeability applies for models where the areal grid size resolution is close to the drainage area of the well. Figure 1-58 and Figure 2-9 shows how this assumption is approximately accomplish.

- Defining the Excess Permeability (χ):

The KH from PBU interpretations - $kh)_{PBU}$ -, when compared to the KH from log interpretations[43] - $kh)_{\text{logs}}$ -, this data is used to generate a multiplier known as the excess permeability, which is implicitly related to the critically stressed fracture intensity around a well. This parameter, named as χ, plays an important role for the flow capacity consistency of the model.

$$\chi = \frac{k_T h}{k_m h} = \frac{(k_m + k_f)h}{k_m h} \approx \frac{kh)_{PBU}}{kh)_{\text{logs}}} \qquad \text{2-25.}$$

Reorganizing Eq. 2-25

$$k_f = k_m(\chi - 1) \qquad \text{2-26.}$$

Where

k_T : is the total permeability.
k_m : is the Matrix permeability.
k_f : is the effective fracture permeability.

- From Pressure Transient Analysis **[25]**, Eq. 2-27 is the same equation presented in Chapter 1, Section 1.5.5.

$$k_f = \sigma \cdot k_m \frac{r_w^2}{\lambda} \qquad \text{2-27.}$$

Eq. 2-28 results from combining Eq. 2-26 and Eq. 2-27

[43] For this specific study, it is assumed that the KH from the PBU above the saturation point represents the closest approximation to the total KH of the well, knowing that several factors that increase or decrease these values are due to the presence of the initial water saturation, reservoir pressure that could be below the saturation pressure, the interpretation itself and the pseudo-pressure used to perform the interpretations. There is also an uncertainty related to the KH coming from logs which depends on the correlation or technique used from the porosity-permeability core correlations.

$$k_m(\chi - 1) = \sigma \cdot k_m \frac{r_w^2}{\lambda} \qquad 2\text{-}28.$$

Eq. 2 -29 comes from reorganizing the Eq. 2-18.

$$\chi - 1 = \sigma \frac{r_w^2}{\lambda} \qquad 2\text{-}29.$$

Reorganizing the expression for the excess permeability from Eq. 2-27, then:

$$\chi = \sigma \frac{r_w^2}{\lambda} + 1 \qquad 2\text{-}30.$$

- For Reservoir Simulation purposes **[19]**, using Eq. 1-18 described in Chapter 1, Section 1.5.3.2, Eq. 2-31 shows how the effective fracture permeability $k_{,f}$ is related to the number of critically stressed fractures N_f that crosses an area A' that have and apparent aperture e_0 and an area A. As reference, see the Figure 1-36.

$$k_{,f} = N_f \cdot \left(e_0^2 \cos^2(\alpha)\right) \frac{A}{A'} \rightarrow \qquad 2\text{-}31.$$

Plugging Eq. 2-26 into Eq. 2-31, the following is obtained.

$$k_m(\chi - 1) = N_f \cdot \left(e_0^2 \cos^2(\alpha)\right) \frac{A}{A'} \qquad 2\text{-}32.$$

Organizing Eq. 2-32 to solve for χ:

$$\chi - 1 = N_f \frac{k_{f,in}}{k_m} \frac{A}{A'} \rightarrow \qquad 2\text{-}33.$$

Reorganizing Eq. 2-33

$$\chi = N_f \frac{k_{f,in}}{k_m} \frac{A}{A'} + 1 \qquad 2\text{-}34.$$

Simplifying Eq. 2-34.

$$\chi = N_f \frac{k_{f,in}}{k_m} \frac{e_0}{h} + 1 \rightarrow \qquad 2\text{-}35.$$

$$\chi = \frac{N_f}{h}\frac{k_{f,in}}{k_m}e_0 + 1 \qquad 2\text{-}36.$$

Defining N_f/h as the critically stressed fracture intensity[44] per block length in x, y and z direction.

$$\frac{N_f}{h} = \frac{i_x}{\Delta x} + \frac{i_y}{\Delta y} + \frac{i_z}{\Delta z} \qquad 2\text{-}37.$$

The total pseudo intensity is defined as the sum of the matrix length divided by the length of the grid cells in each direction.

$$i = i_x + i_y + i_z \qquad 2\text{-}38.$$

With

$$i_x = \frac{L_x}{\Delta x},\ i_x = \frac{L_y}{\Delta y},\ i_x = \frac{L_z}{\Delta z} \qquad 2\text{-}39.$$

Where

i_x : is the number of fractures in a cell in the x direction.
i_y : is the number of fractures in a cell in the y direction.
i_z : is the number of fractures in a cell in the z direction.

Replacing Eq. 2-39 into Eq. 2-37.

$$\frac{N_f}{h} = I_x + I_y + I_z \qquad 2\text{-}40.$$

Where

I_x : critically stressed fracture intensity in the x direction, number of fractures/ft.
I_y : critically stressed fracture intensity in the y direction, number of fractures/ft.
I_z : critically stressed fracture intensity in the z direction, number of fractures/ft.

Where I is the total fracture critically stressed Intensity per cell length, # fractures/ft defined in Eq. 2-41.

[44] N_f is sometimes referred as FI (fracture index). It is highly important to define this number as a higher value of N_f will generate an high underestimation of the fracture apertures. In this work it was calibrated N_f with the critical stress fracture theory and analysis. See Figure 2-21

$$I = I_x + I_y + I_z \qquad \text{2-41.}$$

The excess permeability that is used to match the PBU data is related to the critically stressed fracture intensity, intrinsic fracture permeability and fracture aperture as follows:

$$\chi = \left(\frac{i_x}{\Delta x} + \frac{i_y}{\Delta y} + \frac{i_z}{\Delta z} \right) \frac{k_{f,in}}{k_m} e_0 + 1 \qquad \text{2-42.}$$

The excess permeability in Eq. 2-43 is used in Step 9 in the calibration workflow.

$$\chi = I \frac{k_{f,in}}{k_m} e_0 + 1 \qquad \text{2-43.}$$

Furthermore, the fracture intensity is related to the permeability multiplier, the intrinsic permeability and the fracture aperture with the following equation:

$$I = \frac{k_m (\chi - 1)}{k_{f,in} e_0} \qquad \text{2-44.}$$

With either Eq. 2-44 or Eq. 2-45, it is possible to link the intrinsic fracture characteristics at micro scale (from geology and petrophysical – forward static modeling[45]) with the response of the natural fracture system χ (excess permeability).

$$I = \frac{k_m (\chi - 1)}{(e_0 \cos(\alpha)) \cdot e_0} \qquad \text{2-45.}$$

Notice that the fracture's dip (□) impacts the spacing, which is also linked to the Intensity that depends on the number of fractures per well, as it is described in the spacing and fracture porosity correlation, see Figure 1-19.

Figure 2-19 shows the flow chart process to get the match between the excess permeability obtained from the Pressure Transient Analysis, and the apparent aperture of the fractures to generate consistent shape factors.

The aperture match is really an apparent aperture, as the aperture by itself changes from fracture to fracture, and Eq. 2-43 does not include other fracture parameters like the tortuosity and the filling that the fracture aperture can have (i.e Clays that affect the fracture's NTG).

[45] Geological Approach (forward static modeling) and reservoir Engineering Approach (backward dynamic modeling) are described by Utria **[8, pp. 34-39]**.

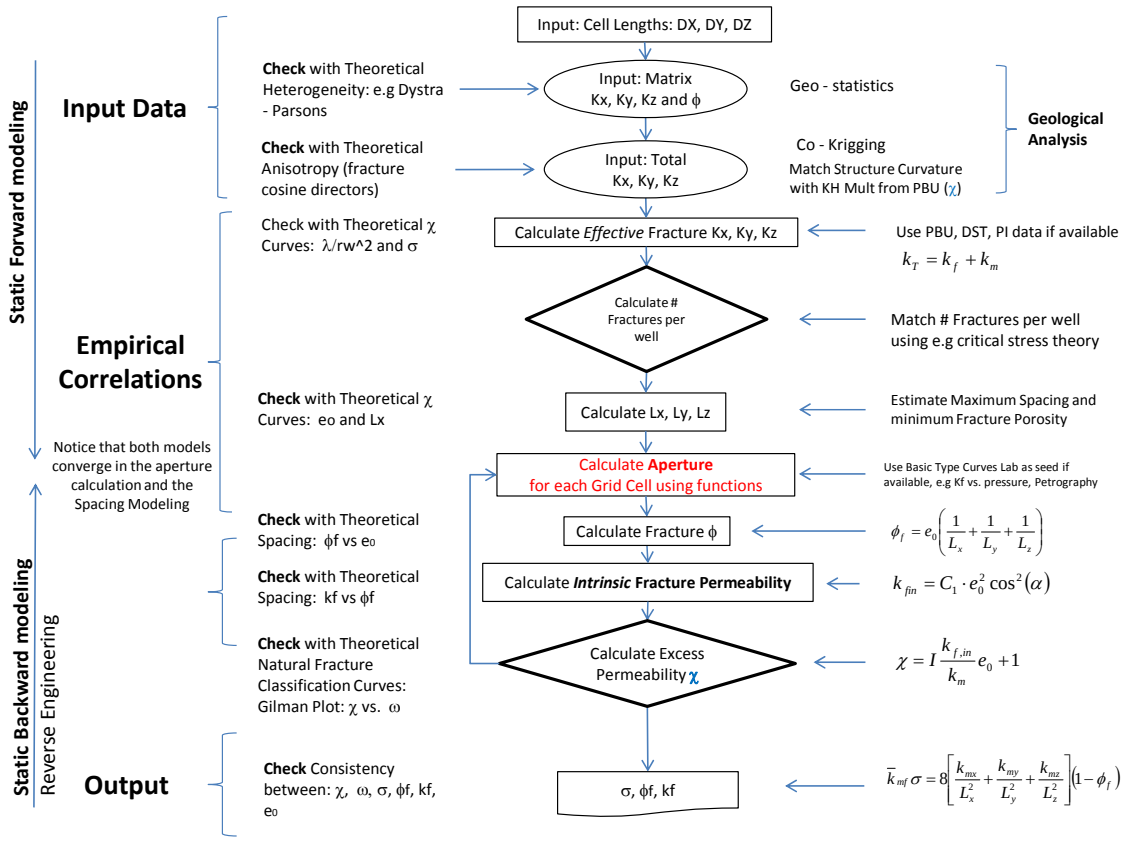

Figure 2-19. Flow Chart to generate a consistent Natural Fracture Model with available Flow Capacities.

2.7.2 Quality Control of the Workflow

There are some terms that are relevant to explain within the context of simulation:

- Calibration: this is related to the use of measured experiments (e.g Laboratory or field data) to refine and limit the parameters required for modeling.

- History Matching: this is related to the match of a certain process using a calibrated model.

2.7.2.1 Calibration

- **Fluids**

Some fluids in eastern Colombian foothills have similar signatures (or fingerprint). Assuming that the previous statement is valid, the Binary Interaction Parameters (BIP's) from an analogue field that has these values calibrated with nitrogen were used. See Section 3.4 for the quality control performed with PVT simulations for the Nitrogen.

- **Natural Fracture Driven Mechanism**

Figure 2-20 shows different alternatives explored to link the distribution of the spatially apparent fracture permeability with different geological fracture drivers (seismic-ant-tracking, net sand, curvature, structural, no trend). The curvature plot in column 3 was highlighted to show that it was selected as the driver mechanism.

The main assumption for this model is that the excess permeability (primary variable) is associated to the curvature of the structure (see 3rd column in Figure 2-20) for each sheet (secondary variable)[46]. For these fields, the curvature is the variable with less uncertainty and more physical meaning for the fracture representation **[26]**[47].

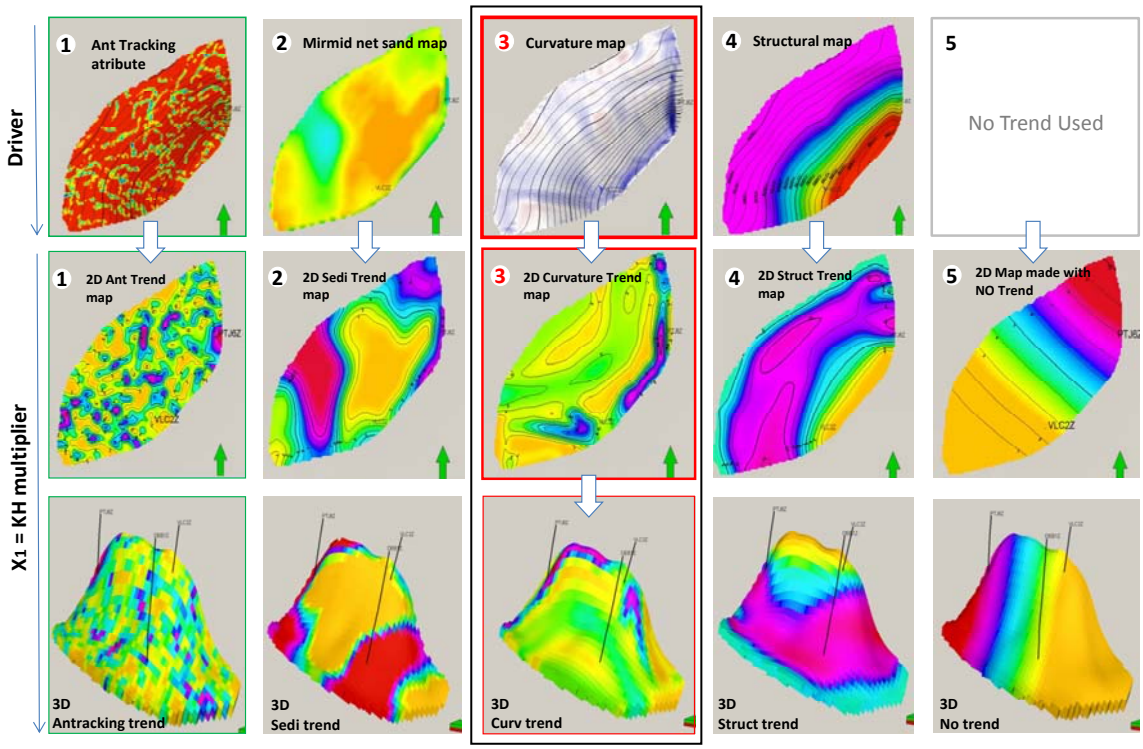

Figure 2-20. 3D Fracture Permeability methodology (from Gutierrez, 2013).

[46] Ant tracking is a workflow that uses the structural shape, Volume amplitude combined with a chaos theory and variance to identify fracture and fault trends. As the seismic quality is considered poor (see Figure 1-3), the ant tracking method could be less accurate finding the fracture distribution.

[47] See Section 1.3 for further information about the structural geology of Pauto and Floreña.

- **Correlation between the critically Stressed Fractures and the Geological Fracture Driver Mechanism.**

Gutierrez **[26]** in 2013 presented a work which uses a combination of the co-kriging geo-statistical technique combined with the curvature map of each sheet to generate the equivalent single porosity model which guarantees that each well correctly matches the KH from PBU.

As the effective permeability of the model is directly related to the permeability due to the geo-statistical and co-kriging process used in this fields, It was assumed that the fracture intensity will also have a direct correlation with the curvature, then a linear correlation between the fracture intensity and the permeability when only one data set of critically stressed fracture were available and a power law correlation ($I = ak_f^b$) when more than two data sets of critically stressed fractures were available,.

Figure 2-21 confirms that the assumption is a good approximation to match the 3D numerical simulation.

- Very good correlations for Pauto Main Sheet Mirador formation (see Plot 4 in Figure 2-21), Floreña Field Mirador (see Plot 1) and Barco (see Plot 2) formations were found, which confirm that the combination of the curvature driver with the number of critically stressed fractures could be a good initial approach.

- A deviation for the predicted power law correlations obtained for Dele Sheet Mirador formation can be explained by 2 reasons, one being that the KH interpretation made in one of the wells that was in the oil section is not directly comparable with the KH for all Pauto where there is gas condensate fluid; and the second being that the deviation happens in one of the wells that is below the dew point, which also affects KH estimations. These two considerations should be taken into account in future works to improve the petrophysical population of the reservoir simulation models.

- Guamalera sheet (see Plot 5) also shows a deviation in one of the wells, which is attributed to a high uncertainty related to the structure, see Section 1.3.2 and Figure 1-3.

  The well that does not match the 45^0 trend, is a new well that was not included in the petrophysical model as it was drilled after the model was created. Great geological efforts had been made to improve the predictability of the structural models, but there is still work to be done to understand the shape and curvature of the model.

- An example for Floreña Guadalupe is presented in Plot 3. The match uses just one data point. Similar to the graph presented for Guamalera Sheet this approximation could present a deviation in future prediction wells in case the shape of the structure is re-interpreted.

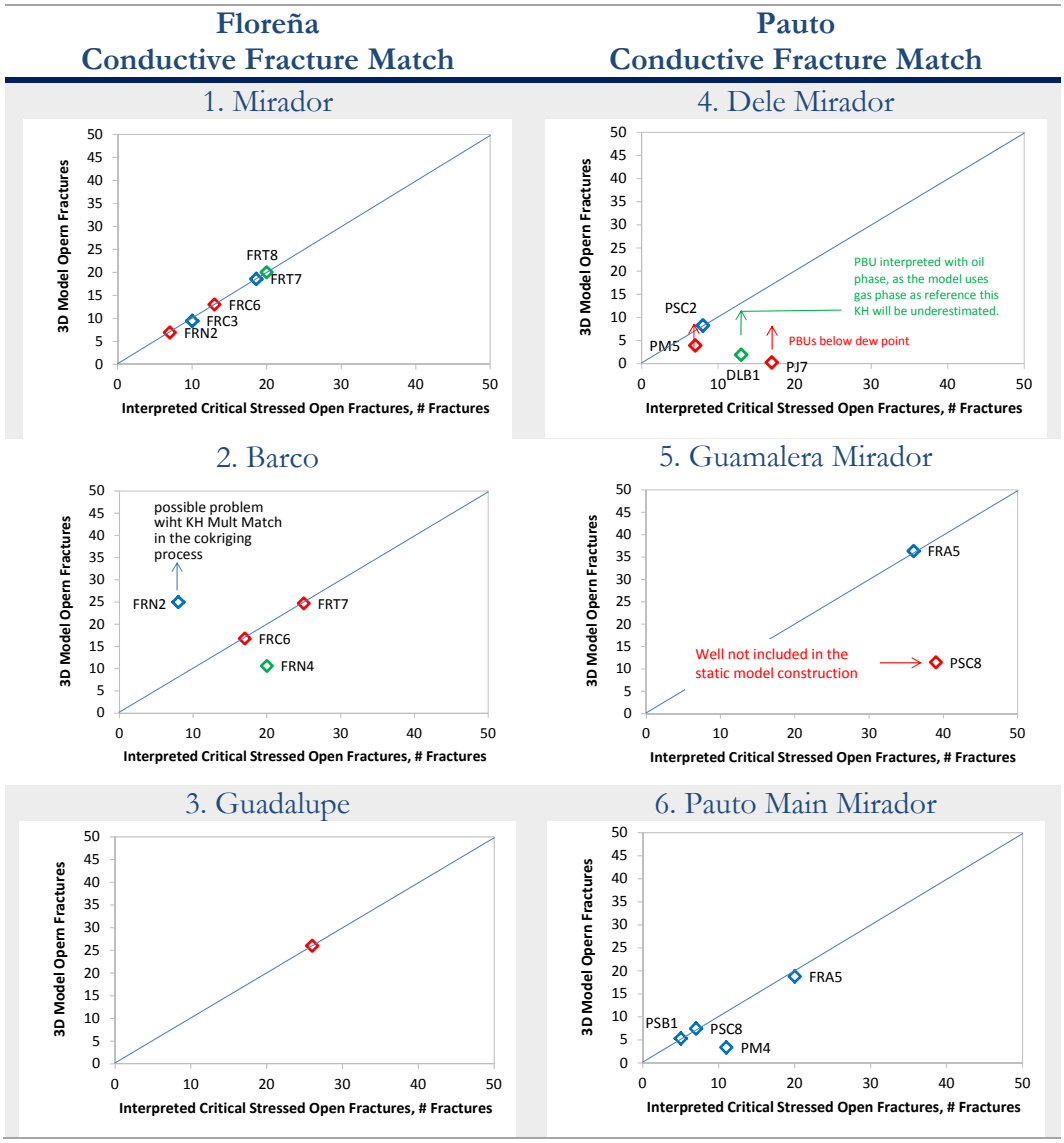

Figure 2-21. Fracture Intensity - Structural Driven Mechanism Match.

- **Pressure transient coefficients Check**

Figure 2-22 shows two main parameters that could be obtained in PBU interpretations when they are analyzed as dual porosity/dual permeability systems.

The purpose of this figure is to compare the storability factor (□) and the inter-porosity factor with the parameters that were presented in Section 1.5.5.

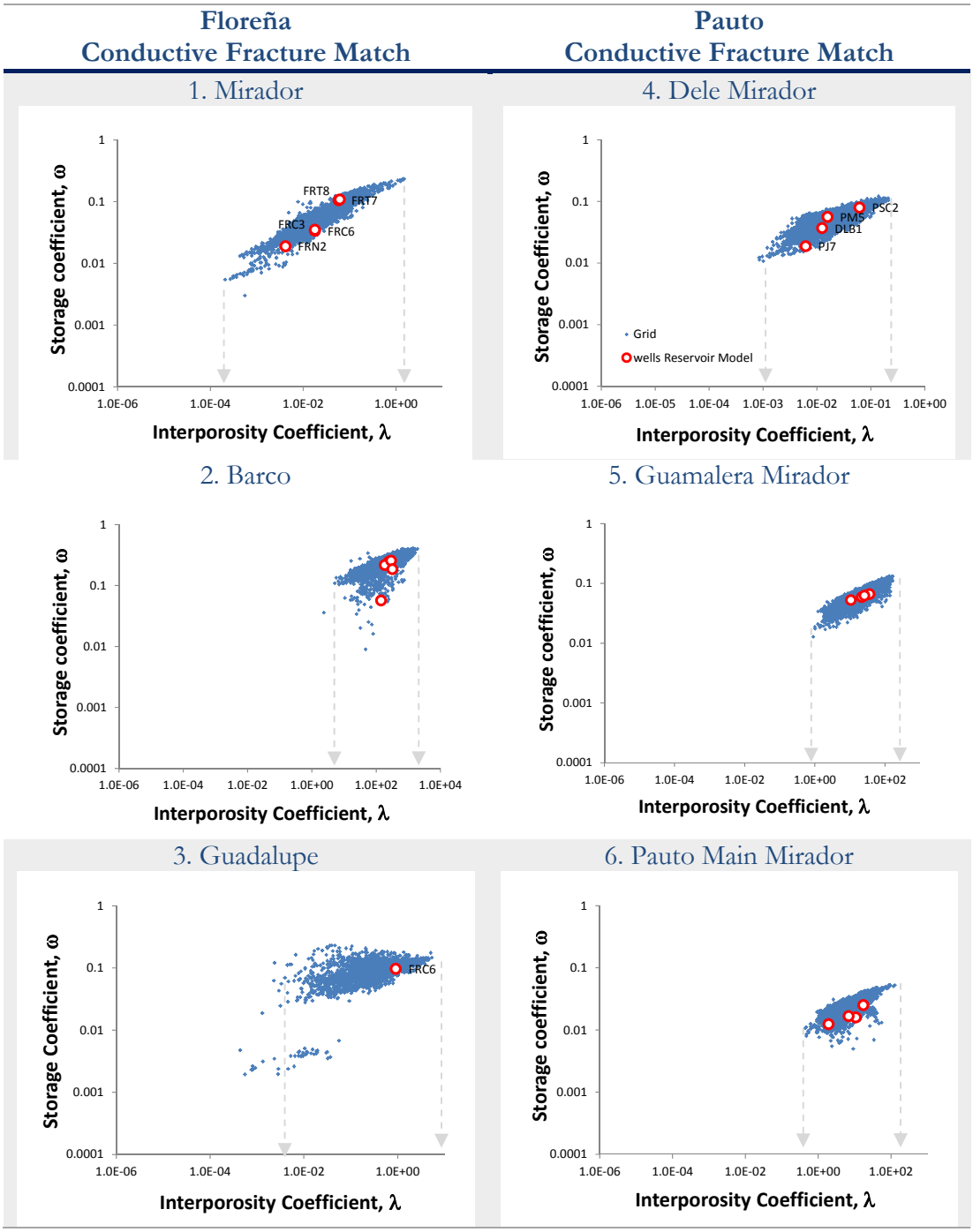

Figure 2-22. Pressure Transient Coefficients.

By using the petrophysical input for the reservoir simulation model in Dele Sheet Mirador formation and comparing the wells of Figure 1-46, the inter-porosity values for well 1 and 2 are $1.4x10^{-2}$ and $3.5\ x10^{-2}$ respectively, which are consistent with theoretical values presented in Figure 1-45.

- **Fracture Spacing, aperture and porosity**

Figure 2-23 and Figure 2-24 (right side graphs) show the apparent fracture aperture estimated for each formation, where it can be observed that the deeper the structure has the lower aperture, which confirms that the proposed methodology links the KH reduction with depth, which is observed in Figure 1-13 so, the workflow is generating consistent values of apertures with depth.

Figure 2-23 and Figure 2-24 (graphs on the right side) also shows an apparent aperture around 0.01 cm which are in the fracture spectrum and not in the micro-fracture spectrum. This quality control is important to keep consistency of the model built in this project.

Figure 2-23 and Figure 2-24 (left side plots) show a range for the fracture spacing in the structures' strike direction (Lx in the perpendicular direction of the maximum horizontal stress).

As the spacing is consistent with the geological observation and image log interpretations (see Figure 1-16 and Figure 1-17), these values directly affect the fracture porosity calculations, obtaining values in the order of $1x10^{-2}$ to $1x10^{-3}$ %, which are smaller compared to previous works **[21]**, where the porosity was in the order of 1%.

Theoretical values for fracture porosities are ~0.01% for apertures of ~0.01 cm, as it is shown in Figure 1-48. Refer to Figure 2-10, where the limits for the fracture porosity and fracture apparent apertures are presented, both which are comparable to the right side plots in Figure 2-23 and Figure 2-24.

Sheets (fields) and Reservoirs	Average Spacing in x direction by well in meters	Fracture Porosity and Aperture per reservoir
Floreña field Mirador formation Average depth ~8.000 ft TVDSS.	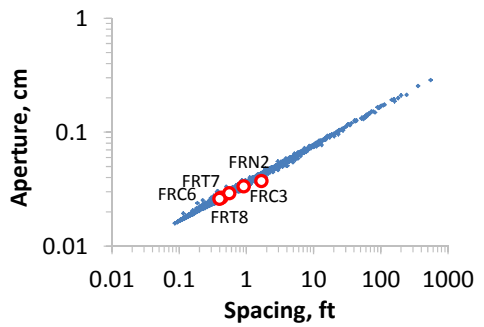	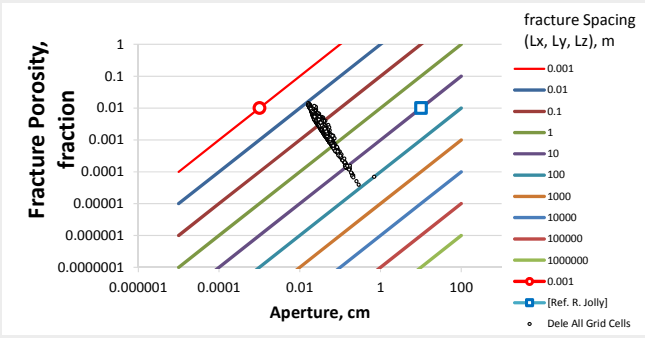
Floreña field Barco formation Average depth ~ 9.500 ft TVDSS.	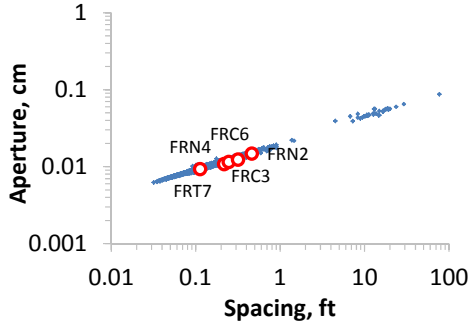	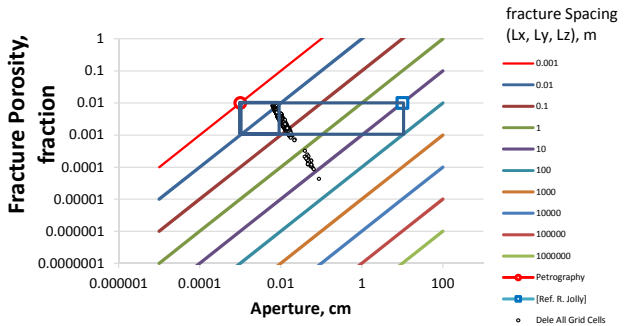
Floreña field Guadalupe formation Average depth ~ 12.000 ft TVDSS.	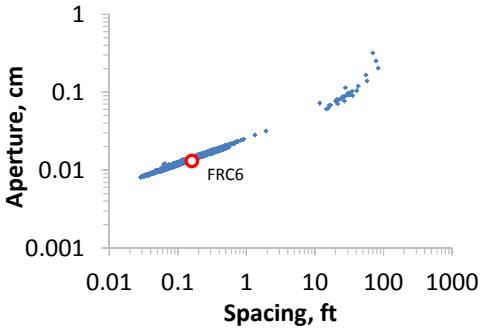	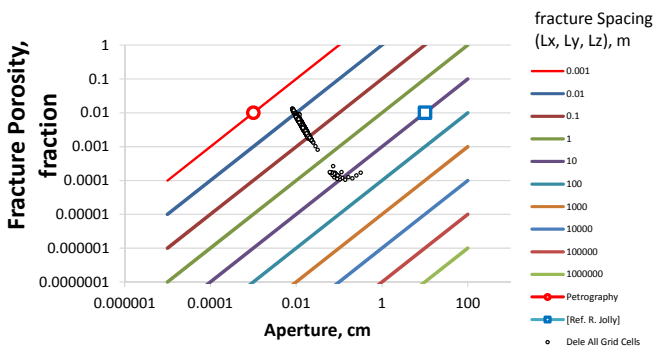

Figure 2-23. Estimations for Floreña Fracture Spacing vs. Aperture (left) and Aperture vs. Porosity (right).

Dele Sheet
Mirador formation

Average depth ~ 13.000 ft TVDSS.

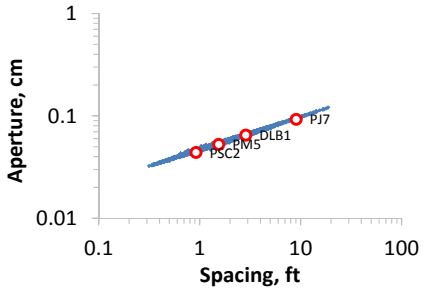

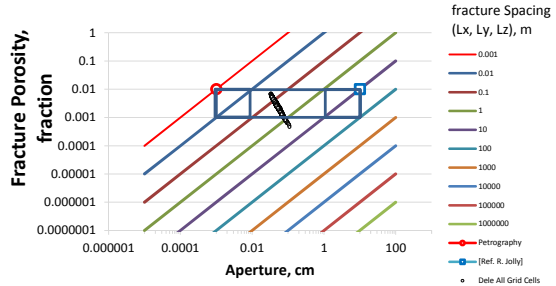

Guamalera Sheet
Mirador formation

Average depth ~ 14100 ft TVDSS.

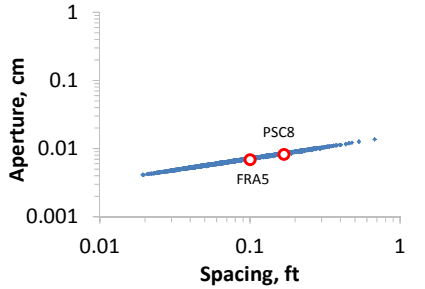

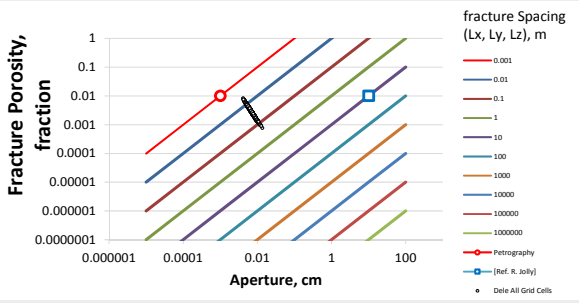

Pauto Main Sheet
Mirador formation

Average depth ~ 12.500 ft TVDSS.

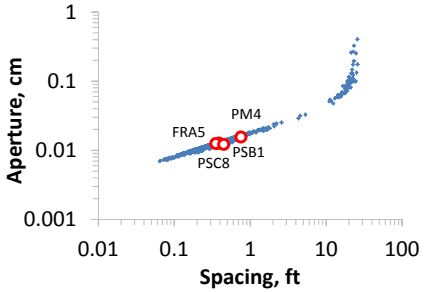

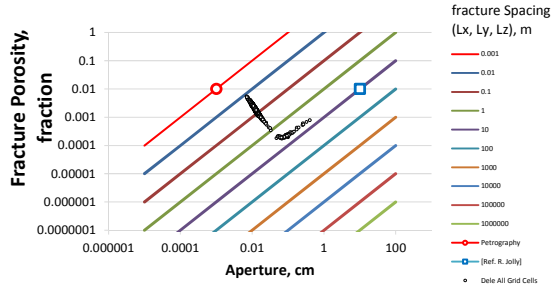

Granadillo Sheet
Mirador formation
(Co- Kriging source See Figure 2-20)

Average depth ~ 12.500 ft TVDSS.

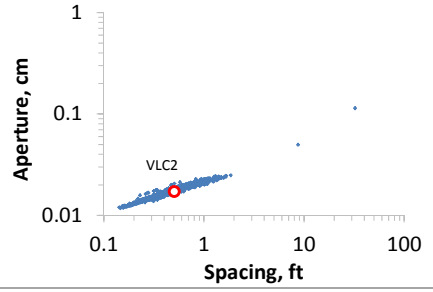

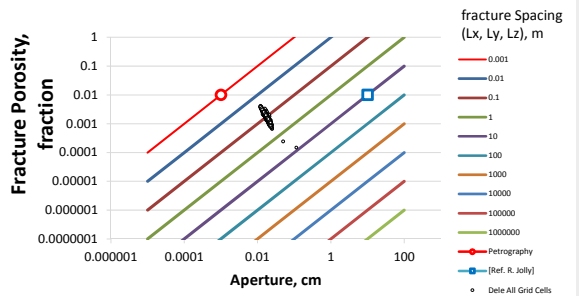

Figure 2-24. Estimations for Pauto Complex Fracture Spacing vs. Aperture (left) and Porosity vs. Aperture (right).

- **Shape Factor Check**

A general rule presented by Gilman **[20]** suggests that a typical natural fracture derived shape in the pressure transient analysis will not develop when $\sigma \cdot k_m > 0.1 md \cdot ft$. Figure 2-25 and Figure 2-26 (right side graphs) show that almost all PDM sheets (compartments) are above this value; this could be one of the reasons why wells that even have fractures are difficult to characterize with PBU interpretations.

As a reference:

- See Figure 1-45, which shows the theoretical behavior where the spacing increases when the inter-porosity values increase. This correlation is also found in Figure 2-25 and Figure 2-26.

- Inter-porosity (□) values obtained in Figure 2-25 and Figure 2-26 correlate with a spacing of 5 ft with average inter-porosity values of $1x10^{-3}$ obtained in Figure 1-45.

Figure 2-25 and Figure 2-26 (left side plots) show the shape factor values obtained for each reservoir, after matching the excess permeability (χ).

Reservoir/Sheets /Formations	Shape Factor (□)	□ .k_{mf}
Pauto Complex Dele	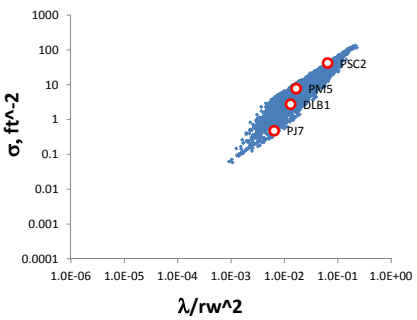	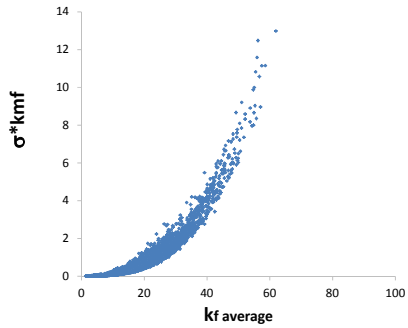
Pauto Complex Guamalera	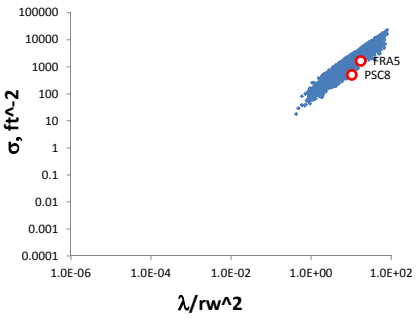	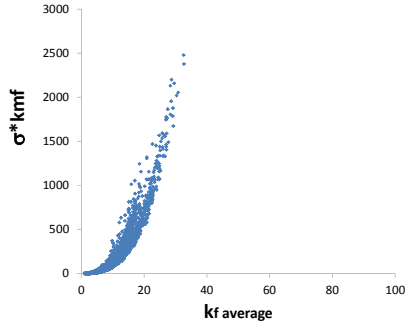
Pauto Complex Pauto Main Mirador	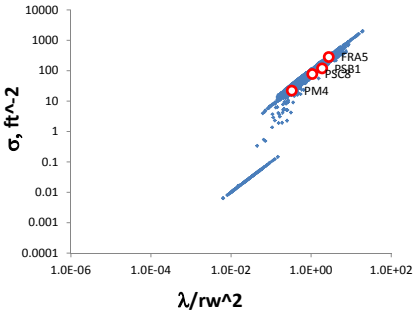	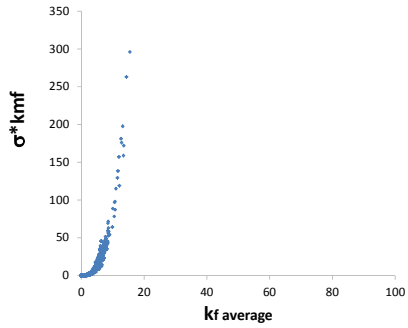
Pauto Complex Granadillo	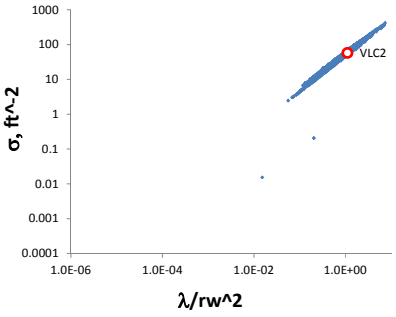	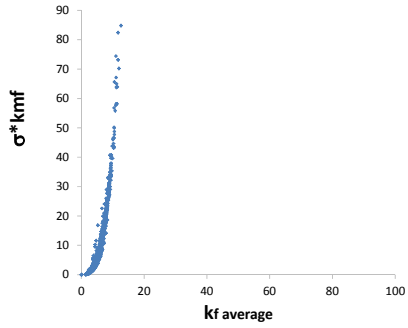

Figure 2-25. Pauto Field - Reservoir Simulation Shape Factor.

Figure 2-25 and Figure 2-26 also show that the shape factor and inter-porosity coefficients are high enough to hide the dual porosity/dual permeability effect described in detail within Section 1.6.5 with Figure 1-45.

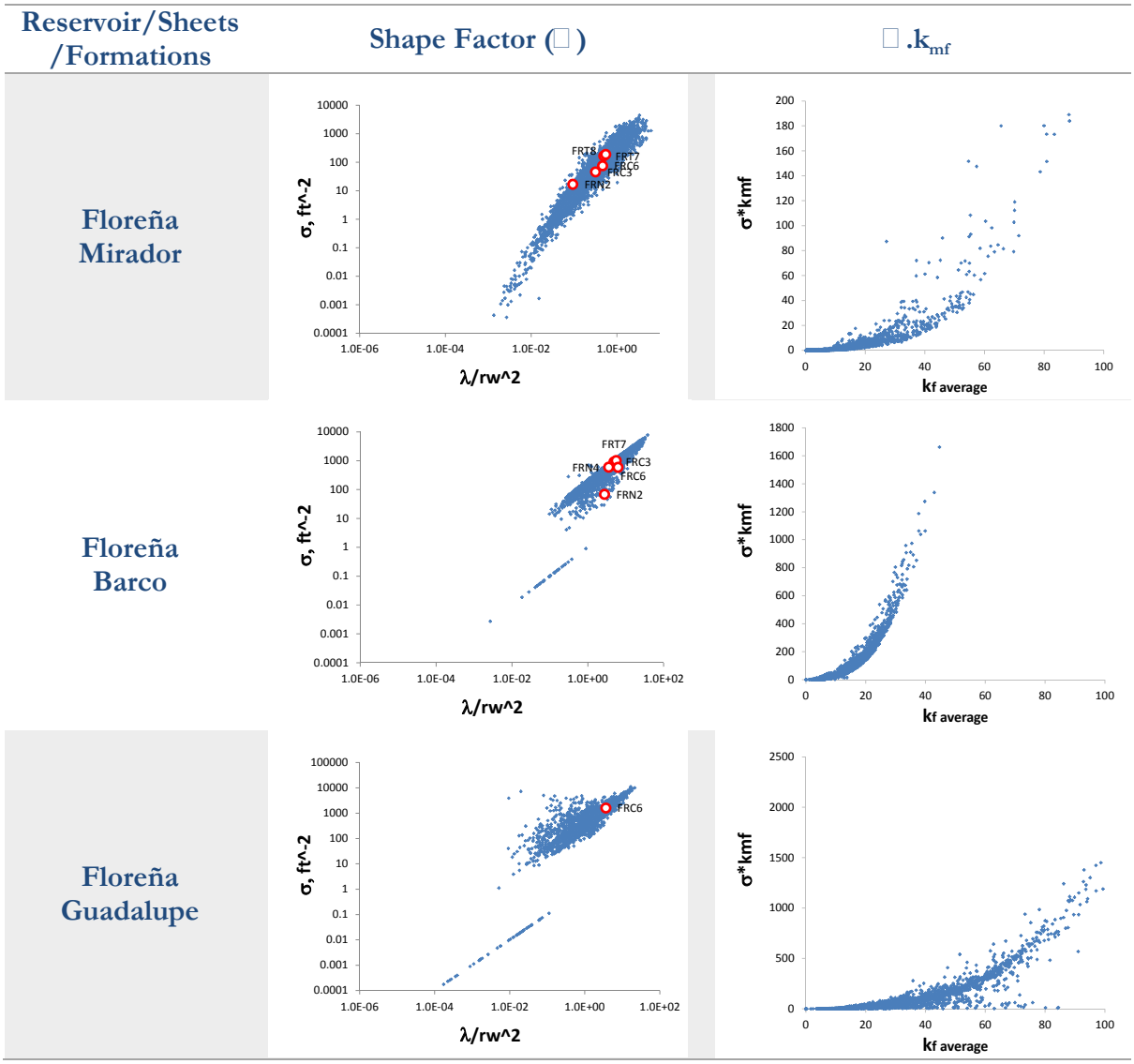

Figure 2-26. Floreña Filed - Reservoir Simulation Shape Factor.

- **Excess Permeability calibration**

Figure 2-27 shows the excess permeability match using this work's proposed methodology.

The *x* axes is the estimated excess permeability obtained with the curvature of the structures and then linked using co-kriging to match the KH of the wells in the static model. This approach was then compared with the estimation of the excess permeability graphed in the *y* axes using Eq. 2-43 by changing the apparent aperture until the match was obtained, in other words until the 45^0 line in Figure 2-27 plots were achieved.

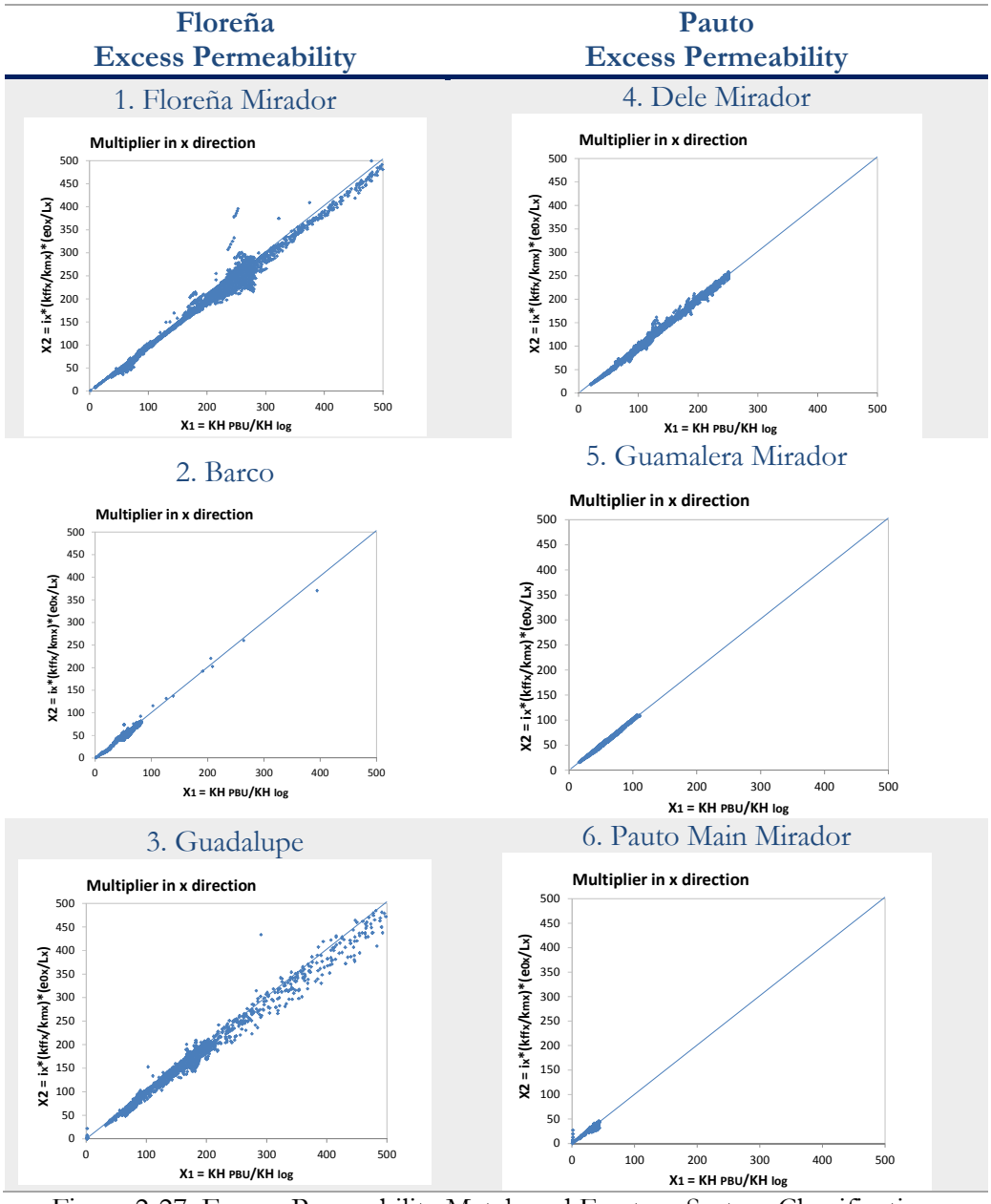

Figure 2-27. Excess Permeability Match and Fracture System Classification.

- **Natural Fracture System Classification**

Gilman Plot for a Natural Fracture Classification shows a lower excess permeability compared to the lines presented by the author **[27]**, see Figure 2-28.

Plot 4 in Figure 2-28 shows the PBU interpretation data (red triangle) reported in Table 1.1 and the comparison with the obtained data using the workflow for the reservoir simulation model (blue dots).

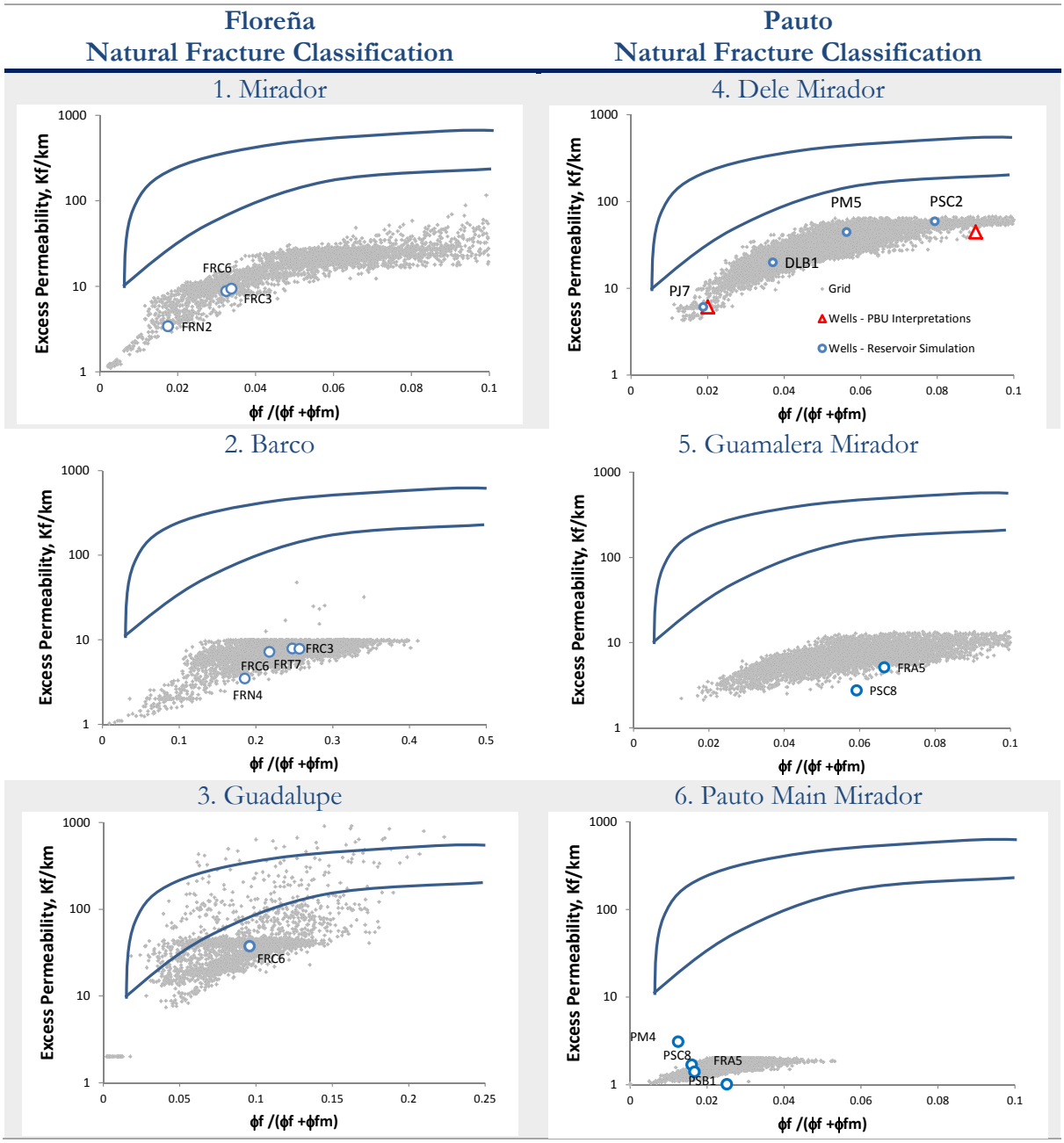

Figure 2-28. Gilman Plots for Fracture System Classification.

Nelson classification shows that the natural fracture system is located from a matrix flow point of view, as type III and type M (M-Matrix dominated flow, sometimes referred as type IV). The fractures play an important role in fluid flow within in type III reservoirs and wells, see Figure 2-29.

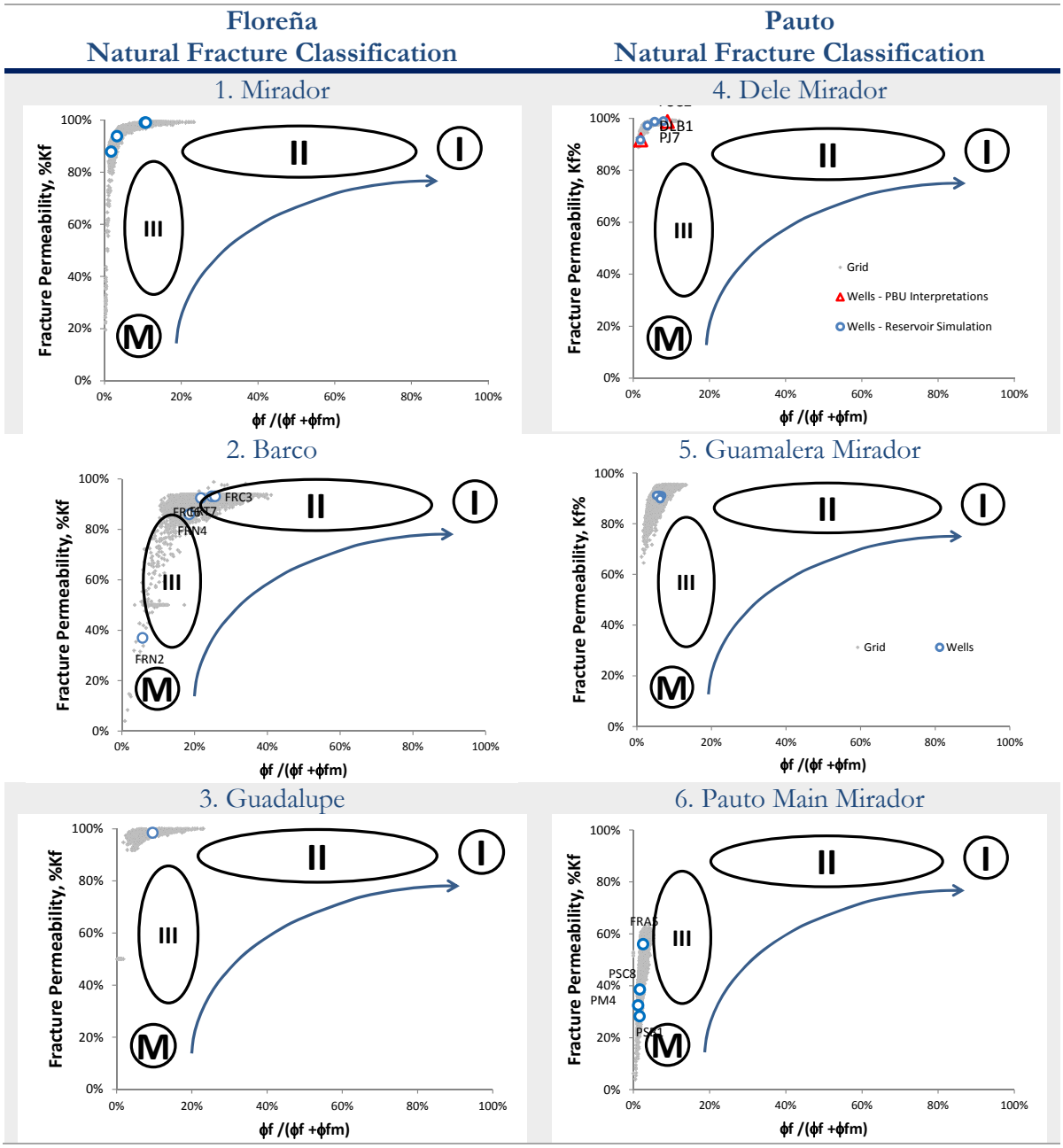

Figure 2-29. Nelson Plots for Fracture System Classification.

2.7.2.2 History Match

The methodology used for the history matching process was as follows:

1. Perform a Quality Control of the input data.

2. Perform a material balance for each reservoir, and compare it to the values obtained from the reservoir simulation model. This is the first step to guarantee that the energy of the system is within the expected limits.

3. Build different models in Rubis[TM, 48] software, which allows the selection of the most probable baffles, faults, and connections between the structures.

4. Afterwards, the static model (petrophysical model and structure) was built in Petrel[49]. **[22]**, which uses the material balance and connectivity analysis made in step 1 and 2.

5. A refined full field reservoir simulation model was then built in Nexus[50]. The refined model was coarsened in the vertical direction to improve the CPU time, see Section 2.6.1.2.

6. A first cycle history match (HM) was run using an Assisted History Matching Application for the coarse model[54].

7. Then, the best HM was selected, and then the History Matching of the model was manually improved.

8. Finally, the vertical coarse single porosity model was converted into a dual porosity model using the workflow presented in Figure 2-19.

Table 2.3 shows the nomenclature used for the sensitivities, where hm stands for history match, sp for single porosity, dp for dual porosity, C for Coarse, F for fine, s for single processor run, and d for dual processor run.

Table 2.3. History Match - Run Names.

Runs	Vertical Grid Size	History Run Name	Comments
1	Coarse	hm_spC1s	Equivalent model – Single Porosity
2	Refined	hm_spF1d	Equivalent model – Single Porosity
Reference	Coarse	hm_dpC1d	Base. Vertical grid size ~150 ft, see Figure 2-9.

[48] Rubis is a flexible reservoir simulation software, developed by Kappa, which allows the reservoir engineer to generate different structural grid shapes and simple petrophysical grid population. This was done due to a high uncertainty in the structural shapes (see Section 1.3).
[49] Petrel is a Schlumberger software package that integrates the petrophysical, geological and reservoir simulation modeling. Especially for this work, Petrel was used to perform the geo-statistical and co-Kriging work required to populate the matrix and fracture permeability for the single porosity and dual porosity/dual permeability static models.
[50] Nexus and DMS are Halliburton software tools used to create complex full field models and perform assisted history matching.

- Speed up factor.

The speed up factor combines the technology and time available; these 2 aspects should be considered as constraints when building a reservoir simulation model. For these cases, the last parallel processing available in the company was used, combined with a vertical coarsening to accelerate the running time.

A vertical coarsening was implemented to speed up the run time, keeping a balance between accuracy and time required for the evaluation.

The CPU time required for the models is presented in Figure 2-30, where the coarse single porosity model (see hm_spC1s) only takes 20 minutes to run, compared to 95.1 hours for the coarse dual porosity/dual permeability (DPDP) model, which was run in parallel mode using 2 processors (see hm_dpF1d2).

To run a DPDP full field model, at least to speed up factors must be considered (see Figure 2-30):

1. The coarsening of the vertical grid cells, which reduces the CPU time from 95.1 hr for the refined dual porosity/dual permeability model (see hm_dpF1d2) to 8.3 hr for the refined fine single porosity model (see hm_spF1d2).

2. The parallel processing with 2 processors reduces the CPU time from 95.1 hrs for the refined dual porosity/dual permeability model (see hm_dpC1s) to 10.9 hrs for the coarse dual porosity/dual permeability model (see hm_C1d2).

3. Current dual porosity/dual permeability models still have limitations for Piedemonte full filed simulation practical purposes, as the CPU times of 10.9 hrs are excessively high. The combination of both factors let the DPDP model run in 10.9 hr (see hm_dpC1d2), compared to the SP model that runs in 0.4 hrs (see hm_spC1s).

4. The proposed workflow generates spacing values of less than 10 ft, which gives a high transmissibility contrast. When spacing values are limited to values higher than 1 ft and the model is run in 4 processors, the CPU time changes from 10.9 hr to 3 hrs.

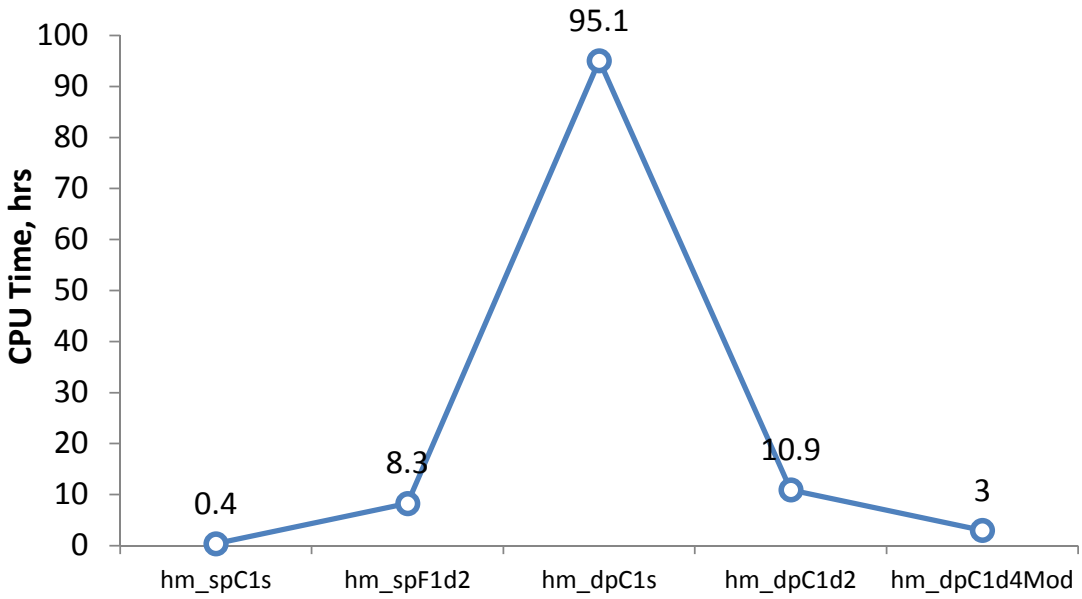

Figure 2-30. CPU Time for the Refined and Coarsened Single and Dual Porosity Models.

- History Match.

As there are several variables and reservoirs to be analyzed in this project, the following graphs were organized in order to synthetize as much as possible the history matching results for the single and DPDP models.

Figure 2-31 shows the reservoir pressure behavior by sheet, which indicates a similar behavior between the SP model and the DPDP model.

Figure 2-31, Figure 2-32, Figure 2-33 and Figure 2-34 show that the refined model does not generate big changes in pressure and production matching, allowing to work with the coarse model as the base case in this project.

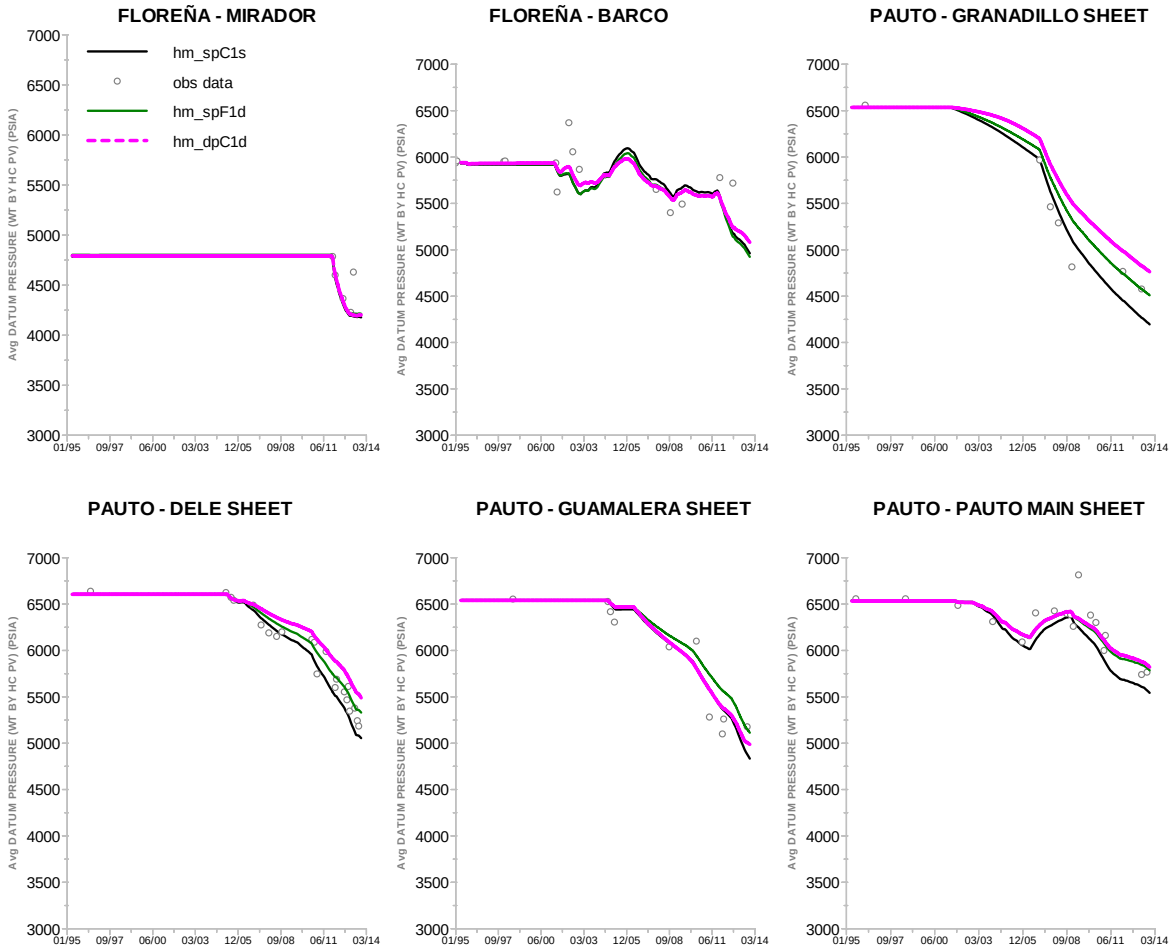

Figure 2-31Pauto and Floreña Fields - Observed and Simulated Data for the SP and DPDP System.

See Figure 1-6 as a reference to see a map and the location of each sheet in the field.

Figure 2-32 shows the production variables at field level, which includes both fields Pauto Complex and Floreña.

The main achievement by implementing the natural fracture system and the proposed workflow in Figure 2-19 is an improvement in water production while keeping a similar history match in both the single porosity model and the DPDP model.

The main reason for the slight improvement in water production was because of a better representation achieved with the pore space and permeability for the water moving from the aquifer to the wells.

As the SP model represents an equivalent permeability (for the matrix and fracture system) with the porosity coming from the matrix, the water has a higher mobility to flow from the aquifer to the wells.

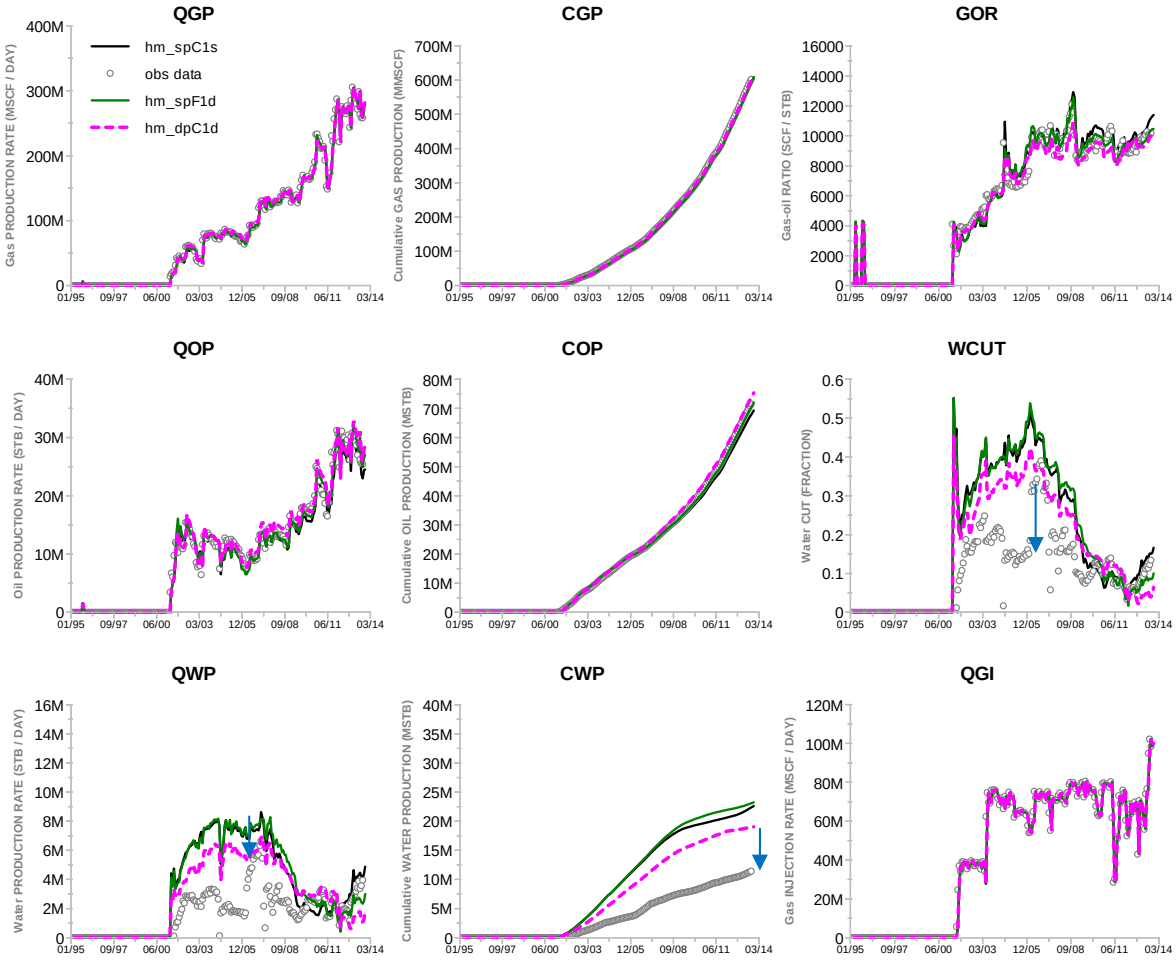

Figure 2-32. Field - Observed and Simulated Data for the SP and DPDP.

Figure 2-33 shows the effect of the slight improvement in the GOR evolution of a selected well in a gas condensate blow down section when modeling the reservoir as a DPDP system. This improvement is due to a better representation of the sheet's pressure depletion and a better condensate flow in the fractures. Notice that the condensate flow in the fractures affects the GOR evolution of the wells.

For practical purposes, the history match of the SP and DPDP models have the same behavior.

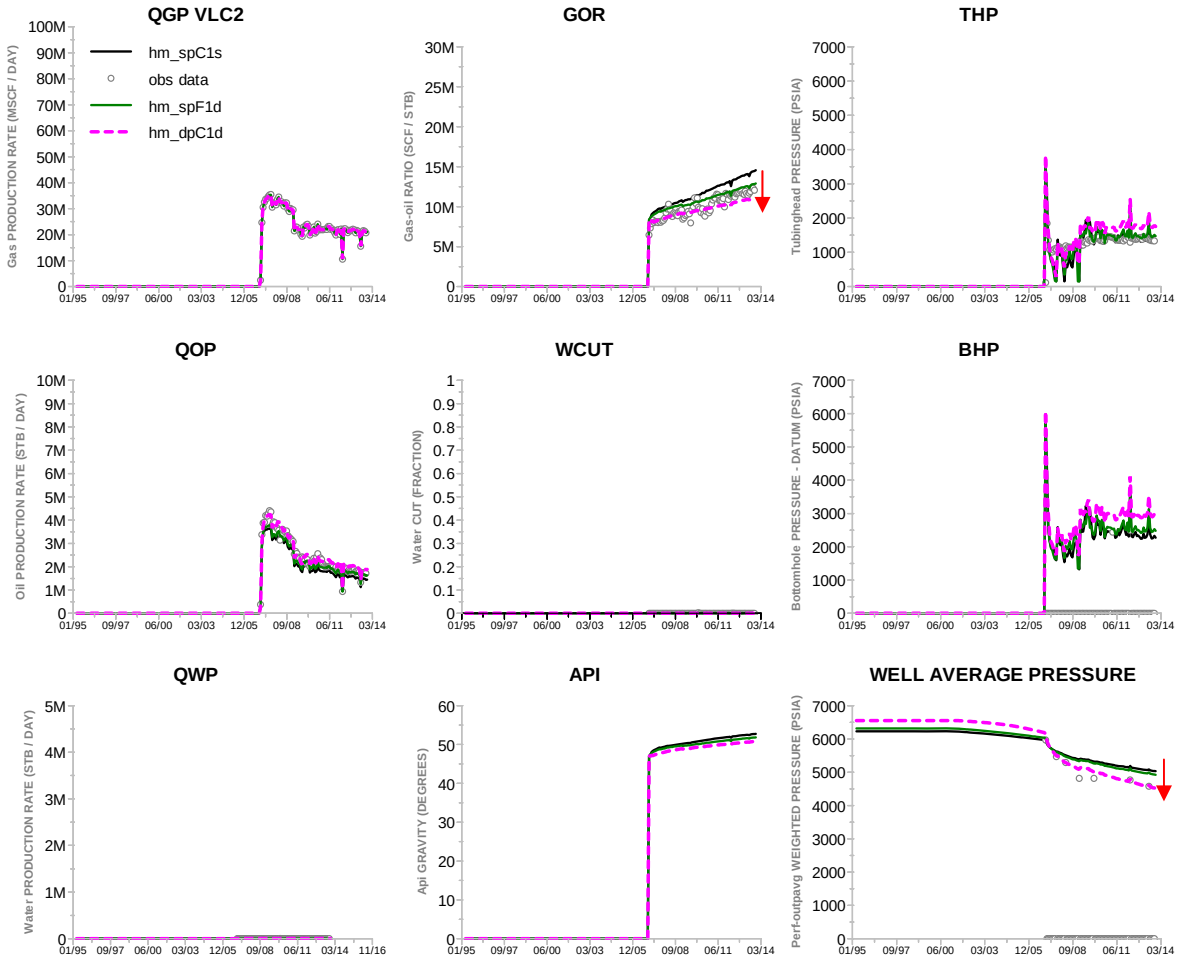

Figure 2-33. Selected Gas Condensate Well under Pressure Depletion – Granadillo Sheet-Observed and Simulated Data for the SP and DPDP Systems.

Figure 2-34 shows a well located in the oil zone of Floreña with miscible gas injection. Both models, the SP and the DPDP have a similar history match. The history match was basically achieved by keeping the same volumetric and especially the same KH values for the well following the proposed workflow in Figure 1-1 and Figure 2-19.

So, by using the simple workflow proposed in Section 2.7.1, it was possible to guarantee a similar flow capacity in the well, which gave good results for the history matching of the DPDP model.

Figure 2-34 shows a good improvement in the THP values, which can be reflected in a possible improvement in the BHP values as well. In the DPDP model, the fractures allow the well to produce with a higher BHP; this is observed when comparing the SP model (hm_sp, the gray and green solid lines) with the DPDP model (hm_dp, the dashed magenta line).

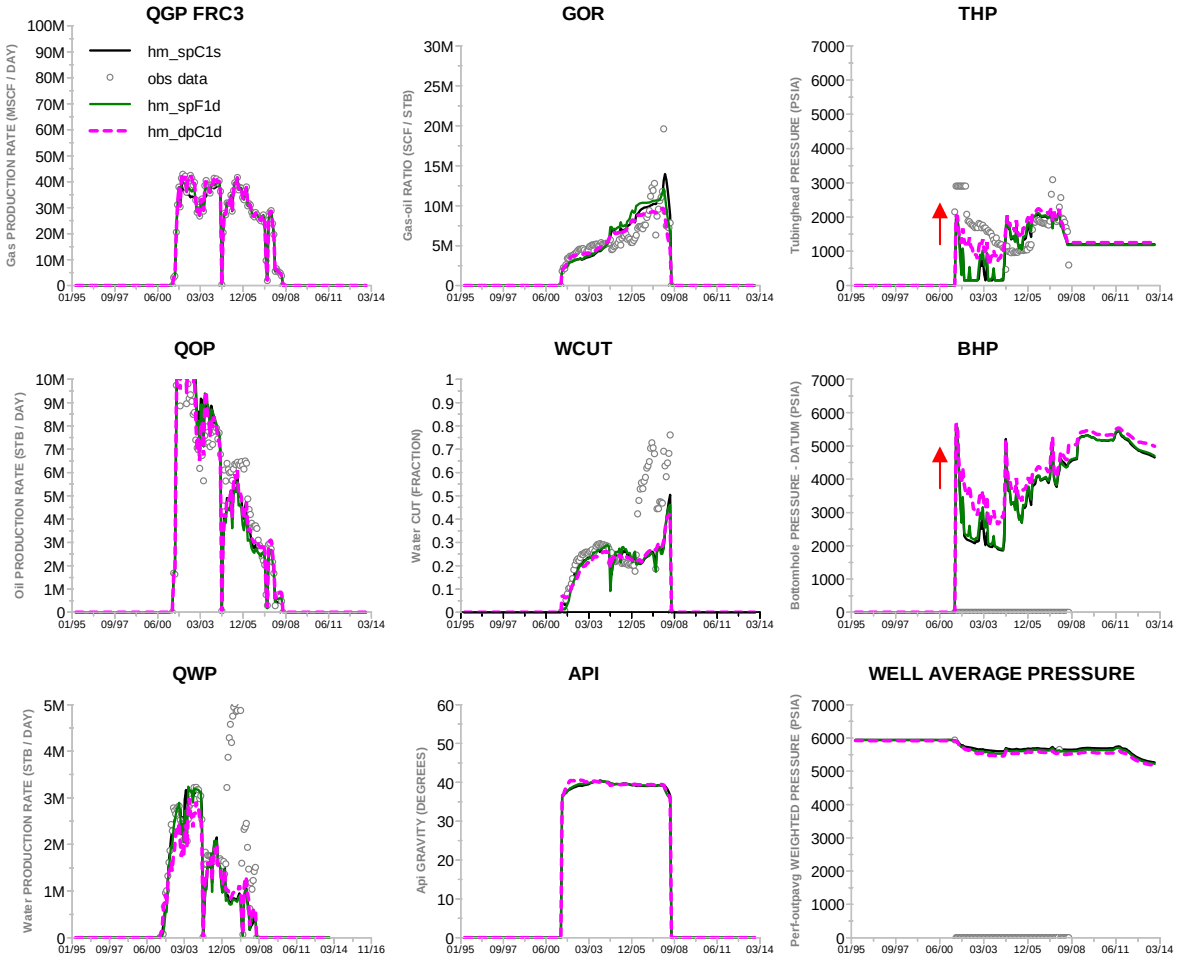

Figure 2-34. Selected Volatile Oil Well with Miscible gas Injection - Observed and Simulated Data for the SP and DPDP Systems.

Figure 2-35 shows an aerial view of the oil saturation distribution at field level for Pauto and Floreña fields, with some places reaching values of around 20% (see green areas).

The following figures are presented to analyze the flow in the reservoir. Additional oil density and viscosity analysis is presented in Appendix C, as the resolution of Figure 2-35 is not enough to define the impact of the oil saturation in the field.

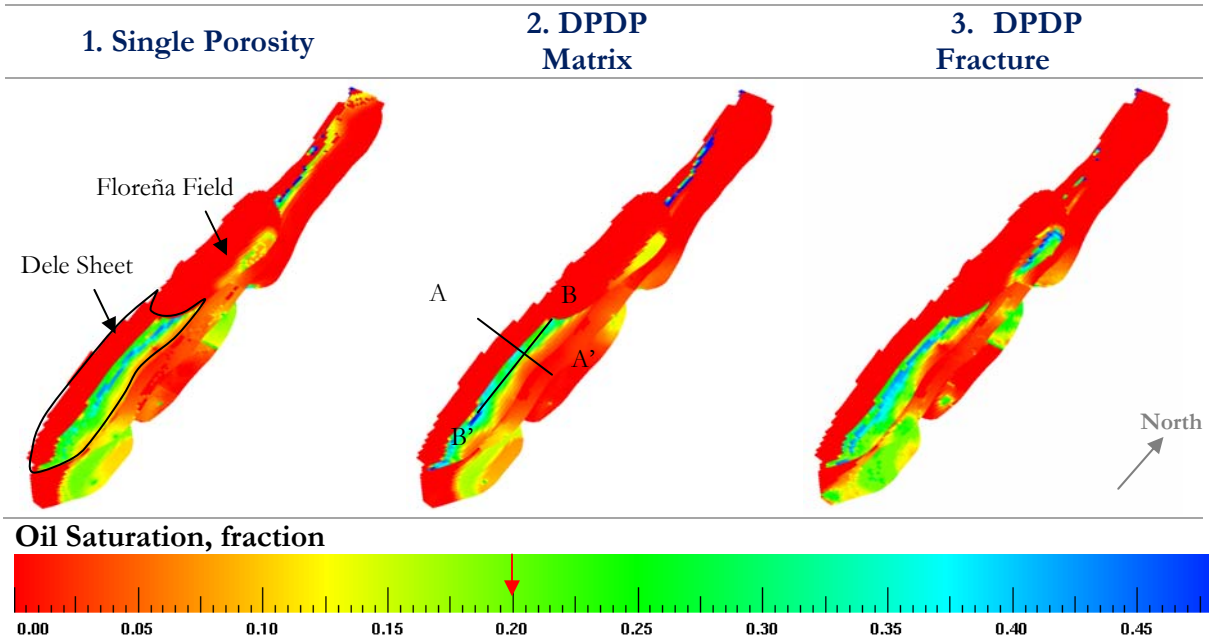

Figure 2-35. Field Oil- Saturation Comparison of SP and DPDP – end of History matching process.

This section still does not consider the Nitrogen injection, for comparative purposes see in the Section 3, the Figure 3-17 and Figure 3-18.

- **Oil Saturation.**

Even if the history match for the SP and the DPDP models are almost the same (see Figure 2-31 to Figure 2-34), there is a huge difference in the oil saturation distribution (higher in the fracture system compared to the SP model).

Figure 2-36 shows a higher vertical oil segregation within the fracture for DPDP model (see Plot 3), compared to the SP model (see Plot 1).

Figure 2-36 represents a cross section in the *x* and *y* direction, which is highlighted in the middle plot of Figure 2-35 (Plot 2).

As a reference, this cross section will be used in the analysis presented in Chapter 3.

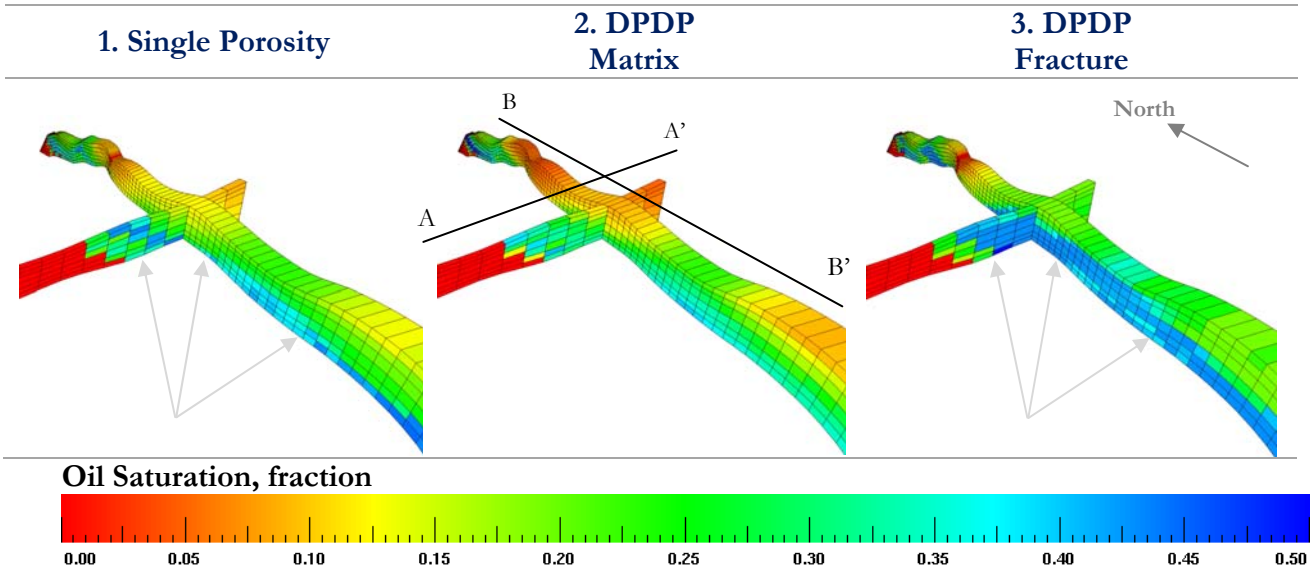

Figure 2-36. Dele Sheet Ternary Oil- Saturation Comparison of SP and DPDP – end of History matching process.

- **Horizontal oil flow.**

Figure 2-37 shows the difference in the flow behavior between the SP and DPDP models.

- Point A in Figure 2-37 shows oil flow at the bottom of the structure for the SP model, while the DPDP model shows that there is no oil flow at the bottom of the structure.
- Point C in Figure 2-37 shows that the oil flow in the DPDP model is right in the middle of the structure and slightly less than in the SP model.
- Point B in Figure 2-37 shows that there is no oil flow in the matrix system of the DPDP model, while the SP model shows that there is oil flow.

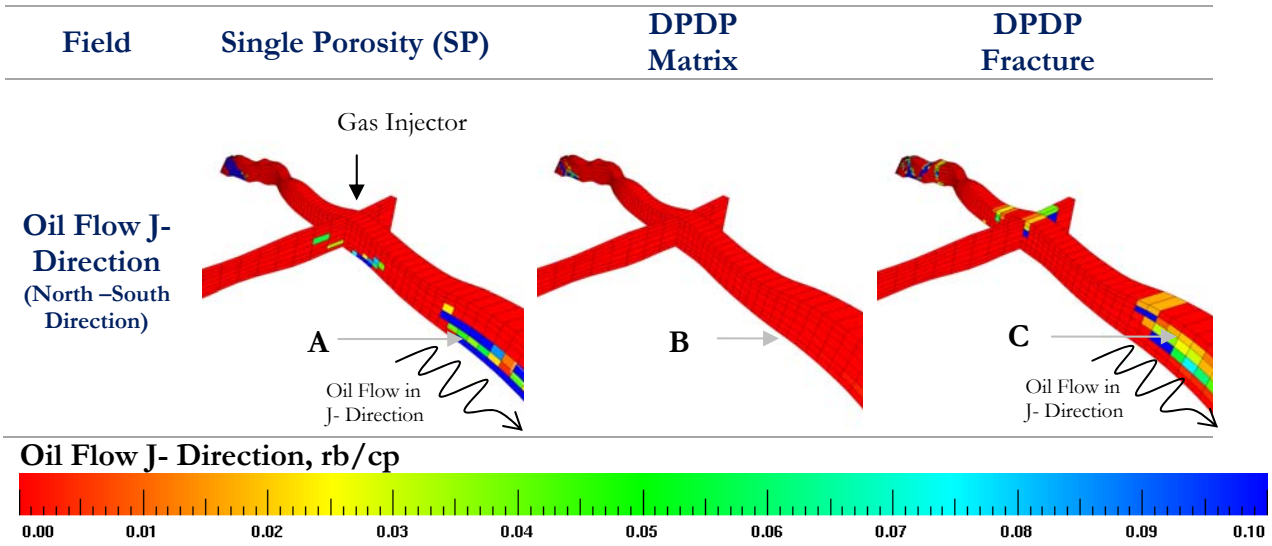

Figure 2-37. Dele Sheet - Oil Flow J- Direction Comparison of SP and DPDP – end of History matching process.

Figure 2-38 shows the oil, gas and water saturation at the end of the history matching process, and the arrow represents the approximate limit of the displacement front.

While the matrix has a similar 3 phase fluid distribution compared to the SP model, the fracture system exhibits a very different distribution, showing higher degree of oil saturation at the top of the structure.

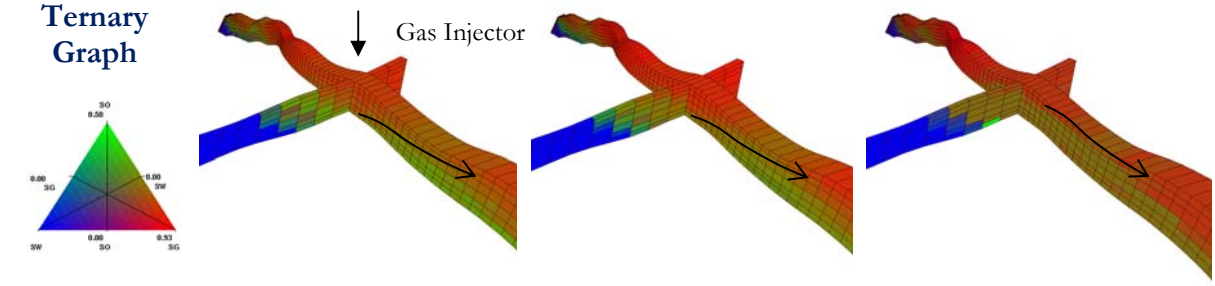

Figure 2-38. Dele Sheet – Oil, Gas and Water Ternary Saturation. Comparison of SP and DPDP – end of History matching process.

- **Oil Segregation.**

The blue cells in Figure 2-39 represent a higher oil flow in the K+ direction (vertical direction).

The oil segregation represented in the single porosity model is lower than in the matrix and fracture of the DPDP model (see points A, B and C).

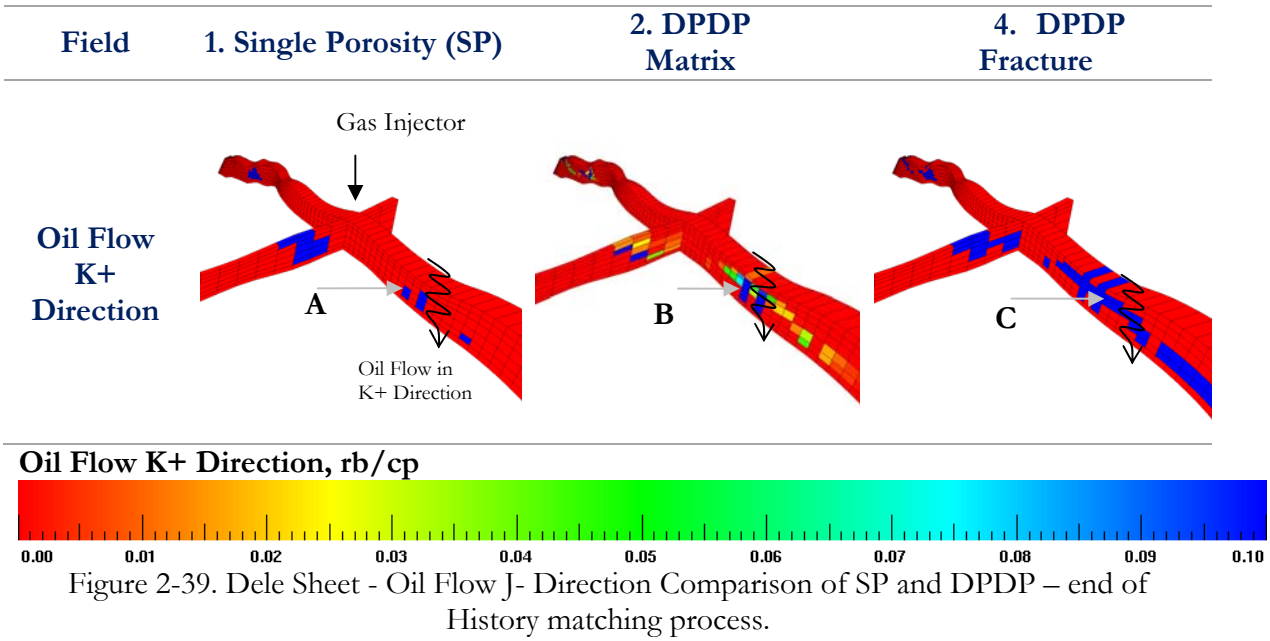

Figure 2-39. Dele Sheet - Oil Flow J- Direction Comparison of SP and DPDP – end of History matching process.

Figure 2-40 shows that there are very low oil relative permeability (kro) values for oil saturation fraction from 0.2 to 0.4 for the SP model (left side plot, Plot 1) and the matrix system in the DPDP model (middle plot, Plot 2), those values are tied to the relative permeabilities presented in Section 2.6.3.5.

For the fracture system of the DPDP model (right side plot, Plot 3), there is higher oil saturation at the bottom of the structure with slightly better oil relative permeabilities.

Even if there is some mobility of oil as observed in Figure 2-40, the net flow in those cells is still very low as it can be seen in Figure 2-37.

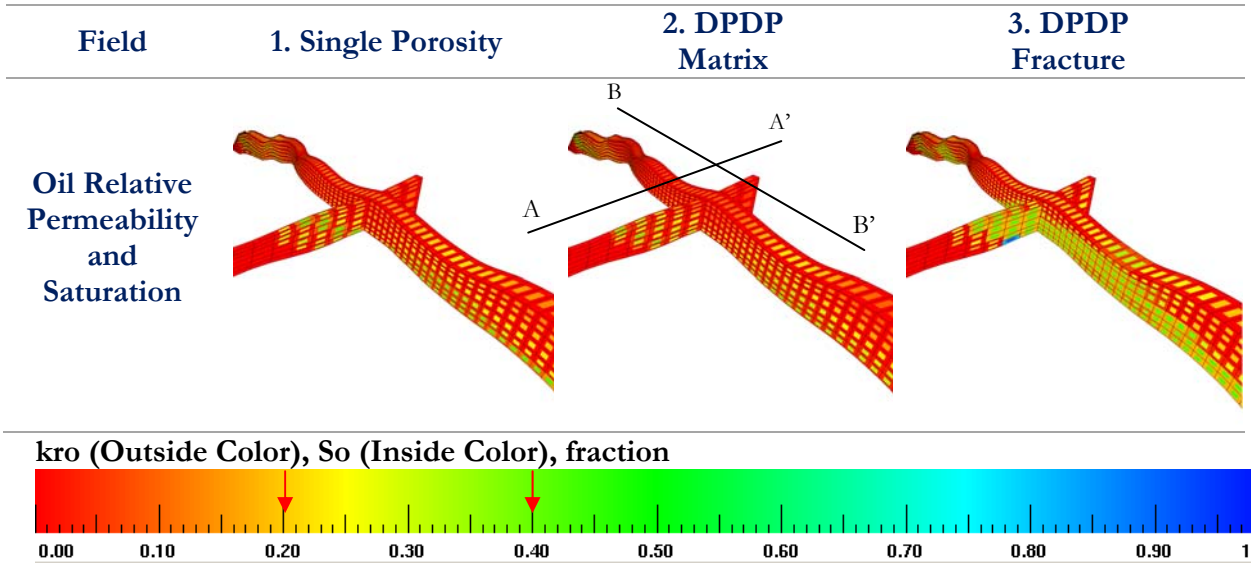

Figure 2-40. Dele Sheet - Oil Relative Permeability and Oil Saturation- Direction Comparison of SP and DPDP – end of History matching process.

2.8 Summary and Conclusions

1. It is possible to pose a detailed mathematical and numerical model with compositional fluids and a dual porosity/dual permeability system to represent the fluid flow in the reservoir, see Section 2.4 and Appendix A.

2. The proposed workflow and equation to build a dual porosity/dual permeability model by estimating the apparent apertures successfully links the static and dynamic models to estimate the shape factor, fracture porosity and permeability to calibrate the field data, see Eq. 2-43, Figure 2-19, Section 2.5.2.1.

3. The methodology proved to be successful to achieve a history match of Pauto and Floreña fields, see Figure 2-31 to Figure 2-34 in Section 2.8.2.2.

4. With the methodology that was proposed in this work, it was possible to estimate that the average apparent apertures are in the order of 0.005-0.01 cm, see Figure 2-23 and Figure 2-24.

5. The high the critical stressed fracture intensity created in the model is related to high fracture dips, which generate theoretical fracture spacing of less than 10 ft, see Figure 2-21, Figure 2-23 and Figure 2-24).

6. Spacing and apparent aperture are strongly related with the fracture porosity and permeability, as it was explained in Figure 1-19; both parameters were used effectively to obtain consistency in the data used for the dual porosity/dual permeability model construction, as it is seen in Figure 2-10, Figure 2-23 and Figure 2-24.

7. The expected storability coefficient (□) for Pauto and Floreña fields are between 0.01 to 0.1, and the inter-porosity coefficient (□) is in the order of 10^{-2} when the excess permeability is higher than 10 (see). These values make it difficult to observe the characteristic DPDP pressure derivate behavior, as it is necessary to have low fracture porosities (<1%) and lower inter-porosity values (~10^{-6}) to see the characteristic pressure derivative shape from pressure transient analysis, see Figure 2-22 and Figure 1-47.

8. Even if the match in production and pressure between the SP and DPDP models where very close, 2 main differences were observed: 1) a higher vertical condensate segregation generated in the fracture system compared with the single porosity model (see Figure 2-36 and Figure 2-39) and 2) a higher reduction in the mobility of the liquid drop out generated in the matrix compared with the single porosity model (see Figure 2-37).

9. To run a DPDP full field model, at least to speed up factors must be considered, 1) the coarsening of the vertical grid cells reduces the CPU time from 95.1 hr to 8.3 hr, compared to the refined SP model, 2) the parallel processing, reduces the CPU time from 95.1 hrs to 10.9 hrs compared to the DPDP model that was run in a single processor. The combination of both factors let the DPDP model run in 10.9 hr, compared to the SP model that runs in 0.4 hrs, see Figure 2-30.

2.9 References

1. C. WHITSON AND M. BRULE. Phase Behavior. Monograph Volume 20 SPE. First Printing. Texas, USA. 2000.

2. A. CASTILLO Y J. MONTOYA. Modelamiento Numérico del Comportamiento del Banco de Condensado en las Cercanías del Pozo. Trabajo de Grado en Ingenieria de Petroleos. Universidad Nacional de Colombia, Sede Medellín. 2003.

3. J. WARREN AND P. ROOT. The Behavior of Naturally Fractured Reservoirs. Soc. Pet. Eng. J. pg. 245-255. Sep 1963.

4. M. SAHIMI. Flow and Transport in Porous Media and Fractured Rock. From Classical methods to modern approaches. Second, revised and enlarged Edition. 2009.

5. D. BELIVEAU, ET AL. Analysis of the Waterflood Response of Naturally Fractured Reservoir. SPE 22946. Dallas, USA. October 6-9 1961.

6. J. RINGER ET AL. Experimental and Numerical Studies if Gas Injection in Fractured Carbonates: Pressure and Compositional effects. International Symposium of the Society of Core Analysis held in Toronto, Canada, 21-25 August 2005.

7. T. BRATTON ET AL. The Nature of Naturally fractured Reservoirs. Oilfield Review. 2006.

8. L. UTRIA. Estimación Teórica de permeabilidad en yacimientos naturalmente fracturados verticalmente. Universidad Industrial de Santander. Trabajo de Grado. Bucaramanga, Colombia. 2007.

9. L. F. AYALA ET AL. Analysis of Condensate Buildup and Flow Impairment of Retrograde Gases in Fissured Reservoirs. Presented in the SPE Latin American and Caribbean Petroleum Engineering Conference-. SPE 107870. April 2007.

10. V. AMUNDSE. Effects of Fracture Capillary Pressure and non-straight Relative Permeability Lines. Norwegian University of Science and Technology. Thesis. May 2012.

11. M. HONG ET AL. The Up-scaling of Discrete Fracture Models for Faster, Coarse-Scale Simulations of IOR and EOR Processes for Fractured Reservoirs SPE 166075., Society of Petroleum Engineers. Copyright 2013.

12. W. AKAND ET AL. A Review on SPE´s Comparative Solution Projects (CSPs). The University of Texas. Journal of Petroleum Science Research (JPSR) Volume 2 Issue 4, October 2013.

13. R. HINKLEY ET AL. Nexus Technical Publications. https://www.landmark.solutions. SPE 106069-MS, SPE 87813-PA, SPE 163619-MS. 2013.

14. M. JAMIOLAHMADY ET AL. A Generalized correlation for predicting gas –condensate relative permeability at near wellbore conditions. Journal of Petroleum Science and Engineering. Elsevier B.V. 2009.

15. M. JAMIOLAHMADY ET AL. Gas/condensate Relative Permeabilities in Propped-Fracture Porous Media: Coupling vs. Inertia. SPE 115726. July 2008.

16. M. JAMIOLAHMADY ET AL. Gas/Condensate Relative Permeability of a Low Permeability Core: Coupling vs. Inertia. SPE 120088. April 2010.

17. G. PEÑUELA. Prediction of the Gas-Condensate Well Productivity and Field Implementation using a Compositional Model, M.Sc. Thesis, U. of Oklahoma, OK 1999.

18. NEXUS TECHNICAL REFERENCE. Halliburton. December 2013.

19. K. COATS. Implicit Compositional Simulation of Single-Porosity and Dual-Porosity Reservoirs. SPE 18427, presented at the SPE Symposium on Reservoir Simulation in Houston, Texas, USA. Feb. 1989.

20. J. GILMAN. Practical Aspects of Simulation of Fractured Reservoirs. International Forum on Reservoir Simulation. Littleton, CO, USA. pg. 15. June 23-27 2003.

21. R. JOLLY. Floreña Fracture Characterization and Modeling. Equion Energia LTDA. Internal Report. Bogota, Colombia. October 2002.

22. Z. GUITERREZ Piedemonte Static Model Construction. Equion Energia LTDA. Internal Report. Bogota, Colombia. 2013.

23. F. MEDINA. Consideraciones sobre el índice Gini para medir la concentración del ingreso. Serie: Estudios Estadísticos y Prospectivos. División de Estadística y Prospecciones Económicas. Santiago de Chile. Marzo de 2001.

24. D. GOMEZ AND C. HERRERA. Modelos Radiales Campo Cupiagua: Daño por Banco de Condensado. BP Internal Report. Bogota, Colombia. Enero 2008.

25. V. GOLF-RACHT, T.D. Fundamentals of Fractured Reservoir Engineering. Amsterdam: Elsevier Scientific. Amsterdan – Oxford – New York. 1982.

26. Z. GUTIERREZ. Piedemonte 2013 Static Model. Equion Energia Internal Report. Bogota, Colombia. 2013.

27. J. GILMAN ET AL. A New Classification Plot for Naturally Fractured Reservoirs. Canadian Unconventional Resources Conference. SPE 146580. Alberta, Canada. 15-16 November 2011.

3. NITROGEN INJECTION

3.1 Introduction

The objectives of this work are to model nitrogen injection process in a natural fracture system and evaluate the impact of the main static uncertainties like gas trap saturation, permeability, relative permeabilities and dynamic uncertainties like nitrogen injection rates and composition on the recovery efficiency for Piedemonte fields.

A dual porosity/dual permeability model that was built using a new and simple workflow proposed in Chapter 2 and the surveillance data explained in Chapter 1 was used to carefully evaluate and understand the impact of nitrogen injection on the oil and gas recoveries of the matrix and fracture systems.

It is known that the Minimum Miscibility Pressure (MMP) of the oil decreases when the C7+ molecular weight decreases and C2-C6 mole fraction increases **[1, 2, 3]**. On the other hand, both fractures and Matrix begin to change the proportion of C7+Molecular Weight to C2-C6 mole fraction through time, which changes the Miscibility pressure in each system when nitrogen is injected, as shown in Figure 3-2 and Figure 3-38.

Two main injection sensitivities were tested in order to equilibrate the potential losses of nitrogen injection compared to lean gas injection and improve the efficiency of oil and gas matrix displacement: 1) Different injection rates (see Section 5.6.2) and 2) different N_2 composition combinations with CO_2 (see Section 5.7.2).

The results show that once the liquid had dropped out in the reservoir, the pressure maintenance scenario with the N_2 injection is limited due an injection capacity constraint at reservoir level which limits the nitrogen injection to a maximum incremental gas injection volume of 200 MMscfd, see Figure 3-11. This amount of injected nitrogen is not enough to re-vaporize the liquid that had been affected by gravity due to pressure depletion in the reservoirs under the surfaces conditions evaluated, see Figure 2-36, Figure 3-19 and Figure 3-20.

The results show that liquid losses can be reduced by having a higher amount of CO_2 in the N_2 stream and gives the best performance with CO_2 injection. The oil production losses are, with respect to the base case, 4 MMstb in 10 years with a constant gas sales plateau, which gives a maximum incremental gas sales of 0.9 Tcf in 10 years, see Figure 3-44.

The results show a higher sweep efficiency with the dual porosity/dual permeability model, compared to the single porosity model due to an improvement in the matrix - matrix, fracture - fracture communication combined with matrix - fracture communication, making possible that more fluids move from the reservoir to the wells (see Figure 3-32).

The results for the static uncertainty parameters show that the matrix vertical permeability (kmV) and the gas trap saturation (Sgt) are two of the parameters that have the highest

uncertainty. When kmV is increased by a factor of 10, it generates a more efficient sweep of the matrix system compared to the reference case, which is reflected in an increase on the cumulative oil production of 16 MMstb in 10 years. When the Sgt is not considered, there is an increase in the cumulative oil production of 11 MMstb in 10 years, see Figure 3-77.

In conclusion, the high connectivity between the matrix and fracture systems brings up higher oil production losses with the dual porosity/dual permeability system than that with the single porosity system.

3.2 State of the Art

The most common approaches use nitrogen as a pressure maintenance technique in oil reservoirs (e.g volatile oil and black oil). The following review presents some of this work and some other literature related to compositional nitrogen injection in natural fracture gas condensate reservoirs.

Since 1979, some laboratory works **[1, 2, 3]** reported that the MMP decreases when the C2-C6 molar fraction increases and the Molecular Weight (MW) of C7+ decreases **[4].** Some gas condensate fields located in Wyoming-USA have reported some simulation and pilots tests **[5]**, as well as full field implementations **[6, 7, 8]** of nitrogen injection processes. Those field are structurally and compositionally analogue to the PDM fields. These studies show different strategies to increase efficiency, such as injection of hydrocarbon gas buffers followed by nitrogen injection **[8]**, or by using foams combined with nitrogen to increase the volumetric sweep efficiency **[4]**. It is also highlighted that an integrated field development approach is required for a successful project, including the processing facility design, as different operational efficiencies could generate a huge impact on the recovery **[7]**.

Limon et al. **[9]** showed in 1999 an update for the black oil Cantarell field development, where a production increase in 40% was obtained with 66 new wells which was achieved by giving pressure support with nitrogen injection. Guzman **[10]** performed in 2014 a summary of Cantarell nitrogen injection project, showing that modules of 300 MMscfd have been increasingly implemented since 2000 until reaching an average nitrogen injection of 1500 MMscfd, obtaining an incremental oil recovery of 28% up to 2014. The costs reported by both studies for the nitrogen are 0.23 - 0.56 USD$/Mscfd, in which it is also reported that nitrogen molecular weight of 28 g/mol compared to 16.46 g/mol for natural gas, makes nitrogen a good candidate for pressure support if the same volume of natural gas is used as a reference.

Vicencio **[11]** in 2007 performed a reservoir simulation study for a naturally fractured carbonate - Cantarell field considering the natural fractures (dual porosity/dual permeability model) and the nitrogen injection. Apertures in the order of 10 to 300 μm were used to model a capillary discontinuity; the model also presented small reservoir property variations. He concluded that 1) gas densities play an important role in gravity drainage, which generates a secondary gas cap and segregation of oil into the bottom of the structure. 2) a temperature higher than 900 °F decreases the reservoir gas density, and 3) matrix vertical sub gridding is required when gravity drainage is an important production mechanism.

Then Lawrence **[12]** in 2002 and 2010 presented laboratory tests performed on the carbonate volatile oil - Jay Field, where ~25% of residual oil saturation with water was displaced by nitrogen (from Sorw: 0.35 to Sorm: 0.07). From compositional measurements, it was observed that light components were initially produced, which gradually changing to heavier components. An incremental oil recovery of 10% was also estimated using a reservoir simulation with the Todd-Longstaff model for miscible displacement.

Linderman et al **[13]** in 2008 and Abdulwahab et al in 2010 presented key references to this project, as they analyzed analogue gas condensate fluid properties compared to Pauto with a

liquid drop out of ~20% with an NGL/LPG plant incorporated into the analysis. These studies present a reservoir simulation study in a single porosity system with N_2 and CO_2 injection in a retrograde gas fluid located in Abu Dhabi. The reported gas production capacity of the field is 1800 MMscfd, with a nitrogen injection capacity of 1700 MMscfd.

The first study performed by Linderman et al **[13]** in 2008, identified 4 principal aspects for the N2 injection in the gas condensate field. 1) Even if N_2 increases the saturation pressure, liquid drop out is much less at abandonment pressures; for that reason the loss of condensate in the reservoirs seems not to be significant as it was conventionally thought. 2) Even if the CO_2 injection could increase the recovery factor over the nitrogen injection, the difference in total equivalent barrels are not significant; also the cost of CO_2 could be higher than N_2 if CO_2 sources are not near the reservoir. 3) Cryogenic plants (ASU-Air Separation Units) are recommended to extract the N_2. 4) N_2 injection generates a marginal impact on the NGL production of less than 1%, and 5) the N_2 injection rate is an important factor that affects the rapid increase of N_2 concentration in the producers. 6) It is also proposed that nitrogen injection could be a good option for reservoirs with high depletion and with oil rims.

The second study performed by Abdulwahab et al **[14]** in 2010 presents different surface and subsurface alternatives to manage the N_2 breakthrough in the producers to maximize the gas value. Some of them are: 1) re-distribution of production/injection with time. 2) Flue gas re-cycling. 3) Increasing the make-up gas amount from external sources. 4) Selective nitrogen injection in the field (by regions), and 5) implementing a N_2 Rejection Unit (NRU) installation to separate the nitrogen from the methane.

Rivera et al **[15]** in 2001 performed a Special Core Analysis test in the laboratory using Berea plugs combined with a Slimtube to guarantee the Miscibility process. These tests were performed with different nitrogen injection rates for the plugs saturated with volatile oils from the Eastern Colombian foothills. The efficiencies reported were 50%, 65% and 80%, being inversely proportional to the injection rates.

3.3 Nitrogen Injection Performance

There are mainly 2 general aspects for a good nitrogen injection process at subsurface level. One is pressure and the second is the displacement efficiency. Both are related with the Minimum Miscibility Pressure (MMP), which will impact the breakthrough time.

Knowing that there are some theoretical optimum conditions for the maximum displacement efficiency, then the next important step is to identify the uncertainties and their impact in the recovery factor[51]. Table 3.1 describes some of them:

Table 3.1. Factors that affect Nitrogen Injection Efficiency.

Uncertainties	Impact
• Pore size distribution. • *Vertical Permeability*[52]. • *Matrix Permeability.* • *Heterogeneity and Anisotropy.* • *EOS Parameters.* • Wettability Changes. • Surface Tension. • Capillary Pressure. • Gas-Water Relative Permeability behavior. • *Hysteresis Behavior.* • *Gas Trap Saturation.* • Oil Saturation. • Capillary imbibition of retrograde condensate. • *Condensate release into the fracture.* • Condensate re-infiltration. • Dispersed hydrocarbon liquids. • Reactions and Fluid behavior in presence of Water minerals. • Reactions and Fluid behavior in presence of Asphaltenes. • Reactions with clays.	**Reservoir Level** Recoveries • *Break through times.* • *Sweep Recovery Efficiency.* • *On C5+ Production.* • *Condensate Bank Saturation development in the matrix and fractures.* • *Condensate viscosity reduction.* • *Retrograde condensation.* • *Gravity Drainage.* • Viscous cross flow. • Nitrogen losses due to dissolution in water or adsorption in the rock. Formation Damage (Flow Assurance) • Pore throats Blockage due to precipitations of salts, asphaltenes or clays swelling. **Surface Level** • *Produced Gas composition (quality).* • *Hydrocarbon Production (decline).*

[51] Variables written in *Italics* are those studied in this wok.
[52] See **Section 3.7** for the main selected uncertainties.

3.4 Fluids' Quality Control with Nitrogen Injection: PVT Simulations

For the prediction phase, due to the lack of laboratory experiments up to the moment this work was done, validating the nitrogen injection process was not possible so, in order to account for the uncertainty, a set of analogue data was used so as to delimit the problem in some degree.

For this purpose, Minimum Miscibility Pressure (MMP) simulations were done using the interaction coefficients from other fields that have laboratory tests with nitrogen, like Cupiagua (see Table 2.2). In addition, the swelling test was compared with a similar work performed by Linderman **[13]** where an analogous fluid behavior is observed.

Figure 3-1 and Figure 3-2 show the 3 main tests per sheet (compartment) and per reservoir, that relates the change in saturation pressure (column 1), liquid drop out (column 2) and Minimum Miscibility Pressure (Column 3) with different injection fluids: Nitrogen, Methane, Carbon dioxide and lean gas.

The composition used for the simulation of the MMP comes from the liquid composition of the CVD at 4000 psia following an average reservoir pressure in the simulated predictions (i.e see Plot 9 in Figure 3-9).

- **Pauto**

Figure 3-1 shows that the highest liquid drop out (LDO) in Pauto field belongs to Dele Sheet[53], which also has a high excess permeability (see Figure 1-13).

As a reference, the Swelling tests (Column 2 in Figure 3-1) show a slight difference when comparing the CO2 and the Lean gas at 4000 psia (see the red vertical line with dots-surrounded by the gray areas). Both fluids show similar efficiencies when reducing the LDO.

On the other hand, N_2 shows a lower efficiency as the generated liquid fraction is higher, which means that N_2 helps the gas condensate to produce more condensate.

Floreña proves to be much more sensitive to the gas injection composition in the gas condensate zones than Pauto field does. This is observed with the bigger liquid drop out dispersion observed in Column 2 of Figure 3-2 compared to Figure 3-1.

Sheet	1. Saturation Pressure	2. Swelling Test	3. MMP
Dele	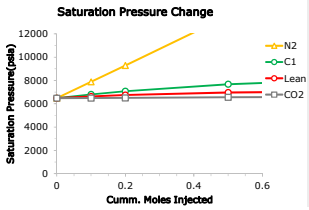	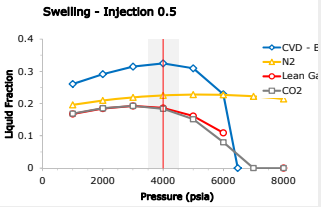	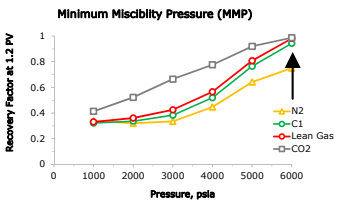
Comment	Big increase in the saturation pressure with N_2 compared with other gases.	**Slight** increase from 0.18 to 0.22 in the liquid dropout with the Lean gas injection and N_2 at 4000 psia.	No miscibility is reached with nitrogen in case the criteria is to have a RF >90%
Guamalera / Granadillo	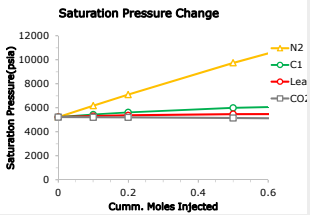	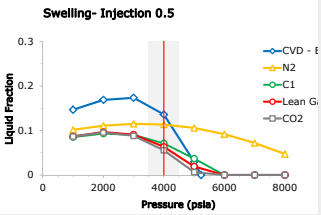	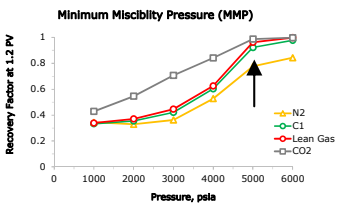
Comment	Big increase in the saturation pressure with N_2 compared with other gases.	**Medium** difference in the liquid dropout (from 0.05 to 0.11) compared lean gas with N_2 injection with Dele fluids at 4000 psia.	No miscibility is reached with nitrogen in case the criteria is to have a RF >90%
Pauto Main Mirador	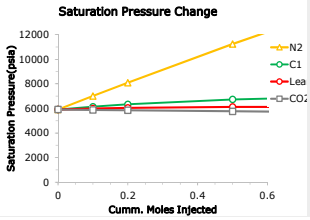	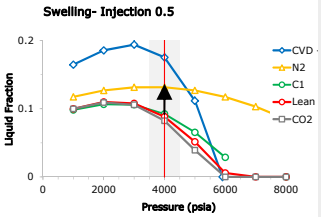	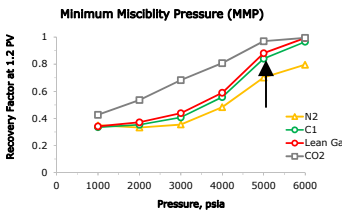
Comment	Big increase in the saturation pressure with N_2 compared with other gases.	**Higher** difference in the liquid dropout (from 0.08 to 0.13) compared lean gas with N_2 injection with Dele fluids at 4000 psia.	No miscibility is reached with nitrogen in case the criteria is to have a RF >90%

Figure 3-1. Pauto's Fluid Behavior with N_2, Lean gas and CO_2 Injection. Saturation Pressure (left side plots), Swelling Test (middle section plots) and MMP Simulations (right side plots).

[53] See Figure 1-6 as a reference to locate the sheets (compartments) in the map.

- **Floreña**

The MMP is around 5000 psia for the gas condensate and volatile oil sections with lean gas and CO_2, while N_2 does not achieve the Recovery Factor Criteria where miscibility conditions are considered to be reached when the RF is higher than 90%, see Colum 3 in Figure 3-2.

The condensate from gas cap zones has a better RF compared to the volatile oil zones for the 4 injected fluids (CH_4, Lean gas, CO_2 and N_2), see Colum 3 in Figure 3-2.

At 4000 psia, the volatile oil from Barco shows a similar liquid drop out behavior with lean gas and nitrogen. On the other hand, the volatile oil located in Guadalupe shows a lower LDO with N_2; this phenomenon happens due to a higher amount of C7+ that Guadalupe fluids have compared to Barco fluids, see Column 2 in Figure 3-2.

The reduction in the volatile oil section's LDO proves that N_2 is a more inefficient injection fluid compared to lean gas, methane (C1) and CO_2.

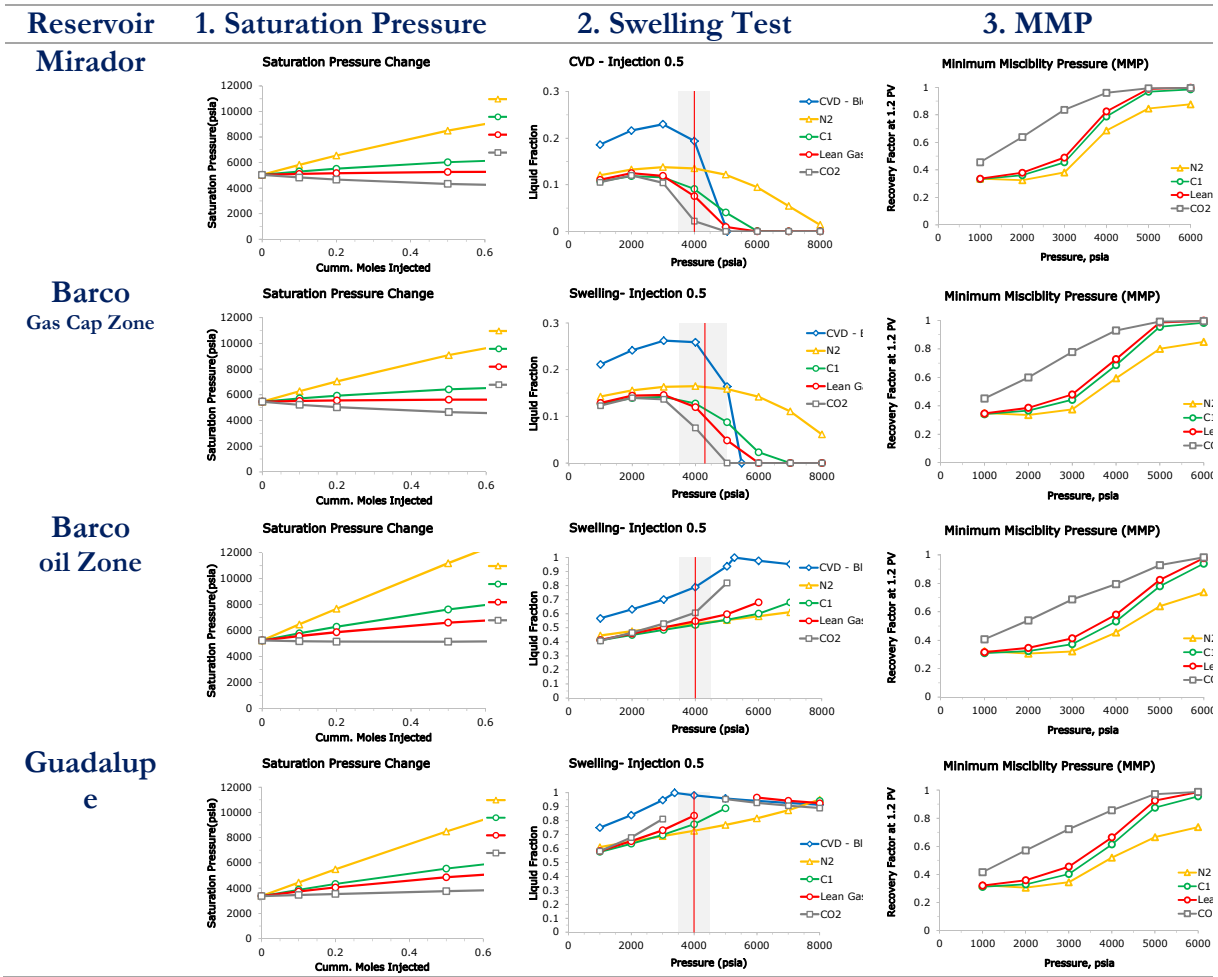

Figure 3-2. Floreña's Fluid Behavior with N_2, Lean gas and CO_2 Injection. Saturation Pressure (left side plots), Swelling Test (middle section plots) and MMP Simulations (right side plots).

3.5 Assumptions on Nitrogen Operational Specifications

Careful detailed surface engineering is required to define and determine the specifications and work ranges for the Air Separation Unit (ASU), compressors and Nitrogen Rejection Unit (NRU) that are used to separate the hydrocarbon gas from nitrogen.

A first conceptual approach to the system that is known by the author is presented in Figure 3-3 and Figure 3-4, where the NRU[54] is located at the end of the process, as it is in this location that almost all the hydrocarbon is separated, and it is where the highest amount of methane and nitrogen that must be separated is, in order to guarantee that the gas sales composition is free of nitrogen. This configuration conveys the project's global concept of the surface system.

In Figure 3-3, A_FR-EPF is the node where all production is collected (i.e slug catcher), SEP1 is a node where the separators are defined (i.e high, medium and low separators), NGL is the node used for the separation of the NGL, where V means vapor phase and L means liquid phase. NRU is the node for the separation of nitrogen from methane.

The arrows represent the gas used for fuel, flare or sales. At the end of the process, there are 2 nodes, where one is related to the gas cycling (NRU_ADD), and the other is related to the N_2 that is separated once the wells begin to have a N_2 breakthrough (NRU_N2_ADD); this node controls de N_2 recycling process.

As a reference, the efficiency assumed in the NRU was 0.98. Also the NRU was considered to have no restriction in the capacity.

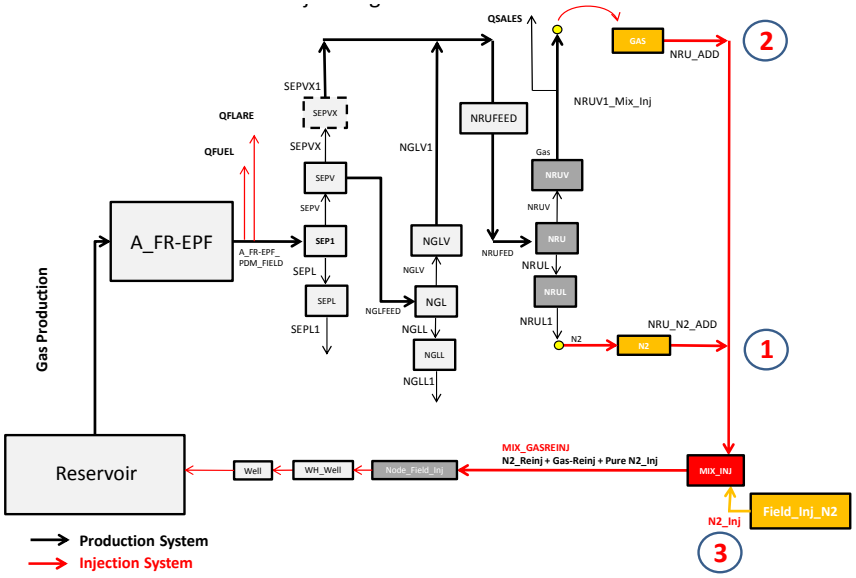

Figure 3-3. Production System - Nitrogen Plant Sketch.

[54] Notice that the NRU representation only considers the module that separates the N_2 from the hydrocarbons, in reality the NRU is a full plant that has incorporated the NGL/LPG units plus other especial equipment.

Figure 3-4 shows the injection systems, where the NRU_GAS collects the gas for reinjection after the gas sales target, and the NRU_N2 node collects the N_2 separated from the NRU. Both streams are collected in the MIX_INJ node, with additional N_2 coming from the ASU unit, which is the node that generates the makeup N_2 for injection.

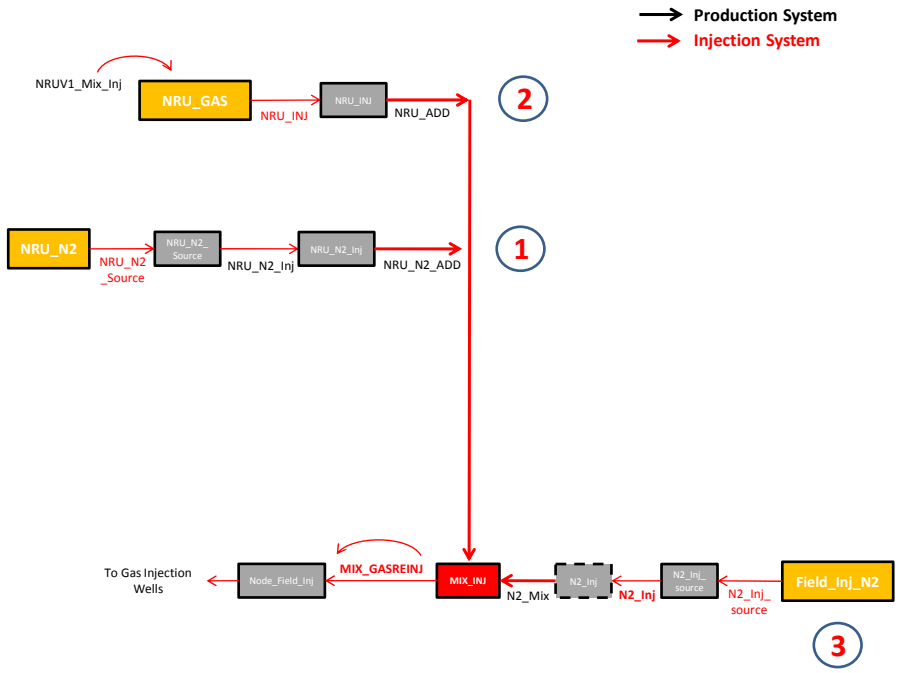

Figure 3-4. Injection System - Nitrogen Plant Sketch.

The following increase in fuel gas required for the new nitrogen system was assumed for this project. The assumption is based on the following equation: $Fuel\ gas\ Rate = 0.04 \cdot Q_{gi} + 1.6 \cdot$

Table 3.2. Fuel Gas Assumption.

Nitrogen Injection	Fuel Gas
100	6
200	10
300	14

Main Assumption:

All the process and reservoir behavior is tied to the selected Facility; for the purpose of this study it was keep constant the NGL plant with an unrestricted NRU plant so, other facilities configurations will give different production and injection results.

3.6 Nitrogen Injection and Gas Sales Sensitivities

To give a context on the selection of different scenarios, a mix of techniques were used to select the nitrogen evaluation option[55]. To start with, the problem was identified, being the lack of demand for gas in Colombia after 2018 **[22],** followed by A. Ocampo's idea of reviewing the injection of non-hydrocarbon gases in order to access the re-injected gas for sale. This leads to a deeper investigation until finding the opportunity, after several technical meetings, of injecting nitrogen as an option to solve the problem.

Thereafter, the main attributes and alternatives to evaluate nitrogen injection in this study are: 1) Reservoir management with specific gas injection rates. 2) Evaluate the blow down scenario (no gas injection), lean gas reinjection and nitrogen injection. 3) Select the variables that will be studied (e.g the oil, gas and total hydrocarbon incremental recovery).

3.6.1 Base Case Description

Table 3.5 shows a summary for the base case runs, which were named as spC1s_FM13_GS0_Base and dpC1p_FM13_GS0_Base, where sp means single porosity model and dp for dual permeability model; s or p after number 1 means single or dual processor run; FM13 stands for the 13th Full field Model version; GS0 for 0 Incremental Gas Sales; and Base indicates that this is going to be the base case for the incremental oil and gas recovery comparison.

Table 3.3. DP-DPDP approach – Prediction Run Names.

Runs	Approach	Run Name	Comments
	Single Porosity	p_spC1s_FM13_GS0_Base	This is a single porosity model that assumes 0 additional Gas Sales (GS0)
Base	Method CGH	p_dpC1d_FM13_GS0_Base	This is a dual porosity/dual permeability model that assumes 0 additional Gas Sales (GS0)

Table 3.4 indicates the average and general production constraints used in these models:

Table 3.4. Reference Case Description.

Gas	Gas, MMscfd	Condition
Production	500	Declining
Fuel and Flare	18	Constant
Sales	105	Constant
Re-injection	400	Declining
Gas Makeup	0	No Makeup gas

Figure 3-5 shows the behavior of production with the single porosity model (solid dark gray line) and the dual porosity/dual permeability model (dashed light gray line):

[55] Notice that the selected evaluation option is dependent of the reservoir management that is wanted for the reservoirs.

- Plot No. 1, Plot No. 4, Plot No. 7 in the first column and Plot No. 9 show the gas, oil, and water rates, and the injection rates, respectively. It can be observed that the DPDP model shows a better production potential due to a higher fluid mobility within the fracture network, which is related to high matrix-matrix mobility with the fracture-fracture mobility combined with the matrix-fracture mobility.

- Plot No. 2, Plot No. 5 and Plot No. 8 in the 2nd column show the cumulative gas, oil and water production respectively, related to the material balance and volumetrics of the system. A combination of poor pressure support and a slightly better rock quality distribution in the SP compared to the DPDP model make these zones have a higher water encroachment compared to the total field behavior, see Appendix C for more details.

- Plot No. 3 and Plot No. 6 in Column 3 show that the SP model (solid line) has an isotropic permeability in the x and y direction, while the DPDP model (dashed line) exhibits a permeability anisotropy of 1.3 (see Figure 2-14 for more details), giving a small delay in the GOR evolution compared to the SP model, and a better water encroachment control due to gas injection.

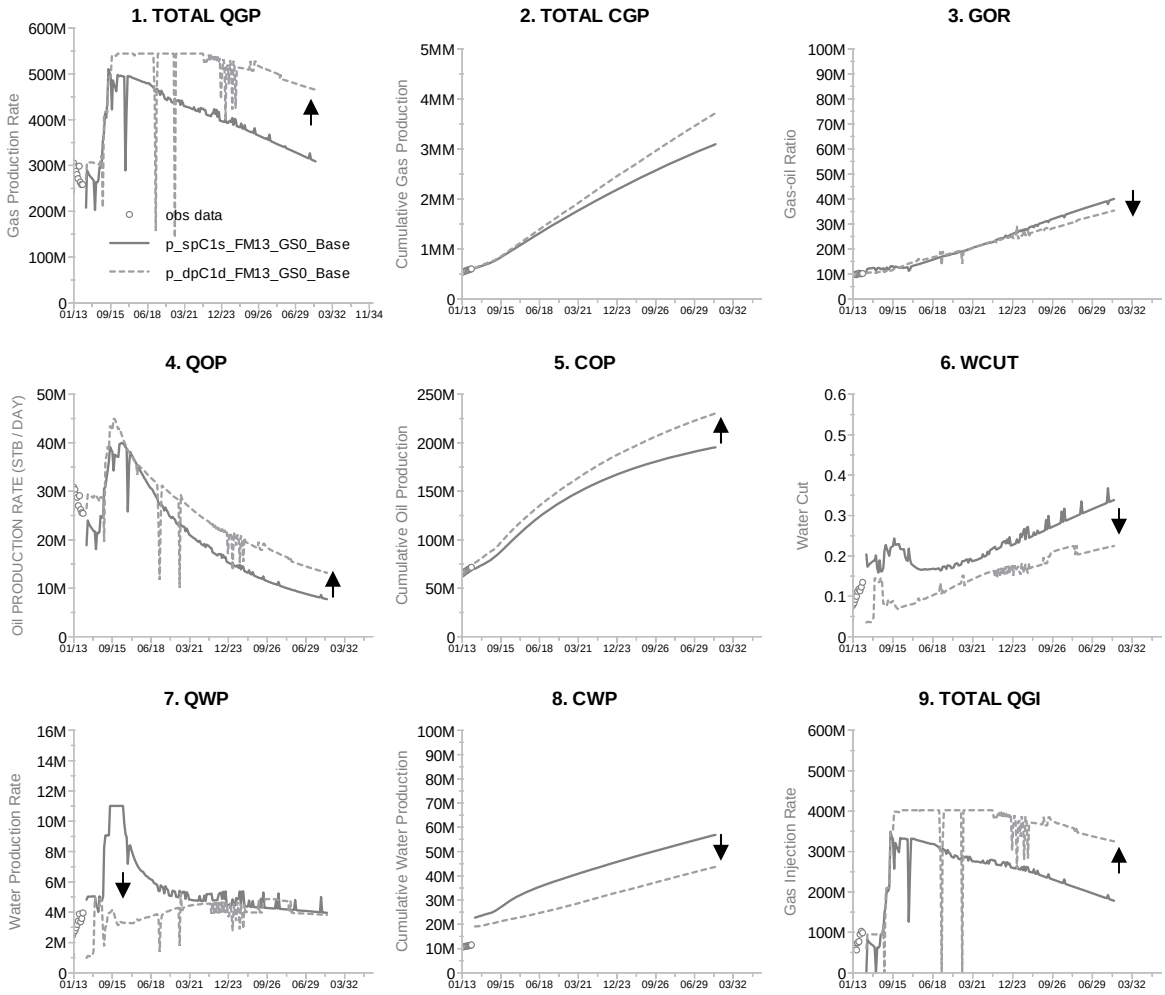

Figure 3-5. Field Surface Water Production – SP and DPDP.

- **Saturation, density and viscosity**

The density increases in the fracture system, generating a higher segregation of condensate from the top to the bottom of the structure than the SP model does.

For the selected cells, Floreña shows higher gas saturation in the fractures compared to Pauto Complex; this increases the fracture oil density and viscosity.

The injection line was intentionally left in the graph for comparative purposes with the nitrogen injection process presented in Figure 3-38.

Sheets	Saturation	Density	Viscosity
Dele	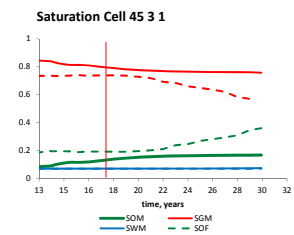	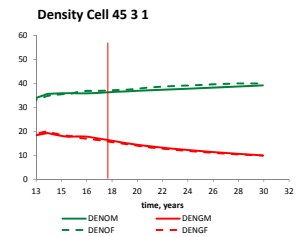	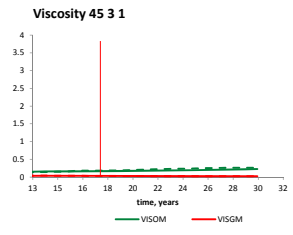
Guamalera	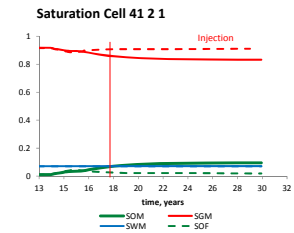	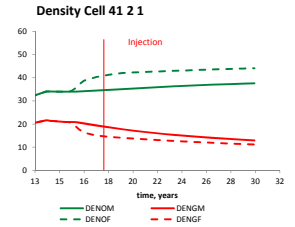	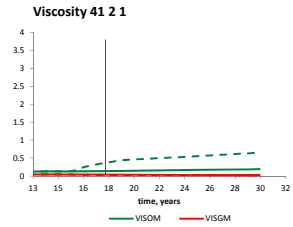
Pauto Main Mirador	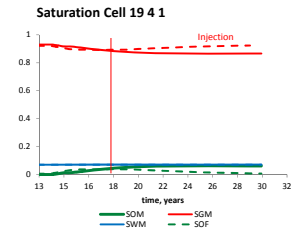	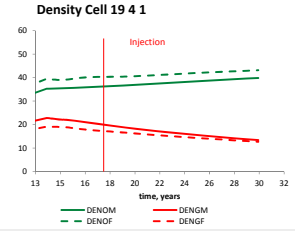	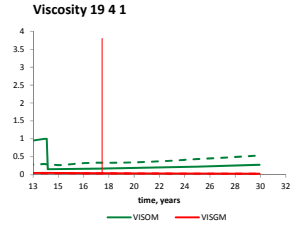
Floreña Mirador	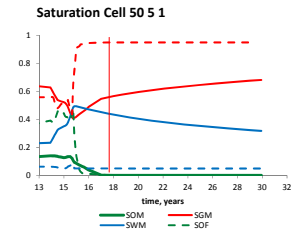	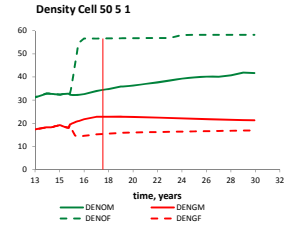	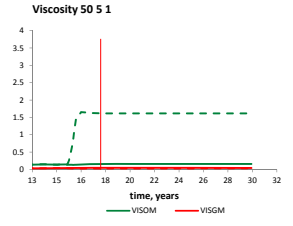
Floreña Barco Gas Cap Zone	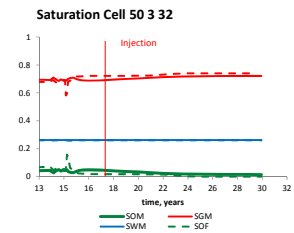	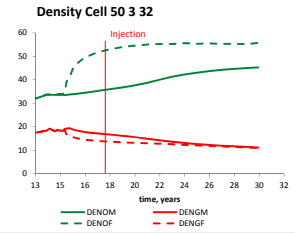	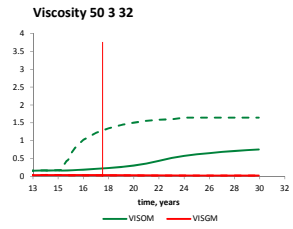

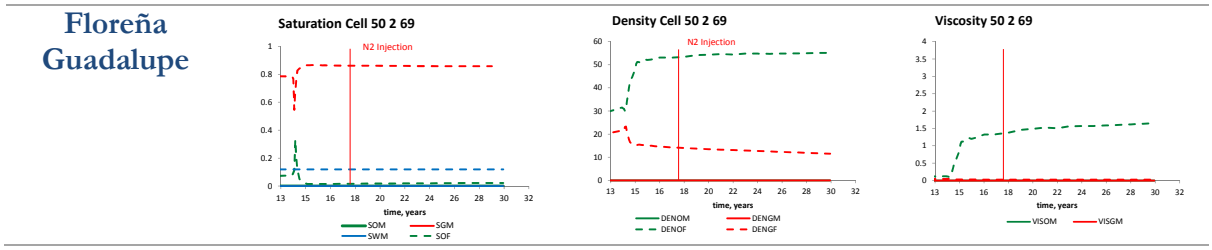

Figure 3-6. Subsurface Saturation (fraction), Density (gr/cc) and Viscosity (cp) distribution – Base Case.

- **Composition**

Figure 3-7 shows the matrix and fracture k values for the intermediate components (1st column plots) and the heavy components (2nd column).

There is a transition from C3 to C4 components where lighter components tend to be in the fracture while heavier components tend to be in the matrix (dashed and solid lines).

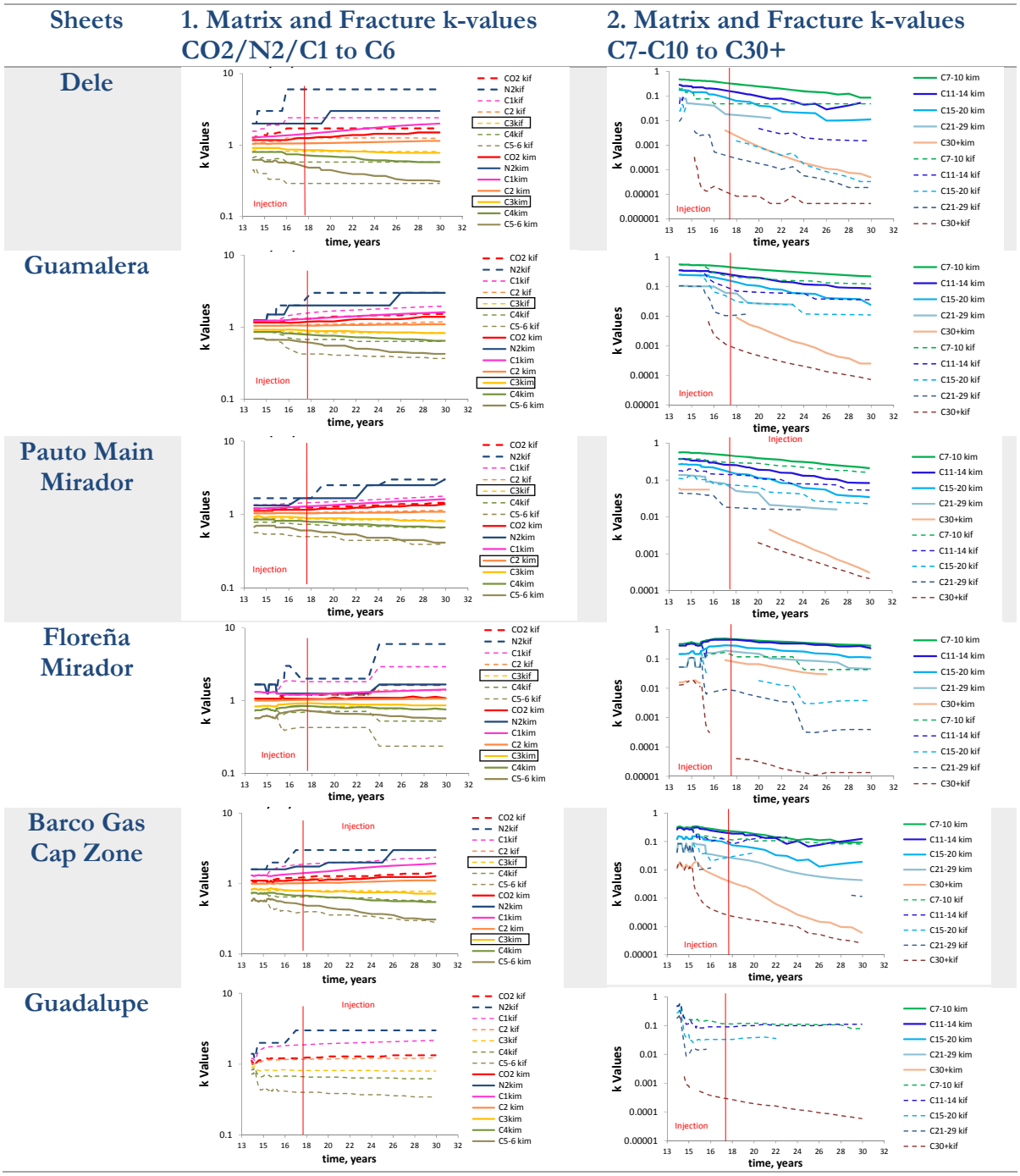

Figure 3-7. Subsurface k-values and Concentrations – Reference Case.

3.6.2 Injection Scenarios

The aim of this section is to provide useful and informed scenarios so as to identify the critical point where additional energy added into the system will not result in significant incremental oil and gas production. The uncertainty section (see Section 3.7) presents an extended analysis.

The gas injection rate is probably the closest reservoir management condition to resemble reality, as it reflects the desired gas amount to be injected into the field controlled with easy surface management, without constraining the production, which could sometimes happen when taking into account the voidage replacement option and pressure support option.

Table 3.5 presents the run codes used to perform the sensitivity study. The idea behind the run codes is a way to shorten the characteristics of each run in order to quickly and easily compare among them.

Table 3.5. Injection Rates – Prediction Run Names.

Runs	Nitrogen Injection (N), MMscfd	Gas Sales (GS), MMscfd	Prediction Run Name
0	0	0	p_dpC1d_FM13_GS0_Base
1	0	100	p_dpC1d_N0_GS100
2	100	100	p_dpC1d_N100_GS100
3	200	100	p_dpC1d_N200_GS100
4	300	100	p_dpC1d_N300_GS100
5	0	200	p_dpC1d_N0_GS200
6	100	200	p_dpC1d_N100_GS200
7	**200**	**200**	p_dpC1d_**N200_GS200**
8	300	200	p_dpC1d_N300_GS200

Figure 3-8 shows the incremental gas inflection point at 200 MMscfd of N_2 injection with 200 MMscfd of gas sales (Case 7). It is a point where increasing nitrogen injection clearly won't bring more incremental benefits.

The maximum incremental gas sales are not due to a N_2 overriding phenomena but because the maximum injection limit is achieved in the system (see Figure 3-11, Plot No. 2) which constraints the possible benefits from pressure support (see Figure 3-11, Plot No. 4 and Plot No. 9).

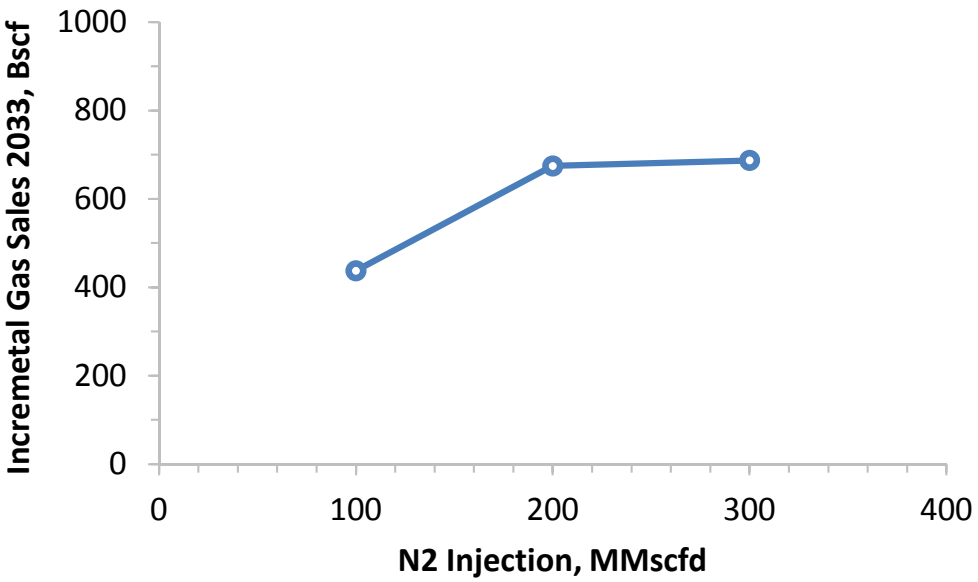

Figure 3-8. Cumulative Production vs. N_2 Injection for different Gas Sales Scenarios.

- **Production**

Figure 3-9 shows comparative cases for the partial blow down scenario (no additional gas make for injection and an increase in the gas sales).

Plot No. 4 and No. 5. for the DPDP Model show that some wells have some choked back oil production, so when the cases that don't inject N_2 with 100 (magenta line) and 200 MMscfd (red line) gas sales, there is an oil production maintenance compared to the base case with gas injection (ray line), up to a point where water encroaches and there is an increase in the decline of oil related to the relative permeability behavior.

Previous observations stated that the blow down scenario reduces the oil production impact compared to the base case, but this analysis does not include the time that is required for optimizing this apparent benefit with no additional gas injection.

Plot No 6 reveals that, due to the lack of pressure support in the system, there is an increase in the WCut 2 years after the blow down begins (see points A and B). Point C in the oil production Plot No. 4 shows how production begins to decline once the water begins to encroach into the system, which occurs at 4500 psia (see point D in Plot No. 9).

Plot No. 2 and 7 show the drastic gas injection reduction due to the increase in the gas sales. For the case of 200 MMscfd gas sales, the injection is dramatically reduced to zero after 8 years.

The case with no N_2 injection and the gas sales of 100 MMscfd shows that the oil production impact for the first 10 years is in the order of 16 MMstb (see point E in Plot No. 4). This effect only happens with the DPDP model, where the oil has a higher mobility in the fracture system compared to the SP system.

Plot No. 9. The average pressure of the field is reduced in almost 1000 psia in 10 years of blow down.

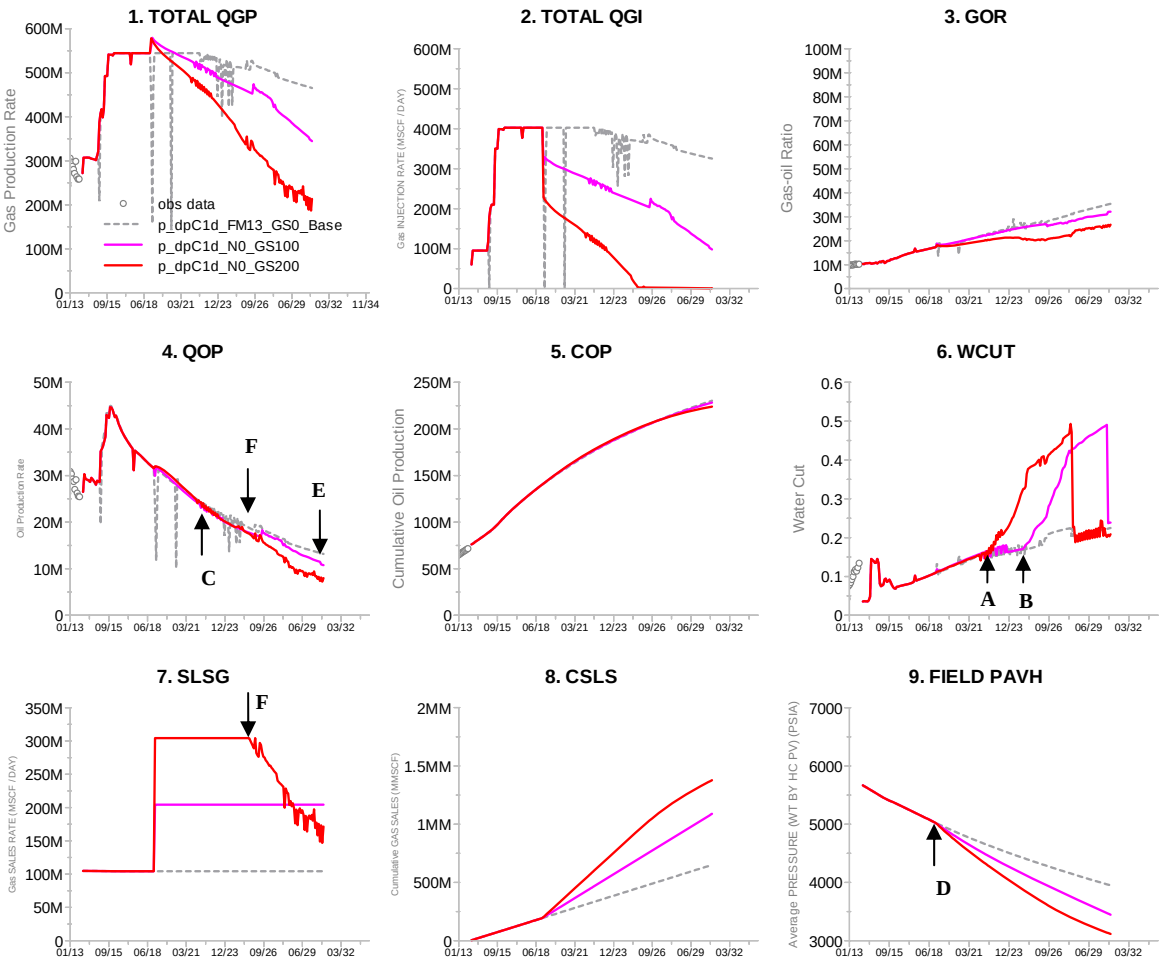

Figure 3-9. Field Surface Production – Gas Sales 100-200 MMscfd and No N_2 Injection.

Figure 3-10 exhibits for comparative purposes a case where there is a similar gas injection and different gas sales rates. One of the cases is with 100 MMscfd of N_2 injection with 200 MMscfd hydrocarbon gas sales and the other case is with 200 MMscfd nitrogen injection with 200 MMscfd hydrocarbon gas sales.

This case was selected to compare the volumes rather than the mass. It was found that a similar gas injection and gas production compared to the base case was achieved by injecting 100 MMscfd of N_2 and 100 MMscfd of hydrocarbon gas.

For low N_2 injection rates (Plot No. 2) and low gas sales rates (Plot No. 7), the decline of oil production is reduced (Plot No. 4 Point E) and the gas sales plateau is increased (Plot No. 7) compared to the base case (gray line),

Plot No. 3. With higher N_2 injection, there is higher GOR evolution.

Plot 6. Gas Injection controls the water production increase compared to the partial blow down case.

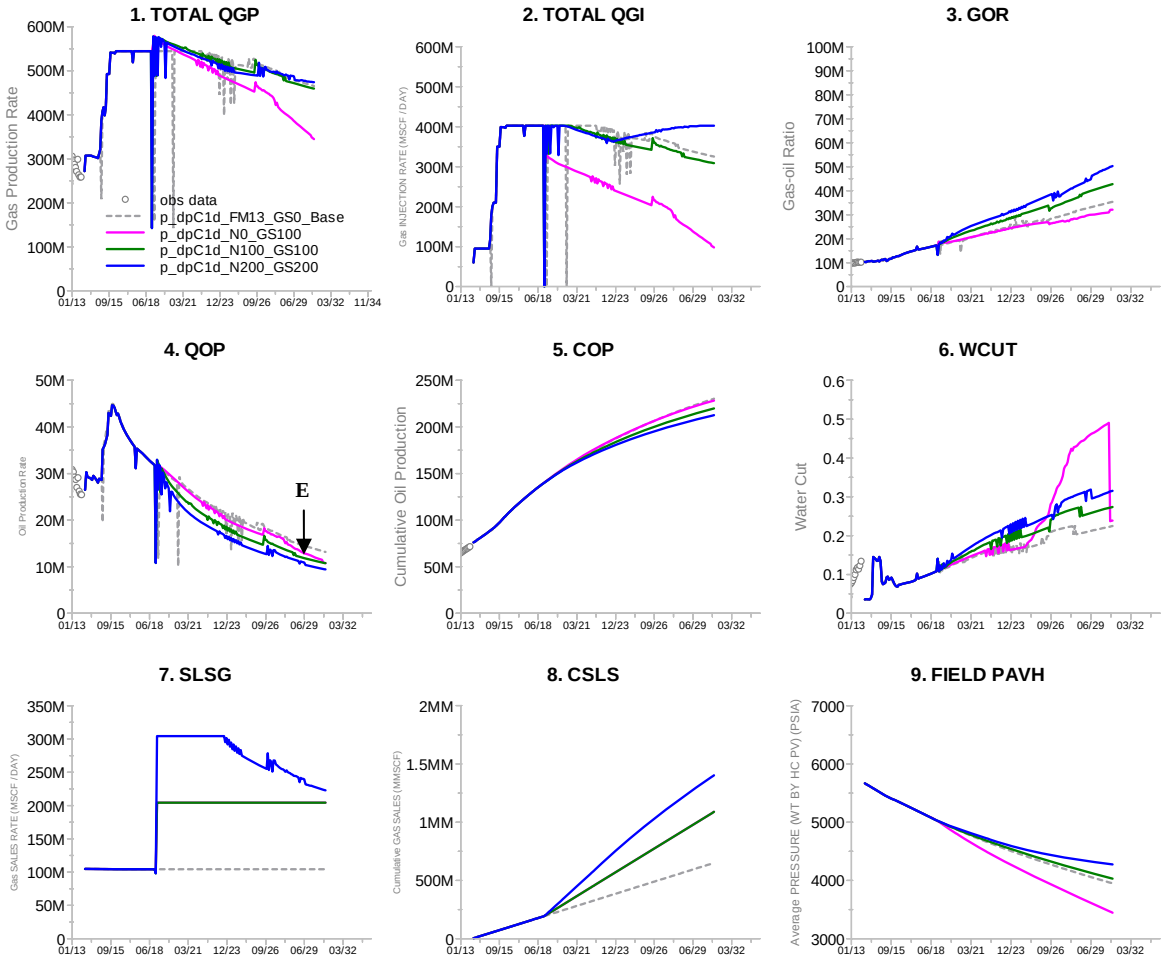

Figure 3-10. Field Surface Production – Gas Sales 100 MMscfd - N_2 Injection. 100, Gas Sales 200 MMscfd - N_2 Injection. 200 MMscfd.

Figure 3-11 displays the sensitivities that were performed, keeping gas sales of 100 MMscfd of gas constant with 3 different N_2 injection cases: 100, 200 and 300 MMscfd. The objective of this sensitivity was to study the effect of pressure on oil production.

Plot No. 7 shows that it is possible to achieve a gas sales plateau for the 3 N_2 injection cases.

Plot No. 9. As N_2 injection gets higher, higher is the pressure support until it reaches a gas injection limit of 300 MMscfd, which constraints the field reservoir management so as to have a control on pressure support or voidage replacement.

Plot No. 4. Nitrogen injection increases the decline of oil production. Increasing N_2 injection rates to avoid this loss does not substantially decrease the oil decline.

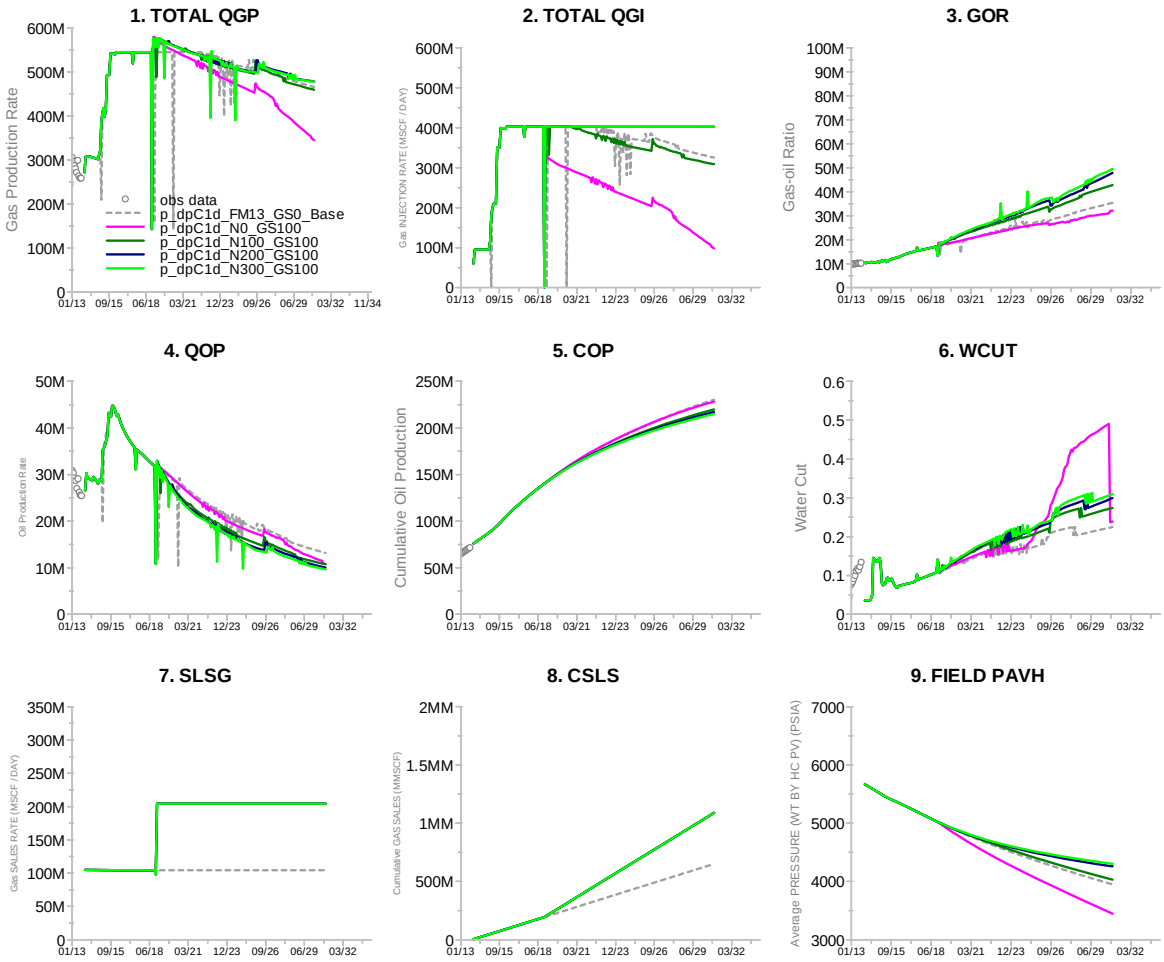

Figure 3-11. Field Surface Production – Gas Sales 100 MMscfd with 100-200-300 MMscfd N_2 Injection.

Similar to Figure 3-11, Figure 3-12 shows the sensitivities performed keeping gas sales of 200 MMscfd of gas constant with 2 different N_2 injection cases: 200 and 300 MMscfd.

The objective of this sensitivity analysis was to study the effect that pressure has on oil production and to prove if it was possible to increase the gas sales, but due to a restriction in wells' injectivity as a result of low KH values, there is a threshold where forcing the simulator to inject 300 MMscfd of N_2 is not possible, so the cases when injecting 200 MMscfd (blue line in Figure 3-12) and 300 MMscfd (light green line in Figure 3-12) give similar results.

Plot No. 4 in Figure 3-12 exhibits a higher impact on oil production compared to the same plot in Figure 3-11, where there is an increase in Gas Sales from 100 MMscfd to 200 MMscfd.

The reason for the lower oil production impact of the no Nitrogen injection case having 200 MMscfd of gas sales (red line N0_GS200) compared to the base case (dashed light gray line FM13_GS0) is because in the N0_GS200, the well head pressure of the wells are gradually reduced to (THP).

Plot No 2. Because of reservoir injectivity constraints, it was found that it is almost the same to try to inject 200 and 300 MMscfd, which generate a limitation in the re-pressurization target so as to avoid oil loss.

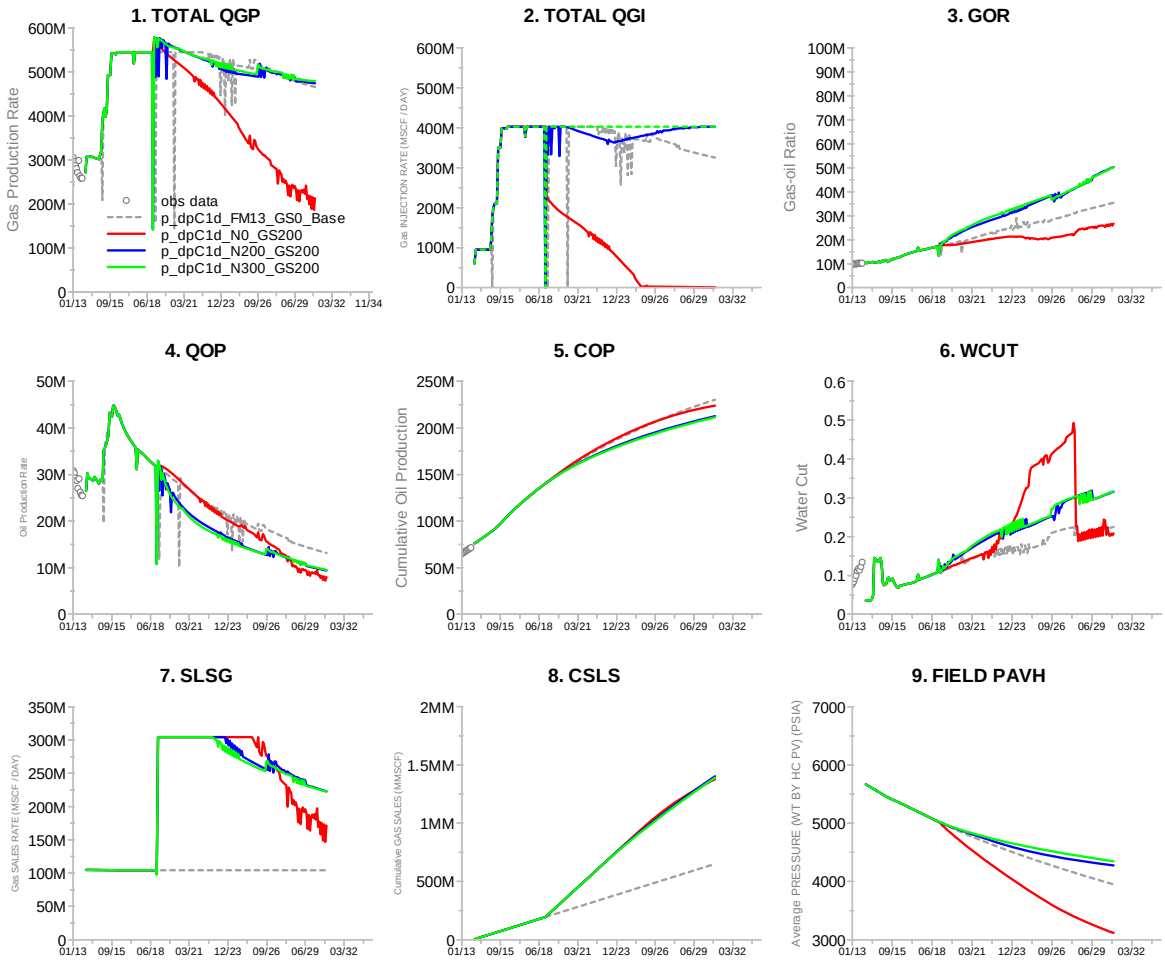

Figure 3-12. Field Surface Production – Gas Sales 200 MMscfd with 200-300 MMscfd N_2 Injection.

- **Composition**

In Figure 3-13, it can be observed that the higher the N_2 injection rates are, the higher N_2 invasion in the matrix is (see the size of the blue regions in all 4 Plots), especially en Floreña.

It can also be appreciated that there is a more homogeneous matrix invasion in Dele (see points B in the Plots) compared to Floreña Mirador, which present a channeling effect (see point A in the Plots).

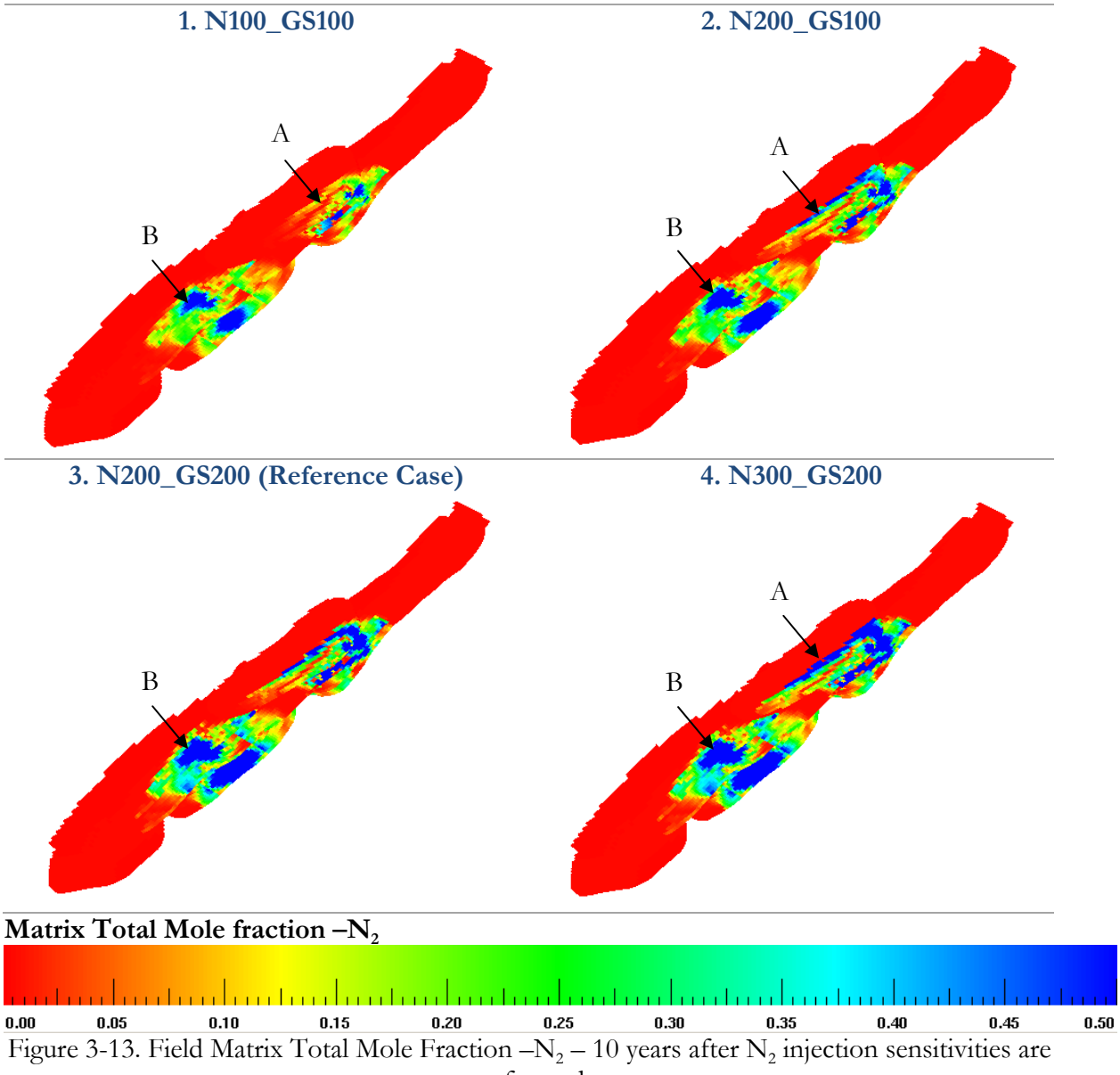

Figure 3-13. Field Matrix Total Mole Fraction $-N_2$ – 10 years after N_2 injection sensitivities are performed.

Figure 3-14 notes that there is a higher N_2 invasion when the N_2 injection rate is higher. This is seen when comparing the blue region intensity of 100 MMscfd of N_2 injection (see Plots No. 1 and 2) with 200 MMscfd of N_2 injection (see Plots 3 and 4).

It can also be observed that there are still regions with no gas injection that could limit the benefits of N_2 injection areal sweep and pressure support.

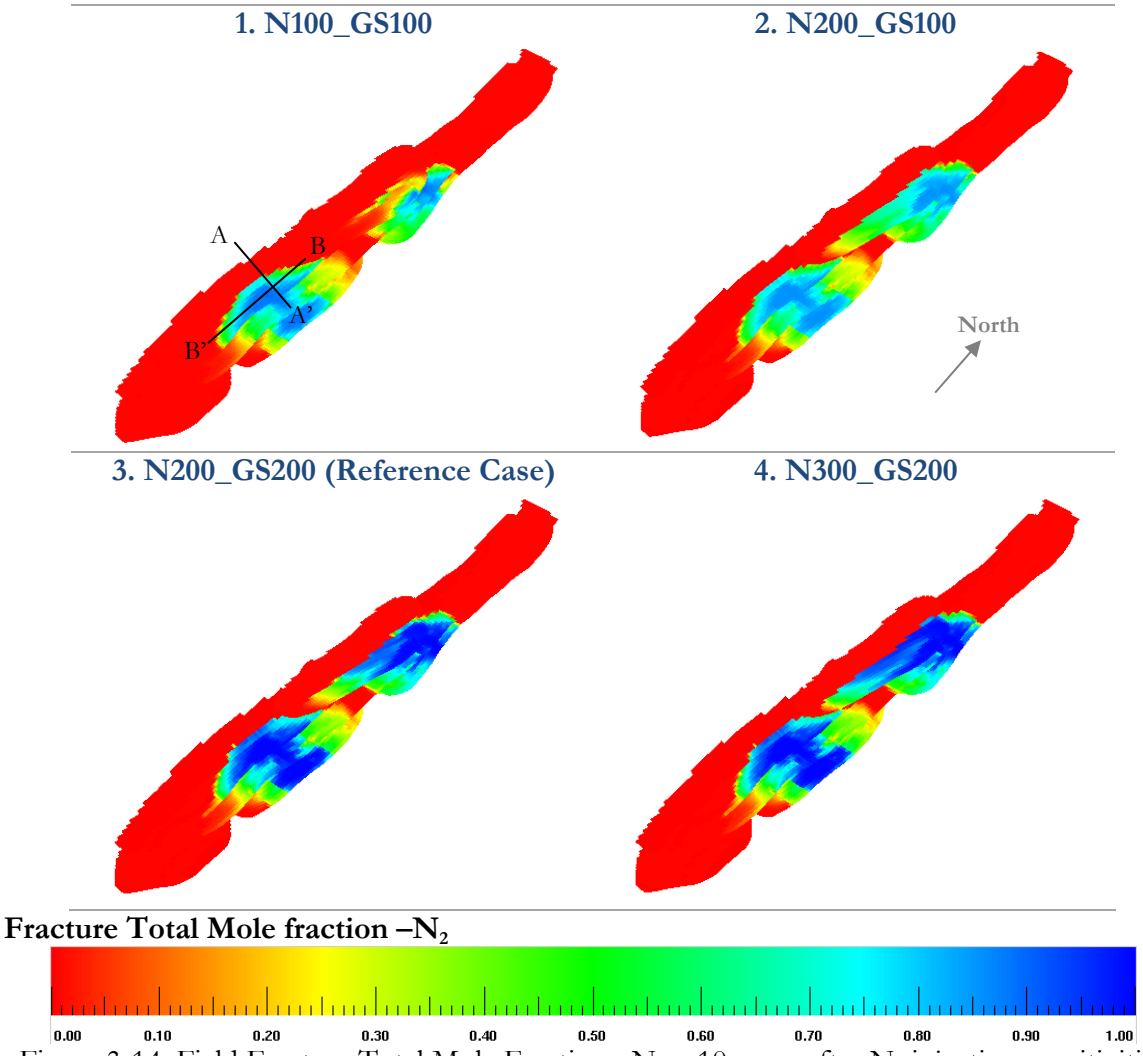

Figure 3-14. Field Fracture Total Mole Fraction –N_2 – 10 years after N_2 injection sensitivities are performed.

Figure 3-15 shows a cross section in Dele Sheet (see Figure 3-13 for reference).

Matrix N_2 molar composition tends to increase in the top of the structure, being higher with higher N_2 injection and higher gas sales rates.

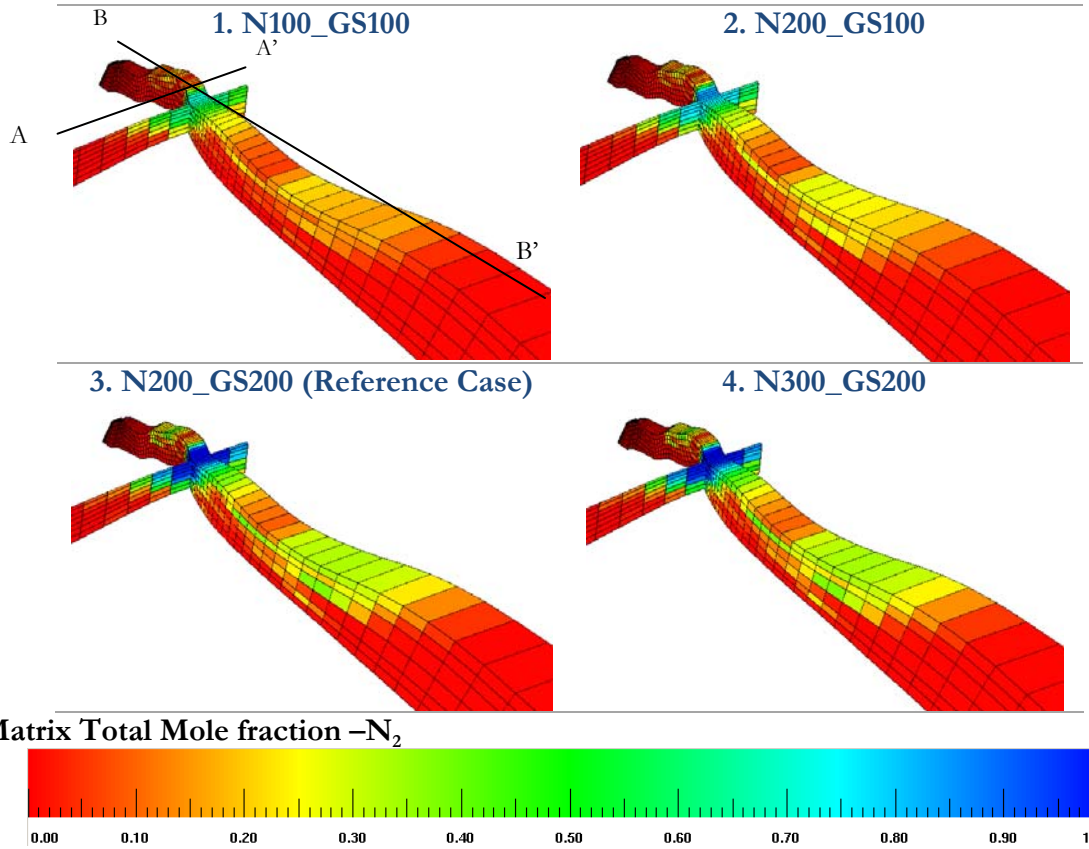

Figure 3-15. Dele Matrix Total Mole Fraction –N_2 – 10 years after N_2 injection sensitivities are performed.

Figure 3-16 shows a cross section in Dele Sheet (see Figure 3-14 for reference).

Fracture N_2 molar composition tends to increase in the top of the structure, being higher with higher N_2 injection and higher gas sales rates.

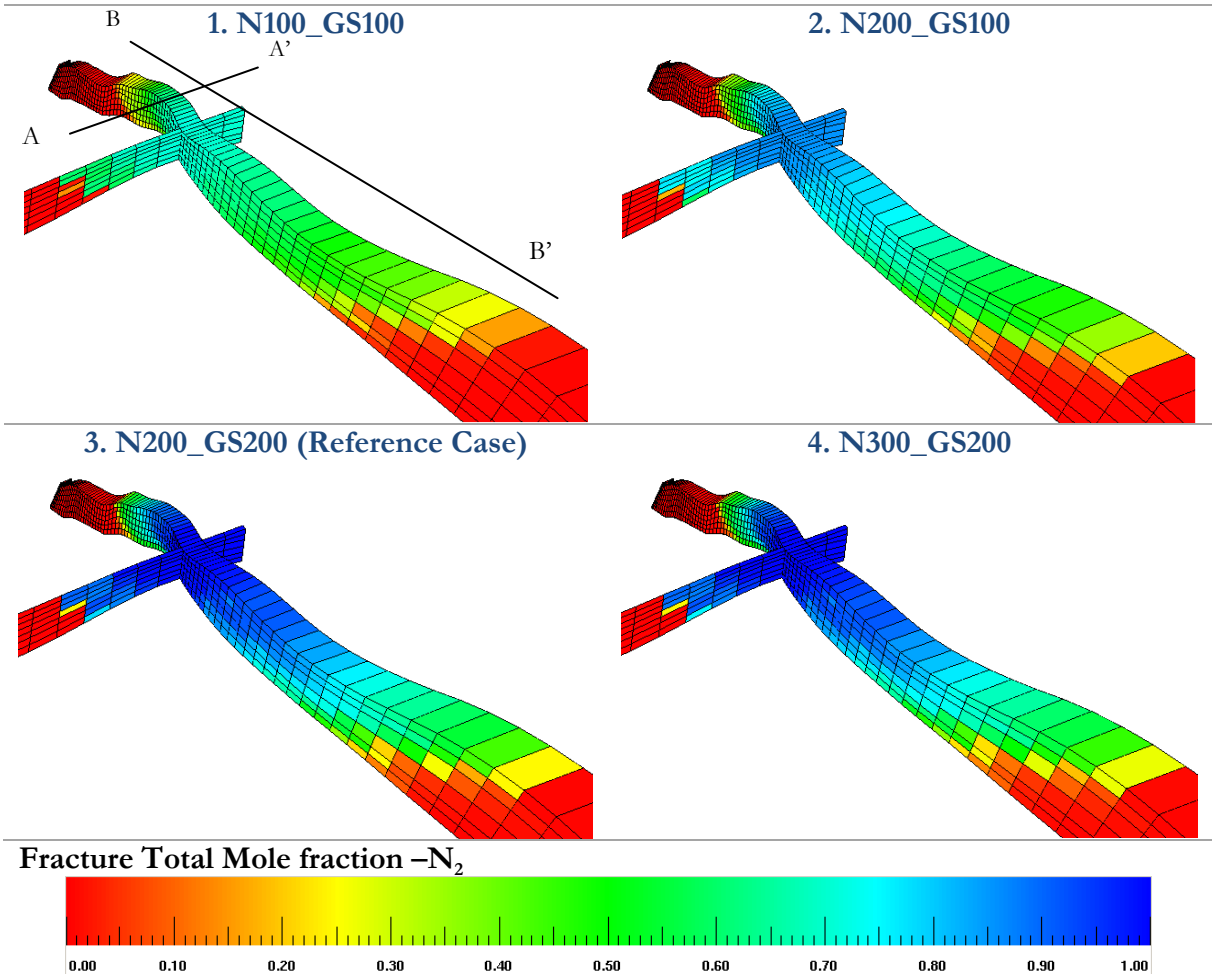

Figure 3-16. Dele Fracture Total Mole Fraction –N_2 – 10 years after N_2 injection sensitivities are performed.

- **Saturation**

Figure 3-17 shows an aerial view of the matrix oil saturation, where there are similar results with different gas injection cases, meaning that N_2 is not able to sweep additional oil from Dele matrix system when the N_2 injection rate is increased.

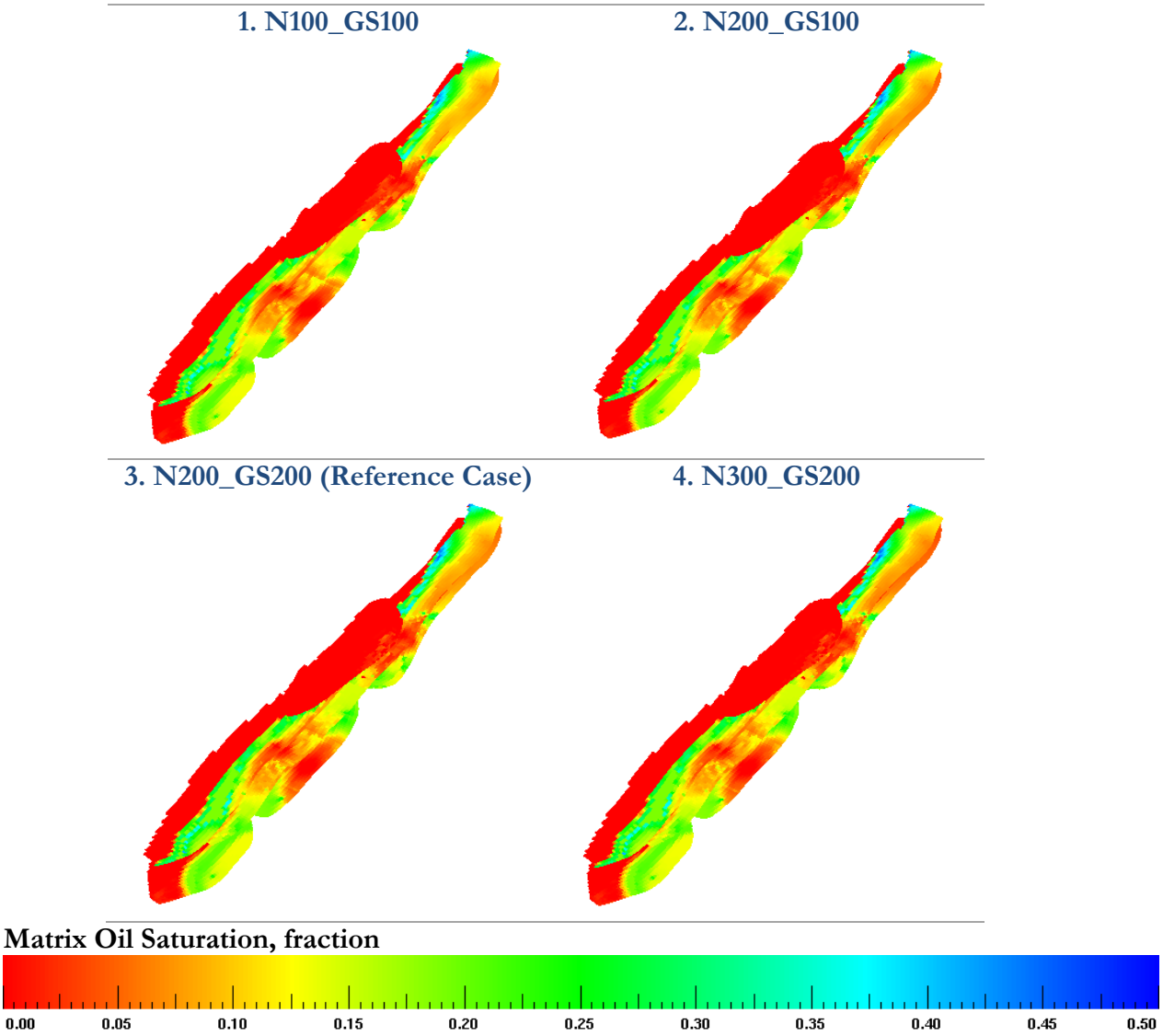

Figure 3-17. Field Matrix Oil Saturation –N_2 – 10 years after N_2 injection sensitivities are performed.

Minimum fracture oil saturation variations are observed in Figure 3-18. The results show that having an injection of 100 or 200 MMscfd with 100 and 200 MMscfd gas sales, a similar displacement front is generated.

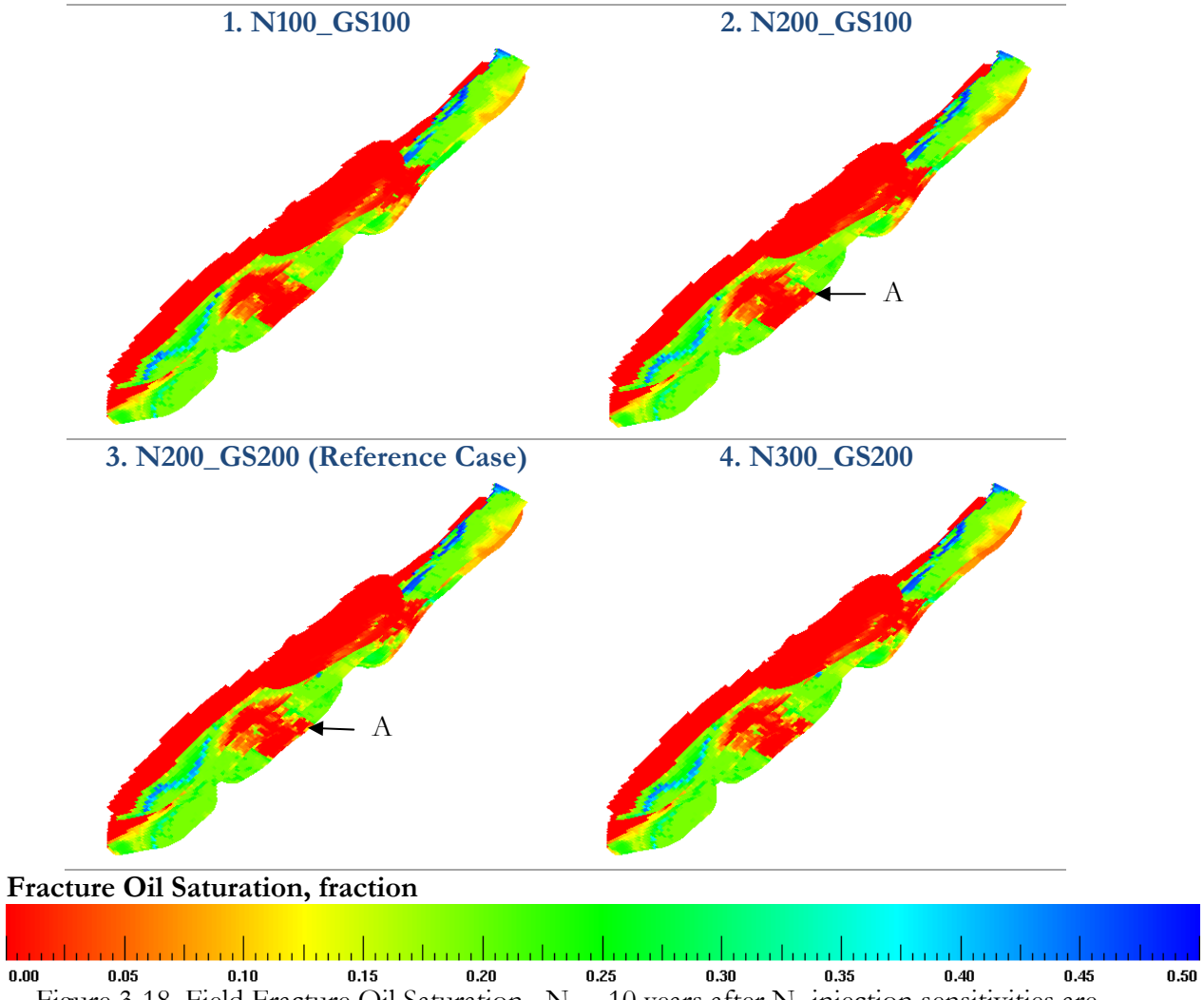

Figure 3-18. Field Fracture Oil Saturation –N_2 – 10 years after N_2 injection sensitivities are performed.

For practical purposes, Figure 3-19 shows that all cases have the same matrix oil saturation in Dele Sheet, meaning that increasing the N_2 injection rate does not necessarily mean that it will be possible to sweep additional oil from the matrix.

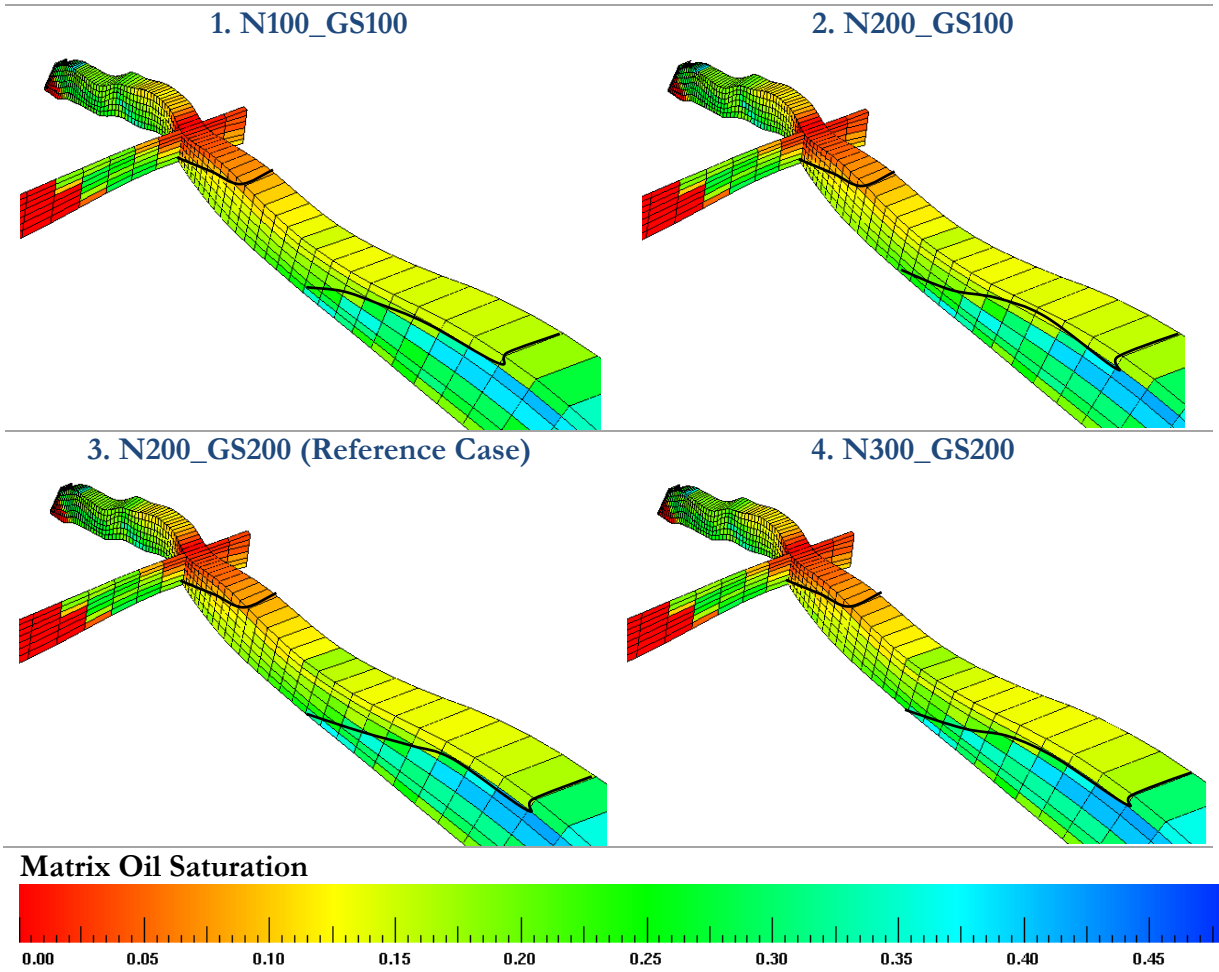

Figure 3-19. Dele Matrix Oil Saturation – 10 years after N_2 injection sensitivities are performed.

Figure 3-20 shows a very low variation in the fracture oil saturation for all nitrogen injection cases. This low variation among the cases is in agreement with the small oil production increase presented in Plot No. 4 of Figure 3-10, Figure 3-11 and Figure 3-12.

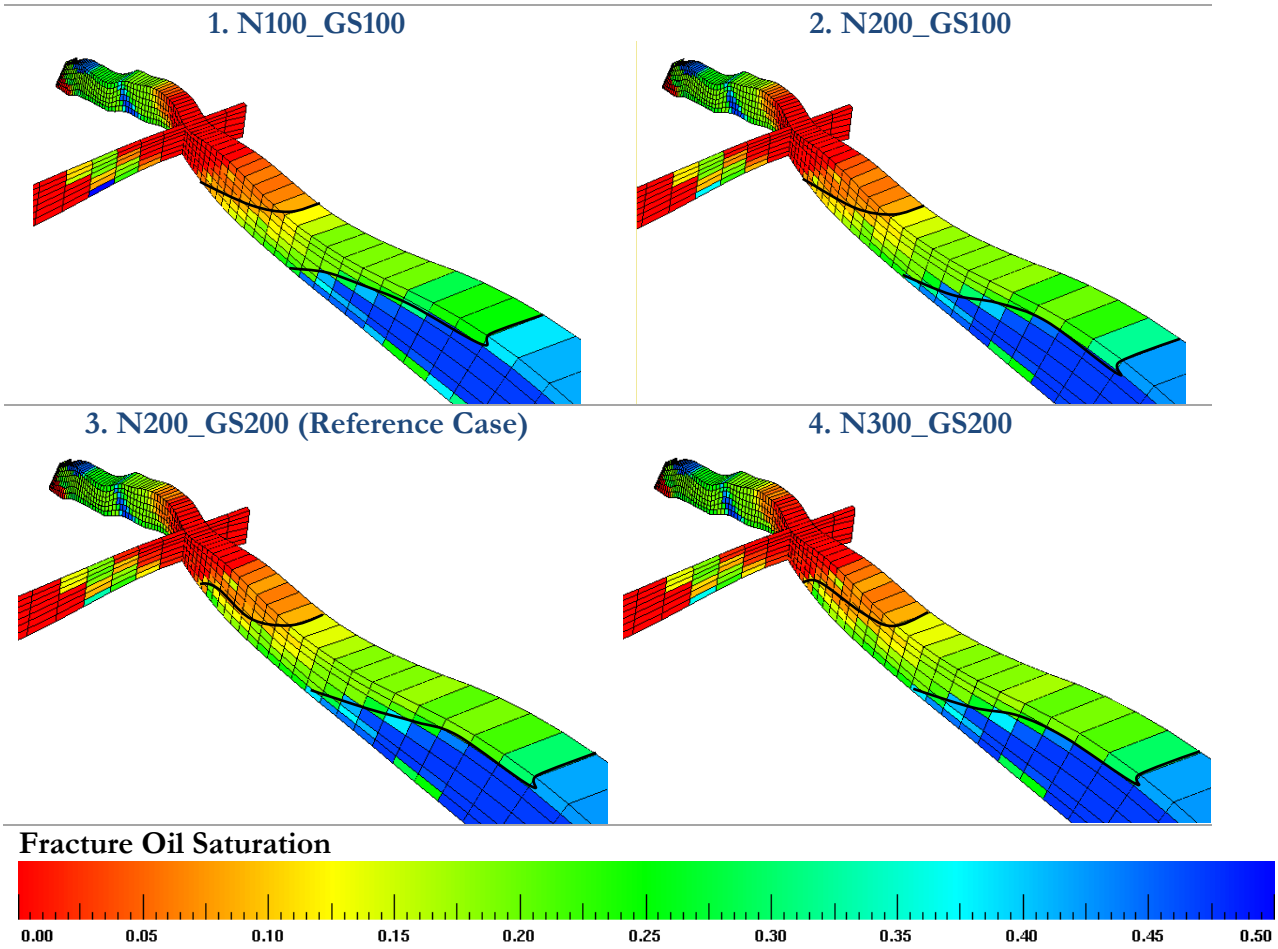

Figure 3-20. Dele Fracture Oil Saturation – 10 years after N_2 injection sensitivities are performed.

- **Oil and Gas Relative Permeability**

Figure 3-21 displays small variations for gas relative permeability just behind the displacement front. This can be observed when comparing point A in Plot No. 1 and 3. The highlighted cell shows a slight increase in the fracture gas relative permeability, as the reference case presents a higher N_2 injection rate than case 1, which only injects 100 MMscfd.

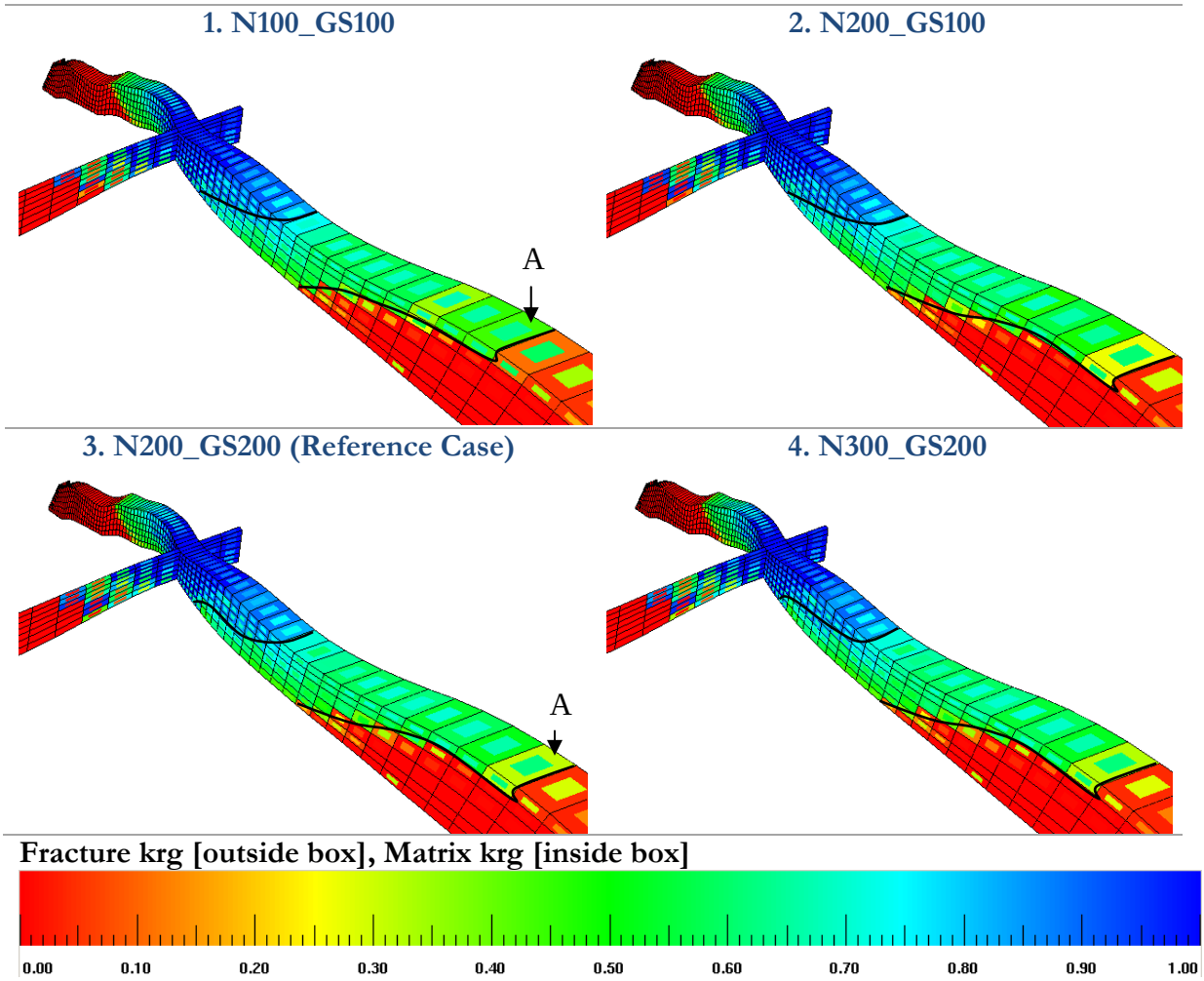

Figure 3-21. Dele Matrix and Fracture Gas Relative Permeability– 10 years after N_2 injection sensitivities are performed.

Using a scale range from 0 to 1, Figure 3-22 shows that kro develops 2 principal regions governed by the fracture oil relative permeability. The first region goes from the injector up to the displacement front (see Point 1 in Figure 3-22), and the second region goes from the displacement front up to the producer well (see Point 2 in Figure 3-22).

The first region is characterized by a very low to null fracture oil relative permeability, even if the zone has some oil in it; and the second region is characterized by a fracture oil relative permeability around ~0.3 with a null to some matrix oil relative permeability of ~0.1 (see Point A in Figure 3-22).

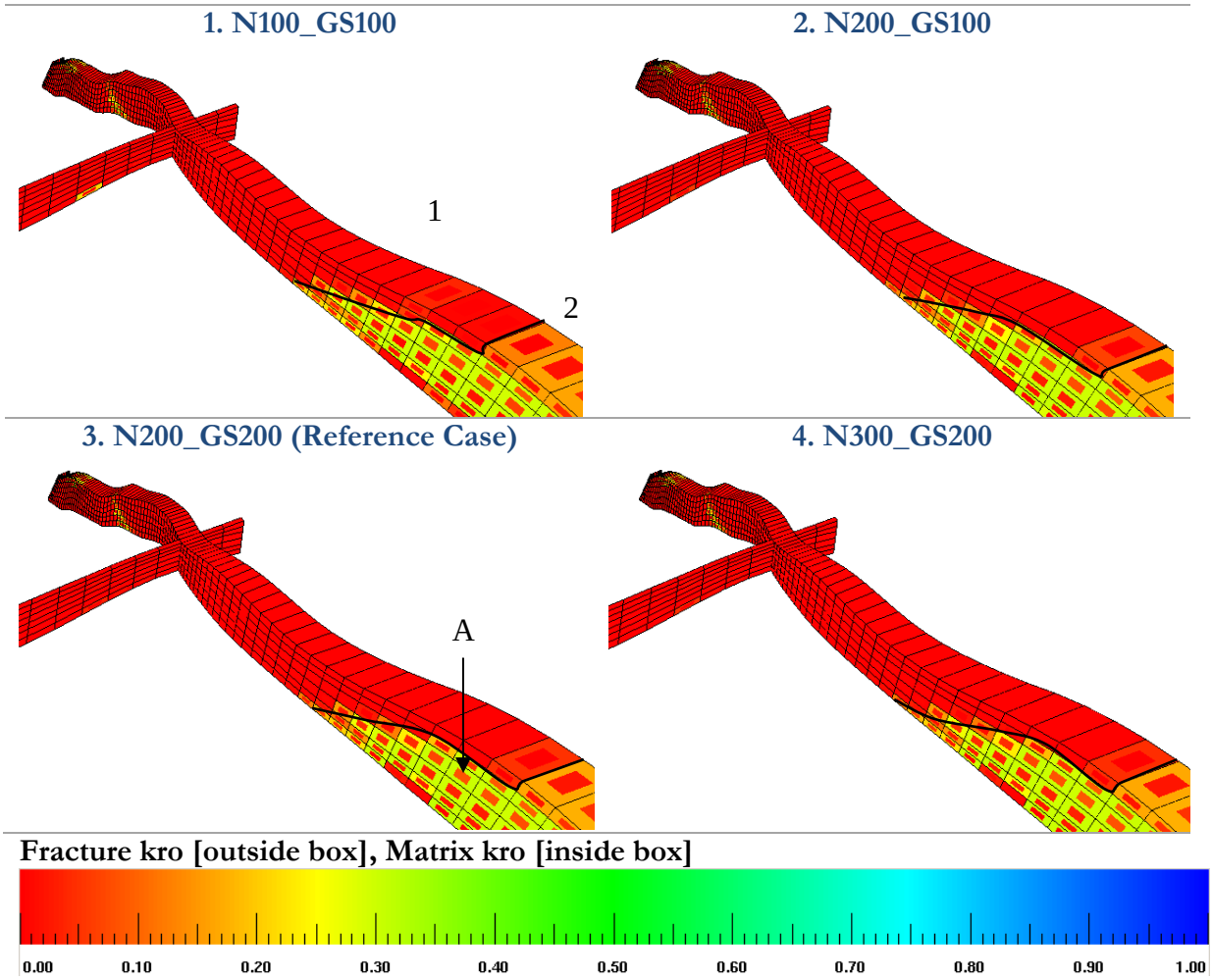

Figure 3-22. Dele Matrix and Fracture Oil Relative Permeability– 10 years after N_2 injection sensitivities are performed.

- **Relative Permeability and Saturation**

Figure 3-23 highlights 3 general displaced zones. One that is very close to the injector, where the fracture oil saturation is close to the Sorm~0.05 (red region) and the matrix oil saturation is close to the Sor~0.2 (orange region). This region is named as 1 in Figure 3-23.

There is a second region where the fracture oil saturation is close to ~0.2 and the matrix oil saturation is ~0.15.

And finally, there is a 3rd region close to the producer where the N_2 has not fully penetrated, where the fracture oil saturation is higher than 0.5 and the matrix oil saturation is 0.25 or higher.

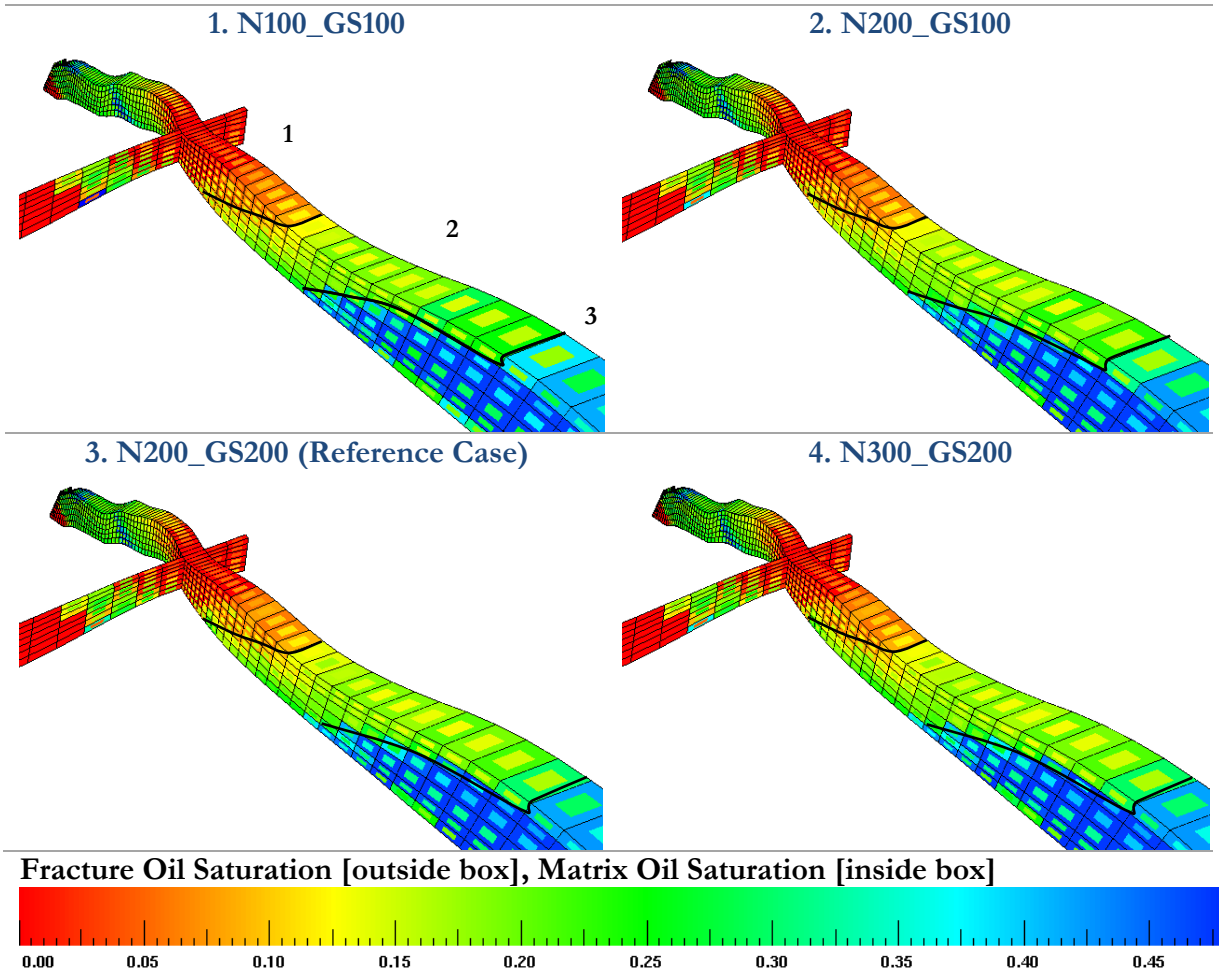

Figure 3-23. Dele Matrix and Fracture Oil Saturation– 10 years after N_2 injection sensitivities are performed.

Figure 3-24 presents a combination of fracture oil relative permeability (outer box) with fracture oil relative permeability, with the aim of observing the regions where there is some oil locked by very low or even null oil relative permeability.

Region 2 presented in Figure 3-24 shows that the oil is locked in the fracture system, which is related to the relative permeabilities presented in Section 2.7.3.5.

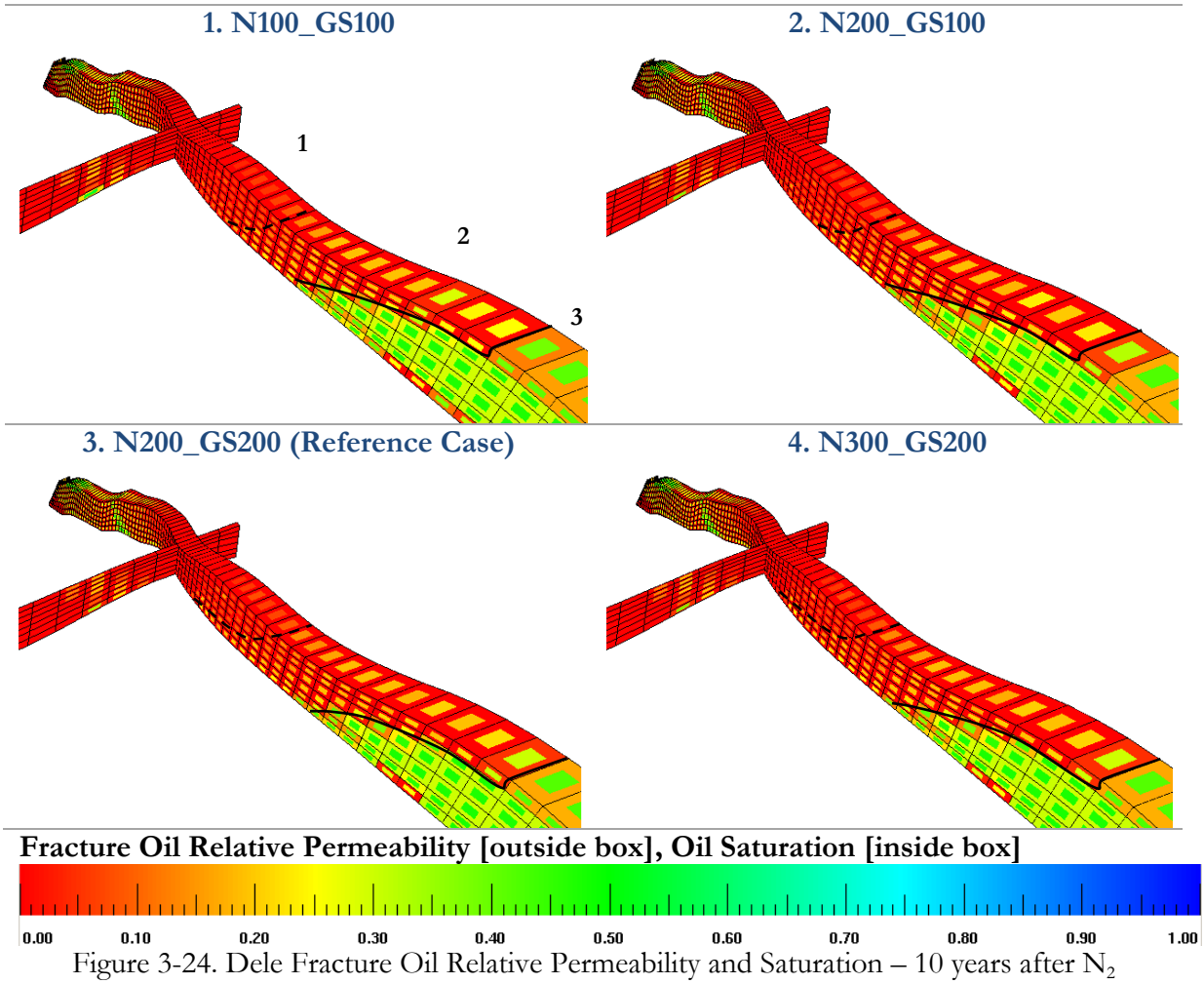

Figure 3-24. Dele Fracture Oil Relative Permeability and Saturation – 10 years after N_2 injection sensitivities are performed.

Figure 3-25 shows how matrix oil (represented in the inner box) is locked because of a low oil relative permeability (represented in the outer box).

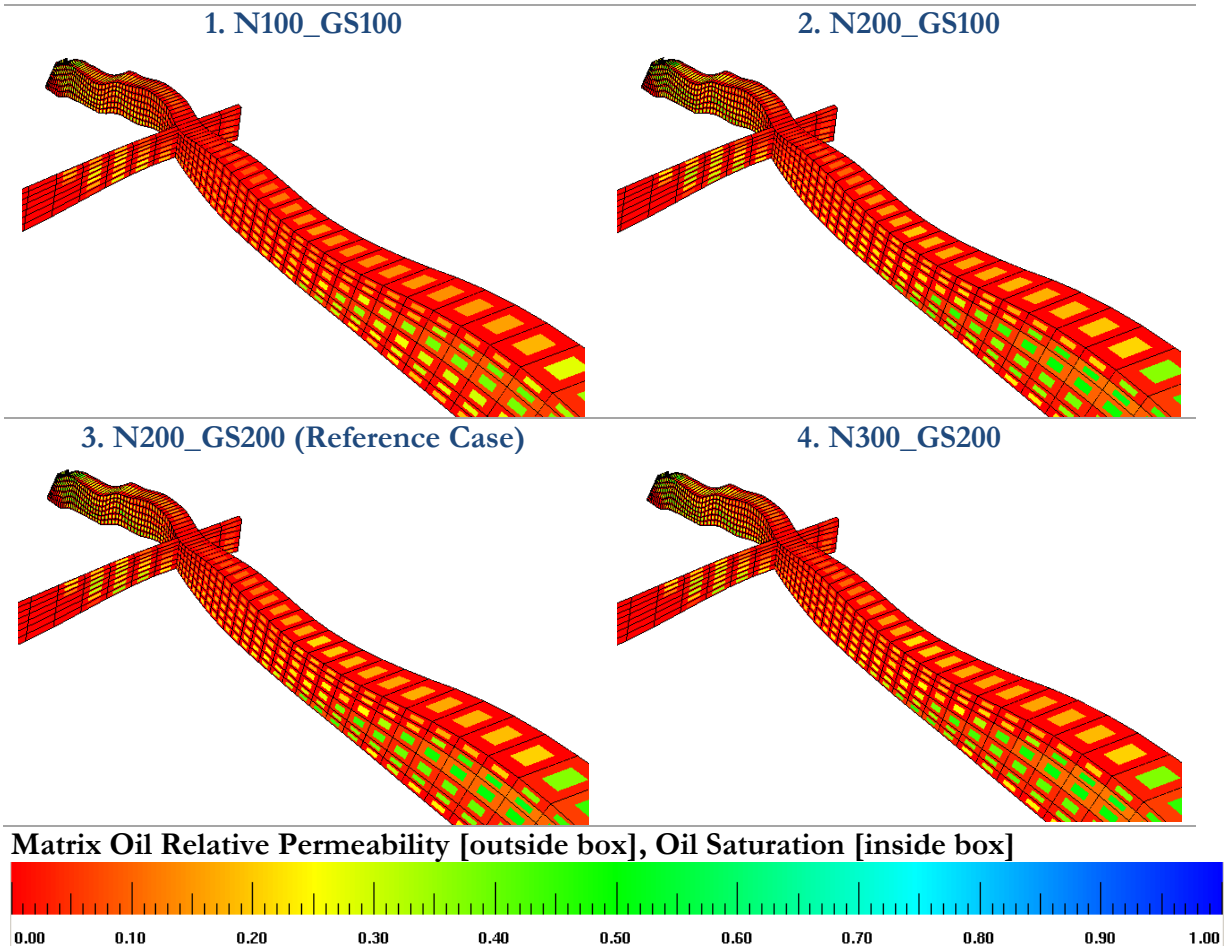

Figure 3-25. Dele Matrix Oil Relative Permeability and Saturation – 10 years after N_2 injection sensitivities are performed.

3.7 Uncertainty Sensitivity Analysis

Two main impacts were investigated, that were related to nitrogen injection in the reservoir:

- One is the impact of nitrogen injection on condensate recovery.
- Second is the impact of nitrogen injection on total hydrocarbon recovery.

Using a deductive approach, three levels of analysis are presented, going from the top (global) view down to a deeper level of analysis, as follows:

- In the production level: Colombia Energy interest. Qo, Qg, Qw.
- In the saturation level: Reservoir Engineering Interest: So, Sg, Sw.
- In the compositional level: Master investigation interest: k Values (k is the yi/xi ratio, which gives a measure of the tendency a component has to pass to the other phase. When k>1, the component tends to be concentrated in the gas phase **[24]**).

A design of 200 MMscfd of gas sales and 200 MMscfd of N_2 injection was selected as a reference case to understand the impact that nitrogen injection has over oil and gas production , having selected some uncertainties, like the following: 1) the workflow used to build the DPDP Model. Two important fluids parameters: 2) Makeup injected gas concentration and 3) N_2 Interaction Coefficient parameters); two main matrix parameters: 4) Sgt and 5) relative permeability; two fracture variables: 6) horizontal permeability anisotropy and 7) vertical fracture permeability.

The objective of Figure 3-26 is to show the oil production loss and gas sales gain when injecting N_2 into the system, compared to the base case with the DPDP model.

In Figure 3-26, *QA* means Quick Analysis (see Plot No. 5 in Figure 3-32, Section 3.7.1), *N2%gi* means different N_2 mixtures with CO_2 (N0CO100 means 100% injected CO_2 and N50CO50 means 50% of N_2 and 50% of CO_2, see Section 3.7.2), *BICS0* means that there are zero Binary interaction coefficients with other pseudo-components (see Section 3.7.3), *Sgt* means Maximum Gas Trap Saturation (where Sgt0 means no gas trap saturation, while Sgt60 means 60% of maximum gas trap saturation, see Section 3.7.4), *kr* is related to the relative permeability sensitivities (where Allkrf means using the krf for both the matrix and fracture system, while allkfm means using the krm for the matrix and fracture system; both sensitivities where made at reservoir level, see Section 3.7.5), *kf* means that kx and ky are the same (isotropic case , see Section 3.7.6), *kv* means vertical permeability (where kmV means increasing the matrix vertical permeability kmz by a factor of 10, and kfV means decreasing the fracture kfz by a factor of 10, see Section 3.7.7).

One 1st clear observation is that all sensitivity cases show oil production loss with N_2 being injected compared to the base case (no N_2 injection).

A 2nd very interesting case is when the vertical matrix permeability is increased (see kmV parameter in Figure 3-26), which impacts oil production with additional 1.7 MMstb. This is a highly important parameter, as the base case considers a value of kmz = 0.1 * kmy.

A 3rd important observation is related to pure CO_2 injection (see N0CO100 parameter) which shows an oil loss of just 3.8 MMstb with respect to the base case. This result confirms that CO_2 has much more compatible properties with condensate gas than Nitrogen does. This case also increases gas sales to its maximum value during the 10'year period of evaluation.

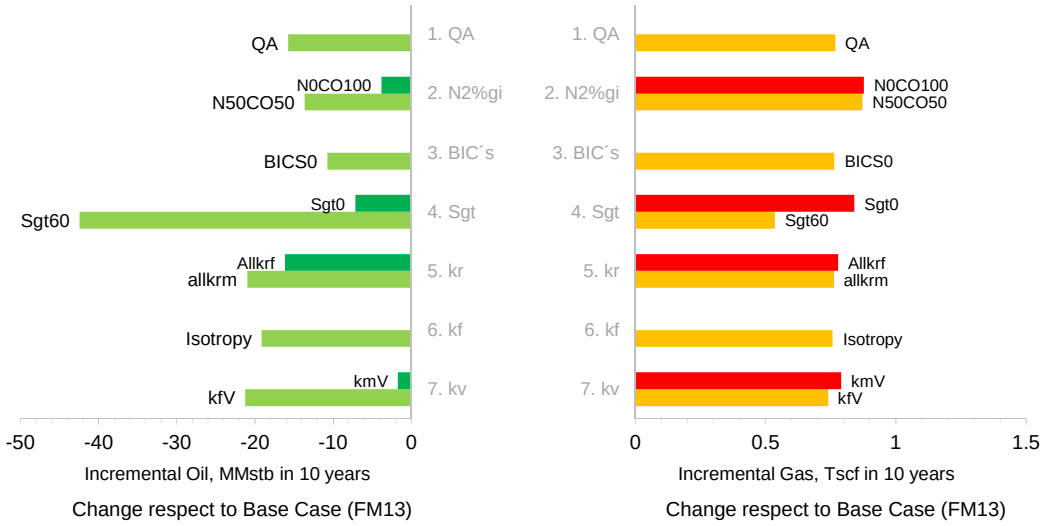

Figure 3-26. Tornado Graph – Surface Oil and Gas Sales Cumulative Production Summary of the Uncertainty Impact with respect to the Base Case (FM13).

Figure 3-27 has similar results as with Figure 3-26, but in this case using the Recovery Factor parameter. The average oil recovery loss with N_2 is between 1 to 3%, and for the incremental gas recovery, the gain is between 9 to 14%.

In other words, the oil recovery loss is within the uncertainty of the final recovery for the reference case (see Figure 3-30).

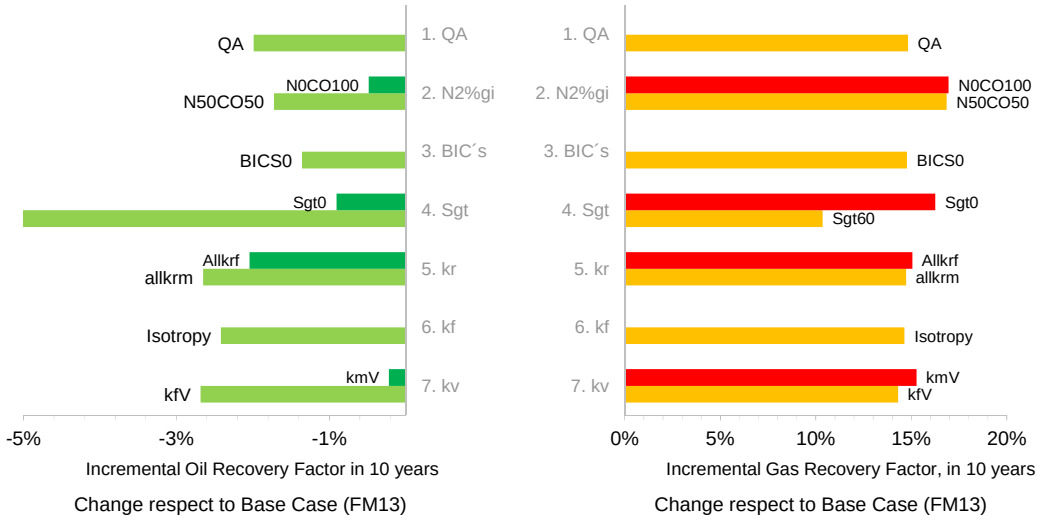

Figure 3-27. Tornado Graph – Surface Oil and Gas Sales Recovery Summary of the Uncertainty Impact with respect to the Base Case (FM13).

Figure 3-28 shows the total net incremental recovery with 200 MMscfd of gas injection with 200 MMScfd of gas sales. The total incremental recovery is between 78 MMBOE and 110 MMBOE.

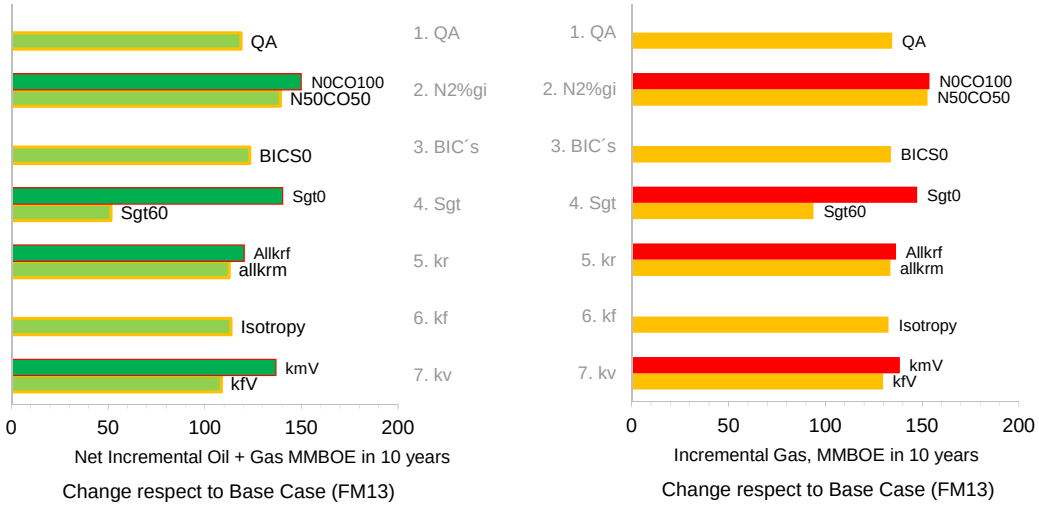

Figure 3-28. Tornado Graph – Surface Net Oil and Gas Sales and Gas MMBOE Production Summary of the Uncertainty Impact with respect to the Base Case (FM13).

The objective of Figure 3-29 is to present how much impact do the uncertain variables selected for this evaluation have on the results when injecting 200 MMscfd of N_2 with 200 MMscfd of Gas Sales making use of the DPDP model.

As expected, the same 3 parameters described in Figure 3-26 have the biggest impact compared to the reference case.

Figure 3-29 shows that the gas trap saturation evaluation (Sgt) generates one of the biggest positive and negative variations in oil and gas response.

The aim for this evaluation was to capture the importance of tuning the Sgt value in order to avoid over- or underestimating the benefits of injecting N_2. This was the reason for the analysis of this variable presented in Section 1.6.3.3.

The analysis of Section 1.6.3.3 gives some confidence about the Sgt value of 0.3 used in the reference case, so that this parameter can be considered tuned, but it still should be tied to future rock typing methodology.

The composition of the injected fluid is related to its surface manageability, so it is possible to optimize the injection by adding CO_2 into the N_2 stream.

Finally, the biggest uncertainty with lowest manageability parameter that is the matrix vertical permeability, which makes up huge oil production differences in the recovery. kmV could increase cumulative oil production in 16.2 MMsctb.

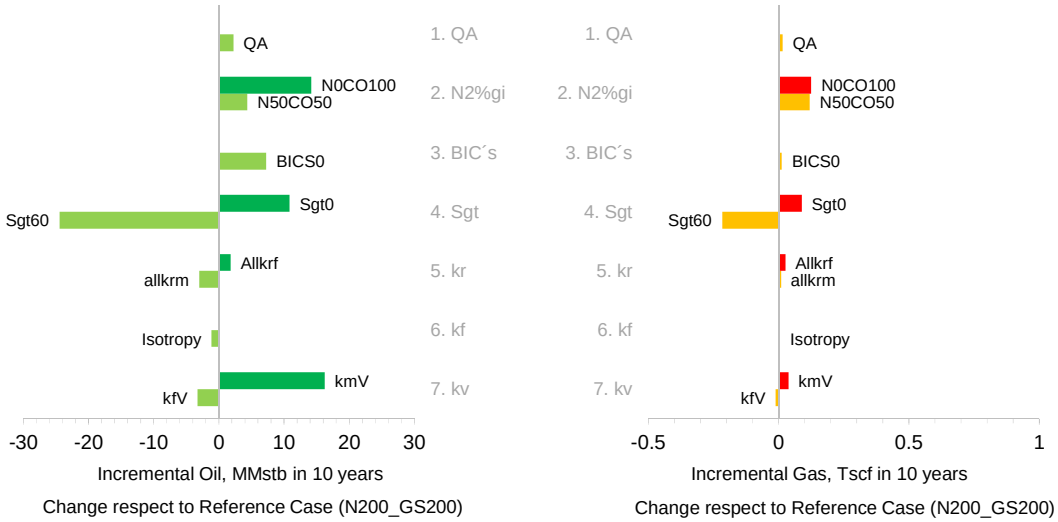

Figure 3-29. Tornado Graph – Surface Oil and Gas Sales Cumulative Production Summary of the Uncertainty Impact with respect to the Reference Case (N200_GS200).

Figure 3-30 shows the oil and gas recovery variation around the reference case, which can be interpreted as the uncertainty related to the recovery factor while injecting 200 MMscfd of N_2 with 200 MMscfd of gas sales.

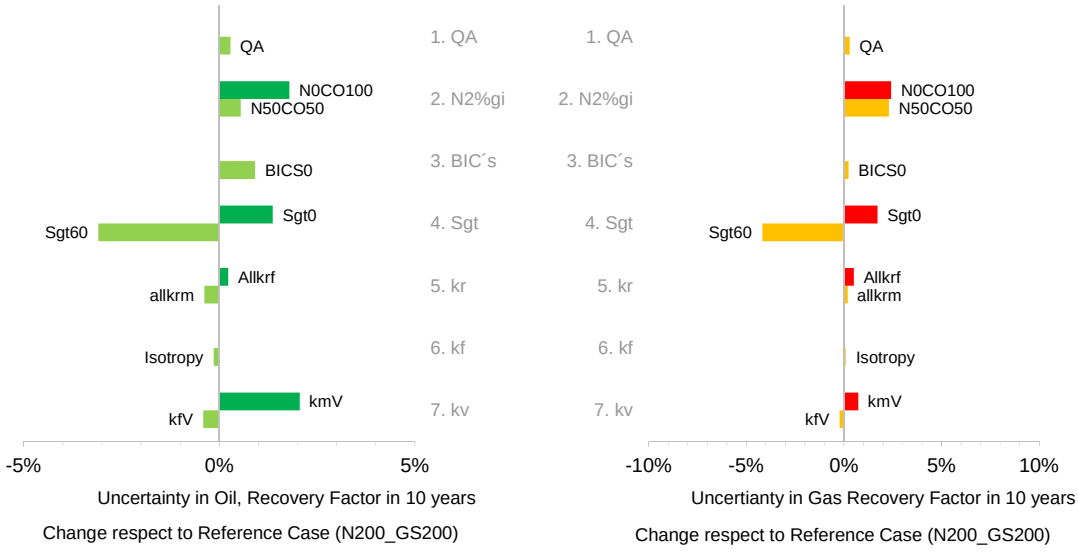

Figure 3-30. Tornado Graph – Surface Oil and Gas Sales Recovery Factor Summary of the Uncertainty Impact with respect to the Reference Case (N200_GS200).

Figure 3-31 shows the sum of oil and gas production in the left side tornado plot, in order to quantify the uncertainty with respect to the reference case. A similar analysis that was presented before shows that the matrix vertical permeability is an important uncertain parameter that may play a difference when deciding whether to perform or not the project.

Figure 3-31 also presents if when combining N_2 with CO_2 it increases the possibilities of a higher recovery factor for the project.
The right side tornado in Figure 3-31 shows the uncertainty in gas sales in MMBOE around the reference case, where the injection of CO_2 increases the recovery in 20.9 MMBOE, while the kmV just makes up an incremental 6.6 MBOE of gas.

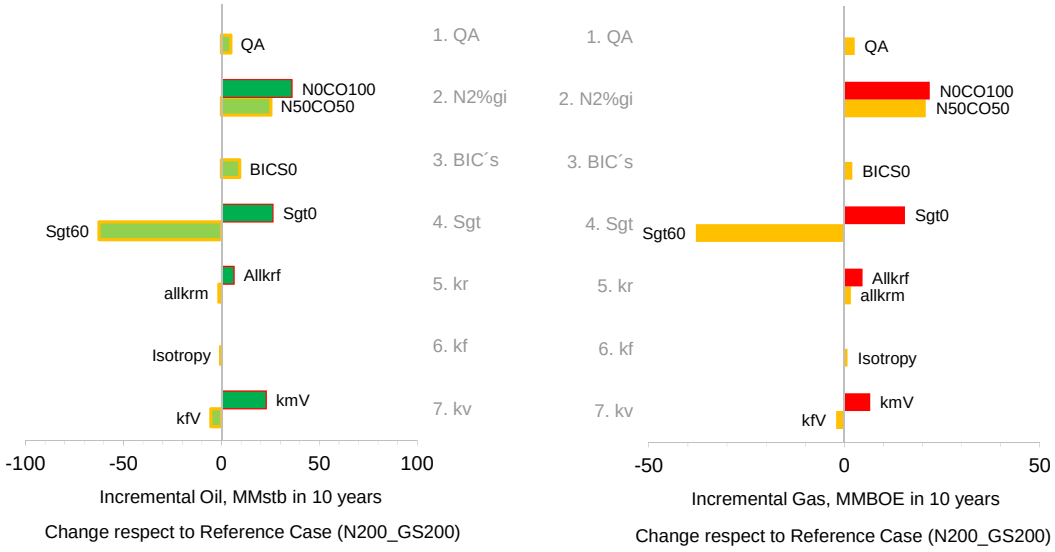

Figure 3-31. Tornado Graph – Surface Net Oil and Gas Sales and Gas MMBOE Summary of the Uncertainty Impact with respect to the Reference Case (N200_GS200).

3.7.1 Fracture Porosity

A simple rule to estimate the fracture permeability with $\phi_f < 0.1 \cdot \phi_m$ [56] when $\phi_m < 10\%$ was used, and the results were compared with the reference case, which used Eq. 1-4 (see Figure 2-23 and Figure 2-24 for reference).

Table 3.6 displays the nomenclature used for the sensitivity study in this section.

Table 3.6. Quick DPDP approach – Prediction Run Names.

Runs	Approach	Run Name	Comments
	Single Porosity	p_spC1s_N200_GS200	Equivalent model
Reference	Method CGH	p_dpC1d_N200_GS200	Reference Case: with workflow presented in **Section 2.8**
1	Quick Approach: QA	p_dpC2d_N200_GS200_QA	See Assumption above.

All plots in Figure 3-33 show that the Quick Approach (solid blue line) compared to the proposed Method (dashed magenta line) gives a better oil production. The reason for this slight improvement is due to an increase in fracture porosity when making use of the general rule $\phi_f < 0.1 \cdot \phi_m$.

See also Appendix D for a detailed analysis per sheet.

- **Production**

The oil and gas production comparison between the quick approach using this work's proposed methodology (see Section 2.8) and the SP Approach shows a big difference in the displacement. As the SP Model does not present anisotropy, the cells' relative permeability is higher, which allows for a better sweep of oil and there is no high vertical permeability compared to the DPDP model.

Figure 3-32 presents 6 plots that are related to the general production variables at field level.

- Plot No. 1 in Figure 3-32 displays gas production, where there is a clear difference between gas production at field level when using the SP model (solid black line) and the DPDP (dashed magenta and solid blue lines). Two reasons for this big change are concerned with permeability and the relative permeability used in each model.

- Plots No. 4 and 5 in Figure 3-32 show that the oil production potential is higher when modeling the field as a DPDP system compared to the SP system. This effect is related to the relative permeability curves used in the DPDP model.

- Plot No. 3 in Figure 3-32. GOR evolution with time shows a slightly higher evolution for the SP model than with the DPDP model after 10 years of N_2 injection. The slower GOR evolution in the DPDP model is related to the anisotropy that was implemented,

[56] This approximation assumes that the storage coefficient (ω) is constant and approximately equal to 0.1.

which has a lower effective permeability between the injectors and producers (see Figure 2-14). Refer also to Figure 3-39 and Figure 3-40 to see this effect within the nitrogen concentration map.

- Plot No. 6 in Figure 3-32. WCut evolution with time is steeper in the SP model.

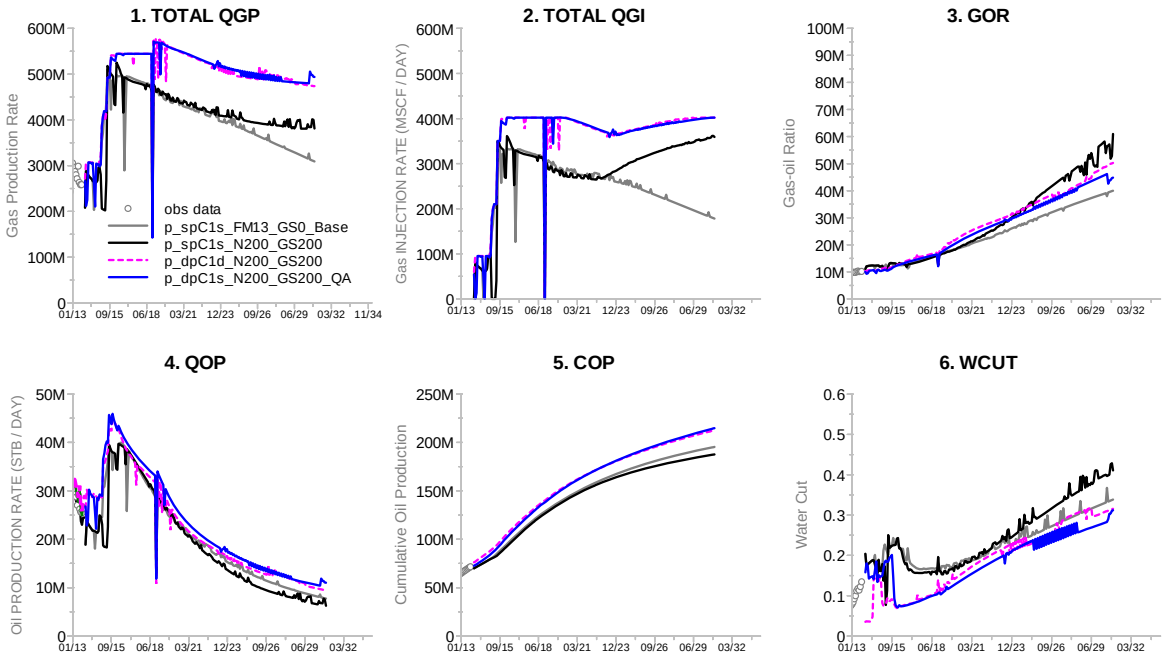

Figure 3-32. Field Surface Production – DPDP Quick Approach (QA) Sensitivity.

The Figure 3-33 displays 9 plots that are related to gas production, gas sales and gas injection, and the impact they have on the average field hydrocarbon pressure.

- Plot No. 3 in Figure 3-33 shows the N_2 gas injection increase with time due to the recycling process, and Plot No. 6 shows the N_2 production. Both plots show the recycling process beginning after 1 year; refer also to Figure 3-39 and Figure 3-40 to observe this effect within the nitrogen concentration map.

- Plot No. 5 in Figure 3-33 shows a fast hydrocarbon gas injection decline (with time), as this gas is used for gas sales (see Plot No. 7). In less than 5 years, hydrocarbon gas injection is reduced to 0.

- Plot No. 7 in Figure 3-33 shows a 2 year delay for gas sales decline in the DPDP model compared to the SP model.

- Plot No. 9 shows a slightly weaker pressure support (200 psia) for the DPDP model than for the SP model.

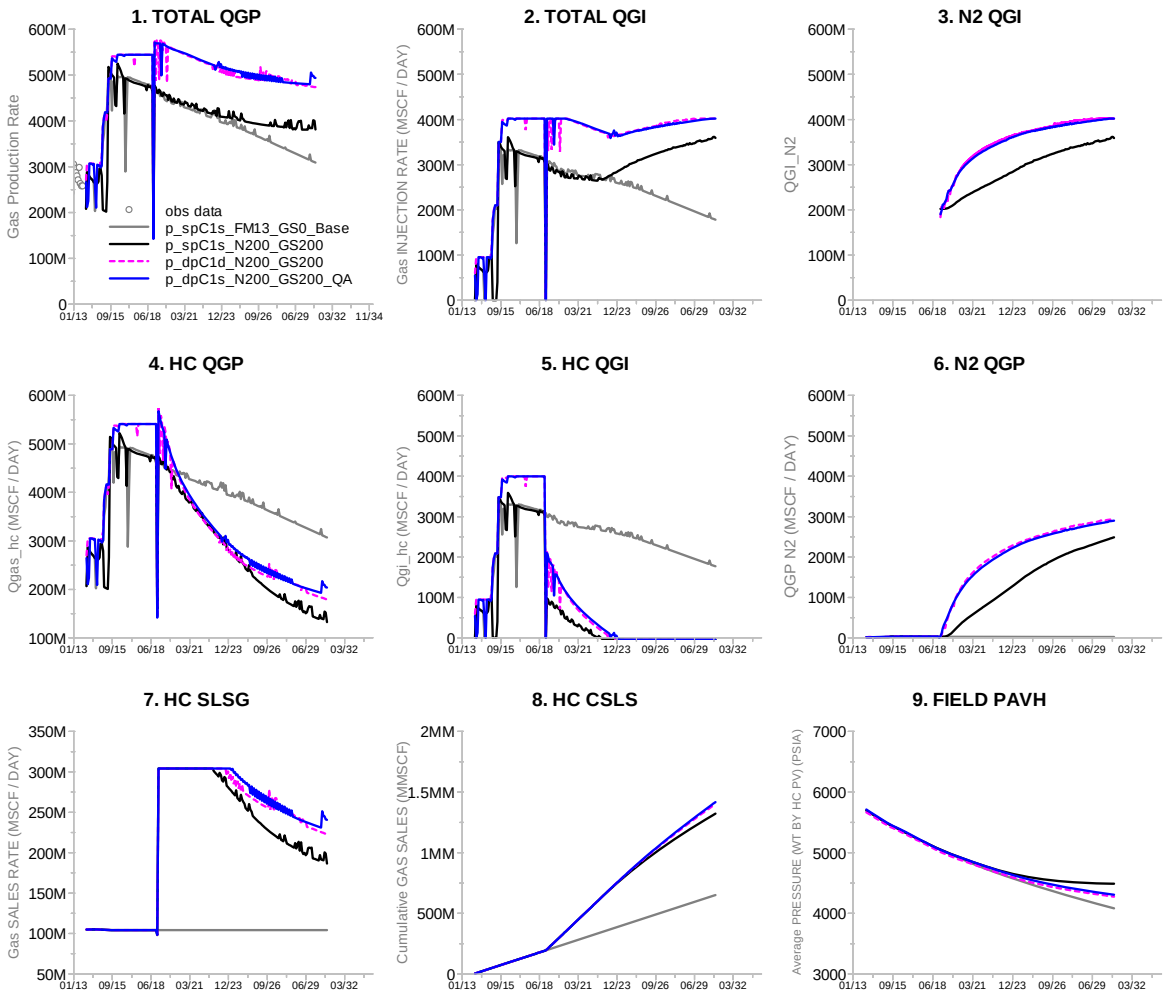

Figure 3-33. Field Surface Gas Behavior – DPDP Quick Approach (QA) Sensitivity Analysis.

- **Saturation, density and viscosity**

Figure 3-34 shows a summary of oil saturation, density and viscosity in Dele Sheet, where small differences are pinpointed with an arrow, when comparing the cases with and without N_2 injection. See Appendix D for further analysis about the changes in depth for the different PDM sheets.

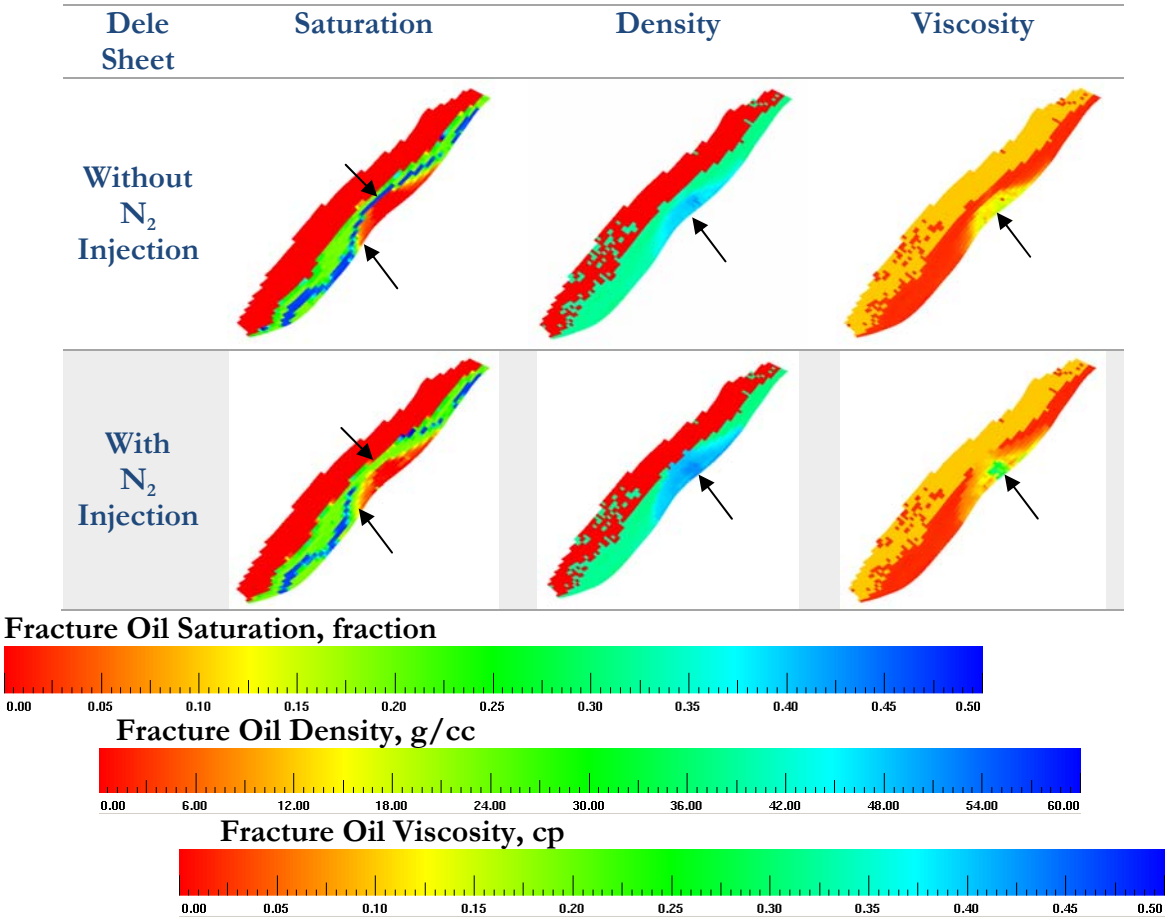

Figure 3-34. Fracture Oil Saturation Example – Quick DPDP Approach – 10 years after N_2 Injection – Layer 4 (Bottom).

Figure 3-35 shows that saturation changes are more pronounced with depth when comparing the SP with the DPDP_QA model, proving that N_2 injection generates a higher liquid drop out in the reservoir that tends to segregate to the bottom of the structure (see point A and B in Figure 3-35).

As expected, gas saturation increases faster in the fractures than within the matrix.

Density and viscosity quickly increases in the fracture system, showing a direct correlation with the k- values' evolution as there is a continuous loss of intermediate and heavy components located in the fracture.

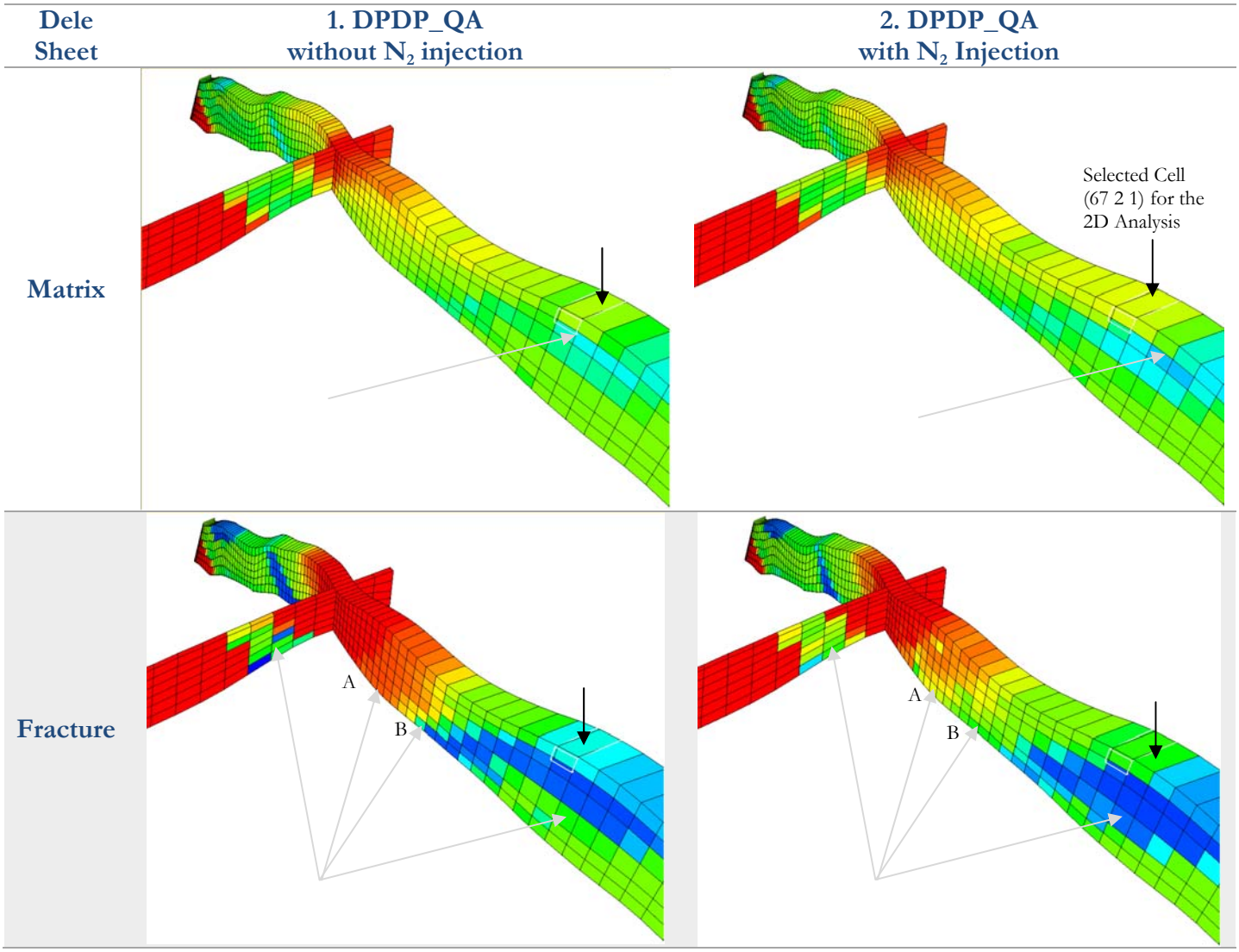

Figure 3-35. Dele Saturation X-Section– without N_2 Injection (left side Plot) and with N_2 Injection - Quick DPDP Approach – 10 years after N_2 Injection.

Comparing Figure 3-6 with Figure 3-36, there is a significant change from ~40 gr/cc to 60 gr/cc in oil and gas density when nitrogen is injected in Dele Sheet, especially within the fracture system.

There is an observable change in oil viscosity within the fracture system. Oil viscosity begins to increase once nitrogen begins to contact the oil that is located inside the fracture and the matrix. This effect is much more noticeable in Floreña Barco Gas Cap zone, as both the matrix and fracture have better petrophysical properties for this reservoir.

Sheets	1. Saturation	2. Density	3. Viscosity
Dele	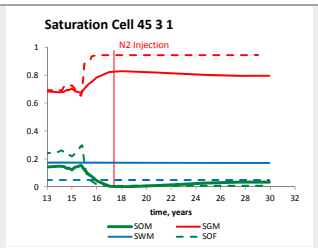	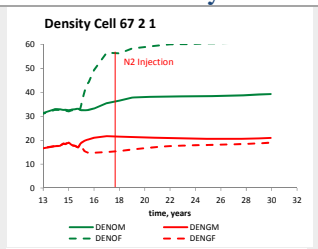	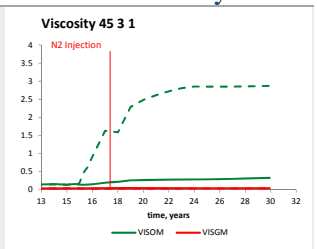
Guamalera	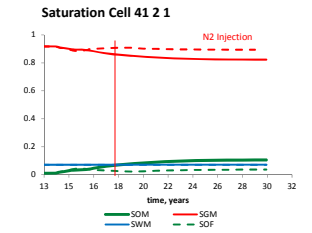	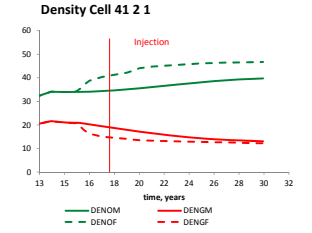	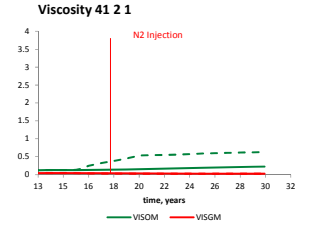
Pauto Main Mirador	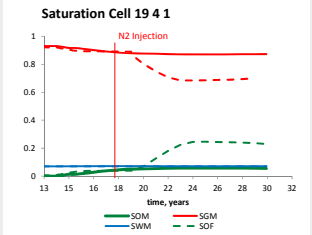	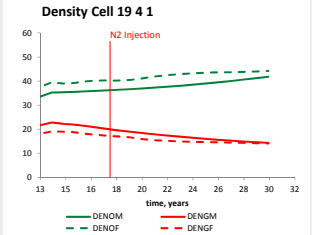	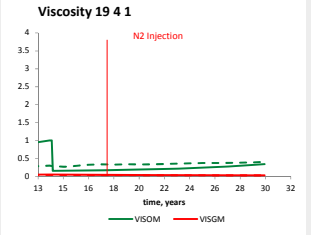
Floreña Mirador	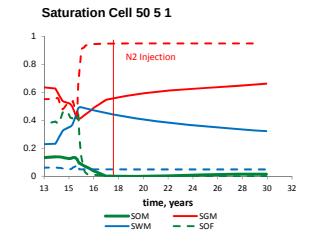	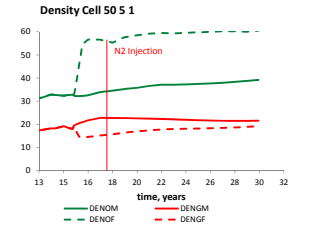	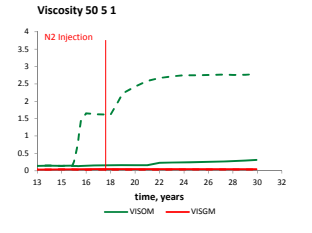
Floreña Barco Gas Cap Zone	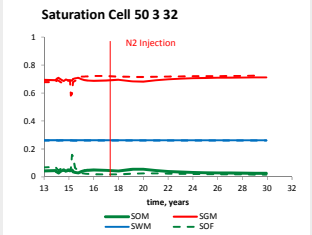	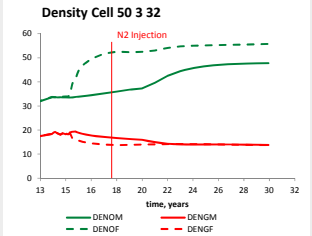	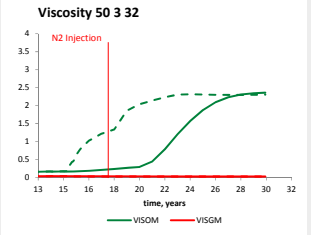
Floreña Guadalupe	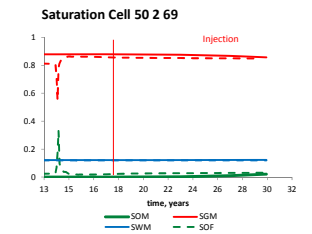	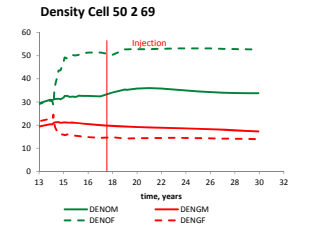	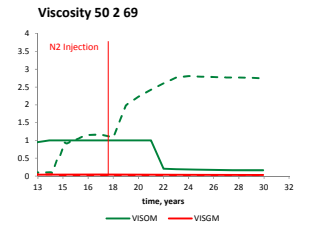

Figure 3-36. Subsurface Saturation, Density and Viscosity distribution – Quick DPDP Approach with N_2 Injection.

- **Composition**

Figure 3-37 shows the distribution of N_2 mole fraction within the matrix and fracture system at the beginning of 2030 (10 years after the N_2 injection).

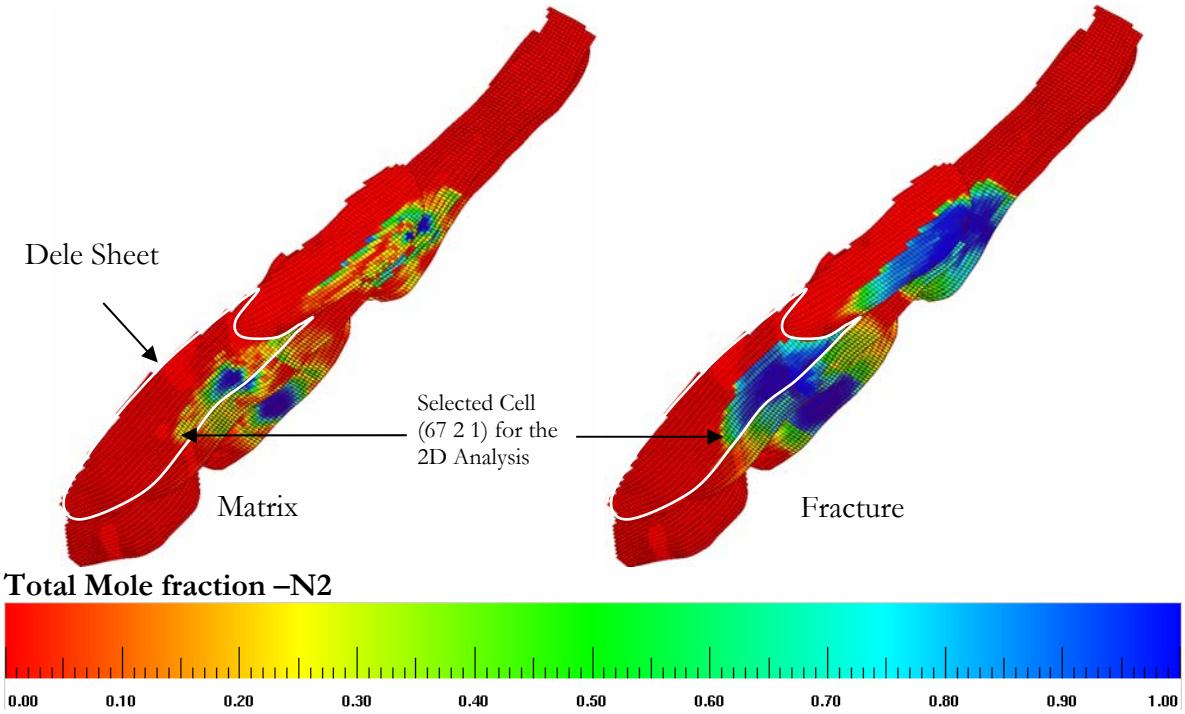

Figure 3-37. Pauto Complex Total Mole Fraction –N_2 – Quick DPDP Approach – 10 years after N_2 Injection.

When comparing the behavior of the k values with and without N_2 injection (see Figure 3-38 and Figure 3-7, respectively), it is observed that the fracture system (dashed lines) quickly begins to lose intermediate (column 1 in Figure 3-38) and heavy components (column 2 in Figure 3-38) from the gas phase. This phenomenon serves as a start to explain the oil production loss presented in Figure 3-32.

In other words, when the k-values have a relatively constant behavior through time, as seen in Figure 3-7, it means that the pseudo-components tend to be in the same proportion in each phase (oil and gas); once nitrogen begins to be injected, the K-values begin to deviate steeply from a value of 1.0, displaying a fan-like shape.

Figure 3-38 shows that C3 pseudo-component is reduced within the fracture system when comparing the N_2 injection with the no N2 injection cases.

It can also be observed that the point where the matrix and fracture seem to be unaltered is now with the C2 pseudo-component (with no N_2 injection in Figure 3-7, the point where the matrix and fracture seem to be unaltered is with the C3 pseudo-component).

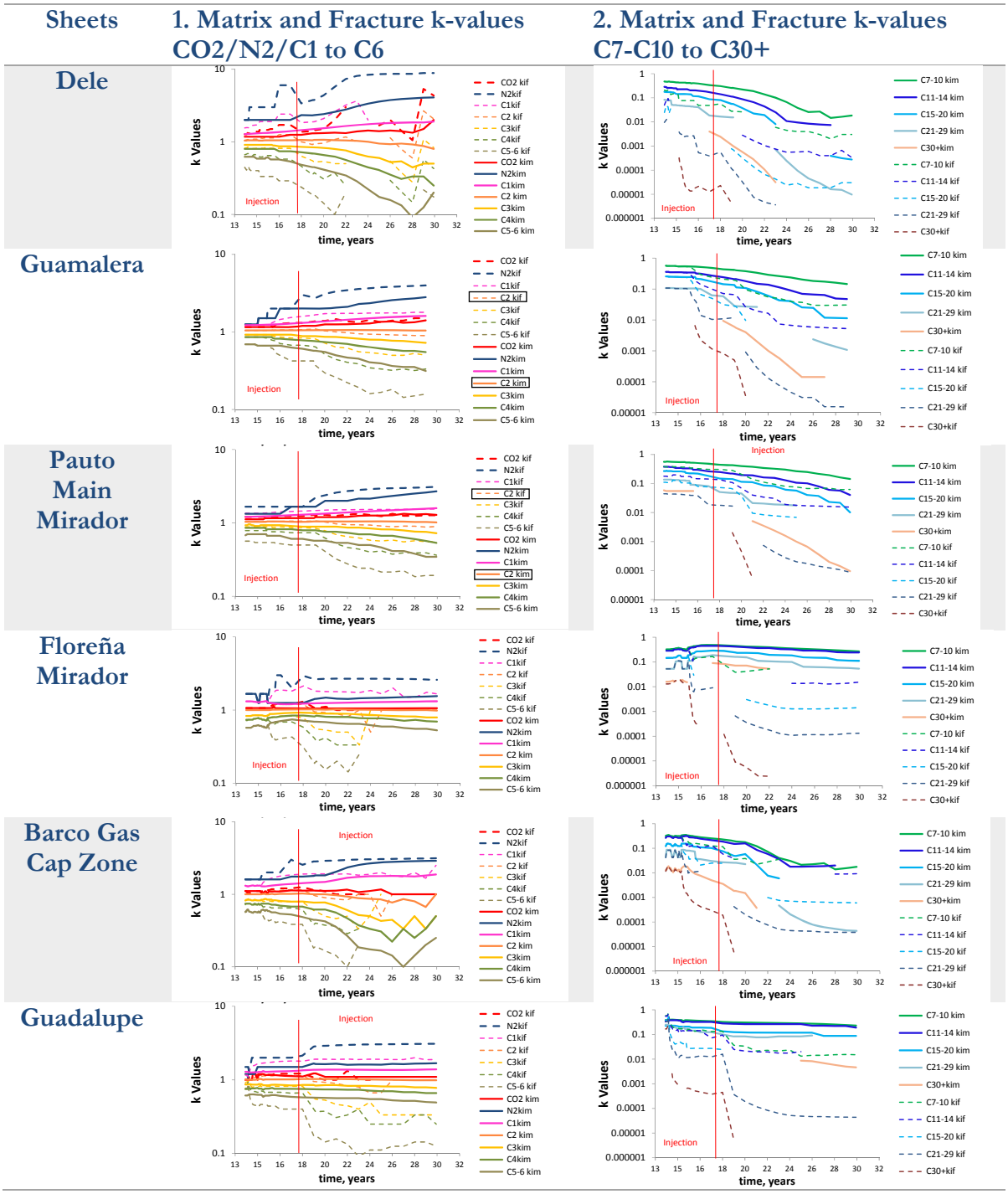

Figure 3-38. Subsurface k-values and Concentrations – Quick DPDP Approach with N_2 Injection.

Total mole fraction of Nitrogen after 1 year of N_2 injection - Dele Sheet Example.

N_2 travels a higher distance in 1 year through the fracture system of the DPDP model (see Point A in Figure 3-39) compared to the distance it travels through the SP model (see Figure 3-40).

This effect is also appreciated in the N_2 injection evolution with time. See point B, Plot No. 3 in Figure 3-33 when comparing the SP model with the DPDP model.

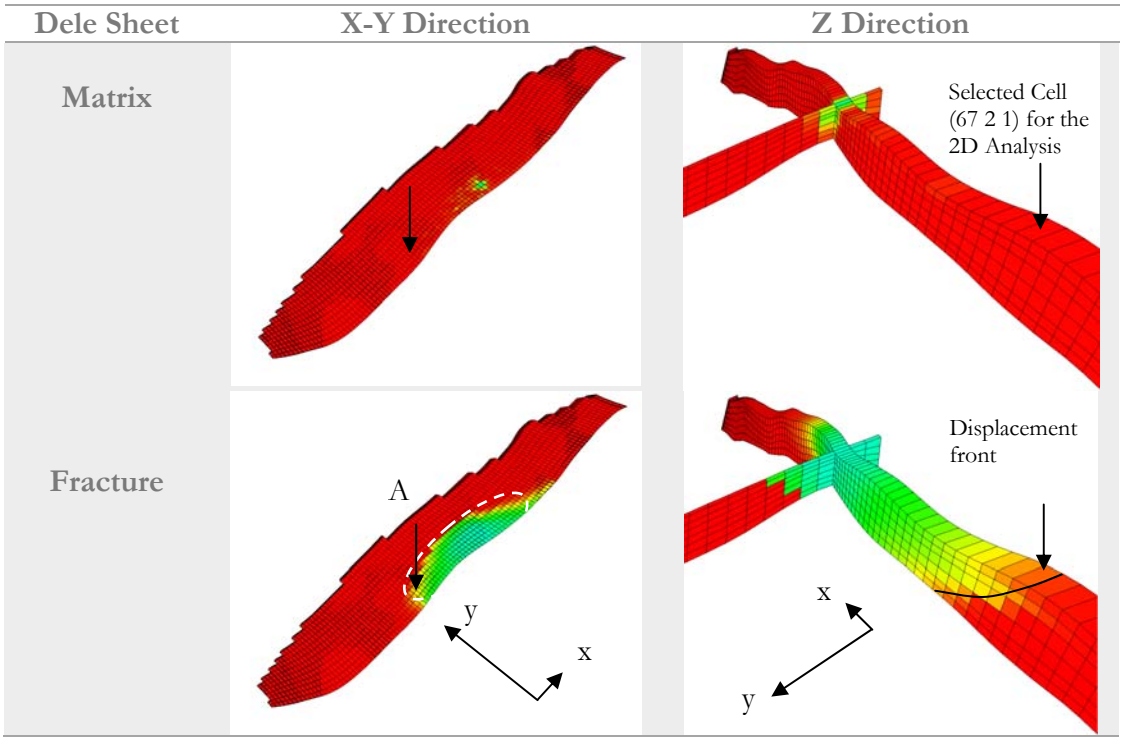

Figure 3-39. Dele Sheet Total Mole Fraction –N_2 – Quick DPDP Approach – 1 year after N_2 Injection.

In Figure 3-40, it is easy to also appreciate that the shock front of the oil displacement is more stable in the SP model compared to the fracture displacement front in Figure 3-39 of the DPDP model. The displacement front is very close to the yellow grid cells (0.2 N_2 molar concentration) for both figures.

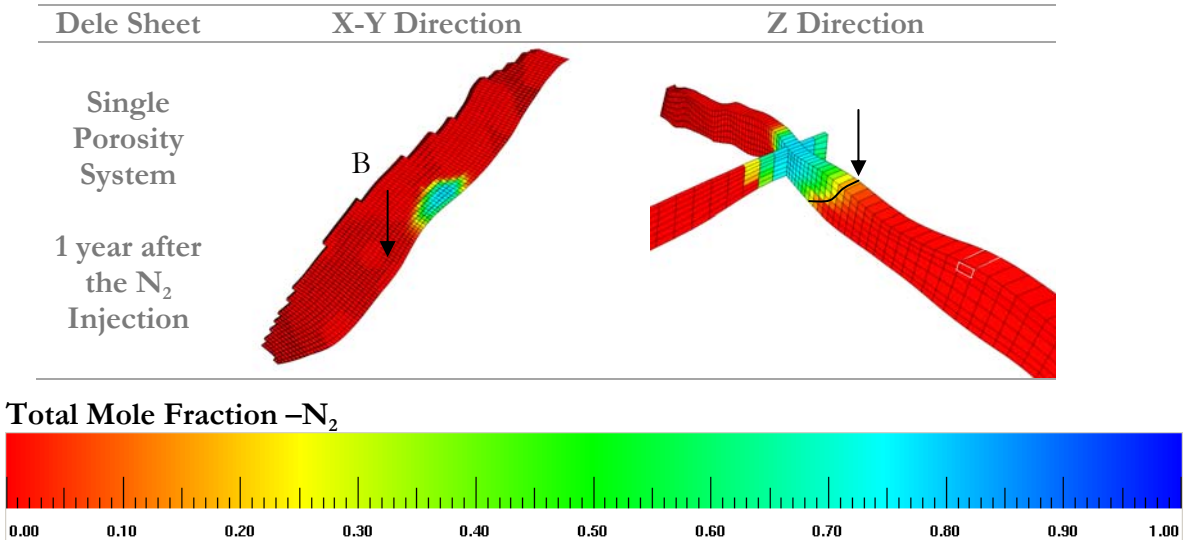

Figure 3-40. Dele Sheet Total Mole Fraction –N_2 –SP Approach. 1 year after the N_2 Injection.

Total mole fraction of Nitrogen after 10 years of N_2 injection - Dele Sheet Example.

Figure 3-41 shows that, looking at the matrix N_2 mole fraction, there is a poor sweep, meanwhile the fracture's N_2 mole fraction indicates a very fast movement through the fracture. In other words, there is an overriding effect for rich gas located in the matrix due to high mobility (high permeability of N_2 through the fractures).

Even if there is a well-defined fracture effective permeability anisotropy with a better permeability in the *y* direction (see Figure 2-12), the DPDP model makes it clear that the pressure difference between the producer and injectors is more important in creating an ellipsoidal drainage area shape in the *x* direction than in the *y* direction.

Comparing the dashed and the ellipsoidal areas in Figure 3-41 and Figure 3-42, it can be seen that the fracture areal sweep is more homogenous compared with the SP model, which means that the anisotropy helps achieving a better areal sweep efficiency.

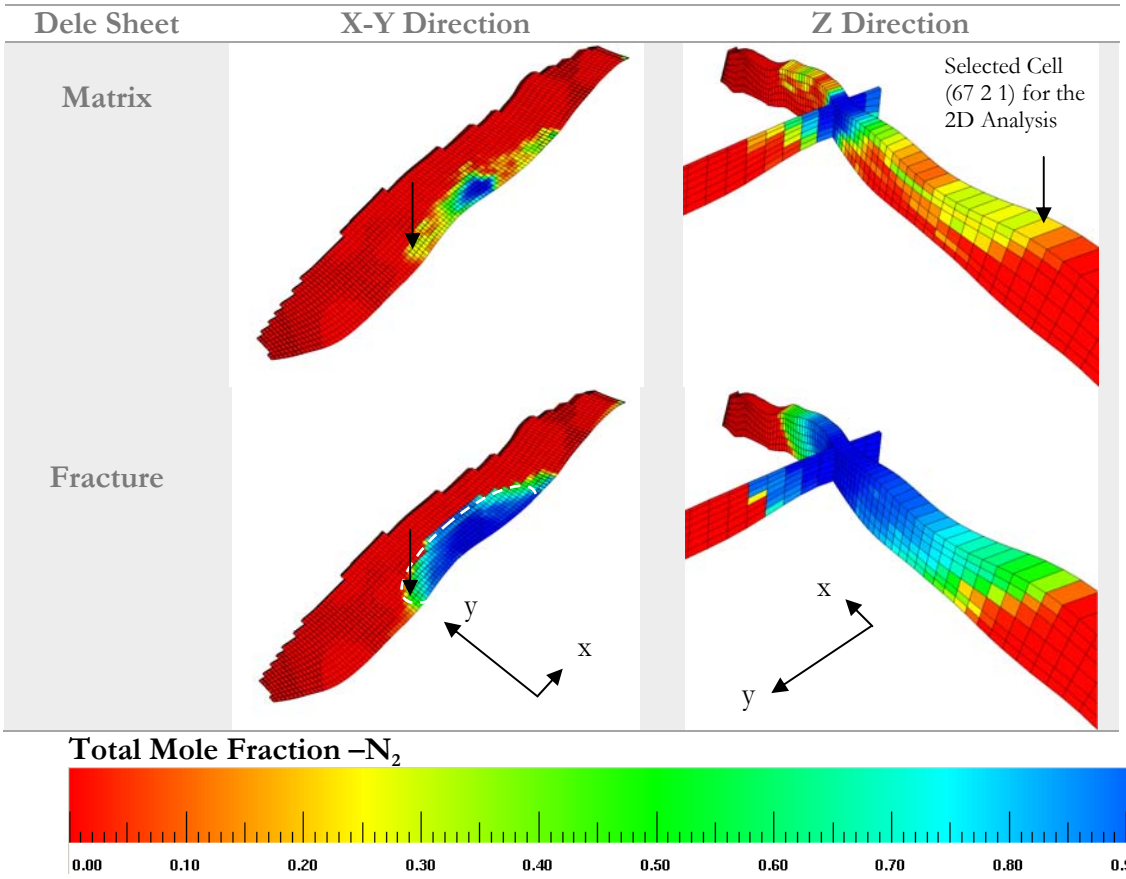

Figure 3-41. Dele Sheet Total Mole Fraction –N_2 – Quick DPDP Approach – 10 years after N_2 Injection.

Figure 3-42 shows the N_2 mole fraction for the SP system. An intermediate areal sweep can be observed, compared to the matrix and fracture systems, as it was expected, which in turn gives a better sweep for the rich gas (see Figure 3-41).

It is also possible to observe in the SP model, that the gravitational segregation of nitrogen in the top of the structure is much more pronounced compared to the DPDP model (see Figure 3-41).

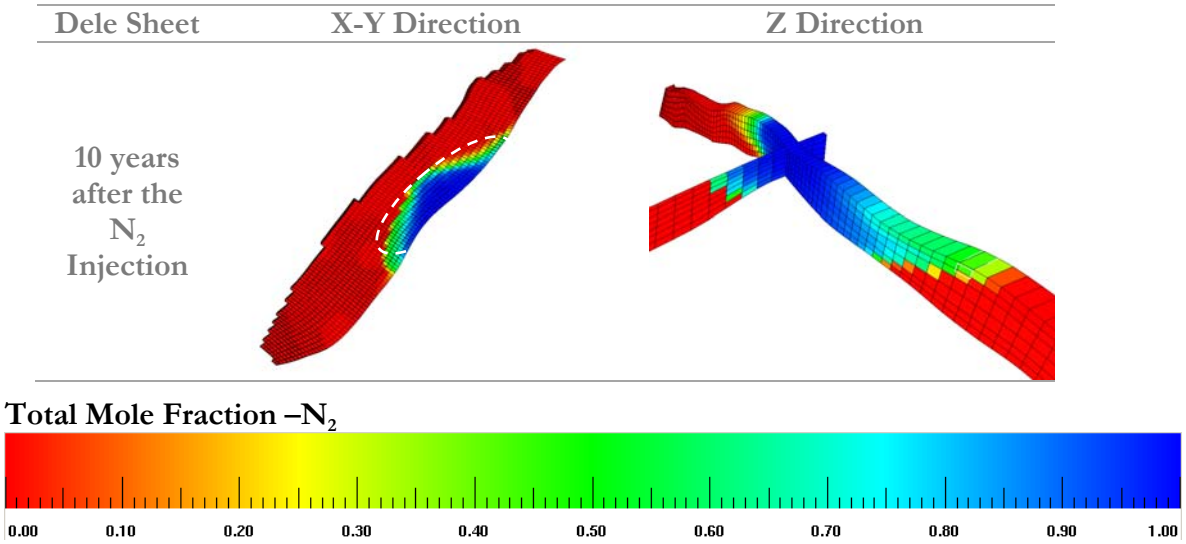

Figure 3-42. Dele Sheet Total Mole Fraction –N_2 –SP Approach. 10 years after the N_2 Injection.

3.7.2 Fluids: Selected Design among different N_2 Qualities

The following sensitivity analysis was done by changing the composition[57] of 100% pure nitrogen injection to 50% N_2 and 50% CO_2, and to 100% CO_2, in order to measure the impact of replacing N_2 with CO_2.

For this specific case, the same injection volumes were not kept, as the recycled N_2 was reduced when CO_2 injection was increased. Also, any CO_2 solubility that could occur in the reservoir was not taken into account.

Table 3.7 shows the nomenclature used for this section's sensitivities.

Table 3.7. Nitrogen Injection Composition Sensitivities – Prediction Run Names.

Runs	SC	N_2	CO_2	Prediction Run Name	Comments
0	1	100%	0%	p_dpC1d_N200_GS200	Reference Case
2	1	50%	50%	p_dpC1d_N200_GS200_**N50CO50**	Keeps the same additional Gas injection target of 200 MMscf but changing the composition of the gas injection stream to 50% N_2 / 50% CO_2.
4	1	0%	100%	p_dpC1d_N200_GS200_**N0CO100**	Keeps the same additional Gas injection target of 200 MMscf but changing the composition of the gas injection stream to 0% N_2 / 100% CO_2. In other words this case assumes 100% CO_2 injection with no CO_2 re-cycling.

The purpose of this section was to intentionally show that the CO_2 in PDM fields will have a better oil sweep, as the literature demonstrates and was explained in the introductory section of this document.

As a summary, CO_2 injection shows a better performance compared to N_2 due to 1) a lower N_2 volume injection, 2) a higher CO_2 contact with the matrix fluids and 3) more compatible properties with hydrocarbon fluids.

- **Production**

By injecting the same 200 MMscfd but contaminating pure nitrogen with different %Mol of CO_2, it is a clear the subsurface benefit of implementing CO_2.

Figure 3-43 shows 6 plots related to the general production variables at field level.

- Plot No. 1 shows a reduction in gas production rate (see the dashed black line, N0CO100 case) that is related to the lower N_2 recirculation (see Plot No. 3) once there is an increase in CO_2 injection.

[57] See references 13, 14 where the CO_2 evaluation was compared to N_2 injection in a gas condensate reservoir.

- Plots No. 4 and 5 show an expected oil recovery improvement by adding CO_2 into the reservoir, as the CO_2 has better properties to sweep oil. Notice that a 100% CO_2 injection has almost the same oil recovery effect, pressure support, GOR (Plot No. 3) and WCut Evolution (Plot No. 6), compared to the base case (no N_2 injection, gray line), which allows accessing the gas resources for sales.

  Pure CO_2 injection will reduce the liquid loss; this can be observed when comparing the base case (grey line) with the N0CO100 run (black line).

- Plot No. 3. Lower GOR evolution when injecting pure CO_2 was achieved, but the reason for this was a lower N_2 injection (see Plot No. 3 in Figure 3-45) and N_2 recirculation (see Plot No. 6 in Figure 3-45).

- Plot No. 6 shows how the WCut evolution is controlled by adding CO_2 into the system.

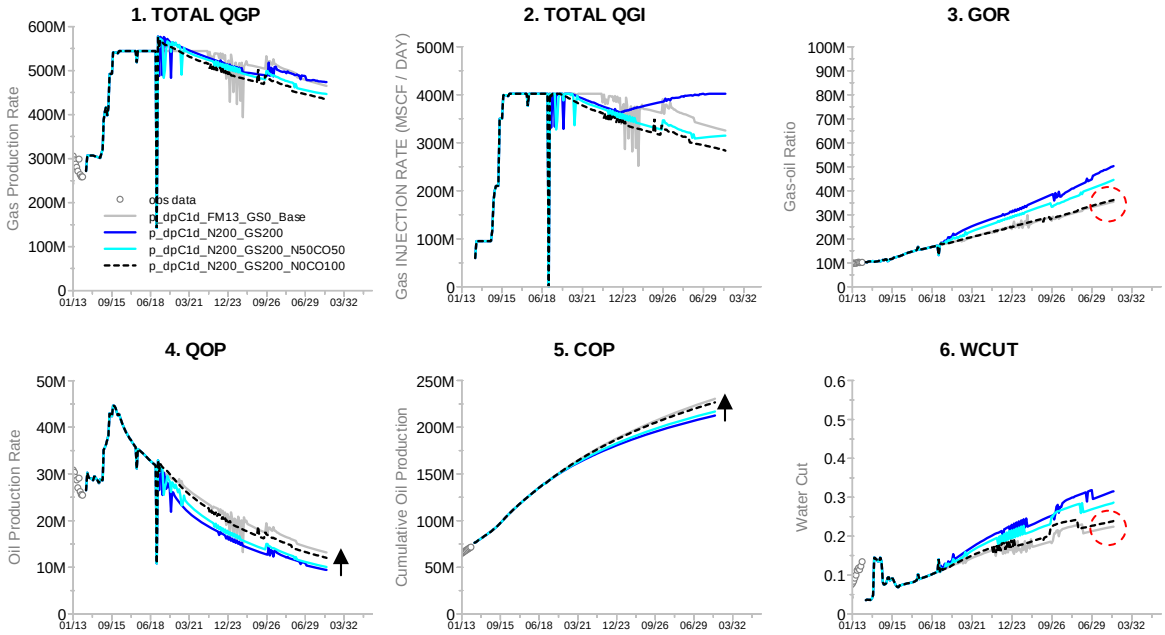

Figure 3-43. Field Surface Production – DPDP Gas Injection Composition.

Figure 3-44 shows the following:

- Plot 7 exhibits a significant Gas Sales sustainability and plateau by adding CO_2 into the system (see the dashed black line). This behavior is attributed to a lower N_2 recirculation. When using 50% CO_2 and 50% N_2, gas sales are extended for 6 years (see points A and B).

- Plot No. 4 shows a higher hydrocarbon gas production with 100% CO_2 injection (see the dashed black line, N0CO100) than with 100% N_2 injection (see blue solid lines), which helps extend gas sales production (see points C, D and E).

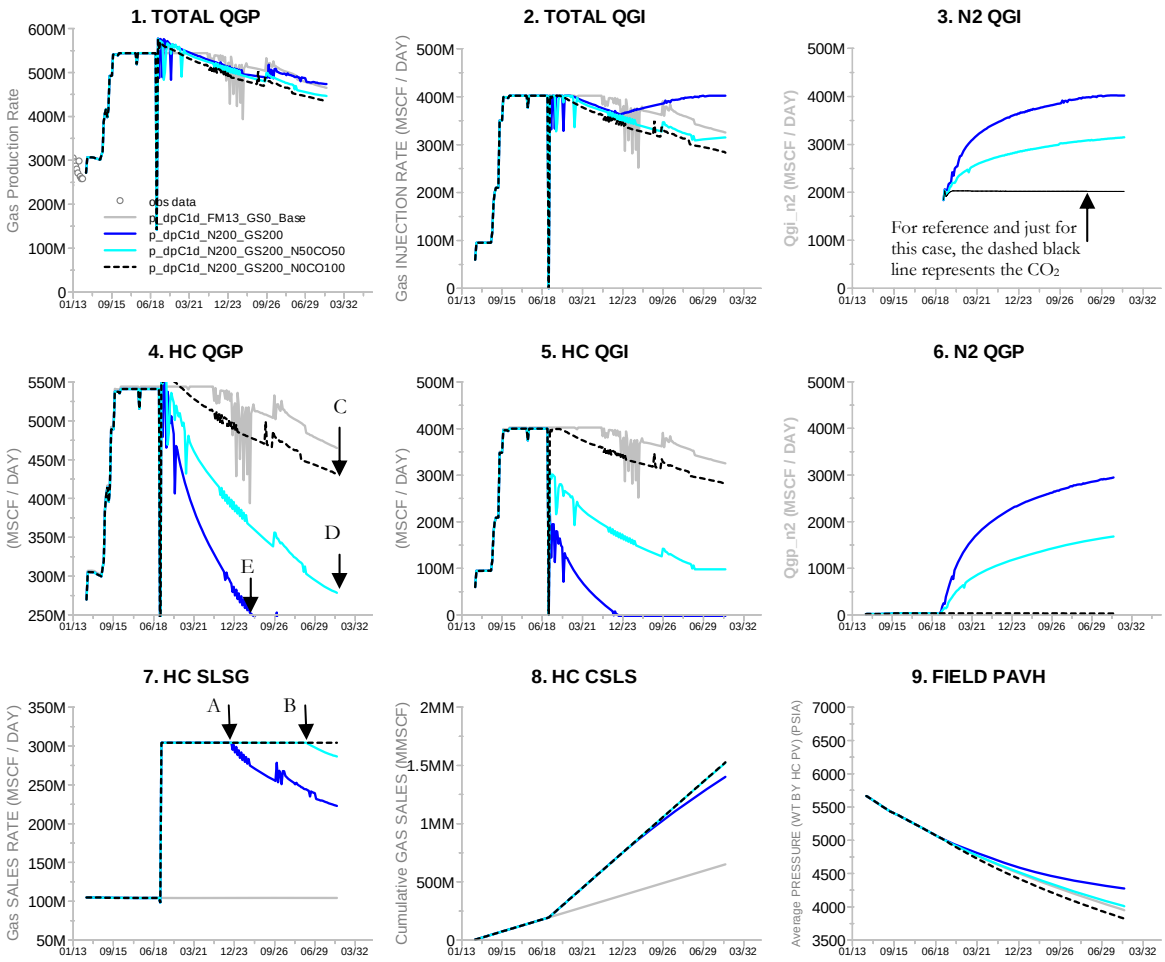

Figure 3-44. Field Surface Gas Behavior – DPDP Gas Injection Composition.

- **Saturation**

When comparing the transition zone that is formed between regions 1 and 2, Figure 3-45 shows a better oil sweep with pure CO_2 (see Plot No. 4, region 1).

As CO_2 has a higher molecular weight compared to N_2, CO_2 tends to have a more stable displacement allowing the total change of the transition zone shape between regions 1 and 2. In other words, CO_2 tends to have a higher sweep of the bottom of the structure compared to N_2 (see Plot No. 2).

N_2 injection (see Plot No. 2), compared to the base case (see Plot No. 1), tends to segregate into the bottom of the structure. This is related to an increase in the injection rate as the N_2 case has 200 MMscfd, which allows the gas to channelize.

This inefficiency is controlled by CO_2 injection, as it can be observed by gradually increasing CO_2 concentration to 50% (see Plot No. 3), up to a point where there is 100% CO_2 being injected (see Plot No. 4).

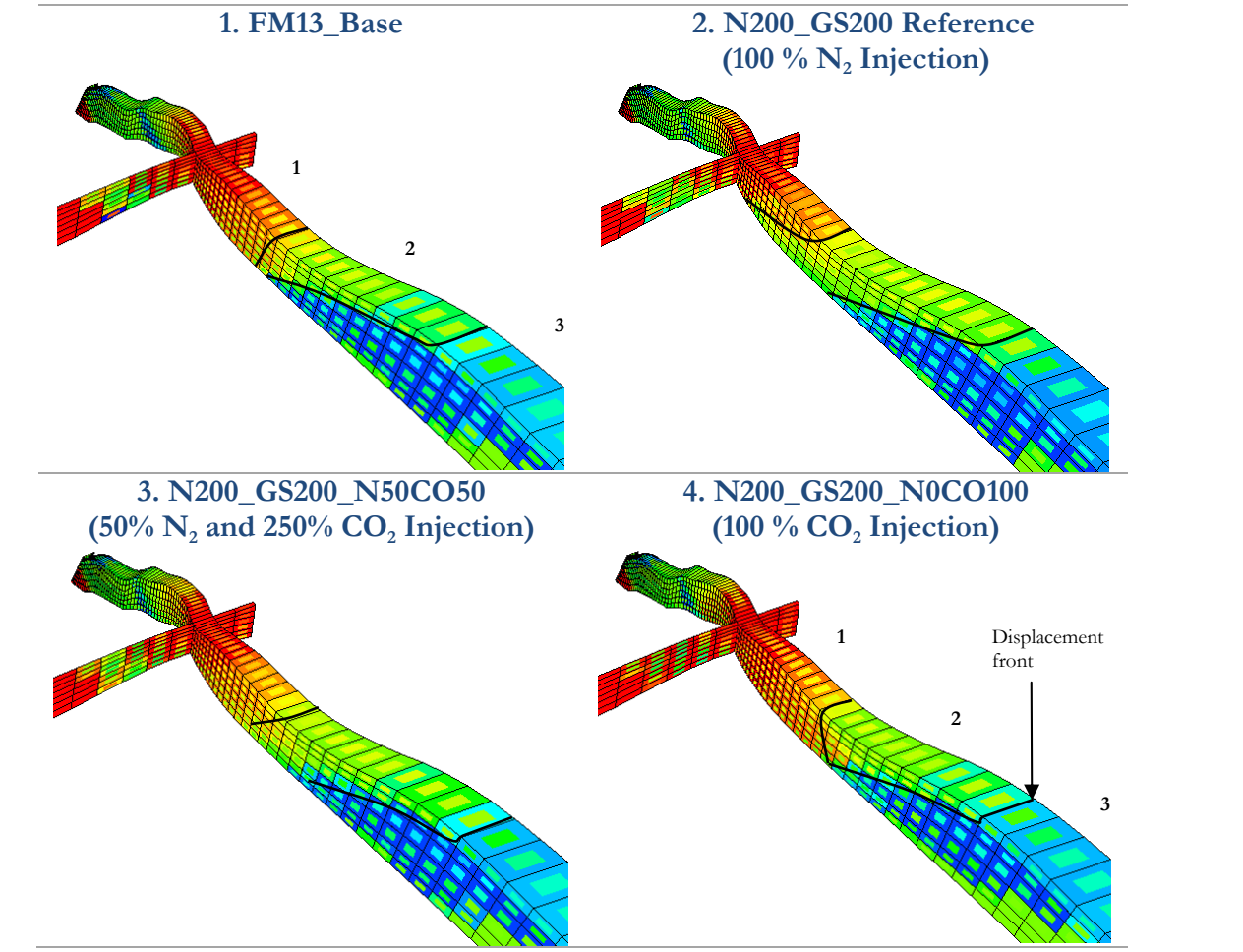

Figure 3-45. Dele Matrix-Fracture Oil Saturation – 10 years after N_2 injection sensitivities are performed. DPDP Gas Injection Composition.

Figure 3-46 shows the same effect described in Figure 3-45, where there is a better oil sweep from the bottom of the structure with CO_2 (see Plot No. 4). This is reflected by an improvement in the fracture gas relative permeability at the bottom of the structure.

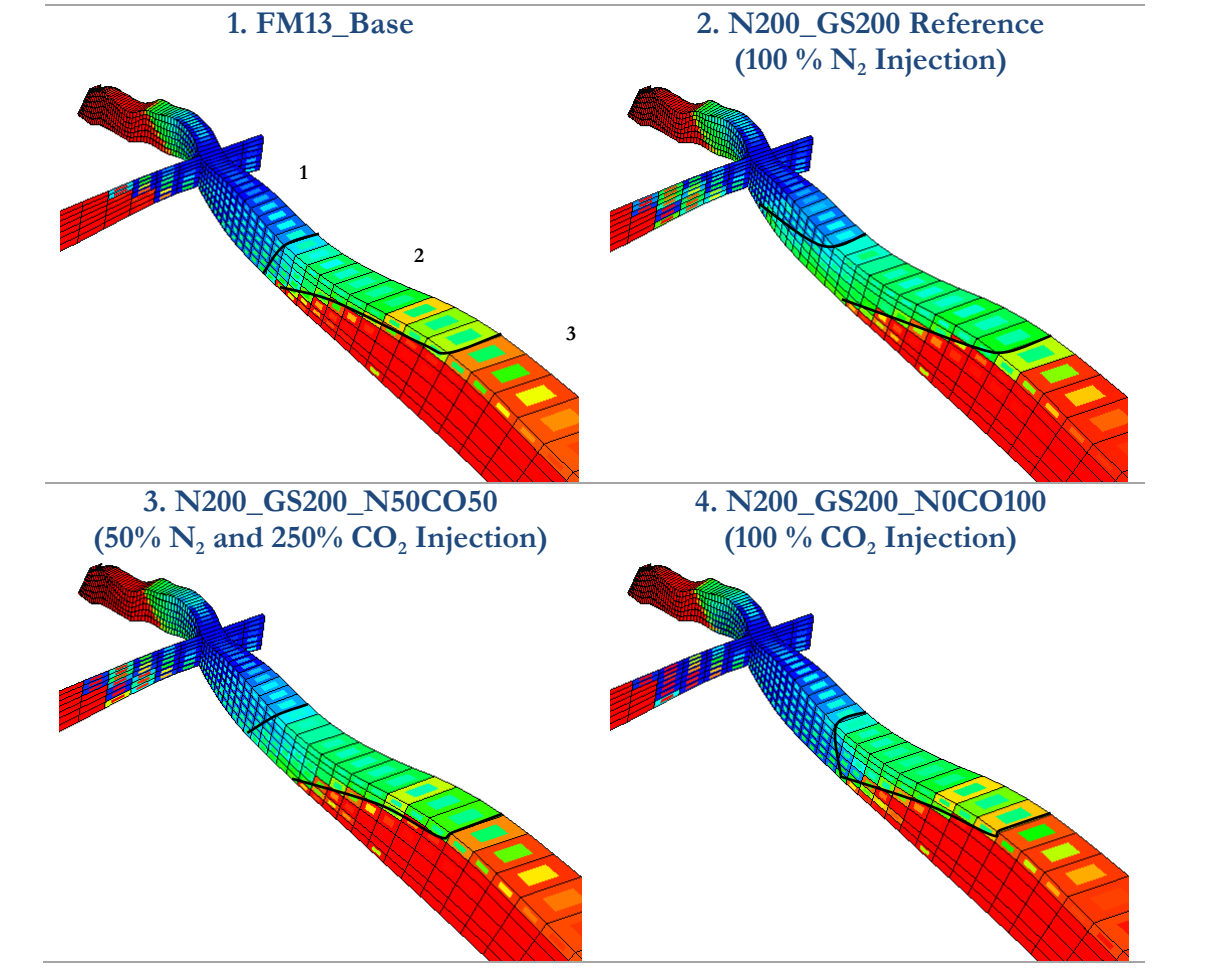

Figure 3-46. Dele Matrix and Fracture Gas Relative Permeability– 10 years after N_2 injection sensitivities are performed. DPDP Gas Injection Composition.

- **Composition**

Figure 3-47 demonstrates how the displacement front's concentration of N_2 is delayed when the injection is combined with CO_2. CO_2 increases the chance of contacting the matrix fluid, making up a more stable displacement front.

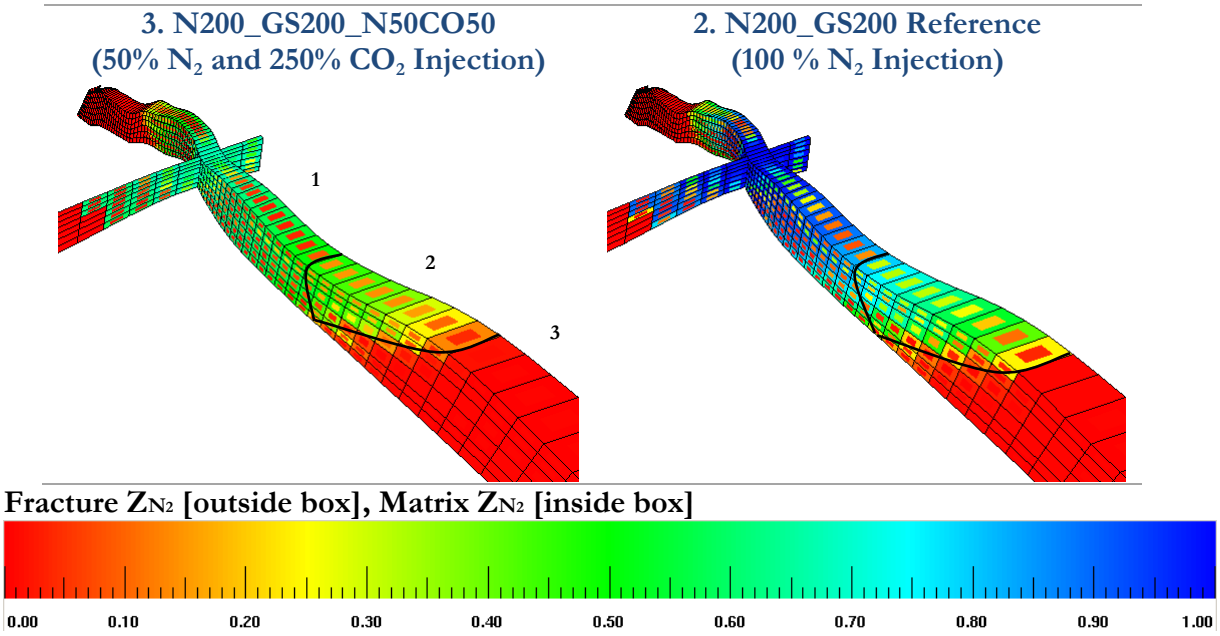

Figure 3-47. Dele Sheet Total Mole Fraction –N_2 – 10 years after N_2 Injection. DPDP Gas Injection Composition.

Notice in Figure 3-48 how the difference between the matrix and fracture N_2 concentration is lower (~25%) with 50% N_2/50% CO_2, than with 100% N_2 (~40%).

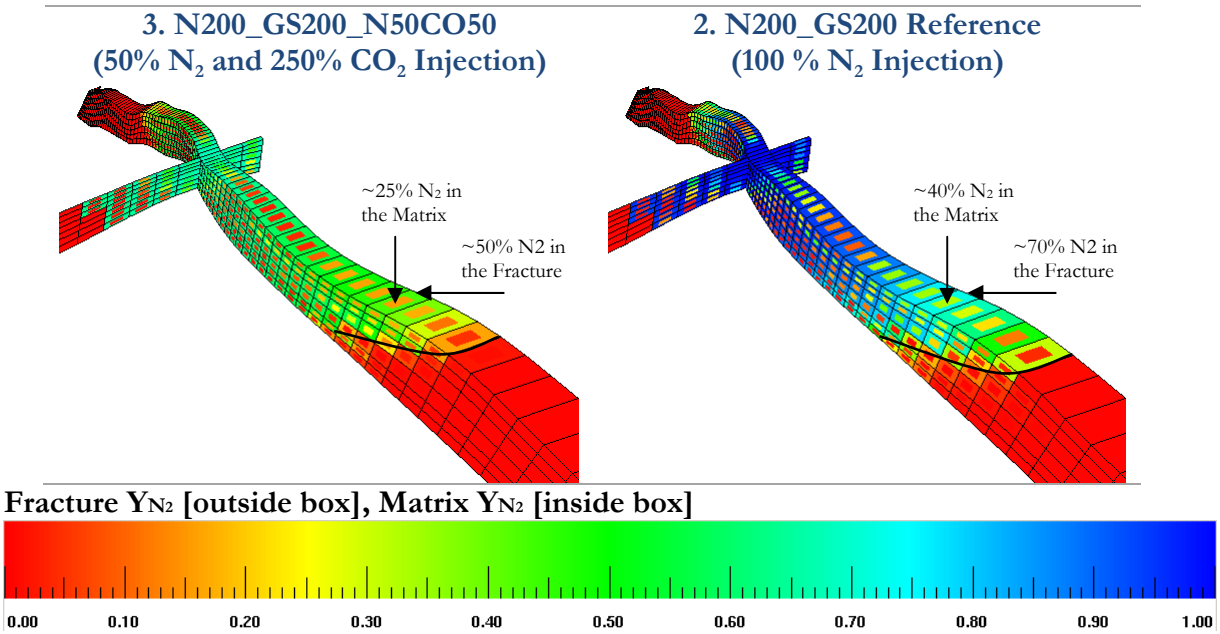

Figure 3-48. Dele Sheet Gas Mole Fraction –N_2 – 10 years after N_2 Injection. DPDP Gas Injection Composition.

Figure 3-49 shows how nitrogen concentration is reduced in the fracture liquid fraction, when the injected gas is combined with CO_2 (see Plot No. 3).

Also, nitrogen concentration in both cases is almost 0% in the matrix, meaning that nitrogen tends to be more in the gas phase of the matrix.

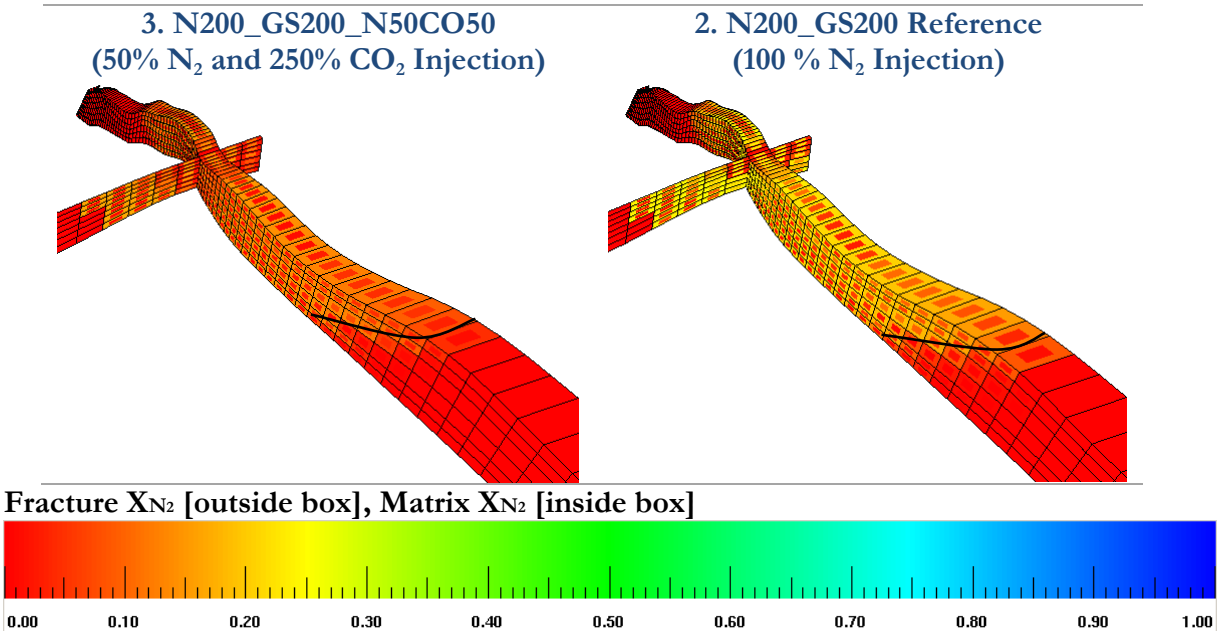

Figure 3-49. Dele Sheet Oil Mole Fraction –N_2 – 10 years after N_2 Injection. DPDP Gas Injection Composition.

Comparing the case of 50% N_2/50% CO_2 Injection (Plot No. 1) with 100% CO_2 Injection (Plot No. 2) in Figure 3-50, shows that higher the CO_2 concentration, better and more stable is the displacement front.

Figure 3-49 also shows the capacity for CO_2 to have a more homogenous distribution between the matrix and the fracture. For example, cells located behind the displacement front have a CO_2 concentration in the matrix of around ~20%, and the fracture system has 40%. On the other hand, Figure 3-48 shows that for the case of 100% of N_2 injected (see Plot No. 2), the difference between the matrix and fracture N_2 concentration is higher: while the matrix has around ~40% N_2 concentration, the fracture has ~70% of N_2.

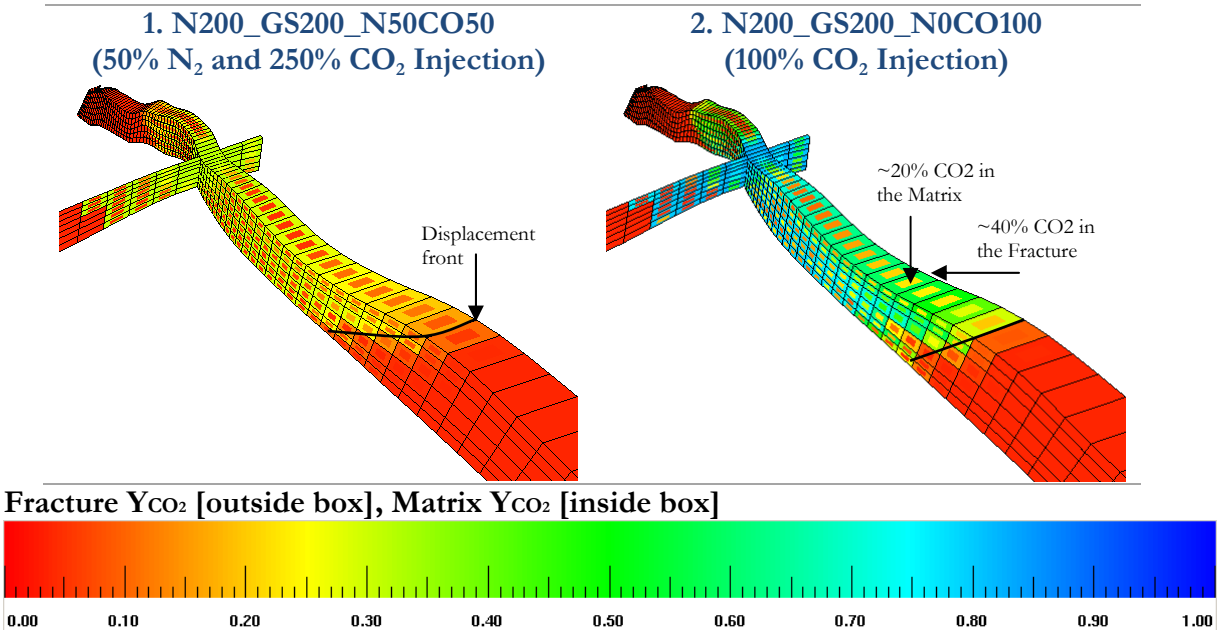

Figure 3-50. Dele Sheet Oil Mole Fraction –CO_2 – 10 years after N_2 Injection. DPDP Gas Injection Composition.

3.7.3 Fluids: Nitrogen Binary Interaction Parameters

The model uses the Binary Interaction Parameters (BIP's) from an analogue field that has the EOS tuned with nitrogen (see Section 2.7.4), so it slightly constrains the nitrogen results. A sensitivity run with zero interaction of nitrogen with the other pseudo-components was performed.

Table 3.8 shows the nomenclature used for the sensitivities.

Table 3.8. BIP´s – Prediction Run Names.

Runs	BIPs	Prediction Run Name	Comments
	from Analogue Field	p_dpC1d_N200_GS200	Reference Case, see also **Ref [1]** and **Section 2.7.4** for further details.
1	0	p_dpC1d_N200_GS200_BIPs0	Zero BIP´s between N_2 and the other pseudo components.

When using the Zero BIC´s in the Equation of state, the N_2 interaction with other pseudo components are minimized to its maximum, meaning that the N_2 will not favor the drop out of intermediate and heavy components from the gas phase, being this last the main fluid that flows in the porous media. The consequence would be a richer gas that is produced, compared to the reference case, increasing oil production.

As the difference between the reference case and the sensitivity runs performed with the N_2 BIP's are not significant, 3D Figures were not presented.

- **Production**

Figure 3-51 and Figure 3-52 show that no significant change in the production variables happen when changing the N_2 Binary coefficients. The only production variable that is altered is oil production, where there is an increase with Zero N2 BIP´s.

The analysis presented in Section 3.7.1 with regards to the composition item shows that N_2 injection helps the gas phase lose intermediate and heavy components.

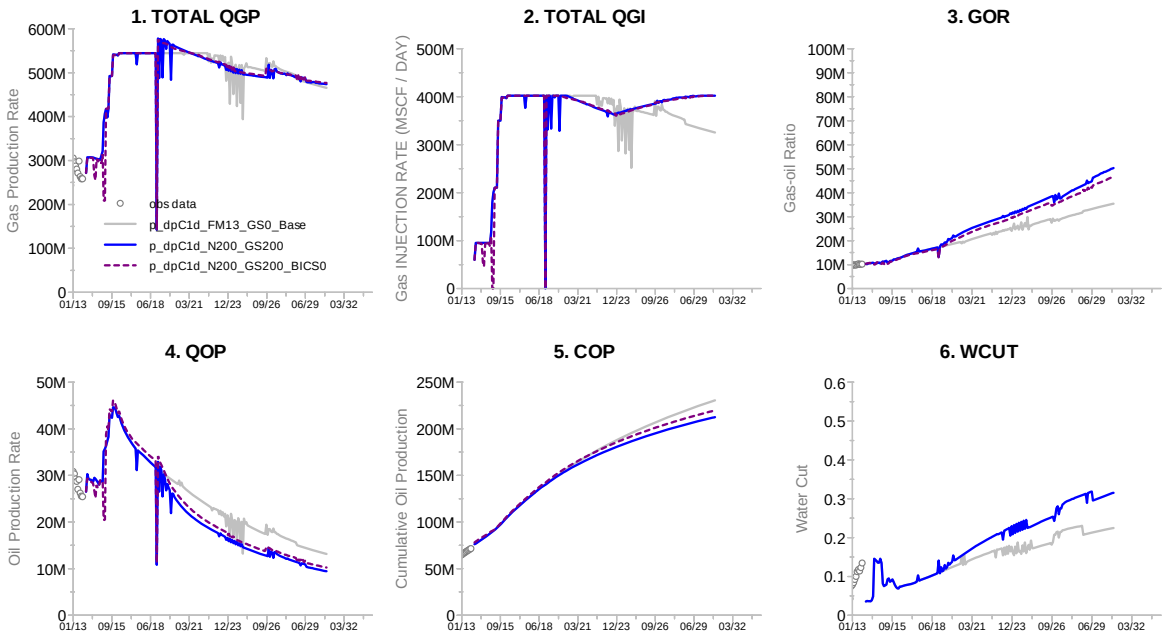

Figure 3-51. Field Surface Production – DPDP BIP´s Sensitivity Analysis.

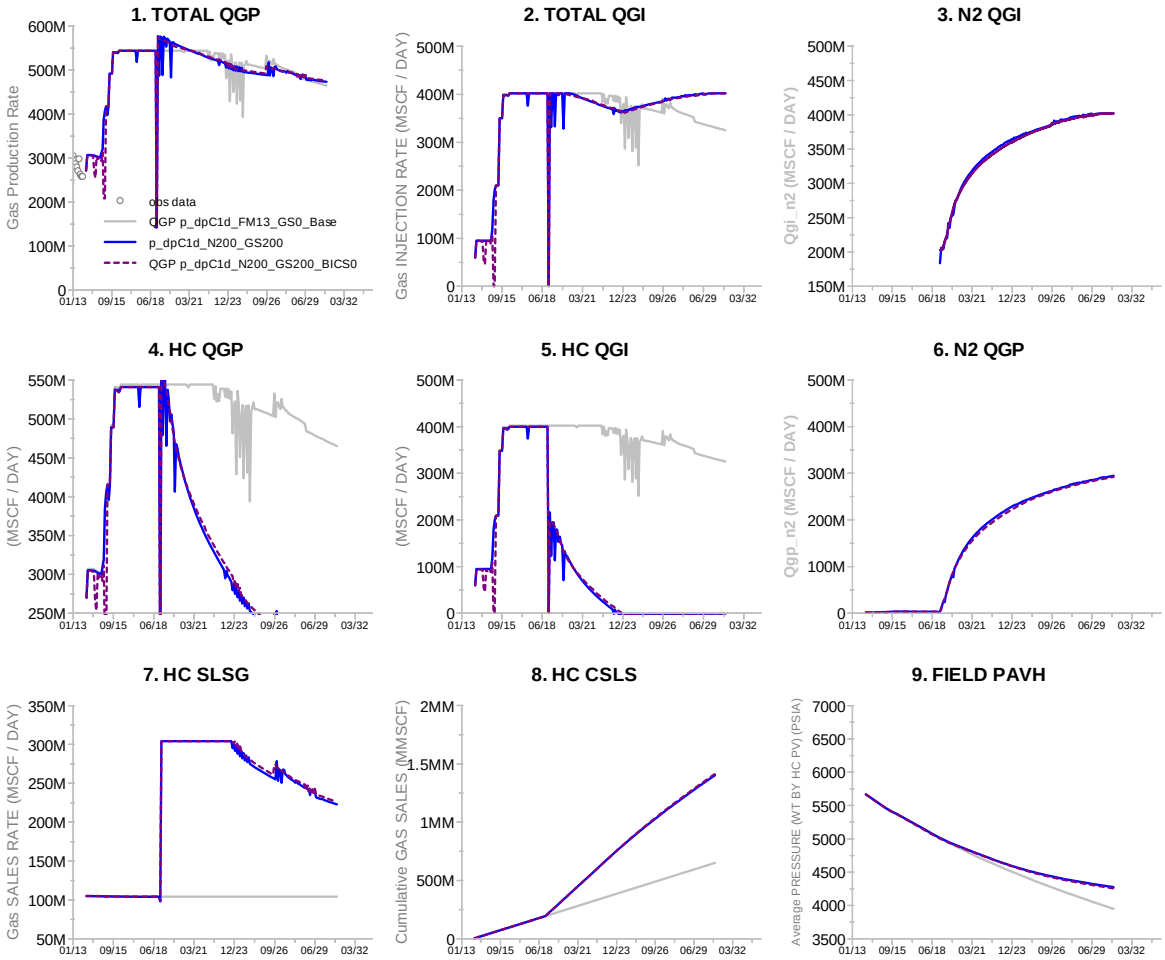

Figure 3-52. Field Surface Gas Behavior – DPDP BIP´s Sensitivity Analysis.

3.7.4 Maximum Gas Trap Saturation

Maximum gas trap saturation[58] not only plays an important role during the depletion stage but also during the gas injection process, as it will be shown in this section. See Section 1.6.3.3 for further details about the estimation of gas trap saturation.

Table 3.9 shows the nomenclature for sensitivity cases that are studied in this section.

Table 3.9. Maximum Gas Trap Saturation – Prediction Run Names.

Runs	Sgt	Prediction Run Name	Comments
1	0	p_dpC1d_N200_GS200_Sgt0	No gas trap saturation.
Reference	0.4	p_dpC1d_N200_GS200	Reference Case: Following the lowest limit of the HW Correlation, see Figure 1-34.
2	0.6	p_dpC1d_N200_GS200_Sgt60	Sgt Max. from porosity trend, see Figure 1-34.

The sequence of events to understand the Sgt impact is as follows: the gas trap saturation will affect the gas relative permeability so as to reduce gas production, so the higher gas trap saturation is, the higher will be the reduction on gas production.

The lower the gas production is, the lower is the oil production, as the rich gas that is produced in the well carries the intermediate and heavy components that are reported as the oil production stream (QOP).

- **Production**

Figure 3-53 shows 6 plots related to the general production variables at field level. A general observation is that the Sgt impact on gas and oil production behavior is huge when considering a maximum gas trap saturation of 0% or 60%.

- Plot No. 1 shows a higher gas production potential when Sgt is 0%, and a considerable reduction of potential when Sgt is 60%. The impact is clearly observed even if the Wcut evolution (Plot No. 6) is almost the same for all cases.

- Plot No. 2. The lower the Sgt is, the higher the gas injection is, as there will be no restriction for gas to be injected in the system.

- Plots No. 4 and 5. A huge impact on oil production occurs when changing gas trap saturation. An Sgt of 60% generates a negative impact on production of 24.5 MMstb, while the case with no Sgt generates a positive impact on production of 10.8 MMstb compared to the reference case, which has an Sgt value of 30%

- Plot No. 3. GOR evolution does not drastically change, as gas will be reduced but not its richness.

[58] A key factor in the Enhance Oil Recovery process is the residual oil saturation (Sor). This can be used as an analogue to understand the Enhance Gas Recovery (EGR) process, as here the objective is to partially or totally access the gas that is trapped in the reservoir due to capillary forces.

- Plot No. 6. For this case, the Wcut remains almost the same when changing the Sgt. The water that is present in the reservoir will impact gas production in a higher way when the Sgt is higher.

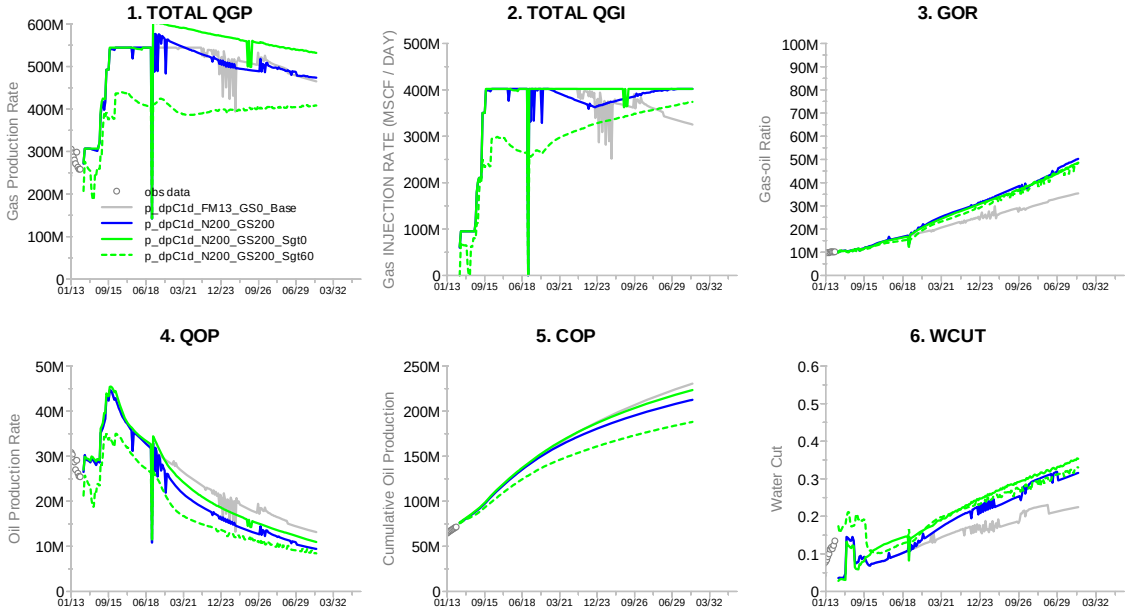

Figure 3-53. Field Surface Production – DPDP Gas Trap Saturation Sensitivity Analysis.

Figure 3-54 shows a huge increase in gas production and gas sales when the Sgt is 0%. The Gas sales plateau is extended 5 years compared to the reference case, where the Sgt is 30%. Compare points A and B in Plot No. 7.

Plot No. 8 shows a reduction in cumulative gas sales of 200 Bcf when the Sgt is 60%, compared to the reference case.

Plot No. 9 shows a lower pressure depletion behavior with higher Sgt values, as there is less voidage in the system, keeping oil, gas and water volumes higher in the reservoir.

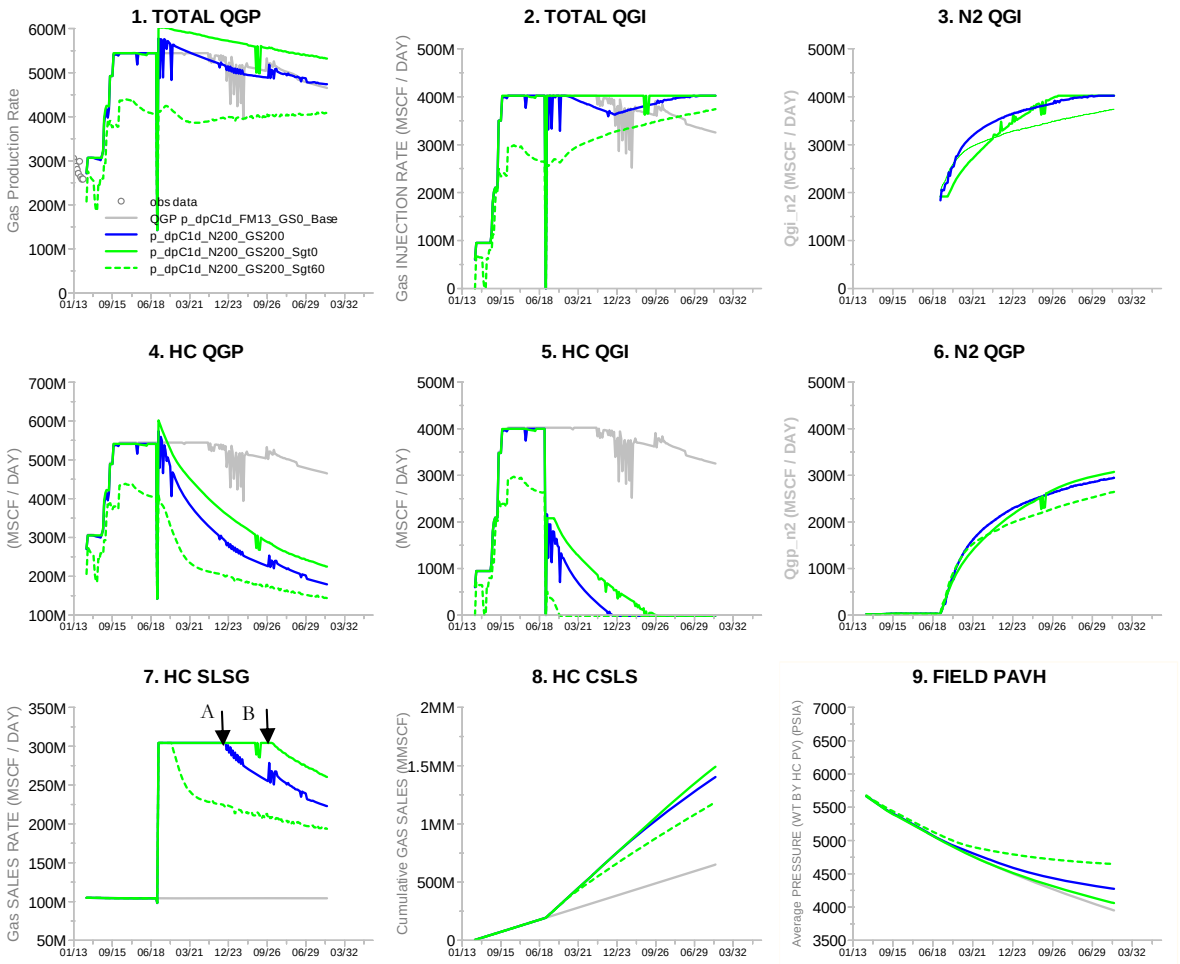

Figure 3-54. Field Surface Gas Behavior – DPDP Gas Trap Saturation Sensitivity Analysis.

- **Saturation**

Figure 3-55 shows the big impact on oil saturation distribution at different Sgt values.

Comparing the red region near the injection point, it can be observed that the Sgt of 60% (Plot No. 4) generates a higher gas injection restriction.

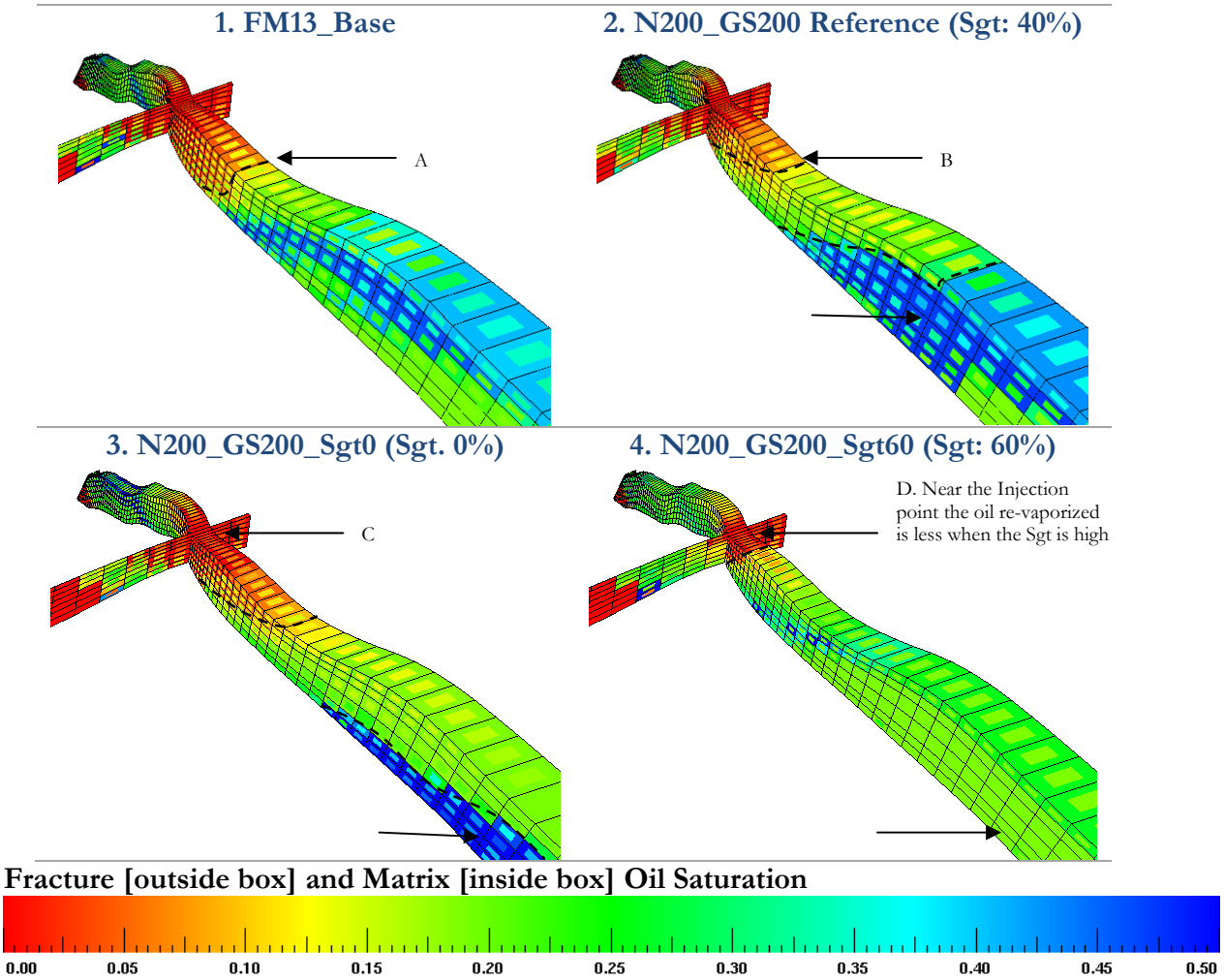

Figure 3-55. Dele Matrix-Fracture Oil Saturation – 10 years after N_2 injection sensitivities are performed. DPDP Gas Trap Saturation Sensitivity Analysis.

Figure 3-56 shows how the gas relative permeability is behind and in front of the shock front. Figure 3-56This figure also shows the fracture gas relative permeability in the outer box, and the matrix gas relative permeability in the inner box.

It can be observed how the gas has a better relative permeability when the Sgt is 0 (see Plot No. 3), compared to the Sgt of 60%. As it was mentioned, the higher the Sgt is, the higher is the restriction for gas to flow in the reservoir.

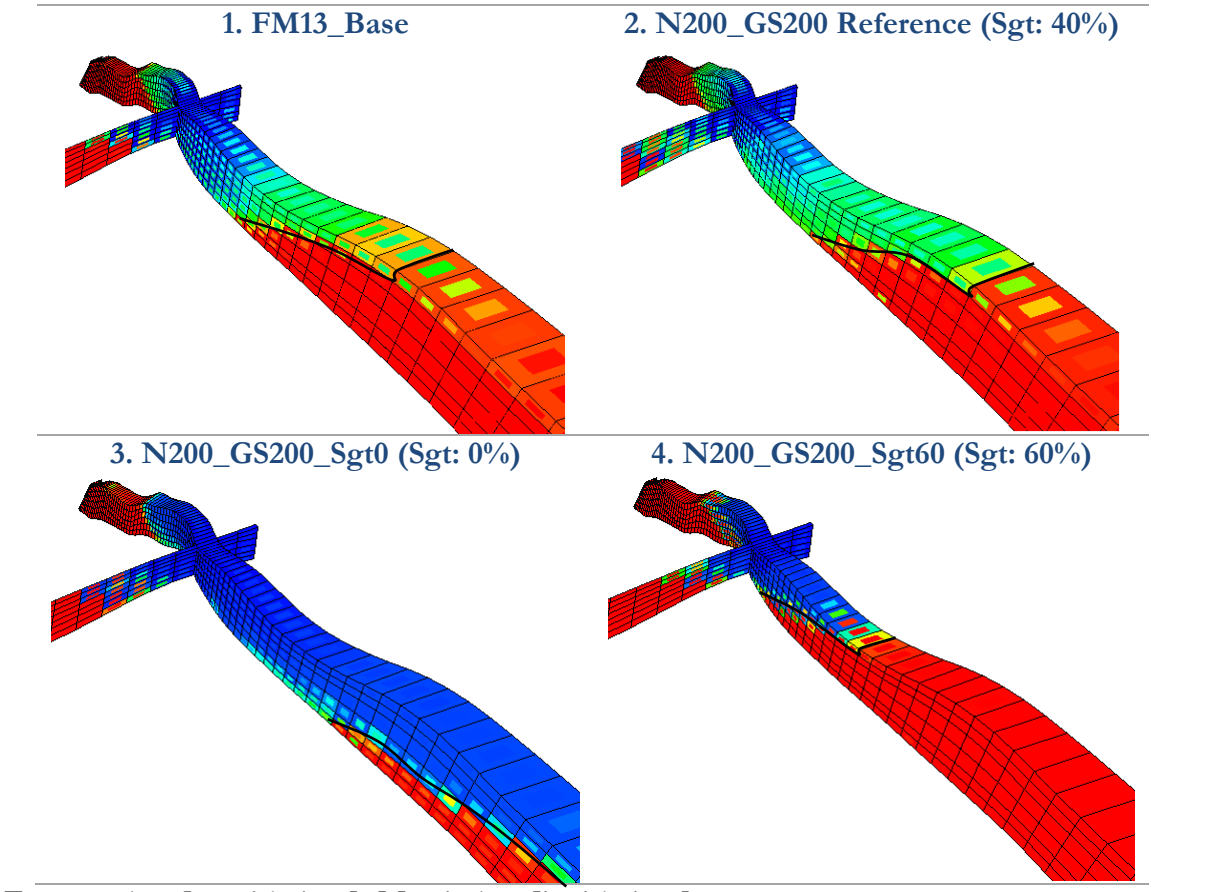

Figure 3-56. Dele Matrix and Fracture Gas Relative Permeability– 10 years after N_2 injection sensitivities are performed. DPDP Gas Trap Saturation Sensitivity Analysis.

Figure 3-57 shows that the oil relative permeability of the oil bank ahead of the displacement front is dramatically changed using gas trap saturation of 0%, 40% and 60%.

Figure 3-57 also shows the fracture oil relative permeability in the outer box, and the matrix oil relative permeability in the inner box.

With an increase in the Sgt, there is a drastic change in oil and gas saturation, which are related to the relative permeabilities. These saturation changes generate different kro distributions in the grid.

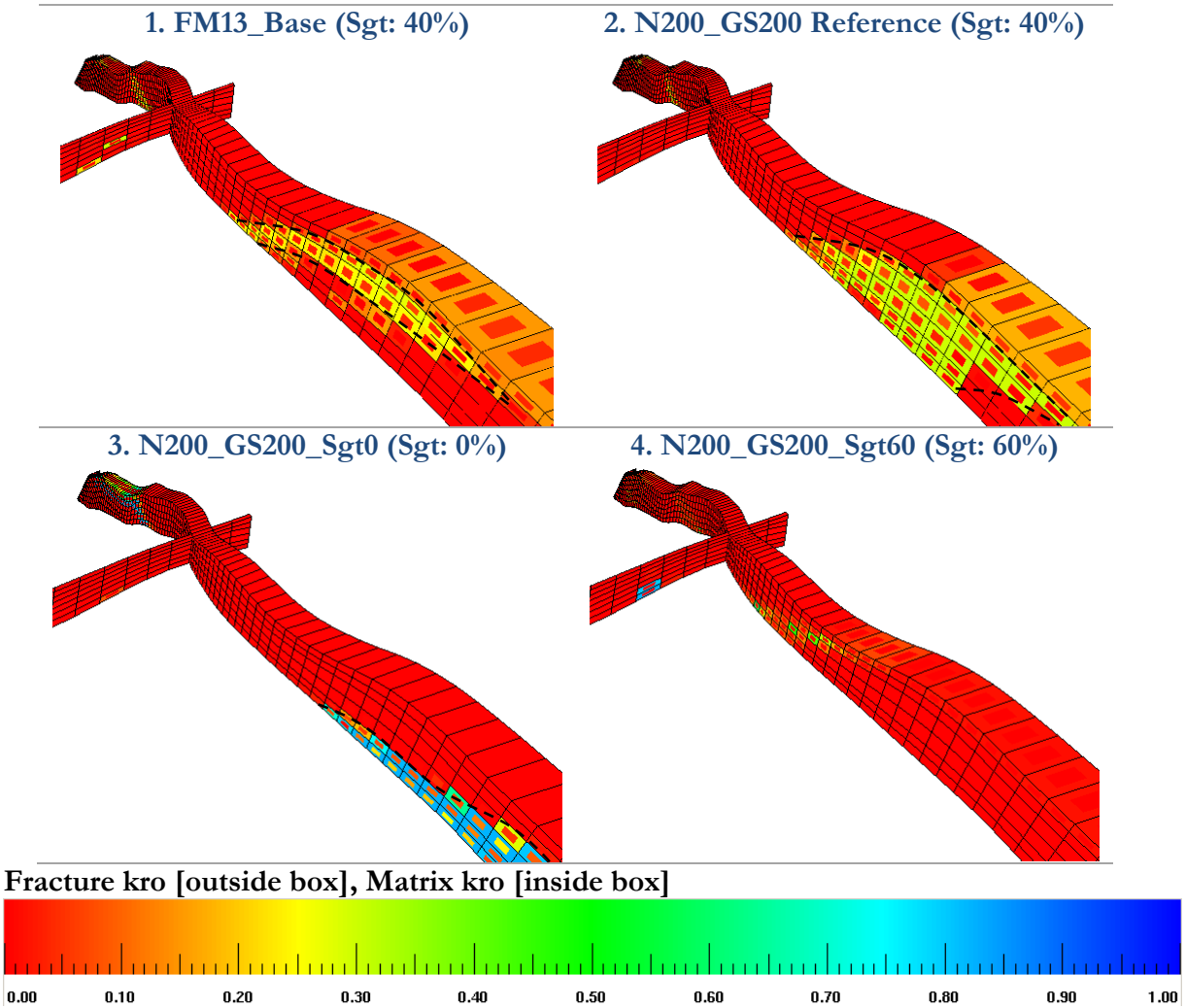

Figure 3-57. Dele Matrix and Fracture Oil Relative Permeability– 10 years after N_2 injection sensitivities are performed. DPDP Gas Trap Saturation Sensitivity Analysis.

- **Composition**

The higher the gas trap saturation is, the shorter is the displacement front, as it can also be observed in Figure 3-58. This is due to a reduction in gas injection, which in turn is due to an increase in the gas flow restriction as explained in Figure 3-53, Plot No. 2.

When Sgt is high (see Plot No. 4), nitrogen travels a shorter distance (see points B, C and D).

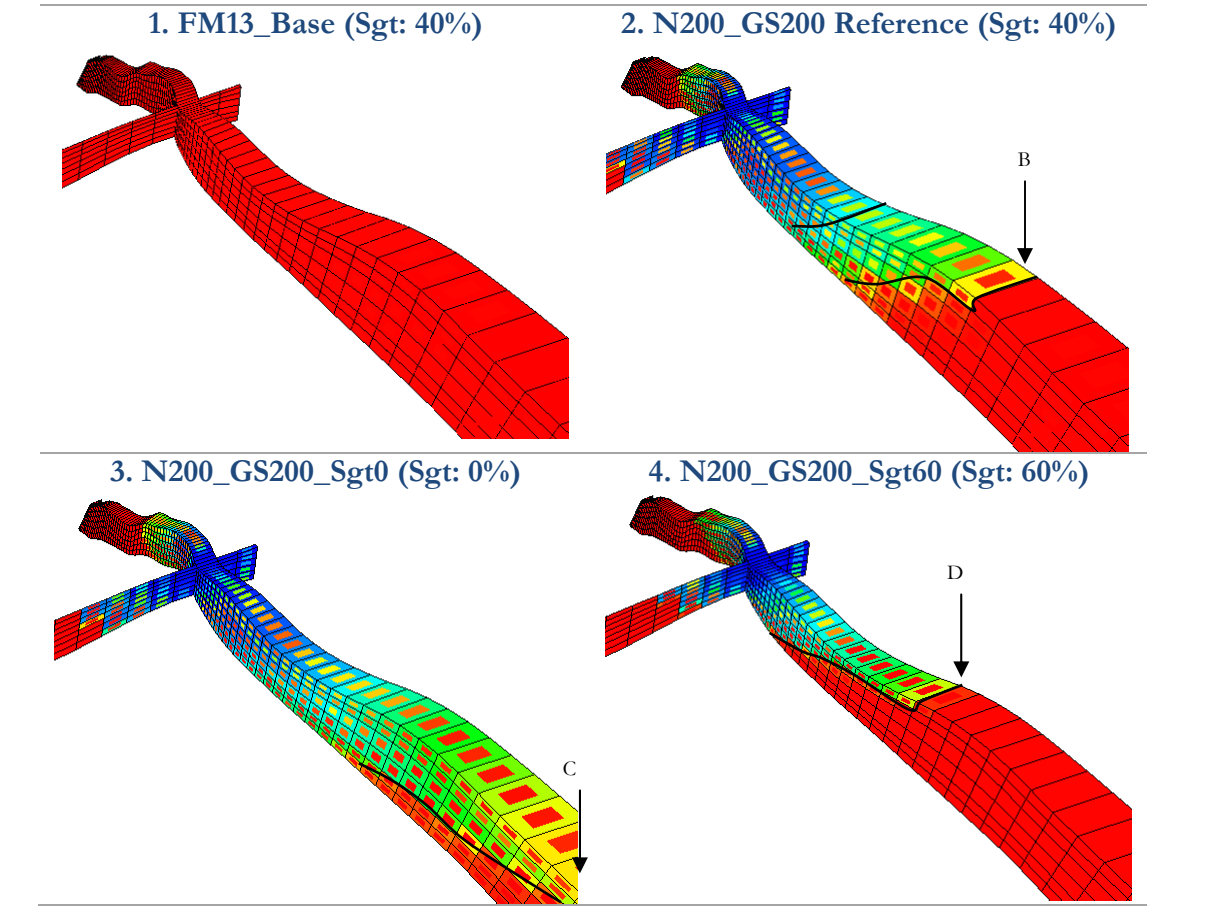

Figure 3-58. Dele Sheet Total Mole Fraction –N_2 – 10 years after N2 injection is performed. DPDP Gas Trap Saturation Sensitivity Analysis.

Figure 3-59 shows the same observation described in Figure 3-58, where the displacement front is delayed with a higher Sgt due to an additional restriction to gas flow.

Comparing Plot No. 3 with plot No. 4, it is possible to observe that the higher the gas trap saturation is, the higher will be the delay of N_2 breakthrough and its evolution with time (see Figure 3-54 Plot No. 6).

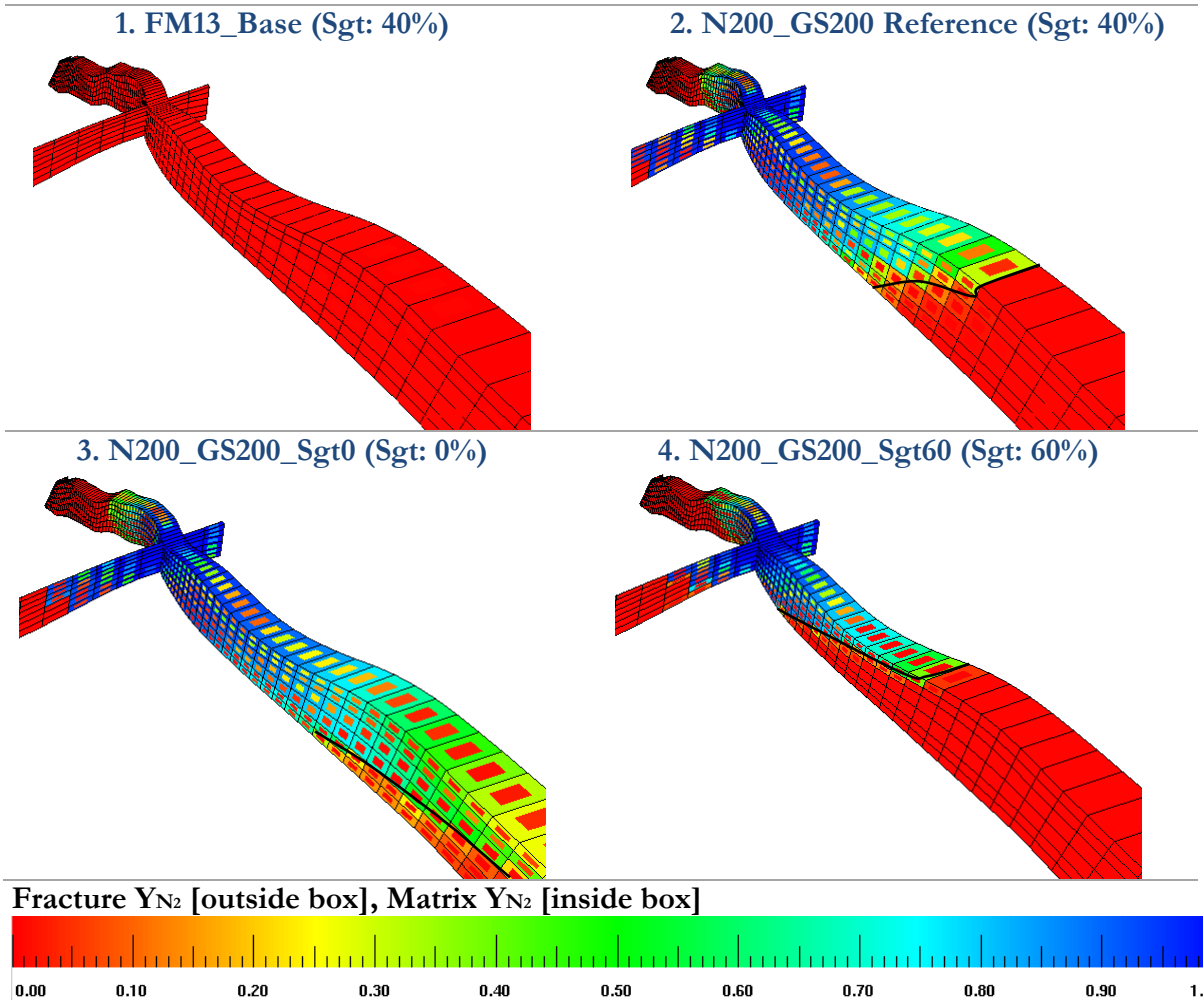

Figure 3-59. Dele Sheet Gas Mole Fraction –N_2 – 10 years after N_2 injection is performed. DPDP Gas Trap Saturation Sensitivity Analysis.

Figure 3-60 shows how the liquid fraction is contaminated with N_2, and its relationship with the gas trap saturation.

Comparing Plot No. 4 and Plot No. 3, it is possible to observe that the higher the Sgt is, the lower the liquid fraction contamination with nitrogen is.

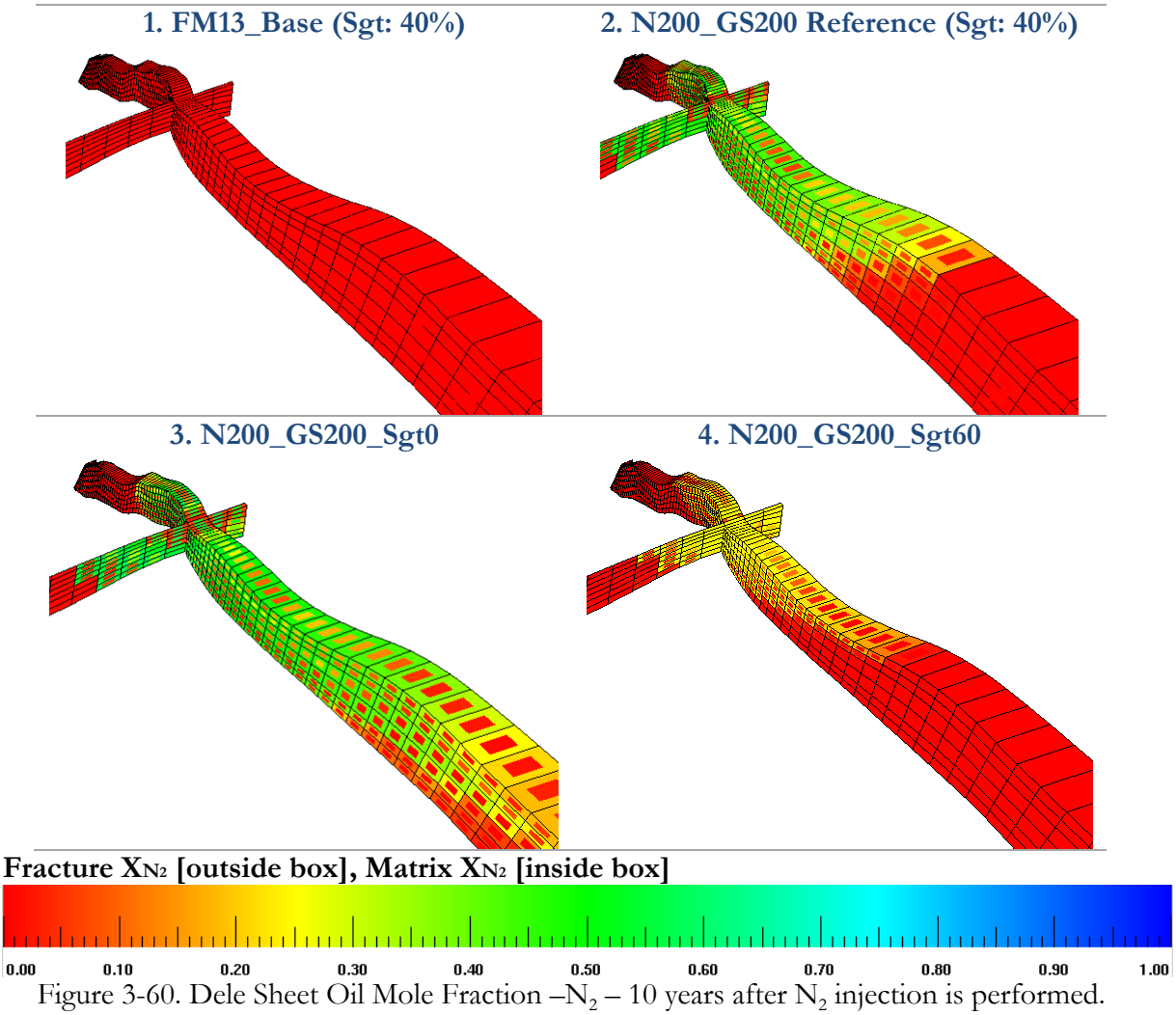

Figure 3-60. Dele Sheet Oil Mole Fraction –N_2 – 10 years after N_2 injection is performed. DPDP Gas Trap Saturation Sensitivity Analysis.

3.7.5 Relative Permeability

The model was designed in order to capture the macro process of fluid flow in the natural fracture system, so micro-fractures were not represented explicitly (see the assumption made in item 5 for the physical model, in Section 2.3). Table 3.10 shows the nomenclature for the sensitivities cases studied through this section.

As this factor could represent an important role in the production of wells **[10, Chapter 2]**, 2 sensitivity cases using the same relative permeability (kr) for the matrix and the fracture were performed. One sensitivity case uses the matrix kr for both the matrix and the fracture of the reservoir, and the second sensitivity case uses the fracture kr for both the matrix and the fracture system of the reservoir.

Notice that the changes that were made were on the reservoir system, keeping the same wellbore relative permeabilities (see Section 2.6.3.5 for a full description). This was only done to consider the impact of the kr at reservoir level, as the impact of using the matrix kr for the matrix and fracture system did not allow the wells to produce and inject.

Table 3.10. Fracture Spacing – Prediction Run Names.

Runs	krm	Prediction Run Name	Comments
Reference		p_dpC1d_N200_GS200	Reference Case. Section 2.6.3.5 for the full description of the kr used in the model
1	krm=krf	p_dpC1d_N200_GS200_Allkrf	Assuming that the matrix is highly fractured it was used the same reservoir relative permeabilities from the fracture system (see Figure 2-16 Colum 2)
2	krf=krm	p_dpC1d_N200_GS200_allkrm	Assuming that the fracture has the same relative permeability than the matrix, (see Figure 2-16 Colum 1).

- **Production**

Figure 3-61 shows 6 plots related to the general production variables at field level. It was observed that oil and gas production do not have significant changes when using either the matrix kr for the fracture or the fracture kr for the matrix system as sensitivities.

The relative permeability sensitivity at reservoir level does not have a big impact on oil and gas production. This is explained in Figure 2-16 with a very small improvement from 0.05 to 0.15 in the oil and gas relative permeability sum when comparing the matrix and fracture relative permeabilities at 50% oil saturation.

There is a slight improvement in gas production, gas injection and gas sales when using the fracture relative permeability for both the matrix and fracture system at reservoir level (see Allkrf sensitivity analysis), see Figure 3-62.

The gas production increase observed in Figure 3-62 when using the fracture kr, is a consequence of a better sweep in the matrix, as it can be observed in the saturation graphs (see Figure 3-64).

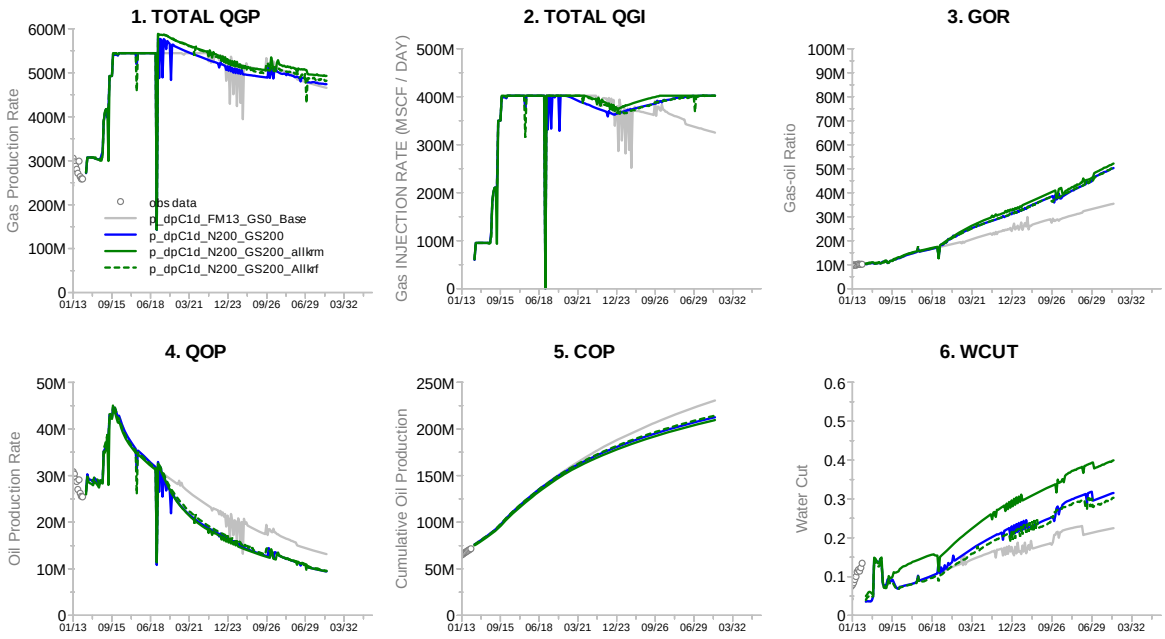

Figure 3-61. Field Surface Production – DPDP Matrix Relative Permeability Sensitivity Analysis.

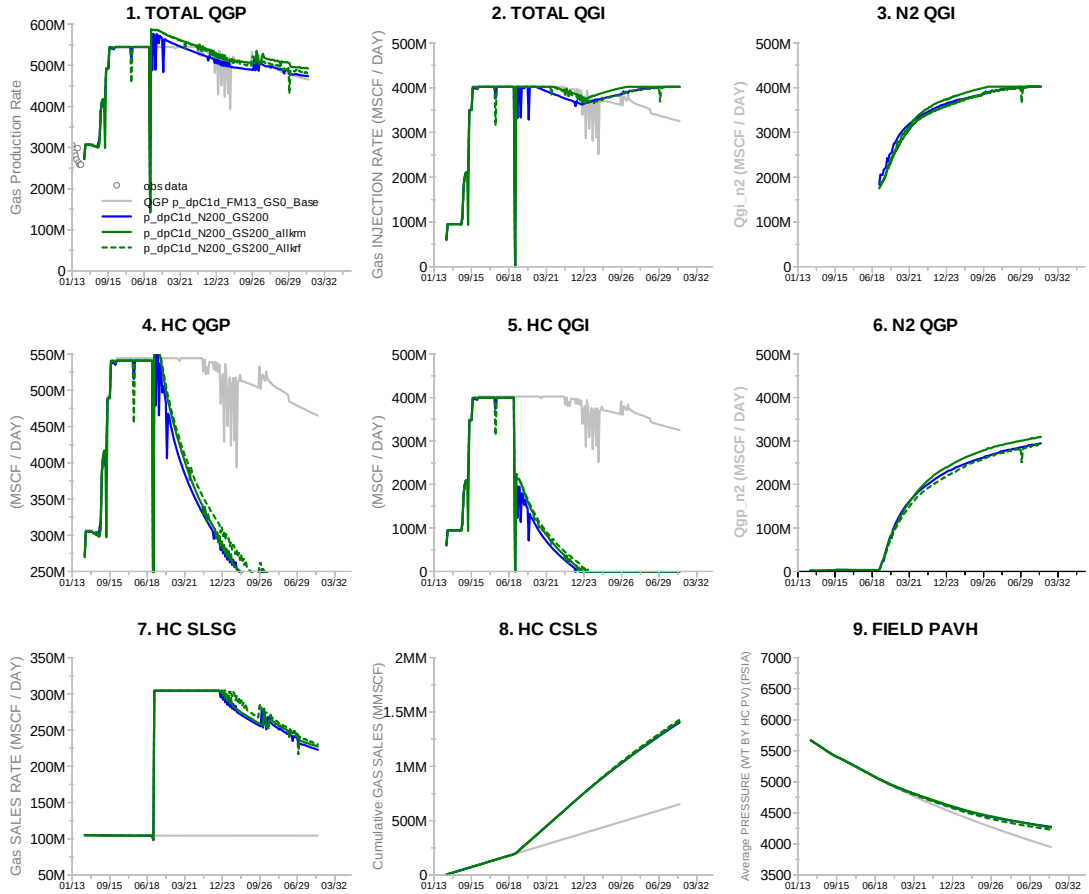

Figure 3-62. Field Surface Gas Behavior – DPDP Matrix Relative Permeability Sensitivity Analysis.

- **Composition**

Figure 3-63 shows that, when using the fracture kr for the matrix and fracture system (Allkrf sensitivity analysis, see Plot No. 4), N_2 progress through the fracture system is increased, but the matrix N_2 progress remains the same as happens with the reference case.

The reason for this behavior is related to the high contrast that exists between the matrix and fracture permeabilities, which restricts N_2 to enter the matrix, even if the change in the kr was from 0.3 (matrix kr, see Figure 2-16. Plot No. 1) to 0.4 (fracture kr, see Figure 2-16. Plot No. 1), having a gas saturation of around ~0.7.

In other words, the matrix and fracture kr used in this study produce a very low change in the oil and gas saturations behind the displacement front, which in turn make almost identical the results when using the matrix or fracture kr.

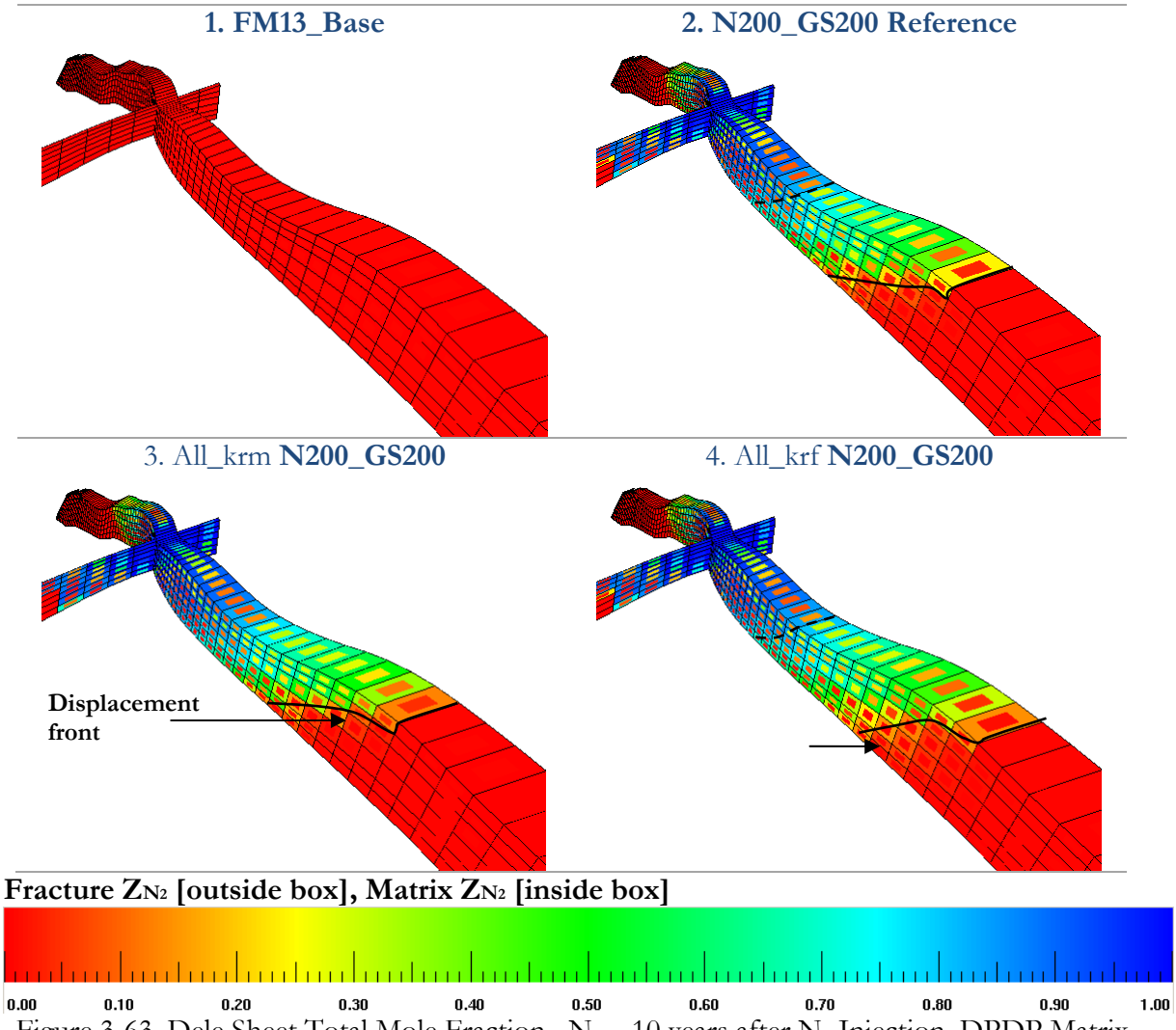

Figure 3-63. Dele Sheet Total Mole Fraction –N_2 – 10 years after N_2 Injection. DPDP Matrix Relative Permeability Sensitivity Analysis.

- **Saturation**

In Figure 3-64 there are 4 Plots for comparison purposes. Plot No. 2 shows the Nitrogen injection reference case.

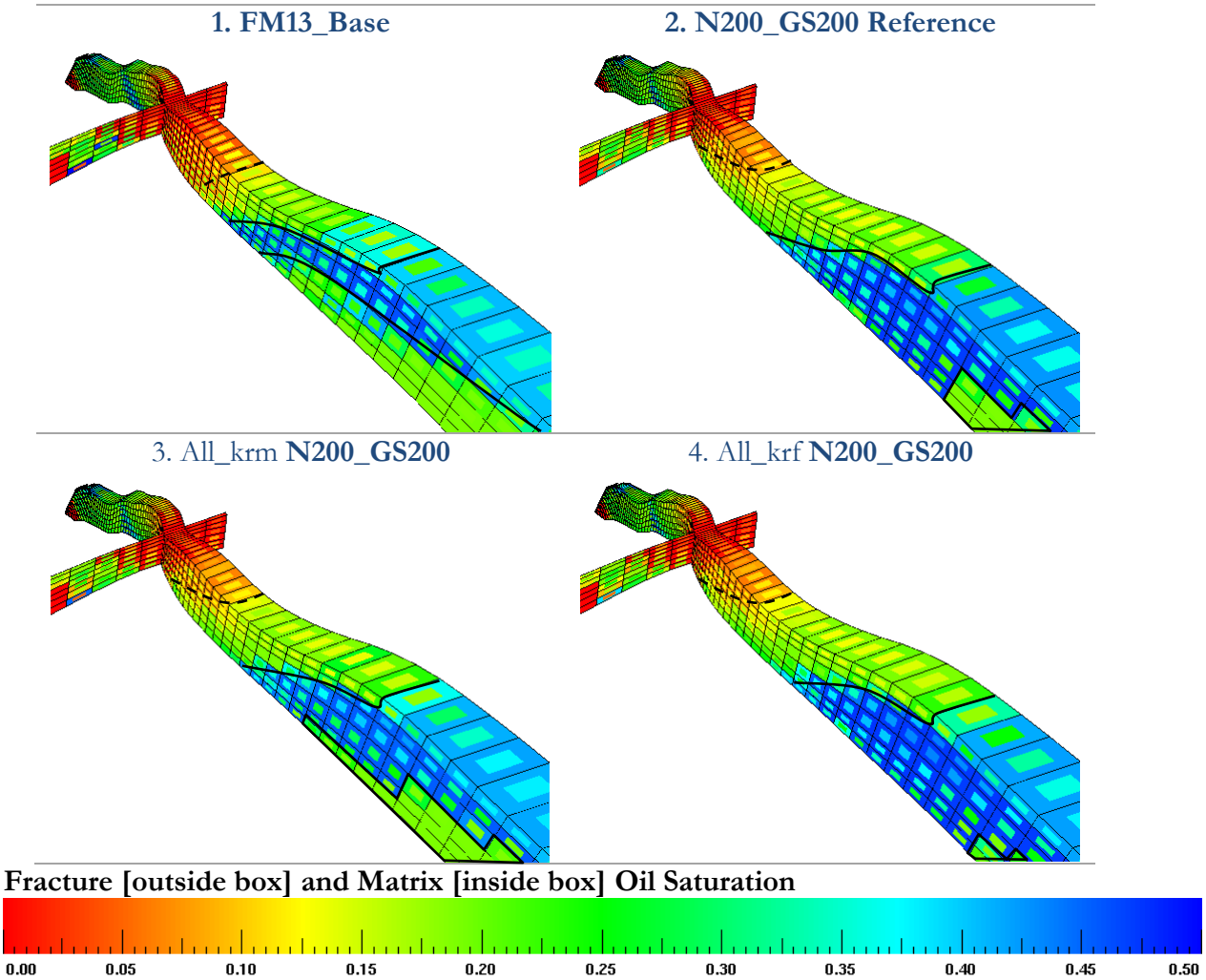

Figure 3-64. Dele Matrix-Fracture Oil Saturation – 10 years after N2 injection sensitivities are performed. DPDP Matrix Relative Permeability Sensitivity Analysis.

It was identified that gas injection develops 3 regions, see Figure 3-65:

- The 1st region has a fracture gas relative permeability (krgf) of ~1.
- The 2nd region has a krgf of around 0.5.
- The 3rd region has a krgf of ~0.

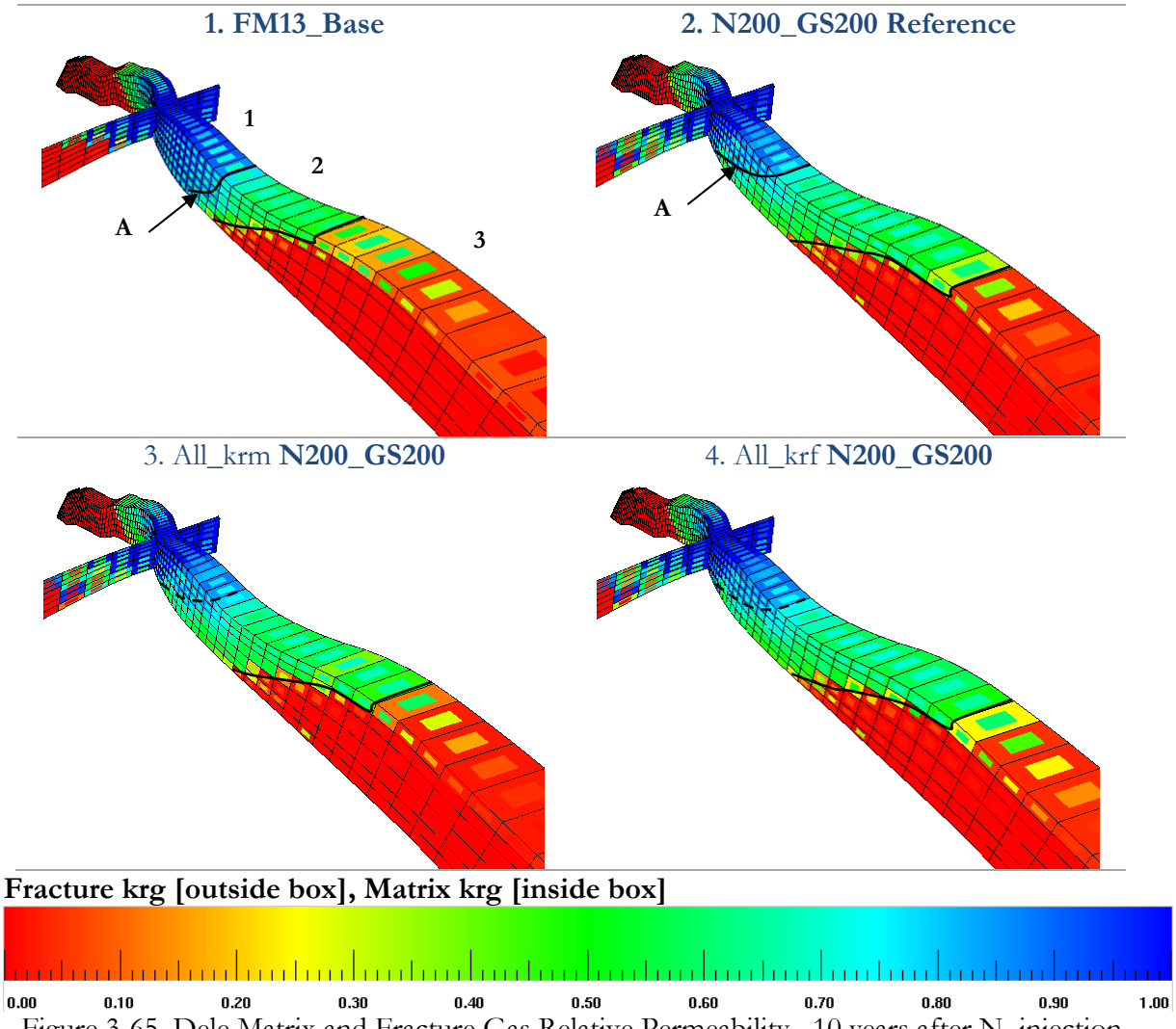

Figure 3-65. Dele Matrix and Fracture Gas Relative Permeability– 10 years after N_2 injection sensitivities are performed. DPDP Matrix Relative Permeability Sensitivity Analysis.

Figure 3-66 shows for the Allkrf sensitivity analysis, an increase in the fracture oil relative permeability ahead of the displacement front, which is associated to higher oil saturation in the fracture system, and an opposite behavior for the allkrm sensitivity analysis.

When comparing the inner boxes that represent the matrix oil relative permeability, the changes are so low that they won't generate a high impact on oil production as shown in Figure 3-61 Plot No. 4.

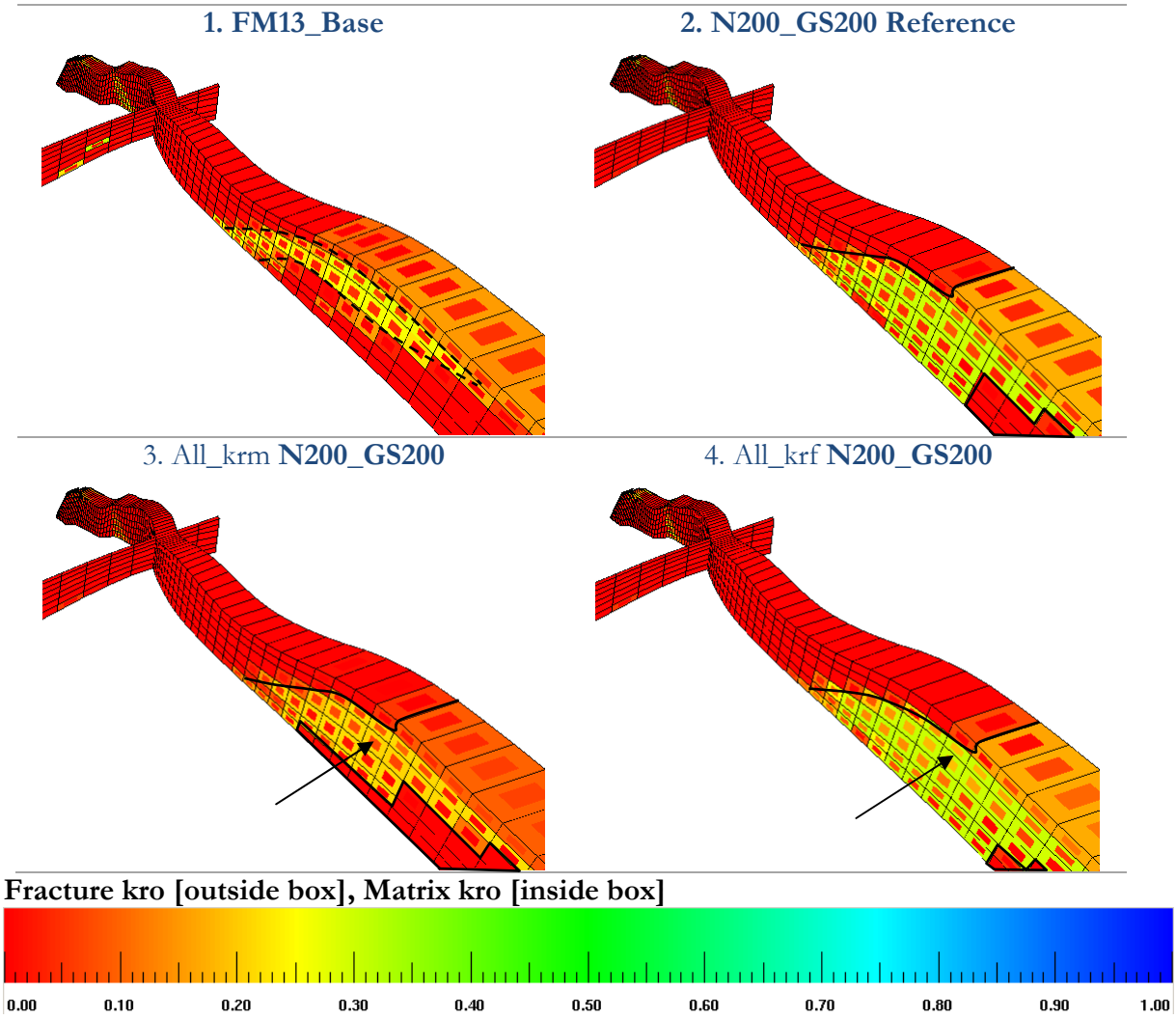

Figure 3-66. Dele Matrix and Fracture Oil Relative Permeability– 10 years after N_2 injection sensitivities are performed. DPDP Matrix Relative Permeability Sensitivity Analysis.

Figure 3-67 shows that the N_2 front accelerates when using the fracture kr for both the matrix and fracture system (see point D in Plot No. 4), compared to the delay in the N_2 front for the model that uses the matrix relative permeability for both the matrix and fracture system (see point C in Plot No. 3).

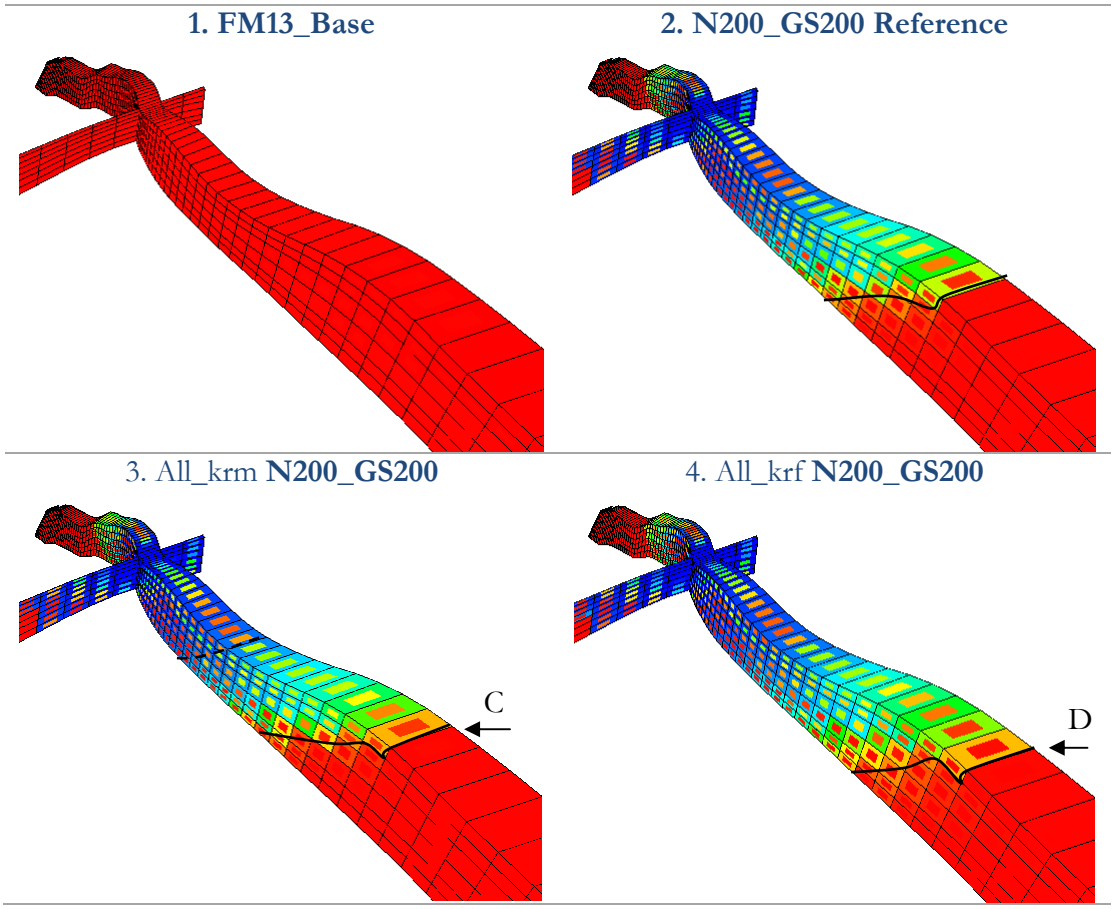

Figure 3-67. Dele Sheet Gas Mole Fraction –N_2 – 10 years after N_2 Injection. DPDP Matrix Relative Permeability Sensitivity Analysis.

3.7.6 Fracture Permeability - Horizontal Anisotropy

The base case considers an anisotropy factor of 1.3, which comes from the permeability tensor described in Figure 2-14 (see Section 2.6.3.3).

The sensitivity analysis performed consisted in using an anisotropy factor of 1 (no anisotropy or Isotropic case) to understand the impact of including the horizontal anisotropy.

Table 3.11 shows the nomenclature for sensitivities cases that are studied through this section.

Table 3.11. Fracture Permeability Anisotropy – Prediction Run Names.

Runs	A	Prediction Run Name	Comments
Reference	1.3	p_dpC1d_N200_GS200	Reference Case: This model has anisotropy of 1.3 explained in Section 2.7.3.3.
1	1	p_dpC1d_N200_GS200_Isotropy	No horizontal anisotropy is implemented in the system, same permeability in x and y direction

The results show that, even if the anisotropic and isotropic cases generate small changes in the production behavior, N_2 evolution in the anisotropic case is slower than in the isotropic case, which partially explains the hypothesis presented in Section 1.8 about the low velocity that tracers have in between the injector and producer in Pauto Main Sheet.

- **Production**

Figure 3-68 shows 6 plots related to the general production variables at field level. A general observation is that the anisotropic and isotropic cases do not generate a significant change in the oil, gas or water pressure behavior.

Plots No. 1 and 2. For PDM fields, the horizontal anisotropy generates a very small change in gas production and injection, which means that the estimated horizontal anisotropy of 1.3 does not make a big change in fluid flow behavior.

Figure 3-69 shows a slight increase in N2 evolution (see Plot No. 6). The other variables that are presented in the figure have undetectable changes.

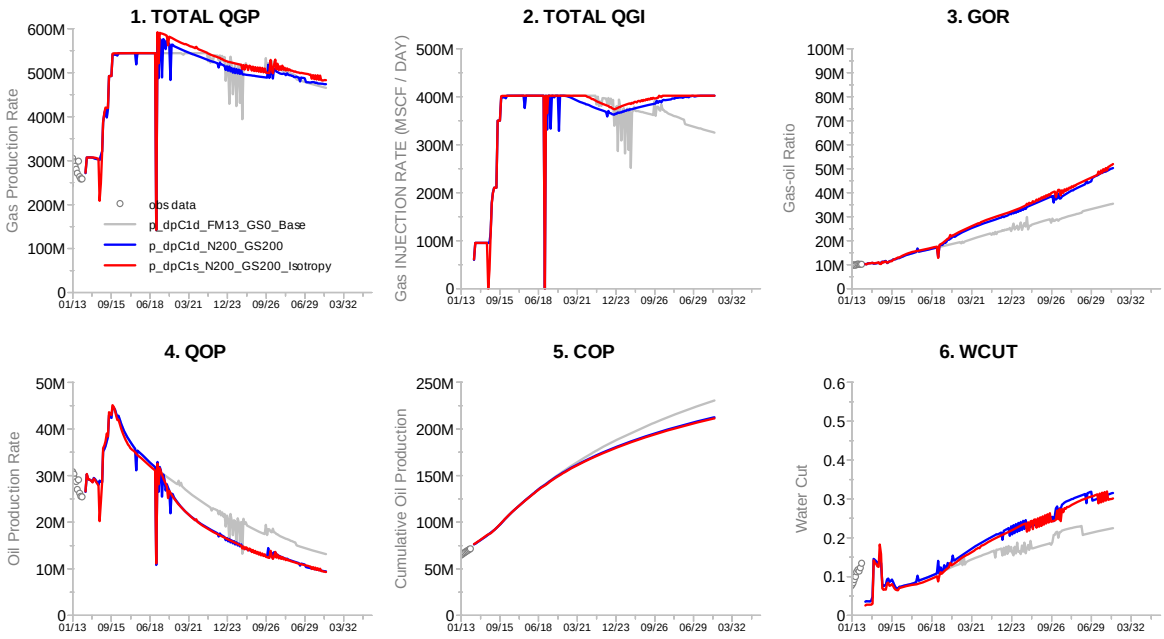

Figure 3-68. Field Surface Production – DPDP Fracture Permeability Isotropy Sensitivity Analysis.

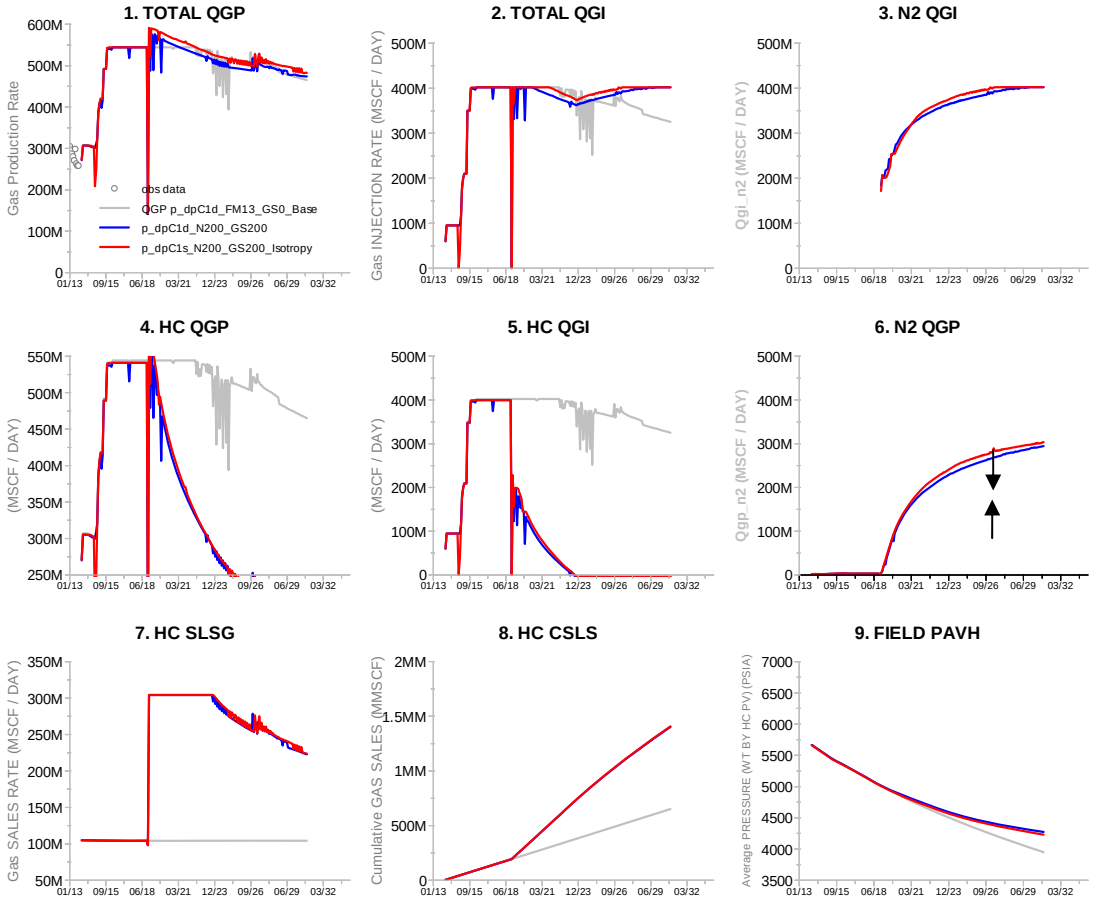

Figure 3-69. Field Surface Gas Behavior – DPDP Fracture Permeability Isotropy Sensitivity Analysis.

- **Saturation**

When there is no anisotropy. there is an increase in permeability in the north-south direction. This produces a higher liquid drop out in the cells, as the pressure depletion from the producer has a bigger influence area, which is shown in Figure 3-70 on points A and B.

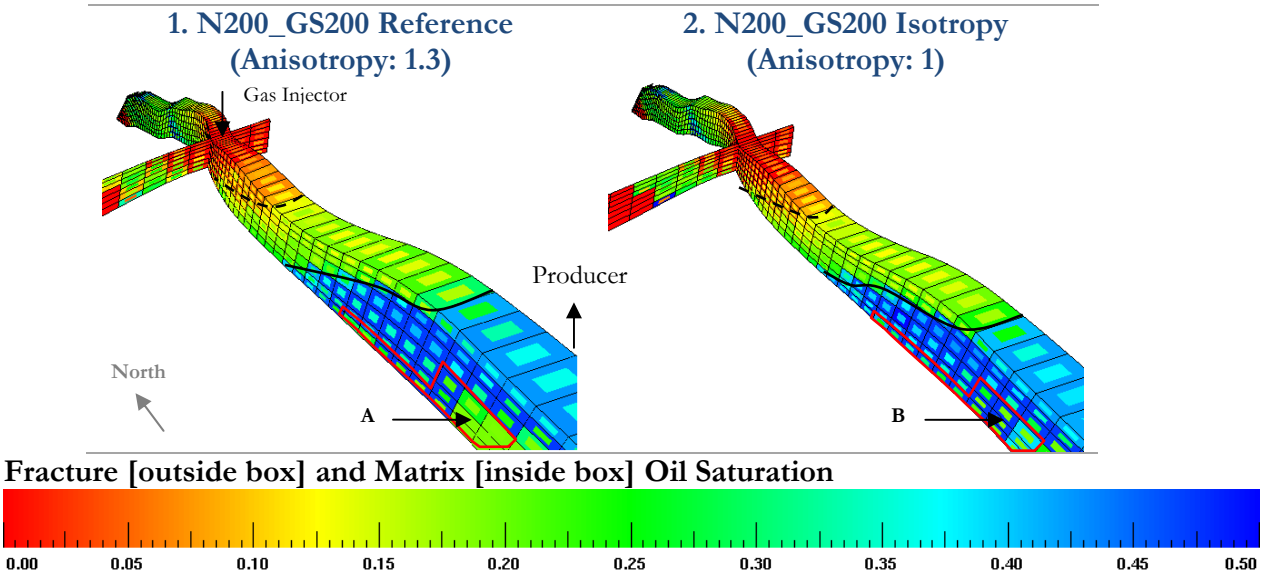

Figure 3-70. Dele Matrix-Fracture Oil Saturation – 10 years after N_2 injection sensitivities are performed. DPDP Fracture Permeability Isotropy Sensitivity Analysis.

Figure 3-71 shows that the lower the anisotropy is, the faster the N_2 travel time is (see points A and B). For this specific case, this happens due to an increase in the y direction permeability (North-south), which favors an increase in permeability.

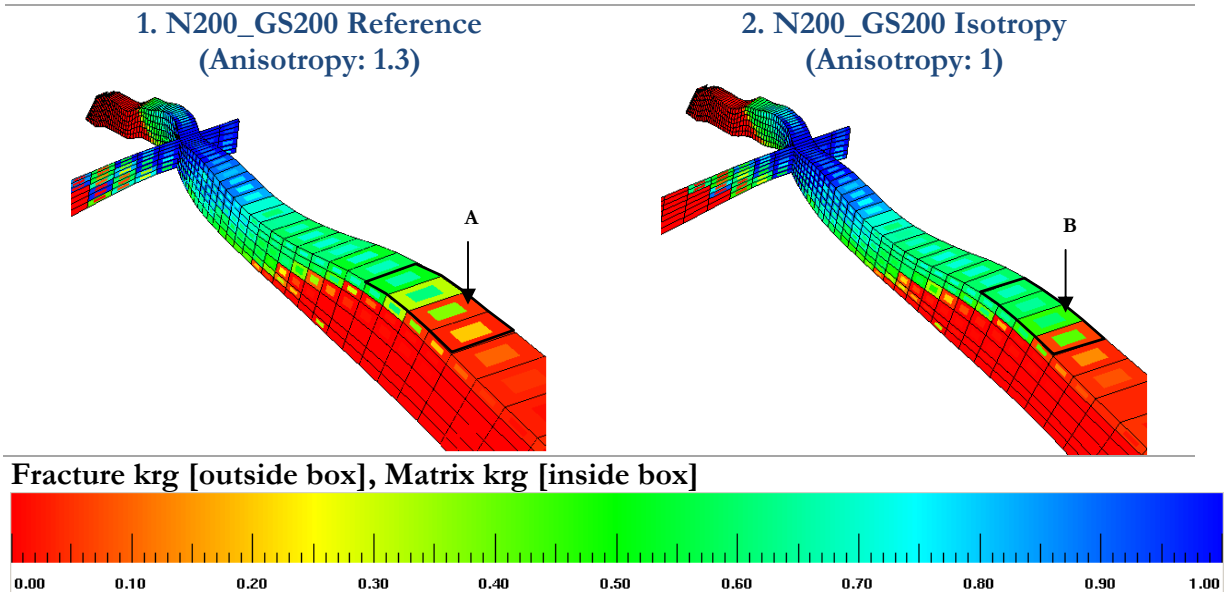

Figure 3-71. Dele Matrix and Fracture Gas Relative Permeability– 10 years after N_2 injection sensitivities are performed. DPDP Fracture Permeability Isotropy Sensitivity Analysis.

When there is no anisotropy, there is an increase in permeability in the north-south direction. This generates a higher liquid drop out, which generates an increase in the fracture oil relative permeability in the cells, as the pressure depletion from the producer has a bigger influence area, which is shown in Figure 3-72 in points A and B.

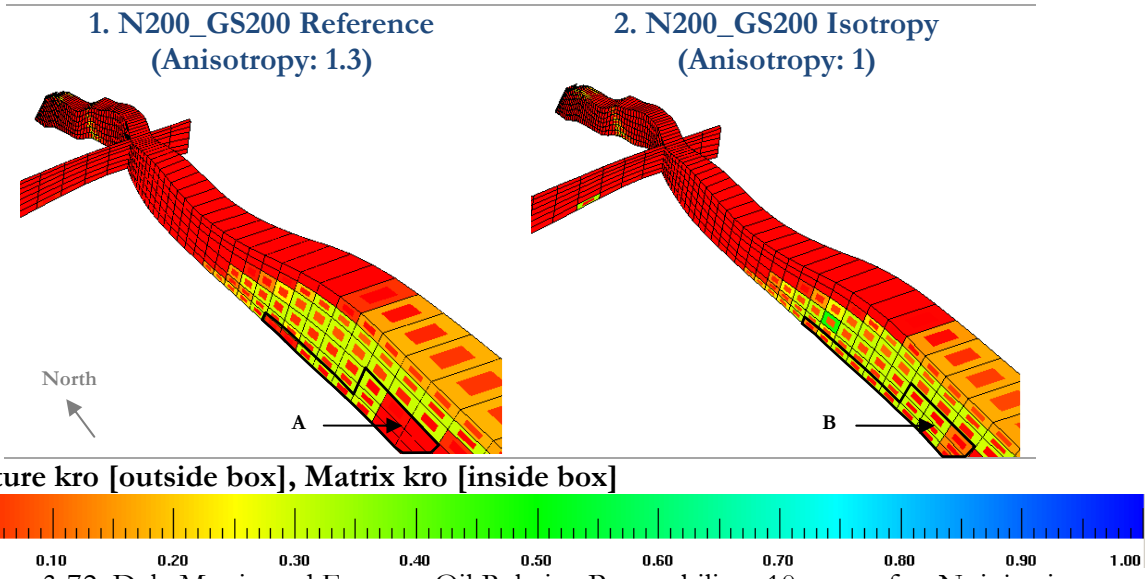

Figure 3-72. Dele Matrix and Fracture Oil Relative Permeability– 10 years after N_2 injection sensitivities are performed. DPDP Fracture Permeability Isotropy Sensitivity Analysis.

- **Composition**

The same observation is presented in the fracture gas relative permeability (see Figure 3-71) which also applies for Figure 3-73, where the lower the anisotropy is, the faster the N_2 travel time is (see points A and B).

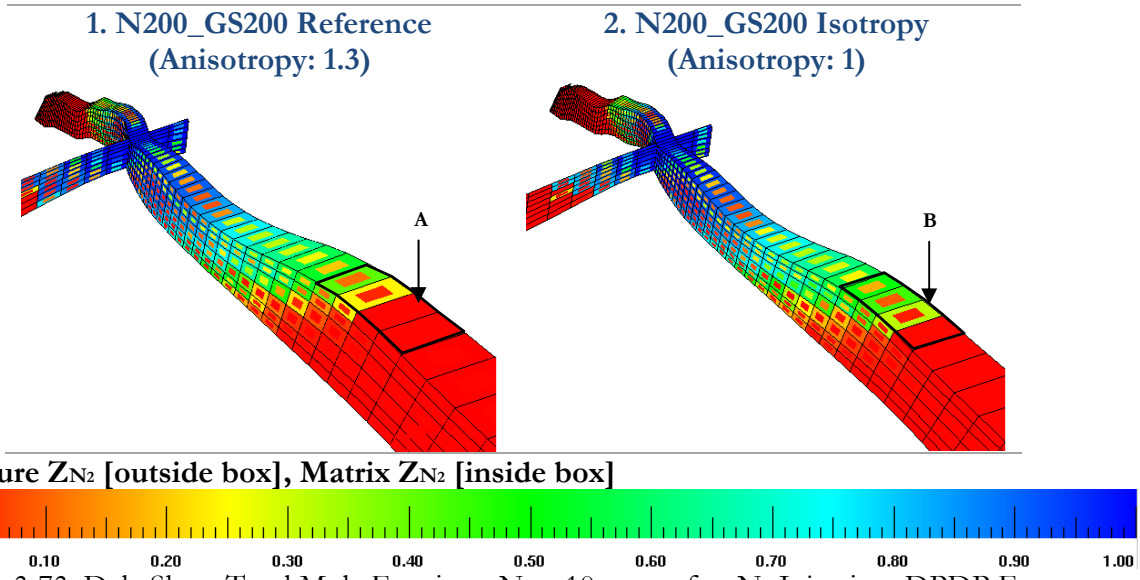

Figure 3-73. Dele Sheet Total Mole Fraction –N_2 – 10 years after N_2 Injection. DPDP Fracture Permeability Isotropy Sensitivity Analysis.

Figure 3-74 shows points A and B as for comparison purposes, where a slight increase in N_2 composition is observed when the model has no anisotropy included. This reflects a less restricted progress for the injected N_2, as the permeability in the *x* and *y* direction are the same. As the anisotropy factor is not quite low, changes in the N_2 flow in the reservoir are low.

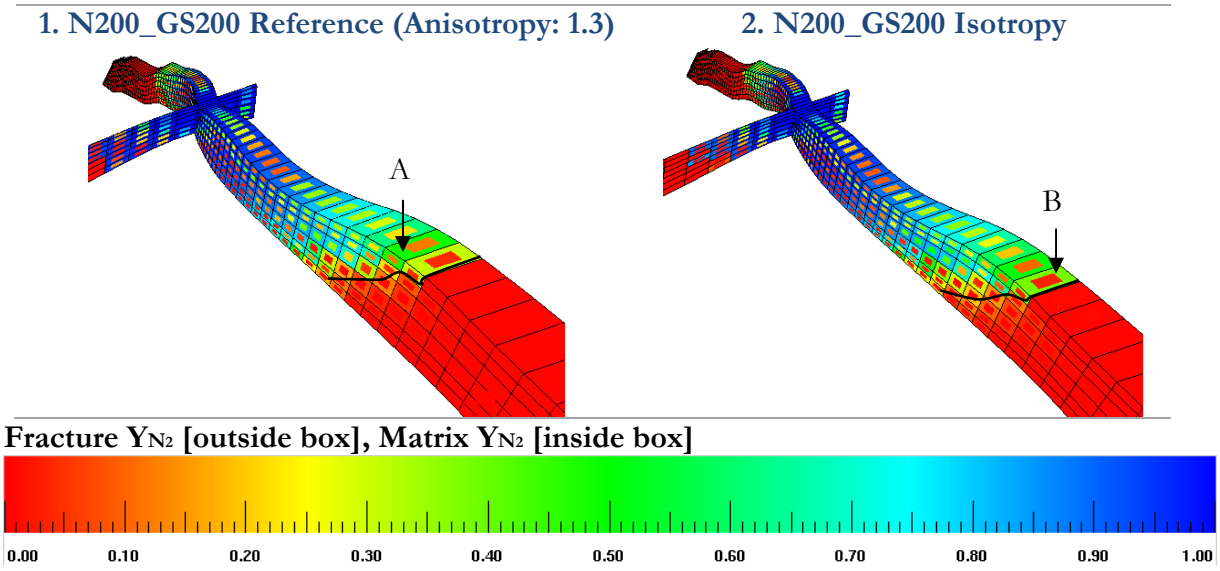

Figure 3-74. Dele Sheet Gas Mole Fraction –N_2 – 10 years after N_2 Injection. DPDP Fracture Permeability Isotropy Sensitivity Analysis.

Figure 3-75 shows how N_2 travels to the flank of the structure with the anisotropy that was implemented; this is because there is a higher fracture permeability in the east-west than in the north-south direction for this case (see in Plot No. 1- Point A). Plot No. 2 - Point B shows a reduction in the N_2 Fraction in the flank of the structure for the isotropic case, as there is an increase in the north – south permeability. Point C in Figure 3-75 shows how N_2 travels more in the liquid phase in the isotropic case than in the anisotropic run.

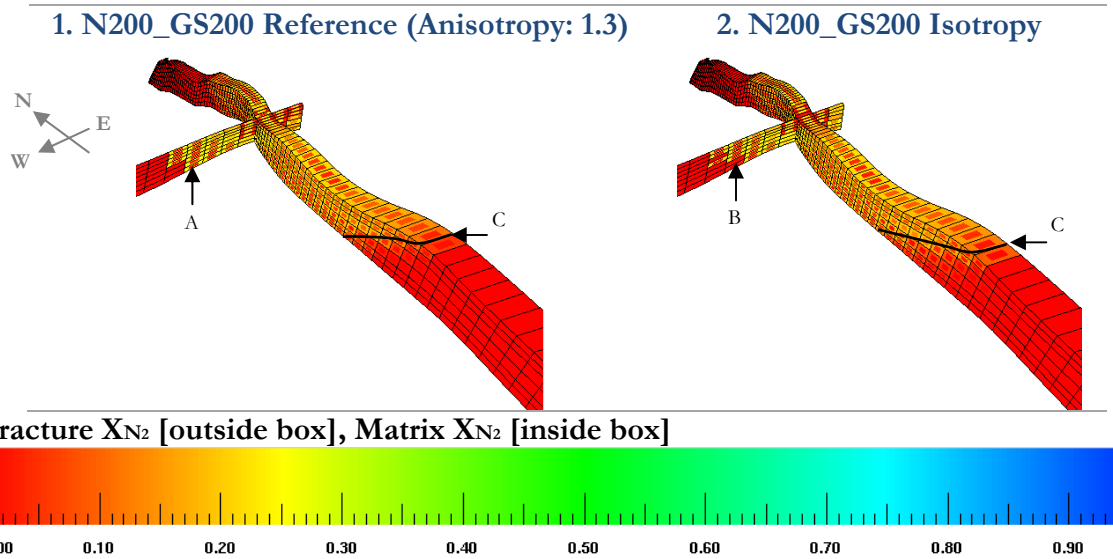

Figure 3-75. Dele Sheet Oil Mole Fraction –N_2 – 10 years after N_2 Injection. DPDP Fracture Permeability Isotropy Sensitivity Analysis.

3.7.7 Vertical Permeability

Following a general rule, the Single porosity model (equivalent model) uses a matrix vertical permeability of 0.1*kym. This assumption was used to build the DPDP model. But as it is shown in Figure 3-76, the ratio is higher than 0.1[59].

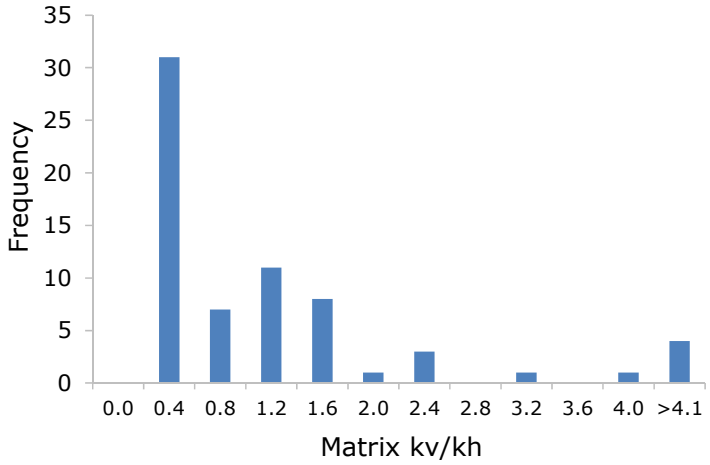

Figure 3-76. Matrix kv/kh ratios.

On the other hand, the vertical permeability of fractures in the dual porosity/dual permeability model is almost the same as in the ky direction, as it was presented in Section 2.6.3.3, which is the highest permeability achievable in the horizontal direction.

A sensitivity analysis with the matrix vertical permeability of 1* kmy and a fracture vertical permeability of 0.1*kfy were run in order to measure the impact of the vertical permeability on the oil and gas flow.

Table 3.12. Fracture Vertical Permeability – Prediction Run Names.

Runs	Kz Multiplier	Prediction Run Name	Comments
Reference	kzm = 0.1 * kym, kzf = 1 * kyf	p_dpC1d_N200_GS200	Reference Case.
1	kzm = 1 * kym	p_dpC1d_N200_GS200_kmV	Increase 10 times the matrix vertical permeability.
2	kzf = 0.1 * kyf	p_dpC1d_N200_GS200_kfV	Decrease 10 times fracture vertical permeability.

Notice that there is a big change in the sensitivity analysis proposed, as the vertical permeability has a 90% increase for the matrix vertical permeability (kmv) sensitivity, and a reduction of 90% for the fracture vertical permeability (kfv) compared to the reference case.

Figure 3-77 shows that the kmv has a huge impact on oil production in the DPDP model, producing a positive cumulative oil production of 16.2 MMstb after 10 years (see also Figure 3-29), and giving the lowest impact on oil production compared to the base case (no gas injection), see Figure 3-26.

[59] To the best of our knowledge, the kv/kh ratio values are not well understood up to this moment, as these values could depend on rock characteristics (e.g stratification) or on micro-fractures, as shown in Figure 1-31.

- **Production**

Figure 3-77 shows 6 plots related to the general production variables at field level. A general observation is that an increase in the kmV reduces the resistivity for the flow of oil, gas and water in the reservoir, and to the wellbore, which increases the production of all three phases.

- Plot No. 1 shows an improvement on gas rate at the end of 2032, with an increase on the kmV. This is due to a better hydrocarbon gas sweep with N2 injection.

- Plots No. 4 and 5 show that a better oil production is achieved with higher matrix permeability in the vertical direction. An increase in the kfv did not generate an observable change. As the matrix has a higher storability factor, then the higher the kmV is, the higher is the matrix transmissibility , achieving higher oil production.

  It can also be observed that, at certain point, there is a steeper oil decline compared to the reference and base cases (blue and gray lines respectively, Point A in Figure 3-77), that follow a typical natural fracture behavior, where there is a more pronounced decline once the matrix begins to be depleted.

- Plot No. 6 exhibits a higher Wcut evolution when increasing either the vertical permeability of the matrix (see the solid magenta line) or the kfv (see the blue line – reference case).

  The reason for this behavior is because, when the fracture vertical permeability is low, the water is able to flow by layers from the aquifer to the well. And when the kmV is increased, water has a better communication in the internal matrix-matrix system, allowing a better communication of water from the aquifer to the well.

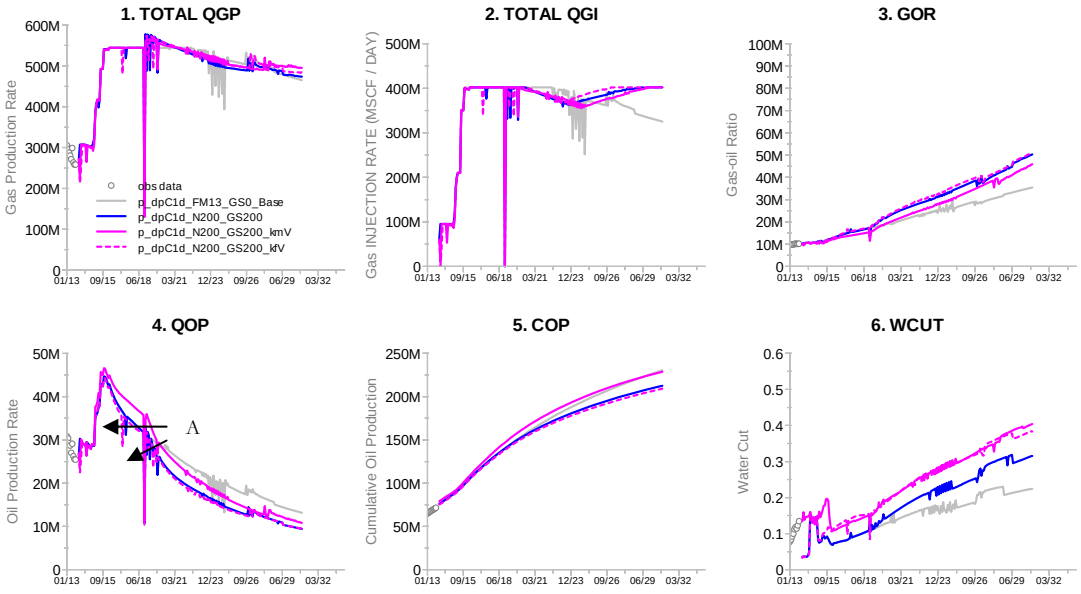

Figure 3-77. Field Surface Production – DPDP Matrix and Fracture Vertical Permeability Sensitivity Analysis.

Plots No. 1 and 7 in Figure 3-78 show a slightly better gas production and gas sales when the matrix vertical permeability is increased; this is due to an increase in the matrix transmissibility, which allows the hydrocarbons that are locked in the matrix to be more easily accessed.

Plot No. 6 in Figure 3-78 reveals that when reducing the fracture vertical permeability, there is a small increase in N_2 production evolution; this is because N_2 has better transmissibility in the horizontal direction than in the vertical direction, allowing for the N_2 to flow faster through the horizontal plane.

This is confirmed when observing the opposite behavior, when the kmV is increased, allowing the N_2 to fill more space, which in turn slightly delays N_2 evolution with time.

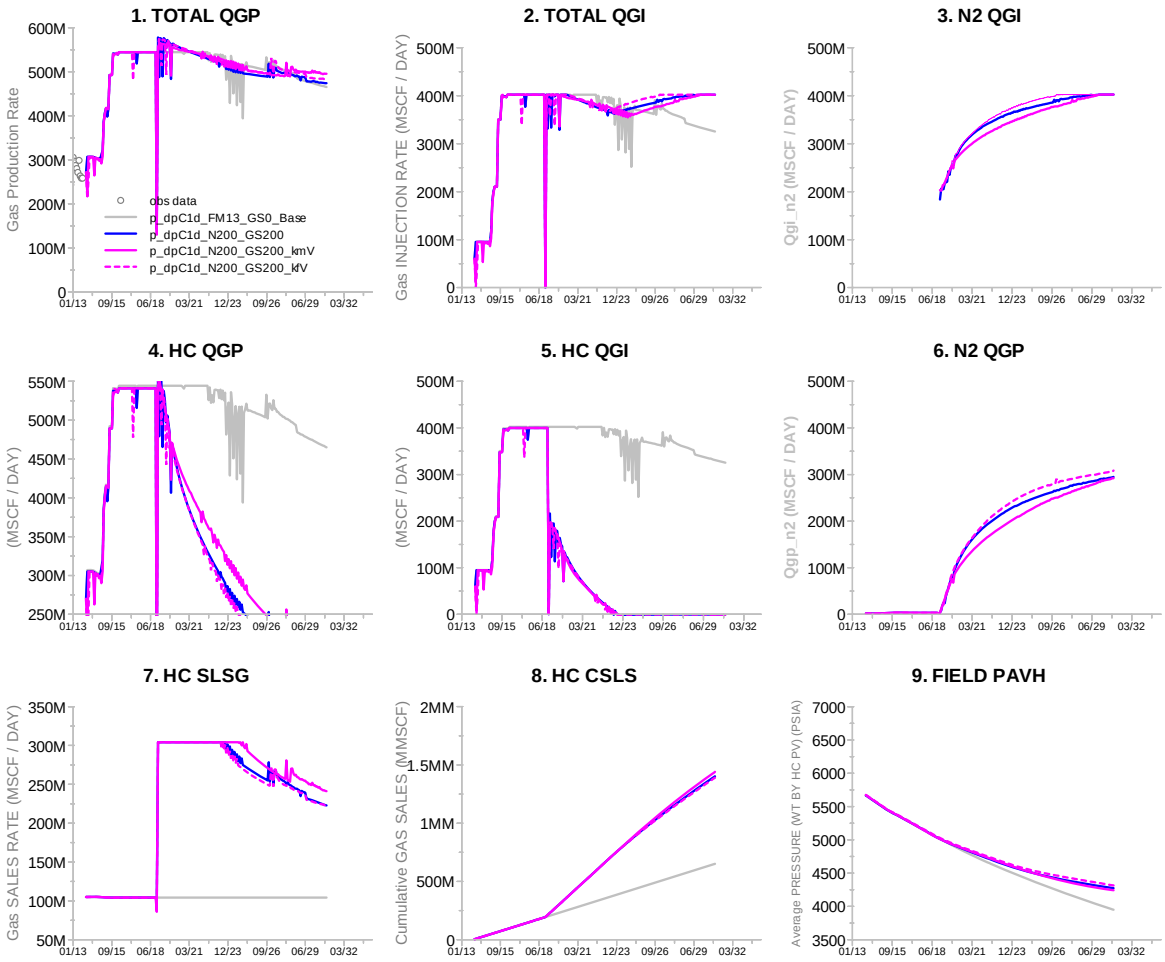

Figure 3-78. Field Surface Gas Behavior – DPDP Matrix and Fracture Vertical Permeability Sensitivity Analysis.

- **Saturation**

When comparing the oil saturation with the reference case in Figure 3-79, there is a slight increase in oil saturation at the bottom of the structure when kfv is higher (see points B and D in that Figure).

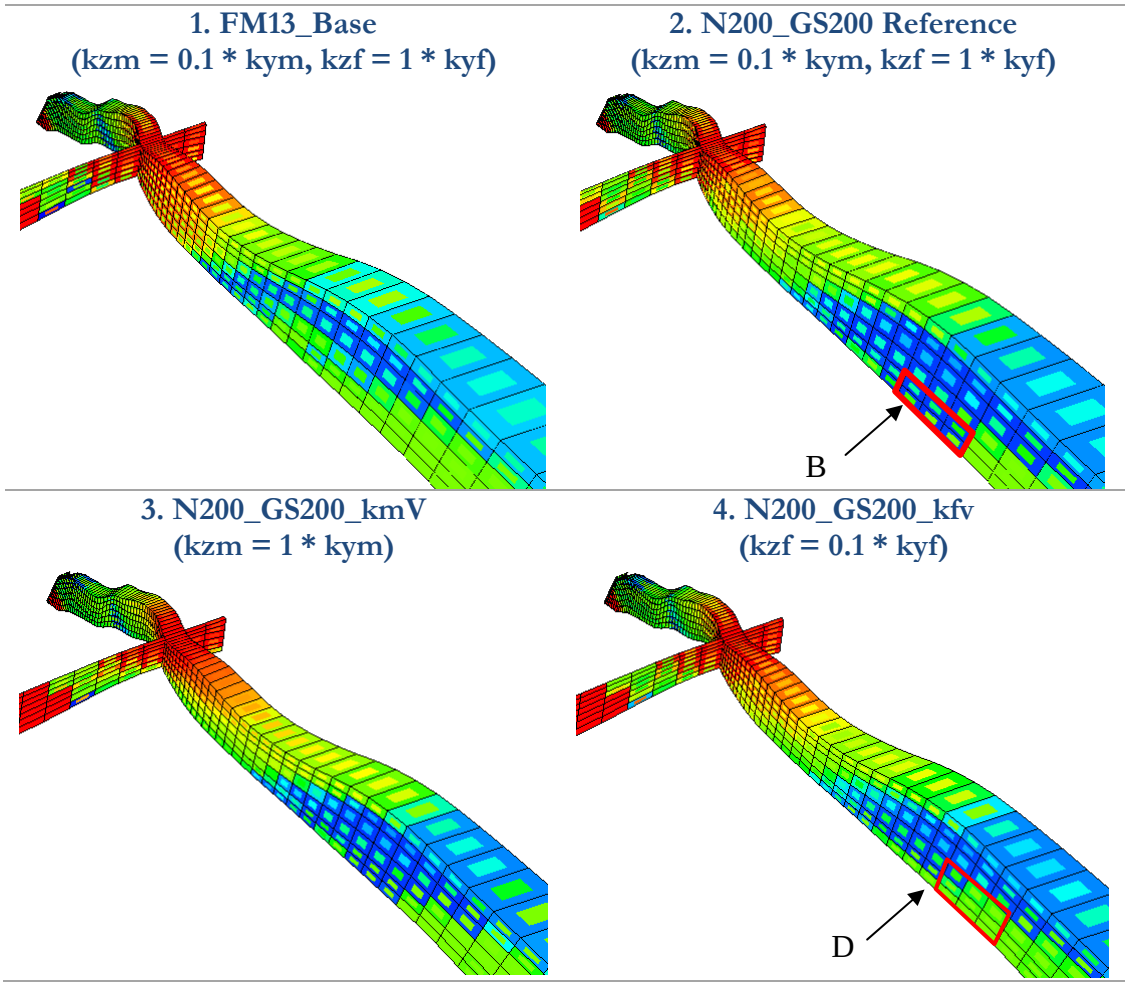

Figure 3-79. Dele Matrix-Fracture Oil Saturation – 10 years after N_2 injection sensitivities are performed. DPDP Matrix and Fracture Vertical Permeability Sensitivity Analysis.

Figure 3-80 shows an improvement in matrix relative permeability when the matrix vertical permeability is increased (see point C) when compared to the base case (see point B).

This is due to a flow improvement through the matrix system, which allows improving gas mobility. On the other hand, gas flow through fractures does not show a significant reduction in terms of gas relative permeability.

The matrix and fracture sensitivity analysis helps to identify that the impact of low matrix petrophysical properties are key parameters that allow the reservoir to deliver more gas for production and sales, as observed in Figure 3-78 Plot No. 7.

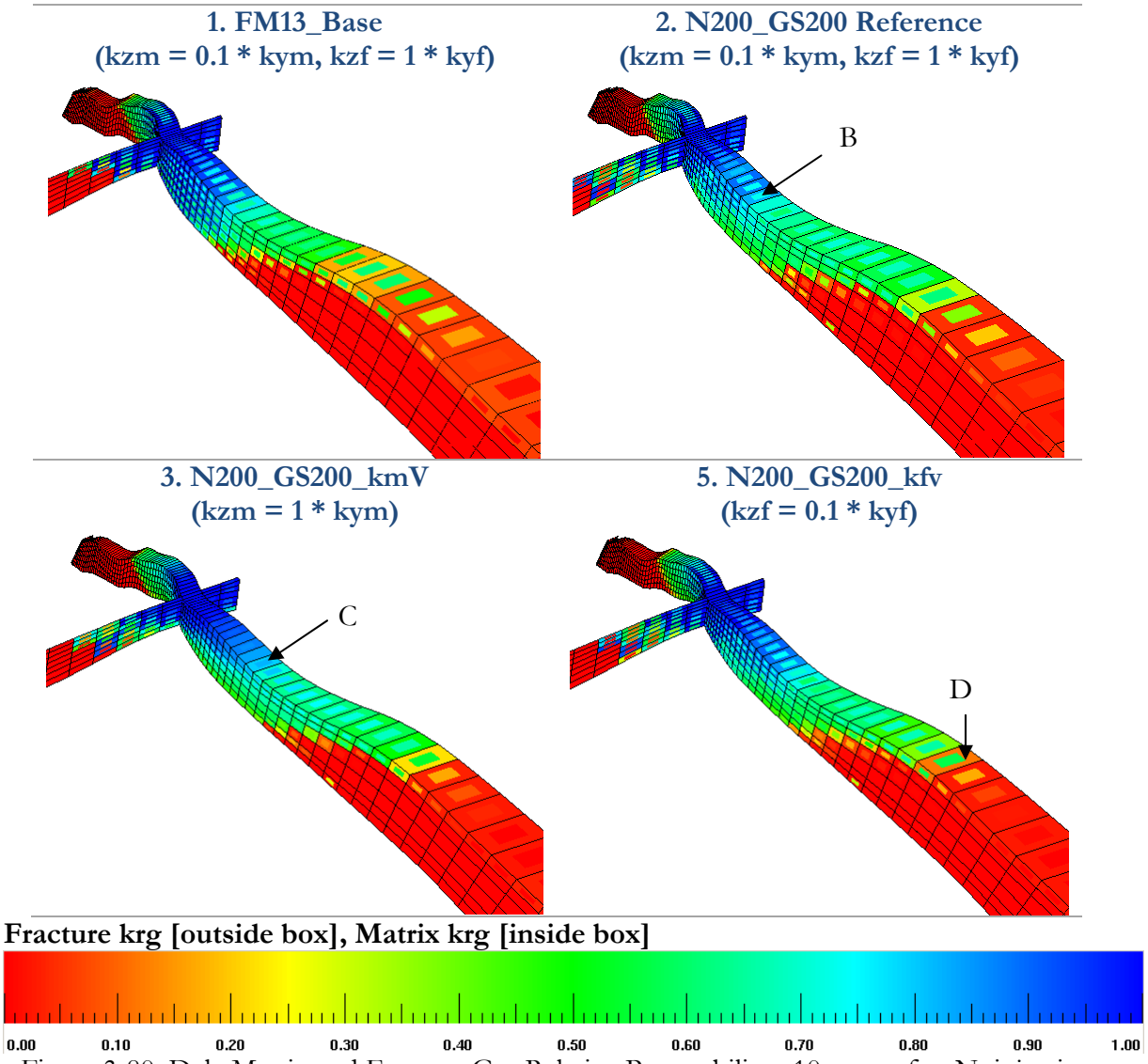

Figure 3-80. Dele Matrix and Fracture Gas Relative Permeability– 10 years after N_2 injection sensitivities are performed. DPDP Matrix and Fracture Vertical Permeability Sensitivity Analysis.

Figure 3-81 shows the corresponding reduction in fracture oil relative permeability at the bottom of the structure, which is tied to the oil saturation description presented in Figure 3-79. In other words, krof is higher due to a higher kfv.

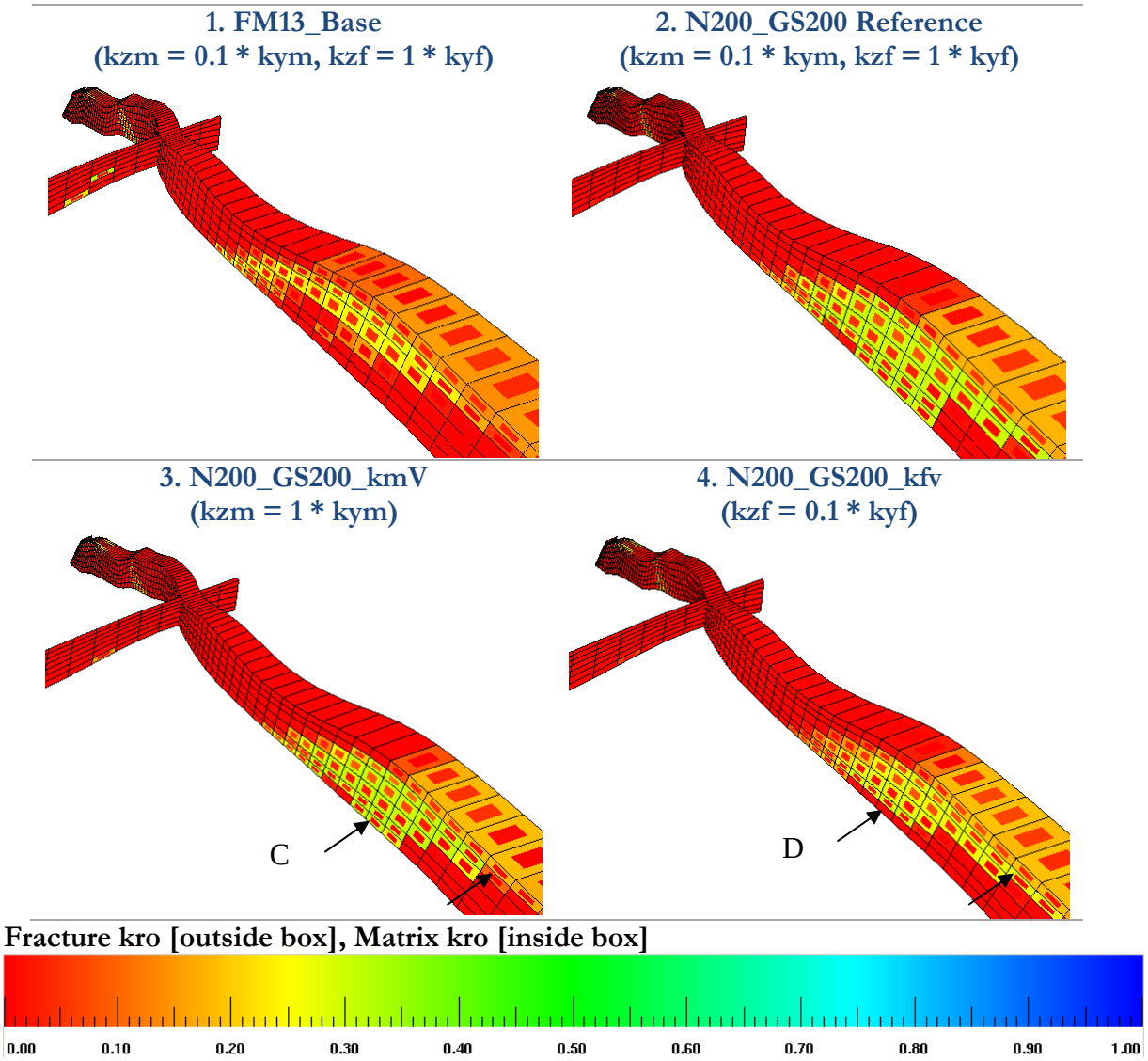

Figure 3-81. Dele Matrix and Fracture Oil Relative Permeability– 10 years after N_2 injection sensitivities are performed. DPDP Matrix and Fracture Vertical Permeability Sensitivity Analysis.

- **Composition**

Figure 3-82 shows an increase in N2 concentration within the matrix when the kmv is increased (see point C) compared to the reference case (see point B). This is due to an increase in the matrix transmissibility that allows N2 to enter into the matrix blocks.

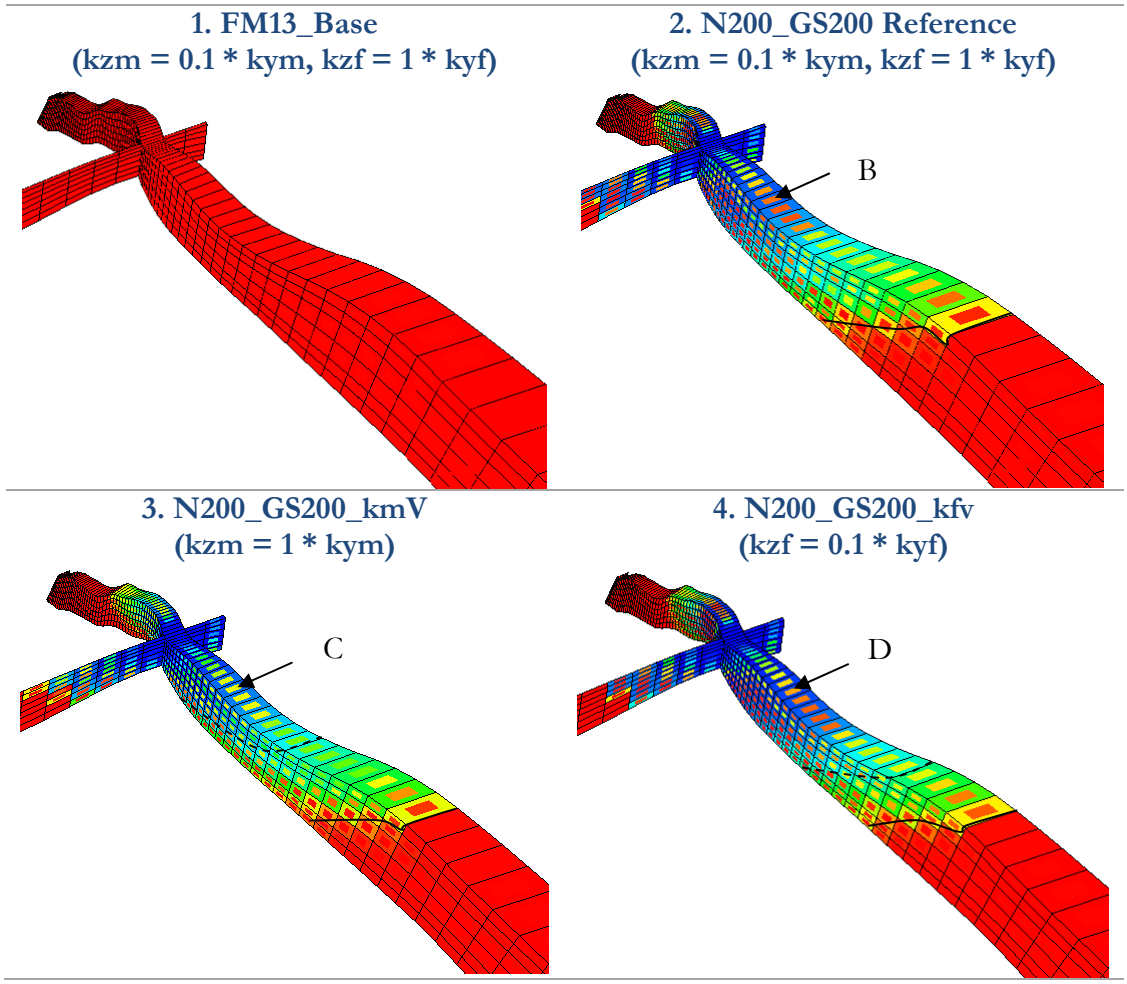

Figure 3-82. Dele Sheet Total Mole Fraction –N_2 – 10 years after N_2 Injection. DPDP Matrix and Fracture Vertical Permeability Sensitivity Analysis.

A comparison with the reference case (see Plot No. 2) in Figure 3-83 shows a slight increase in fracture N_2 composition (see Plot No. 4, blue region) when kfv is decreased, without having any impact on the matrix N_2 composition.

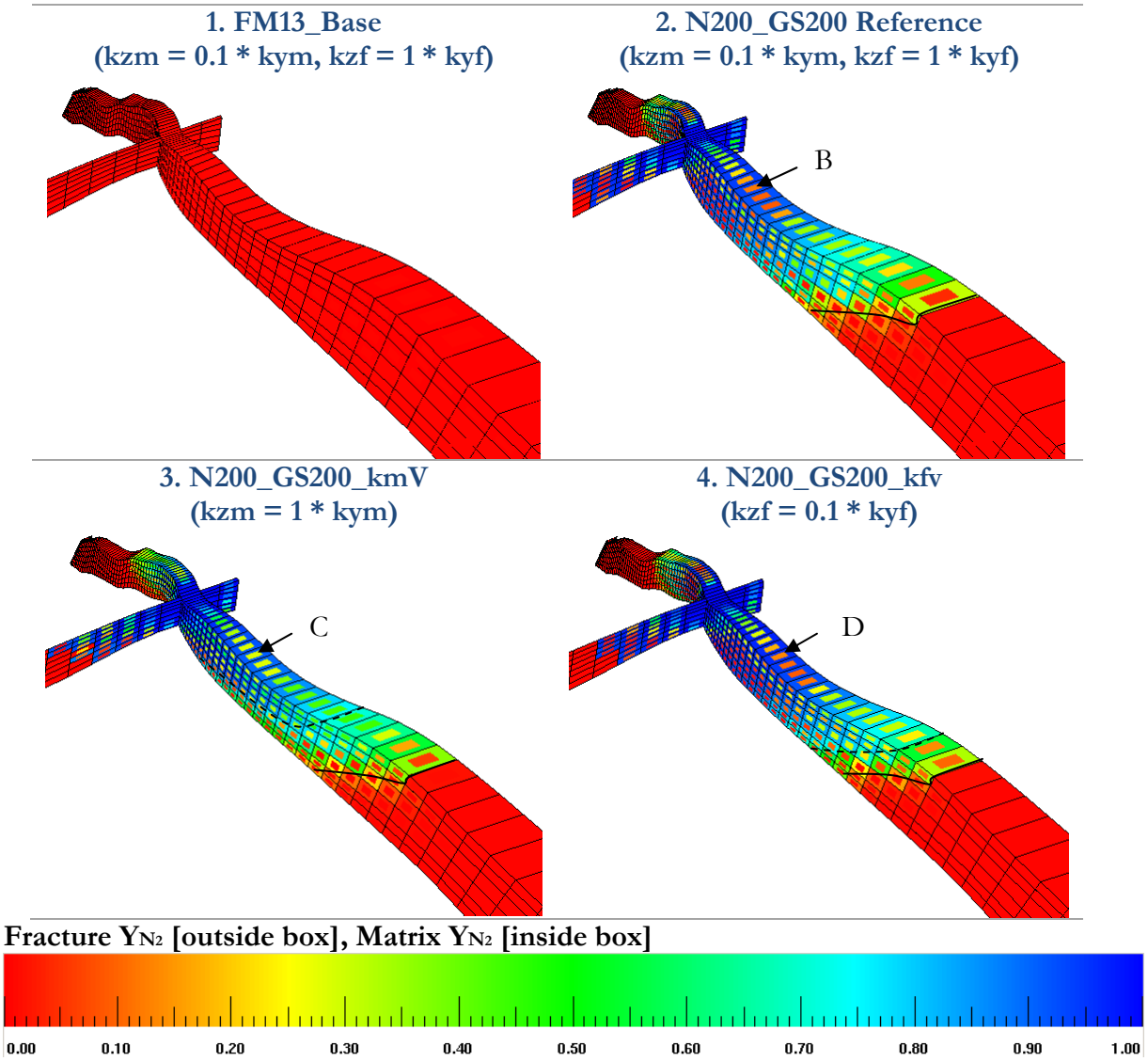

Figure 3-83. Dele Sheet Gas Mole Fraction –N_2 – 10 years after N_2 Injection. DPDP Matrix and Fracture Vertical Permeability Sensitivity Analysis.

Figure 3-84 marks point A in Plots 2, 3 and 4, where a reduction in the fracture vertical permeability (see kfv sensitivity analysis in Plot 4) or an increase in the matrix vertical permeability (see kmV sensitivity analysis in Plot 3) permits the N_2 displacement front to travel a longer distance compared to the reference case (see Plot 2).

The difference between the kmV and kfv sensitivity analysis is the evolution of the displacement front. While kfv produces a more stable front for the liquid located in the fracture (see point C), kmV generates a slight segregation of N_2 to the structure (see point B).

The reason for this behavior is that an increase in matrix vertical permeability allows a better segregation of N_2 to the top, while a reduction in fracture vertical permeability helps to avoid fluid segregation to the top of the structure.

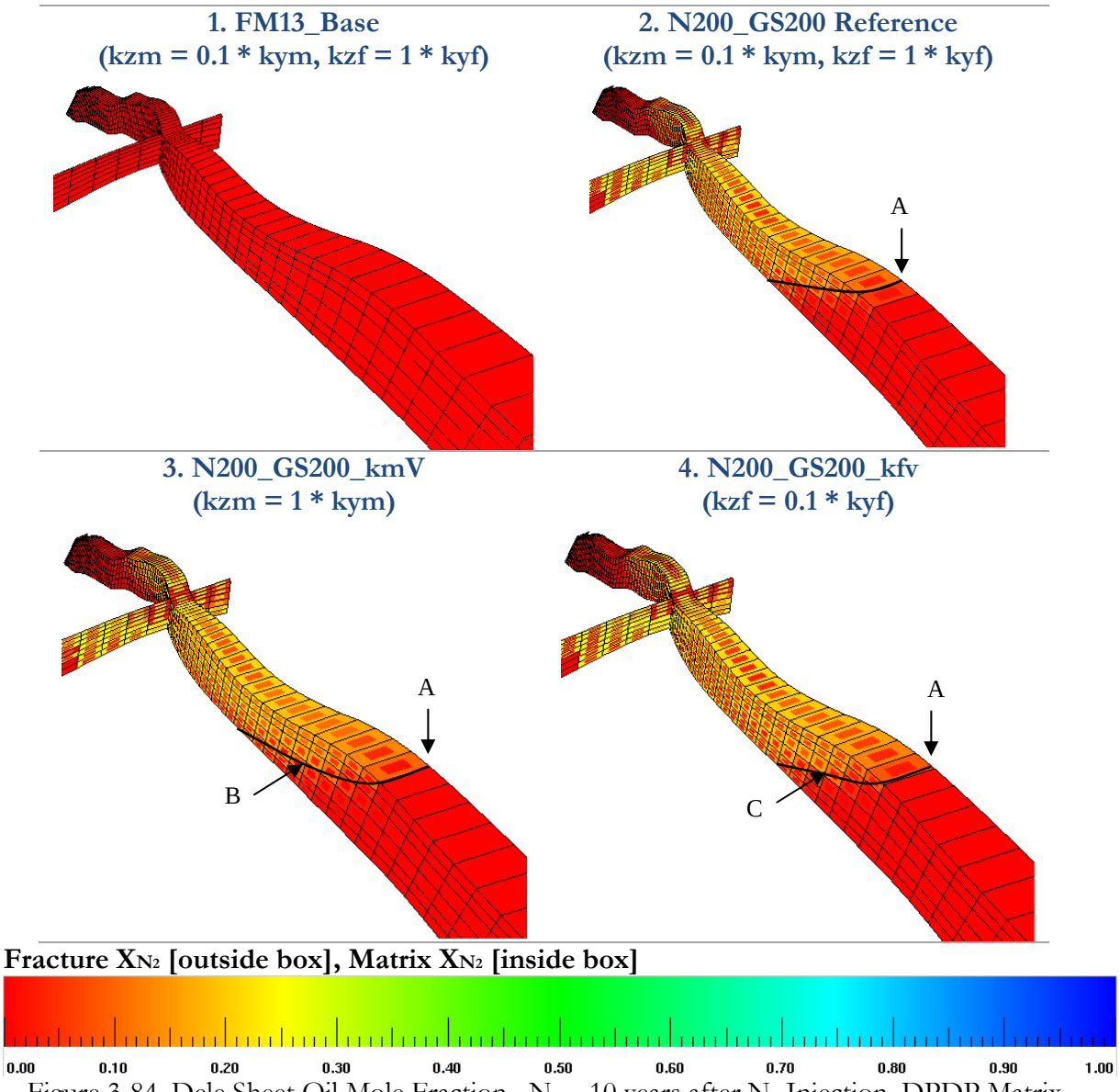

Figure 3-84. Dele Sheet Oil Mole Fraction –N_2 – 10 years after N_2 Injection. DPDP Matrix and Fracture Vertical Permeability Sensitivity Analysis.

3.8 Summary and Conclusions

1. The maximum incremental gas sales are not due to an overriding N_2 phenomenon but due to a maximum reservoir injection limit that is achieved in the system, being 200 MMscfd of N_2 injection with 200 MMscfd of gas sales, see Plot 2 in Figure 3-11 and Case 7 in Figure 3-8.

2. A nitrogen injection process that was modeled in a natural fracture system shows that the gas recovery factor is between 9% and 14%, with an initial liquid loss, compared to the lean gas, of between 1% and 3% in 10 years for the reference case (200 MMscfd of N_2 injection and 200 MMscfd of gas sales). This option generates a net incremental volume of between 78 to 110 MMBOE for PDM fields

3. Higher sweep efficiency was observed with the dual porosity/dual permeability model, compared with the single porosity model, due to an improvement in the matrix-matrix, fracture-fracture communication combined with matrix-fracture communication, which allowed more fluids to be moved from the reservoir to the wells, see Figure 3-32.

4. The lower the critically stressed fracture intensity is, the higher is the displacement efficiency. The main reason for this quite homogeneous displacement in Pauto Main is due to the fact that this sheet has the lowest excess permeability, see Figure F.3.

5. Once the liquid had dropped out in the reservoir, the pressure maintenance scenario with N_2 injection is limited due to reservoir injectivity problems, as there is an injection capacity constraint that allows a maximum additional gas volume of 200 MMscfd (see Figure 3-11) to be injected. Under the surface facilities configuration (NRU without limits), this amount of N_2 is not enough to re-vaporize liquids that had been affected by gravity in the past due to reservoir pressure depletion, see Figure 2-36, Figure 3-19 and Figure 3-20.

6. The fracture system has a higher oil saturation in the displacement front when nitrogen is being injected, compared to no injection of nitrogen. This is due to a higher liquid dropout being generated by nitrogen, see Figure F.1 and Figure 3-1.

7. The analysis indicates that when there is high critically stressed fracture intensity, the gas being injected, either if it is lean gas or nitrogen, tends to bypass more oil that is located in the matrix than when the excess permeability is low, see Figures E.7, E.8 and E.9.

8. Increasing the N_2 injection rate does not necessarily sweep additional oil from the matrix. Figure 3-19 shows that all N_2 injection cases have the same matrix oil saturation in Dele Sheet.

9. 3 general displaced zones where identified with N_2 displacement. The 1st region is very close to the injector, where the fracture oil saturation is close to the Sorm ~0.05 and the matrix oil saturation is close to the Sor~0.2. There is a 2nd region where the fracture oil saturation is close to ~0.2 and the matrix oil saturation is ~0.15. And finally there is a 3rd

region close to the producer where N_2 has not fully penetrated, where the fracture oil saturation is higher than 0.5 and the matrix oil saturation is 0.25 or higher.

10. When using the Zero BIP´s in the Equation of state the interactions of N_2 with other pseudo-components are minimized. Then, N_2 the vaporization of intermediate and heavy components are reduced which generates a lower oil production compared with the lean gas injection up to certain point where the pressure support given by the N_2 swap this behavior.

11. Condensate Liquid losses generated by N_2 injection under the surface conditions modeled can be reduced by having a higher amount of CO_2 in the N_2 stream. The minimum condensate losses results with CO_2 injection as the oil production losses respect to the base case are ~4 MMstb in 10 years with a constant gas sales plateau (see Figure 3-44) gives a maximum incremental gas sales of 0.9 Tcf in 10 years.

12. When the Sgt is not considered, there is an increase in the cumulative oil production of 11 MMstb in 10 years.

13. The higher the gas trap saturation is, the shorter is the displacement front, as it can be observed in Figure 3-58. This reduction in gas injection is due to an increase in gas flow restriction (see Plot 2 and Figure 3-53). When the Sgt is high (see Plot 4), nitrogen travels a shorter distance (see points B, C and D).

14. The sensitivity the relative permeability at reservoir level does not have a big impact on oil and gas production. Very small improvements from 0.05 to 0.15 in the oil and gas relative permeability sum is observed in the measured data when comparing the matrix and fracture relative permeabilities at 50% oil saturation, see Figure 2-16.

15. For Piedemonte fields, the horizontal anisotropy generates a very small change in gas production and injection, which means that the estimated horizontal anisotropy of 1.3 does not generate a significant change in fluid flow behavior, see Plot 1 and Plot 2 in Figure 3-68.

16. Matrix vertical permeability (see kmV paramenter) is one of the most influential parameters that affect the production results. When kmV is increased by a factor of 10, it gives a better sweep efficiency for the matrix system compared to the reference case, which is reflected in an increase in cumulative oil production by 16 MMstb in 10 years.

17. An improvement on gas rate at the end of 2032 with an increase in the matrix vertical permeability is achieved due to a better hydrocarbon gas sweep with N_2 injection, see Figure 3-77 Plot No. 1.

18. There is an evident impact for intermediate components that are lost from the gas phase when comparing the base case (FM13, no N_2 injection) with the reference case (N200_GS200). Even if N_2 has some capacity to vaporize intermediate components, it does not have the same efficiency compared to lean gas injection under the surface facilities conditions evaluated, see Figure G.1 and G.2.

19. C3 and C4 pseudo-components located in the matrix have the highest impact with N_2 injection. Also with the N2 injection, the pseudo-components from C5 to C8 begin to be lost from the gas phase at 4000 psia compared to 3000 psia, see Figure G.3 and G.4.

3.9 References

1. J. CALVIN ET AL. An Evaluation of nitrogen Injection as a Method of Increasing Gas Cap Reserves and Acceleration Depletion – Ryckman Creek Field, Uinta Country, Wyoming.. SPE 8384. September 1979.

2. S. SAYEGH ET AL. Multiple contact phase behavior in the displacement of Crude oil with Nitrogen and Enriched Nitrogen. JCPT 87-06-02. December 1987.

3. C. ALCOCER. The Compositional Approach to Study Dynamic miscibility in nitrogen Injection is Practical and Reveal Mechanisms to Achieve Miscibility. SPE 23726. 1994.

4. D. KUEHNE ET AL. Design and Evaluation of a Nitrogen-Foam Field Trial. SPE 17381-PA. April 1990.

5. J. HANSSEN. Nitrogen as a Low-Cost Replacement for Natural Gas Reinjection Offshore. SPE 17709. June 13-15 1988.

6. D. WENDSCHLAG ET AL. Field wide Simulation of the Anschutz Ranch East Nitrogen Injection Project with a generalized Compositional Model. SPE 12257. Dallas, USA. November 1983.

7. S. KLEINSTEIBER ET AL. A Study for Development of a Plan of Depletion in a Rich Gas Condensate reservoir: Anshutz Ranch East unit, Summit County, Utah, Uinta Country, Wyoming. SPE 12042. Dallas, USA. October 1983.

8. X. WU ET AL. Nitrogen Injection Experience to Development Gas and Gas Condensate Fields in Rocky Mountains. IPTC 16830. Bejin, China. March 2013.

9. T. LIMON ET AL. Overview of the Cantarell Field Development Program. OTC 10.4043/10860-MS. Offshore Technology Conference. Houston, Texas. 1999.

10. M. GUZMANN. Review of a Forgotten Technology with High Potential – The World Largest Nitrogen Based IOR Project in the Supergiant field Catarell, Mexico. SPE 171239-MS. Moscow, Russia. October 2014.

11. O. VICENCIO. Nitrogen Injection into Naturally Fractured Reservoirs. Phd Thesis. University of Texas Austin. 2007

12. J. LAWRENCE. Jay Nitrogen Tertiary Recovery Study: Managing a Mature Field. SPE 78527. 2002

13. J. LINDERMAN ET AL. Substituting Nitrogen for Hydrocarbon Gas in a Gas Cycling Project. SPE 117952. Abu Dahbi, UAE. November 2008.

14. H. ABDULWAHAB ET AL. Managing the Breakthrough of Injected Nitrogen at gas Condensate Reservoir in Abu Dhabi. SPE 137330. 2010.

15. J. RIVERA ET AL. Evaluations of displacement Efficiency in Volatile oil reservoirs under nitrogen injection. SPE 70053. 2001.

16. L. SOTO ET AL. Gas-injection Redistribution Revitalizes a Mature Volatile Oil Field: Cusiana Field Case Study. SPE 103593. San Antonio, TX, USA. September 2006.

17. M. AGUILAR ET AL. Factibilidad de Reemplazar los procesos de re-inyección de gas por Inyección de Nitrógeno en el campo Cusiana. Tesis de grado. Universidad América. Bogota, Colombia. Agosto 2007.

18. R. OSORIO. Curso Hidrocarburos de Yacimiento y PVT. Bogota, Colombia. Noviembre 1 de 2011.

19. R. CASTRO, G. MAYA ET AL. Enhance Oil Recovery (EOR) Status – Colombia. SPE 139199. 2010.

20. S. MARTINSEN AND C. WHITSON. Pauto Complex Fluid Characterization and fluid Initialization. PERA. Equion Internal Report. Trondheim, Normay. February 2009.

21. C. WHITSON AND M. BRULE. Phase Behavior. Monograph Volume 20 SPE. First Printing. Texas, USA. 2000.

22. Perspectivas de oferta y demanda de gas natural en Colombia 2014-2022. Unidad de Planeación Minero Energética. Bogota, Colombia. Abril 2014.

23. C. HERRERA ET AL. Modelamiento Numérico de Inyección de CO2 para un Piloto en el Campo Cusiana. ACIPET. Bogota, Colombia. 26-28 Agosto 2015.

24. C. PALENCIA ET AL. Building a Petrophysical model for a Low Porosity and Highly Tectonized Reservoir. Field Case: Pauto Complex – Colombia. Society of Petrophysicist and well log analysis. SPWLA. 2012.

RECOMMENDATIONS

Static Models

1. **Quality Check:** This is recommended when a new static model is built check 1) check if the grid cells have a low variance in their size; 2) check if the matrix porosity and permeability represent all the measured range; 3) check if the permeability anisotropy is represented; 4) check if the excess permeability matches with the KH from PBUs at the same reference conditions (e.g. above saturation pressure, all referred to at kr@Swi); 5) check if the porosity represents the volumetric estimations; 6) and if the critical stress fractures match the power law correlations.

2. **Selection of Reference Permeability:** It is recommended to use gas permeability at the initial pressure instead of the absolute (Klinkemberg) permeability, in order to avoid underestimating the flow capacity. This will have an impact on either this or further models that consider the geomechanical effect.

3. **Excess Permeability:** KH multipliers should be carefully reviewed as this is the main source for the construction of the natural fracture model. KH from logs has a big impact on KH multipliers as it defines the base for the multiplier, see Figure 2-27.

4. **Permeability and Pressure:** The relationship between the KH from PBU's and the KH Multiplier with regards to the number of opened critically stressed fractures and their orientation interpreted from image logs, could be affected by changes in the reservoir bottom-hole pressures. It is recommended to do an additional work in order to compare these variables at the same pressure and avoid misleading conclusions.

5. **Fracture Spacing:** A specialized geological software tool is required to reduce the uncertainty of the number of fractures per cell. This will greatly affect the fracture spacing, which in turn will affect the porosity, the transfer capacity between the matrix and the fracture, and the fracture's aperture (and fractures' permeability).

6. **Vertical permeability** should be carefully implemented in either the dual porosity/dual permeability model or in the single porosity model. This variable is generally the last parameter to take into account, but it has been shown that gravity drainage has a big effect on the liquid drop out. Without taking this parameter into account, big differences in gas injection recovery estimates can result, since the model could underestimate the gas injection sweep due to a high matrix vertical permeability, underestimating the gas segregation going to the top of the structure due to a high fracture vertical permeability.

7. **Anisotropy:** As interference tests between wells seem not to be a liable option due to high response times between wells, a better understanding of the anisotropy by using several other techniques should be used (e.g fractures' orientation of main fracture families that contribute to the flow, combined with tracer, compositional analysis and

surveillance, articulating this information with sonic logs using the S and P velocities relationships).

One of the assumptions for the model that was developed in this work was to use a constant anisotropy factor. With a specialized software tool, it would be possible to use the orientation, dip and dip azimuth of fractures to implement a variable anisotropy factor for each reservoir in each of the grid cells. It also must be considered that there is not enough information (e.g interference tests) so as to fully validate this possible improvement. This parameter should be included within the single porosity models so as to improve their physical representation of the displacement process inside the reservoir.

8. **Drivers:** The assumption that fracture permeability only depends on the curvature per sheet (the driver mechanism for fracture generation is mechanical) could be refined by including the petrophysical variations with depth and also the rock characterization, in order to include not only the classical porosity-permeability-capillary pressure relationship with the hydraulic diffusion but also including some geomechanical input such as the brittleness (the lithological driver mechanism for fractures, or by coming up with a correlation that includes the young modulus and/or the Poisson ratio, and stress variation across the field), see the Section 2.8.1. Additionally, it is recommended to estimate a curvature index to relate it with the number of fractures and with the fracture permeability.

9. **Geometric Description.** It is recommended to estimate the fractal dimension for each sheet and each reservoir, and to understand the fluid flow dimension. This information will help to fill the gaps where no information is available at different spatial scales (e.g when estimating the fracture properties affected by fracture geometry), which will impact the modeling and prediction at different scales.

10. **Fracture Porosity:** Even when estimated from petrology, PBU analysis and other reports, fracture porosity is in the order of 0.3% to 1%. It is suggested that fracture compressibility should be checked, because micro-fractures at reservoir conditions could be different, resulting in different porosity ranges. Theoretical fracture porosity estimations suggest that fracture porosity could be as low as 0.01%.

Grids

1. **Grid Cell Size:** In case new dual porosity and dual permeability models are built, it is recommended to have a low variance in the grid cell distribution, as it will directly affect the estimation of the shape factor and the fluid flow in the model.

2. **Vertical Grid Size:** Because of the fact that the highest uncertainty is related to the structure, and because of the time required to build new models, a suggested way to build Piedemonte models is to make them vertically refined, so as to easily coarsen them later, for a quick evaluation, and leave a space to shorten or expand the main faults. This is especially important when modeling the liquid that is affected by gravity drainage.

3. **Resolution:** Notice that coarse models are highly useful to populate the dual porosity/dual permeability full field models, and should only be used for that purpose. Special and high resolution grids would have a different purpose; for example, the ones used to describe near wellbore modeling and its population are different, as some cells would only be matrix, and others would have both matrix and fractures.

Petrophysics

1. **Cores:** It is recommended to improve the data sampling from rock types that show production, as some of the data samples (e.g porosity and permeability) are concentrated and skewed to a lower porosity and permeability. There are other several more economic techniques (e.g side wall coring) that capture a better range for these important parameters. They impact the static and dynamic models and the consistency with material balances.

2. **Logs:** Detailed comparisons of resistivity logs, PLT (flow and temperature), image logs, sonic and VSP (well geophysics) with the critical stress fractures could be done for having a better identification and characterization of fractures.

3. **Tomography:** it is recommended to perform a tomography and digital 3D images to understand the impact that micro-fractures have on matrix flow behavior for Piedemonte Fields. This information will help refine the type of fluid flow and its impact on the evolution of saturation with pressure for matrix blocks. It could be possible to create a micro fracture index (e.g number micro fracture/volume).

4. **Micro-Fractures Identification.** Porosity and permeability Cross plots, Capillary pressures, and micro-graphs could help identify possible trends for the matrix and matrix having micro-fractures.

5. **Rock Types:** Future models should include a petrophysical model that links the maximum gas trap saturation and other end points with the rock type. The sensitivity analysis performed to this variable (Sgt) suggests that this parameter will make a huge difference in improving history matching, and will impact the predictions, especially at the end of the production life of wells, in case they are affected in the blow down scenario.

6. **Relative Permeability:** Further simulations should include the rate dependent factor in the relative permeability in order to improve the phenomenological behavior of fluid flow in porous media, in the short and medium term. Additionally it would be important to explore new correlations that included changes in the relative permeability due to changes in the viscosity and densities as it was presented in Figure 3-36 and Figure 3-38.

7. **SCAL:** when performing EOR/EGR studies, there is a close relationship between interfacial tension, wettability (contact angles) and residual oil saturation. It is recommended to have a close look and get measurements of these values to obtain better expected sweep and recovery values for the fields. Also, further relative permeability data require a clearer report on the rates used in the displacement.

8. **Molecular Diffusion:** Further simulations should include molecular diffusion studies in order to improve the phenomenological behavior of fluid flow in porous media in the long term. Nitrogen diffusion highly depends on pressure, and the recovery will be affected in case of an acceleration or delay on this application, as time will be related to pressure depletion of the reservoirs (higher depletion causes a higher diffusion, which in turn gives lower breakthrough times, resulting in earlier gas sales contamination).

Geomechanics

1. **Permeability Changes:** one of the aspects that was investigated in this work was the recovery factor. Another important aspect that may play a considerable impact is the damage performed by different mechanisms, and one of them is the consideration of the geomechanical impact on fractures' permeability due to different pressure depletion scenarios.

2. **Activation or deactivation of Natural Fractures.** The incorporation of geomechanics within the dynamic modeling could capture in a much more appropriate way the activation or deactivation of fractures that affects fluid flow in either history or prediction scenarios.

3. **Fracture and Micro-fracture Compressibility**. It is recommended to estimate these parameters, which will impact the prediction of fracture and matrix behavior.

4. **The linkage with geology and Petrophysics:** Identifying the correlation among the Young modulus, Poisson ratio, and relative permeability end points will improve the knowledge and predictability of rock behavior and its impact on oil and gas production.

Fluids

1. **Compositional Surveillance:** It is recommended that each well should have a gas and liquid chromatography study. This will help in different ways: 1) Increase the resolution as to better understand the natural fracture system; 2) it could be used as refined data to calibrate the static models; 3) it can monitor nitrogen evolution with time for reservoir management purposes; and 4) it can be used to match transport models that will close the loop in the reservoir simulation modeling approach (flow and transport modeling).

2. **Micro fluid Mechanics:** Knudsen threshold to define the limit for slip flow and continuous flow are reported to be either at 0.01 **[Chapter 1, 19]** or 0.001. These changes in a great measure the assumptions made for the matrix fluid flow, and will highly impact the apparent permeability, especially at the end of the reservoir production life. This should be considered for later and more specialized works.

Well Modeling

1. **Wellbore modeling:** Vertical lift performance tables were used in this study. It is recommended to discretize the tubing and to use a correlation that allows the reservoir simulation model to manage the changes in the evolution of gas rate without restrictions.

Reservoir Engineering

1. **Screening Criteria.** The first step in EOR and EGR evaluation is to perform a screening diagnosis. All proposed methodologies include the heterogeneity factor as estimated in Section 2.6.3.3. This approach does not capture the reservoir's anisotropy, which could play an important role in fluid flow behavior. It is recommended to include this basic estimation in order to identify possible channeling effects, and understand if recoverable oil and gas volumes could be affected by this parameter.

2. **Micro-fracture Modeling:** An option to represent micro-fractures in a full field model is by developing an analytical model that represents the increase in flow capacity and gravity drainage inside the matrix. An approximation used for this study was performing a sensitivity analysis to the matrix vertical permeability.

3. **Transmissibly multipliers:** Conventional reservoir simulation models do not capture nowadays slip flow with compositional fluids. An approach to handle this fluid flow mechanism is by estimating transmissibility multipliers that depend on the slip flow permeability, which in turn depends on fluid composition and pressure.

4. **Gravity Drainage:** further evaluations considering the impact of the structure's dip should include pseudo capillary pressures and pseudo relative permeabilities. Also, the reservoir simulation gridding effect should be considered in high dip structural sections, for example in Floreña's flank.

5. **Transport Modeling:** This work only considers flow modeling, but could be improved by including transport modeling, which includes molecular diffusion of tracers and injected nitrogen (e.g hydrocarbon gas and oil contamination). Huff and Puff models and experiments could help understand and partially differentiate advective flow effects (e.g channeling governed by viscosity forces) and diffusive flow (e.g diffusion governed by molecular forces).

6. **Practical Purpose Model.** By just activating the sheet or reservoir that wants to be studied, significant CPU time reduction can be achieved in a DPDP model. So, when evaluating day-to-day depletion plans for new wells, and workover options like stimulation, lateral drilling, etc., it is also possible to activate the region that surrounds, following a drainage area analysis.

7. **Sensitivities.** Additional sensitivity analysis can be achieved to understand the model by testing the behavior that relative permeabilities have, and the change on end points (e.g Sor) with different N_2 and CO_2 conditions, below and above miscible conditions (a combination of the sensitivity analysis performed in Section 3.7.2 and 3.7.5).

Nitrogen Injection

1. **Advanced PVT Experiments:** PVT Laboratory tests must be done to tune the EoS with N_2 injection, as this uncertainty greatly affects decisions like on how to operate the field, the amount of gas required for an optimal development, and also in quantifying the ultimate oil recovery. Otherwise, a big risk must be accepted with limited manageability options. Multi-contact tests are recommended (backward and forward).

2. **Conformance:** One of the main conclusions from this work is to mix pure nitrogen either with lean gas or with CO_2. There is a third option, and is using chemical EOR alternatives (e.g foams).

3. **Temperature Gradients:** Some sheets and reservoirs have a constant temperature gradient. This could generate slight variations in nitrogen miscibility as it is dependent on temperature.

4. **Reservoir Model Usage.** Improvements on this model can be used to predict oil, gas and water volumes; understand compositional phenomena and their causes; adequately optimize the injection points and resources; and identify nitrogen contaminated reservoir regions.

5. **Nitrogen Optimization:** it is recommended to perform further sensitivity studies to optimize the design when either foam injection, buffer CO_2 injection, or NGL/LPG production are considered, which were not reported in this document.

6. **PBU interpretations:** When interpreting a natural fracture, it is highly recommended to check the interpretation done for storage coefficients, in order to adequately measure them; otherwise, fracture porosity could be highly overestimated, as this parameter is related to fracture spacing. In other words, inter-porosity and storage coefficients from PBU interpretations that are used for natural fracture systems, must be quality controlled (e.g theoretical graphs of Shape factors vs. inter-porosity coefficients with different excess permeability values) using theoretical values for the excess permeability (χ) and the apparent fracture apertures (e_0) in order to avoid misinterpretations.

APPENDIX A. Compositional and Dual Porosity/Dual Permeability Equations

A.1 Deduction for a Compositional Multiphase flow in a Natural Fracture System.

A.1.1 For the hydrocarbon System

The fundamental flow equation for a compositional model in a Cartesian System

n_{io}, n_{ig} : Number of moles of component i in the oil and gas phase[60].

n_o, n_g : Number of total moles in the oil and gas phase, respectively.

$x_i = \frac{n_{io}}{n_o}$, $y_i = \frac{n_{ig}}{n_g}$: Molar fraction of component i in the oil and gas phase.

$M_o = \frac{m_o}{n_o}$, $M_g = \frac{m_g}{n_g}$: Molecular weight for oil and gas.

$\rho_o = \frac{m_o}{V_o}$, $\rho_g = \frac{m_g}{V_g}$: Oil and gas densities, respectively.

Apparent and "real" velocities

$v_o = \frac{V_o}{A\Delta t}$, $v_g = \frac{V_g}{A\Delta t}$: Darcy velocity is the apparent velocity of oil and gas phases.

$u_o = \frac{V_o}{A\phi\Delta t}$, $u_g = \frac{V_g}{A\phi\Delta t}$: Volumetric "real" velocity for oil and gas phases.

The moles of component i in the oil and gas phase per unit of area and time is defined as follows:

[60] **Mole:** is the mass of substance equals to its molecular weight in pounds, grams, kilograms or other mass units. e.g the molecular weight of ethane is 30.68, so 1 pound mole of ethane are 30.068 pounds of ethane, 1 gram mole of ethane are 30.068 grams of ethane.

For oil: $\dfrac{i\ Moles\ in\ the\ oil}{Area\cdot\Delta t}=\dfrac{n_{io}}{A\Delta t}=\dfrac{n_{io}}{n_o}\dfrac{1}{\dfrac{m_o}{n_o}}\dfrac{m_o}{V_o}\dfrac{V_o}{A\Delta t}=x_i\dfrac{\rho_o}{M_o}\phi u_o$, A1.1-1.

For gas: $\dfrac{i\ Moles\ in\ the\ gas}{Area\cdot\Delta t}=\dfrac{n_{ig}}{A\Delta t}=\dfrac{n_{ig}}{n_g}\dfrac{1}{\dfrac{m_g}{n_g}}\dfrac{m_g}{V_g}\dfrac{V_g}{A\Delta t}=y_i\dfrac{\rho_g}{M_g}\phi u_g$ A1.1-2.

- **Molar balance in the matrix and fracture**

Assuming a closed system without chemical reactions, the total number of moles for each component remains constant.

$$\sum_{\beta=1}^{\theta}n_{i\beta}=0, i=1,2,...,n_c \quad \text{A1.1-3.}$$

Performing a molar balance in an infinitesimal element with volume $V_T=\Delta x\Delta y\Delta z$:

$$\begin{bmatrix}i\ moles\ into\\ the\ element\ x\end{bmatrix}_{\Delta t}-\begin{bmatrix}i\ moles\ out\ of\\ the\ element\ x+\Delta x\end{bmatrix}_{\Delta t}\pm\begin{bmatrix}i\ moles\\ Source\ and\ Sink\end{bmatrix}_{\Delta t}=\begin{bmatrix}i\ moles\\ Acumulated\\ inside\ the\ element\end{bmatrix}_{\Delta t} \quad \text{A1.1-4.}$$

Eq. A1.1-4 could also be understood as:

$$[i\ moles\ in]_{\Delta t}-[i\ moles\ out]_{\Delta t}\pm\begin{bmatrix}i\ moles\\ produced/injected\end{bmatrix}_{\Delta t}=\begin{bmatrix}i\ moles\\ Acumulated\end{bmatrix}_{\Delta t} \quad \text{A1.1-5.}$$

The moles of *i* that go into the element *x* are the input of i moles of oil, gas and water in the 3 flow directions

$$\begin{bmatrix}Moles\ que\\ entran\ de\ i\end{bmatrix}_{\Delta t}=\left(x_i\frac{\rho_o}{M_o}\phi u_{ox}\right)\Delta y\Delta z\Delta t+\left(x_i\frac{\rho_o}{M_o}\phi u_{oy}\right)\Delta x\Delta z\Delta t+\left(x_i\frac{\rho_o}{M_o}\phi u_{oz}\right)\Delta x\Delta y\Delta t+$$

$$\left(y_i\frac{\rho_g}{M_g}\phi u_{gx}\right)\Delta y\Delta z\Delta t+\left(y_i\frac{\rho_g}{M_g}\phi u_{gy}\right)\Delta x\Delta z\Delta t+\left(y_i\frac{\rho_g}{M_g}\phi u_{gz}\right)\Delta x\Delta y\Delta t \quad \text{A1.1-6.}$$

The output of i moles that go out of the element in a specific interval of time are the same moles that go into the volume plus an incremental number of moles passing from point x to $x+\Delta x$.

$$\left[\begin{matrix}Moles\,que\\ salen\ de\,i\end{matrix}\right]_{\Delta t}=\left[x_{io}\frac{\rho_o}{M_o}\phi u_{ox}+\Delta\left(x_i\frac{\rho_o}{M_o}\phi u_{ox}\right)\right]\Delta y\Delta z\Delta t+\left[\left(x_i\frac{\rho_o}{M_o}\phi u_{oy}\right)+\Delta\left(x_i\frac{\rho_o}{M_o}\phi u_{oy}\right)\right]\Delta x\Delta z\Delta t$$

$$+\left[\left(x_i\frac{\rho_o}{M_o}\phi u_{oz}\right)+\Delta\left(x_i\frac{\rho_o}{M_o}\phi u_{oz}\right)\right]\Delta x\Delta y\Delta t+ \qquad \text{A1.1-7.}$$

$$+\left[y_i\frac{\rho_o}{M_o}\phi u_{ox}+\Delta\left(y_i\frac{\rho_o}{M_o}\phi u_{ox}\right)\right]\Delta y\Delta z\Delta t+\left[\left(y_i\frac{\rho_o}{M_o}\phi u_{oy}\right)+\Delta\left(y_i\frac{\rho_o}{M_o}\phi u_{oy}\right)\right]\Delta x\Delta z\Delta t$$

$$+\left(y_i\frac{\rho_g}{M_g}\phi u_{gz}+\Delta\left(y_i\frac{\rho_g}{M_g}\phi u_{gz}\right)\right)\Delta x\Delta y\Delta t \qquad \text{A1.1-8.}$$

Defining the hydrocarbon flow as $\tilde{q}_{hci}$:

$$\tilde{q}_{hci}=\frac{Moles\ del\,componente\ i\ que\ entran\ ó\ salen\ por\ fuentes\ ó\,sumideros}{Volumen\ del\ \ diferencial\,x\,tiempo} \qquad \text{A1.1-9.}$$

$$\tilde{q}_{hci}=\tilde{q}_{oi}+\tilde{q}_{gi} \qquad \text{A1.1-10.}$$

The subscript *hc* refers to hydrocarbon, which implies that oil and gas could have some non-hydrocarbons that belong to either oil or gas hydrocarbon phases.

Then:

$$Moles\,de\ i\ \ que\,entran\ ó\,salen\ por\ \ fuentes\,ó\,sumideros=\tilde{q}_{hci}\Delta x\Delta y\Delta z\Delta t \qquad \text{A1.1-11.}$$

The accumulation of moles of i can be expressed as:

$$\left[\begin{matrix}Acumulación\,ó\,agotamiento\\ de\,moles\,de\ i\end{matrix}\right]_{\Delta t}=\left[Moles\,de\ i\right]_{t+\Delta t}-\left[Moles\,de\ i\right]_t \qquad \text{A1.1-12.}$$

$$Moles\,del\,componente\ i\,en\,el\ petróleo=x_i\frac{\rho_o}{M_o}S_oV_p=x_i\frac{\rho_o}{M_o}S_o\left(\phi\Delta x\Delta y\Delta z\right) \qquad \text{A1.1-13.}$$

$$Moles\ \ del\,componente\ i\ \ en\ el\ gas=y_i\frac{\rho_g}{M_g}S_gV_p=y_i\frac{\rho_g}{M_g}S_g\left(\phi\Delta x\Delta y\Delta z\right) \qquad \text{A1.1-14.}$$

$$\begin{bmatrix} Acumulación\,ó \\ agotamiento \\ de\,moles\,de\ i \end{bmatrix}_{\Delta t} = \left(x_i \frac{\rho_o}{M_o} \phi S_o \Delta x \Delta y \Delta z + y_i \frac{\rho_g}{M_g} \phi S_g \Delta x \Delta y \Delta z \right)_{t+\Delta t}$$

$$- \left(x_i \frac{\rho_o}{M_o} \phi S_o \Delta x \Delta y \Delta z + y_i \frac{\rho_g}{M_g} \phi S_g \Delta x \Delta y \Delta z \right)_t$$

$$- \Delta \left(x_i \frac{\rho_o}{M_o} \phi u_{ox} \right) \Delta y \Delta z \Delta t - \Delta \left(x_i \frac{\rho_o}{M_o} \phi u_{oy} \right) \Delta x \Delta z \Delta t - \Delta \left(x_i \frac{\rho_o}{M_o} \phi u_{oz} \right) \Delta x \Delta y \Delta t$$

$$- \Delta \left(y_i \frac{\rho_g}{M_g} \phi u_{gx} \right) \Delta y \Delta z \Delta t - \Delta \left(y_i \frac{\rho_g}{M_g} \phi u_{gy} \right) \Delta x \Delta z \Delta t - \Delta \left(y_i \frac{\rho_g}{M_g} \phi u_{gz} \right) \Delta x \Delta y \Delta t = \tilde{q}_i \Delta x \Delta y \Delta z \Delta t +$$

$$\left(x_i \frac{\rho_o}{M_o} \phi S_o \Delta x \Delta y \Delta z + y_i \frac{\rho_g}{M_g} \phi S_g \Delta x \Delta y \Delta z \right)_{t+\Delta t} - \left(x_i \frac{\rho_o}{M_o} \phi S_o \Delta x \Delta y \Delta z + y_i \frac{\rho_g}{M_g} \phi S_g \Delta x \Delta y \Delta z \right)_t \quad \text{A1.1-15.}$$

Diving the previous equation by $\Delta x \Delta y \Delta z \Delta t$ and taking the limit $\Delta' s \to 0$, we now have the differential equation

$$- \frac{\partial}{\partial x} \left(x_i \frac{\rho_o}{M_o} \phi u_{ox} \right) - \frac{\partial}{\partial y} \left(x_i \frac{\rho_o}{M_o} \phi u_{oy} \right) - \frac{\partial}{\partial z} \left(x_i \frac{\rho_o}{M_o} \phi u_{oz} \right)$$

$$- \frac{\partial}{\partial x} \left(y_i \frac{\rho_g}{M_g} \phi u_{gx} \right) - \frac{\partial}{\partial y} \left(y_i \frac{\rho_g}{M_g} \phi u_{gy} \right) - \frac{\partial}{\partial z} \left(y_i \frac{\rho_g}{M_g} \phi u_{gz} \right) = \tilde{q}_{hci} +$$

$$\frac{\partial}{\partial t} \left(x_i \frac{\rho_o}{M_o} \phi S_o + y_i \frac{\rho_g}{M_g} \phi S_g \right) \quad \text{A1.1-16.}$$

Reorganizing the previous equations

$$- \frac{\partial}{\partial x} \left(x_i \frac{\rho_o}{M_o} \phi u_{ox} + y_i \frac{\rho_g}{M_g} \phi u_{gx} \right) - \frac{\partial}{\partial y} \left(x_i \frac{\rho_o}{M_o} \phi u_{oy} + y_i \frac{\rho_g}{M_g} \phi u_{gy} \right) - \frac{\partial}{\partial z} \left(x_i \frac{\rho_o}{M_o} \phi u_{oz} + y_i \frac{\rho_g}{M_g} \phi u_{gz} \right)$$

$$\frac{\partial}{\partial t} \left(x_i \frac{\rho_o}{M_o} \phi S_o + y_i \frac{\rho_g}{M_g} \phi S_g \right) \quad \text{A1.1-17.}$$

- **Conservation of momentum – Darcy Law**

The volumetric velocity for oil and gas phases is given by:

$$v_o = \frac{V_o}{A\Delta t} = \phi u_o \qquad \text{A1.1-18.}$$

Then, using the relationship between the apparent velocity and the volumetric velocity (Darcy law equation):

$$v_{ox} = \phi u_{ox} = -\frac{k_{rox}k_x}{\mu_o}\frac{\partial \Phi_o}{\partial x};\ v_{oy} = \phi u_{oy} = -\frac{k_{roy}k_y}{\mu_o}\frac{\partial \Phi_o}{\partial y};\ v_{oz} = \phi u_{oz} = -\frac{k_{roz}k_z}{\mu_o}\frac{\partial \Phi_o}{\partial z} \qquad \text{A1.1-19.}$$

$$v_{gx} = \phi u_{gx} = -\frac{k_{rgx}k_x}{\mu_g}\frac{\partial \Phi_g}{\partial x};\ v_{gy} = \phi u_{gy} = -\frac{k_{rgy}k_y}{\mu_g}\frac{\partial \Phi_g}{\partial y};\ v_{gz} = \phi u_{gz} = -\frac{k_{rgz}k_z}{\mu_g}\frac{\partial \Phi_g}{\partial z} \qquad \text{A1.1-20.}$$

Replacing Eq. A.1.1-19 and Eq. A.1.1-20 into Eq. A.1.1-17.

$$-\frac{\partial}{\partial x}\left(x_i \frac{\rho_o}{M_o}\frac{k_{ro}k_x}{\mu_o}\frac{\partial \Phi_o}{\partial x} + y_i \frac{\rho_g}{M_g}\frac{k_{rg}k_x}{\mu_g}\frac{\partial \Phi_g}{\partial x}\right)$$

$$-\frac{\partial}{\partial y}\left(x_i \frac{\rho_o}{M_o}\frac{k_{ro}k_y}{\mu_o}\frac{\partial \Phi_o}{\partial y} + y_i \frac{\rho_g}{M_g}\frac{k_{rg}k_y}{\mu_g}\frac{\partial \Phi_g}{\partial y}\right)$$

$$-\frac{\partial}{\partial z}\left(x_i \frac{\rho_o}{M_o}\frac{k_{ro}k_z}{\mu_o}\frac{\partial \Phi_o}{\partial z} + y_i \frac{\rho_g}{M_g}\frac{k_{ro}k_z}{\mu_o}\frac{\partial \Phi_o}{\partial z}\right)$$

$$\frac{\partial}{\partial t}\left(\phi\left(x_i \frac{\rho_o}{M_o}S_o + y_i \frac{\rho_g}{M_g}S_g\right)\right) \qquad \text{A1.1-21.}$$

The previous equation is the fluids' diffusivity equation. It is important to highlight that this diffusivity is related to the hydraulic diffusivity.

$$k_o = k_{ox}\cdot\vec{i} + k_{oy}\cdot\vec{j} + k_{oz}\cdot\vec{k} \qquad \text{A1.1-22.}$$

Reorganizing the diffusivity equation

$$\nabla\cdot\left(x_{io}\frac{\rho_o}{M_o}\frac{k_o}{\mu_o}\nabla\Phi_o\right) + \nabla\cdot\left(y_i\frac{\rho_g}{M_g}\frac{k_g}{\mu_g}\nabla\Phi_g\right) = \tilde{q}_{hci} + \frac{\partial}{\partial t}\left(\phi\left(x_i\frac{\rho_o}{M_o}S_o + y_i\frac{\rho_g}{M_g}S_g\right)\right) \qquad \text{A1.1-23.}$$

The flow potential of phase α is defined as the sum of the kinetic potentials (Φ_α) given by the hydraulic pressure (P_α) and the gravitational potential $\left(\rho_\alpha \frac{g}{g_c} D\right)$.

$$\Phi_o = P_o - \rho_o \frac{g}{g_c} D, \Phi_o = P_o - \gamma_o D \qquad \text{A1.1-24.}$$

$$\Phi_g = P_g - \rho_g \frac{g}{g_c} D, \ \Phi_g = P_g - \gamma_g D \qquad \text{A1.1-25.}$$

Assuming $\frac{g}{g_c} = 1$, g is the local gravitational constant and g_c is the universal gravitational constant.

Using the definition of potential in the vertical direction for oil and gas phases:

$$\frac{\partial \Phi_o}{\partial z} = \frac{\partial P_o}{\partial z} - \frac{g}{g_c} \frac{\partial (\rho_o D)}{\partial z} \rightarrow \frac{\partial \Phi_o}{\partial z} = \frac{\partial P_o}{\partial z} - \frac{g}{g_c} \left[\rho_o \frac{\partial D}{\partial z} + D \frac{\partial \rho_o}{\partial z} \right] \qquad \text{A1.1-26.}$$

$$\frac{\partial \Phi_g}{\partial z} = \frac{\partial P_g}{\partial z} - \frac{g}{g_c} \frac{\partial (\rho_g D)}{\partial z} \rightarrow \frac{\partial \Phi_g}{\partial z} = \frac{\partial P_g}{\partial z} - \frac{g}{g_c} \left[\rho_g \frac{\partial D}{\partial z} + D \frac{\partial \rho_g}{\partial z} \right] \qquad \text{A1.1-27.}$$

$$P_g = P_o + P_{cog} \ \rightarrow \Phi_g = P_o + P_{cog} - \gamma_g h \qquad \text{A1.1-28.}$$

Replacing

$$\frac{\partial}{\partial x}\left(\frac{x_i \rho_o}{M_o} \frac{k_x k_{ro}}{\mu_o} \frac{\partial (P_o - \gamma_o D)}{\partial x} + \frac{y_i \rho_g}{M_g} \frac{k_x k_{rg}}{\mu_g} \frac{\partial (P_g - \gamma_g D)}{\partial x} \right)$$

$$+ \frac{\partial}{\partial y}\left(\frac{x_i \rho_o}{M_o} \frac{k_y k_{ro}}{\mu_o} \frac{\partial (P_o - \gamma_o D)}{\partial y} + \frac{y_i \rho_g}{M_g} \frac{k_y k_{rg}}{\mu_g} \frac{\partial (P_g - \gamma_g D)}{\partial y} \right)$$

$$+ \frac{\partial}{\partial z}\left(\frac{x_i \rho_o}{M_o} \frac{k_z k_{ro}}{\mu_o} \frac{\partial (P_o - \gamma_o D)}{\partial z} + \frac{y_i \rho_g}{M_g} \frac{k_z k_{rg}}{\mu_g} \frac{\partial (P_g - \gamma_g D)}{\partial z} \right)$$

$$= \tilde{q}_{hci} + \frac{\partial}{\partial t} \phi \left(\frac{x_{io} \rho_o S_o}{M_o} + \frac{y_{io} \rho_g S_g}{M_g} \right) \qquad \text{A1.1-29.}$$

Developing the equations using P_o as a primary variable:

$$\frac{\partial}{\partial x}\left(\frac{x_i\rho_o}{M_o}\frac{k_x k_{ro}}{\mu_o}\frac{\partial\left(P_o-\gamma_o D\right)}{\partial x}+\frac{y_i\rho_g}{M_g}\frac{k_x k_{rg}}{\mu_g}\frac{\partial\left(P_o+P_{cog}-\gamma_g D\right)}{\partial x}\right)$$

$$+\frac{\partial}{\partial y}\left(\frac{x_i\rho_o}{M_o}\frac{k_y k_{ro}}{\mu_o}\frac{\partial\left(P_o-\gamma_o D\right)}{\partial y}+\frac{y_i\rho_g}{M_g}\frac{k_y k_{rg}}{\mu_g}\frac{\partial\left(P_o+P_{cog}-\gamma_g D\right)}{\partial y}\right)$$

$$+\frac{\partial}{\partial z}\left(\frac{x_i\rho_o}{M_o}\frac{k_z k_{ro}}{\mu_o}\frac{\partial\left(P_o-\gamma_o D\right)}{\partial z}+\frac{y_i\rho_g}{M_g}\frac{k_z k_{rg}}{\mu_g}\frac{\partial\left(P_o+P_{cog}-\gamma_g D\right)}{\partial z}\right)$$

$$=\tilde{q}_{hci}+\frac{\partial}{\partial t}\phi\left(Z_i\left(\frac{\rho_o S_o}{M_o}+\frac{\rho_g S_g}{M_g}\right)\right) \qquad \text{A1.1-30.}$$

$$=\tilde{q}_{hci}+\frac{\partial\left(\phi\Gamma Z_i\right)}{\partial t} \qquad \text{A1.1-31.}$$

Where Γ is defined as:

$$\Gamma=\frac{\rho_o S_o}{M_o}+\frac{\rho_g S_g}{M_g} \qquad \text{A1.1-32.}$$

Reorganizing the internal term

$$\frac{x_{io}\rho_o}{M_o}\frac{k_x k_{ro}}{\mu_o}\frac{\partial P_o}{\partial x}-\frac{x_{io}\rho_o}{M_o}\frac{k_x k_{ro}}{\mu_o}\frac{\partial\left(\gamma_o D\right)}{\partial x}$$

$$\frac{y_{ig}\rho_g}{M_g}\frac{k_x k_{rg}}{\mu_g}\frac{\partial P_o}{\partial x}+\frac{y_{ig}\rho_g}{M_g}\frac{k_x k_{rg}}{\mu_g}\frac{\partial P_{cog}}{\partial x}-\frac{y_{ig}\rho_g}{M_g}\frac{k_x k_{rg}}{\mu_g}\frac{\partial\left(\gamma_g D\right)}{\partial x} \qquad \text{A1.1-33.}$$

Re-organizing the previous equation

$$\frac{\partial}{\partial x}\left(\left(\frac{x_i\rho_o}{M_o}\frac{k_x k_{ro}}{\mu_o}+\frac{y_i\rho_g}{M_g}\frac{k_x k_{rg}}{\mu_g}\right)\frac{\partial P_o}{\partial x}+\frac{y_i\rho_g}{M_g}\frac{k_x k_{rg}}{\mu_g}\frac{\partial P_{cog}}{\partial x}\right.$$

$$\left.-\frac{x_i\rho_o}{M_o}\frac{k_x k_{ro}}{\mu_o}\frac{\partial\left(\gamma_o D\right)}{\partial x}-\frac{y_i\rho_g}{M_g}\frac{k_x k_{rg}}{\mu_g}\frac{\partial\left(\gamma_g D\right)}{\partial x}\right)$$

$$+\frac{\partial}{\partial y}\left(\left(\frac{x_i\rho_o}{M_o}\frac{k_y k_{ro}}{\mu_o}+\frac{y_i\rho_g}{M_g}\frac{k_y k_{rg}}{\mu_g}\right)\frac{\partial P_o}{\partial y}+\frac{y_i\rho_g}{M_g}\frac{k_y k_{rg}}{\mu_g}\frac{\partial P_{cog}}{\partial y}\right.$$

$$-\frac{x_i\rho_o}{M_o}\frac{k_y k_{ro}}{\mu_o}\frac{\partial(\gamma_o D)}{\partial y}-\frac{y_i\rho_g}{M_g}\frac{k_y k_{rg}}{\mu_g}\frac{\partial(\gamma_g D)}{\partial y}\Bigg)$$

$$+\frac{\partial}{\partial z}\Bigg(\Bigg(\frac{x_i\rho_o}{M_o}\frac{k_z k_{ro}}{\mu_o}+\frac{y_i\rho_g}{M_g}\frac{k_z k_{rg}}{\mu_g}\Bigg)\frac{\partial P_o}{\partial z}+\frac{y_i\rho_g}{M_g}\frac{k_z k_{rg}}{\mu_g}\frac{\partial P_{cog}}{\partial z}$$

$$-\frac{x_i\rho_o}{M_o}\frac{k_z k_{ro}}{\mu_o}\frac{\partial(\gamma_o D)}{\partial z}-\frac{y_i\rho_g}{M_g}\frac{k_z k_{rg}}{\mu_g}\frac{\partial(\gamma_g D)}{\partial z}\Bigg)$$

$$=\tilde{q}_{hci}+\frac{\partial(\phi\Gamma Z_i)}{\partial t} \qquad \text{A1.1-34.}$$

Where the compositional mobility in each direction is defined as:

$$\lambda_{cx}=\frac{x_{io}\rho_o}{M_o}\frac{k_x k_{ro}}{\mu_o}+\frac{y_{ig}\rho_g}{M_g}\frac{k_x k_{rg}}{\mu_g} \qquad \text{A1.1-35.}$$

$$\lambda_{cy}=\frac{x_{io}\rho_o}{M_o}\frac{k_y k_{ro}}{\mu_o}+\frac{y_{ig}\rho_g}{M_g}\frac{k_y k_{rg}}{\mu_g} \qquad \text{A1.1-36.}$$

$$\lambda_{cz}=\frac{x_{io}\rho_o}{M_o}\frac{k_z k_{ro}}{\mu_o}+\frac{y_{ig}\rho_g}{M_g}\frac{k_z k_{rg}}{\mu_g} \qquad \text{A1.1-37.}$$

Re-organizing

$$\frac{\partial}{\partial x}\Bigg((\lambda_{cx})\frac{\partial P_o}{\partial x}+\Bigg(\frac{y_i\rho_g}{M_g}\frac{k_x k_{rg}}{\mu_g}\frac{\partial P_{cg,o}}{\partial x}\Bigg)-\Bigg(\frac{x_i\rho_o}{M_o}\frac{k_x k_{ro}}{\mu_o}\frac{\partial(\gamma_o D)}{\partial x}+\frac{y_i\rho_g}{M_g}\frac{k_x k_{rg}}{\mu_g}\frac{\partial(\gamma_g D)}{\partial x}\Bigg)\Bigg)$$

$$+\frac{\partial}{\partial y}\Bigg((\lambda_{cy})\frac{\partial P_o}{\partial y}+\Bigg(\frac{y_i\rho_g}{M_g}\frac{k_y k_{rg}}{\mu_g}\frac{\partial P_{cg,o}}{\partial y}\Bigg)-\Bigg(\frac{x_i\rho_o}{M_o}\frac{k_y k_{ro}}{\mu_o}\frac{\partial(\gamma_o D)}{\partial y}+\frac{y_i\rho_g}{M_g}\frac{k_y k_{rg}}{\mu_g}\frac{\partial(\gamma_g D)}{\partial y}\Bigg)\Bigg)$$

$$+\frac{\partial}{\partial z}\Bigg((\lambda_{cz})\frac{\partial P_o}{\partial z}+\Bigg(\frac{y_i\rho_g}{M_g}\frac{k_z k_{rg}}{\mu_g}\frac{\partial P_{cg,o}}{\partial z}\Bigg)-\Bigg(\frac{x_i\rho_o}{M_o}\frac{k_z k_{ro}}{\mu_o}\frac{\partial(\gamma_o D)}{\partial z}+\frac{y_i\rho_g}{M_g}\frac{k_z k_{rg}}{\mu_g}\frac{\partial(\gamma_g D)}{\partial z}\Bigg)\Bigg)$$

$$=\tilde{q}_{hci}+\frac{\partial}{\partial t}\phi(Z_i\Gamma) \qquad \text{A1.1-38.}$$

Eliminating the gravitational component in the x and y directions, as it is assumed that it only acts in the vertical direction:

$$\frac{\partial}{\partial x}\left(\left(\lambda_{cx}\right)\frac{\partial P_o}{\partial x}+\left(\frac{y_i\rho_g}{M_g}\frac{k_x k_{rg}}{\mu_g}\frac{\partial P_{cg,o}}{\partial x}\right)\right)+\frac{\partial}{\partial y}\left(\left(\lambda_{cy}\right)\frac{\partial P_o}{\partial y}+\left(\frac{y_i\rho_g}{M_g}\frac{k_y k_{rg}}{\mu_g}\frac{\partial P_{cg,o}}{\partial y}\right)\right)$$

$$+\frac{\partial}{\partial z}\left(\left(\lambda_{cz}\right)\frac{\partial P_o}{\partial z}+\left(\frac{y_i\rho_g}{M_g}\frac{k_z k_{rg}}{\mu_g}\frac{\partial P_{cg,o}}{\partial z}\right)-\left(\frac{x_i\rho_o}{M_o}\frac{k_z k_{ro}}{\mu_o}\frac{\partial\left(\gamma_o D\right)}{\partial z}+\frac{y_i\rho_g}{M_g}\frac{k_z k_{rg}}{\mu_g}\frac{\partial\left(\gamma_g D\right)}{\partial z}\right)\right)$$

$$=\tilde{q}_{hci}+\frac{\partial}{\partial t}\phi\left(Z_i\Gamma\right) \qquad \text{A1.1-39.}$$

Replacing the oil and gas derivatives that included the gravitational component:

$$\frac{\partial}{\partial x}\left(\left(\lambda_{cx}\right)\frac{\partial P_o}{\partial x}+\left(\frac{y_i\rho_g}{M_g}\frac{k_x k_{rg}}{\mu_g}\frac{\partial P_{cg,o}}{\partial x}\right)\right)+\frac{\partial}{\partial y}\left(\left(\lambda_{cy}\right)\frac{\partial P_o}{\partial y}+\left(\frac{y_i\rho_g}{M_g}\frac{k_y k_{rg}}{\mu_g}\frac{\partial P_{cg,o}}{\partial y}\right)\right)$$

$$+\frac{\partial}{\partial z}\left(\left(\lambda_{cz}\right)\frac{\partial P_o}{\partial z}+\left(\frac{y_i\rho_g}{M_g}\frac{k_z k_{rg}}{\mu_g}\frac{\partial P_{cg,o}}{\partial z}\right)\right.$$

$$\left.-\left(\frac{x_i\rho_o}{M_o}\frac{k_z k_{ro}}{\mu_o}g\left[\rho_o\frac{\partial D}{\partial z}+D\frac{\partial\rho_o}{\partial z}\right]+\frac{y_i\rho_g}{M_g}\frac{k_z k_{rg}}{\mu_g}g\left[\rho_g\frac{\partial D}{\partial z}+D\frac{\partial\rho_g}{\partial z}\right]\right)\right)$$

$$=\tilde{q}_{hci}+\frac{\partial}{\partial t}\phi\left(Z_i\Gamma\right) \qquad \text{A1.1-40.}$$

Re-organizing the equation

$$\lambda_c=\lambda_{cx}\cdot\vec{i}+\lambda_{cy}\cdot\vec{j}+\lambda_{cz}\cdot\vec{k} \qquad \text{A1.1-41.}$$

$$K=k_x\cdot\vec{i}+k_y\cdot\vec{j}+k_z\cdot\vec{k} \qquad \text{A1.1-42.}$$

$$\nabla\cdot\left(\left(\lambda_c\right)\nabla P_o+\left(\frac{y_i\rho_g}{M_g}\frac{Kk_{rg}}{\mu_g}\nabla P_{cgo}\right)-\left(\frac{x_i\rho_o\gamma_o}{M_o}\frac{kk_{ro}}{\mu_o}+\frac{y_i\rho_g\gamma_g}{M_g}\frac{kk_{rg}}{\mu_g}\right)\nabla z\right)$$
$$=\tilde{q}_i+\frac{\partial\left(\phi\Gamma Z_i\right)}{\partial t} \qquad \text{A1.1-43.}$$

where

$$\frac{\partial(\phi\Gamma)}{\partial t} = \frac{1}{\Gamma}\frac{\partial\Gamma}{\partial P} + \frac{1}{\phi}\frac{\partial\phi}{\partial P} \qquad \text{A1.1-44.}$$

$$c_{tf} = \frac{1}{\Gamma}\frac{\partial\Gamma}{\partial P} \qquad \text{A1.1-45.}$$

$$c_{vp} = \frac{1}{\phi}\frac{\partial\phi}{\partial P} \qquad \text{A1.1-46.}$$

Re-organizing

$$\nabla\cdot\left(\lambda_c\nabla P_o + \left(\frac{y_i\rho_g}{M_g}\frac{Kk_{rg}}{\mu_g}\nabla P_{cgo}\right) - \left(\frac{x_i\rho_o\gamma_o}{M_o}\frac{kk_{ro}}{\mu_o} + \frac{y_i\rho_g\gamma_g}{M_g}\frac{kk_{rg}}{\mu_g}\right)\nabla z\right)$$

$$= \tilde{q}_{hci} + \left(\phi\Gamma c_{tf} + \phi\Gamma c_{vp}\right)\frac{\partial P}{\partial t} \qquad \text{A1.1-47.}$$

Re-organizing and assuming that there is no porosity change with pressure ($c_{vp} = 0$)

$$\nabla\cdot\left(\lambda_c\nabla P_o + \left(\frac{y_i\rho_g}{M_g}\frac{Kk_{rg}}{\mu_g}\nabla P_{cgo}\right) - \left(\frac{x_i\rho_o\gamma_o}{M_o}\frac{kk_{ro}}{\mu_o} + \frac{y_i\rho_g\gamma_g}{M_g}\frac{kk_{rg}}{\mu_g}\right)\nabla z\right) = \tilde{q}_{hci} + \phi\Gamma c_{tf}\frac{\partial P}{\partial t} \qquad \text{A1.1-48.}$$

Now, as a summary, the resulting equations for the matrix and fracture are

$$\nabla\cdot\left(\lambda_c\nabla P_o + \left(\frac{y_i\rho_g}{M_g}\frac{Kk_{rg}}{\mu_g}\nabla P_{cgo}\right)_x - \left(\frac{x_i\rho_o\gamma_o}{M_o}\frac{kk_{ro}}{\mu_o} + \frac{y_i\rho_g\gamma_g}{M_g}\frac{kk_{rg}}{\mu_g}\right)\nabla z\right)_x$$

$$= \bar{q}_{hci} + \bar{q}_{mfi} + \phi\Gamma c_{tf}\frac{\partial P}{\partial t} \qquad \text{A1.1-49.}$$

The relative permeabilities are a function of saturation, which can be modeled by a correlation (e.g Corey and Brook, LET, etc).

$$k_{rg} = f(S_g) \qquad \text{A1.1-50.}$$

$$k_{ro} = f(S_o) \qquad \text{A1.1-51.}$$

$$k_{rw} = f(S_w) \qquad \text{A1.1-52.}$$

$$S_o + S_g + S_w = 1.0 \qquad \text{A1.1-53.}$$

A.1.2 Differential model for water

- **Mass balance**

$$\begin{bmatrix} masa\ entra \\ de\ aceite \end{bmatrix}_{\Delta t} - \begin{bmatrix} masa\ sale \\ de\ aceite \end{bmatrix}_{\Delta t} \pm \begin{bmatrix} fuentes / sumideros \\ de\ aceite \end{bmatrix}_{\Delta t} = \begin{bmatrix} acumulacion / agotamiento \\ de\ aceite \end{bmatrix}_{\Delta t} \quad \text{A1.1-54.}$$

Each term has the following expression:

$$\begin{bmatrix} masa \\ entra \end{bmatrix}_{\Delta t} = \rho_w u_{wx} \Delta y \Delta z \Delta t + \rho_w u_{wy} \Delta x \Delta z \Delta t + \rho_w u_{wz} \Delta x \Delta y \Delta t \quad \text{A1.1-55.}$$

$$\begin{bmatrix} masa \\ sale \end{bmatrix}_{\Delta t} = \rho_w u_{wx} \Delta y \Delta z \Delta t + \Delta\left(\rho_w u_{wx} \Delta y \Delta z\right)\Delta t \quad \text{A1.1-56.}$$

$$+ \rho_w u_{wy} \Delta x \Delta z \Delta t + \Delta\left(\rho_w u_{wy} \Delta x \Delta z\right)\Delta t + \rho_w u_{wz} \Delta x \Delta y \Delta t + \Delta\left(\rho_w u_{wz} \Delta x \Delta y\right)\Delta t \quad \text{A1.1-57.}$$

Defining $\tilde{q}_w$ as the mas of fluid that goes into or out from the source or sink (producer or injector wells) per unit of reservoir volume and time.

$$\begin{bmatrix} fuentes / \\ sumideros \end{bmatrix}_{\Delta t} = \tilde{q}_w \cdot \rho_w \cdot \Delta x \Delta y \Delta z \cdot \Delta t \quad \text{A1.1-58.}$$

$$\begin{bmatrix} Acumulacion / \\ Agotamiento \end{bmatrix}_{\Delta t} = \left(\rho_w V_w\right)_{t+\Delta t} - \left(\rho_w V_w\right)_{t+\Delta t} = \rho_w A \Delta x \cdot \left(\frac{\phi \cdot S_w}{B_w}\right)_{\Delta t} \quad \text{A1.1-59.}$$

$$\begin{bmatrix} Acumulacion / \\ Agotamiento \end{bmatrix}_{\Delta t} = \rho_w \Delta x \Delta y \Delta z \cdot \left(\frac{\phi \cdot S_w}{B_w}\right)_{\Delta t} \quad \text{A1.1-60.}$$

From Eq. A1.1-55 to A1.1-57 into A1.1-54.

$$\rho_w u_{wx} \Delta y \Delta z \Delta t - \left[\rho_w u_{wx} \Delta y \Delta z + \Delta\left(\rho_w u_{wx} \Delta y \Delta z\right)\right] \cdot \Delta t$$

$$+ \rho_w u_{wy} \Delta x \Delta z \Delta t - \left[\rho_w u_{wy} \Delta x \Delta z + \Delta\left(\rho_w u_{wy} \Delta x \Delta z\right)\right] \cdot \Delta t$$

$$+ \rho_w u_{wz} \Delta x \Delta y \Delta t - \left[\rho_w u_{wz} \Delta x \Delta y + \Delta\left(\rho_w u_{wz} \Delta x \Delta y\right)\right] \cdot \Delta t + \tilde{q}_w \cdot \rho_w \Delta x \Delta y \Delta z \cdot \Delta t$$

$$= \rho_w \Delta x \Delta y \Delta z \cdot \left(\frac{\phi \cdot S_w}{B_w}\right)_{\Delta t} \quad \text{A1.1-61.}$$

Re-organizing terms

$$-\Delta\left(\rho_w u_{wx}\Delta y\Delta z\right)\Delta t-\Delta\left(\rho_w u_{wy}\Delta x\Delta z\right)\Delta t-\Delta\left(\rho_w u_{wz}\Delta x\Delta y\right)\Delta t$$

$$+\tilde{q}_w\cdot\rho_w\cdot\Delta x\Delta y\Delta z\cdot\Delta t=\rho_w\Delta x\Delta y\Delta z\cdot\left(\frac{\phi\cdot S_w}{B_w}\right)_{\Delta t} \qquad \text{A1.1-62.}$$

Dividing the previous equation by $\Delta x\Delta y\Delta z$ and Δt

$$-\frac{\Delta\left(\rho_w u_{wx}\right)}{\Delta x}-\frac{\Delta\left(\rho_w u_{wy}\right)}{\Delta y}-\frac{\Delta\left(\rho_w u_{wz}\right)}{\Delta z}+\tilde{q}_w\cdot\rho_w=\frac{\rho_w}{\Delta t}\cdot\left(\frac{\phi\cdot S_w}{B_w}\right)_{\Delta t} \qquad \text{A1.1-63.}$$

Taking the limit when $\Delta x,\Delta y,\Delta z$ and Δt ->0

$$-\frac{\partial\left(\rho_w u_{wx}\right)}{\partial x}-\frac{\partial\left(\rho_w u_{wy}\right)}{\partial y}-\frac{\partial\left(\rho_w u_{wz}\right)}{\partial z}+\tilde{q}_w\cdot\rho_w=\rho_w\frac{\partial}{\partial t}\left(\frac{\phi\cdot S_w}{B_w}\right)_{\Delta t}$$

$$-\frac{\partial\left(u_{wx}\right)}{\partial x}-\frac{\partial\left(u_{wy}\right)}{\partial y}-\frac{\partial\left(u_{wz}\right)}{\partial z}+\tilde{q}_w=\frac{\partial}{\partial t}\left(\frac{\phi\cdot S_w}{B_w}\right)_{\Delta t} \qquad \text{A1.1-64.}$$

Re-organizing terms

$$u_w=u_{wx}\cdot\vec{i}+u_{wy}\cdot\vec{j}+u_{wz}\cdot\vec{k} \qquad \text{A1.1-65.}$$

Defining the rotational as:

$$-\nabla\cdot\left(u_{wcn}\right)=\tilde{q}_w+\frac{\partial}{\partial t}\left(\frac{\phi\cdot S_w}{B_w}\right)_{\Delta t} \qquad \text{A1.1-66.}$$

- **Conservation of momentum – Darcy Law**

$$u_{wx}=-\frac{k_{wx}}{\mu_w}\frac{\partial\Phi_w}{\partial x},u_{wy}=-\frac{k_{wy}}{\mu_w}\frac{\partial\Phi_w}{\partial y},\ u_{wz}=-\frac{k_{wz}}{\mu_w}\frac{\partial\Phi_w}{\partial z} \qquad \text{A1.1-67.}$$

$$u_{wx}=-\frac{k_x k_{rw}}{\mu_w}\frac{\partial\Phi_w}{\partial x},u_{wx}=-\frac{k_y k_{rw}}{\mu_w}\frac{\partial\Phi_w}{\partial y},u_{wx}=-\frac{k_z k_{rw}}{\mu_w}\frac{\partial\Phi_w}{\partial z} \qquad \text{A1.1-68.}$$

Defining the capillary pressure as the difference between the non-wetting phase and the wetting phase pressure.

$$P_w=P_o-P_{cow} \qquad \text{A1.1-69.}$$

Where the flow potentials are defined as:

$\Phi_w = P_w - \gamma_w z$ With γ_w as the hydrostatic gradient of water. A1.1-70.

Applying the definition of potential in the vertical direction for the water phase:

$$\frac{\partial \Phi_w}{\partial z} = \frac{\partial P_w}{\partial z} - \frac{g}{g_c}\frac{\partial(\rho_w D)}{\partial z} \quad \text{A1.1-71.}$$

$$\rightarrow \frac{\partial \Phi_w}{\partial z} = \frac{\partial P_w}{\partial z} - \frac{g}{g_c}\rho_w \frac{\partial D}{\partial z} \quad \text{A1.1-72.}$$

$$\rightarrow \frac{\partial \Phi_w}{\partial z} = \frac{\partial P_w}{\partial z} - \gamma_w \frac{\partial D}{\partial z} \quad \text{A1.1-73.}$$

The capillary pressures are defined as following

$$P_{cow} = P_o - P_w = f(S_w) \quad \text{A1.1-74.}$$

$$P_w = P_o - P_{cow} \quad \text{A1.1-75.}$$

Developing the equation and using *Po* as a primary variable.

$$\frac{\partial}{\partial x}\left(\frac{\rho_w}{B_w}\frac{k_x k_{rw}}{\mu_w}\frac{\partial(P_o - P_{cow} - \gamma_w D)}{\partial x}\right) + \frac{\partial}{\partial y}\left(\frac{\rho_w}{B_w}\frac{k_y k_{rw}}{\mu_w}\frac{\partial(P_o - P_{cow} - \gamma_w D)}{\partial y}\right)$$

$$+ \frac{\partial}{\partial z}\left(\frac{\rho_w}{B_w}\frac{k_z k_{rw}}{\mu_w}\frac{\partial(P_o - P_{cow} - \gamma_w D)}{\partial z}\right)$$

$$= \tilde{q}_w + \frac{\partial}{\partial t}\left(\frac{\phi S_w}{B_w}\right) \quad \text{A1.1-76.}$$

Eliminating the gravitational component in the *x* and *y* directions

$$\frac{\partial}{\partial x}\left(\frac{\rho_w}{B_w}\frac{k_x k_{rw}}{\mu_w}\frac{\partial(P_o - P_{cow})}{\partial x}\right) + \frac{\partial}{\partial y}\left(\frac{\rho_w}{B_w}\frac{k_y k_{rw}}{\mu_w}\frac{\partial(P_o - P_{cow})}{\partial y}\right)$$

$$+ \frac{\partial}{\partial z}\left(\frac{\rho_w}{B_w}\frac{k_z k_{rw}}{\mu_w}\frac{\partial(P_o - P_{cow} - \gamma_w z)}{\partial z}\right)$$

$$= \tilde{q}_w + \frac{\partial}{\partial t}\left(\frac{\phi S_w}{B_w}\right) \qquad \text{A1.1-77.}$$

Re-organizing

$$\frac{\partial}{\partial x}\left(\left(\frac{k_x k_{rw}}{\mu_w}\right)\frac{\partial P_o}{\partial x} - \frac{k_x k_{rw}}{\mu_w}\frac{\partial P_{cow}}{\partial x} - \frac{k_x k_{rw}}{\mu_w}\frac{\partial(\gamma_w D)}{\partial x}\right)$$

$$+ \frac{\partial}{\partial y}\left(\left(\frac{k_y k_{rw}}{\mu_w}\right)\frac{\partial P_o}{\partial y} - \frac{k_y k_{rw}}{\mu_w}\frac{\partial P_{cow}}{\partial y} - \frac{k_y k_{rw}}{\mu_w}\frac{\partial(\gamma_w D)}{\partial y}\right)$$

$$+ \frac{\partial}{\partial z}\left(\left(\frac{k_z k_{rw}}{\mu_w}\right)\frac{\partial P_o}{\partial z} - \frac{k_z k_{rw}}{\mu_w}\frac{\partial P_{cow}}{\partial z} - \frac{k_z k_{rw}}{\mu_w}\frac{\partial(\gamma_w D)}{\partial z}\right)$$

$$= \tilde{q}_w + \frac{\partial}{\partial t}\left(\frac{\phi S_w}{B_w}\right) \qquad \text{A1.1-78.}$$

Eliminating the gravitational component in x and y directions

$$\frac{\partial}{\partial x}\left(\left(\frac{k_x k_{rw}}{\mu_w}\right)\frac{\partial P_o}{\partial x} - \frac{k_x k_{rw}}{\mu_w}\frac{\partial P_{cow}}{\partial x}\right)$$

$$+ \frac{\partial}{\partial y}\left(\left(\frac{k_y k_{rw}}{\mu_w}\right)\frac{\partial P_o}{\partial y} - \frac{k_y k_{rw}}{\mu_w}\frac{\partial P_{cow}}{\partial y}\right)$$

$$+ \frac{\partial}{\partial z}\left(\left(\frac{k_z k_{rw}}{\mu_w}\right)\frac{\partial P_o}{\partial z} - \frac{k_z k_{rw}}{\mu_w}\frac{\partial P_{cow}}{\partial z} - \frac{k_z k_{rw}}{\mu_w}\gamma_w\frac{\partial D}{\partial z}\right)$$

$$= \tilde{q}_w + \frac{\partial}{\partial t}\left(\frac{\phi S_w}{B_w}\right) \qquad \text{A1.1-79.}$$

Re-organizing

$$\nabla\cdot\left(\left(\frac{\rho_w}{M_w}\frac{Kk_{rw}}{\mu_w}\right)\nabla P_o - \left(\frac{\rho_w}{M_w}\frac{Kk_{rw}}{\mu_w}\right)\nabla P_{co,w} - \left(\frac{\rho_w\gamma_w}{M_w}\frac{Kk_{rw}}{\mu_w}\right)\nabla z\right) = \tilde{q}_w + \frac{\partial}{\partial t}\left(\frac{\phi S_w}{B_w}\right) \qquad \text{A1.1-80.}$$

A.2 Phase Behavior and Fluid System.

As a flash calculation is done in every cell every time step, it is necessary to know the total composition, Z_i to perform this task. Eq. A2.1.1 is used as a basis to obtain the compositional change in space for each time step (n+1).

$$\frac{\partial}{\partial x}\left(\frac{x_i\rho_o}{M_o}\frac{k_x k_{ro}}{\mu_o}\frac{\partial\Phi_o}{\partial x}+\frac{y_i\rho_g}{M_g}\frac{k_x k_{rg}}{\mu_g}\frac{\partial\Phi_g}{\partial x}\right)+\frac{\partial}{\partial y}\left(\frac{x_i\rho_o}{M_o}\frac{k_y k_{ro}}{\mu_o}\frac{\partial\Phi_o}{\partial y}+\frac{y_i\rho_g}{M_g}\frac{k_y k_{rg}}{\mu_g}\frac{\partial\Phi_g}{\partial y}\right)$$

$$+\frac{\partial}{\partial z}\left(\frac{x_i\rho_o}{M_o}\frac{k_z k_{ro}}{\mu_o}\frac{\partial\Phi_o}{\partial z}+\frac{y_i\rho_g}{M_g}\frac{k_z k_{rg}}{\mu_g}\frac{\partial\Phi_g}{\partial z}\right)=\tilde{q}_{hci}+\tilde{q}_{Ti}+\frac{\partial}{\partial t}\phi\left(\frac{x_i\rho_o S_o}{M_o}+\frac{y_i\rho_g S_g}{M_g}\right)$$

$$=\tilde{q}_{hci}+\tilde{q}_{Ti}+\frac{\partial}{\partial t}\phi\left(Z_i\left(\frac{\rho_o S_o}{M_o}+\frac{\rho_g S_g}{M_g}\right)\right) \qquad \text{A2.4-1.}$$

The total composition must satisfy the following condition.

$$Z_i = Lx_i + Vy_i \qquad \text{A2.4-2.}$$

Where

L : is the fraction of liquid
V : is the fraction of gas

The fractions are defined as:

$$L=\frac{\frac{S_o\rho_o}{M_o}}{\frac{S_o\rho_o}{M_o}+\frac{S_g\rho_g}{M_g}} \qquad \text{A2.4-3.}$$

$$V=\frac{\frac{S_g\rho_g}{M_g}}{\frac{S_o\rho_o}{M_o}+\frac{S_g\rho_g}{M_g}} \qquad \text{A2.4-4.}$$

Replacing Eq. A2.4-3 and Eq. A2.4-4 into Eq. A2.4-2:

$$Z_i = \frac{\frac{S_o\rho_o}{M_o}}{\frac{S_o\rho_o}{M_o}+\frac{S_g\rho_g}{M_g}} x_i + \frac{\frac{S_g\rho_g}{M_g}}{\frac{S_o\rho_o}{M_o}+\frac{S_g\rho_g}{M_g}} y_i \qquad \text{A2.4-5.}$$

Reorganizing Eq. A2.5-5.

$$Z_i\left(\frac{S_o\rho_o}{M_o}+\frac{S_g\rho_g}{M_g}\right) = \frac{S_o\rho_o}{M_o}x_i + \frac{S_g\rho_g}{M_g}y_i \qquad \text{A2.5-6.}$$

Replacing Eq. A2.4-6 into Eq. A2.4-1.

$$\nabla.\left(\frac{x_i\rho_o}{M_o}\frac{k_o}{\mu_o}\nabla\Phi_o\right)_m + \nabla.\left(\frac{y_i\rho_g}{M_g}\frac{kk_{rg}}{\mu_g}\nabla\Phi_g\right)_m$$

$$= \tilde{q}_{hci} + \tilde{q}_{Ti} + \frac{\partial}{\partial t}\phi_m\left(Z_i\left(\frac{S_o\rho_o}{M_o}+\frac{S_g\rho_g}{M_g}\right)\right)_m \qquad \text{A2.4-7.}$$

Z_{im}^{n+1} and Z_{im}^{n}

For the matrix

$$Z_m^{n+1} = \frac{\nabla.\left(\frac{x_i\rho_o}{M_o}\frac{k_o}{\mu_o}\nabla\Phi_o\right)_m + \nabla.\left(\frac{y_i\rho_g}{M_g}\frac{kk_{rg}}{\mu_g}\nabla\Phi_g\right)_m + z_{im}^n\left(\frac{S_o\rho_o}{M_o}+\frac{S_g\rho_g}{M_g}\right)_m - \tilde{q}_{hci} - \tilde{q}_{Ti}}{\frac{\phi_m}{\Delta t}\left[\left(\frac{S_o\rho_o}{M_o}+\frac{S_g\rho_g}{M_g}\right)+\frac{\partial}{\partial t}\left(\frac{S_o\rho_o}{M_o}+\frac{S_g\rho_g}{M_g}\right)\right]_m} \qquad \text{A2.4-8.}$$

For the fracture.

The same procedure is made for the matrix as applied for the fracture system.

$$Z_f^{n+1} = \frac{\nabla.\left(\frac{x_i\rho_o}{M_o}\frac{k_o}{\mu_o}\nabla\Phi_o\right)_f + \nabla.\left(\frac{y_i\rho_g}{M_g}\frac{kk_{rg}}{\mu_g}\nabla\Phi_g\right)_f + z_{im}^n\left(\frac{S_o\rho_o}{M_o}+\frac{S_g\rho_g}{M_g}\right)_f - \tilde{q}_{hci} - \tilde{q}_{Ti}}{\frac{\phi_f}{\Delta t}\left[\left(\frac{S_o\rho_o}{M_o}+\frac{S_g\rho_g}{M_g}\right)+\frac{\partial}{\partial t}\left(\frac{S_o\rho_o}{M_o}+\frac{S_g\rho_g}{M_g}\right)\right]_f} \qquad \text{A2.4-9.}$$

APPENDIX B. Dele Sheet Slim Tube Simulation Fluid Properties.

The following Figures show a summary for Dele Sheet fluid properties and composition using different fluids (Nitrogen, Methane, lean gas and Carbon dioxide) and pressures.

- **Saturation and fluid properties.**

Figure B.1 shows the properties of the results from the MMP simulations using nitrogen.

The general reservoir pressure behavior, especially in Dele sheet, stabilizes at 4000 psia (see Figure 3-9 Plot No. 9).

Figure B.1 shows that at 4000 psia, the MMP simulation with N_2 injection is immiscible (comparing point A and B in the figure), which is aligned with the oil production loss displayed in Figure 3-10.

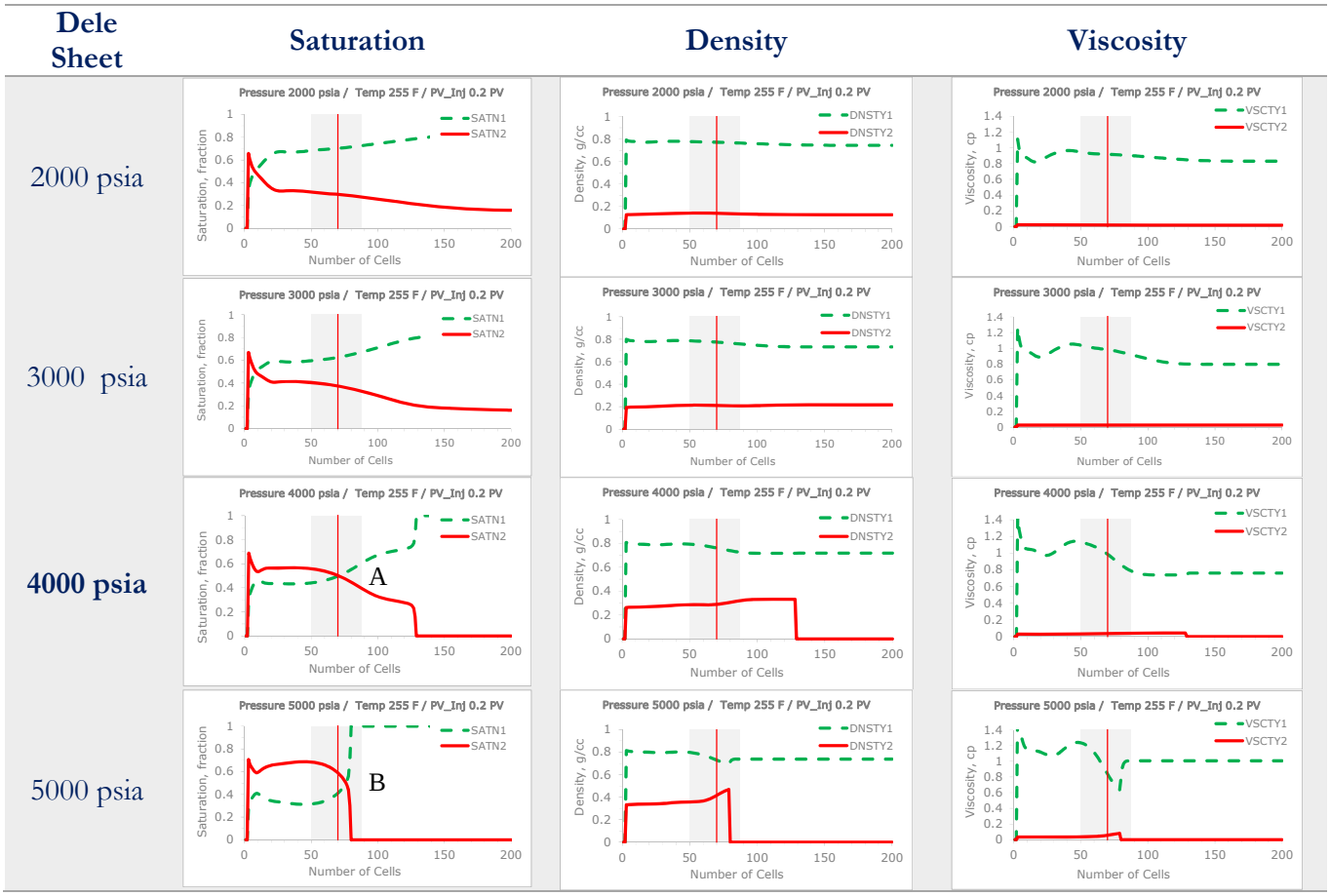

Figure B.1. Pauto Fluid Properties with N_2, Injection from MMP Simulation.

Figure B.2 shows the oil and gas saturation, density and viscosity tests performed at 4000 psia.

Comparing N_2 injection (see point A) with methane (see point B), lean gas (see point C) and CO_2 (see point D), it can be observed that the best fluid for gas injection is CO_2. This is the reason of how the best performance was achieved, as shown in Figure 3-43.

Notice how the residual oil saturation behind the displacement front is lower with CO_2 than compared with N_2 (see the dashed green line).

Also, the viscosity behavior with CO_2 is lower behind the displacement front, compared to N_2 and lean gas.

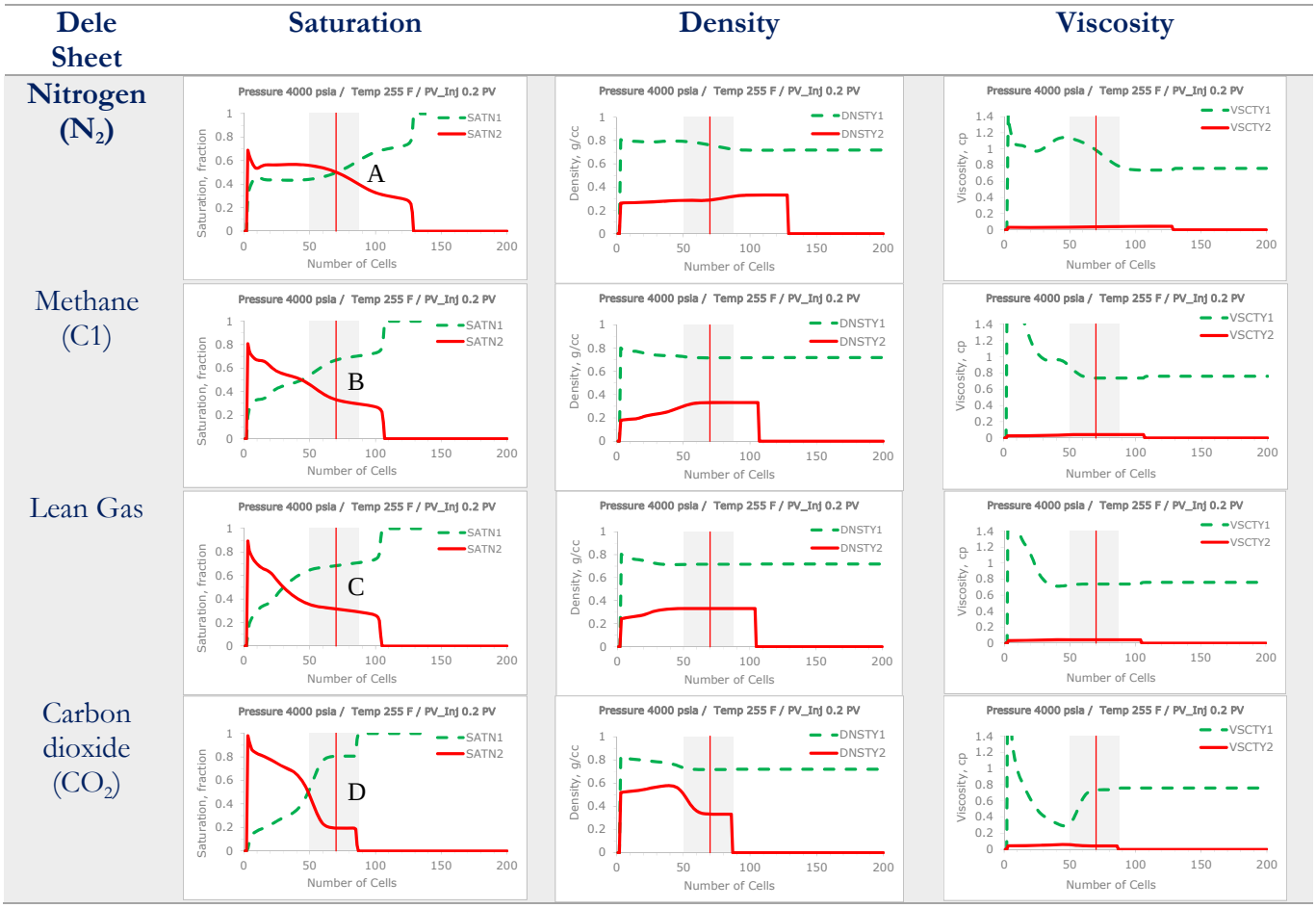

Figure B.2. Pauto Fluid Properties with N_2, Lean gas and CO_2 Injection from MMP Simulation – 4000 psia.

APPENDIX C. Reference Case History Match Description

Figure C.1 shows a ternary graph at the end of the history matching process. In this graph, the oil, gas and water ternary saturation graph slightly hides the oil liquid drop out originated in the reservoir due to the system's pressure depletion below the saturation pressure.

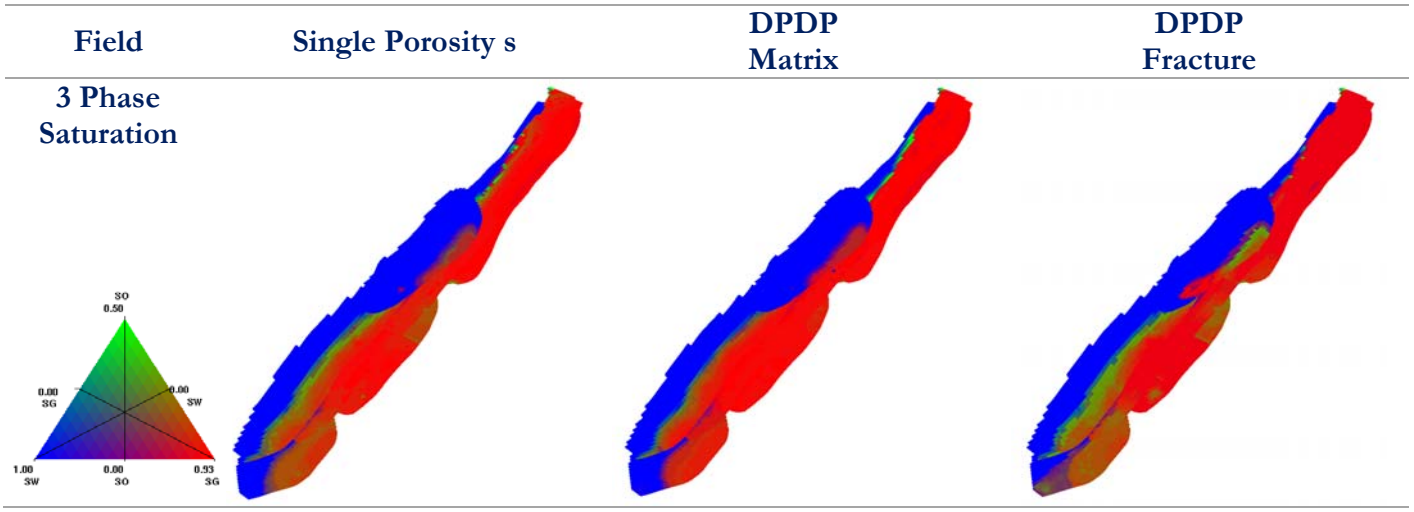

Figure C.1. Field Ternary Oil-gas-water saturation Comparison SP and DPDP – end of History matching process.

As a reference, Figure 1-50 and Figure 1-51 show the maximum liquid drop out (LDO) for Pauto and Floreña, this is within the range of 20% to 30%.

To visualize the oil saturation magnitude, Figure C.2 and Figure C.3 present oil saturation in a 0 to 0.5 scale.

In Figure C.2 (at field level) and Figure C.3 (for Dele Sheet), it can be appreciated that the hypothetical radial condensate banking effect is no longer valid; instead, there are regions with different oil saturations that extend across the field.

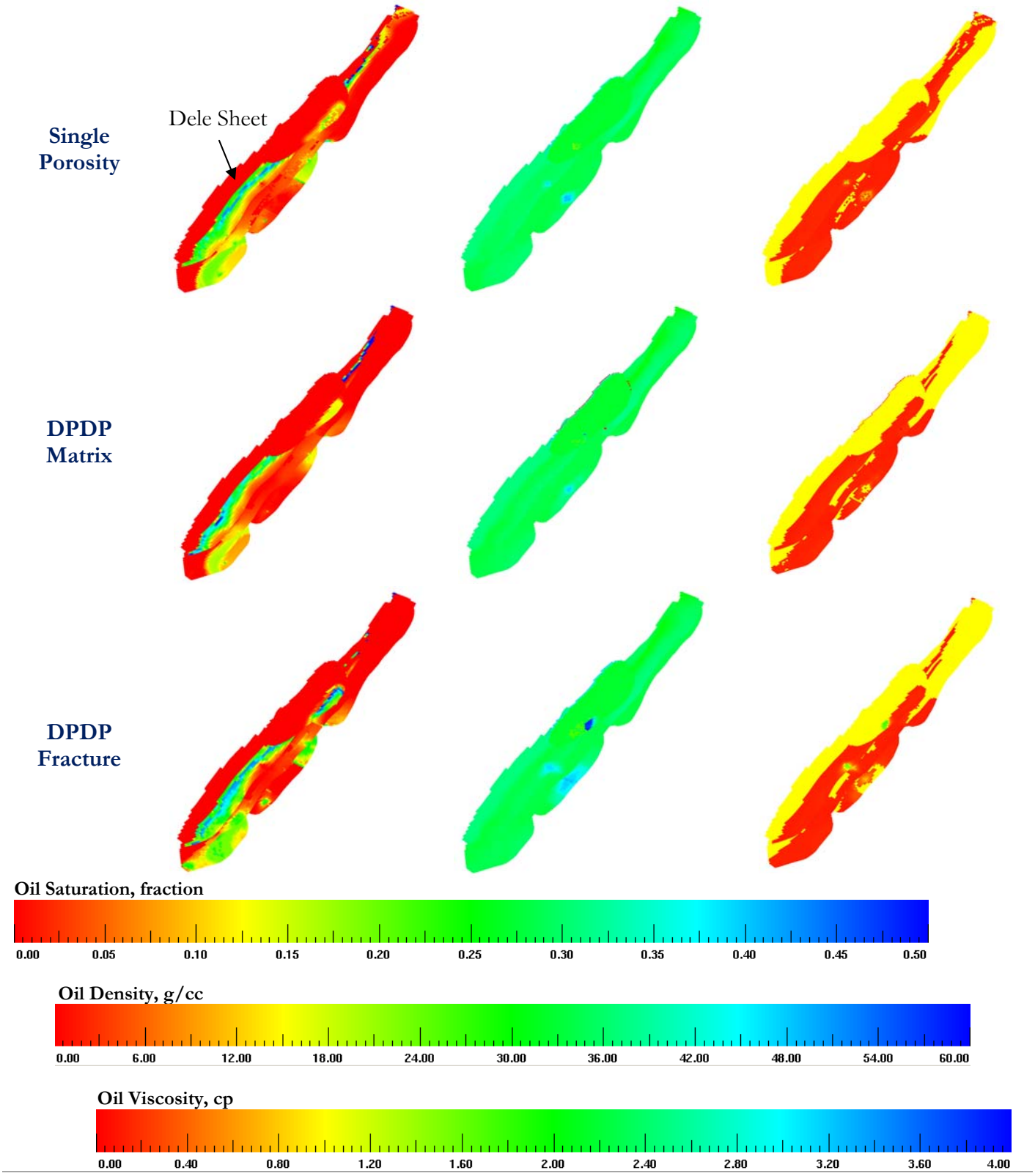

Figure C.2. Field - Oil Saturation, density and viscosity Comparison SP and DPDP – end of History matching process.

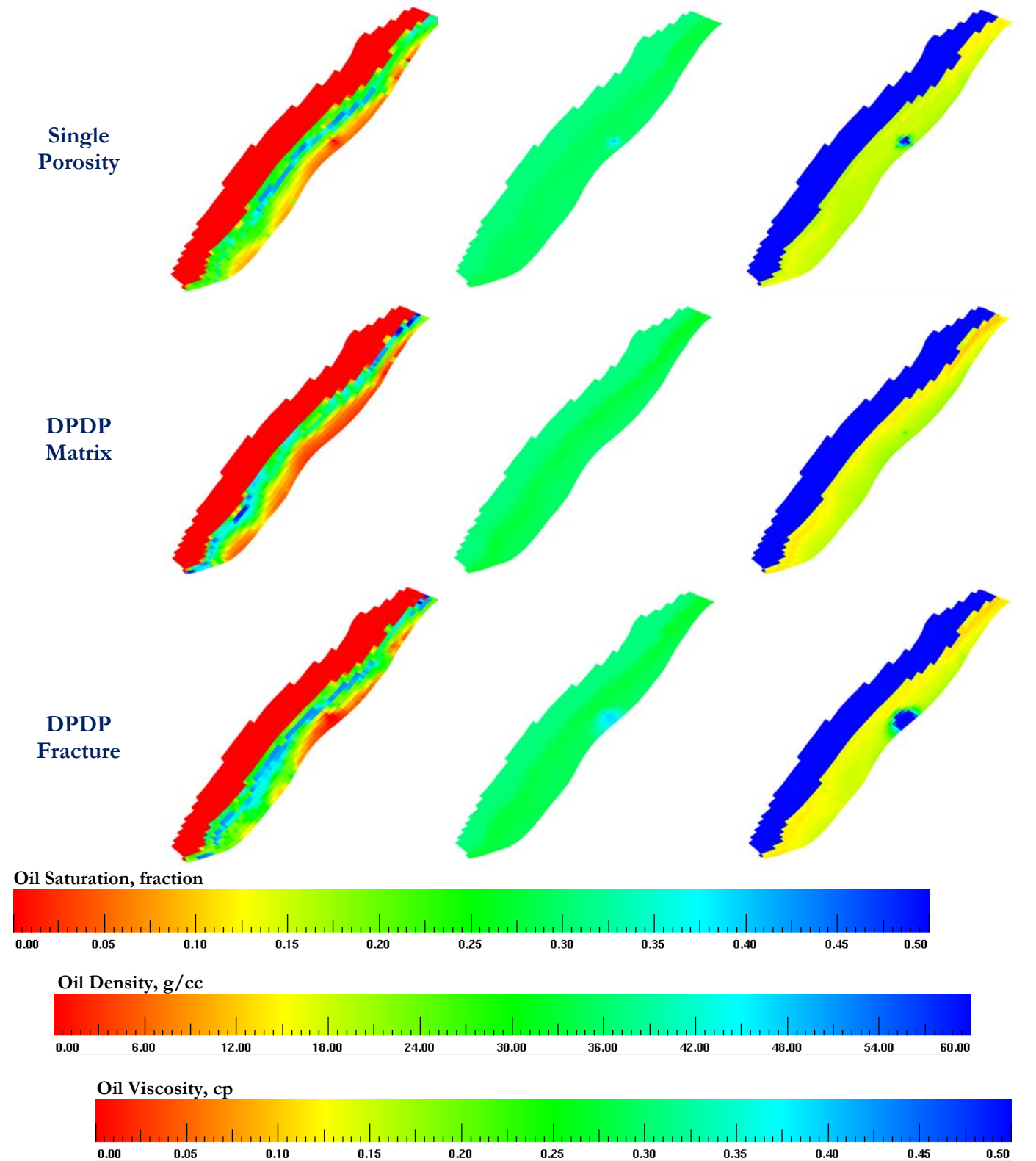

Figure C.3. Dele Sheet - Oil Saturation Comparison SP and DPDP – end of History matching process.

APPENDIX D. Reference Case Prediction

Figure D.1 shows the permeability distribution in the *x*, *y* and *z* directions for PDM field, with highlighted zones where a higher water encroachment happens at field level.

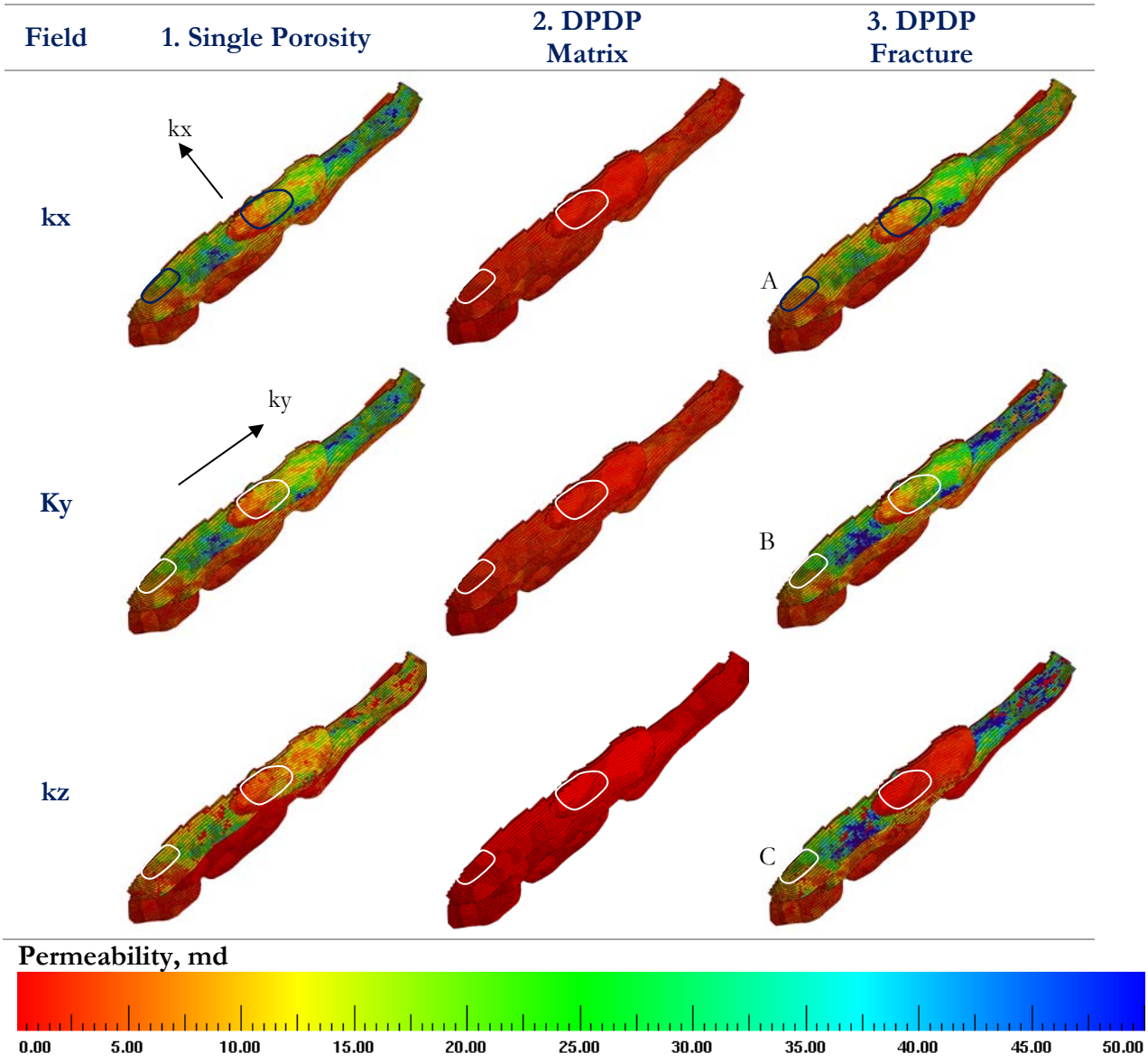

Figure D.1. Field Permeability – SP and Quick DPDP Models Approach.

Figure D.2 shows the regions where water encroachment happens with higher the critical stressed fracture intensity. One circle points out the southern area in Dele sheet (see point D) and the other one is in Floreña Mirador (see point E).

In Floreña (point B) SP model shows a higher water encroachment flow (blue regions) from the aquifer compared to the DPDP model.

Also in Dele Sheet (point A), the SP model shows higher water encroachment (green region) compared to the DPDP model.

A combination of poor pressure support and a slightly better rock quality distribution in the SP model compared to the DPDP model (see Figure D-1 points A, B and C) result in that these zones have a higher water encroachment compared to the total field behavior.

For Dele Sheet, it also refers to the analysis presented in Figure 1-52.

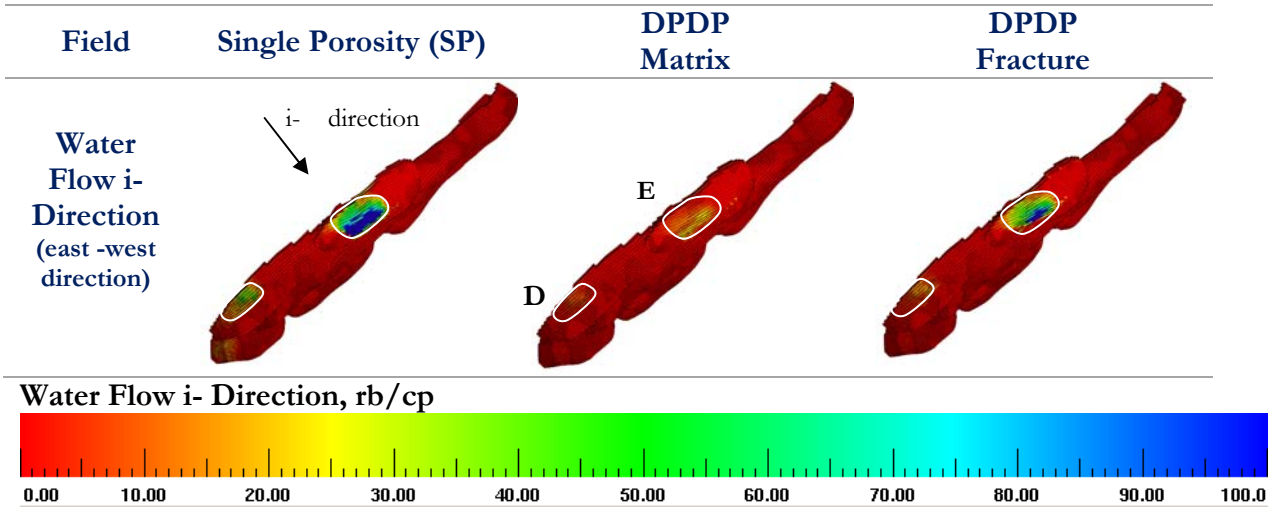

Figure D.2. Water Flow in K+ direction (bottom-up direction) – SP and Quick DPDP Models Approach.

APPENDIX E. Injection Scenarios DPDP Model Approach - Additional 3D Graphs

The figures presented in this section are complimentary graphs for Section 3.6.2 for the cases with N2 injection rates and gas sales rates presented in Table 3.5.

The concentrations are presented using an external box to show the fracture composition, and an internal box to represents the matrix composition

- **Matrix and Fracture Liquid CO2/N2/C1 to C6**

Notice that the scale for CO_2 concentration is up to 0.03, which is a very low value. There is an incipient CO_2 distribution associated to the injection, where CO_2 tends to be located in the fracture system in a higher proportion.

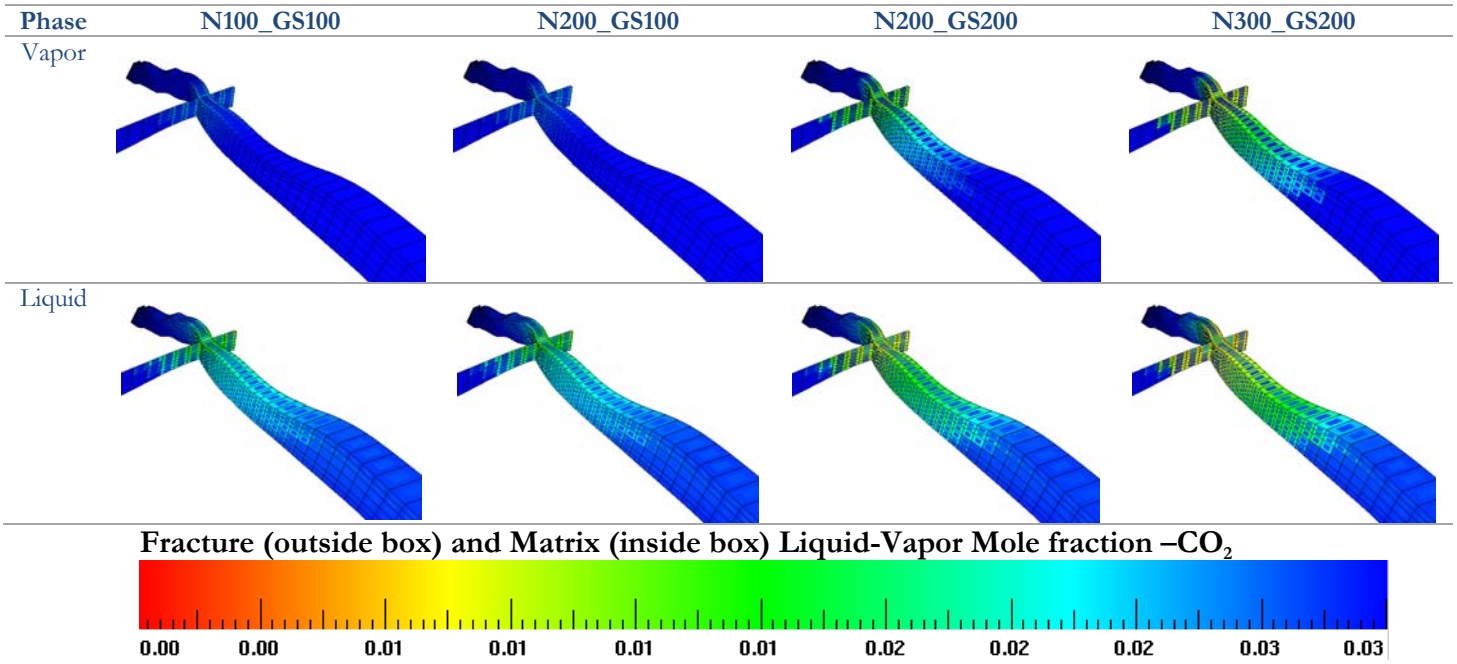

Figure E.1. Dele Matrix Liquid-Vapor Mole Fraction Cross-Section – CO_2 – 10 years after N_2 injection sensitivities are performed.

Figure E.2 clearly shows N_2 channeling through the fracture system (see plot 3V and 4V).

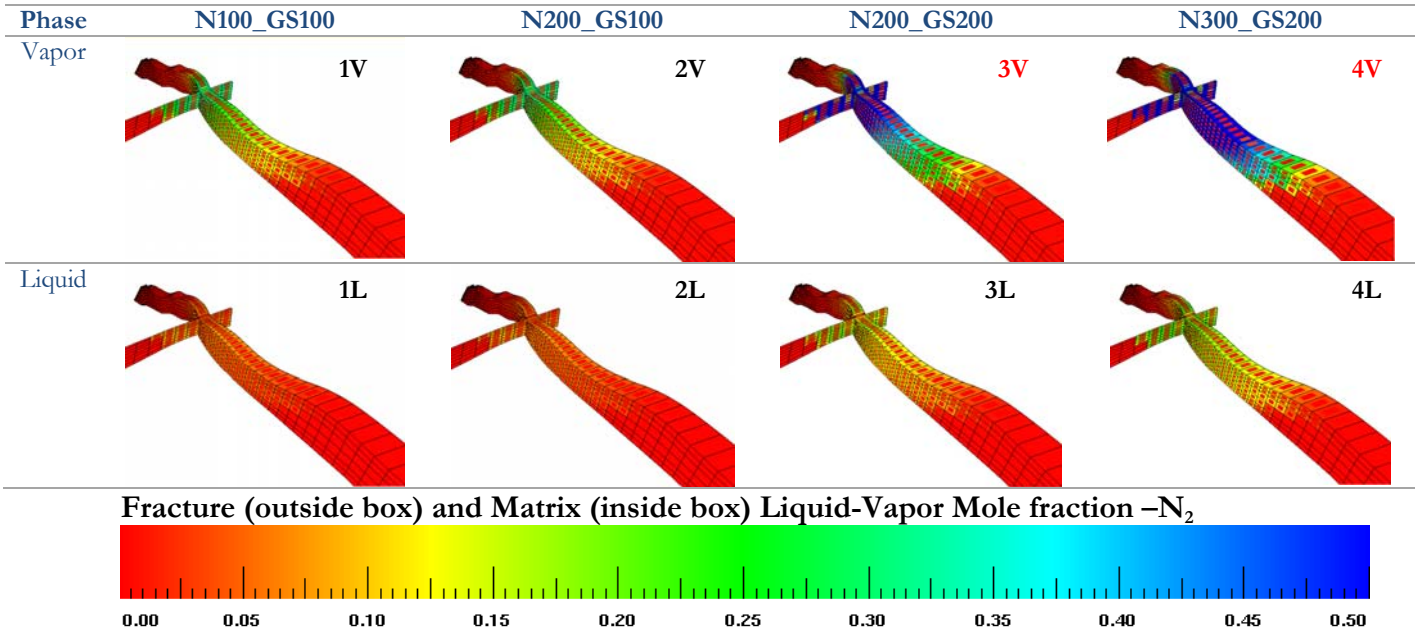

Figure E.2. Dele Matrix Liquid-Vapor Mole Fraction –N_2 – 10 years after N_2 injection sensitivities are performed.

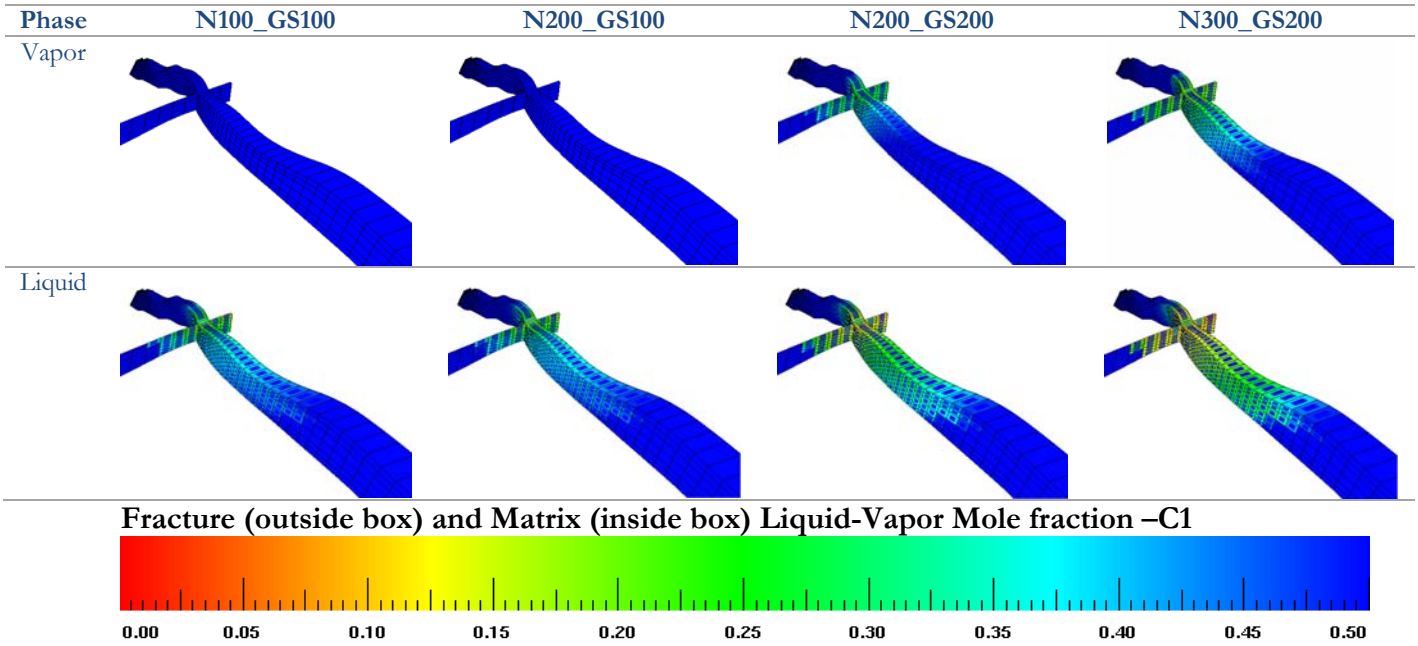

Figure E.3. Dele Matrix Liquid-Vapor Mole Fraction –C1 – 10 years after N_2 injection sensitivities are performed.

As presented in Figure 3-38, there is thresholds where the C2 and C3 have a similar proportion in the fracture and in the matrix, as shown in Figure E.3 and Figure E.4.

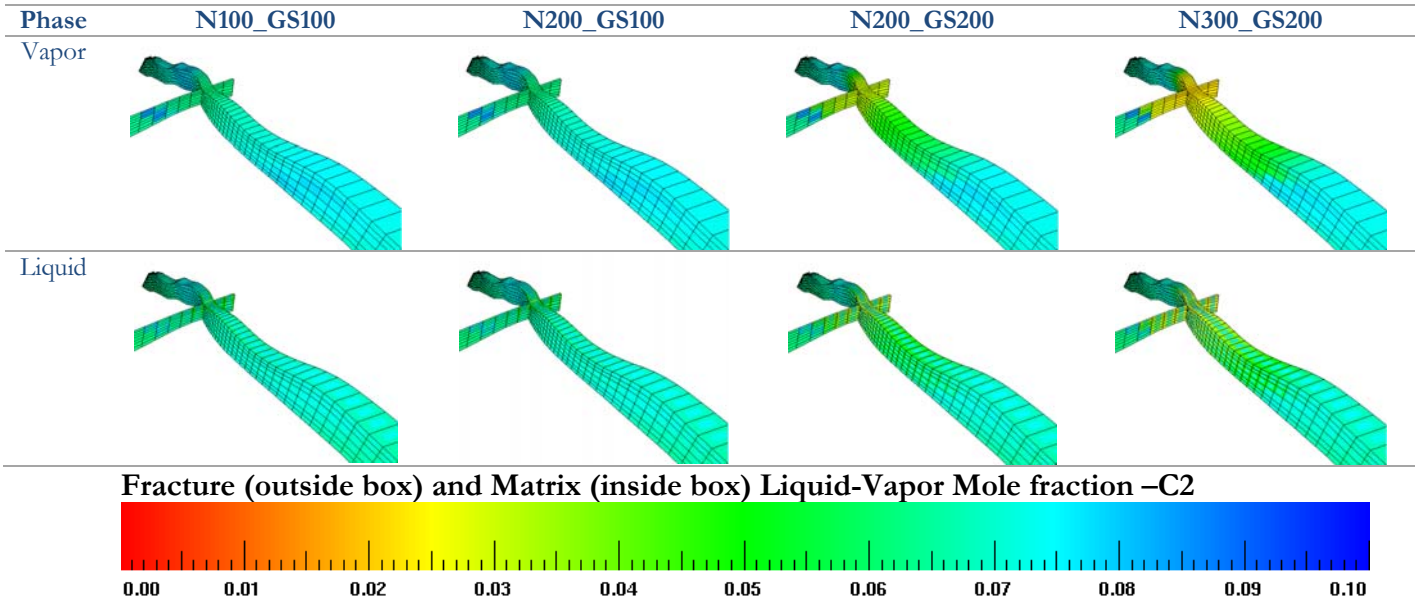

Figure E.4. Dele Matrix Liquid-Vapor Mole Fraction –C2 – 10 years after N_2 injection sensitivities are performed.

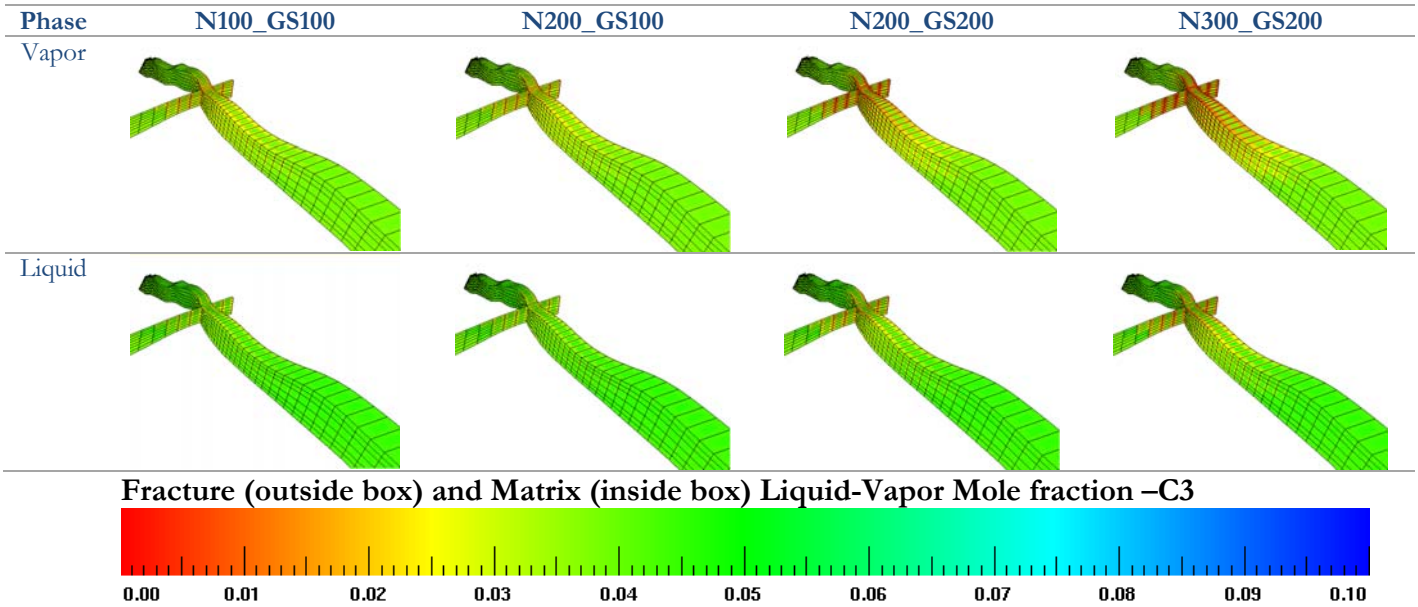

Figure E.5. Dele Matrix Liquid-Vapor Mole Fraction –C3 – 10 years after N_2 injection sensitivities are performed.

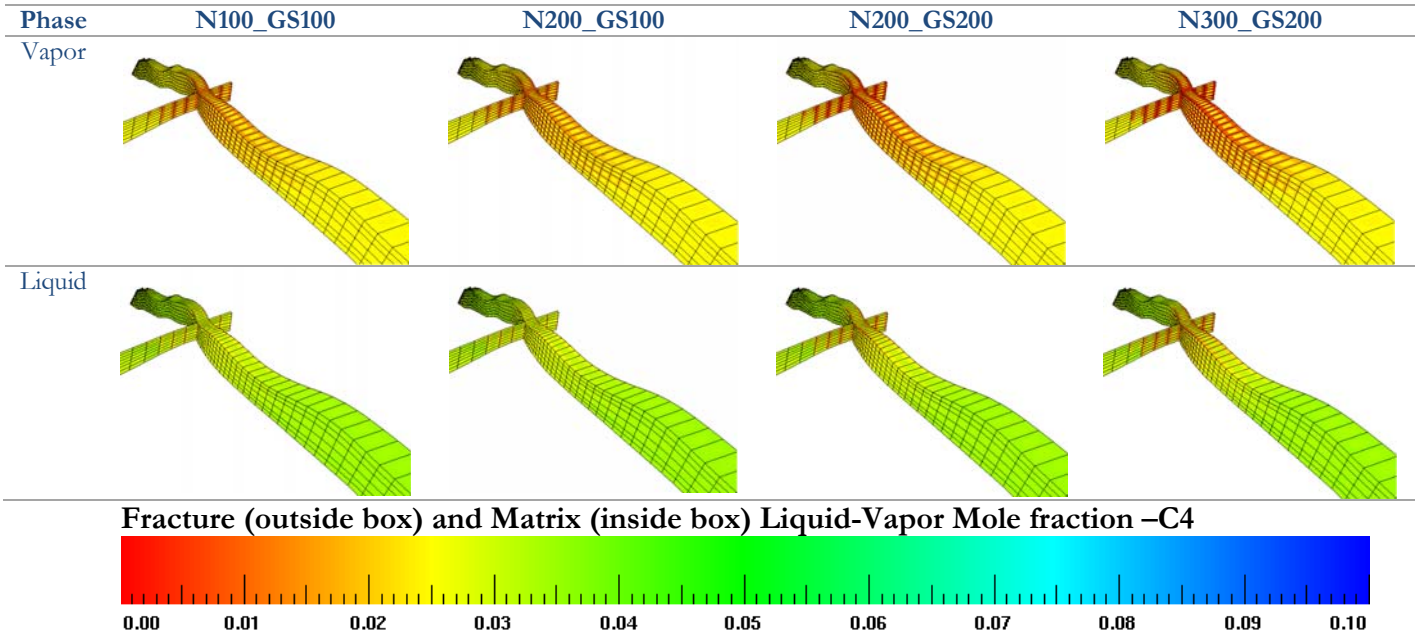

Figure E.6. Dele Matrix Liquid-Vapor Mole Fraction –C4 – 10 years after N_2 injection sensitivities are performed.

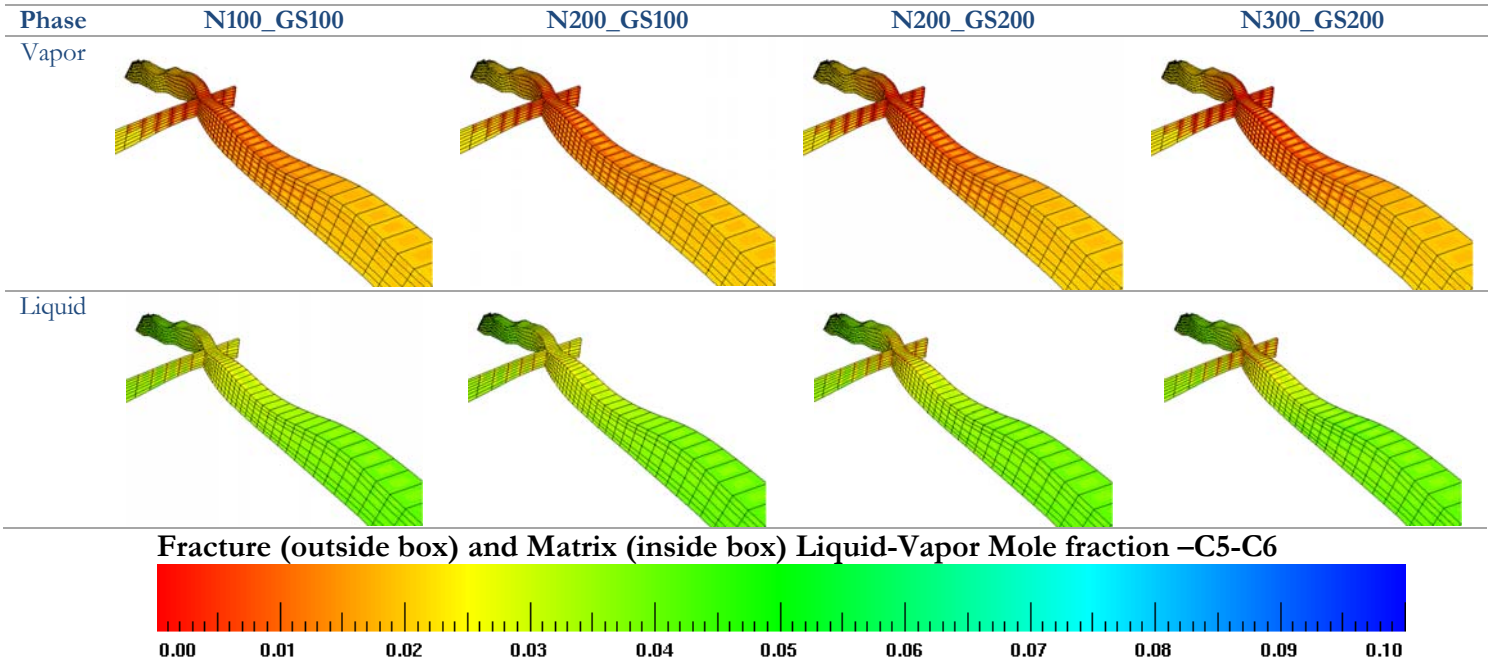

Figure E.7. Dele Matrix Liquid-Vapor Mole Fraction –C5-C6 – 10 years after N_2 injection sensitivities are performed.

- **Matrix and Fracture Liquid C7-C10 to C30+**

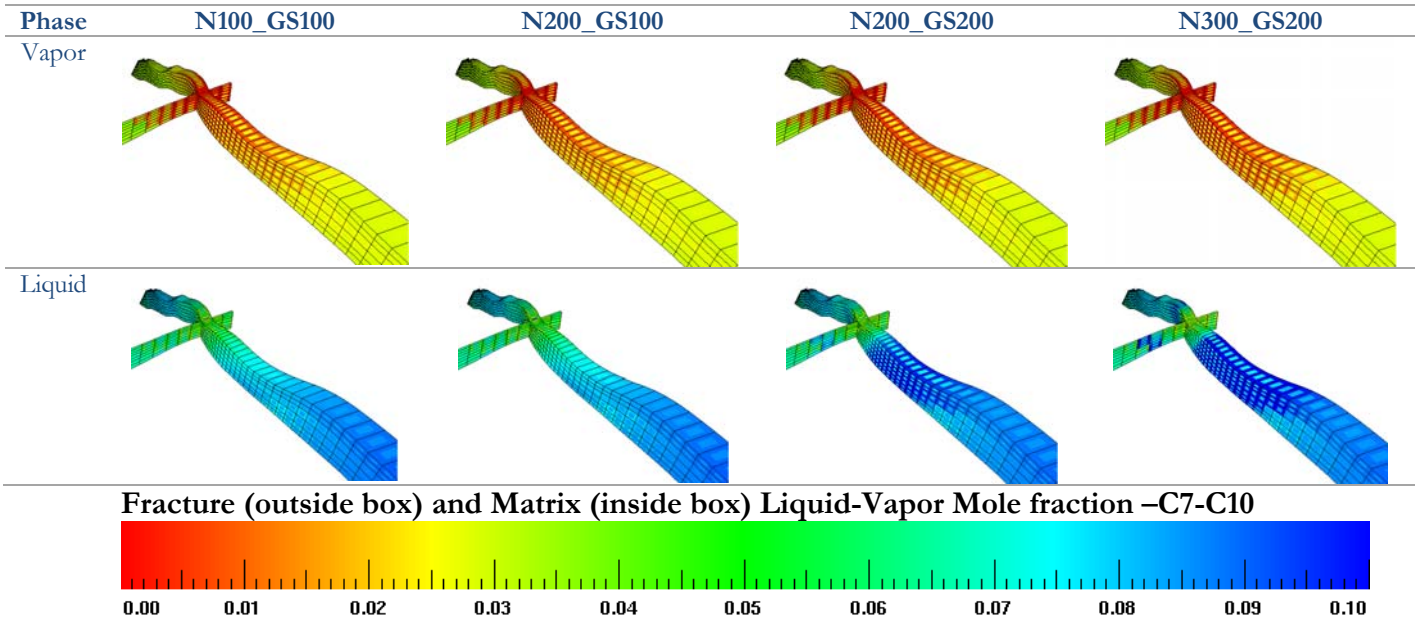

Figure E.8. Dele Matrix Liquid-Vapor Mole Fraction –C7-C10 – 10 years after N_2 injection sensitivities are performed.

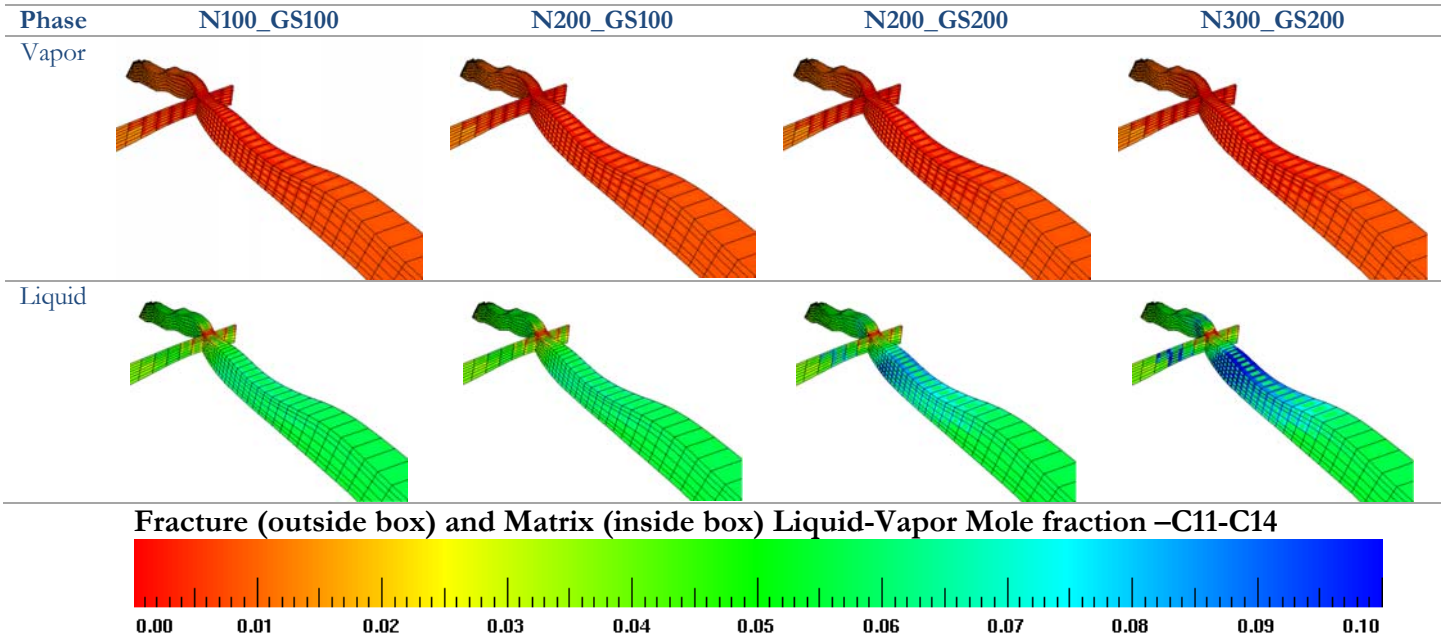

Figure E.9. Dele Matrix Liquid-Vapor Mole Fraction –C11-C14 – 10 years after N_2 injection sensitivities are performed.

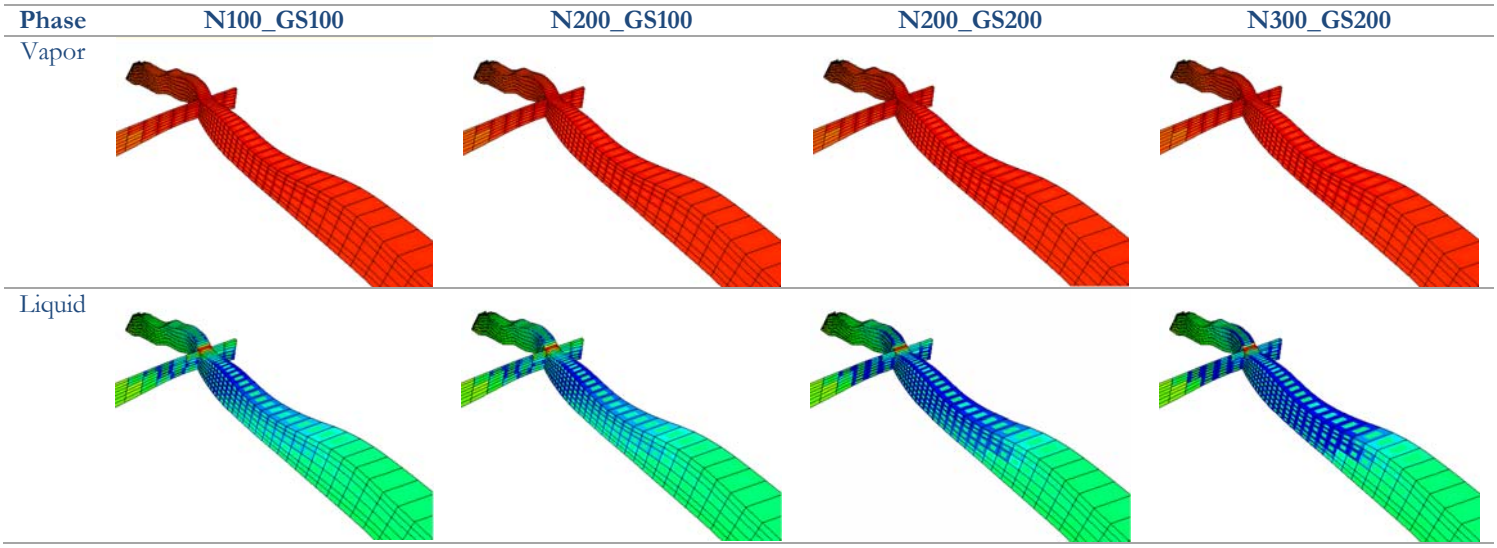

Figure E.10. Dele Matrix Liquid-Vapor Mole Fraction –C15-C20 – 10 years after N_2 injection sensitivities are performed.

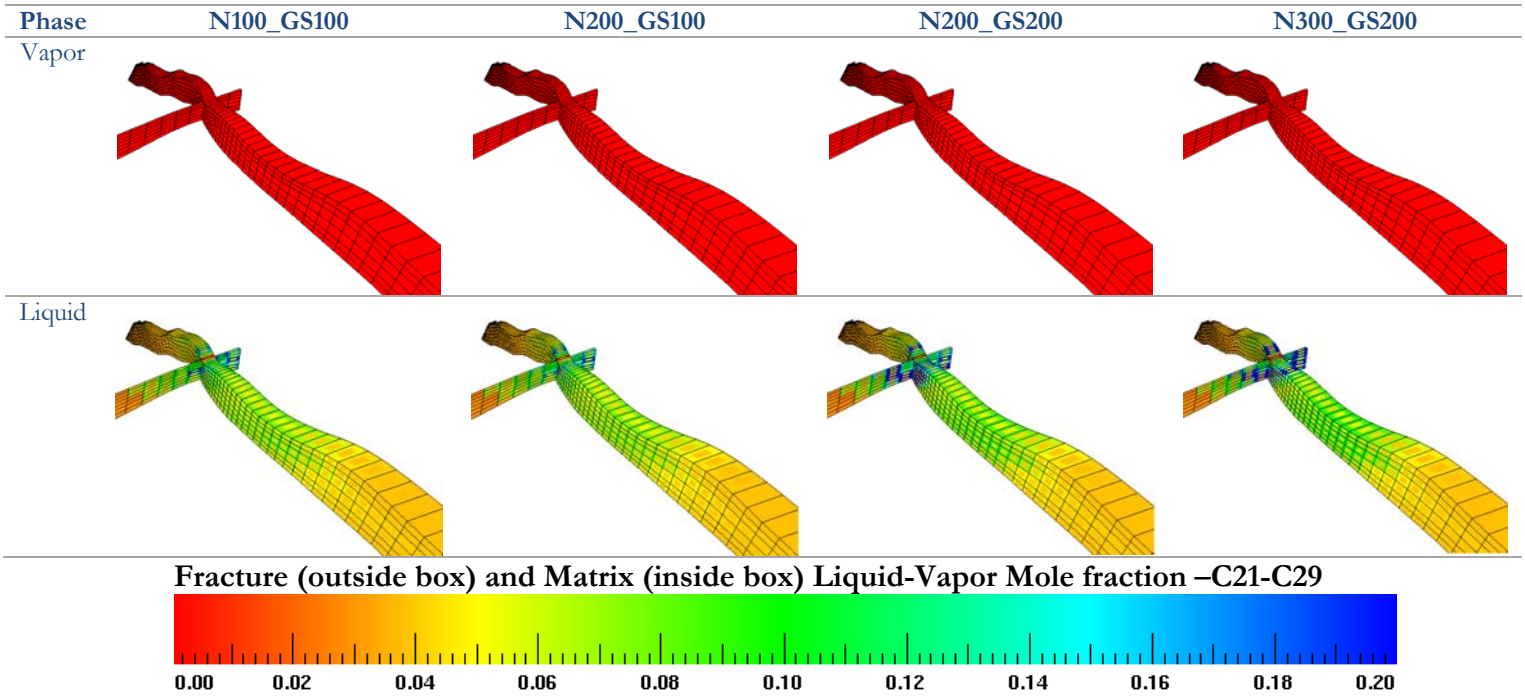

Figure E.11. Dele Matrix Liquid-Vapor Mole Fraction –C21-C29 – 10 years after N_2 injection sensitivities are performed.

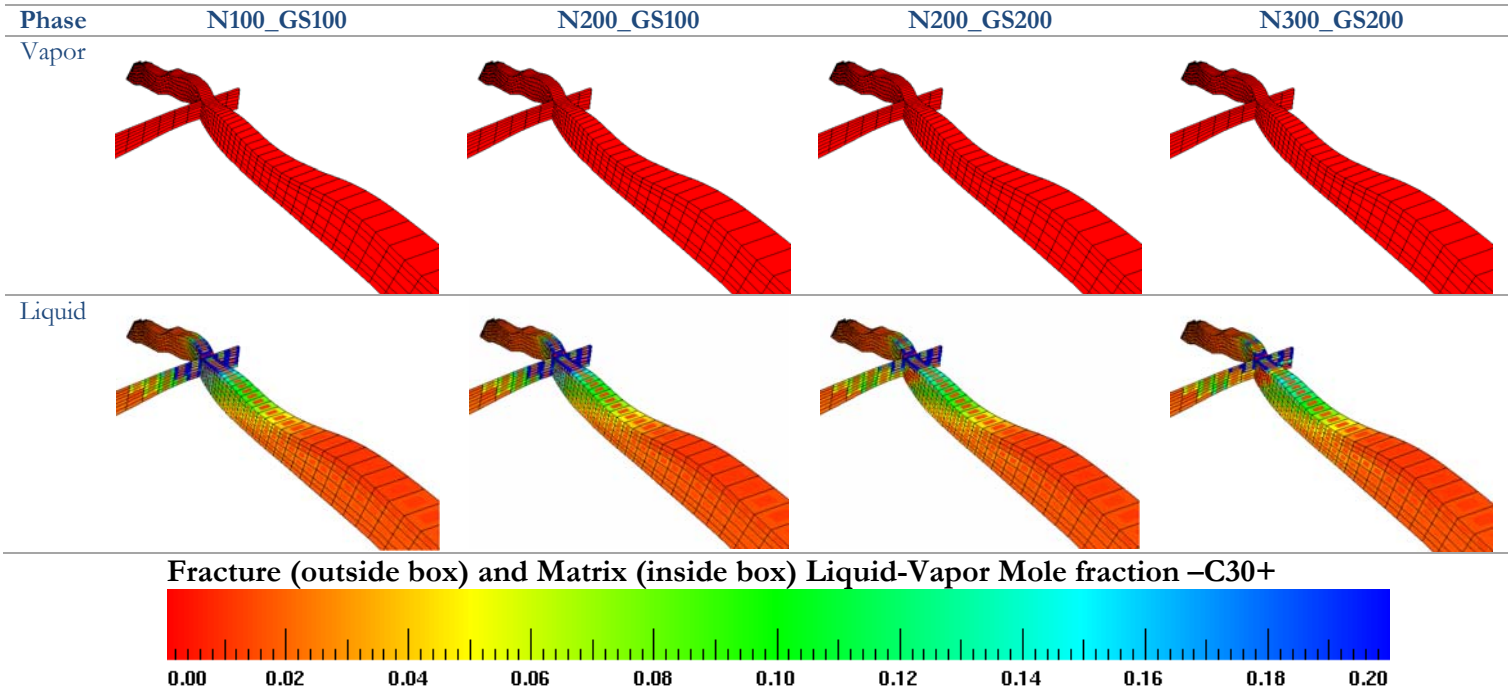

Figure E.12. Dele Matrix Liquid-Vapor Mole Fraction –C30+– 10 years after N_2 injection sensitivities are performed.

APPENDIX F. Dual Porosity/Dual Permeability (DPDP) Model - Additional 3D Graphs

The following figures show the analysis for the case of 200 MMscfd of N_2 injection and 200 MMscfd of gas sales (reference case), and are complimentary graphs for Section 3.6.3 for the sensitivity analysis presented when building a DPDP model using general rules.

- **Oil Saturation**

For all sheets, there is an increase in oil saturation at the bottom of the structures when nitrogen is injected. This happens because of a higher liquid drop out generated by nitrogen compared to hydrocarbon gas.

Figure F.1 shows that the matrix does not have a clear change in saturation with and without nitrogen injection.

Figure F.1 displays that the fracture system has higher oil saturation in the displacement front when nitrogen is being injected, compared to the case of no nitrogen injection. This is a result of a higher liquid dropout generated by nitrogen (see Figure 3-1). When comparing the sizes of the highlighted areas with the dashed and solid lines, there is an increase on oil saturation with depth due to gravity segregation through fractures.

When reviewing the liquid drop out (LDO) presented in Figure 3-1, where Dele sheet has a higher LDO compared to Guamalera and Pauto Main sheets, this behavior is reflected in the oil saturation behavior of the matrix and fracture systems in Figures F.1, F.2 and F.3. Oil saturation is even higher in some places in Dele sheet (see the blue regions in Figure F.1) than the LDO due to the accumulation term presented in Equation 2.1.

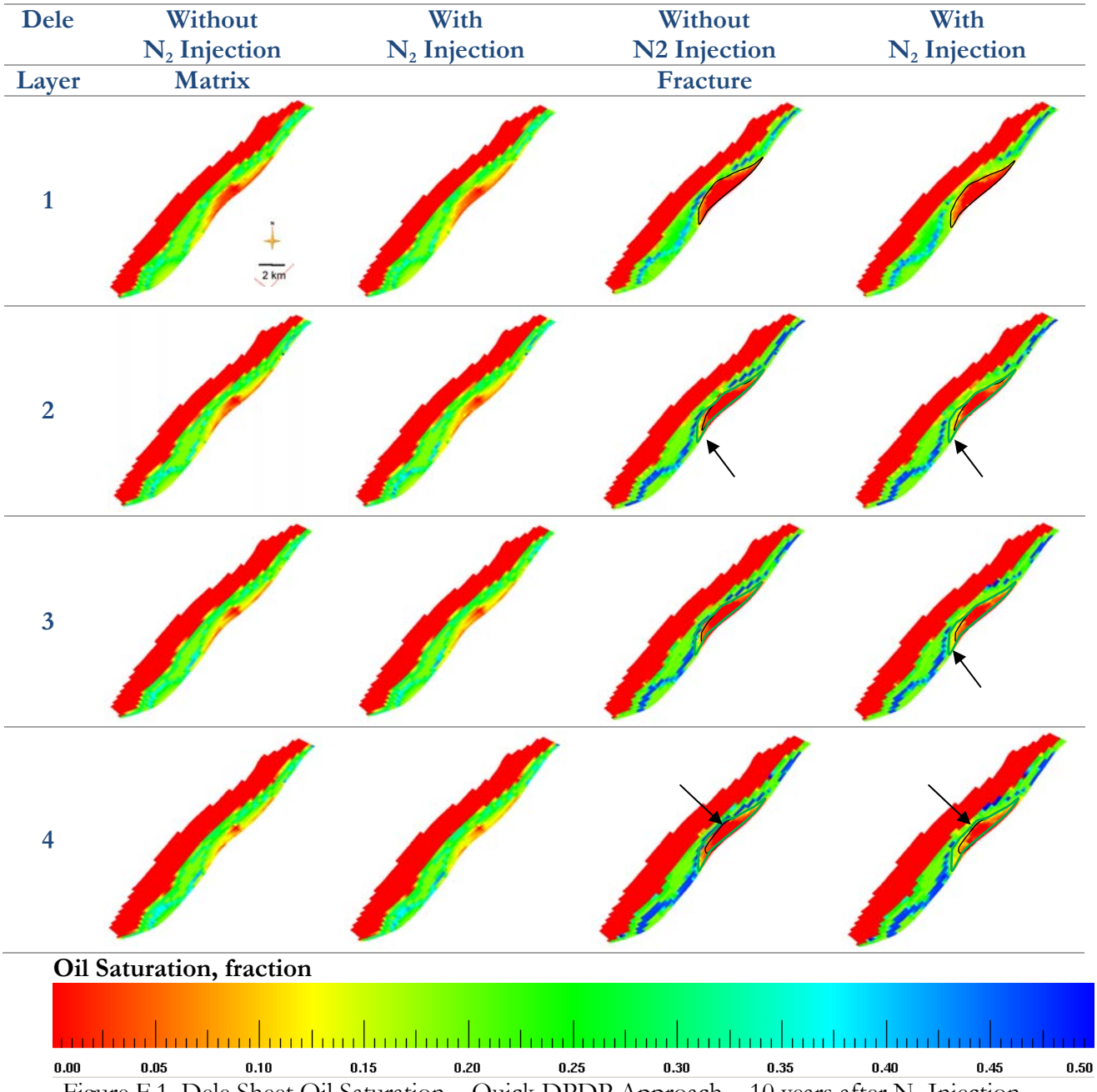

Figure F.1. Dele Sheet Oil Saturation – Quick DPDP Approach – 10 years after N_2 Injection.

Refer to Figure 1-1 for field dimensions.

Figure F.2 shows that the matrix oil saturation is the same for the cases with and without N_2 injection after 10 years.

For the fracture system, there is an evident increase in the oil saturation with N_2 injection (see the pinpointed area with an arrow).

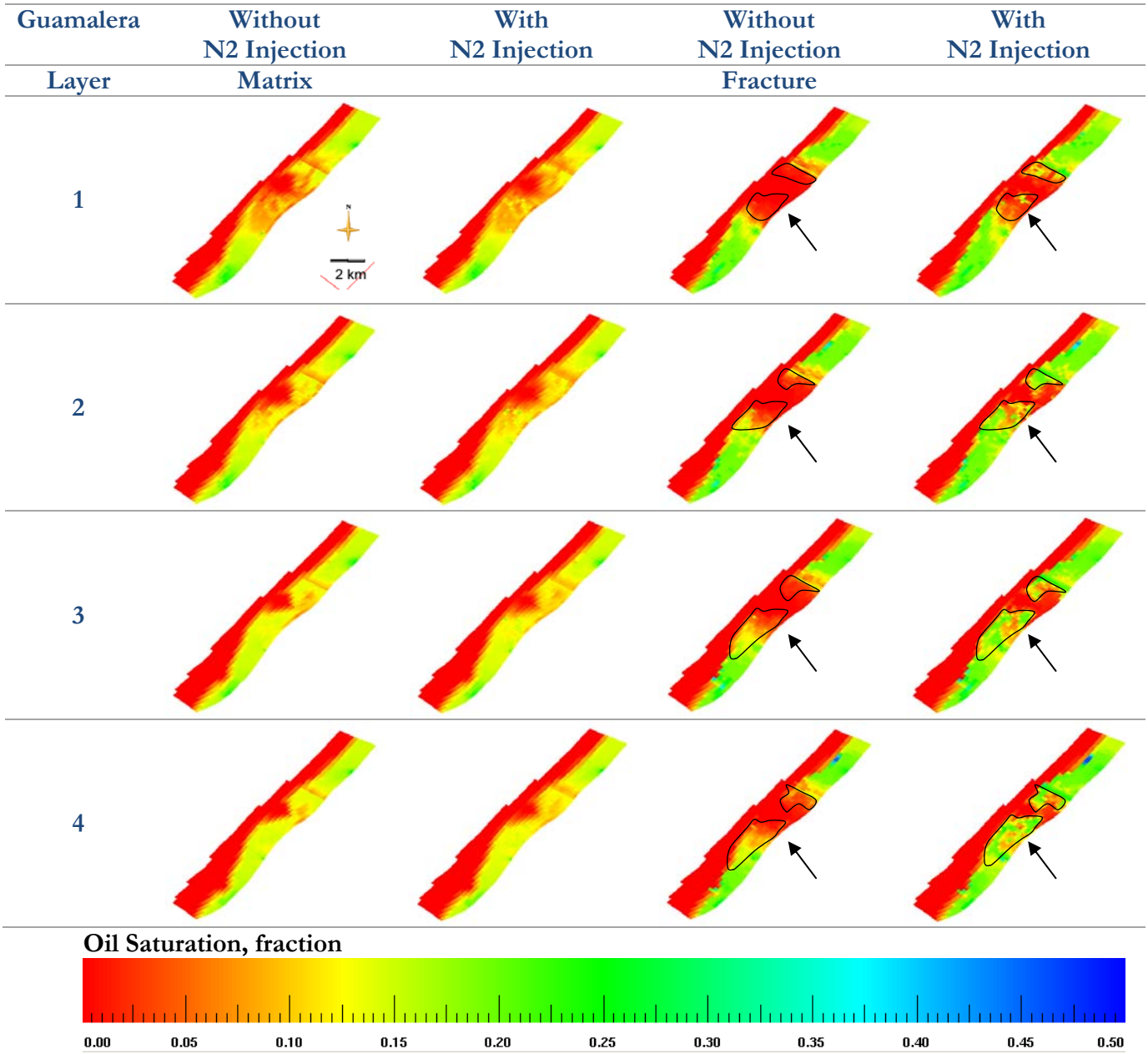

Figure F.2. Guamalera Sheet Oil Saturation – Quick DPDP Approach – 10 years after N_2 Injection.

Figure F.3 displays the oil saturation 10 years after N_2 injection in Pauto Main sheet. The highlighted lines in the plots show an area where there is a difference in oil saturation when injecting N2 and Lean gas.

It can be appreciated that there is a much more homogeneous displacement in this sheet compared to Dele and Guamalera sheets, and the difference between N_2 and Lean gas injection is not that high.

The main reason for this quite homogeneous displacement is due to the fact that this sheet has the smallest excess permeability; in other words, the lower the critical stressed fracture intensity is, the higher is the displacement efficiency.

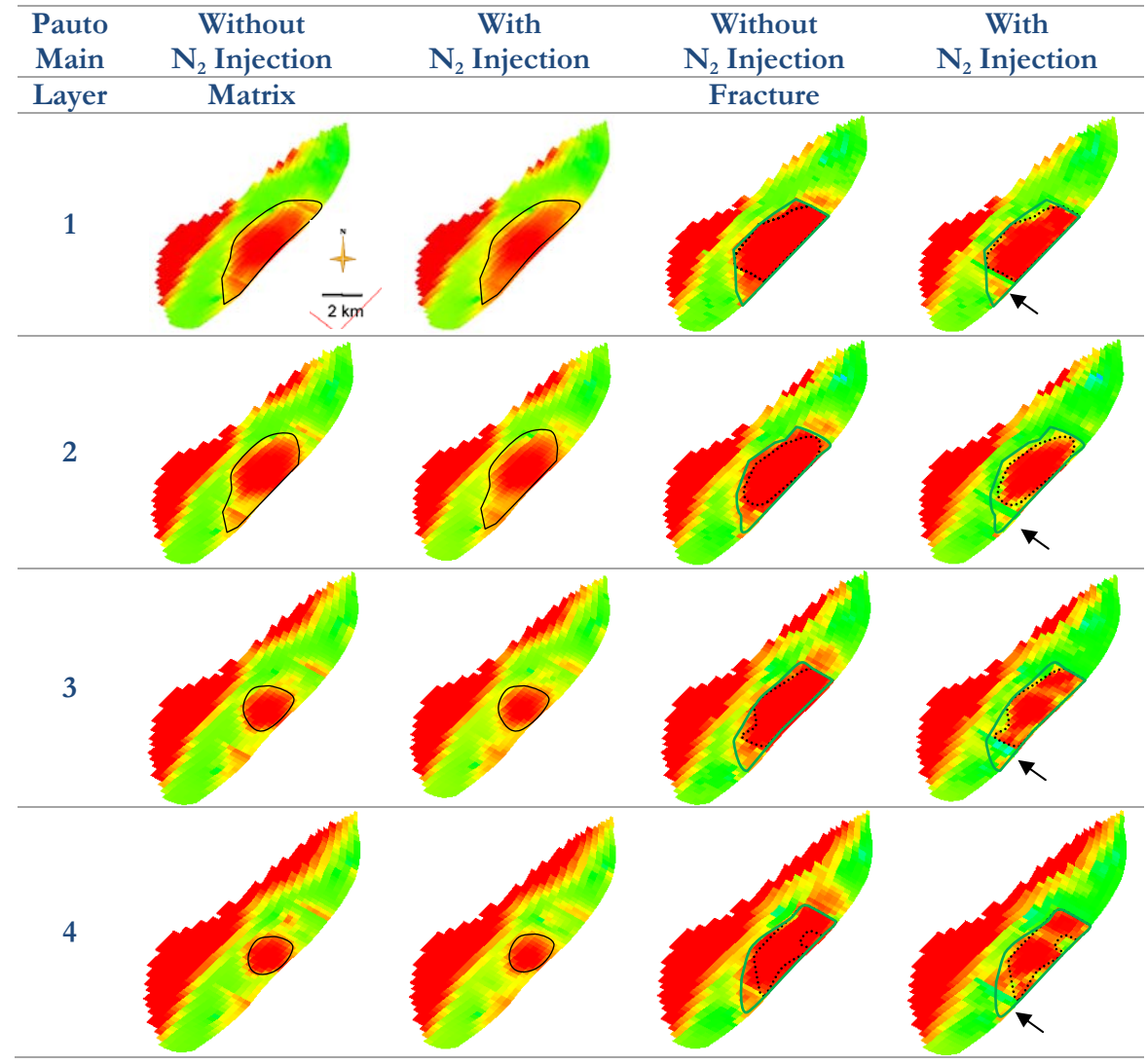

Figure F.3. Pauto Main Sheet Oil Saturation – Quick DPDP Approach – 10 years after N_2 Injection.

- **Oil Density**

Figure F.4 shows the oil density for Dele Sheet in the matrix and fracture systems, with and without N_2 injection. The nitrogen injection produces a higher density increase in the oil that remains around the injector; this is due to intermediate components that are re-vaporized, and a lack of hydrocarbon exchange that happens when lean gas is injected.

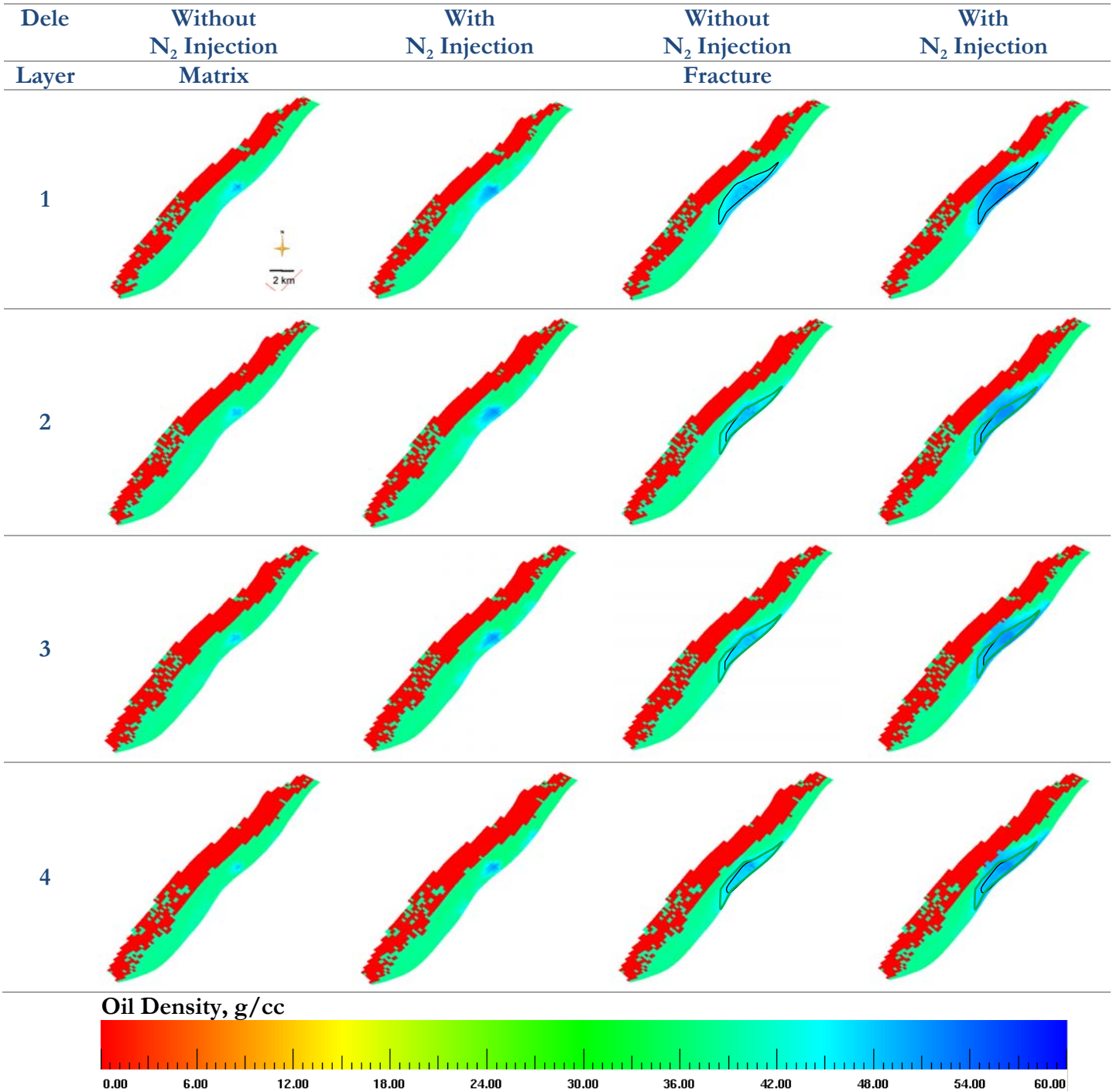

Figure F.4. Dele Sheet Oil Density – Quick DPDP Approach – 10 years after N_2 Injection.

Figure F.5 shows the oil density areal distribution in Guamalera Sheet, where a difference is observed when comparing Dele and Pauto Main behaviors. While Dele has a crestal gas injection and N_2 tends to flow upwards the structure due to a higher χ that results in a higher kfv, Guamalera N_2 injection is located in the flank very close to the WOC.

This difference results in that the displacement is less homogeneous, presenting higher oil properties distribution along this sheet. The highlighted areas come from the oil saturation differences observed in Figure F.2. Region A is the one with the highest oil saturation changes, but still with densities that are not affected by nitrogen injection. These places could be used for future developments.

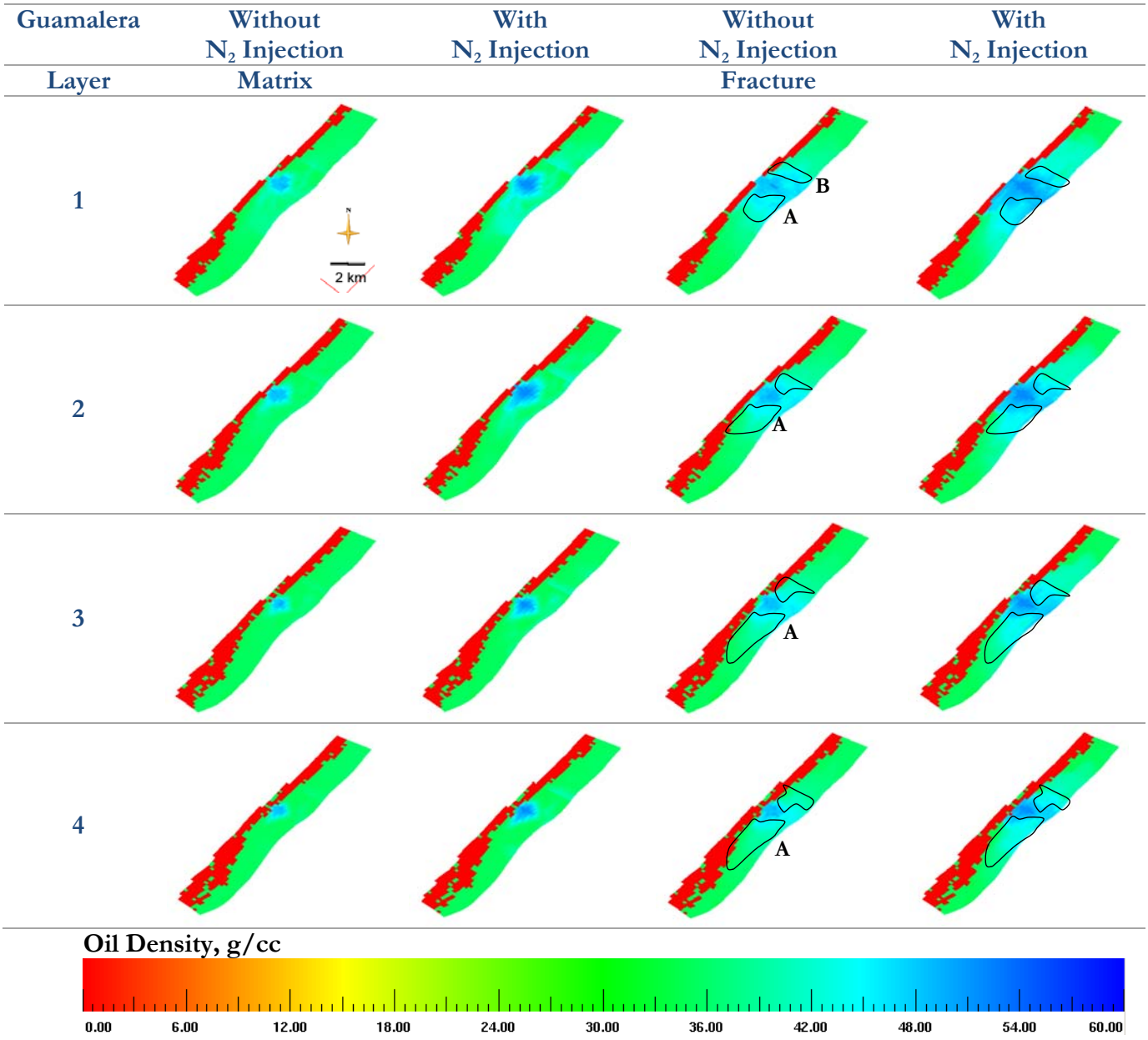

Figure F.5. Guamalera Sheet Oil Density – Quick DPDP Approach – 10 years after N_2 Injection.

Figure F.6 shows the oil density for Pauto Main sheet in the matrix and the fracture with and without N_2 injection, with a highlighted line, where a difference in the oil saturation (see Figure F.3) with and without N_2 injection can be appreciated.

High oil density changes are appreciated around the injection points, where oil saturation is low. There is a slight increase in oil density from 36 gr/cc to ~44 gr/cc in the displacement front.

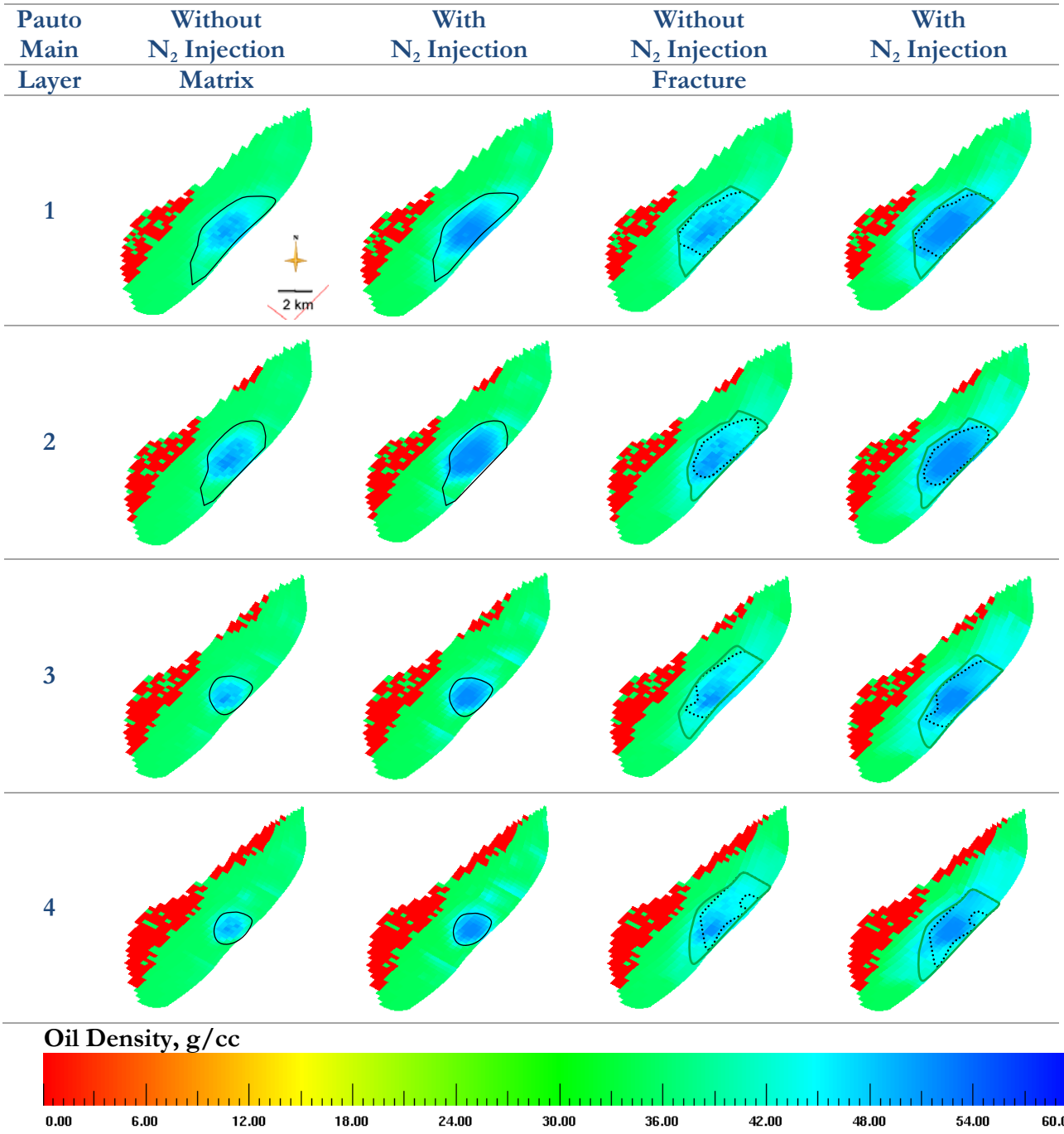

Figure F.6. Pauto Main Sheet Oil Density – Quick DPDP Approach – 10 years after N_2 Injection.

- **Oil Viscosity**

The Figures show the coarsened layers organized from top (layer) to bottom (layer 4) so as to relate the change in areal properties with depth.

Notice in Figures F.7, F.8 and F.9 how viscosity increases in some places to values of up to 2.5 cp (light green areas), which is higher than water viscosity. Even if oil viscosity changes are related to the vaporization of intermediate components due to gas injection, see Figure 1-50 as a reference to observe the change of oil viscosity with pressure.

In Figure F.7, the N_2 injection case shows a slightly higher viscosity increase around the injection point in the fracture system (see point B) compared to the case without N_2 injection (see point A). This happens as a higher gas injection volume is reached when injecting N_2 as a makeup gas, allowing the viscosity to increase due to the vaporization of intermediate components.

In Figure F.7, there is not a significant change in matrix oil viscosity with and without N_2 injection (see point D and point C, respectively).

To compare the matrix oil viscosity with depth, the first layer of Dele (Figure F.7 point D), Guamalera (Figure F.8 point E) and Pauto Main Sheet (Figure F.9 point F) were taken, which show that the area where the oil matrix viscosity increases is where the system has less excess permeability.

The analysis indicates that when there is higher fracture intensity, the injected gas, either if it is lean gas or nitrogen, tends to bypass more oil located in the matrix than when the excess permeability is lower.

Figure F.9 points F and G show that a more homogeneous displacement in the matrix and fractures is achieved when the excess permeability is low (see Figure 2-28).

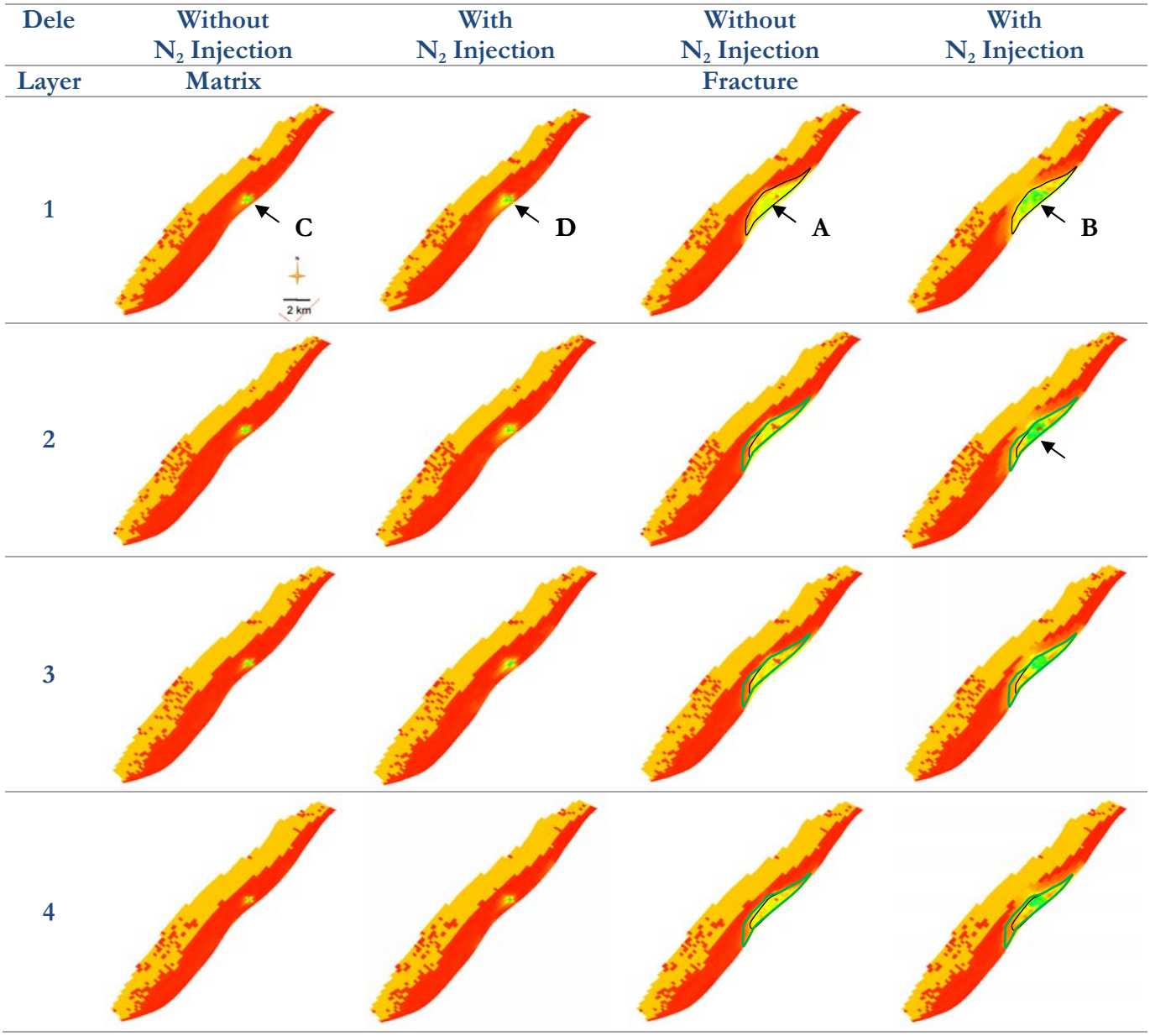

Figure F.7. Dele Sheet Oil Density – Quick DPDP Approach – 10 years after N2 Injection.

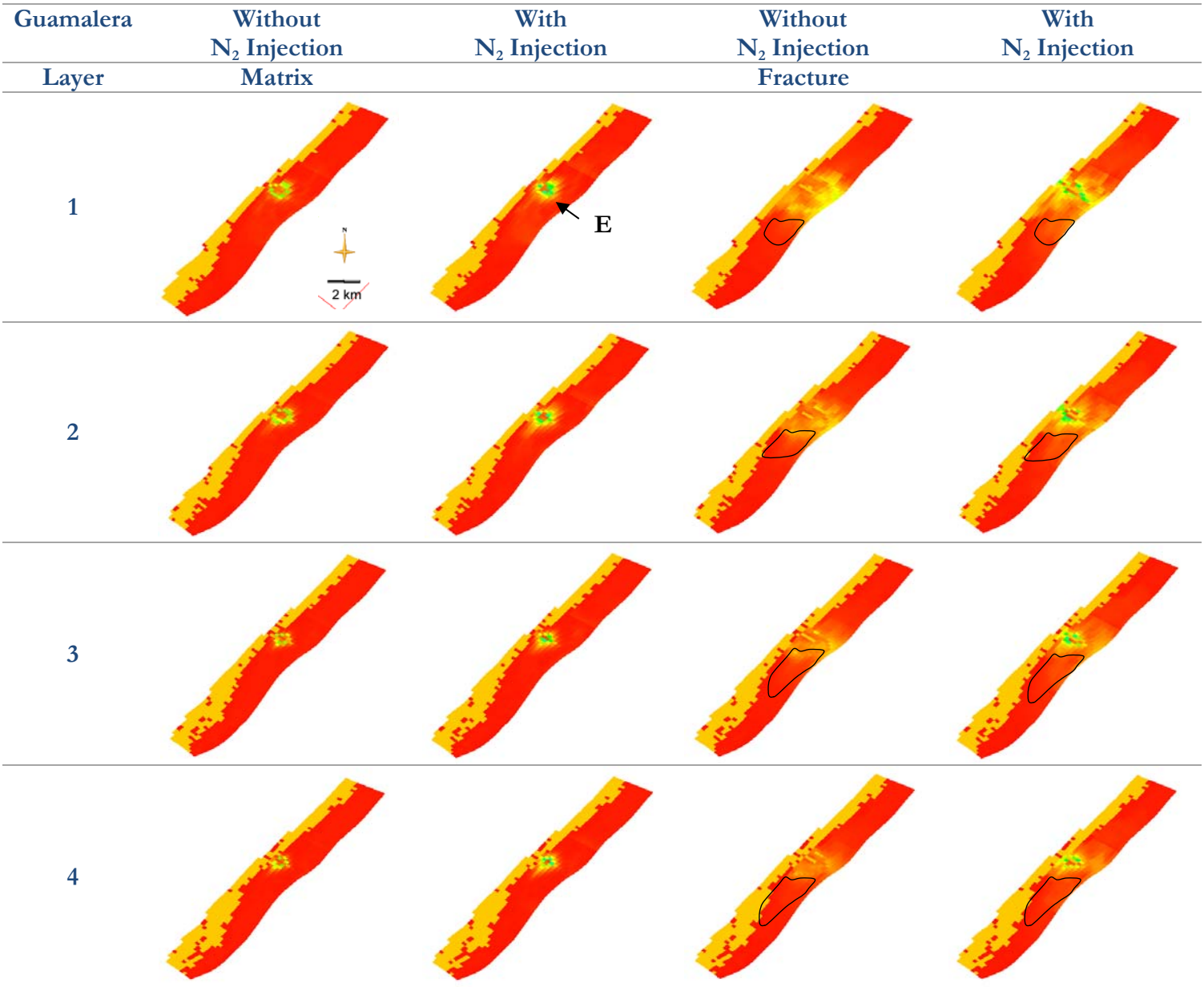

Figure F.8. Guamalera Sheet Oil Density – Quick DPDP Approach – 10 years after N_2 Injection.

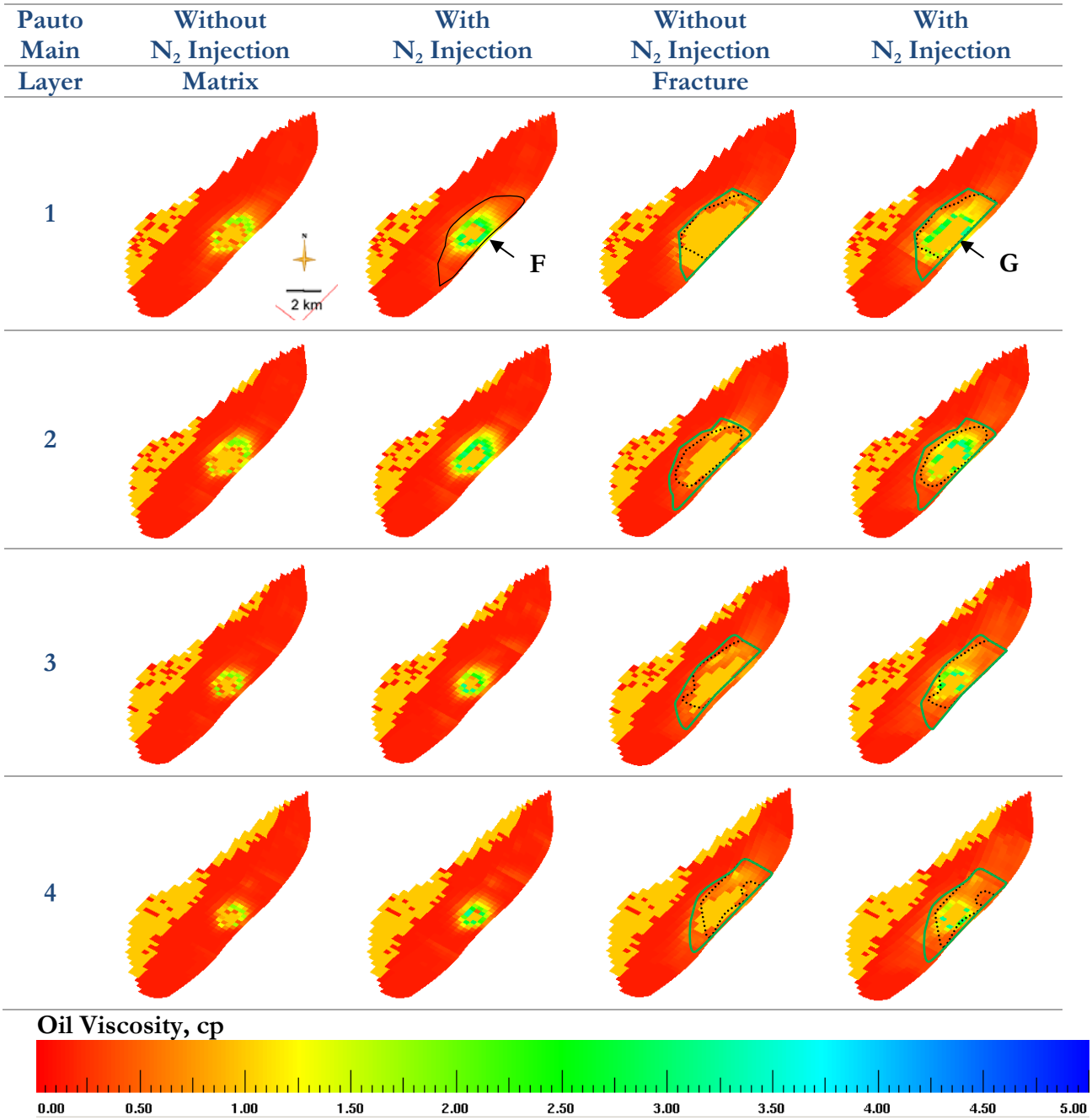

Figure F.9. Pauto Main Sheet Oil Density – Quick DPDP Approach – 10 years after N_2 Injection.

APPENDIX G: Grid and Field Pseudo-Components Analysis

Figure G.1 shows the comparison between the pseudo-components evolution with time at field level with and without N_2 injection (black and blue lines, respectively).

The dashed line is related to the gas phase and the solid lines are related to the liquid phase.

Plot 1, Plot 8, Plot 9 and Plot 12 show how N_2 produces an increase in mole % of CO_2, C1, C7-C10, C11-C14, C30+ in the liquid fraction. See the green bars in Figure G.2, where the tornado graph shows the impact that is generated.

All Plots show that when N_2 is injected, there is a drastic reduction in % mole of all hydrocarbon components located in the gas phase. This is the reason for the oil production loss compared to the base case for the operational surface conditions modeled. See the red bars in Figure G.2, where the tornado graph shows the impact that is generated.

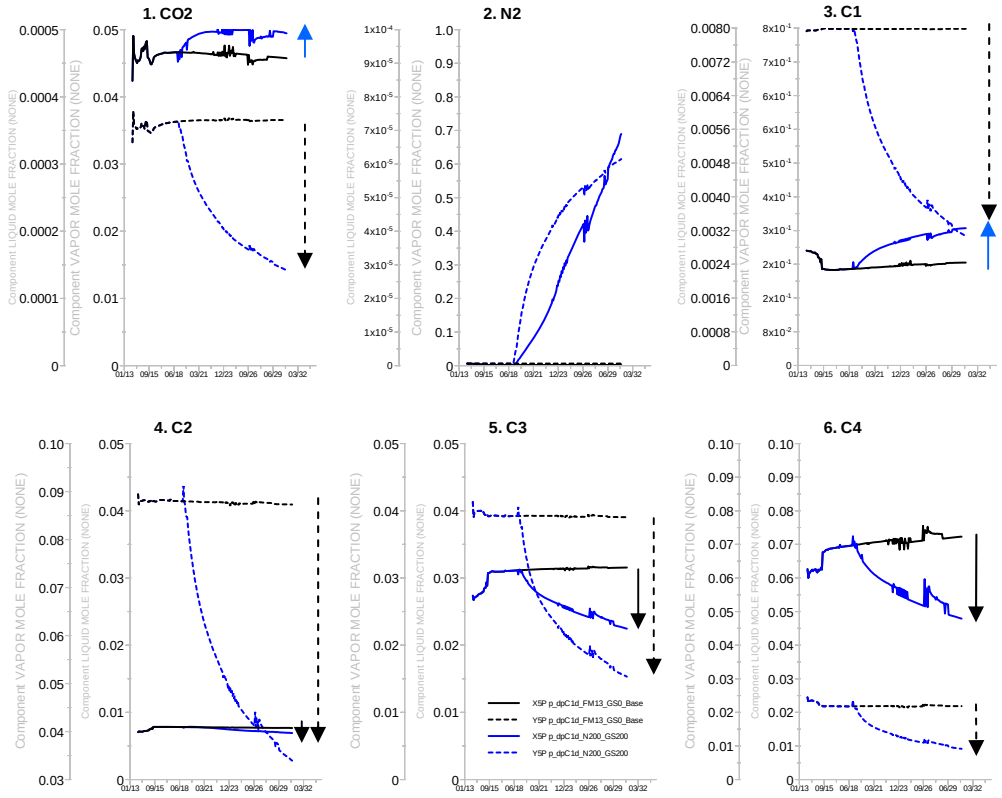

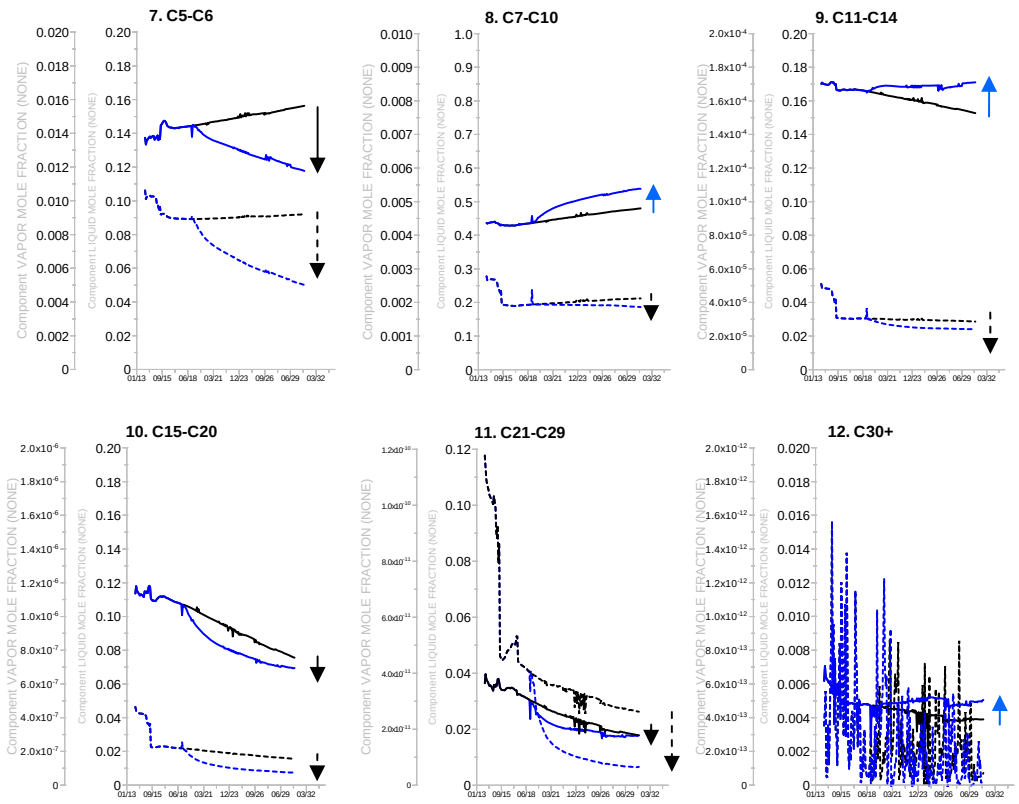

Figure G.1. Field Pseudo-components evolution with time
Base Case vs. Reference Case.

Figure G.2 shows the molar concentration 10 years after the N_2 injection. The data comes from Figure G.1. There is an evident impact on the intermediate components that are lost from the gas phase comparing the base case (FM13, no N_2 injection) with the reference case (N200_GS200). Even if N_2 has some capacity to vaporize intermediate components, it has not the same efficiency compared to lean gas injection.

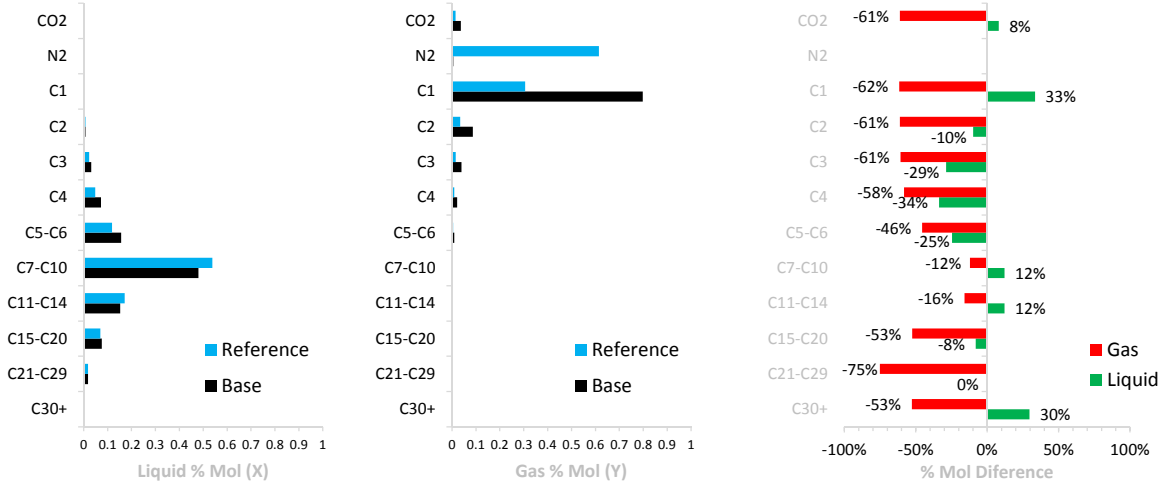

Figure G.2. Field Pseudo-components impact 10 year after N_2 Injection
Base Case vs. Reference Case.

Figure G.3 and Figure G.4 display a loss of intermediate and heavy components in the matrix and fracture system (see the dotted blue line) from the vapor phase in Dele Grid after 10 years when there is N_2 injection. This happens at higher reservoir pressures (~4000 psia) compared to the base case at 3000 psia (no N2 injection, black dots).

Figure G.3 and Figure G.4 also show that C3 and C4 pseudo-components behave differently to other pseudo components that are lost from the gas phase with N2 at 4000 psia, while the lean gas injection (base case - black dots) do not have that loss, and remain in a higher proportion in the gas phase.

As a summary, C3 and C4 pseudo-components located in the matrix have the highest impact with N_2 injection. Also with the N2 injection, the pseudo-components from C5 to C8 begin to be lost from the gas phase at 4000 psia compared to 3000 psia.

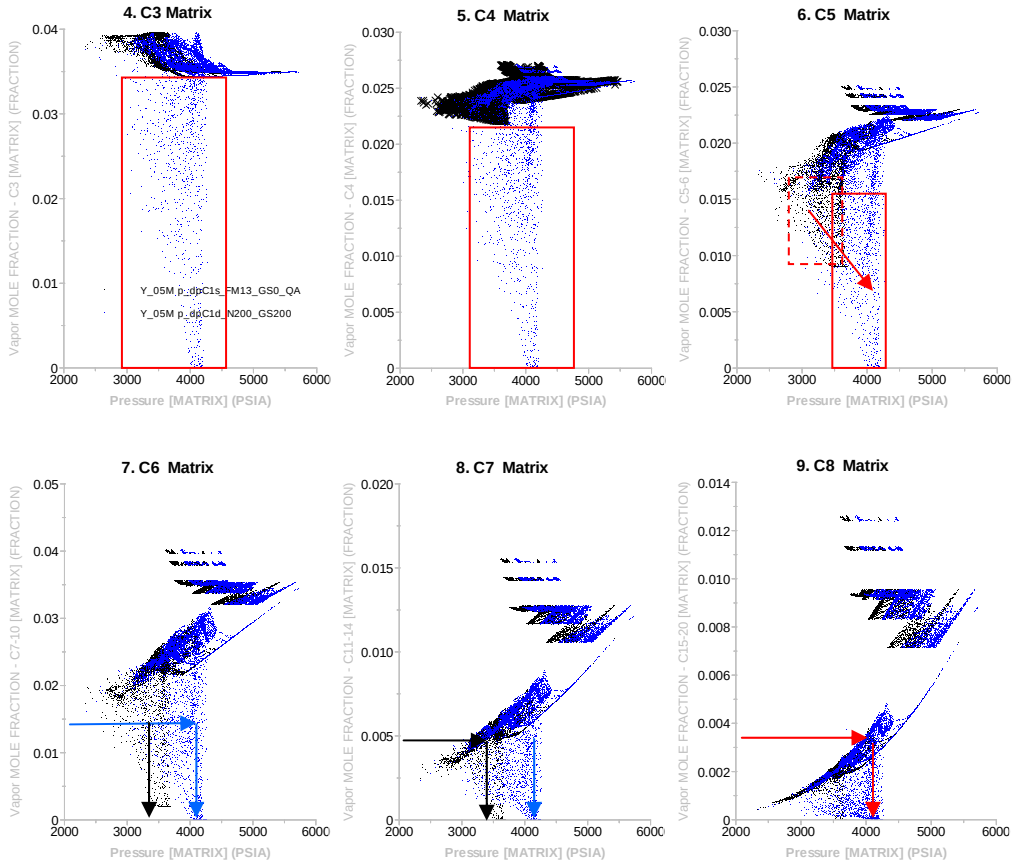

Figure G.3. Dele Matrix Grid Cells Vapor Pseudo-components evolution with pressure Base Case vs. Reference Case.

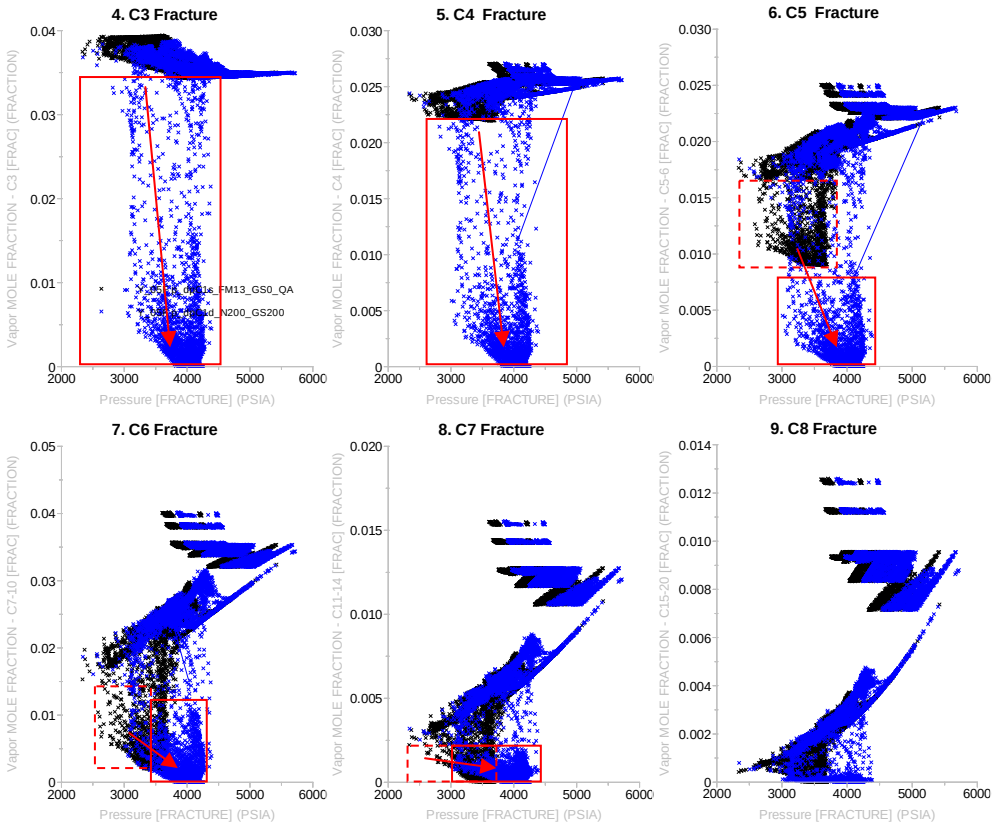

Figure G.4. Dele Fracture Grid Cells Pseudo-components evolution with pressure Base Case vs. Reference Case.

Figure G.5 shows the increase in oil viscosity and oil density with N_2 concentration increase that happens in Dele Grid after 10 years of N_2 injection.

Figure G.5 is a complimentary graph to Figure E.4 and Figure E.7, where there is a higher increase in oil density and viscosity near the injector.

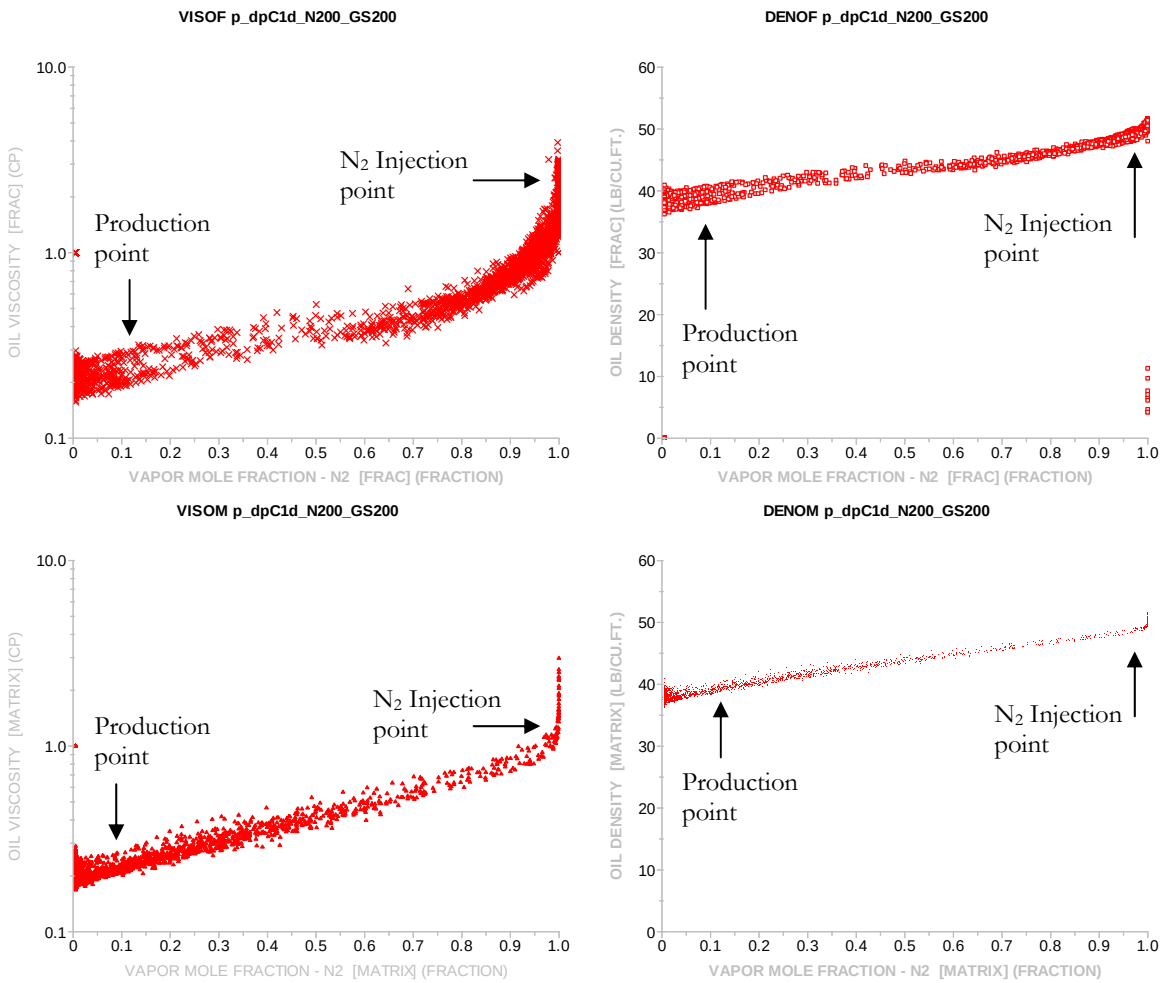

Figure G.5. Dele Grid – Matrix and Fracture - Density and Viscosity vs. Nitrogen Concentration for the reference case.